Higher Degree Examinations

THE ACADEMIC REGISTRAR,
Room 261,
UNIVERSITY OF LONDON,
SENATE HOUSE,
MALET STREET,
LONDON, WC1E 7HU

WRITE ON THIS SIDE ONLY

UNIVERSITY OF LONDON
SENATE HOUSE WC1E 7HU

With the Compliments of the
ACADEMIC REGISTRAR

I understand from Dr. Thompson that you have kindly agreed to examine this candidate, for which we are most grateful.

C.A. Gregory

C.A. Gregory
Academic Division.

University of London

Telegrams UNIVERSITY LONDON
Telephone 01-636 8000

SENATE HOUSE
MALET STREET
LONDON
WC1E 7HU

Extension 3018, 3019

Our ref AR/HDE/INT/APP
Your ref

15 June 1983

Dear Examiner,

I am writing to inform you that, subject to your consent to act, you have been appointed as an Examiner for the candidate named below who has submitted a thesis for the degree stated.

Examiners are required to examine the candidate orally unless, after they have read the thesis and without further test, they determine that the candidate has not satisfied them. The Internal Examiner has been asked whether he can make the necessary arrangements for the oral examination with the co-examiner(s) and the candidate. If this is not possible, I will summon the candidate to attend for the oral examination when the Internal Examiner has suggested a suitable time and place.

The Examiners are asked to write their joint report on the candidate's entry form which is sent to the Internal Examiner and which must be signed by each Examiner. Please return the enclosed thesis with the Examiners' report.

I enclose a copy of the Instructions to Examiners and of the Scheme of Payment.

Yours faithfully,

P. Taylor.

Academic Registrar

Co-Examiner(s): Dr. R.N. Thompson,
Dept. of Geology,
Imperial College.

Candidate's name: John Anthony Wolff.

Examination: PhD or MPhil Ph.D.

Professor R.A. Howie,
Dept. of Geology,
King's College.

UNIVERSITY OF LONDON

PAYMENTS TO EXAMINERS

7.—PH.D. AND HIGHER DOCTORATE EXAMINATIONS IN 1983

(For M.D. and D.Vet.Med. See Document 3)

(1) Ph.D. Examinations

To each of two examiners who act in the first instance and to a third if called upon by the Principal £50

If an examiner is the candidate's Supervisor or, under the Scheme for Research Institutions, the candidate's External or University Supervisor .. £20

If three examiners are appointed to act in the first instance, the following fees will be payable:

Internal Examinations under the Scheme for Research Institutions.—A fee of £15 to the External Supervisor or University Supervisor, a fee of £30 to a teacher of the University (other than the University Supervisor) and a fee of £50 to not more than one examiner external to the University (other than the External Supervisor).

Other Internal Examinations.—A fee of £15 to the Supervisor and/or a teacher from the candidate's School; a fee of £30 to a teacher of the University from any other School or Institute, and a fee of £50 to not more than one examiner external to the University.

External Examinations.—A fee of £50 to each examiner, provided that the appointment of the three examiners has been specifically approved by the External Council after consideration of a special report of the appropriate Board of Studies.

For re-examination of a candidate submitting the same thesis or a thesis in a revised form, the fees payable are half the fees prescribed above for the first examination.

For re-examination of an aggrieved candidate under SM 4858 of July 1972, the original examiners who act each receive half the fee prescribed above for the first examination, full fees being payable to each other examiner who acts.

(2) D.D., D.Lit., LL.D., D.Mus., D.Sc., D.Sc.(Eng.), D.Sc.(Econ.)

To each Examiner who acts, inclusive fee, per candidate £75

For re-examination of an aggrieved candidate under SM 4858 of July 1972, the original examiners who act each receive half the fee prescribed for the first examination, full fees being payable to each other examiner who acts, together with a fee of £10 to each examiner taking part in an oral examination.

Travelling Expenses

(i) For each occasion on which *an examiner who is external to the University* is required to attend a practical examination, oral examination, or examiners' meeting, he may claim the return railway fare and the cost of travel by underground and/or public road transport (bus or coach) for all necessary journeys actually performed together with the following subsistence allowances:—

For a necessary absence from home not involving a night:—

For a period of 5-10 consecutive hours £4

For a period of more than 10 consecutive hours £8

For each necessary period of absence up to 24 hours involving a night away from home, £36

(ii) For each occasion on which *an examiner who is a teacher of the University* is required to attend a practical examination, oral examination or examiners' meeting he may claim from the University the return railway fare and the cost of travel by underground and/or public road transport (bus or coach) *from the School or Institute at which he is a teacher* for all necessary journeys actually performed.

Any claim for travelling expenses under these provisions shall be included with the examiners' report.

(iii) For each occasion on which *an examiner who is a teacher of the University* is required to attend a practical examination, oral examination or examiners' meeting for an examination conducted solely for External Students and/or Internal Students at Institutions having Recognised Teachers, the travelling expenses set out in (ii) will be met together with the following subsistence allowances:

For a necessary absence from the teacher's School or Institute:—

For a period of 5-10 consecutive hours £4

For a period of more than 10 consecutive hours £8

(iv) In the event of travel from a vacation address the travelling expenses shall be agreed by the Administrative Secretary before they are incurred.

P. TAYLOR
Clerk of the Senate

November 1982

Printed by Edson Printers Ltd., Watford, Herts.
C2740/4,800/11.82/27699 S

J-A. NOLFF 1:C - PWJ

Title..... Examination

Examiner .....
(Name and Title, block letters)

Subject .....

Department .....

Month and year of examination.....19.....

School/Institute .....

UNIVERSITY OF LONDON

Travelling Expenses to Teachers

For each occasion on which an examiner who is a teacher of the University is required to attend a practical examination, oral examination, or examiners' meeting he may claim from the University the return railway fare and the cost of travel by underground and/or public road transport (bus or coach) *from the School or Institute at which he is a teacher* to the place of the examination or examiners' meeting.

For each such occasion on which the examination in question is conducted *solely for External Students and/or Internal Students at Institutions having Recognised Teachers,* the following subsistence allowances will be payable in addition to the travelling expenses specified above:

For a necessary absence from the teacher's School or Institute*:

(*a*) For a period of 5-10 consecutive hours—£4.00

(*b*) For a period of more than 10 consecutive hours—£8.00

Cost of return travel by train, underground and/or public road transport from your School/Institute	Amount claimed £	
To..... on.....		
To..... on.....		
To..... on.....		
To..... on.....		
To..... on.....		
To..... on.....		
To..... on.....		
Subsistence allowances (Examinations for External Students Only)		
(*a*) .....days at £4.00 (five to ten hours):		
Dates		
(*b*) .....days at £8.00 (more than ten hours):		
Dates		
Postage and telephone expenses.....		
Total payable		

Signature of Examiner ..... Date .....

Certified ..... Accounting Division

This form should be completed and returned promptly to the Senior Payments Officer (fees), University of London, Senate House, Malet Street, London, WC1E 7HU, for payment together with the examination fee where applicable. Examiners are asked to submit only one claim form for all expenses in respect of one examination.

The University will not normally meet small claims which are received after the fees for the examination have been paid.

* In the event that these rates are increased after this form is issued the new rates will be applied automatically.

For office use only

	Form Type			Cost Centre Code Expenses		Examination Number			Form No.		Examiner Number		T. T.			Expenses	
☐	E	F	★	★	P A 3 O D N	★		★	★		☐		★		★	★	.	☐
														TOTAL		★	★	.	☐

Printed by Edson Printers Ltd., Watford, Herts.
B8751/5,000/1.81/26247 S.

UNIVERSITY OF LONDON

GENERAL INSTRUCTIONS FOR APPOINTMENT OF EXAMINERS AND FOR CONDUCT OF EXAMINATIONS FOR PH.D. FOR INTERNAL STUDENTS

1. Appointment of Examiners

1.1 **General**

1.1.1. At least one of the examiners for each candidate shall, whenever practicable, have had experience in examining for the Ph.D. Degree of the University.

1.1.2 If the examiners appointed do not include the Supervisor (or either of two Joint Supervisors) under whom the research has been carried out, then:

(a) The Supervisor (or one of two Joint Supervisors) shall be invited to attend the oral examination of his Ph.D. candidate as an observer without the right to question the candidate or participate in any way (see also 3.5. below)

(b) The examiners may, at their discretion, consult the Supervisor before completing their Report, particularly if they have doubts relating to the appropriate recommendation to make.

(c) The Supervisor or Joint Supervisor(s) shall be entitled to receive a copy of the examiners' Report on request for his own information only. Any Report so given is issued in the strictest confidence to the Supervisor or Joint Supervisor(s) concerned and may not be passed to any third party.

1.1.3. Examiners are advised that all matters relating to the examination must be treated as confidential. Examiners are not permitted to divulge the content of previously unpublished material contained in a candidate's thesis until such time as any restrictions on access to the thesis, which may have been granted by the Academic Council, have been removed.

1.2 **For Candidates working at a School of the University or at an Institution having Recognised Teachers**

1.2.1 For each candidate Boards of Studies shall normally appoint two persons to act as Examiners, but the Board of Studies may if they consider it desirable, appoint three persons to act as examiners jointly. At least one of the examiners shall be a visiting examiner (i.e. external to the University or from a School where the candidate was not registered). If two of the examiners appointed are external to the University, a special request for the additional fees payable has to be made to the Finance of University Examinations Sub-Committee. The Academic Council will therefore require from Boards of Studies submitting any such proposal a statement of the reasons for it.

1.2.2 If three examiners are appointed to act in the first instance of whom two are the candidate's teachers, these two shall be considered as one examiner for the purpose of decision.

1.2.3 When two examiners are appointed in the first instance Boards of Studies shall also appoint, either at the same time or when required, an additional examiner to act only if called upon by the Principal at the request of the examiners. The original examiners shall so request before they report formally that they are unable to arrive at an agreement and may do so at any time, if they consider it desirable. Wherever possible the additional examiner shall be of professorial status and shall have considerable experience of examining for the Ph.D. Degree of this University. This provision shall also apply when two of three examiners appointed in the first instance are the candidate's teachers and count as one for the purpose of decision under paragraph 1.2.2.

1.3 **For Candidates registered under the Scheme for Public Research Institutions and Industrial Research Laboratories**

1.3.1. For each candidate Boards of Studies shall normally appoint three persons to act as examiners jointly who must include:

(i) An expert in the field of the candidate's research who is not the External Supervisor nor a member of the academic staff of the School at which the candidate is registered.

(ii) An Appointed Teacher in the general field of study who is not a member of the academic staff of the School at which the candidate is registered.

(iii) A third examiner who may, if the Board so wishes, be either the University or the External Supervisor.

If two of the examiners (other than the External Supervisor) are external to the University, a special request for the additional fees payable has to be made to the Finance of University Examinations Sub-Committee. The Academic Council will therefore require from Boards of Studies submitting any such proposal a statement of the reasons for it.

Only in exceptional circumstances with the permission of the Academic Council may both the University and External Supervisors be appointed as Examiners.

1.3.2. The University Supervisor and/or the External Supervisor if not appointed as Examiner(s) shall be invited to attend the oral as observer(s) in accordance with the conditions set out in paragraph 1.1.2.

2. Thesis

2.1 The thesis must form a distinct contribution to the knowledge of the subject and afford evidence of originality, shown either by the discovery of new facts and/or by the exercise of independent critical power. A full bibliography and references will be required.

2.2 The thesis must be written in English and the literary presentation must be satisfactory. The standard of the Ph D thesis shall be such that, if not already published in an approved form, it must be suitable for publication, either as submitted or in an abridged form or modified form.

2.3 The candidate must indicate how far the thesis embodies the result of his own research or observation, and in what respects his investigations appear to him to advance the study of his subject.

2.4 A candidate may submit the results of work done in conjunction with his supervisor and/or with fellow research workers provided that the candidate states clearly his own personal share in the investigation and that the statement is certified by the supervisor.

2.5 A candidate will not be permitted to submit as his thesis one which has been submitted for a degree or comparable award in this or any other university or institution, but a candidate shall not be precluded from incorporating in a thesis covering a wider field work which he has already submitted for a degree or comparable award in this or in any other university or institution, provided that he shall indicate on his entry form and also on his thesis any work which has been so incorporated.

2.6 Copies of all successful theses, whether published or not, will be deposited for reference in the University Library.

3. Conduct of Examination

3.1 Each report of the Examiners shall state (a) the subject of the thesis submitted by the candidate; (b) a list of his other original contributions (if any) to the advancement of his subject; (c) a concise statement of the grounds upon which the Examiners base their recommendation.

3.2 After the Examiners have read the thesis, they may, if they think fit, and without further test, determine that the candidate has not satisfied them in the examination. Such a candidate will not be permitted to re-enter for the examination but he may apply to register *de novo* for a further period of study leading to the submission of a thesis on a different topic.

3.3 Except as provided in paragraphs 3.2 and 3.10 the Examiners after reading the thesis shall examine the candidate orally and at their discretion by written papers or practical examinations or by both methods on the subject of the thesis, and, if they see fit, on subjects relevant thereto. If an additional examiner is called upon to act (see paragraph 1.2.3 above) after an oral examination has been held, the examiners acting jointly and after considering all relevant circumstances shall determine whether to hold a further oral examination and whether that examination (if any) shall be conducted by the additional examiner alone or in concert with one or more of the original examiners.

3.4 In addition to the provision in para 3.3 above for the Examiners to examine any candidate orally on subjects relevant to his thesis a candidate registered under the Public Research Institution or Industrial Research Laboratories Schemes may be tested at his oral examination on the background he has acquired as a result of his prescribed course of study. At the time of entry to the examination the University Supervisor is required to submit a brief statement on the components of the course of study.

3.5 Oral examinations shall be held in private.

3.6 If the thesis is adequate and the candidate satisfies the Examiners in all other parts of the examination, the Examiners will report that the candidate has satisfied them.

3.7 The examiners may require the candidate to make specified minor amendments to the thesis. These must be made within a period of one month and the amended thesis will be submitted to the examiners or to one of their number nominated by them for confirmation that the amendments are satisfactory.

3.8 If the thesis is adequate but the candidate fails to satisfy the Examiners at the practical or written examination held in connection therewith, the Examiners may determine that the candidate be exempted on re-entry from presentation of the thesis and permitted to submit to a further practical or written examination within a period specified by them and not exceeding 18 months.

3.9 If the thesis is adequate but the candidate fails to satisfy the Examiners at the oral examination, the Examiners may determine that the candidate be permitted to re-present the same thesis and submit to a further oral examination within a period not exceeding 18 months specified by them.

3.10 If the thesis, though inadequate, shall seem of sufficient merit to justify such action, the Examiners may determine that the candidate be permitted to re-present his thesis in a revised form within 18 months. Examiners shall not, however, make such a decision without submitting the candidate to an oral examination. The Examiners may at their discretion exempt from a further oral examination on re-presentation of his thesis a candidate who under this section has been permitted to re-present his thesis in a revised form.

3.11 When a candidate for Ph.D. Degree in the field of Statistics has not a preliminary degree in Statistics the Examiners are recommended to test the candidate's general knowledge of statistical method and theory outside the special field covered by his thesis.

3.12 If, after completion of the examination including the oral examination or re-examination for the Ph.D., the examiners determine that a candidate has not reached the standard required for the award of the degree nor for the re-presentation of the thesis in a revised form for that degree, they may determine, if they think fit, that the candidate has reached the standard required for the award of the M.Phil subject to any minor amendments which may be required.

3.13 A candidate whom the examiners have adjudged to have reached the standard required for the award of the M.Phil. under paragraph 3.12 shall be subject to the following conditions and procedures:

3.13.1 The candidate will be informed that he has been unsuccessful at the examination for the Ph.D. but that he has reached the standard required for the award of the M.Phil.; and that he may be considered for the award of the M.Phil. if he indicates within two months that he wishes to be so considered.

3.13.2 A candidate who indicates that he wishes to be considered for the award of the M.Phil. Degree under this Regulation will not be required to submit the thesis as may be required under the Regulations for the M.Phil. Degree or to undergo an oral examination thereon, but will be required to fulfil the requirements for the M.Phil. Examination in all other respects including the passing, at the next following occasion on which they are held, of any written papers or other tests prescribed for the M.Phil. Degree in the relevant field.

3.13.3 If additional forms of examination are prescribed, the candidate will be informed that he must satisfy the examiners in such forms of examination, and that if he fails, re-entry will be governed by the Regulations for the M.Phil. so far as applicable.

3.13.4 A candidate who applies for the award of the M.Phil. degree under these regulations must make any minor amendments that may be required by the examiners within a period of one month.

3.13.5 A candidate who has reached the standard for the award of the M.Phil. who does not indicate that he wishes to be considered for the award of that degree within the period given in 3.13.1 above will be informed that he has failed to satisfy the examiners for the Ph.D., and that he may no longer be considered for the award of the M.Phil.

Printed by Edson Printers Ltd., Watford, Herts.
C0687/2/5000/11.81/33624 S

PETROLOGY OF QUATERNARY PYROCLASTIC DEPOSITS FROM TENERIFE, CANARY ISLANDS

Thesis submitted for the degree of Doctor of Philosophy

by

JOHN ANTHONY WOLFF

Geology Department
Imperial College
London SW7 2BP

June 1983

To Mum and Dad

ABSTRACT

A widespread Late Quaternary phonolitic pumice series on Tenerife provides a record of several tens of thousands of years of violently explosive volcanism centred on the Las Canadas caldera. The field characteristics of the constituent plinian pumice fall deposits, ignimbrites and mudflows are described and their formation mechanisms reviewed with particular regard to the extent to which the petrological features of individual units are representative of the precursory magma bodies.

Whole-pumice compositions are variable, both within the products of individual eruptions and through the series as a whole. Crystal fractionation, magma mixing and country-rock contamination are provisionally identified as processes governing pumice geochemistry. Particularly noteworthy is compatible behaviour of some rare earth elements, tentatively ascribed to the fractionation of minor quantities of sphene.

Petrographically heterogeneous deposits are common and have been studied in detail. Most contain a trachyandesitic magmatic component, identified on the basis of phenocryst mineralogy and glass compositions, intermixed with phonolitic material. Some additionally bear an alkali basaltic component. It is proposed that a zoned magma chamber, in which phonolitic magma stratified above an intermediate layer, was the source of the pumice series. This chamber was subject to occasional replenishment by more primitive basaltic magma. Mixing of chamber contents may have triggered eruptions in some cases.

Iron-titanium oxides equilibrated between 830°C and 940°C in the phonolitic and intermediate magmas. Equilibrium thermodynamics are applied to the phenocryst assemblages in several deposits to obtain values for the fugacities of the volatile species H_2O, H_2, S_2, H_2S, SO_2, SO_3 and O_2 before eruption.

Nepheline syenite xenoliths provide solidified representatives of phonolitic magma and the respective mineralogies of syenites and pumices are described and discussed. Syenites are generally similar to undersaturated alkaline bodies exposed elsewhere in the world.

Welding and related processes in alkaline pyroclastic deposits are discussed with reference to Tenerife, Gran Canaria

and Pantelleria. Laminar viscous flowage structures in Gran Canaria ignimbrites are largely the product of secondary flow or rheomorphism. Chemical composition of the hot deposit is identified as a major factor affecting the development of welding and rheomorphism. The role of agglutination, or primary impact welding, in the compaction of salic and basaltic air-fall tephra is examined theoretically, and a thermal facies model for pumice fall deposits is tentatively proposed.

ACKNOWLEDGEMENTS

Research for this thesis was funded by the Natural Environment Research Council of Great Britain, whom I thank for a studentship and for financing fieldwork in the Canary Islands. Work at Imperial College was supervised by Dr. G.D. Borley, and, latterly, by Dr. R.N. Thompson. I am grateful to Dr. Thompson, to whom fell the task of critically reading this thesis, for offering supervision following Dr. Borley's retirement.

I have been very fortunate to have had the benefit of Prof. G.P.L. Walker's guidance and inspiration in the field, especially as regards tuition in the methods of study of pyroclastic rocks. Prof. Walker and Dr. B. Booth very generously gave unlimited access to a vast amount of unpublished field data on the Tenerife pumices, without which the value of many of the results reported in this thesis would have been severely diminished.

Use of analytical facilities has relied on the help and goodwill of many people. I especially wish to thank Dennis Bailey for polishing some difficult slides, Paul Suddaby and Neil Wilkinson for instruction in the use of the electron microprobe, Geoff Bullen and Robin Parker for assistance with XRF work, Peter Watkins for supervising wet chemical analysis, Roy Lowry, Susan Parry and Nick Rogers for help with neutron activation analysis and associated data processing, and Roy Lowry and Robin Parker for computing assistance and for use of programs written by them.

In the course of research and the somewhat protracted gestation period of this thesis, many useful and stimulating discussions were held with friends and colleagues at Imperial College and elsewhere. Research collaboration with John Wright

and Mick "Barnacle Bill" Storey has been particularly fruitful. Thanks must also go to Kate Brodie, Lawson Brown, Brian Clough, Graham Cunmingham, Roy Lowry, Bob Maddock, Allan Mann, Ann Morrison, Jack Nolan, Dave Savage, Alan Smith, Steve Sparks, Bob Thompson, George Walker and Colin Wilson. Some good mates, without whom life and geology would have been more quiet, are Lawson Brown, Roy Lowry, Steve Soldin, Mick Storey and John Wright.

Finally, and more than anyone, I must thank my wife Beverley, for her love and support, and for putting up with me during the writing.

TABLE OF CONTENTS

	Page
ABSTRACT	3
ACKNOWLEDGEMENTS	5
CHAPTER I. GEOLOGICAL BACKGROUND AND PHYSICAL CONSIDERATIONS	22
I.1 GEOLOGICAL SETTING AND PREVIOUS WORK	22
I.1.i The Canary Islands	22
I.1.ii Tenerife: Physiography and climate	24
I.1.iii Previous work on Tenerife	27
I. 1.iv General geology of Tenerife	28
The Ancient Series	29
The Canadas Series	33
Younger volcanics	34
Discussion	36
I.1.v Collapse structures and the origin of Las Canadas	37
I.2 PHYSICAL FEATURES OF PYROCLASTIC ROCKS: NOMENCLATURE, ORIGIN, AND RELEVANCE TO GEOCHEMICAL SAMPLING	41
I.2.i Nomenclature	41
Components	42
Types of deposit	43
Welding	46
I.2.ii Genesis of pyroclastic rocks	47
Eruption	47
Transport and deposition	50
Post-eruptive processes	53
I.2.iii Factors affecting petrological study	55
Extraction of magma	55
Fragmentation of magma	59
Transport of tephra	66

Recommendations for geochemical sampling of pyroclastic deposits 70

I.3 FIELD CHARACTERISTICS OF THE TENERIFE PUMICE SERIES 72

I.3.i General aspects 73

I.3.ii The Granadilla Series 84

I.3.iii The Fasnia Series 95

I.3.iv The Adeje area 104

I.3.v Sub-Granadilla Series pumice deposits 113

CHAPTER II. WHOLE-ROCK GEOCHEMISTRY OF THE PUMICE SERIES 116

II.1 INTRODUCTION 116

II.1.i Effects of eruptive and post-eruptive processes on pumice chemistry 116

II.2 COMPOSITIONAL VARIATIONS AMONG ANALYSED SAMPLES 122

II.2.i Behaviour of elements in the pumice series 123

II.2.ii Features of individual deposits 126

II.2.iii Variation in rare-earth elements (REE) 127

II.2.iv Variation in Nb/Ta ratio. 127

II.3 DISCUSSION 134

II.3.i Differentiation mechanisms 134

II.3.ii Behaviour of REE in Tenerife pumices 137

II.3.iii Behaviour of Nb and Ta 139

II.3.iv Relationship of phonolite to trachyandesite 141

II.3.v Variation within individual deposits 142

II.3.vi Concluding remarks 147

CHAPTER III. PUMICE MINERALOGY AND MAGMA MIXING 149

III.1 GENERAL PETROGRAPHY AND MINERALOGY 149

III.1.i Feldspar 151

III.1.ii Feldspathoids 155

III.1.iii Pyroxene 156

III.1.iv Olivine 164

III.1.v Amphibole 164

III.1.vi Biotite 166

III.1.vii Sphene 172

III.1.viii Fe-Ti oxides 172

III.1.ix Apatite 174

III.1.x Pyrrhotite 175

III.1.xi Glass 175

III.2 THE TAJAO IGNIMBRITE 179

III.2.i Petrography and mineralogy 179

III.2.ii Glasses 193

III.2.iii Estimation of original magma compositions 200

III.2.iv Summary 207

III.3 IGNIMBRITE O 207

III.3.i Petrography and mineralogy 207

III.4 OTHER DEPOSITS 214

III.4.i Airfall and ignimbrite E 215

III.4.ii The Adeje red ignimbrite 215

III.4.iii Pumice fall J 219

III.4.iv Remaining deposits 220

III.5 DISCUSSION 221

III.5.i Qualitative model for the genesis of Tenerife pumice deposits 224

III.5.ii Suggestions for further study 248

Addendum 250

CHAPTER IV. TEMPERATURES AND VOLATILE COMPONENTS OF THE PUMICE-FORMING MAGMAS 251

IV.1 THERMODYNAMIC BACKGROUND 252

IV.2 GEOTHERMOMETERS 257

IV.2.i Iron-titanium oxides geothermometer 258

IV.2.ii Clinopyroxene - ilmenite geothermometer 268

IV.2.iii Olivine - clinopyroxene geothermometer 269

IV.2.iv Plagioclase - alkali feldspar geothermometer 271

IV.2.v Nepheline - alkali feldspar geothermometers 271

IV.2.vi Nepheline geothermometer 271

IV.3 THE PRE-ERUPTIVE VOLATILE COMPONENT OF THE PUMICE-FORMING MAGMAS 272

IV.3.i Estimation of temperature and oxygen fugacity 272

IV.3.ii Estimation of water fugacity and concentration 273

IV.3.iii Estimation of hydrogen fugacity 276

IV.3.iv Estimation of sulphur fugacity 277

IV.3.v Estimation of f_{H_2S}, f_{SO_2}, f_{SO_3} 280

IV.3.vi Discussion 281

Accuracy 281

General limitations 282

Comparison with other magma types 283

Rough estimation of f_{H_2O} for non-biotite bearing samples 287

Magmatic water contents 288

Some volcanological implications 290

CHAPTER V. SYENITE XENOLITHS FROM THE PYROCLASTIC SERIES 292

V.1 INTRODUCTION 292

V.1.i General aspects of the nepheline syenite xenoliths 293

V.1.ii Petrography of the nepheline syenites 294

V.2 MINERALOGY OF THE NEPHELINE SYENITES 299

V.2.i Feldspar 299

V.2.ii Nepheline and sodalite 300

V.2.iii Aegirine-augite and aegirine 305

V.2.iv Amphibole 313

V.2.v Other minerals 317

Lavenite 317

Sphene 319

Biotite 319

Ilmenite 319

Loparite 320

Remaining minerals 323

V.2.vi Discussion 325

Conditions of formation 325

Comparison with the mineralogy of the phonolites 330

General considerations 331

V.3 THE MEDANO XENOLITHS 333

V.3.i Occurrence 333

V.3.ii Petrography 333

V.3.iii Plagioclase 337

V.3.iv Feldspathoids 339

V.3.v Mafic phases 341

V.3.vi Other phases 342

V.3.vii Discussion 343

CHAPTER VI THE WELDING OF ALKALINE PYROCLASTIC DEPOSITS 346

VI.1 INTRODUCTION 346

VI.2 WELDED TUFFS ON TENERIFE 349

VI.2.i Ignimbrites 349

Petrology of the Adeje red ignimbrite 351

Discussion 352

VI.2.ii Welded air-fall tuffs 354

The Boca de Tauce tuff 354

VI.3 THE WELDED IGNIMBRITES OF SOUTH-WESTERN GRAN CANARIA 356

VI.3.i General field characteristics 357

VI.3.ii Petrology of ignimbrite E 363

Phenocrysts 367

Groundmass phases 367

VI.3.iii Flowage structures 370

Extensional structures 370

Imbricate structure 371

Flow folds 371

Discussion 377

Origin of structural relations 390

VI.3.iv Discussion 393

VI.4 THE GREEN TUFF OF PANTELLERIA 394

VI.4.i General field characteristics 395

VI.4.ii Petrology 395

Phenocrysts 396

Groundmass phases 398

Discussion 399

VI.4.iii Estimation of physical parameters for the eruption 403

VI.4.iv Discussion 405

VI.5 AGGLUTINATION OF FLUID TEPHRA 408

VI.5.i Modelling agglutination processes 409

Equal-volume deformation of non-vesicular pyroclasts 410

Porosity-loss flattening of vesicular tephra 412

VI.5.ii Discussion 416

Effect of non-Newtonian rheology 421

Application to basaltic eruptions 423

VI.5.iii Suggested thermal facies model for plinian air-fall deposits 427

REFERENCES 430

APPENDIX A. WHOLE-ROCK ANALYSIS 452

Sample preparation 452

Analysis 454

Results, and their quality 455

APPENDIX B. ELECTRON MICROPROBE ANALYSES 462

Procedure 462

Quality of analyses 463

The data 463

B.1 FELDSPARS 470

B.2 NEPHELINES 482

B.3 SODALITE-GROUP MINERALS 485

B.4 PYROXENES 487

B.5 AMPHIBOLES 501

B.6 BIOTITES 506

B.7 OLIVINES 508

B.8 LAVENITES 510

B.9 AENIGMATITES 512

B.10 SPHENES 514

B.11 GLASSES 516

B.12 IRON-TITANIUM OXIDES 521

B.13 LOPARITES 537

B.14 APATITES 539

B.15 PYRRHOTITES 541

ENCLOSURES (bound in at rear of text)

WOLFF, J.A. & STOREY, M., 1983. The volatile component of some pumice-forming alkaline magmas from the Azores and Canary Islands. Contrib. Mineral. Petrol. 82, 66-74.

WOLFF, J.A. & STOREY, M., in press. The use of tephra studies to determine volatile release during large explosive volcanic eruptions. Tech. Rep. Planet. Volatiles Conf., Lunar Planet. Inst.

WOLFF, J.A. & WRIGHT, J.V., 1981a. Rheomorphism of welded tuffs. J. Volcanol. Geotherm. Res. 10, 13-34.

WOLFF, J.A. & WRIGHT, J.V., 1981b. Formation of the Green Tuff, Pantelleria. Bull. Volcanol. 44, 681-690.

WOLFF, J.A., WRIGHT, J.V., SMITH, A.L., CLOUGH, B.J., ROOBOL, M.J. & SELF, S. Mixed pumice eruptions: field

characteristics. Trans. IX Carib. Conf. 1, 355-365.

FIGURES

Page

CHAPTER I

1.1 The Canary Islands 23

1.2 Topographic map of Tenerife 26

1.3 Geological map of Tenerife 32

1.4 Teide and Viejo 35

1.5 The Guimar Valley 38

1.6 Geometry of pumice deposits 44

1.7 Schematic section through a typical pumice deposit 49

1.8 Magma extraction patterns 58

1.9 Grain size distribution in a plinian eruption column 60

1.10 Relationship between phenocryst size and spacing 62

1.11 Modification of pumice chemistry by crystal loss 64

1.12 Volume erupted between ejection of two adjacent pyroclasts of different sizes 68

1.13 Volume erupted between ejection of two adjacent pyroclasts of same size 69

1.14 Inter-relations of pumice deposits in the field 77

1.15 Location map of SE Tenerife 80

1.16 Area vs. thickness plot 82

1.17 Pumice fall A 85

1.18 Deposits D & E 87

1.19 Ignimbrite F 90

1.20 Deposit G 94

1.21 Deposit J 98

1.22 Deposits K & L 101

1.23 Deposits M & N 102

1.24 Section through Adeje succession 105

1.25 Sketch map of the Adeje area 106

1.26 The Adeje red ignimbrite 110

1.27 Fall deposit overlying red ignimbrite 112

1.28 Sub-Granadilla Series succession 115

CHAPTER II

2.1 Major elements vs. LOI 119

2.2 Chemical profiles through deposit G 121

2.3 Normalised element diagram 124

2.4 REE plots for deposit A 128

2.5 REE plots for deposit D 129

2.6 REE plots for deposit E 130

2.7 REE plots for deposit G 131

2.8 REE plots for deposit J 132

2.9 Comparison of REE contents in pumice deposits 133

2.10 REE distribution coefficients for sphene/bulk rock 138

2.11 Nb/Ta vs. Th 140

2.12 Chemical profiles through deposit E 143

2.13 Comparison of base, middle and top of fall deposit G 145

CHAPTER III

3.1 Feldspar compositions in mixed pumices 153

3.2 Al vs. Mg in a zoned titanaugite 158

3.3 Al vs. Mg for all pyroxenes in mixed pumices 159

3.4 Mg - (Fe^{2+} + Mn) - Na for pyroxenes 162

3.5 (Na + K) vs. Si for amphiboles from mixed pumices 165

3.6 Mg/(Mg + Fe) for biotites from mixed pumices 167

3.7 Compositional relations in Ti-rich biotites 170

3.8 (Ti + Al) vs (M^{2-} + Si) in Ti-rich biotites 171

3.9 MgO vs. ulvospinel content of titanomagnetites 173

3.10 Streaky mixed pumice from the Tajao ignimbrite 177

3.11 Amphibole in salic glass, Tajao ignimbrite 182

3.12 Feldspar compositions, Tajao ignimbrite 184

3.13 Pyroxene compostions, Tajao ignimbrite 185

3.14 Minor element content of Fe-Ti oxides, Tajao ignimbrite 186

3.15 Summary of phenocryst compositions, Tajao ignimbrite 187

3.16 Bytownite crystal, Tajao ignimbrite 188

3.17 Amphibole-plagioclase-oxide aggregate grain, Tajao ignimbrite 189

3.18 Aegirine-augite, Tajao ignimbrite 190

3.19 Olivine and titanomagnetite, Tajao ignimbrite 191

3.20 Titanaugite-oxide aggregate grain, Tajao ignimbrite 192

3.21 Classification of glasses from Tajao ignimbrite 197

3.22 Variation diagrams vs. SiO_2, Tajao ignimbrite glasses 198

3.23 Variation diagrams vs. CaO, Tajao ignimbrite glasses 199

3.24 Calculation of initial liquid compositions, Tajao ignimbrite 202

3.25 Plagioclase flotation in pahoehoe basalt 205

3.26 Feldspar compositions, ignimbrite O 210

3.27 Minor element content of Fe-Ti oxides, ignimbrite O 211

3.28 Pyroxene compositions, ignimbrite O 212

3.29 Variation diagrams vs. SiO_2, ignimbrite O glasses 213

3.30 Variation diagrams vs. SiO_2, E and Adeje red ignimbrite glasses 216

3.31 Minor element content of Fe-Ti oxides, E, J and Adeje ignimbrite 217

3.32 Feldspar compositions, Adeje ignimbrite 218

3.33 Densities of Tenerife magmas 223

3.34 Cartoon of proposed magma chamber under Las Canadas 228

3.35 Degree of basalt crystallisation and H_2O-saturation 236

3.36 Possible magma mixing mechanism 237

3.37 Cooling rate of lower layer in stratified magma system 240

3.38 Interface thickness in stratified magma system 241

3.39 Suggested model of magma mixing in zoned chamber 245

3.40 Effect of bubble rise through zoned magma chamber 247

CHAPTER IV

4.1 T - f_{O_2} diagram, Boca de Tauce tuff 262

4.2 T - f_{O_2} diagram, deposit E 263

4.3 T - f_{O_2} diagram, Adeje red ignimbrite 264

4.4 T - f_{O_2} diagram, all samples analysed 274

4.5 f_{S_2} data 279

4.6 Fugacity data 284

4.7 Comparison of fugacity data with other areas 285

4.8 Rough estimation of f_{H_2O} for non-biotite bearing samples 289

CHAPTER V

5.1 Perthite, nepheline syenite block 297

5.2 Albite overgrowth, nepheline syenite block 298

5.3 Nepheline compositions in $NaAlSiO_4$ - $KAlSiO_4$ - SiO_2 302

5.4 All analysed aegirine and aegirine-augite compositions in Di - Hed - Ac 307

5.5 Zoning in an aegirine-augite 308

5.6 Zoning in four aegirine-augites 309

5.7 Sector zoning in aegirine-augite 312

5.8 Extreme zoning in aegirine-augite 314

5.9 Compositions of late-stage acicular aegirines 315

5.10 Compositions of amphiboles in nepheline syenites 318

5.11 REE plot for five loparites 321

5.12 REE plot for a loparite 322

5.13 Igneous lamination, Medano xenolith 335

5.14 Plagioclase and titanaugite, Medano xenolith 336

5.15 Plagioclase compositions, Medano xenoliths 338

5.16 Nepheline, amphibole and plagioclase, Medano xenolith 340

CHAPTER VI

6.1 Boca de Tauce welded air-fall tuff 355

6.2 Distribution of ignimbrites on Gran Canaria 358

6.3 Ignimbrite key sections, Gran Canaria 359

6.4 Infilling of basal hollows, Gran Canaria ignimbrites 360

6.5 Basal layer, Gran Canaria ignimbrite 361

6.6 Imbricated fiamme, base of ignimbrite 364

6.7 Imbricated fiamme, undesignated ignimbrite 365

6.8 Cooling joint deforming foliation 366

6.9 Amphibole compositions, Gran Canaria ignimbrite E 368

6.10 Lineations on sub-horizontal surface 372

6.11 Tension cracks in stretched pumice lapillus 373

6.12 Rotation of fragments by laminar viscous flow 374

6.13 Fold size distributions 378

6.14 Dip of axial surface vs. interlimbangle for flow folds 379

6.14 Schematic drawing of fold development during viscous flow 380

6.16 Harmonic analysis of fold surface shapes 381

6.17 Fold layer shapes 382

6.18 Recumbent fold, Gran Canaria ignimbrite E. 383

6.19 Refolded fold, Gran Canaria ignimbrite E. 384

6.20 Folding of welding-zone boundary, Gran Canaria ignimbrite E. 385

6.21 Relations around topographic step, ignimbrite E. 386

6.22 Flow curves for various materials 392

6.23 Pyroxene compositions, Green Tuff of Pantelleria 397

6.24 T - f_{O_2} diagram for the Green Tuff, Pantelleria 401

6.25 Fe/(Fe + Al) in feldspar vs. $NaFeSi_2O_6$ content of pyroxene, Green Tuff, Pantelleria 402

6.26 Lithic size vs, distance from vent, Green Tuff 406

6.27 Discharge rate vs. vent radius for the Green Tuff eruption 407

6.28 Clast size vs. clast viscosity for agglutination of tephra by equal-volume deformation 413

6.29 Clast size vs. yield strength required for agglutination 414

6.30 Clast size vs. clast viscosity for agglutination by porosity-loss compaction 417

6.31 Lava flow depth vs. yield strength 426

APPENDIX B

B.1 Histograms of standard jadeite analyses 467

B.2 Histograms of standard olivine analyses 469

TABLES

CHAPTER I

1.1 Comparison of stratigraphic schemes for Tenerife 30

1.2 Total erupted volumes of major pumice fall deposits on Tenerife 83

CHAPTER III

3.1 Mineral assemblages of Tenerife pumice deposits 152

3.2 Correlations of phenocryst phases in the Tajao ignimbrite 181

3.3 Correlation matrix for major elements in Tajao ignimbrite glasses 194

3.4 Analytical error as a fraction of compositional variation in Tajao ignimbrite glasses 195

3.5 Modal analysis of streaky pumice from the Tajao ignimbrite 203

3.6 Compositions of Tajao ignimbrite magmas before mixing 204

CHAPTER IV

4.1 Comparison of results from Fe-Ti oxides and ilmenite-clinopyroxene geothermometers 266

4.2 Estimated magmatic water contents 278

4.3 Abundances of species in the system H-O-S 286

CHAPTER V

5.1 Modal analyses of selected nepheline syenite blocks 295

5.2 Temperatures of cessation of exsolution in perthites 329

5.3 Assemblages of Medano xenoliths 334

CHAPTER VI

6.1 Suggested thermal facies model for plinian deposits 429

APPENDIX A

A1 Major- and trace-element contents of whole pumice samples 457

A2 Precision of major-element XRF determinations 458

A3 Errors in trace-element determinations 459

A4 Errors in REE determinations 460

A5 Comparison of determined REE contents of U.S.G.S. standard rocks with recommended values 461

APPENDIX B

B.i Precision of microprobe analyses 465

B1 Feldspar analyses 473-81

B2 Nepheline analyses 483-4

B3 Sodalite analyses 486

B4 Pyroxene analyses 488-500

B5 Amphibole analyses 502-5

B6 Biotite analyses 507

B7 Olivine analyses 509

B8 Lavenite analyses 511

B9 Aenigmatite analyses 513

B10 Sphene analyses 515

B11 Glass analyses 517-20

B12 Iron-titanium oxide analyses 523-36

B13 Loparite analyses 538

B14 Apatite analyses 540

B15 Pyrrhotite analyses 542

CHAPTER I

GEOLOGICAL BACKGROUND AND PHYSICAL CONSIDERATIONS

I.1 GEOLOGICAL SETTING AND PREVIOUS WORK

I.1.i The Canary Islands

The eastern North Atlantic Ocean between latitudes 14°N and 40°N contains a number of island groups collectively known as Macronesia. The islands are largely the products of Tertiary and Quaternary alkaline volcanism which continues to the present, with several eruptions this century (Mitchell-Thome, 1981). The Canary Islands (Figure 1.1), the largest group with a total land area of 7,500 km^2, lie between 100 km and 550 km of the African coast around latitude 28°N. Known to the Ancients, the archipelago was re-discovered by Iberian adventurers in the 14th century; by the end of the 15th, the aboriginal Guanche population had been bloodily subdued and the islands came under Spanish control. At present they are part of metropolitan Spain.

The topography of the two easternmost islands, Fuerteventura and Lanzarote, is relatively gentle; the relief of the remaining five is impressive, particularly Tenerife, La Palma and Hierro, all of which are young volcanoes with spectacular collapse features (the word caldera, in its geological sense, originates in the Canaries). An overall summary of Canarian geology has been given by Mitchell-Thomé (1976) to whom the reader is directed for a full bibliography; salient aspects are briefly mentioned here. The islands lie on a

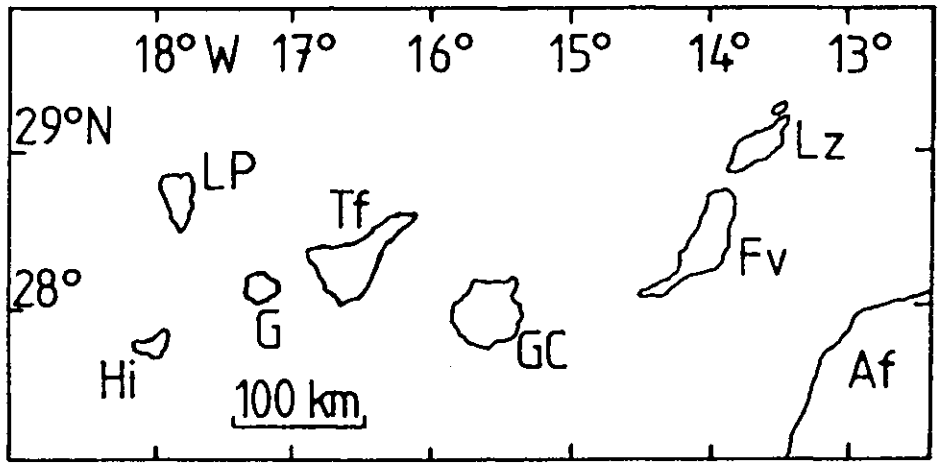

Fig. 1.1 Location of the Canary Islands in the Eastern Atlantic Ocean. Af = Africa, Fv = Fuerteventura, Lz = Lanzarote, GC = Gran Ganaria, Tf = Tenerife, G = Gomera, LP = La Palma, Hi = Hierro.

crustal fracture zone extending off the African continent, perhaps related to the formation of the Atlas Mountains (Bosshard, 1969). Fuerteventura and Lanzarote lie on the continental slope; Gran Canaria rises from transitional continental-oceanic crust, while the western islands are truly oceanic. Isotopic age determinations (Abdel-Monem et al., 1971, 1972) demonstrate an overall westward younging of the oldest rocks on each island. Alkali basalt shield volcanism predominates, with more evolved magmas on all islands except Hierro. The volcanics are markedly sodic and usually highly undersaturated, although trachytes occur on most islands and pantelleritic ignimbrites outcrop on Gran Canaria (Schmincke, 1970; see also Chapter VI). Sub-volcanic plutonic complexes are exposed on Gran Canaria, La Palma, Gomera and Fuerteventura, and inferred from xenoliths on Tenerife. A deeper common plutonic basement has been postulated (Borley et al., 1971) although bathymetry shows that each island is the tip of a large individual volcanic edifice.

I.1.ii Tenerife: Physiography and climate

Tenerife (Figure 1.2) is the largest island, with an area of 2058 km^2, and also has the highest peak in the Atlantic Ocean (Teide, 3718 m a.s.l.). The island is roughly triangular, elongated into the Añaga peninsula in the north-east. This and the Teno area in the north-western corner are deeply dissected and are formed of the oldest rocks on the island. Most of the land rises towards the central area of Las Canadas, a wide semi-circular depression bounded by a steep wall to the east, south and south-west. Rising from the northern part of Las Canadas is the twin stratovolcano of Teide-Viejo. Locally the topography of Tenerife is dominated by

Fig. 1.2 Topographic map of Tenerife with contours at 500m intervals. Also shown is part of the 500m submarine contour. The rim of the Las Canadas wall is shown by the dashed line. Unmarked localities mentioned in the text are shown in Fig. 1.15.

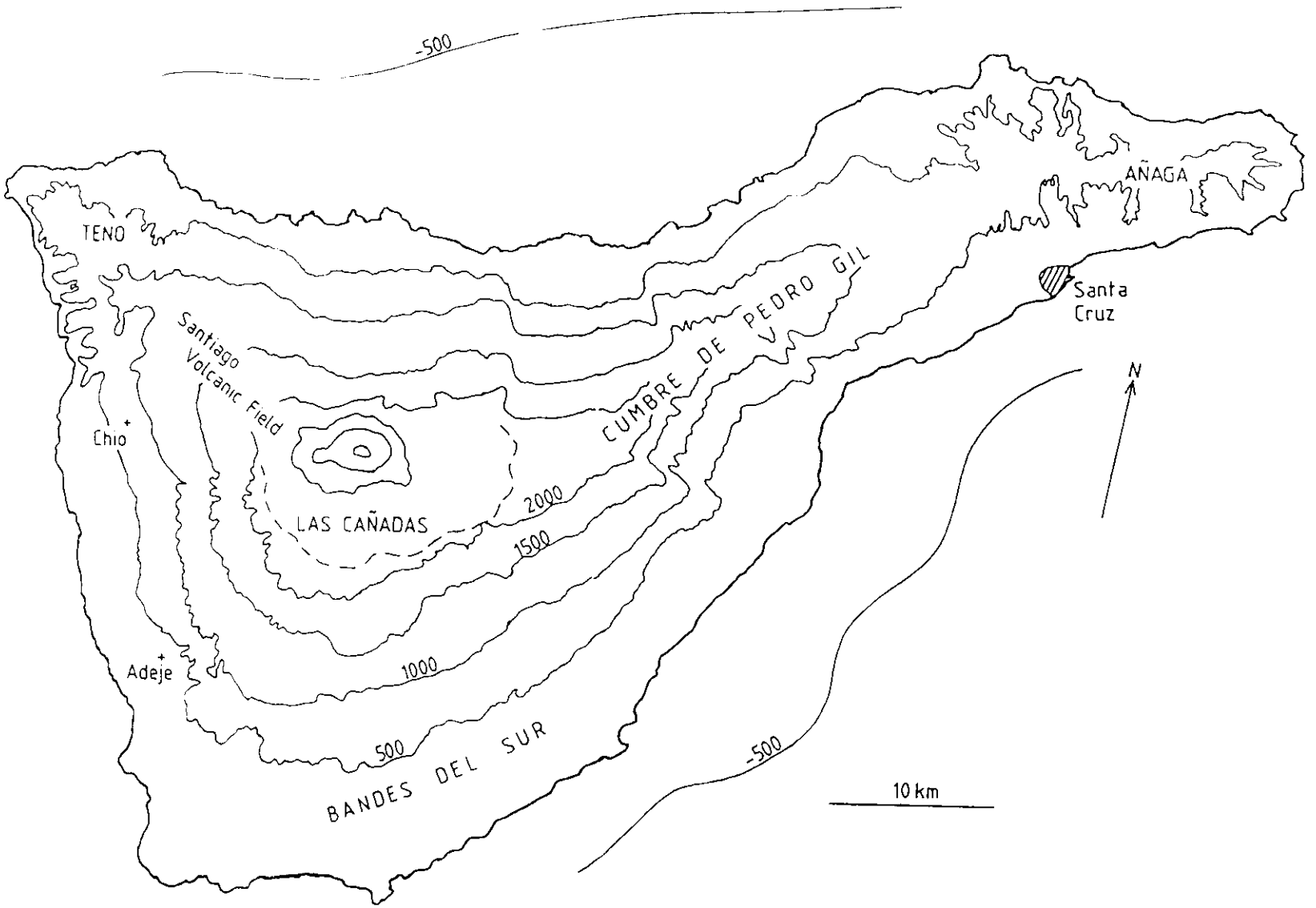
-500
TENO
AÑAGA
Santa Cruz
CUMBRE DE PEDRO GIL
Santiago Volcanic Field
Chio
LAS CAÑADAS
2000
1500
1000
500
-500
Adeje
BANDES DEL SUR
N
10 km

enormous landslip scars (I.1.v), the best examples being the Orotava and Guimar valleys, each covering >100 km^2. The relief is responsible for a very great climatic variation, from sub-tropical on the lower slopes of the windward northern side ascending through temperate zones to the peak of Teide, which is snow-covered for much of the year. Rainfall is much less on the southern side; temperate vegetation persists down to below the 1000 m contour giving way to the semi-arid region of Bandes del Sur, and eventually to the desert conditions of southern coastal Tenerife. Climatic variation has had a marked effect on the state of preservation of pyroclastic material (I.3). Ephemeral streams have cut numerous steep, narrow canyons called barrancos, often affording excellent sections through the outer part of the volcanic pile. The constant pleasant climate at low altitudes (mean annual temperature 21°C) has attracted travellers since the days of the ancient Phoenicians, and the enormous upsurge of tourism in the last 15 years has considerably improved the economic condition of the islands in general. Banana and tomato exports and oil refining (at Santa Cruz de Tenerife) are other important commercial activities.

I.1.iii Previous work on Tenerife

There is a substantial body of geological literature dealing with Tenerife dating back to the early 18th century, mostly in languages other than English. The first reasonably detailed account is that of Hausen (1956), which includes a map and stratigraphic column. Little subsequent material appeared until the late 1960s, with the publication of another general treatment (Fuster et al., 1968) and several papers dealing with specific aspects of the geology, volcanology, petrology, geophysics and geochronology of Tenerife

and the other islands. Ridley (1968) proposed a volcanic stratigraphy partly based on that of Hausen (1956), and in a series of papers reported a detailed investigation of the geology and petrology of Las Canadas, with particular reference to the phonolite lavas (Ridley, 1970a, b, c, 1971a, b). Bosshard (1969), Bosshard and MacFarlane (1970), Dash and Bosshard (1969) and MacFarlane and Ridley (1968) give comprehensive regional and local geophysical data; the last authors, on the basis of a gravity survey, proposed the existence of a large basic mass, with a fractionated upper zone, under Las Canadas. Abdel-Monem et al. (1972) give 25 K-Ar age determinations and Watkins (1973) and Watkins et al. (1966) discuss paleomagnetic data. Scott (1970, 1976) has given a detailed treatment of the ferromagnesian mineralogy of the volcanic series, concentrating on the pyroxenes. Borley (1974) has given a further general geological and petrological account, and Borley et al. (1971) discuss the mineralogy of basic and ultrabasic xenoliths from Teno and Anaga. Booth (1973) and Booth and Walker (in prep.) have carried out a detailed tephrochronological study of the widespread young phonolitic pyroclastics, the petrology of which forms the principal subject of this thesis.

I.1.iv General geology of Tenerife

Any attempt to place the young pyroclastics within the overall geological framework of Tenerife necessarily depends on the extent to which the geological evolution of the island is understood; unfortunately there is only a loose consensus of published opinion. This section attempts to present a broad outline of Tenerife geology including the pumice series (omitted from previous general accounts as a group). The most widely quoted stratigraphic succession, that

of Fuster et al. (1968) is unnecessarily complex from a general viewpoint and contains, by the authors' admission (Fuster et al., 1968, p.206), some unwarranted stratigraphic divisions. This account therefore relies more on the work of Hausen (1956) and Ridley (1968), supplemented by this author's own observations. A comparison of the three previously-proposed successions is shown in Table 1.1. A geological map is given in Figure 1.3.

The Ancient Series

All workers are agreed that the rocks of the deeply dissected areas of Anaga and Teno are much older than the rest of the island, and are thought to be the remnants of a large basaltic shield which may have originally included Gomera. Flows of alkali basalt and ankaramite are intercalated with layers of altered basaltic scoria, and occasional sections through cinder cones buried by later flows are seen. The Anaga flows dip northwards, those of Teno to the west, suggesting eruption from more than one centre or set of fissures. Rocks of Anaga and Teno yield K-Ar ages between 15.7 and 4.7 m.y. (Abdel-Monem et al., 1972). They are cut by a network of basic and phonolitic dykes, sheets, and plugs.

The upper limit of this series is difficult to define. Eroded basalt lava sequences, assigned to the same formation by previous workers, outcrop as isolated peaks surrounded by younger volcanics and as occasional "windows" in barranco floors in the Bandes del Sur. Also considered to be "Ancient" are the basalts exposed in the southern wall of the Guimar valley, which has a maximum height of 600 m. These latter are pahoehoe basalts, visibly fresher than the

Hausen (1956)	Ridley (1968)	Fuster et al.(1968)	This work
Basaltic adventive volcanoes	Basalts from adventive cones	Recent basic series	Younger volcanics
Pyroclastic formation ? ?	Teide & Viejo flows	Teide-Viejo trachybasalts and phonolite	
	Post-Vilaflor basanites ? ?	Basaltic Series III	Canadas Series (including Granadilla & Fasnia Series) and contemporaneous basalts.
Phonolitic-trachyphonolitic-trachytic formation	Vilaflor Complex	Trachytic-trachybasaltic Series	
		Upper Canadas Series	
		Lower Canadas Series	
Ancient basaltic formation	Ancient basaltic formation	Old Basalt Series	Ancient Series

Table 1.1. Comparison of stratigraphic schemes for Tenerife.

Fig. 1.3 Geology of Tenerife, modified after Ridley (1968), Hausen (1956), Booth (unpublished) and the map of the Instituto Geologico y Minero de Espana. See text for discussion of stratigraphic divisions. Pumices are contemporaneous with the Canadas Series but are separated on the map to indicate chief areas of exposure. Age range of cinder cones and other vents probably spans the last 1 m.y.

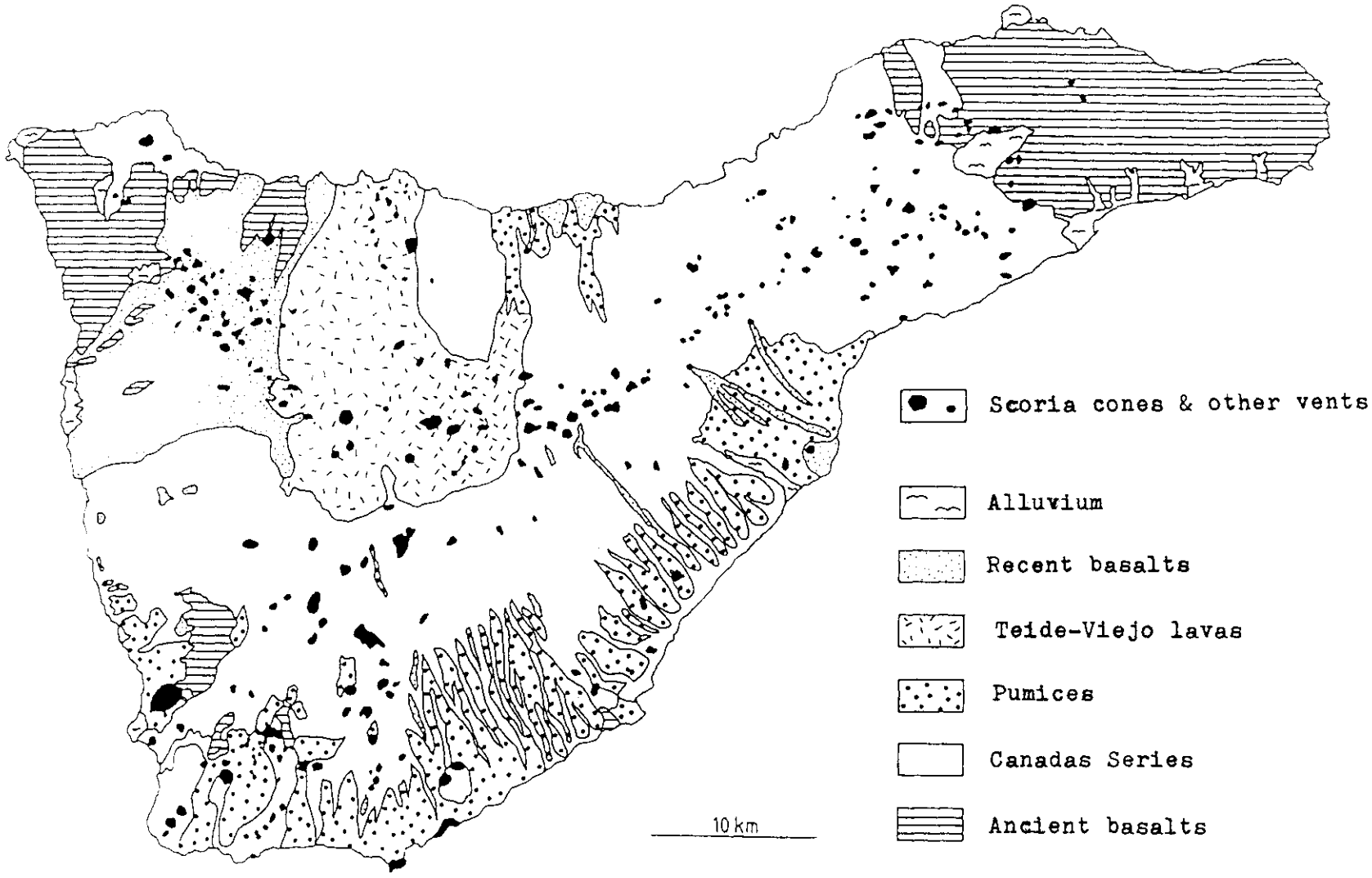
Scoria cones & other vents
Alluvium
Recent basalts
Teide-Viejo lavas
Pumices
Canadas Series
Ancient basalts
10 km

Teno and Añaga rocks. Flow units are typically 1-2 m thick and appear to have been emplaced in rapid succession. A distinct erosional horizon occurs approximately half-way up the scarp (B. Booth, pers. comm.). Abundant empty vesicles in flows at the base of the scarp testify that they were never buried to any great depth in a volcanic pile. These flows have been dated at 1.85 M.Y. - 0.81 M.Y. (Abdel-Monem et al., 1972) and are thus roughly contemporaneous with the Lower Canadas Series of Fuster et al. (1968). They dip towards the south-east.

The Canadas Series

The Canadas Series (Vilaflor Complex of Ridley, 1968) is exposed in the walls of Las Canadas and the upper slopes outside the caldera. The lowest exposed rocks are basalts, trachybasalts, and phonolite lavas and pyroclastics, the basalts being indistinguishable from, and possibly equivalent to, the "Ancient" flows of the Guìmar valley scarp. The youngest members are phonolitic pumices and welded tuffs which mantle the wall and are thus later than the scarp rocks. Ages of samples from the scarp range from 1.54 M.Y. to $<$0.2 M.Y. (Abdel-Monem et al., 1972).

The Las Canadas wall is divisible into three sections separated by faults; age relations between these are unknown. The westernmost section is composed chiefly of basalts and trachybasalts. A fault at Roques de Garcia divides this from the central section in which phonolite lavas predominate, while west of Las Pilas these give way to phonolitic pumices and welded tuffs. The compositional contrast is reflected by later eruptive centres within the caldera; Viejo and the Santiago volcanic field are predominantly composed of alkali basalts and trachybasalts, while Teide and its satellites such as

Mna. Rajada are dominantly phonolitic. The possible significance of this compositional localisation is discussed in Chapter III.

The volcanological nature of many of the Las Canadas wall phonolites is uncertain. The author has observed welded air-fall tuffs, previously mapped as pyroclastic flows or "eutaxites", at several localities (e.g. Boca de Tauce, Chapter VI); furthermore Booth and Walker (pers. comm.) report that several units with the characteristics of lavas grade laterally into welded air-fall tuffs, and thus would appear to be rheomorphic welded tuffs (Wolff and Wright, 1981a).

The top of the Canadas Series is contemporaneous with the pumice succession of S. Tenerife, one late member of which has been identified on the western part of Las Canadas rim (I.3). Another unit, the Pilas ash-flow of Ridley (1968) which also occurs on the rim, may be equivalent to a welded ignimbrite which forms part of the southern pumice succession on the lower slopes (I.3). These occurrences date the uppermost parts of the Canadas Series at $<$30,000 yrs B.P. (I.3).

Younger volcanics

Fuster et al. (1968) place several stratigraphic units above the Canadas Series. However, two of these (Basaltic Series III, Trachytic-trachybasaltic Series) are intercalated with or predate the pumice succession and are thus contemporaneous with the Canadas Series. Of probable younger age is the Teide-Viejo complex (Figure 1.4), which clearly postdates the formation of the Las Canadas wall, although the relationship to the pumice series is uncertain. Any of the eruptions represented in southern Tenerife would

Fig. 1.4 Teide (right) and Viejo, viewed from 5km to the SW. Note well-developed levees on Teide lavas. Right of centre in the middle distance are the Roques de Garcia, buried to the N by Teide and Viejo lavas. The Roques form a thin wall protruding from the scarp of Las Canadas (Fig. 1.15), and may be an erosional remnant of the division between, originally, two adjacent calderas.

have draped a thick, perhaps welded, pyroclastic layer over the entire Las Canadas area; no such layers are visible on Teide or Viejo (although recent small pumice eruptions from Teide summit and flank centres have occurred). Thus the exposed parts, at least, of the twin peaks are comparitively youthful.

Numerous cinder cones dot the outer slopes of Tenerife. These span a considerable age range; most are older than the pumice series. Younger examples are found in the Santiago volcanic field west of Viejo, which has been historically active (most recently Chinyero, 1909) and isolated cones elsewhere (e.g. in the Guimar valley).

Discussion

From the foregoing it is apparent that the stratigraphy of Tenerife is somewhat confused and poorly understood, partly because of a determination on the part of previous workers to assign stratigraphic divisions on the basis of rock composition. On Tenerife, as on many volcanoes, spatial localisation of magma composition is at least as important as temporal. Basaltic activity has been more or less continuous throughout the subaerial history of the island, but has been accompanied by the eruption of evolved magmas during the last 1.5 m.y. or so. The southern pumice succession may be assigned to the uppermost part of the Canadas Series, predating the Teide and Viejo lavas. Far from being a past episode, the Canadas Series may thus be viewed as still in the process of formation, as there is every reason to suppose that future large pumice eruptions will take place within Las Canadas (Booth and Walker, in prep.). The continuity of central activity over the past 1.5 m.y. represented in the series lends strength to the concept of Tenerife as a huge

single volcano (adopted hereafter for convenience). Construction of a detailed stratigraphy which reflects the actual evolution of such a complex edifice should preferably rely on the recognition of individual eruptive units over a wide area. Re-mapping of Tenerife is urgently required.

I.1.v Collapse structures and the origin of Las Canadas

Collapse structures are common features on young volcanoes, especially calderas formed by the "cauldron subsidence" mechanism, generally presumed to be the consequence of partial emptying of an underlying magma chamber. Collapse features on Tenerife depart significantly from the classic closed circular or elliptical caldera shape, the most prominent being Las Canadas and the Orotava and Guimar valleys (Figure 1.2). The origin of Las Canadas has been speculated upon for 150 years, being variously ascribed to erosion, explosion, true caldera collapse (Hausen, 1956), landsliding (Ridley, 1968), trap-door collapse (Ridley, 1971), and progresive subsidence (Booth, 1973).

The Orotava and Guimar valleys are less equivocal landslip scars. In both cases, an even-floored wide valley sloping down to a low, gently convex coastline is bounded by near-vertical scarps (Figure 1.5). Outside the valleys the terrain is rugged and terminates in high, cliffed coasts. These features are all suggestive of a landslip origin. Supporting evidence comes from the inshore bathymetric contours, which indicate a submarine topographic ridge downslope from the Guimar valley (Figure 1.2). Huge landslip scars of similar form are known on other volcanoes (Duffield et al, 1982).

Fig. 1.5 The Guimar Valley, viewed from the top of the Ladera scarp which forms the SW wall of the valley. Note the topographic contrast of the dissected landscape beyond the valley with the smooth valley floor. The prominent cinder cone is contemporaneous with the pumice series

Similar features of the terrain and coastline adjacent to the open northern side of Las Canadas led Ridley (1968) to postulate a landslide origin for all three features. Ridley also identified several older collapse scars on the island. Subsequently, while retaining a common origin for the three structures, Ridley (1971) abandoned the landslip mechanism in favour of a "trap-door collapse" hypothesis. In this model, the "hinge" of a trap-door block is downslope from the head region where maximum subsidence takes place. For the reasons given above, the later hypothesis of Ridley (1971) is rejected for the Orotava and Guimar valleys.

No single process can easily account for the formation of Las Canadas; however it is geologically dissimilar from the landslide features. Isopach maps of the pumice deposits of southern Tenerife (Figures 1.18-1.23), several of which have volumes $> 10\ km^3$ (Table 1.2), demonstrate that, with one exception, all were erupted from Las Canadas. The presence of welded air-fall tuffs in the southern wall (such tuffs are near-vent deposits, Sparks and Wright, 1979), cone-building activity in the centre (Teide and Viejo) and position in the summit region of Tenerife also point to the importance of Las Canadas as a volcanic focus. In contrast, activity in the Orotava and Guimar valleys is limited to small-volume basaltic strombolian and lava eruptions. Borley (1974) and Booth and Walker (in prep.) suggest that Las Canadas is a true collapse caldera, modified by later landsliding which destroyed the northern coastal region. Booth (1973) noted that the volume of Las Canadas, plus that of a missing pre-caldera cone (estimated by extrapolation of present ground slopes to have been ca. 5000 m high) is roughly equal to the total dense-rock equivalent volume of the southern pumice succession, and suggested

that the caldera floor subsided piston-wise in response to progressive emptying of a shallow magma chamber by successive plinian/ignimbrite eruptions. There are a number of problems with this hypothesis, quite apart from the complex nature of the caldera itself. Firstly, the sub-volcanic magma chamber is compositionally inhomogeneous and may have been periodically replenished (Chapter III). Secondly, if the caldera was largely formed before the eruption of ignimbrites late in the series, the pyroclastic flows would have had to surmount the barrier of Las Canadas wall in order to reach their present positions in southern Tenerife. Although the ability of pyroclastic flows to move uphill is well documented (Miller and Smith, 1977; Francis and Baker, 1977; Walker et al., 1980), whether or not they can climb near-vertical walls and retain their essential character is far less certain. Thirdly, the total volume of ignimbrite erupted from Las Canadas is unknown. Several, of young age but unknown stratigraphic position, occur in the north, while their abundance in the southern coastal region implies that significant volumes may have entered the sea. Finally, a considerable thickness of ignimbrite is highly likely to have ponded within Las Canadas itself if caldera formation predated any eruptions in which flows formed; in this case the volume estimate for the caldera would be erroneous, since it is partly filled with highly vesicular pumice. Nonetheless, in the light of the evidence for Las Canadas as the source of considerable volumes of pumice it seems difficult to avoid the conclusion that the feature is a true caldera or group of overlapping calderas, although the precise relations of collapse to eruption episodes is unknown. The collapse followed by landsliding theory of Borley (1974) and Booth and Walker (in prep.) seems the most satisfactory.

An interesting possibility of structural control of the location of post-landsliding volcanism then arises. Teide and Viejo, which clearly post-date collapse, lie on the northern side of Las Canadas along with several satellite and monogenetic cones. Evidence of activity in the southern part is, however, almost entirely lacking (Figure 1.3). The disappearance of a large sector of caldera wall and flank material would have substantially decreased the local lithostatic load, and thus magma could find easier pathways to the surface in that area. The composition of magma erupted then simply reflects that locally available (Chapter III), and volcanic piles accumulate where resistance to uprise is least. If Teide and Viejo post-date the most recent large pumice eruption, they may thus be acting as safety-values to the magma chamber by releasing magma in several small eruptions rather than allowing a large volume to become volatile-saturated over a long repose period culminating in a major explosive event.

I.2 PHYSICAL FEATURES OF PYROCLASTIC ROCKS: NOMENCLATURE, ORIGIN, AND RELEVANCE TO GEOCHEMICAL SAMPLING

I.2.1 Nomenclature

The purpose of this section is to provide an outline of the physical characteristics, including criteria for field recognition, and formation mechanisms of the various types of pumice deposit and to discuss how geochemical examination should best be conducted in the light of these processes. Obviously, a system of nomenclature

is a necessary prelude to any such discussion. The terminology of pyroclastic rocks has yet to be standardised and is notoriously confusing. The author has employed the following simple system; it is primarily suited to the study of Quaternary pyroclastics, since many of the diagnostic characteristics on which the system is based are destroyed by age, alteration, and burial to depths greater than a few hundred metres. Only terms used in this thesis are defined below, and the system is thus especially suited to petrological studies of pyroclastic rocks; it should be noted that the physical volcanologist may require a more detailed and general terminology, and the reader is referred to Wright et al. (1980).

Components

Pumice: This word is used to describe all vesicular magmatic material produced by explosive eruption, irrespective of grain size. It may therefore refer to large blocks or fine glass shards; the latter are commonly called "fine ash" in the field.

Crystals: during the explosive eruption of porphyritic magmas, a proportion of the crystals are liberated from pumice and form a discrete juvenile component. Here these are referred to loose crystals; those still included in pumice are termed phenocrysts. The distinction is petrologically important as loose crystals, by reason of grain-size, density, and shape, generally behave differently to pumice during transport.

Lithics: This term embraces all dense material in a pumice deposit. Lithics may be fragments of country rock or non-vesicular juvenile material; there are no generally applicable objective criteria on which the distinction can be made. Consider, for example, the lithic content of a deposit containing an abundance of non-vesicular juvenile glassy fragments (termed "cognate lithics" by Wright et al., 1980) which was erupted through a country rock sequence of obsidian lavas. Similarly, fragments of crystalline, vesicular rock of strongly contrasting composition to the host pumice may have an accidental origin, or be "cognate lithics" introduced by magma-mixing mechanisms (Eichelberger, 1980; Wolff et al., 1980). Those lithics of unequivocal accidental origin, such as plutonic blocks, are here termed xenoliths.

Types of deposit

Sparks and Walker (1973) proposed three basic types of pyroclastic deposit: pyroclastic fall, pyroclastic flow, pyroclastic surge (Figure 1.6).

Pyroclastic fall deposits: In pyroclastic fall eruptions, fragments are ejected from the vent into the atmosphere and thence fall freely to earth. The form of the resultant deposit is principally dependent on eruption column conditions and wind velocity. Fall deposits show mantle bedding (draping of topography, Figure 1.6a) are well size-sorted and usually exhibit internal stratification. All the pumice falls investigated in this thesis are plinian in the classification of Walker (1973), that is, the isopach (thickness contour) of one-tenth maximum thickness encloses an area greater than 500 km^2 .

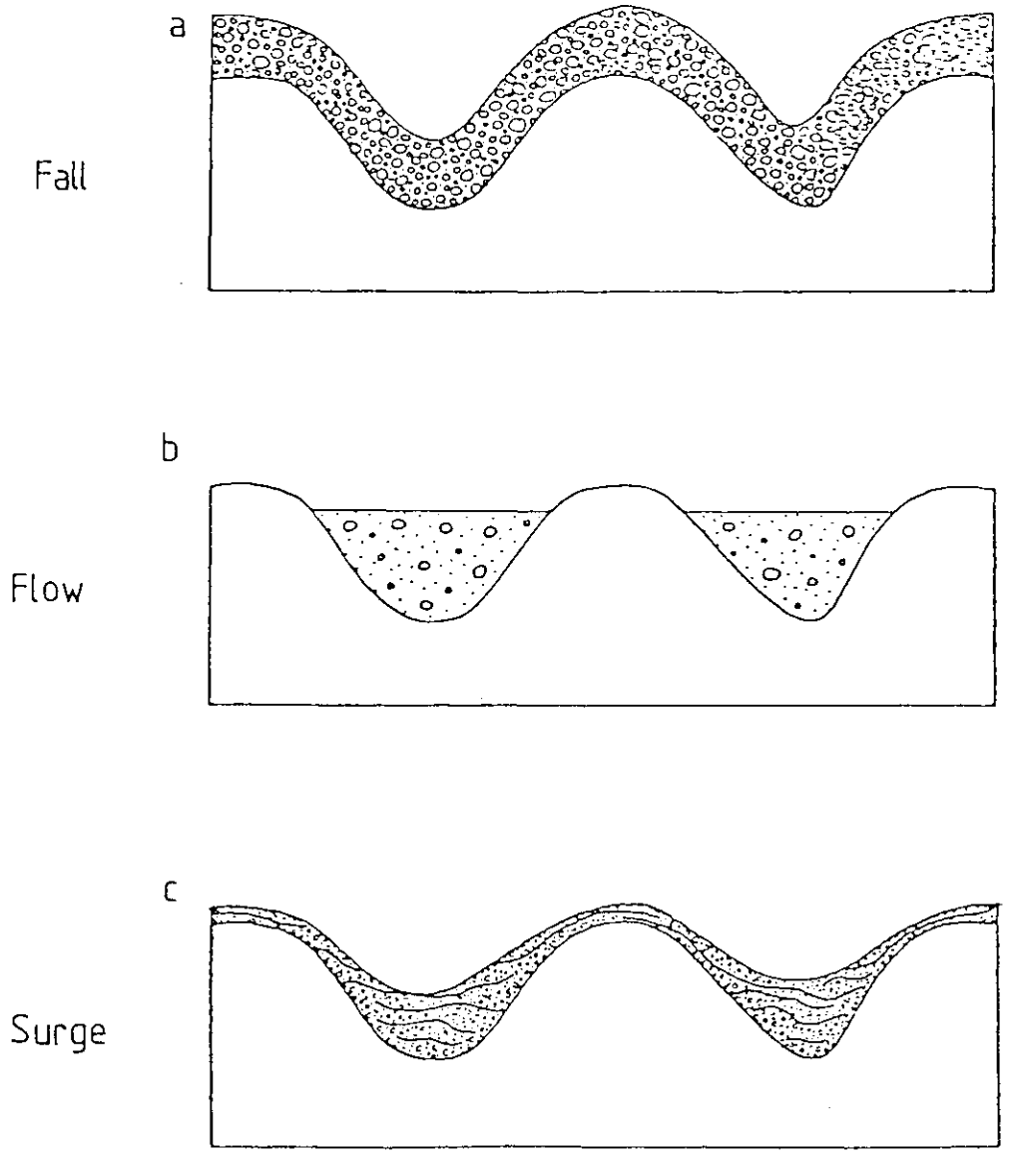

Fig. 1.6 Geometric relations of the three principal types of pumice deposit overlying the same topography (after Wright et al., 1980).

Pyroclastic flow deposits: Pyroclastic flows are hot, high-concentration gas-solid dispersions which move as gravity-controlled flows. In general, flow deposits infill topography (Figure 1.6b), are poorly sorted, lack internal stratification, and usually display a comparitively fine-grained basal layer. Ignimbrite describes a deposit or dense rock formed from pyroclastic flows composed predominantly of pumice; the term is used irrespective of the size of the deposit or the degree of post-depositional welding or other induration. Unwelded ignimbrites typically consist of pumice and lithic clasts dispersed in a finer matrix of pumice and loose crystals. An ignimbrite is the product of one eruption and usually consists of many individual flow units. Superposition of flow units can result in a misleading stratified appearance, for example, ignimbrite E of Sparks (1976). Non-welded ignimbrites can easily be confused with mudflows formed by the remobilisation of previously deposited pyroclastic material by surface water. Ignimbrites are normally accompanied by one or more types of deposit which result from the flow-producing activity (see below). All of the pyroclastic flow deposits investigated here are ignimbrites.

Pyroclastic surge deposits: Pyroclastic surges involve the lateral movement of particles in highly expanded, turbulent, low concentration gas-solid dispersion. Their deposits show sedimentary bedforms (e.g. cross-stratification) in which individual laminae are well-sorted, mantle bedding with a tendency to accumulate in depressions (Figure 1.6c) and (frequently) preferential enrichment in dense fragments.

Mudflows: Volcanic mudflows (lahars) are of secondary origin; they consist of volcanic debris remobilised by water. They are frequently generated during large explosive eruptions as a result of the accompanying catastrophic rainfall, but may also form independently from the downslope slumping of old waterlogged pyroclastic material. Pumice-rich examples may be indistinguishable from non-welded ignimbrites, though, in general, mudflows contain a higher proportion of lithic debris. On Tenerife there exists a complete gradation between the products of lithic-rich and almost lithic-free flows, sometimes along the same stratigraphic horizon (I.3).

Welding

A welded tuff is a pyroclastic deposit which has become coherent through sintering of hot, still-plastic clasts (usually pumice); all three types of primary pyroclastic deposit can become welded, although few examples of welded surges have been noted (Wright et al., 1980). Sillar is coherent ignimbrite in which the constituent clasts are undeformed; it can be formed by point-contact sintering of pumice, by vapour-phase crystallisation of non-welded pumice, or by weathering of previously unconsolidated material. Flattening of clasts is only achieved during welding sensu stricto and is accompanied by a partial loss of porosity to give partly welded tuff; complete loss of porosity results in densely welded tuff. In both grades of welding, pumice clasts are flattened to form characteristic fiamme, aligned in eutaxitic texture. In certain types of ignimbrite, fiamme may also have formed by the shearing of juvenile clasts as the pyroclastic flow halts (Self, 1973). Welded tuffs typically display zones of varying degrees of welding (Smith, 1960b). A densely welded tuff deposited on a gradient

may flow downslope as a coherent mass if sufficiently plastic; the resulting rock is termed a rheomorphic welded tuff (Wolff and Wright, 1981a).

I.2.ii Genesis of pyroclastic rocks

Plinian air-fall deposits, ignimbrites, and pyroclastic surges are formed during large explosive eruptions of (usually) salic magma. The mechanisms of these eruptions, and by which the various kinds of pumice deposit attain their final form, are now partly understood, although direct confirmation of existing models is unlikely due to the violence of the phenomena concerned. The summary which follows is drawn largely from Fisher (1979); Ragan and Sheridan (1972); Riehle (1973); Sheridan (1979); Sparks (1974, 1976, 1978a, b); Sparks and Walker (1973, 1977); Sparks and Wilson (1976); Sparks and Wright (1979); Sparks, Self and Walker (1973); Sparks, Wilson and Hulme (1979); Walker (1971, 1972); Walker et al. (1980); C.J.N. Wilson (1980); L. Wilson (1976, 1980); Wilson, Sparks, Huang and Watkins (1978); Wilson, Sparks and Walker (1980); Wolff and Wright (1981a); Wright and Walker (1977, 1981) and Wright et al. (1980); only processes pertinent to the genesis of the Tenerife pumice deposits are considered here.

Eruption

Explosive eruptions are driven by the rapid exsolution of volatile from the magma. Sparks (1978a) has considered the processes of bubble nucleation and growth in detail, and concludes that very small supersaturation pressures are sufficient to cause nucleation. Mechanisms of volatile supersaturation may include uprise of magma, pressure release through fracturing of magma chamber walls, and

mixing with hotter magma. Once nucleated, bubbles grow as magmatic volatiles diffuse into them. In rising salic magma, bubble growth ceases well before the magma disrupts, although pressures within bubbles continue to increase as the magma rises. Eventually the excess pressure causes fragmentation of magma and explosive ejection of pumice away from the surface of the disrupting magma. As the mixture of gas and pumice moves up the volcanic conduit, the conduit walls are rapidly eroded to contribute part of the lithic fraction of the final deposit. The mixture leaves the conduit at the vent to form a jet or blast whose kinetic energy is largely determined by the original volatile content of the magma (L. Wilson, 1980); typical velocities are 200-600 ms^{-1} (Wilson, 1976). The size of particles erupted varies from a few microns to a few metres. The jet, or eruption column, rises due to continuing expansion of the gas for a few km; during this phase air is entrained and heated, thus reducing column density. If this decreases to a value below the ambient atmospheric density, convective uprise may carry the eruption cloud to heights of up to 55 km; this is the case in plinian eruptions. Otherwise, when the rising column reaches zero velocity, it falls back to earth to form pyroclastic flows and surges. This "column collapse" process is envisaged to occur continuously after the manner of a shooting gallery fountain, and is favoured by wide vent radius, low magmatic volatile contents, low muzzle velocities, and high mass eruption rates. Progressive collapse may occur, where the outer low-velocity dilute portion of the eruption column collapses initially to form pyroclastic surges, followed by the denser inner part which forms pyroclastic flows. A natural sequence of eruption, as deeper, less volatile-rich magmatic levels are tapped and the eruptive vent widens, is therefore fall → surge → flow (Figure 1.7). Field evidence indicates that this is typical of ignimbrite-forming eruptions (Sparks et al., 1973).

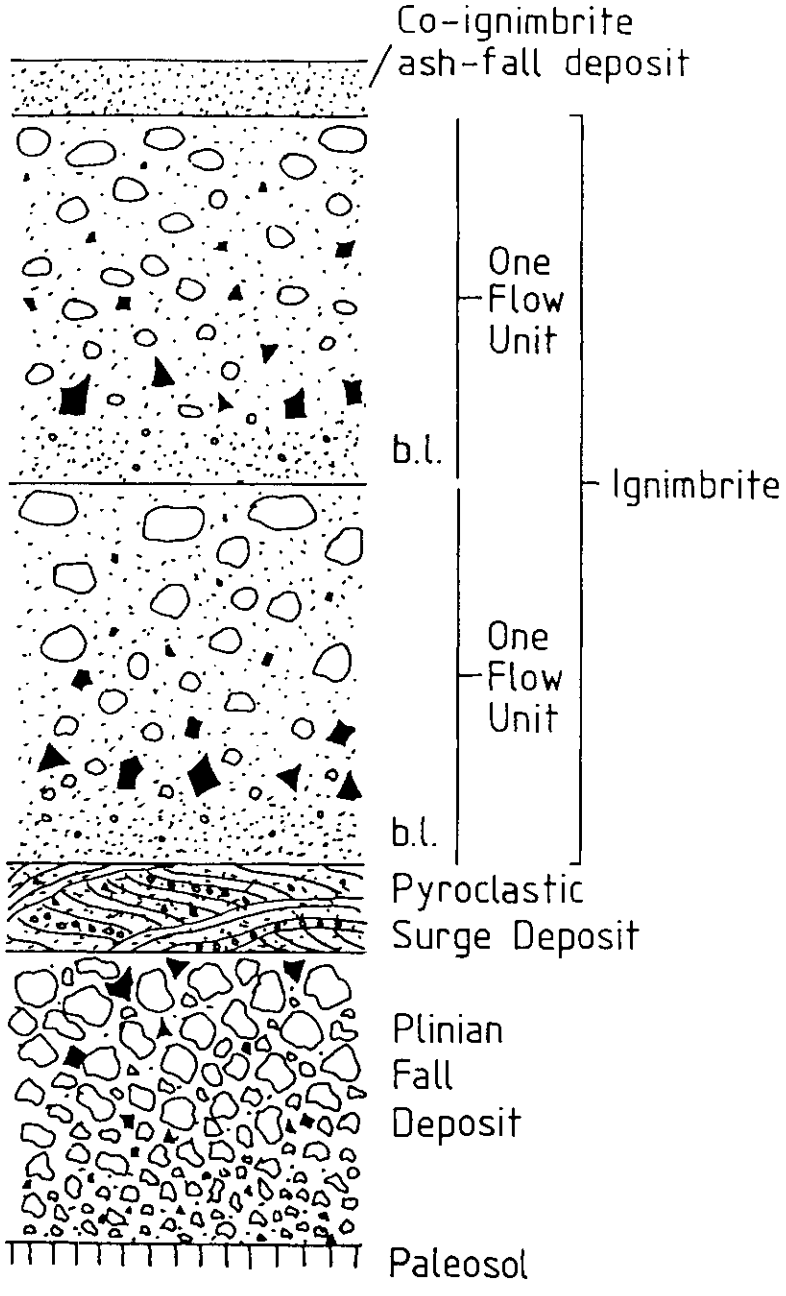

Fig. 1.7 Schematic section through a typical large pumice deposit on Tenerife, modified after Sparks et al. (1973). b.l. = fine-grained basal layer of ignimbrite flow unit (layer 2a of Sparks et al., 1973). Note reverse grading of pumice and lithics in plinian fall deposit, dune-type bedding in surge deposit (layer 1 of Sparks et al., 1973) and reverse grading of pumice with normal grading of lithics in the main part of ignimbrite flow units (layer 2b of Sparks et al., 1973). Co-ignimbrite ash fall deposit (layer 3 of Sparks et al., 1973) may also be found separating successive flow units of the same ignimbrite. Surge deposit is commonly absent on Tenerife, but is included for the sake of completeness. Diagram is not to scale, but the relative thicknesses of layers are qualitatively represented.

Transport and deposition

Pyroclastic falls: A plinian eruption column consists of two portions; a lower gas-thrust part which may extend to a few km above the vent, and the upper convective cloud which constitutes most of the column. The upper portion expands considerably as it rises until its maximum diameter is approximately equal to the height of the column. The height attained is a function of the mass eruption rate. Fall-out from the cloud forms the pumice fall deposit. The distribution of pumice is strongly affected by wind, and thus the great majority of air-fall deposits have non-circular dispersal patterns. Clearly, deposit thickness and grain-size of pumice, lithics and free crystals decrease away from source; the finest material is transported several 1000s of km, although it is not usually possible to trace prehistoric deposits beyond a few tens of km from the vent. Near-source, fall deposits often show well-developed stratification and alternating coarse and fine beds (due to the variation in particle settling rate with grain-size); further away, poorer sorting and stratification are evident. Minor variations in eruptive intensity are thus not recorded in the distal facies of fall deposits, although a gradual increase in column height is frequently recorded in the form of reverse grading. The proportions of pumice, lithics and free crystals in the deposit also varies with distance from source as a function of the grain-size populations of each particle type and that of the entire deposit. Rain-flushing of the eruption cloud, breaks in activity, and changes in wind direction all modify the detailed character of a deposit.

Pyroclastic flows: The collapse of a plinian eruption column produces pyroclastic flows and a number of types of associated deposit. When the collapsing material hits the ground, there is a brief agitation/fluidisation episode of very high gas flow rates through the forming pyroclastic flow, during which large and heavy blocks segregate out to form a very coarse, bedded deposit termed a co-ignimbrite lag-fall deposit. Fine pumice, on the other hand, is elutriated out to produce a cloud which rises above the flow. These effects are greatest during the initial stages of collapse, but persist throughout the collapse episode. During collapse and flow formation, substantial cooling (to an extent determined by the initial volatile content of the magma, the most volatile-rich material cooling to the greatest extent) of the pyroclasts occurs, although a pyroclastic flow, once formed, is a thermally-conservative system. The flow moves away from the vent at high speed (up to 100 ms^{-1}) an effect of the large gravitational head of the collapsing column. Gas-flow rates, principally due to continuing exsolution of volatiles from pumice, are sufficiently high to cause partial fluidisation of the flow. Fine material, continuously generated during flow by attrition of pumice, is elutriated by the upward gas movement and escapes to form the over-riding cloud which is the most obvious physical manifestation of a moving flow. Material of intermediate grain-size forms the fluidised matrix within which the largest, non-fluidised, pumice and lithic clasts are dispersed. These large clasts are therefore free to sink or float, depending on their densities relative to the fluidised matrix, in the flow to produce the distinctive feature of coarse-tail grading in the final deposit. A fine-grained layer usually develops at the contact between the flow and the underlying or confining surface, even where this is vertical. A flow possessing

sufficient kinetic energy may surmount topographic barriers, leaving behind a thin ignimbrite veneer deposit, of similar character to the main flow deposit, as a record of its passage. A pyroclastic flow possesses a yield strength, and when the applied stress due to velocity and/or gravity becomes less than this value, the flow rapidly halts. Common causes are probably decrease of gas-flow rates and decrease of ground slope. Gas release continues after the cessation of movement, resulting in the formation of lithic-rich fumarole pipes. The fine pumice dust elutriated during flow formation and movement settles to produce a widespread co-ignimbrite ash fall deposit whose volume may be equal to that of the ignimbrite. Where the flow has not passed, the ash-fall therefore serves as a valuable ignimbrite stratigraphic marker, although preservation potential is poor unless it is rapidly covered by another eruptive unit.

A typical ignimbrite, such as found on Tenerife, consists of a number of flow units, each with a fine-grained basal layer, displaying reverse grading of large pumices and normal grading of lithics, but otherwise homogeneous. Depending on the emplacement interval, each flow unit may be overlain by a fine ash deposit, or this may only occur at the top of the ignimbrite (Figure 1.7).

Pyroclastic surges: Pyroclastic surges are the least understood of the three main types of pyroclastic deposit. It appears that a number of mechanisms can give rise to surge deposits of basically similar appearance. Surges can form by eruption column collapse where the collapsing material is too dilute to form a true flow; the surge then forms a radially-expanding cloud moving outwards from the vent. Surges may also form from the material

elutriated from a moving pyroclastic flow (Fisher, 1979); since gas flow rates are very much less than lateral flow velocity, elutriated material moves initially at a speed only slightly less than that of the underlying flow. A surge formed by this mechanism is therefore localised in occurrence, overlies its parent ignimbrite, and is intimately associated with co-ignimbrite ash-fall deposits. In the former process, surge formation may be closely followed by flow formation as the eruption column progressively collapses. Surges may also erupt directly from a vent without an accompanying eruption column. Surges move turbulently, and deposition occurs by settling of grains from the turbulent fluid. Their deposits thus often show sedimentary structures such as dunes, antidunes and laminations. Turbulence also results in preferential enrichment in dense and equidimensional fragments such as lithics and heavy mineral grains. It should be emphasised that base surges are a different kind of phenomenon, being the product of phreatomagmatic activity. Base surges are not considered here; they have been found only in one locality on Tenerife, the surtseyan tuff-ring at Medano (I.3).

Post-eruptive processes

Many ignimbrites and the greater part or all of most fall and surge deposits, suffer no physical change after deposition (apart from erosion and weathering). Consolidation of pumice to form tuff is however a common feature, and necessary if the character of the rock is to be preserved for a large part of geological time. If the pyroclasts are sufficiently plastic after deposition, welding may occur in all three types of deposit. Tephra viscosity is controlled by the viscosity, load pressure, and cooling time of the sheet. Thus welding is favoured in thick, near-vent accumulations

of relatively fluid tephra. Very low pumice viscosity may permit agglutination, or simultaneous deposition and welding, to occur; however, this may be shown to be a negligible effect for all cases considered here (see Chapter VI). More usually, welding is initiated during and after deposition and continues for periods of up to several years after deposition. Welding in air-fall deposits is usually restricted to the near-vent region, since the emplacement temperature of air-fall pumice decreases rapidly with distance from source. Flows, however, are efficient conservers of heat and welded ignimbrites covering large areas are a familar geological phenomenon. Welding and compaction occurs by the coalescence of glassy material with accompanying loss of pore space until ultimately a dense rock is produced. Welding may of course cease due to cooling before this stage is reached (see I.2.i). In some cases, sufficiently fluid densely welded tuff may flow downslope as a lava, resulting in substantial modification of internal structures (see Chapter VI for a full discussion).

Post-emplacement processes may also affect unwelded tuffs. Chemical alteration, perhaps initiated by rainwater percolating through hot pumice, may cause induration of a deposit. Ignimbrites are particularly susceptible due to the large amount of fine material they contain. Furthermore, unconsolidated tephra is highly prone to reworking by the forces of erosion. The present appearance of a pyroclastic unit in outcrop may therefore differ substantially from the original form of the material emplaced.

I.2.iii Factors affecting petrological study

Pyroclastic rocks are notoriously beset with traps for the unwary petrologist. Chemical changes occurring after deposition have been well documented, particularly by R.B. Scott (1966, 1969, 1971a, b), and there also exist considerable data on chemical changes accompanying the alteration of volcanic glass (Aramaki et al., 1965; Lipman, 1965; Lipman et al., 1969; Noble, 1967; Zielinski et al., 1977). Post-emplacement chemical alteration of Tenerife pumices is considered in Section I.3 and Chapter II.

Much less attention has been d voted to the effects of physical processes on the petrological character of pyroclastic rocks. An appreciation of these processes is particularly important in view of the current petrological fashion for identifying magmatic heterogeneity on the scale of individual eruptive units (Hildreth, 1979; Sigurdsson and Sparks, 1981; Wright and Walker, 1981; see also Chapters II and III). The importance of distinguishing between phenocrysts and free crystals has already been noted (I.2.i). Processes occurring between magma extraction and deposition will now be more fully discussed.

Extraction of magma

Blake (1981) has modelled the extraction of Newtonian magma from a large, flat-roofed magma chamber into a cylindrical pipe entering at the roof. Under these conditions, the locus of points of magma which will arrive simultaneously at the conduit entrance is sub-spherical, the chamber roof forming a tangent to the sub-sphere at the extraction point. Therefore material from the deepest level tapped within the chamber will be erupted at the same

time as magma in close proximity to the chamber roof. If the magma body is chemically zoned, heterogeneous tephra will therefore be erupted (Figure 1.8a). Blake has calculated that the deepest level currently being tapped contributes roughly 50% of the total material being erupted, however without detailed information on magma rheology and rates of extraction it is not possible to ascertain the scale on which mixing occurs by this mechanism. The widths of bands in streaky pumice suggest that it may commonly be of the order of <1 mm to a few cm (I.3 and Chapter III), and is thus on the same scale as the sizes of pyroclasts commonly encountered in pumice deposits. In order for the equations of Blake to be applicable to an analysed sample and the chemical stratigraphy of the magma chamber reconstructed, it is necessary that the mixing be on a small scale relative to the size of the sample; i.e. large pumice clasts should be sampled.

Extraction patterns are critically dependent on magma chamber morphology. Blake's assumptions may be valid in several cases, for example where a magma chamber underlies a subsiding caldera block, but large deviations from this simple morphology may be envisaged. Lirer et al. (1973) estimate that the products of the AD79 eruption of Vesuvius came from a tall narrow magma chamber measuring approximately 5 km (vertical dimension) by 350 m. In such pipe-like bodies, the conduit diameter is a large fraction of the chamber diameter (Wilson (1976) estimates a vent radius of $\sim$110 m for the Vesuvius, AD79 eruption) and the magma will tend to be extracted with little internal distortion. Thus the resulting pumice deposit will more closely represent an inverted magma chamber stratigraphy (Figure 1.8b). On Tenerife, such variations in the morphology of a zoned

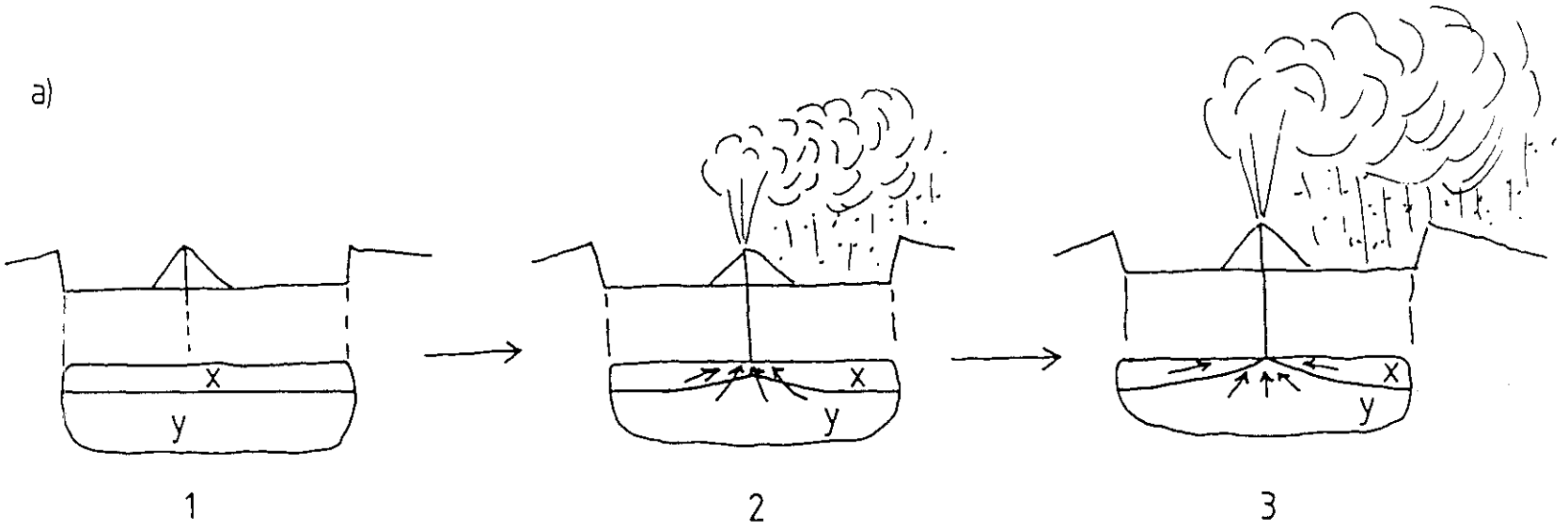

Fig. 1.8 Cartoons showing the effect of magma chamber morphology on magma extraction patterns during eruption. a) Flat-roofed chamber of wide lateral extent, in which magma of composition x overlies magma of composition y. 1. Stable interface between magmas before eruption. 2. Eruption begins; magma x is erupted; interface is deformed as magma is drawn into conduit. 3. Interface is drawn into conduit, and magmas x & y are erupted together, forming a heterogeneous pumice deposit containing banded tephra. b) Tall, narrow, pipe-like chamber containing magmas x & y as before (facing page). 1. Stable interface before eruption. 2. Eruption begins; upward flow of magma draws interface towards surface. 3. Eruption continues; interface drawn into conduit when most of x is exhausted. 4. Magma y erupted after x, and a zoned pumice deposit is formed.

b)

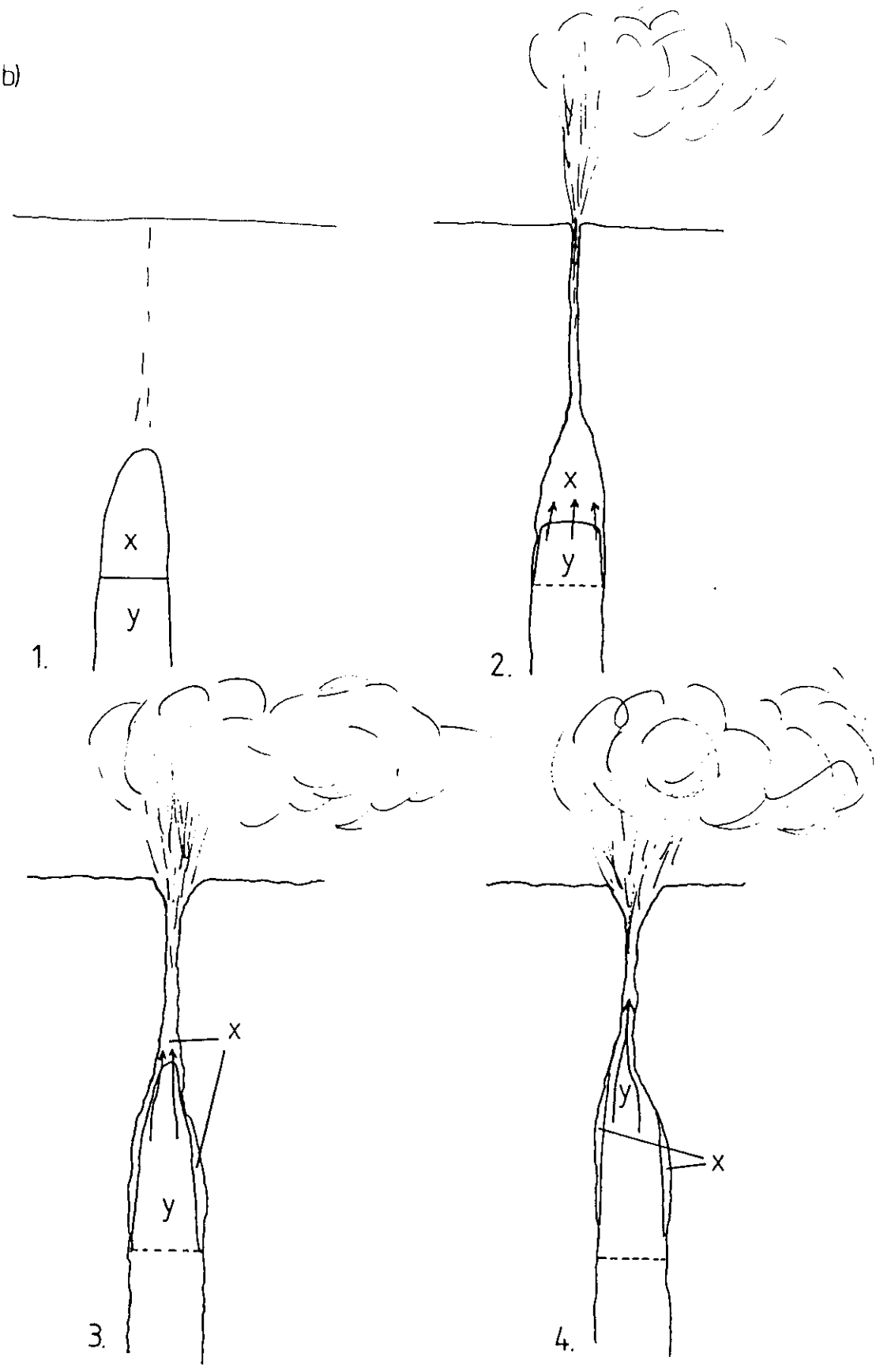

magma chamber may account for the existence of both sharply-zoned deposits and chaotically mixed deposits (I.3 and Chapter III).

Fragmentation of magma

Salic pumice deposits usually contain a few percent or less of phenocrysts, although the mode is difficult to estimate accurately by conventional methods. Completely aphyric deposits are not found on Tenerife.

The presence of phenocrysts in pumice introduces another mechanism for producing geochemical variation by eruptive processes, due to the respective grain-size distributions of pumice clasts and phenocrysts. The primary grain-size distribution of fragmented magma has been estimated by Sparks and Wilson (1976) and is shown in Figure 1.9; the sizes of 98% of primary pyroclasts in a plinian eruption column range across four orders of magnitude. In contrast, a given phenocryst species typically has a size range of one to two orders of magnitude. The median diameter of Sparks and Wilson's (op. cit.) distribution is approximately 1 mm, which is finer than the maximum size typically attained by sanidine phenocrysts in the Tenerife pumices. Therefore over 50% of the total erupted mass of pumice will be automatically unrepresentative of the bulk magma composition before fragmentation. It should also be pointed out that a large phenocryst in a pumice clast of 1 cm diameter or less accounts for a substantial fraction of the dense rock equivalent (D.R.E.) volume of the clast. These problems may be surmounted by sampling large clasts (say >5 cm diameter), if such are available.

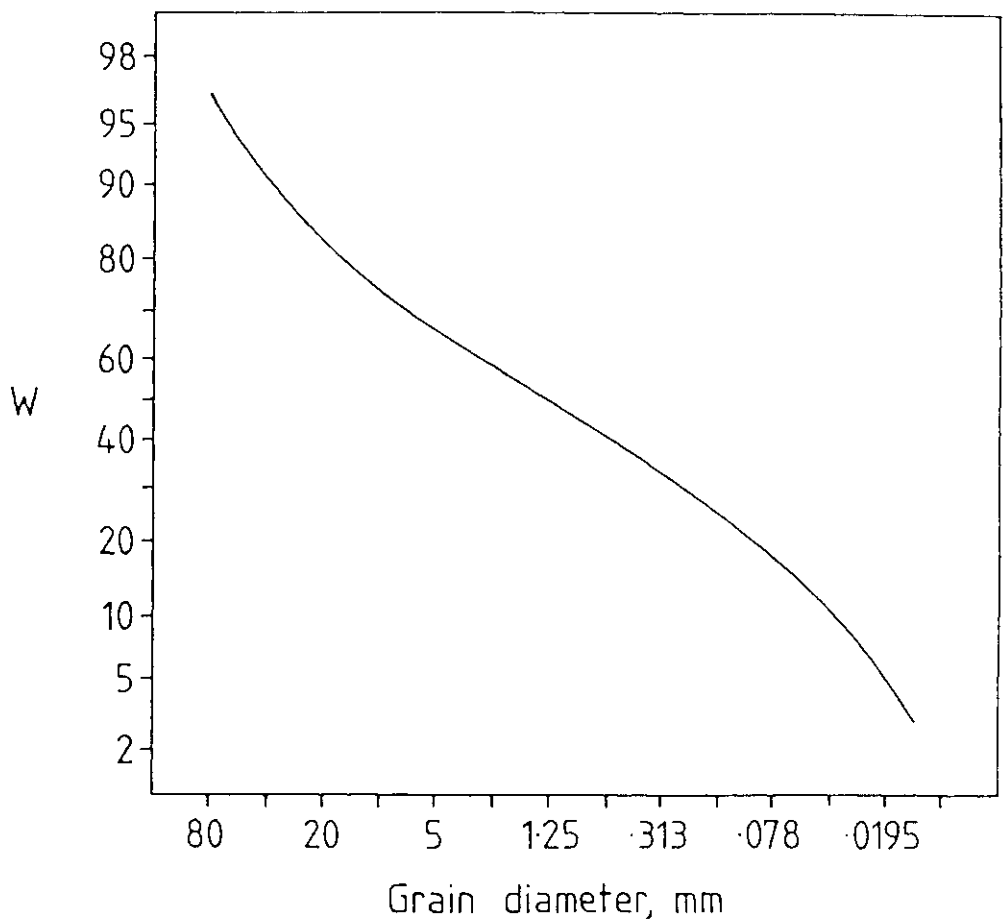

Fig. 1.9 Grain size distribution in a plinian eruption column, after Sparks and Wilson (1976). W is the cumulative weight percentage of particles smaller than a given diameter, plotted against that diameter.

An additional factor is the way in which magma fragments to form pumice. Fragmentation will be partly controlled by the distribution of points of weakness in the magma such as are provided by phenocrysts; hand-specimen examination of porphyritic pumice clasts shows that larger than average vesicles are associated with phenocrysts, presumably since they form sites for bubble nucleation. Thus phenocrysts are preferentially released during fragmentation as free crystals, resulting in apparently aphyric pumice in the finer size grades. (An analogous process may be observed when pumice clasts are artificially cleaned of adhering material by abrasion).

It may be shown that

$$s = d(m^{-1/3} - 1)$$

where s is the average distance between phenocrysts, d is the average diameter of phenocrysts, and m is the volume fraction of phenocrysts in pumice. The relationship is shown graphically in Figure 1.10. Pumice clasts with diameter $< s$ will have suffered serious depletion of phenocrysts. The effect of a maximum degree of depletion occurring in sizes greater than s may be estimated as follows. Assuming that all crystals at the surface of a spherical clast are lost, then the volume of totally depleted material is

$$4/3\pi \left(D/2 \right)^3 - 4/3\pi \left(D/2 - s/2 \right)^3$$

where D is the clast diameter.

This reduces to

$$\frac{\pi}{6} \left(D^3 - (D-s)^3 \right)$$

and the volume of undepleted material is $\frac{\pi}{6}(D-s)^3$.

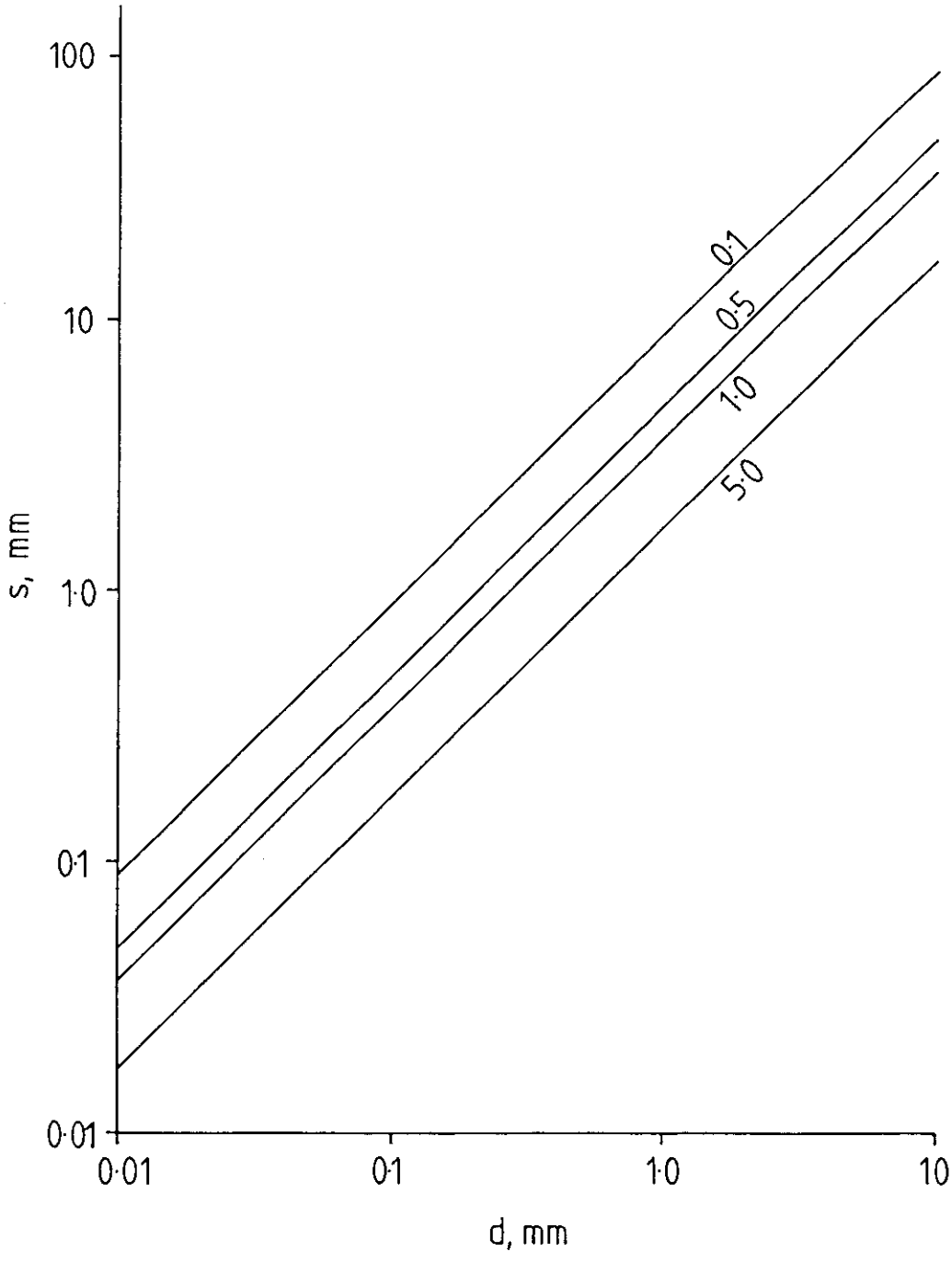

Fig. 1.10 Relationship between average diameter of phenocrysts (d) and spacing between phenocrysts (s) in pumice for four values of the volume abundance of phenocrysts in %.

The masses of depleted and undepleted material are then respectively

$$\rho \frac{\pi}{6} \left(D^3 - (D-s)^3 \right) \quad \text{and} \quad \frac{\pi}{6} (D-s)^3 \left(m(\rho'-\rho) + \rho \right)$$

where ρ = density of pumiceous glass ($\simeq$ bulk pumice density for small m) and ρ' = density of the phenocryst assemblage. Now if the concentration of an element x in the glass is C_x, then its concentration in the phenocryst assemblage is $K_x C_x$, where K_x is the partition coefficient between glass and phenocrysts. The bulk concentration of the element in the porphyritic glass is

$$(1-m)C_x + mK_xC_x = C_x \left(1+m(K_x-1)\right) \qquad 1.$$

Therefore the total mass of the element in the pumice clast is

$$C_x \rho \frac{\pi}{6} \left(D^3 - (D-s)^3 \right) +$$

$$C_x \left(1 + m (K_x-1)\right) : \frac{\pi}{6} (D-s)^3 \left(m (\rho'-\rho) + \rho \right),$$

and its concentration in the clast is

$$\frac{C_x \rho (D^3-(D-s)^3) + C_x \left(1+m(K_x-1)\right) \left(m (\rho'-\rho) + \rho \right) (D-s)^3}{\rho (D^3 - (D-s)^3) + (m(\rho'-\rho) + \rho) (D-s)^3} \qquad 2.$$

Combining (1) and (2), the enrichment, E_x, of element x in the clast due to crystal depletion is the ratio of the actual concentration to the concentration assuming no crystal loss, and so

$$E_x = \frac{\rho (D^3 - (D-s)^3) + \left(1 + m (K_x-1)\right) (m(\rho'-\rho) +\rho) (D-s)^3}{\left(1 + m (K_x-1)\right) (\rho (D^3 - (D-s)^3) + (m(\rho'-\rho)+\rho) (D-s)^3))}$$

This satisfies the requirement that $E_x = 1/(1+m(K_x-1))$ when the clast is fully depleted, i.e. when D = s. Equation (3) is presented graphically in Figure 1.11. For incompatible elements (i.e. $K_x=0$),

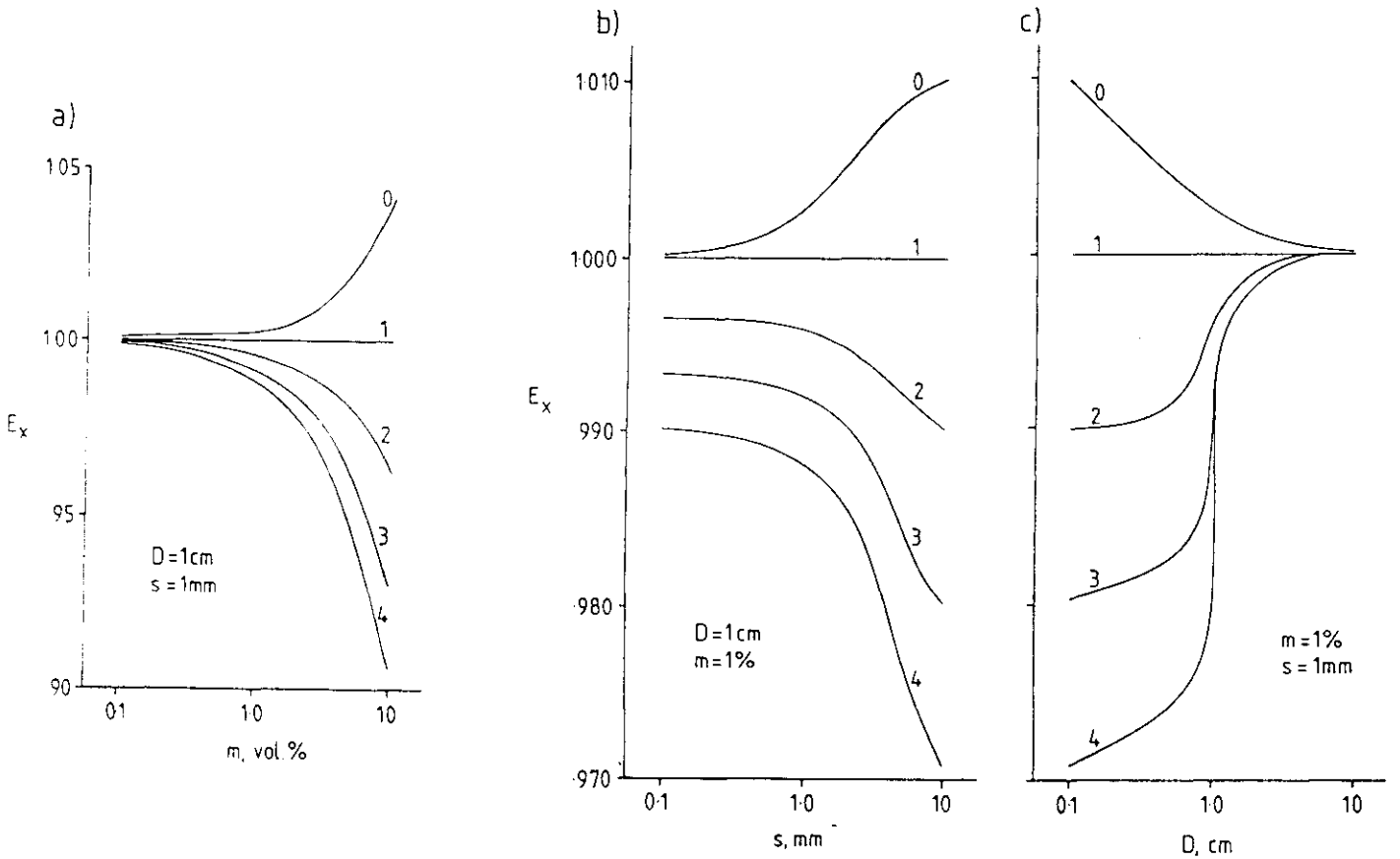

Fig. 1.11 Enrichment, Ex, of element x in a pumice clast due to crystal depletion on magma fragmentation, as a function of clast diameter (D), volume abundance of phenocrysts (m), average distance between adjacent phenocrysts (s), and solid/liquid partition coefficient (Kx). Phenocryst density and pumiceous glass density are taken to be 2.6 g cm^{-3} and 0.5 g cm^{-3} respectively. a) Ex vs s for Kx = 0, 1, 2, 3, 4. b) Ex vs D, as a). c) Ex vs m, as a).

E_x is approximately 1.05 when D=s for a 5% volume abundance of crystals, inserting typical density values. This is the maximum enrichment for an incompatible trace element in a clast with 5% phenocrysts, and is within the precision of several trace-element determinations, particularly of REE. For D=10s, this falls to 1.01, which is within the precision of all trace-element determinations reported in this thesis, and is comparable to the precision of major-element analysis. For elements which partition strongly into a mineral phase which constitutes the bulk of the phenocryst assemblage (e.g. Ba in feldspar), the effect is more serious: when K_x=3.5, m=0.05 and D=10s, E_x=0.975. In this case sampling clasts of 10s size is barely adequate to eradicate the error for some elements.

Equation (3) is undoubtedly a simplification; the phenocryst assemblage is treated as a single phase of uniform composition, vesicles in pumice are assumed to be infinitely small and evenly distributed, and pumice clasts are assumed to be spherical. However, it is considered to represent the maximum "fragmentation effect" to a first approximation, and adequate to indicate sampling requirements for whole rock analysis.

Sampling pumices of the largest available size should help to overcome fragmentation effects. There is a danger here, however. Plinian deposits commonly show reverse grading (I.2.ii - I.3), and thus phenocrysts will comprise a smaller proportion of a sample taken from the base than one from the top. Even were the magma completely homogeneous prior to eruption, sampling the coarsest material in each layer of a reversely-graded deposit might reveal a spurious geochemical trend dominated by crystal fractionation, particularly if

the finer material was within one order of magnitude of the average distance between phenocrysts. It is therefore recommended that the largest available pumices be sampled, but any apparent trends in a profile through a reversely-graded pumice fall deposit should be checked using Equation (3) or Figure 1.11.

Transport of tephra

The tranport mechanisms of the three main types of pyroclastic deposit exert different effects on their ultimate petrological constitution.

Surge deposits are not considered here, as their grain-size characteristics, for reasons noted above, usually prohibit a whole-rock approach. Sufficiently large pumices may be found in near-vent surges, however. Surges are normally very small-volume deposits (compared to fall and especially flow deposits), and their petrological importance is therefore limited.

Walker (1972) described the feature of crystal concentration in ignimbrites, a consequence of the elutriation of fine vitric ash from the eruption column and the moving flow, and concluded that whole-rock ignimbrite samples which include matrix material are of little value for geochemical analysis. Particular care in this regard should be taken with welded ignimbrites, which early workers tended to treat rather like lava flows. Pumice clasts, subject to size restrictions noted above, alone are suitable. Despite this, ignimbrites are potentially the least problematic of deposits in this regard, since they commonly contain single clasts large enough for one or

several samples. Sampling on a flow-unit by flow-unit basis will therefore reliably reveal any change in erupted composition with time. The significance of intra-flow-unit variation is difficult to assess. Wright and Walker (1977, 1980) have shown that a laminar flow mechanism may lead to vertical compositional variation within a single flow unit, whereas plug flow, as developed in some ignimbrites (Wilson, 1980) would presumably favour lateral chemical variation. Provided that individual flow units are small compared to the total volume of the ignimbrite, intra-flow unit variation may be ignored.

The atmospheric transport of pyroclasts in plinian air-fall eruptions is the most significant of all volcanological effects discussed here. Wilson (1972) has computed fall times for pyroclasts in windless conditions for a range of release heights and particle sizes. In Figure 1.12, Wilson's data are used to show the amount of material erupted between the ejection of two pumice clasts which reach the ground at the same time, and thus form part of the same layer in the fall deposit, for various combinations of grain size and release height of particles from the eruption column. The effect of grain size is particularly important (Figure 1.12), especially for low density pumices: for example, 1 km^3 DRE of magma is erupted between the ejection of a 10 cm clast and a 1 cm clast of density 0.5 g cm^{-3}, both particles being released from the top of the eruption column and reaching the ground at the same time. This volume is comparable to that of several of the Tenerife deposits (I.3), and thus any geochemical variation among the erupted products could be entirely masked by the inclusion of a wide size-range of pumice clasts in the analysed sample. Unfortunately, restriction of sample and pumice size to narrow limits may only partly overcome this effect.

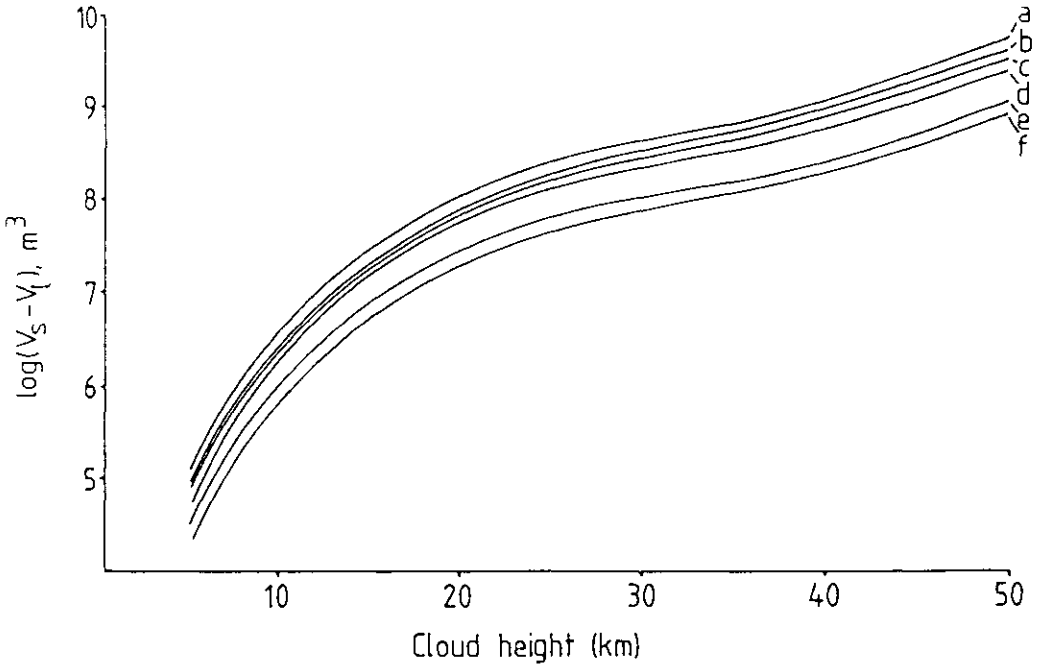

Fig. 1.12 $V_s - V_l$ as a function of eruption cloud height for pyroclasts released from the top of the eruption column, where V_l, V_s are the total volumes erupted at the ejection of a large (l) and small (s) clast respectively, the clasts reaching the ground after atmospheric flight at the same time. Curves constructed for three clast size combinations at two different densities. Labelled curves are a: 10cm/1mm clasts, 0.5 g cm^{-3}; b: 1cm/1mm, 0.5 g cm^{-3}; c: 10 cm/1mm, 1.0 g cm^{-3}; d: 1cm/1mm, 1.0 g cm^{-3}; e: 10cm/1cm, 0.5 g cm^{-3}; f: 10cm/1cm, 1.0 g cm^{-3}. Curves are calculated from the models of Wilson (1976) and Wilson et al. (1978); rise rates in the eruption column are assumed identical for all particles. Thermal efficiency of the column assumed to be 0.7 (Wilson et al., 1978).

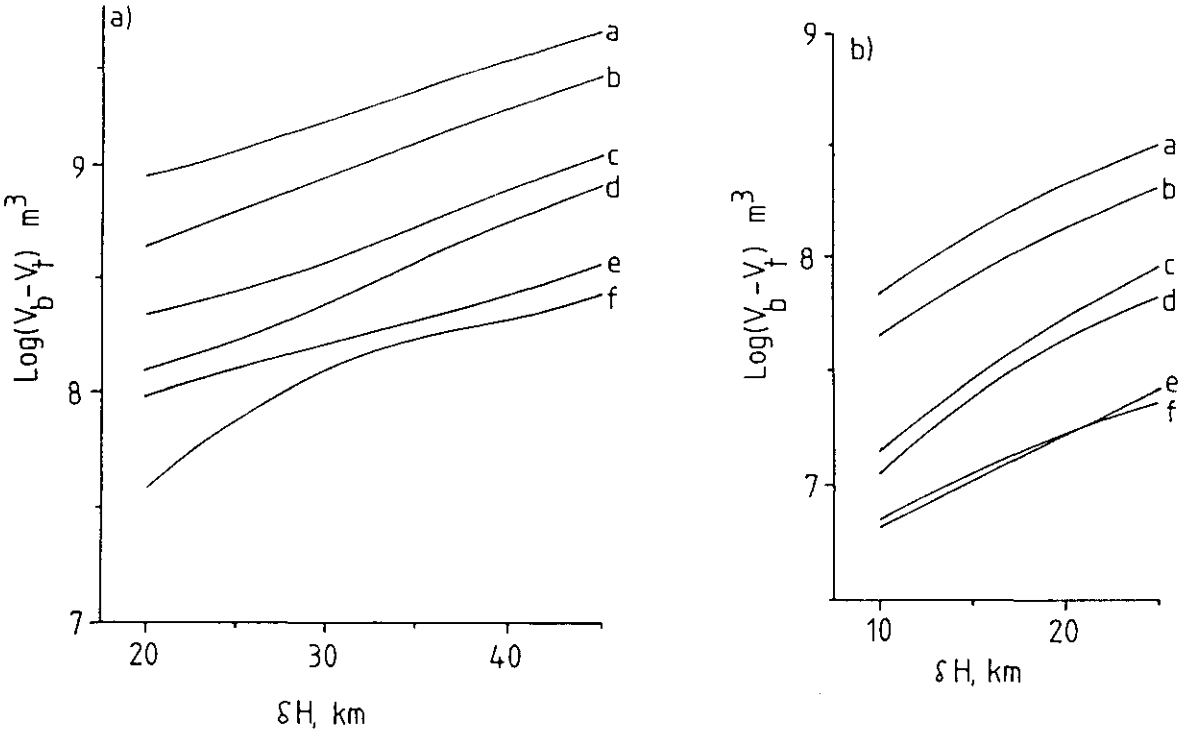

Fig. 1.13 $V_b - V_t$ as a function of release height difference (δH) from the eruption column, where V_t and V_b are the total volumes erupted at the ejection of pyroclasts t and b respectively, where t is released from the top of the eruption column, and b from lower in the column, for a range of clast sizes and densities. a: 1mm clasts, 0.5 g cm^{-3}; b: 1mm, 1.0 g cm^{-3}; c: 1cm, 0.5 g cm^{-3}; d: 1cm, 1.0 g cm^{-3}; e: 10cm, 0.5 g cm^{-3}; f: 10cm, 1.0 g cm^{-3}. Fig. 13a) is for a 50km high column, corresponding to a volumetric eruption rate of $10^6 m^3 s^{-1}$. Fig. 13b) is for a 30km high column, corresponding to a volumetric eruption rate of $10^5 km^3 s^{-1}$. Curves calculated from the models of Wilson (1976) and Wilson et al. (1978), assumptions as in Fig. 1.1 .

During a plinian eruption, clasts are released from the sides of the column at all heights above the vent up to the top of the column. Clearly, the fall time of a clast released from part-way up the column will be less than that of an identical clast released at maximum column height. A considerable volume of magma may therefore have been erupted between the ejection of two pumice clasts of identical size found in the same layer of an air-fall deposit. This volume may again be up to 1 km^3 DRE for 1 cm pumice clasts, at a volumetric eruption rate of 10^6 m^3 s^{-1} (Figure 1.13a) (equivalent to a column height of 50 km, Wilson et al., 1978). For 10 cm clasts, this reduces to 0.15 km^3 DRE. The effect is therefore less serious for large, dense clasts; neither is it so marked in less intense eruptions where column heights are lower (Figure 1.13b). Clasts which have been released from very low in an eruption column may be avoided by sampling at some distance from source, however, this places a limit on the maximum grain size which can be sampled.

Recommendations for geochemical sampling of pyroclastic deposits

Pyroclastic surge deposits are, in general, too fine-grained to permit meaningful whole-rock analysis, not only due to magma extraction and fragmentation effects, but also because of their susceptibility (on Tenerife at least) to post-emplacement alteration; for example, the Tenerife surge (I.3), which is excellently exposed over an area of several hundred square km, is found as a loose deposit in a very few localities. Surges exhibit an extreme development of the crystal-concentration process, and bulk sample composition will therefore bear little relation to the magma chemistry. Whole-rock analysis is therefore not recommended as a method of studying surge petrology.

Ignimbrites show a similar propensity to alteration but, on Tenerife at least, unconsolidated material can usually be found. Ignimbrites commonly consist of several flow units, and, depending on the relations between eruption sequence and flow emplacement, it may be possible to trace geochemical variation through the ignimbrite. Variation within a single flow unit may also occur (Parker, 1979; Wright and Walker, 1977, 1981), presumably where individual flow units are a large fraction of the total erupted volume. Ignimbrites frequently contain large juvenile fragments ($\lesssim$1 m), thus enabling the effects of magma extraction and fragmentation to be overcome by careful sampling. In this regard, unaltered ignimbrites lend themselves to whole-rock analysis more readily than other types of deposit.

The sequence of pumice emplacement in a plinian fall deposit may bear little relation to the sequence of ejection in a large eruption, led alone to the chemical stratigraphy of the magma chamber before eruption. However, the occurrence of compositionally-zoned falls showing a sharp upward change from salic to mafic pumice, considered to represent an inverted magma chamber stratigraphy (Chapter III), shows that this is not always the case. On Tenerife, such occurrences are restricted to comparatively small-volume deposits where the areal distribution and grain-size characteristics suggest that the eruption was of lesser intensity than the principal pumice-forming events (I.3). Heterogeneity of the major deposits, such as E and J, usually finds a more chaotic expression (I.3). In small eruption columns, the time-lag effects due to pumice size and release height are less pronounced (Figure 1.13b) and are insignificant for eruptions of sub-plinian intensity. It is the

largest, coarsest pumice deposits which must be treated with the greatest caution. In general, the selection of large, dense pumices with a restricted grain-size range should best overcome the effects of magma extraction, fragmentation and transport. Where this is not possible, the effects of these processes should be carefully considered before pumice chemistry is related to magma-chamber chemistry.

In summary, physical processes of eruption may result in a rather complex relationship of final pumice deposit to original magma. Whole-rock analysis, by its very nature, records the result of all processes which have participated in the formation of the final rock. Some of the problems discussed here may be circumvented by analysis of separated crystal-free (originally glassy) matrix from pumice clasts, and electron microprobe analysis of glass and phenocrysts. Probe analysis was chiefly employed in this study where there was hand-specimen evidence of heterogeneity, and to deduce information about the magmas, such as temperature, unobtainable by other means (Chapters III and IV). Care was taken during sampling to follow the guidelines laid down here. The geochemical profile in the deposit studied in most detail (G) is not believed to be a sampling artefact (Chapter II).

I.3 FIELD CHARACTERISTICS OF THE TENERIFE PUMICE SERIES

In this section the general stratigraphic relations of the principal members of the pumice succession of south and east Tenerife are described and discussed, together with the specific internal characteristics displayed by each horizon, especially at sampling localities. The content of this section relies heavily on the work

of Booth and Walker (in prep.), who began a stratigraphic and volcanological study of the succession in 1968. Using the principles of tephrochronology, these workers have identified the products of some 40 explosive eruptions in which plinian, ignimbrite-forming, and pyroclastic surge styles of activity are represented. The fifteen most prominent members have been alphabetically designated from A (oldest) to O (youngest). With one exception, these are derived from Las Canadas as indicated by isopach grain-size isopleth maps. The succession divides into two parts separated by a widespread erosion and/or thick soil horizon, the older Granadilla Series being overlain by the Fasnia Series.

In what follows, it has proved impossible to completely separate the contribution of Booth and Walker from that of the author. The overall stratigraphy and distribution of the deposits, the significance of their internal structures, and inferences concerning the progress of the individual eruptions, are entirely due to Booth and Walker. Specific field observations reported here, and sections logged through the succession at sampling localities, are the author's work but most of the logged sections had previously been visited by Booth and Walker. Fieldwork around the Adeje area, and on the sub-Granadilla Series section, was carried out by the author alone.

I.3.i General aspects

When considered in the context of ocean island volcanism, the phonolitic pumice deposits of Tenerife are of impressive dimensions. Most of the plinian deposits are an order of magnitude more voluminous than pumice falls in the Azores (Booth et al., 1978; Self, 1976) and

are comparable to the airfall products of calc-alkaline volcanism (e.g. Walker et al., 1981; Wilson, 1977; Bloomfield et al., 1977). The eruptions were likewise of extreme violence, as evidenced by the frequent occurrence of 20 cm pumice clasts at distances of 20 km from source. Eruption column heights for the most widely dispersed deposits (E, G, J and M) were probably of the order of 40-50 km. Ignimbrites are of comparable dimensions to fall deposits. The general physical features of these deposits correspond to those given in I.2.

The average frequency of big plinian/ignimbrite eruptions is difficult to assess; the two series may have accumulated over the last 70,000 years. Repose periods, as indicated by palaeosol thicknesses, vary from <1000 years to $>10,000$ years. The stratigraphic record is, however, far from complete. The distance between the Las Canadas source area and the nearest exposures is typically 10-15 km, and smaller eruptions may not have deposited a tephra layer thick enough to withstand erosion in southern Tenerife. One known example is the sub-plinian deposit of Montana Blanca at the eastern foot of Teide, which cannot be traced outside Las Canadas. Sometimes, several thin uncorrelated ashes may separate two successive major deposits; thus 5 pumice layers, mean thickness 30 cm, separate D and E at one locality. However, it appears that the Granadilla Series accumulated relatively rapidly (perhaps during ca. 10,000 years), whereas the Fasnia Series formed over a longer period. Only one reliable radiometric age date is available: carbonised wood from pumice J gives a ^{14}C age of $28,500 \pm 1580$ years B.P.

Sections through the succession at altitudes >500 m contrast markedly with those on low ground, in the absence or near-absence of ignimbrites (compare Figures 1.14a and b). This is due to the failure of pyroclastic flows to stick to the steeper slopes (ignimbrite veneer deposits (Walker et al., 1980, 1981) are only locally found on Tenerife); a coastal plain, composed mainly of ignimbrite, forms a pediment-like feature up to several kilometres wide in the south and east. Very few deposits of any type, however, are found above the 1000 m contour and thus the main areas within which fall deposits have survived erosion and ignimbrites occur are broadly similar; faster erosion rates on the steep slopes, and perhaps lack of a protective cover of indurated ignimbrite in some cases have resulted in almost total removal of pumice from the upper ground. However, several thick welded air-fall tuffs are exposed in the walls of Las Canadas, and at least one mantles the caldera wall (see Chapter VI). It is likely that some of these are near-vent equivalents of the larger deposits found on the lower slopes, but lack of intervening exposures has prohibited correlation.

An intractable local problem concerns the distinction between unwelded ignimbrites and mudflows. The undoubted ignimbrites are predominantly vitric, contain abundant pumice clasts often up to 1 m across and have well-defined flow units with clear basal layers. Lithic-enriched pipes or "fossil fumaroles" (Walker, 1972) are, however, only occasionally developed. Other examples contain an increased proportion of lithics, and those with a very high lithic content ($\geqslant$ 50%), a high proportion of large ($\sim$1 m) lithics with little or no coarse-tail grading are regarded as mudflows, especially where an ignimbrite-type flow unit basal layer is lacking or poorly developed.

Fig. 1.14 Sections at two sampling localities to illustrate inter-relations of pyroclastic units, after Booth & Walker. f = fall deposit, ig = ignimbrite, gr = gravels (black ornament). Capital letters are the stratigraphic notation of Booth & Walker, except T ig (Tajao ignimbrite).
a) Motorway km73, the sampling locality for the Tajao ignimbrite;
b) in a barranco 2km ESE of old road km60, and 3.2km NW of motorway km40. Both J ig and O ig contain abundant syenite lithics at this locality, but only O ig yields fresh syenites. G ig* may be an ignimbrite equivalent to one of the fine-grained beds near the base of Gfall seen elsewhere.

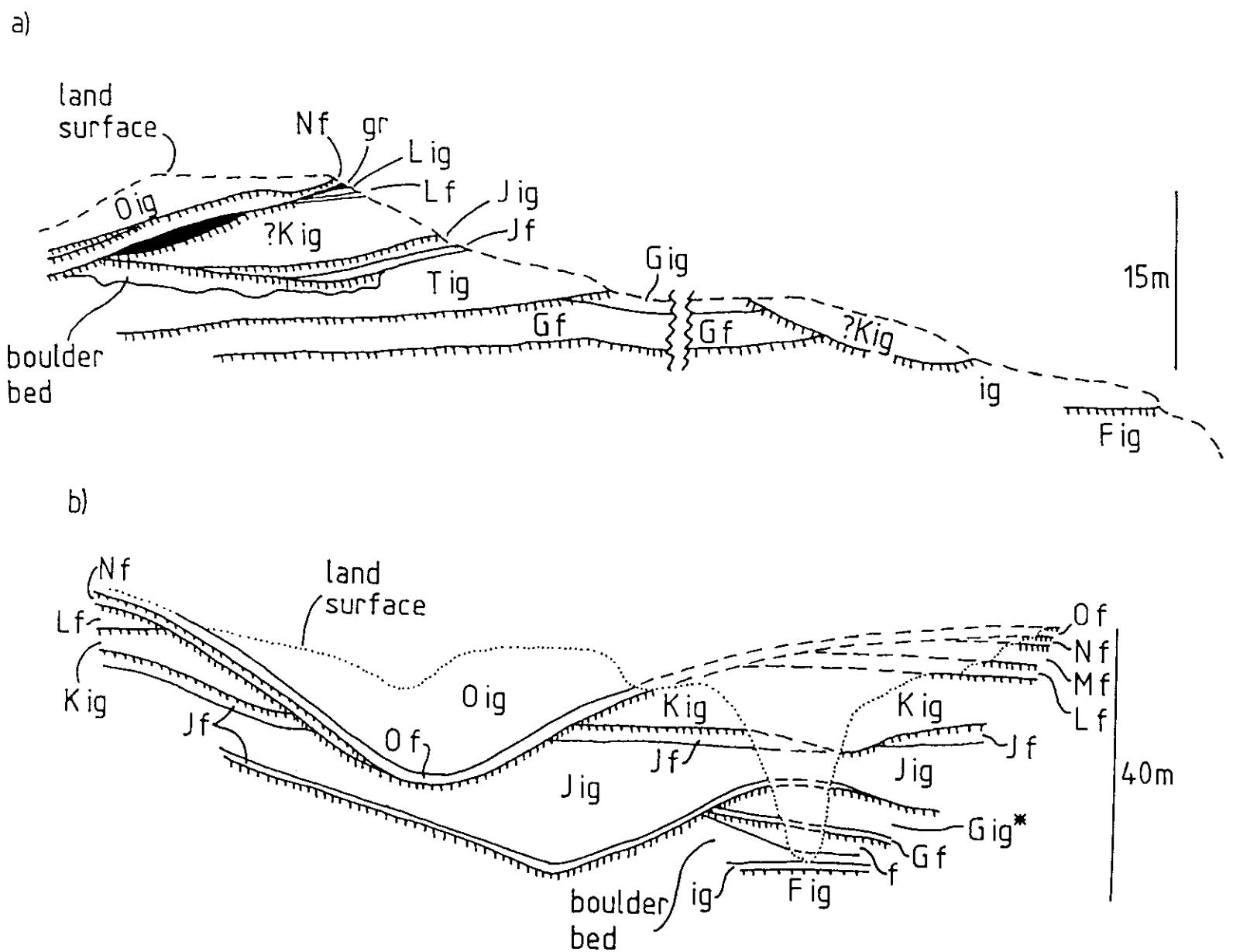
a)
land surface
Nf
gr
Lig
Lf
Jig
Jf
Oig
?Kig
Tig
Gig
Gf
Gf
?Kig
ig
Fig
boulder bed
15m
b)
Nf
Lf
Kig
Jf
land surface
Oig
Of
Kig
Jf
Jig
Kig
Jf
Jig
Of
Nf
Mf
Lf
Gig*
Gf
f
Fig
ig
boulder bed
40m

Many flows are, however, of a highly equivocal nature. The problem is intensified by the apparent close association between ignimbrites and mudflows. Several ignimbrites have mudflows as lateral equivalents; frequently ignimbrite flow units are overlain by deposits with the appearance of mudflows. Mudflows have been observed to form during historic eruptions as a consequence of torrential rain accompanying the eruption, e.g. Mayon, 1968 (Moore and Melson, 1969). The rain is the combined result of water vapour release by the eruption, the atmospheric disturbance, and the probable seeding effect of fine pumice. On Tenerife, it is likely that pumice initially deposited on the steep upper slopes provided the material for mudflow initiation; if so, the proportion of lithics in a flow would partly depend on the quantity of pumice remobilised. Thus mudflows with relatively low lithic contents could develop, and some rocks, appearing to be lithic-rich ignimbrites, could have a mudflow origin. Lithic-rich mudflows are the chief sources of nepheline syenite fragments studied in Chapter V.

Welded ignimbrites at least are undoubted examples of primary pyroclastic flows, although another problem arises in the identification of sillar. Undoubted sillar usually has a white or cream-coloured matrix in which pumices are partly or wholly altered to a golden yellow powder, composed in one case (ignimbrite) of tridymite and clay minerals (x-ray determination by B. Booth). However, the chemical alteration of fall deposits produces a similar-looking rock to sillar, although the well-sorted nature of the pumice is clear on closer inspection. Obviously such alteration will affect non-welded ignimbrites also. In this case the powder formed is usually very pale yellow, allowing distinction from sillar, although

there are again several uncertain cases. Indurated pyroclastics, collectively known as puzzolana, are much used locally as building stone, being light, strong and easy to work.

Ignimbrites are more prone to alteration than fall deposits, perhaps because the fine fraction presents a large surface area to percolating water. Surprisingly, both flow and fall deposits in the arid coastal region are much more strongly altered than at 500 m - 1000 m altitude, where the annual rainfall is much greater. Clearly water alone is not responsible for alteration of pumice; glassy ash survives almost unchanged for $>10^5$ years on the sea floor (e.g. Keller et al., 1978). In the Taupo region, New Zealand, where annual rainfall is high, pumice beds which are permanently wet are usually less altered than those which periodically dry out (C.J.N. Wilson, pers. comm.). Perhaps alteration is greatly accelerated by repeated wetting and drying of pumice.

General features of the fall deposits are their remarkably uniform appearance, poor stratification, low lithic content, and the near-aphyric nature of the pumice. Ignimbrites are commonly unwelded and consist of two or more flow units. The most continuous exposures through the succession are found in roadcuts along the 73 km long motorway which runs between Santa Cruz and Los Christianos, for the most part near the coastline. Becuase of the intense alteration in this region, very few of these exposures yield pumice suitable for geochemical work. Much superior material is found in a belt of largely artificial exposures which runs through the towns of Granadilla, Arico, Fasnia and Guimar, joined by a much older main road. Prominent kilometre posts on both roads (Figure 1.15) greatly

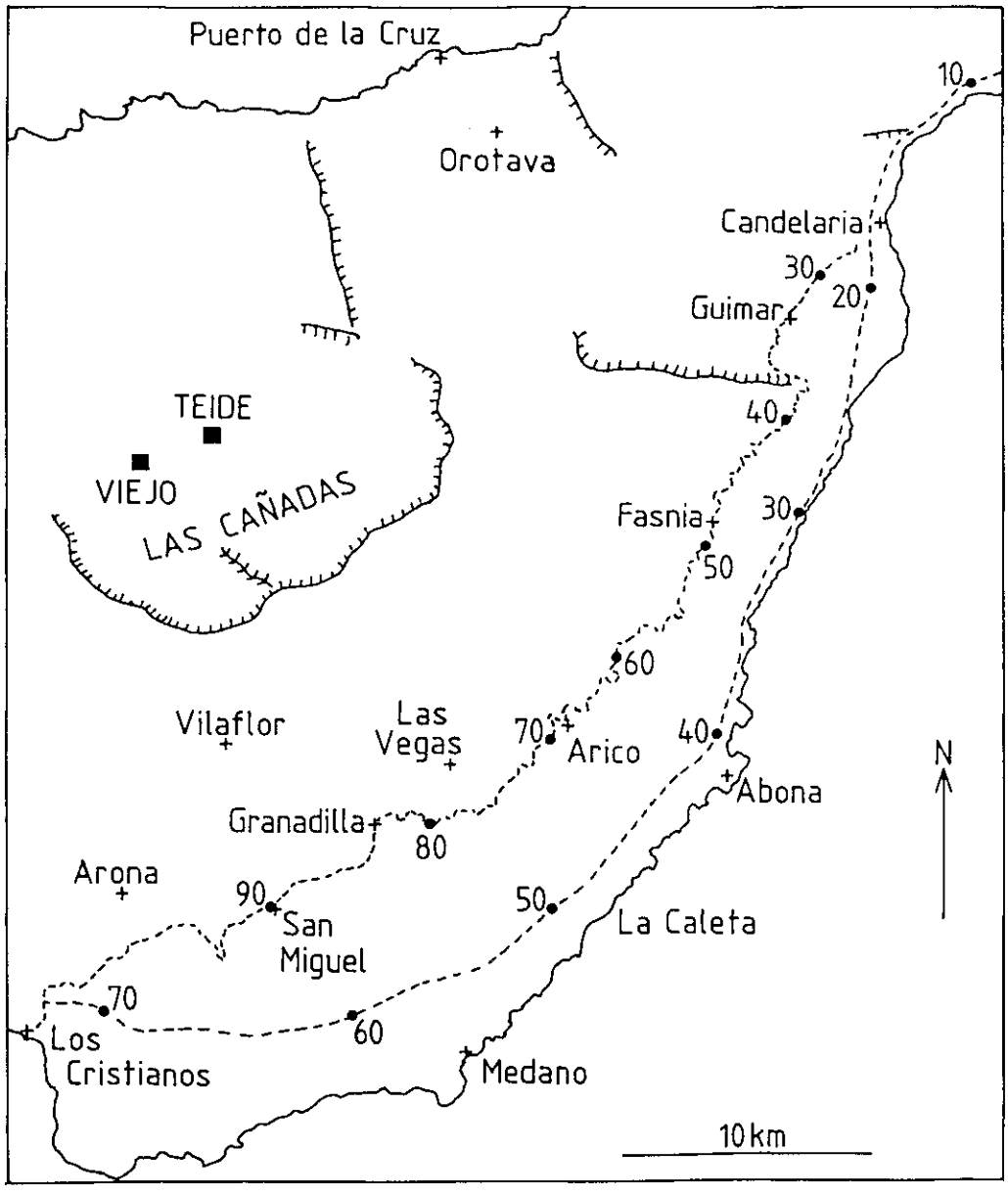

Fig 1.15 Location map of SE Tenerife, showing 10km intervals on the old road (zig-zag dotted line) and the motorway (smooth dotted line near the coast). Scarps bounding Las Canadas, the Orotava valley, and the Guimar valley are also shown.

facilitate determination of field localities. Sampling localities are shown in Figures 1.17-1.23; most are within a few km of the old road.

Volumes of several deposits are given in Table 1.2. Total erupted volumes of widely-dispersed fall deposits are difficult to assess owing to the very considerable quantities of fine ash released during eruption, much of which drifts to distances of several tens of kilometres from source. The preservation potential of thin beds of fine ash is very low, and, on Tenerife, deposits can rarely be traced beyond the 25 cm isopach. To take the fine ash component into account, the author has used a method which depends on the assumption that the products of all plinian eruptions have a broadly similar grain-size distribution. In his study of the Taupo pumice deposit, New Zealand, Walker (1980) employed an independent crystal concentration method to yield the total volume, then drew a straight-line extrapolation of the mapped portion of the deposit on an "area" plot (Figure 1.16) out to an arbitrarily-chosen limiting thickness of 1 μm to satisfy this volume. Subsequently, Walker (1981) treated two other plinian deposits in the same fashion and found that the required extrapolations had virtually identical slopes.

It is important to note that the limiting thickness of 1 μm has no particular significance, but simply that a particular combination of limiting thickness and line slope is required to satisfy the independently-deduced volume. Accordingly, Walker et al. (1981) and Wolff and Wright (1981b), in the absence of independent volume determinations, have extrapolated mapped portions of plinian deposits from Mexico and Pantelleria on an "area" plot parallel to the Taupo extrapolation, to the same limiting thickness. Integration of the area under the curve then yields the volume. The author has

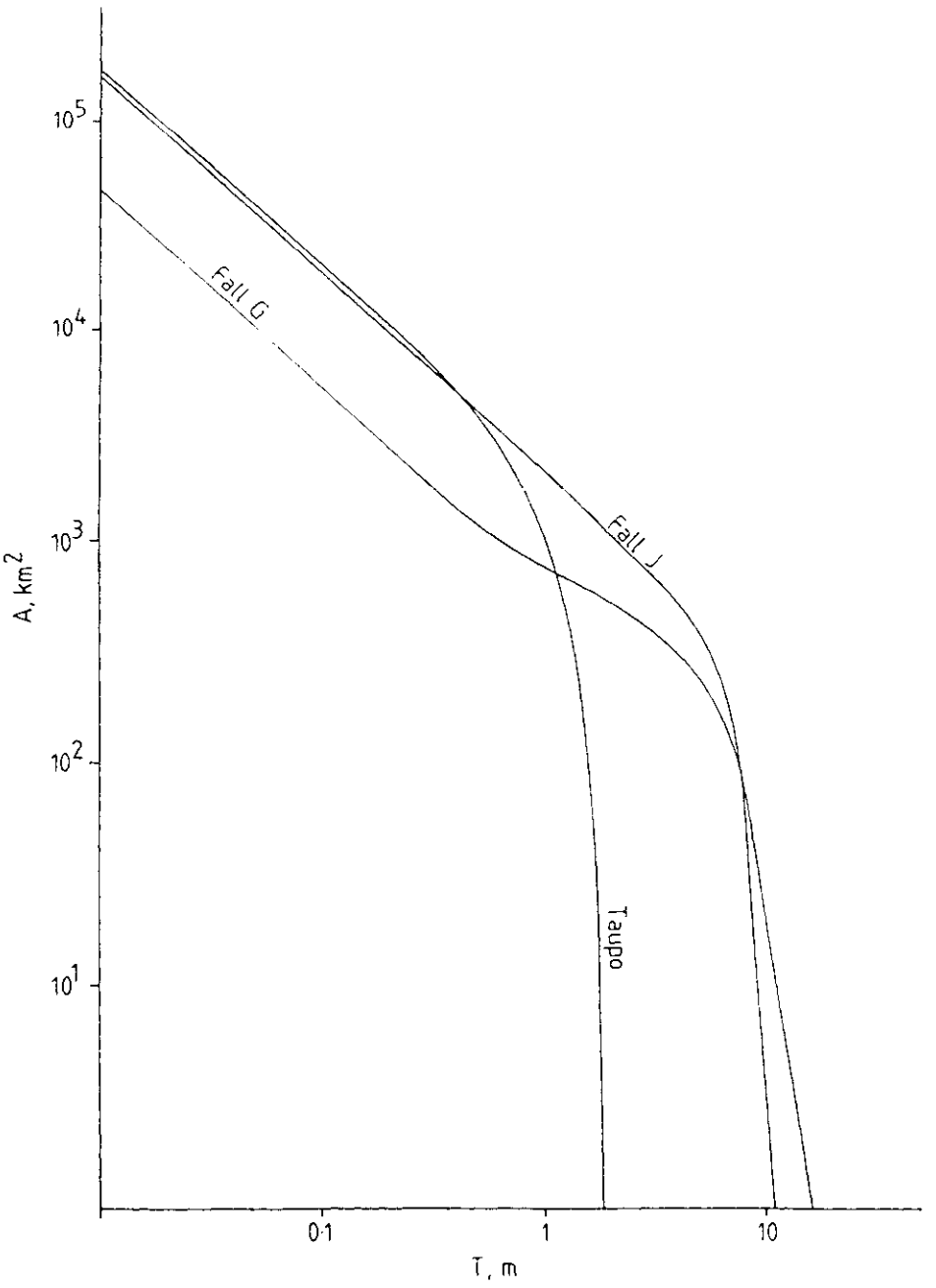

Fig. 1.16 Area vs thickness plot showing the method used to estimate total volume of each major pumice fall deposit from the field data of Booth & Walker. Each curve plots isopachs against the area they enclose; each line is then extrapolated parallel to the slope of the Taupo curve (from the independent volume determination by Walker, 1980) out to a limiting thickness of 1 μm. Curves for two deposits (G, J) are shown. Total volumes of deposits are then given by the area under each curve.

Deposit	Erupted volume (Km^3)	Dense rock equivalent volume (Km^3)
D	14	2.8
E	22	4.4
G	8	1.6
J	24	4.8
K	4.5	0.9
L	6	1.2
M	8	1.6
N	7	1.4

Table 1.2. Total erupted volumes of major pumice fall deposits on Tenerife, deduced by extrapolation of the mapped extent as described in the text. Based on field data of Booth & Walker. Dense rock equivalent volumes calculated assuming mean density of 0.5 g cm^{-3} for pumice, and of 2.5g cm^{-3} for dense rock.

applied this method to the field data of Booth and Walker to find total erupted volumes for several of the Tenerife deposits (Figure 1.16). It was first necessary to extrapolate mapped isopachs beyond the coastline, and thus the deduced volumes (Table 1.2) are only approximate, but are certainly a more accurate reflection of the quantities of erupted magma than the on-land volumes.

I.3.ii The Granadilla series

This series consists of at least twenty plinian and sub-plinian pumice fall deposits and several ignimbrites; of these, seven (designated A to G) are distinctive enough to map by the tephro-chronological methods employed by Booth and Walker.

The lowest, A, is exposed around Las Vegas, and is the best example of a compositionally-zoned deposit in the series. At the sampling locality (Figure 1.17) it consists of 60 cm of white phonolitic pumice overlain by 10 cm of black trachyandesitic pumice. The transition is sudden, although the mafic tephra contains approximately 5% of phonolitic pumice and a small proportion of streaky black-and-white tephra. Any sign of an eruption break associated with the transition, such as a grain-size discontinuity, a fine ash, lithic-rich or erosion horizon is entirely lacking, and the layering is therefore attributed to the continuous eruption of a compositionally-zoned magma from a single vent (further discussed in Chapter III).

Fall deposit B, up to 1.5 m thick, is well-stratified, consisting of five coarse pumice beds separated by thin fine ash layers; it occurs chiefly in the Fasnia region. The relatively minor fall C (maximum thickness 0.3 m), dispersed over a similar area, is

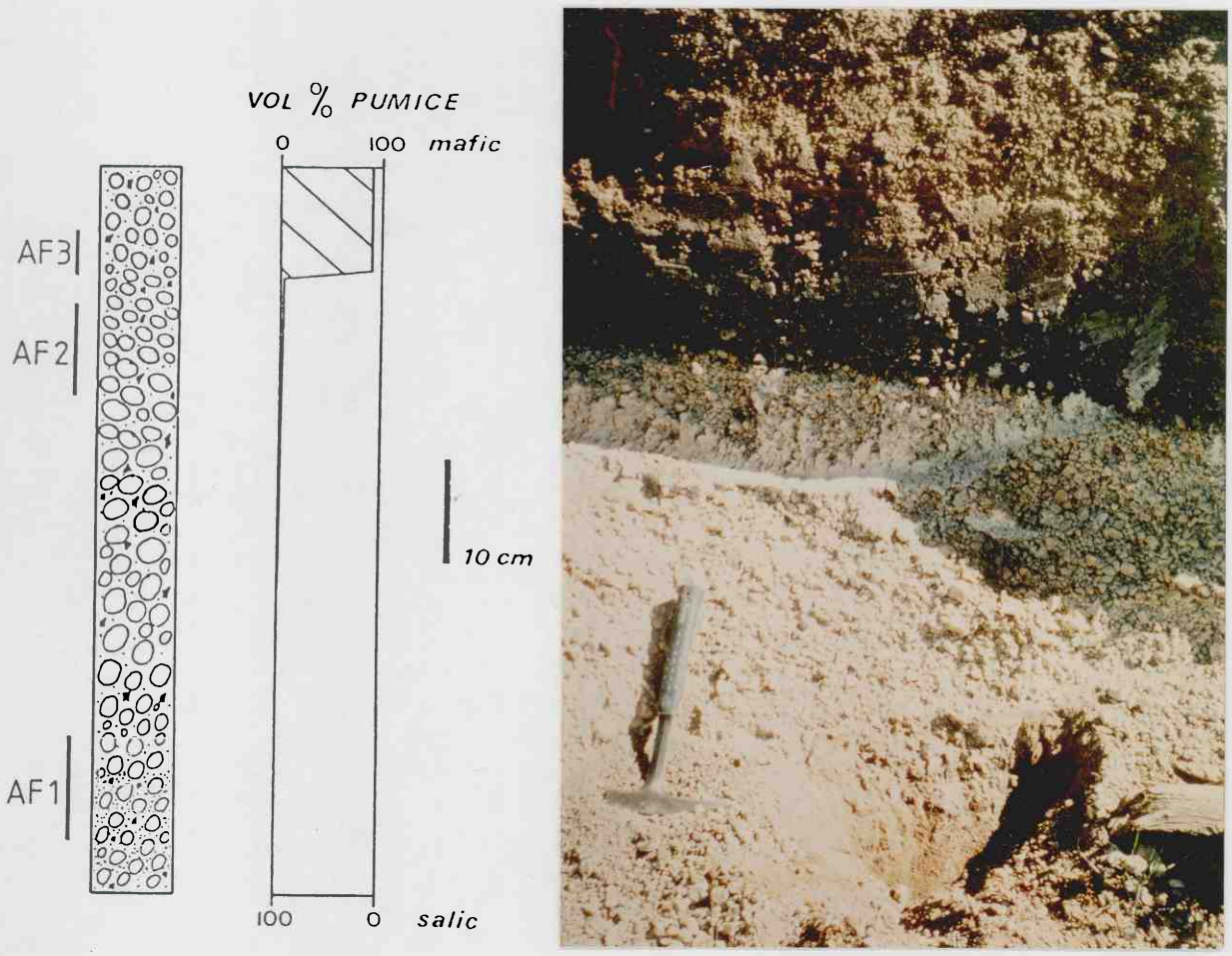

Fig. 1.17 Section through pumice fall A at the sampling locality, showing variation in mafic pumice content and the positions from which samples were taken (vertical bars labelled with sample numbers). Photograph depicts A at this locality; note the upper 10cm of mafic pumice immediately underneath the brown soil. The small pit at lower centre exposes the underlying soil (light orange-brown), the surface onto which A was deposited.

Fig. 1.18 Isopach map, contoured in m, of fall deposits D and E (from the data of Booth & Walker), and sampled sections through these deposits at the point marked D, E. Samples indicated by vertical bars against sections. Mixed pumice from ignimbrite E (see Chap. III) was sampled at the point marked E, illustrated in the photograph. Photograph depicts a road section through the two flow units of ignimbrite E resting on fall E (notebook is positioned nearly half-way up lower flow unit). Note that the upper surface of the lower flow unit is sub-parallel to the upper surface of the fall deposit, suggesting that this unit is in fact an ignimbrite veneer deposit (C.J.N. Wilson, pers. comm.). Note also the very steep erosional truncation of the section on the right of the photograph.

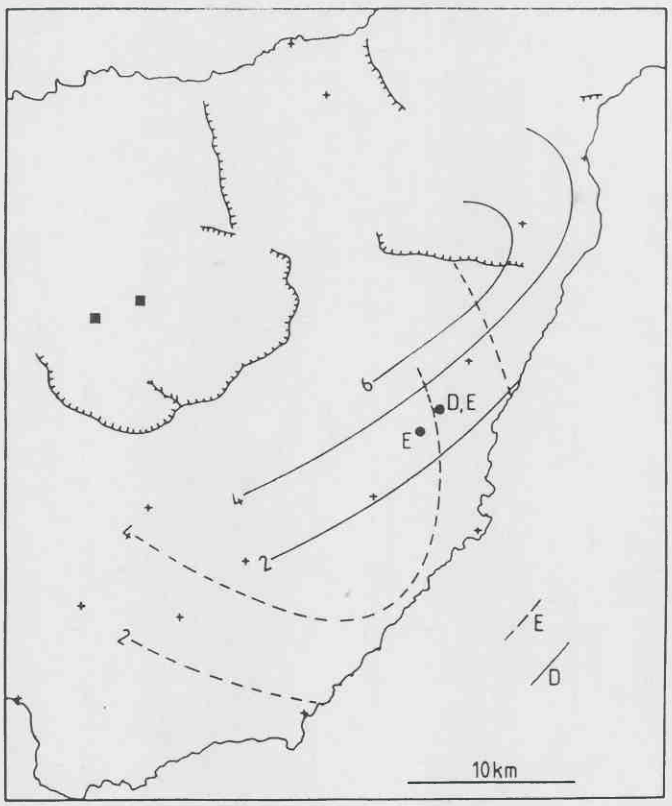
6
4
2
4
2
D,E
E
E
D
10km

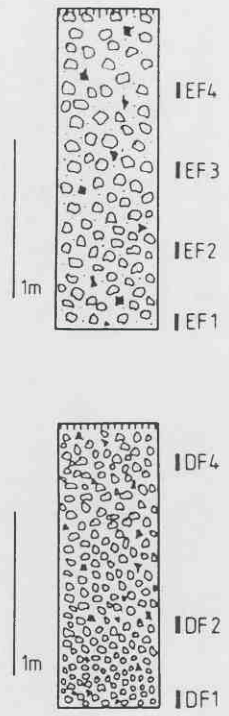
EF4
EF3
EF2
EF1
1m
DF4
DF2
DF1
1m

conspicuous on account of the abundance of lithics in its upper part. B and C were omitted from geochemical study, as exposures of sufficient quality could not be found.

Pumice fall D (Figure 1.18) is one of the largest in the succession. Apart from a fine layer at the base, it is even-grained and homogeneous with a very slight reverse grading. Its maximum thickness is 6.6m on the escarpment overlooking Guimar. Its character changes little over 36 km distance, and maximum pumice size is never more than 7 cm. These features suggest a relatively distant source, probably in the westernmost part of Las Canadas. At most exposures, D has suffered alteration, typically with soluble salt deposits in pumice vesicles. A comparatively thin exposure (1.7 m) was perforce selected for sampling; it lies approximately on the 3 m isopach (Figure 1.18), and thus the upper half may have been removed by erosion.

Fall E (Figure 1.18) is likewise very widespread, but is much coarser (maximum pumice size 25 cm) and more poorly sorted than D. E is easily recognised in the field due to the relatively high content of platy feldspar crystals up to 4 mm long. The poor sorting and lack of a well-defined dispersal axis (Figure 1.18) point to eruption in near-windless conditions. At one locality, the fall is overlain by non-welded ignimbrite E, consisting of three well-defined flow units. The tendency for the upper surface of the lower flow unit to partly follow the previous topography (Figure 1.18) suggests that it may actually be an ignimbrite veneer deposit (G.P.L. Walker and C.J.N. Wilson, pers. comm.). The uppermost few cm of the plinian deposit yields rare clasts of banded and dark pumice;

this is, however, much more abundant in the overlying ignimbrite. The two components are chemically distinct (Chapter III), the mafic being less evolved. Wolff et al. (1980) have suggested that the appearance of a less evolved and relatively volatile-poor magma in the eruption column may have influenced the transition from plinian to ignimbrite-forming activity.

Several thin falls, including a compositionally-zoned deposit similar to A, occur above E. The next significant member is the brown ignimbrite F, unusual for south-eastern Tenerife in having a densely welded zone. F is well-exposed near Arico, where it infills a pre-existing barranco; a new barranco has been cut into its surface, affording good sections through the ignimbrite. This is one of the "eutaxite" localities originally described by Fritsch and Reiss, 1868 (see Chapter VI). Here a non-welded base grades upwards into densely welded ignimbrite with fiamme over a vertical height often less than 1 m. The coarse juvenile component consists of dense phyric obsidian and pumice, with all vesicularity gradations between. Occasional clasts with alternating dense and pumiceous bands are found. Several large blocks have apparently produced thermal aureoles $\simeq$2 cm wide in the surrounding matrix, although a similar effect is seen with some lithic fragments. Lithics of vesicular, phyric and aphyric phonolite are common. The flow exhibits spectacular coarse-tail grading as a downward enrichment in lithics and dense juvenile fragments up to 1 m in diameter (Figure 1.19). F is frequently exposed along an 8 km length of the motorway, suggesting that the pyroclastic flow fanned out on reaching the coastal plain. Welding is less pervasive here and up to 3 flow units, indistinguishable at Arico, are seen. Associated torrent/mudflow deposits rich in rounded obsidian fragments occur in this area. An ignimbrite closely

Fig. 1.19 Welded ignimbrite F resting on the weathered surface of an aa lava flow at Arico. Note the well-developed coarse-tail grading apparent in the concentration of large dense blocks toward the base of the unit. The sub-angular to rounded dark blocks are juvenile obsidian fragments. The ignimbrite passes upwards from pale, non-welded lithic-rich pumice to densely welded tuff with a deep thermal colouration at the top of the exposure. Flow-unit boundaries have not been identified with any certainty in this section.

similar to F (the Pilas ash flow of Ridley, 1967) occurs on the rim of Las Canadas directly upslope from Arico (11 km distant). This flow has not been positively identified as F, but F can be traced continuously in the inaccessible walls of a deep barranco for a few km upslope from Arico, and a correlation is probable. Thus despite the absence of an associated airfall for which an isopach map can be drawn to indicate vent position, a Las Canadas source for F seems likely. F has been the subject of previous petrological studies by Fuster et al. (1968) and Schmincke and Swanson (1967b). It is described here chiefly on account of the presence of abundant non-vesicular juvenile clasts, which, on Tenerife, appears to be peculiar to densely welded ignimbrites (see Chapter VI).

A number of non-welded ignimbrites, including a mixed-pumice deposit, occur between F and the next member, G. Fall deposit G (the Granadilla Pumice) is the best-exposed in the succession, being quarried in several pits around Granadilla. It has been described in detail by Booth (1973). Overall the deposit is reversely graded with a stratified lower part. An exposure 2 km E of Granadilla, lying on the dispersal axis, was selected for sampling (Figure 1.20). Here all four fall units of Booth (1973) are clearly displayed. Fall unit 1, 17 cm thick, rests on a heavy soil (Figure 1.20). Pumice in the basal 2 cm is dark grey and compositionally distinct from the remainder of the deposit (Chapter II); partially disaggregated small mafic crystalline inclusions are common in this dark tephra. Fall unit 1 is restricted to a few km either side of the dispersal axis. Its upper boundary is marked by a fine-grained band which may be a rain-flush bed or possibly a co-ignimbrite ash, the lateral equivalent of an ignimbrite not seen at this locality (such fine

beds are commonly lithified, and were termed "cement-like bands" in the field). The upper surface of this band is rich in lithic sand and free sanidine crystals. Fall unit 2 exhibits a marked grain-size stratification; it is topped by another cement-like band. What could be an ignimbrite equivalent to this is exposed elsewhere (Figure 1.14b) above an airfall resembling the upper part of fall unit 2; it is non-welded and consists of up to five flow units. Immediately above the fine ash band is a lithic-rich layer, which may represent a vent-clearing episode at the resumption of plinian activity after eruption of the pyroclastic flow. Fall unit 3 is also stratified; it grades upwards into the coarse, homogeneous fall unit 4 which forms the bulk of the deposit (Figure 1.20). Unit 4 is reversely graded and the upper part contains in situ nests of pumice fragments formed by the break-up of large blocks on impact. Following the deposition of unit 4, the eruption passed into a pyroclastic-flow phase forming a widespread ignimbrite, well exposed at the sampling locality 5 km E of Granadilla. Here the ignimbrite is ponded in a depression (Figure 1.20) and consists of three or four flow units with a total thickness of 6 m. The lack of layer 3 deposits between flow units suggests rapid successive emplacement. However, partings between some flow units are marked by thin ($\sim$ 5 cm) bands of small (1-2 cm) rounded well-sorted pumice clasts, perhaps formed by winnowing of fines from bulk ignimbrite in the interval between emplacement of successive units. If so, their presence is incompatible with preservation of layer 3 ashes. Flow-unit basal layers are well-developed, and reverse grading of large pumice clasts is common. One very thin (15 cm) but distinct flow unit can only be traced for a few metres; other laterally-impersistent partings occur

Fig. 1.20 Isopach map of pumice fall G, contoured in m (after Booth, 1973), sampling section through pumice fall and ignimbrite G, and photographs depicting: (a) fall unit 1 resting on paleosol (note darker colour of basal 2cm); (b) fall unit 2, showing finer-grained central portion; (c) fall units 2, 3 and 4 with erosional remnant of ignimbrite at top (height of section is 9m); (d) ignimbrite ponding above fall deposit. Sampling section is a composite; ignimbrite was sampled a few km E of the fall, as shown on the map.

(a)

(b)

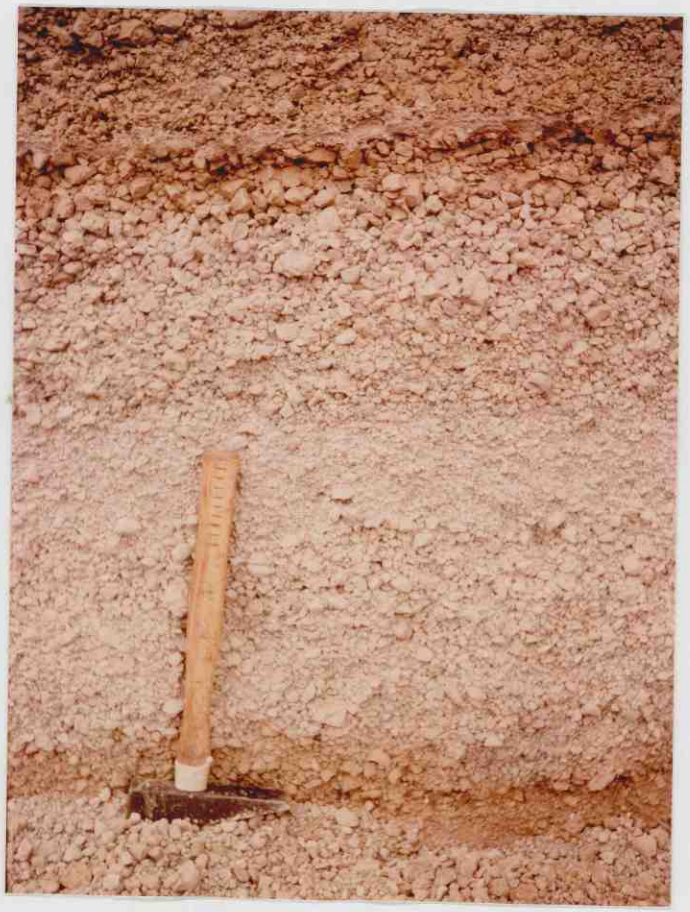

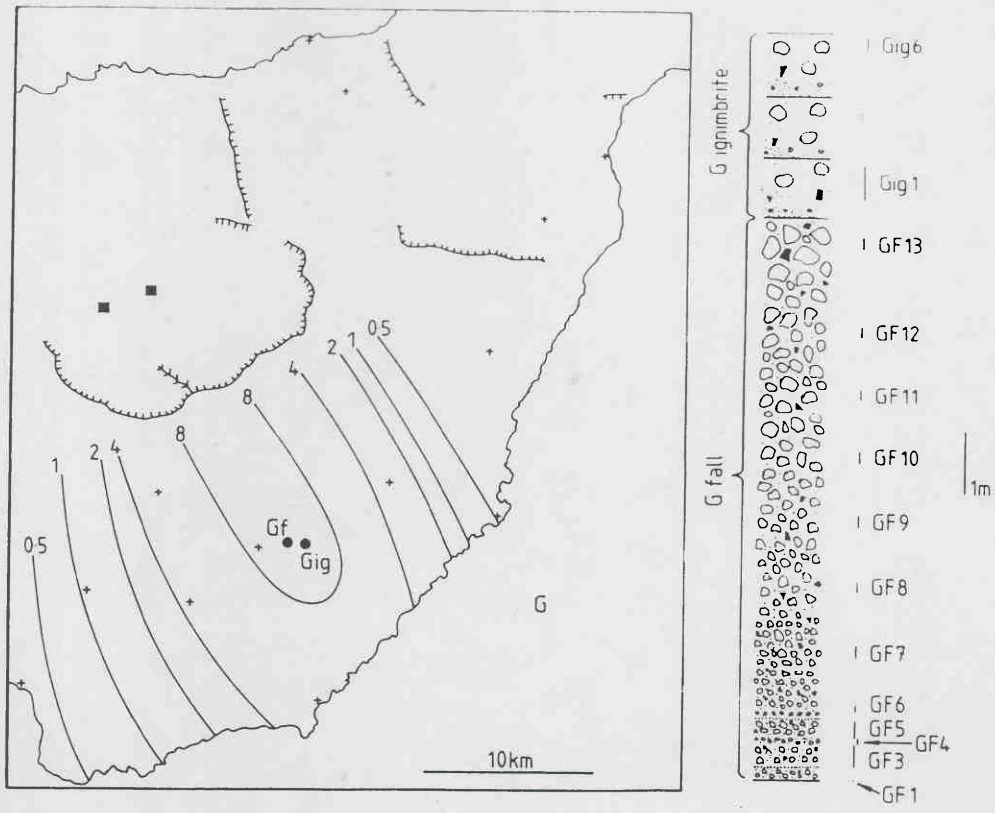
0.5
1
2
4
8
8
4
2
1
0.5
Gf
Gig
G
10km
G ignimbrite
G fall
Gig6
Gig1
GF13
GF12
GF11
GF10
GF9
GF8
GF7
GF6
GF5
GF4
GF3
GF1
1m

(c)

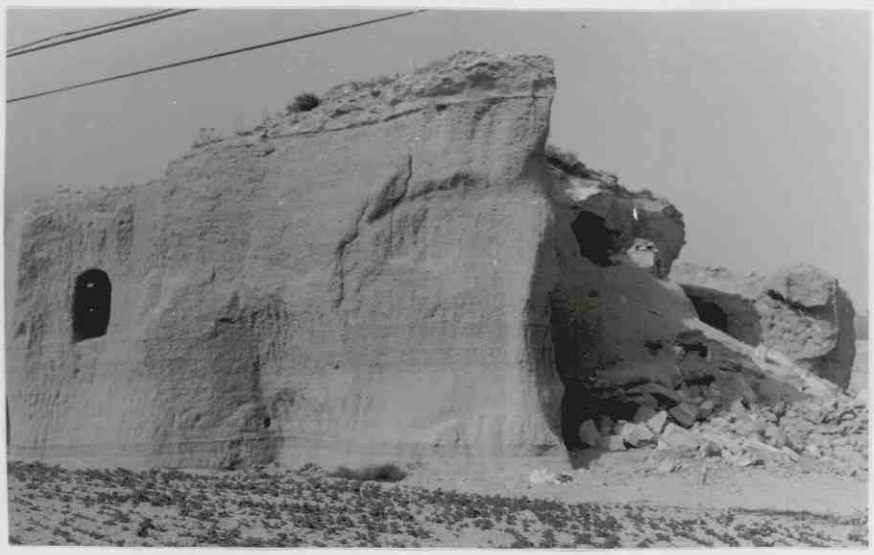

(d)

in the thick uppermost flow unit and illustrate the complex and highly localised nature of the internal stratigraphy of the ignimbrite.

The top of the Granadilla Series is formed by the Tajao ignimbrite (undesignated by Booth and Walker); it is one of the best examples of a mixed-magma deposit in the succession. Exposures are limited due to the major erosional episode separating formation of the Granadilla and Fasnia Series. At the principal exposure in a motorway roadcut (Figure 1.14a) the ignimbrite consists of a single non-welded flow unit containing streaky pumice clasts up to 50 cm size; the total proportion of mafic pumice is approximately 20%. The petrology of this ignimbrite is considered in detail in Chapter III.

I.3.iii The Fasnia Series

The Fasnia series is formed of the products of at least fiften eruptions, of a generally more varied nature than those represented in the Granadilla formation. The Series includes several prominent erosion levels and thick soils, and the average repose period is believed to have been much greater than during formation of the older group.

The lowest member, fall H, is found in the Arona-Los Christianos area. The lower part is stratified and fine-grained with several lithic sand and cement-like horizons, while the upper consists of coarse reversely graded pumice. At all exposures H is more or less heavily altered, and it was excluded from the present study. It is overlain for much of its dispersal area by a closely similar deposit derived from an explosion crater 3 km N of Los Christianos

Over most of the area the base of the Fasnia Series is marked by pumice fall J (Figure 1.21), the most distinctive widespread member of the succession, and, probably, the most voluminous (Table 1.2). J is comparatively well-stratified and contains several partings, fine ash beds, and an extensive pyroclastic surge deposit. It is petrographically distinctive due to the presence of occasional bright blue crystals of haüyne, extremely scarce in other deposits. It is generally lithic-rich; among the lithics is an unusual brown-stained rock thought to have been derived from a fumarolically-altered part of the volcano. Fulgurites are common throughout J. The basal unit is a bed of fine ash locally rich in accretionary lapilli, and containing occasional plant molds formed by the draping of damp ash over vegetation growing from the pre-existing ground surface. This is succeeded by a coarse pumice layer including a horizon rich (ca. 50%) in mafic and streaky mixed pumice, overlain by a well-stratified series of pumice, lithic-rich, and cement-like bands. The entire basal sequence has a maximum thickness of 2.7 m. Its upper boundary is marked by the pyroclastic surge, although ignimbrite and/or mudflow material is sometimes found at the same stratigraphic level. The surge has an erosive base, occasionally cutting right through the underlying sequence to the paleosol, and is frequently cross-bedded with antidune and chute-and-pool structures typical of the near-vent "sandwave" surge depositional facies of Wohletz and Sheridan (1979). The association with mudflows suggests that the surge eruption may have been accompanied by torrential rain. It may be noted that if the dynamics of the moving surge conformed to the model of Wohletz and Sheridan (1979), then the surge cloud must have travelled several tens of km out to sea. The bulk of J, above the surge, consists principally of reversely-graded coarse pumice,

Fig. 1.21 Isopach map (contoured in m), sampling section and photograph of pumice fall J. Sample locality marked by spot on map; stipple indicates areal extent of pyroclastic surge intercalated within the fall deposit. s marks surge on sampling section.

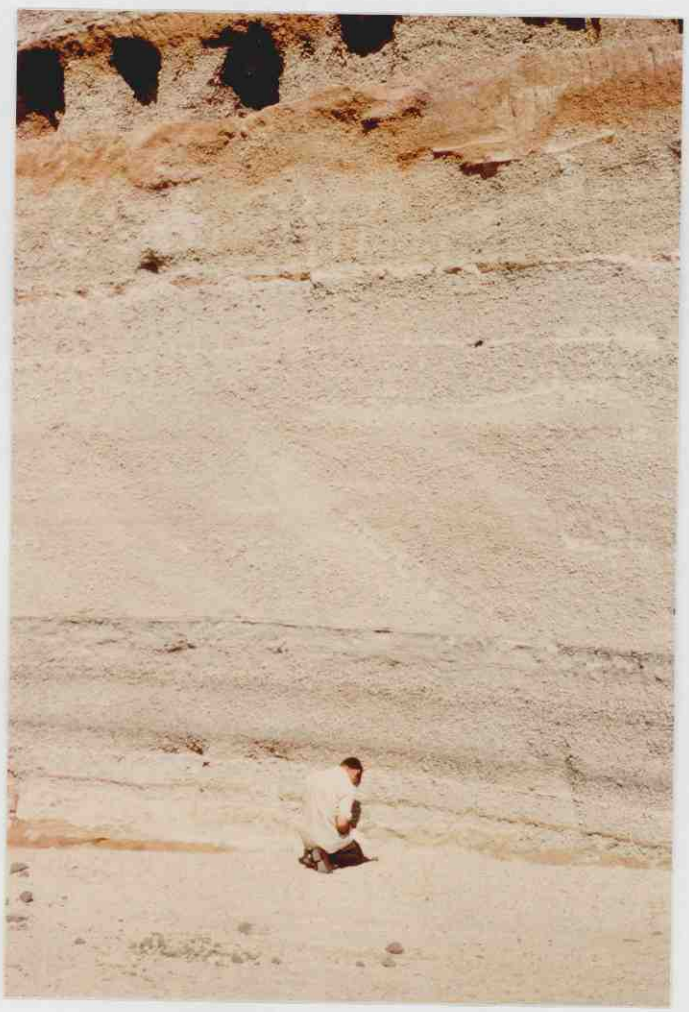

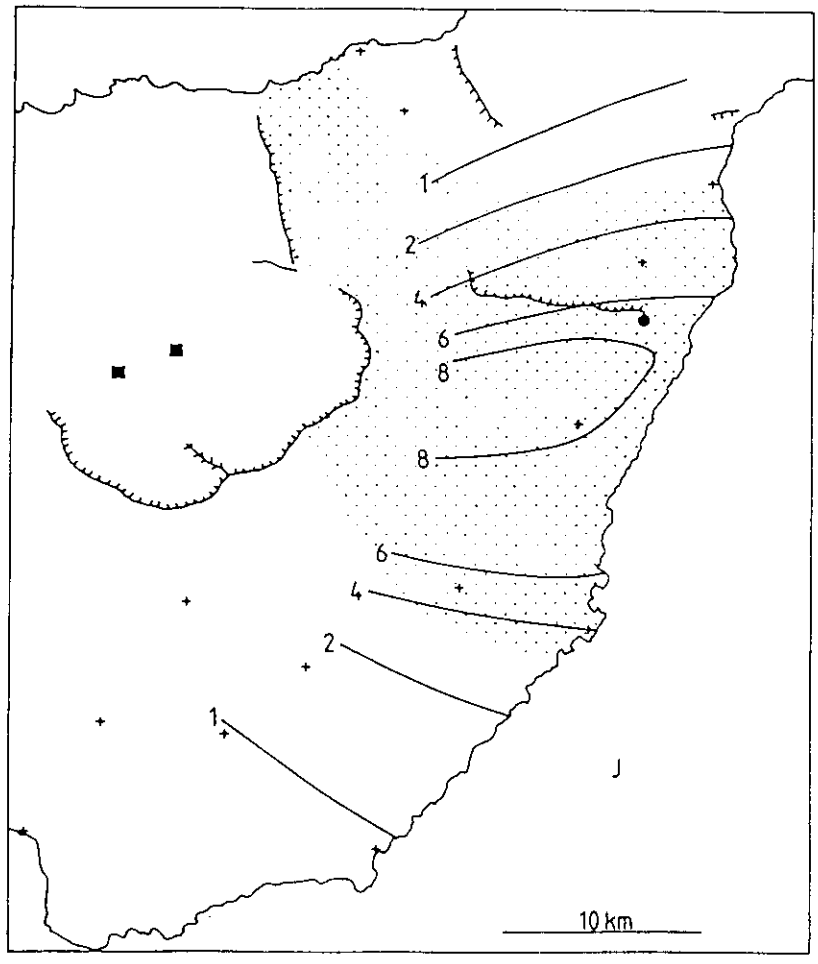
1
2
4
6
8
8
6
4
2
1
J
10 km

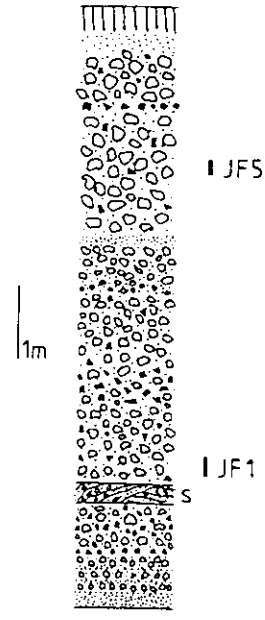
1m
JF5
JF1
S

although the upward grain size variation is rather uneven (Figure 1.21), with two thin (5-10 cm) bimodal ash horizons. The coarser mode in these is identical to that above and below, and the beds differ from the pumice fall only in having an abundant ash matrix. Elsewhere intraformational ignimbrites are found at the same stratigraphic levels, and the fine ash components of the bimodal beds are thus co-ignimbrite ashes (layer 3 deposits) which accumulated at the same time as pumice was falling from a plinian eruption column. Thus if the plinian eruption was interrupted by pyroclastic flow formation, it must have recommenced almost immediately. The main part of J contains rare streaky pumice, and an unusual juvenile fragment of partly-formed intermediate cumulate (see Chapter III) was collected from near the top. J is frequently altered, especially the sub-surge sequence, and sampling was therefore limited to the upper part. The sampling locality was close to the axis of dispersal, at the top of the scarp overlooking Guinar (Figure 1.21).

A poorly exposed mixed pumice ignimbrite separates J from the next big deposit, K. K has a fine, lithic-rich base over part of its extent; otherwise it consists of very coarse pumice. The lower part, separated from the upper by an intraplinian ignimbrite, is never more than 1.7 m thick. The ignimbrite is conspicuous in the Guimar valley, where it consists of three flow units of incipiently-welded sillar. The lowest unit contains numerous tree-molds bearing traces of carbon at several localities. The larger logs were aligned sub-parallel to flow direction; similar log alignment has been described from the Taupo ignimbrite, New Zealand by Froggatt et al. (1981). Where the ignimbrite is missing, as at the sampling locality (Figure 1.22), a bimodal ash similar to those

in J is found. The top of fall K again consists of coarse pumice which is compositionally zoned; the uppermost 20 cm of mafic pumice, best seen around Guimar, is usually incorporated into, or heavily altered by, the soil horizon which marks the top of the deposit.

Fall L has a very low lithic content and consists of pumice clasts with a rather flatter or more tabular shape than is usual. Locally a fine lithic-rich layer is seen at the base and top. The deposit is one of the few that can be traced into the north of Tenerife, and has been identified in Puerto de la Cruz.

Fall M has a distinctive internal stratigraphy. The lowest unit is a fine-grained ash with accretionary lapilli. The second and principal unit contains very coarse pumice but is never more than 2.7 m thick; furthermore the thickness shows rapid lateral variation along the old road (Figure 1.23). Taken together, these features indicate a very powerful short-lived eruption with a strong wind blowing at the time. Rare streaky mixed-magma pumice clasts are found in this unit. The top is marked by a lithic horizon. The next unit is another fine accretionary lapilli ash, which may be in part a co-ignimbrite ash related to an ignimbrite seen in a few exposures of M. The uppermost fall unit consists of coarse pumice, marking a return to plinian activity at the end of the eruption. M is the only deposit to have been identified on the rim of Las Canadas.

Stratigraphic relations above M are imperfectly known; at least nine fall deposits were emplaced after M; one of these is compositionally zoned. The principal deposit of this series,

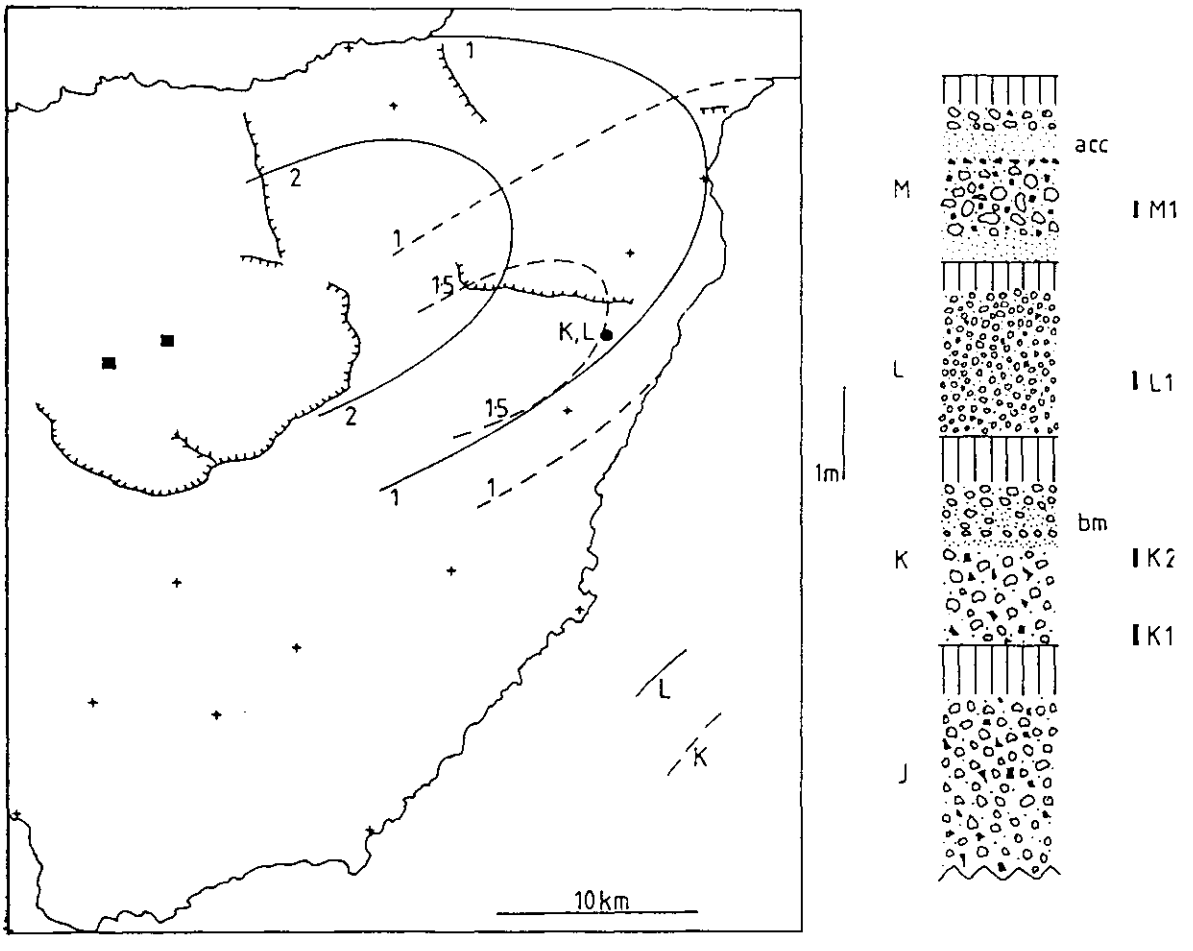

Fig. 1.22 Isopach map (contoured in m) of deposits K and L, and sampling section of K,L and M at the locality shown on the map. acc indicates fine-grained bed with accretionary lapilli; bm denotes bimodal bed.

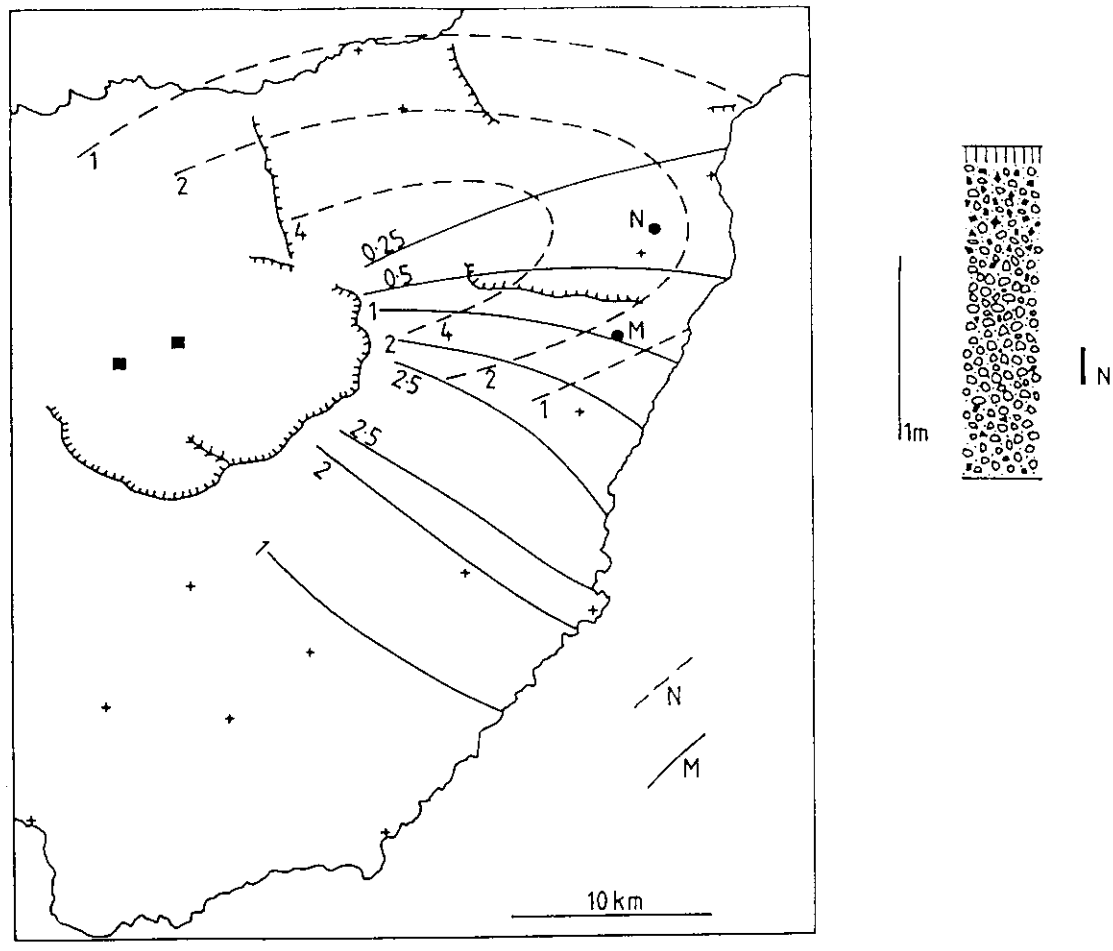

Fig. 1.23 Isopach map (contoured in m) of deposits M and N, and sampling section through pumice fall N. Sampling localities marked by spots on map; section through M shown in Fig. 1.22.

designated as N, is dispersed to the north-east of Las Canadas and is well exposed in the Guimar and Orotava valleys (Figure 1.23). It consists of well-sorted lithic poor pumice, the upper one-third being slightly richer in lithics.

The youngest fall deposit exposed outside Las Canadas, O, is poorly exposed and unexceptional. It was sampled at the locality depicted in Figure 1.14b, where it is overlain by an equivocal ignimbrite/mudflow bearing nepheline syenite xenoliths; elsewhere the top of the succession is marked by an undoubted ignimbrite rich in streaky and mafic pumice, the petrology of which is described in Chapter III. Nepheline syenite blocks are found in gravels immediately overlying this ignimbrite; at other exposures an undoubted mudflow, again with syenite fragments, occurs at the same level. The ignimbrite and mudflow are probably equivalent and represent the final stages of the O eruption, although this is not certain. The petrology of the syenite xenoliths is described in Chapter V.

Booth and Walker (in prep.) stress that all the field evidence indicates that the volcano is at present in a repose period comparable to the longer intervals recorded in the Fasnia Series, and thus that a major pumice eruption will probably occur within the next several thousand years. The pumice series is thus still in the process of formation.

I.3.iv The Adeje area

A prominent, obsidian-bearing densely welded ignimbrite, the Adeje Red Ignimbrite, is well exposed in roadcuts and barrancos in the arid area south-west of Adeje. Occurrences of densely welded ignimbrite are rare on the lower slopes of Tenerife, and the similarity in the field to ignimbrite F at Arico (which is also rich in non-vesicular juvenile material) prompted study of the local volcanic succession in order to establish (or otherwise) the identity of the Adeje flow with F.

The most complete succession, 27.5 m thick, is found near the road junction 2 km SSW of Adeje (Figure 1.25) and is shown in Figure 1.24. The lowest exposed unit is a lithified ignimbrite mudflow with a minimum thickness between 2.5 and 5 m. Locally the eroded top of this unit is overlain by coarse bedded gravels and conglomerates bearing subangular fragments up to 50 cm diameter. A thin (10 cm) bed of fine ash separates this from the next unit, a dark brown rock consisting of blocks of poorly vesicular, crystalline phonolite up to 1 m in diameter in a structureless matrix of smaller fragments and fine ash-sized particles. The brown colouration resembles that developed in densely welded ignimbrites and is considered to be a thermal darkening. This unit, up to 2.5 m thick, is interpreted as a lava-debris flow, formed by the collapse and avalanching of a gravitationally unstable lava dome or flow, and is thus closely similar to the "hot avalanche deposits" described by Francis et al. (1974).

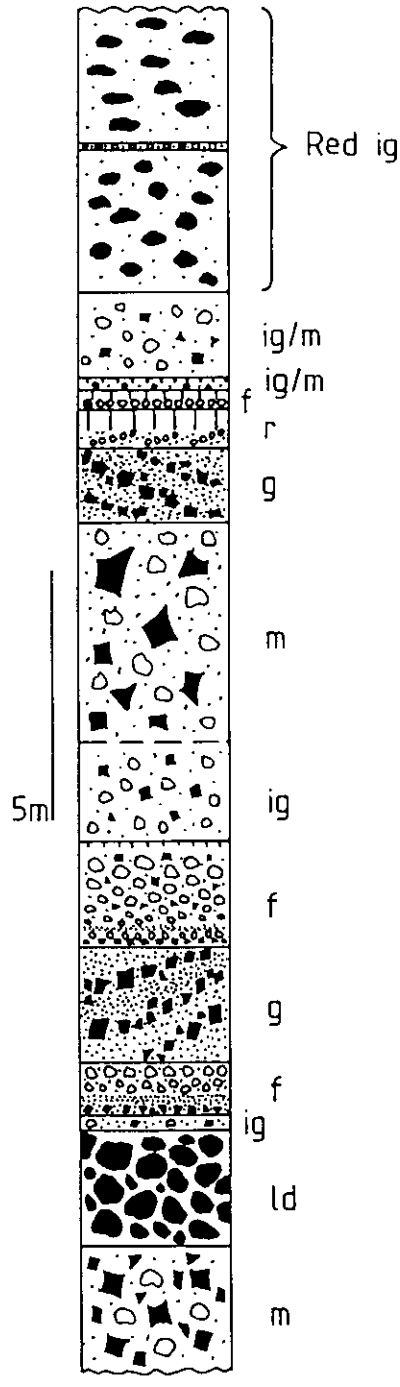

Fig. 1.24 Section through Adeje succession, 4 km SW of Adeje town. m = mudflow, ld = lava debris flow, ig = ignimbrite, f = fall deposit, g = gravels, r = redeposited pumice, ig/m = equivocal ignimbrite/mudflow deposit.

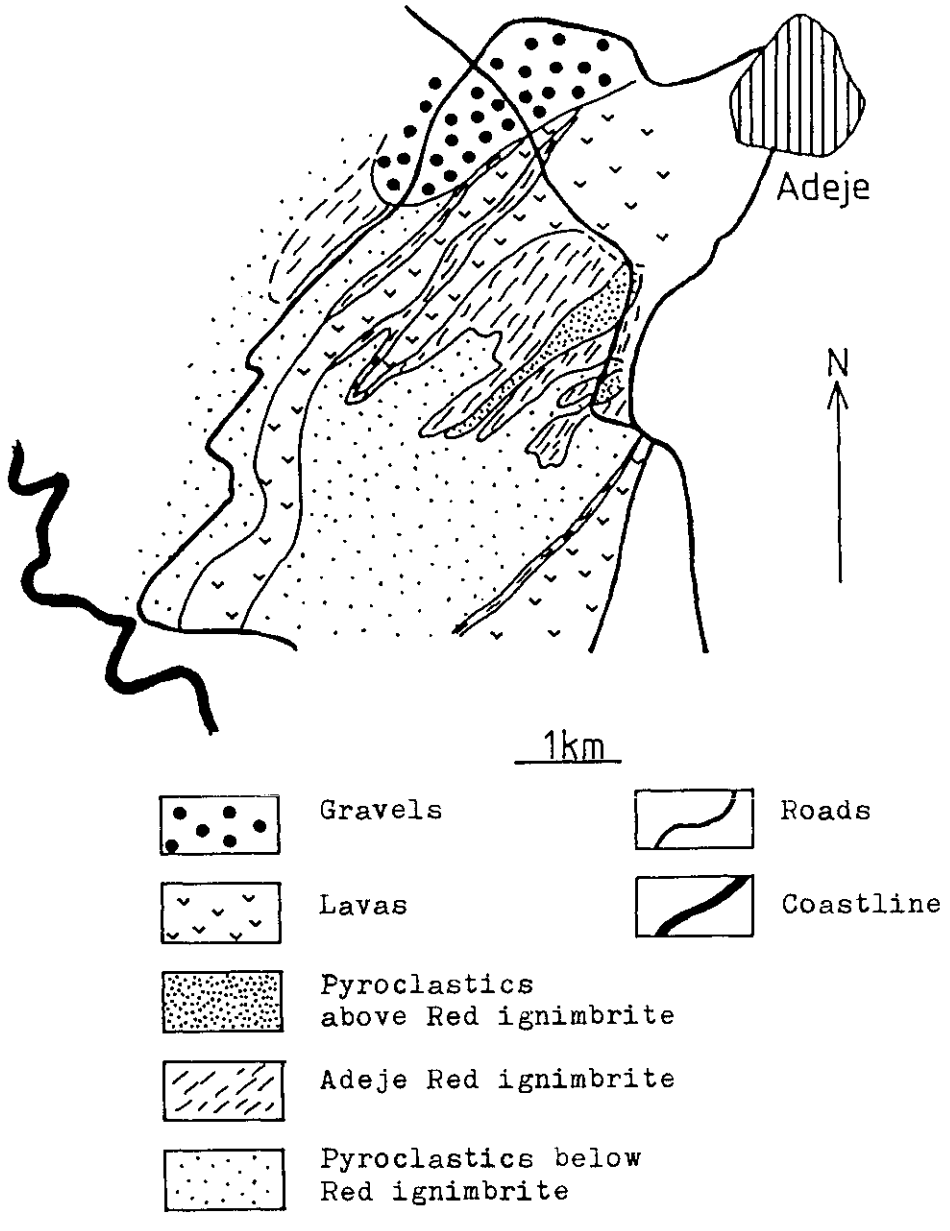

Figure 1.25 Sketch map of the geology of the Adeje area.

A very thin (30 cm) unwelded ignimbrite overlies the debris flow, and is succeeded, with no evidence of a significant hiatus in eruption, by a reversely-graded pumice fall up to 1.5 m thick. The base is lithic-rich, with a lithic sand horizon at 10 cm height. The remainder consists of relatively pure pumice, is strongly reversely graded (fine ash → 2 cm grain size) and has several thin cement-like bands between 10 cm and 40 cm height. The deposit cannot be correlated wth any described by Booth and Walker. It is unconformably overlain by coarse gravels bearing ankaramite boulders. Overlying the gravels is a diagenetised, well-bedded air fall 2.1 m thick. The basal 35 cm consists of fine ash with lithic-rich horizons, overlain by a 6 cm cement-like band which stands out on weathered surfaces. The remainder is a well-bedded, reversely graded, lithic-rich pumice fall (MP 3.5cm). The deposit closely resembles falls H and I of Booth and Walker, both of which, although data are scanty, could have 2 m isopachs in the Adeje region. It differs from H in a lack of streaky pumice, although the intense diagenetisation renders this observation inconclusive. An incipient soil has developed on top of the fall.

The overlying deposit provides an illustration of the problem of distinguishing ignimbrites and mudflows (I.3.i). The basal 2 m is a diagenetised lithic-rich ignimbrite with a basal layer and fossil fumarcles, this last feature being the only unequivocal indication of a pyroclastic flow origin. It is overlain by > 4 m of closely similar rock with a greater abundance of large lithics and no fossil fumaroles. The parting is marked by a sudden increase in lithic content and size, and the disappearance of fumaroles; a basal layer is absent from the upper part, which is interpreted as a mudflow deposited very soon after the ignimbrite. In this

case, it is the absence of fumaroles and a basal layer from the deposit which enables distinction of flow types. The scarcity of fumaroles among Tenerife ignimbrites, and the fact that mudflows sometimes possess a form of basal layer (G.P.L. Walker, pers. comm.), increases the difficulty of making any such clear distinction in many cases.

The mudflow is overlain by up to 2 m of gravels and reworked pumice, upon which a thick boulder-rich soil has developed. Over much of the area the Red ignimbrite rests on these sediments. At the key section a thin (20 cm), well-sorted airfall pumice with a 1 cm fine ash base overlain by a lithic sand layer rests on the soil. This fall is notable for being relatively coarse (maximum pumice size 3.5 cm) for its thickness, suggesting a short-lived but powerful eruption similar to that envisaged for pumice fall M (I.3.iii). Two equivocal mudflow/ignimbrite units, separated by a thin (4 cm) soil horizon, overlie a 20 cm soil developed on the fall. The upper of these shows a thermal darkening through its top 50 cm; this may be due to later heating by the Red ignimbrite which here rests directly on the mudflow/ignimbrite.

Four distinct units were formed during the eruption of the Adeje Red ignimbrite. The lowermost is a locally-exposed mudflow rich in obsidian clasts petrographically and chemically closely similar to those in the overlying ignimbrite.
The mudflow infills depressions in the paleotopography, and a surface soil is lacking. The absence of obsidian clasts in any other deposit in the area, the chemical similarity, and the unusual nature of this composition (Fe-rich peralkaline phonolite) compared to other

Tenerife phonolites, point to a close genetic association with the overlying ignimbrite. Probably the mudflow is redeposited material from an early phase in the same eruption.

The Adeje Red ignimbrite is prominent over a small area ($\sim$ 10 km^2) south-west of Adeje town (Figure 1.25). It cannot be traced far upslope of the main Los Cristianos-west coast road due to a covering of later pyroclastics, torrent deposits, and lavas. It is deeply incised by barrancos, and terminates at an erosional scarp 1½ km from the coast. Its original extent is unknown. The ignimbrite is nowhere more than 10 m thick, and forms a single cooling unit of two main flow units separated over the entire exposed extent by a thin (10 cm) but prominent parting (Figure 1.26) consisting of airfall material. The colour varies upwards from white through grey to the conspicuous oxidised bright orange-brick red thermal colouration which gives the unit its name. Macroscopic clast deformation is never developed, although locally, preferential alignment of elongate clasts may give a false impression of eutaxitic texture. The rock is always coherent and compact, indicating point-contact or sillar welding in the matrix, although the thermal colouration implies emplacement at a slightly higher temperature than, for example, the ignimbrite K sillar near Guimar (I.3.iii). Welding of this deposit is further discussed in Chapter VI.

The coarse juvenile fraction of the ignimbrite comprises pumice and poorly or non-vesiculated sub-rounded obsidian clasts up to 1 m in diameter. These vary from near-aphyric to up to 10% anorthoclase phenocrysts $\leqslant$ 5 mm in length. Vesicle size and frequency increases towards the centres of individual clasts and several have pumiceous interiors, indicating post-eruptive

Fig. 1.26 Adeje ignimbrite resting on cream-coloured equivocal ignimbrite/mudflow, near the locality of Fig. 1.24. Note the prominent parting between the two main flow units of the red ignimbrite. Exposed thickness of the upper flow unit is approx. 5m.

vesiculation. The degree of vesiculation is less in the lower flow unit, true pumice being virtually absent, while vesicle-free clasts are extremely rare in the upper unit. As with ignimbrite F, coarse-tail grading is well-developed in the sinking of obsidian clasts to the flow unit base.

Both main flow units exhibit well-formed basal layers, although in both occasional local partings with poorly developed basal layers are found. The parting between the main units is of particular interest. It is a bimodal ash, comprising 1-2 cm pumice clasts set in a fine matrix. It is closely similar to the bimodal ashes seen in, for example, pumice fall J (I.3.iii) and is considered to have formed by the same mechanism, the fine fraction being the co-ignimbrite ash fall of the lower flow unit. The coarse fraction may thus represent a short-lived plinian precursor to the emplacement of the upper unit by eruption column collapse; if so, the pause between emplacement of the two units must have been of the order of hours, consistent with their forming a single cooling unit. Physical and chemical features of the Adeje Red ignimbrite are further discussed in Chapter III and Chapter VI.

The Red ignimbrite forms the top of the succession over much of the area studied. Locally it is overlain by a pumice fall-ignimbrite/mudflow sequence. The heavily diagenetised fall deposit (Figure 1.27), restricted in exposure to a single pre-existing barranco near the road junction SSW of Adeje (Figure 1.25), is well sorted with a moderate lithic content and overall reverse grading, containing four fine ash beds. The internal stratigraphy (Figure 1.27) and the presence of fulgurites are reminiscent of pumice fall J, but haüyne

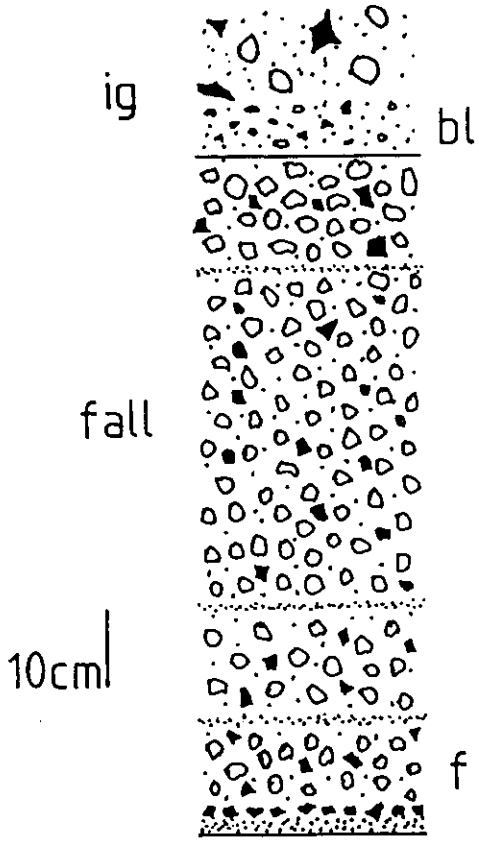

Fig. 1.27 Section through fall deposit and ignimbrite overlying the Adeje Red ignimbrite. bl = basal layer of ignimbrite, f = fulgurite-rich horizon.

is absent. It cannot be correlated with any other deposit in the Granadilla and Fasnia Series. The fall is capped by an ignimbrite/ mudflow over its observed extent. There is no certainty that this is the same flow as elsewhere rests directly on the Red ignimbrite, and is notable on account of a basal lithic concentration zone of trachyte and bedded tuff blocks up to 1 m in diameter in the upper of its two flow units.

The topmost unit of the succession is a widespread basalt lava with well-developed columnar jointing; it usually rests on the Red ignimbrite, with a bright red baked soil at its base.

The Adeje succession is generally similar to that of eastern coastal Tenerife, with airfall material subordinate to clastic flows. Precise correlation is difficult, mainly because the Granadilla and Fasnia Series falls are mostly dispersed well away from Adeje. The recognition of what is probably pumice fall H (or I) provides one reference point, but the stratigraphic position of the Adeje Red ignimbrite remains unknown. Nonetheless, the correlation of H/I indicates that the Red ignimbrite is considerably younger than ignimbrite F, which it closely resembles.

I.3.v Sub-Granadilla Series pumice deposits

The products of five explosive eruptions which pre-date the Granadilla Series are exposed in a barranco about 4 km ENE of Arico (Figure 1.28). The lowest member is an ignimbrite consisting of several flow units, each with well-developed basal layers, normal grading of lithics and reverse grading of pumice. The base is unexposed. It is overlain by redeposited pumice on which a soil

has formed; at one point, where the ignimbrite is unexposed, the same soil containing reworked tephra overlies 30 cm of undisturbed air-fall pumice. Upon the soil lies a coarse, lithic-poor pumice fall, with a central layer of fine pumice and lithic sand. An incipient soil separates this from the next deposit of homogeneous air-fall pumice, itself capped by a poorly-developed soil. The next deposit has several internal features. Overying a thin horizon of fine ash is a very coarse, lithic-rich bed of well-sorted, highly porphyritic pumice, separated from the next fall-unit by a poorly defined fine ash band. Above the ash is 28 cm of strongly reversely-graded pumice, witb a lithic-enriched lower one-third. A prominent cement-like band preceeds the uppermost unit of homogeneous grey pumice. Clearly, this deposit was the product of an eruption of highly variable intensity, as was, say, G or J. The capping soil contains some black pumice clasts, suggesting a compositional zonation similar to falls A and K. The uppermost deposit has been fused by an overlying lava to a pseudo-eutaxitic texture; it consists of two fall units with a fine ash parting. The lower is reversely graded, while the upper displays a slight normal grading. A thick soil horizon, baked by the lava, forms the top of this succession. Upon it rests 20 cm of basaltic scoria and the aa basalt lava.

No attempt was made to search for other exposures of these deposits, and all are heavily indurated and unsuitable for geochemical work. Nonetheless, it is apparent that the styles of explosive activity recorded by the Granadilla and Fasnia formations were established further back in the history of Tenerife.

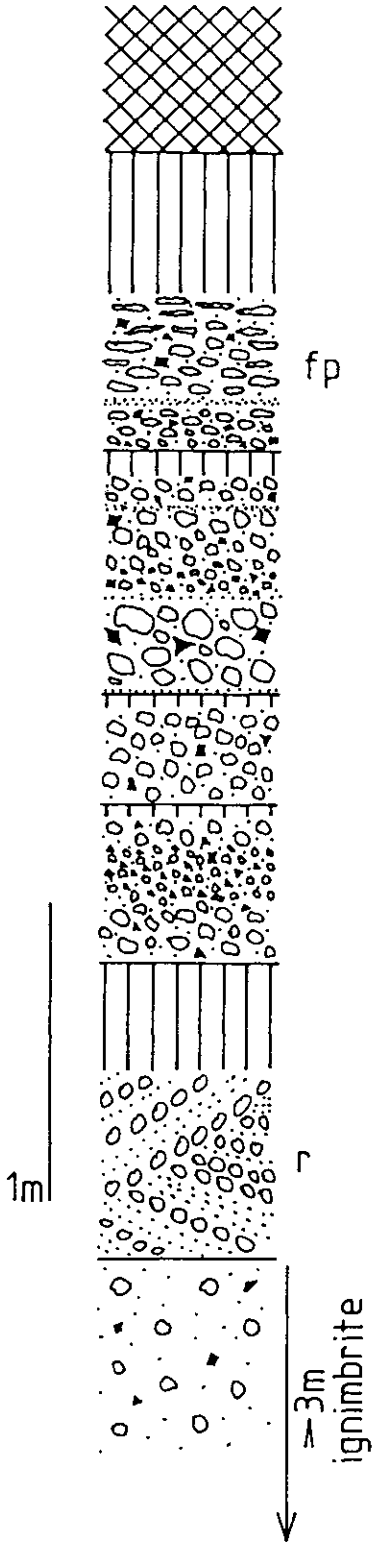

Fig. 1.28 Section through the sub-Granadilla Series succession exposed in a barranco, 4 km ENE of Arico. r = redeposited pumice; fp = fused pumice.

CHAPTER II

WHOLE-ROCK GEOCHEMISTRY OF THE PUMICE SERIES.

II.1. INTRODUCTION.

The original aim of this research project was a detailed geochemical investigation of the Granadilla and Fasnia series. However in view of the petrographically variable nature of the series and of components of individual deposits, it was felt that a general petrological approach, reported in succeeding chapters, was more appropriate. Consequently the geochemical data reported in Appendix A and discussed here are not exhaustive. Attention is concentrated on the Granadilla series, which generally yields less-altered pumice than the Fasnia series. Two samples from pumice fall J are however considered along with data from falls A, D, E and G. Fall G has been sampled in some detail as the exposure which provided the most complete section through G also, fortuitously, yielded the freshest pumice.

II.1.i. Effects of eruptive and post-eruptive processes on pumice chemistry.

The importance of allowing for possible modifications to original magma chemistry due to eruption processes has been discussed in I.2. In sampling, pains were taken to select a narrow grain-size range of the coarsest pumice from each sample for analysis, thus largely overcoming the effects of magma fragmentation and atmospheric transport of pyroclasts (I.2). However the basal pumice in fall G is considerably finer (maximum 1cm) than that at the top of the deposit (maximum 30cm) owing to reverse

grading, which may have reduced the concentrations of some highly compatible elements. However, it will emerge that the base of G is enriched in compatible elements, and thus the arguments presented in II.3. on the origin of compositional variation in this deposit are not qualitatively affected. The effects of magma extraction from the presumed sub-surface reservoir are also discussed in II.3.

The large weight losses on ignition (LOI) of sample powders (Appendix A) indicate substantial post-eruptive hydration of pumice, since primary magmatic water is almost entirely lost within a few hours of eruption (Sparks, 1978b). There is a considerable body of literature on the chemical changes accompanying hydration of volcanic glass. Scott (1971) found that Na loss accompanied hydration of glass shards in rhyolitic ignimbrites. Zielinski et al. (1977) have shown that hydration caused oxidation of iron, loss of Na and Zr, and gain of K, Sr, and Ba by rhyolitic obsidians. They concluded that hydration of rhyolitic glass causes little mobilisation of most trace elements other than alkalis or alkaline-earths, and especially that the REE (including Eu) were immobile and thus useful for evaluating compositional variations in igneous rocks whose fractionation histories had been dominated by feldspar removal. Tsong et al. (1978) have shown that hydration of obsidian results in depletion of Na and K and a lesser depletion in Ca and Mg. However Scheidegger et al. (1978) found little chemical alteration, other than hydration itself, within glass shards from Pleistocene and Pliocene ash layers on the Pacific Ocean floor. Most recently, Clough (1981) compared obsidian-pumice pairs from individual comenditic bread-crust bombs

of Quaternary age from La Primavera volcano, Mexico, and found negligible variation in SiO_2, Al_2O_3, TFeO, Zn, Zr, Rb, Y and Nb due to preferential hydration of pumice, while Na was lost and K gained. There is thus a general consensus of opinion that the alkali contents of hydrated glassy volcanic rocks are not representative of those in the erupted magma. There is a further consensus that the high valency cations (of Si, Ti, Al, REE, Zr, Nb, Hf, Ta, U and Th) are not appreciably mobile under the conditions of low-temperature alteration.

As regards the present study, comparison of whole-rock Na contents with those of variably-hydrated glasses analysed by electron microprobe (Chap. III), and with the Tenerife phonolitic lavas analysed by Ridley (1968, 1970b) shows that substantial Na loss has accompanied pumice hydration. A rather poor correlation exists between major element contents and LOI in the whole-rock samples (Fig. 2.1), suggesting that hydration has affected all major elements. This however, seems unlikely as the correlation is displayed by both mobile and immobile elements. An alternative explanation is that the degree to which the pumice has been hydrated is partly controlled by glass composition, with glasses of evolved magmatic compositions being more susceptible to hydration than those of less evolved types, under similar conditions of low-temperature alteration. This suggestion is supported by the LOI value of the trachyandesitic pumice from fall A, which is considerably lower than that of any of the phonolitic samples (Appendix A).

Here it is assumed that the "high-charge" elements have been unaffected by hydration. The behaviour of any

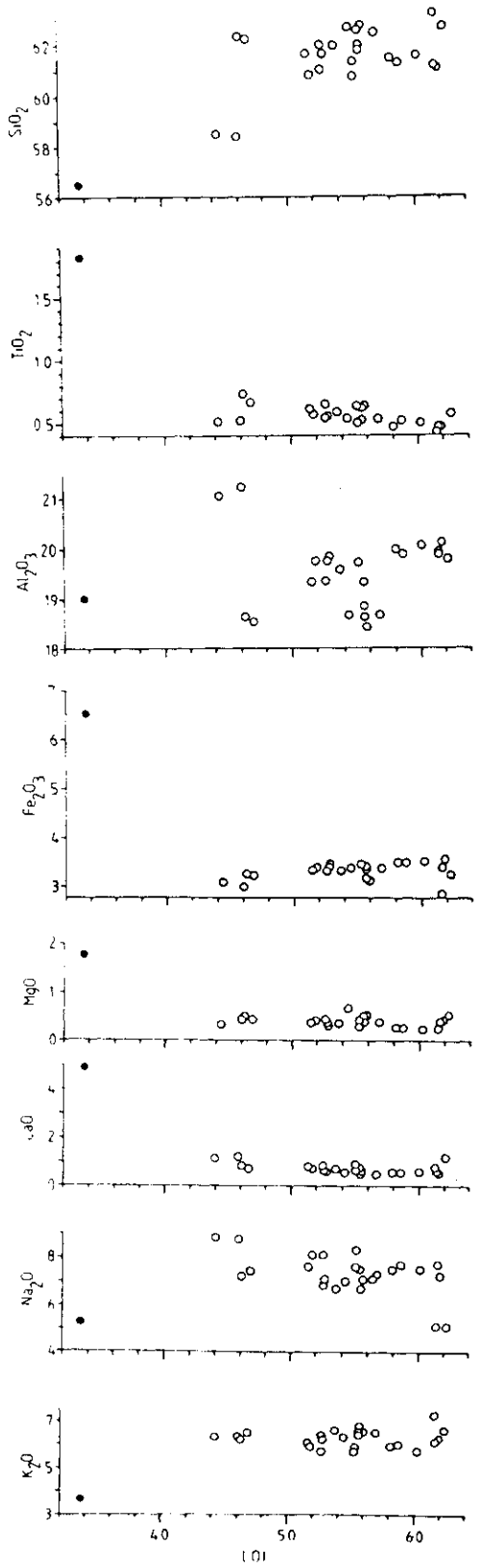

Fig. 2.1 Major element content vs. loss on ignition (LOI) in weight % for all analysed samples. Solid circle is AF3 trachyandesitic pumice, open circles are other samples (phonolitic pumice).

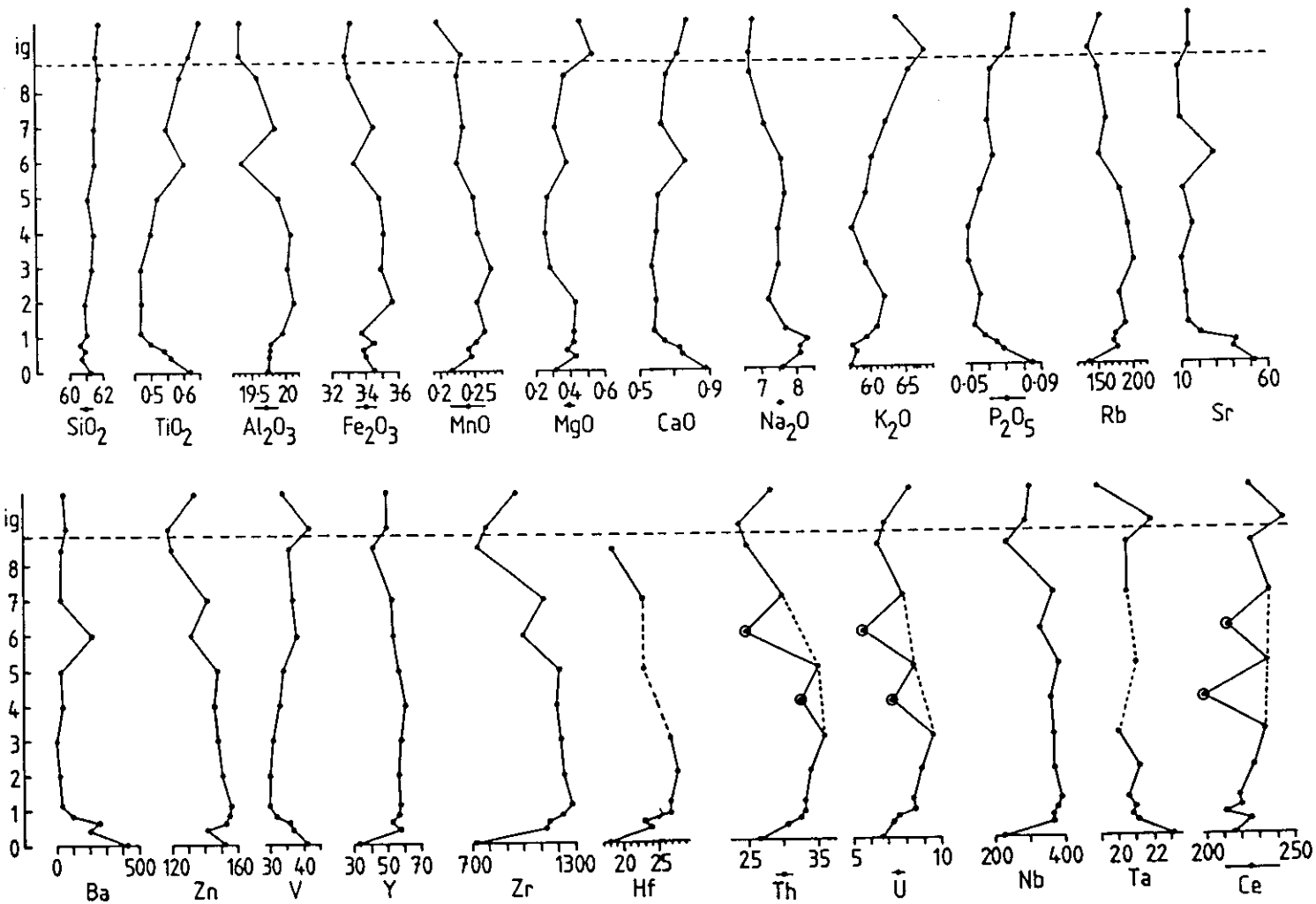
ig
8
7
6
5
4
3
2
1
0
60 62
SiO2
0·5 0·6
TiO2
19·5 20
Al2O3
32 34 36
Fe2O3
0·2 0·25
MnO
0·2 0·4 0·6
MgO
0·5 0·9
CaO
7 8
Na2O
6·0 6·5
K2O
0·05 0·09
P2O5
150 200
Rb
10 60
Sr
0 500
Ba
120 160
Zn
30 40
V
30 50 70
Y
700 1300
Zr
20 25
Hf
25 35
Th
5 10
U
200 400
Nb
20 22
Ta
200 250
Ce

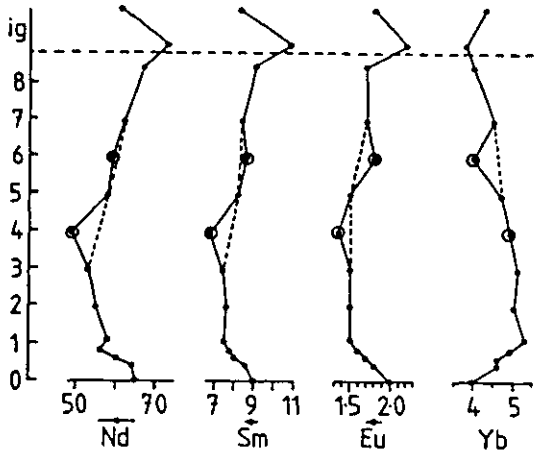

Fig. 2.2 (This page and facing) Variation in all analysed elements with height in pumice fall G and the overlying ignimbrite. Each point represents the centre of each sampled height extent; see Fig. 1.20 for actual vertical extent of each sample. Note that vertical scale (in m above base) applies only to the pumice fall; the two uppermost samples are from the basal and topmost flow units respectively of the ignimbrite. See Chap. I for details of the section. Circled points are not directly comparable with others for certain element profiles due to use of different standards in NAA runs.

element likewise unaffected but which varies through the sample suite should then show a pattern which in some way reflects the patterns of these elements, because if the effects of eruptive and post-eruptive processes have been eliminated, the variation must be due to differences in the composition of the erupted magma. Inspection of Fig. 2.2 indicates that Na, K and Mg are the only elements to have been affected by hydration of pumice (at least in fall deposit G), since the vertical variation of all other elements through G which show a variation is positively or negatively reflected by the immobile elements Ti, Zr, Nb etc. There is some danger here, as the apparent partial influence of glass composition on the degree of hydration noted above could produce a secondary correlation between those elements strongly affected by hydration and those varying greatly with magmatic evolution. This effect does not however appear to be a strong one, however, or the 6m sample in fall G would be enriched in, say, Rb relative to Ti rather than depleted, as predicted by "magmatic" behaviour. The considerable scatter in Fig. 2.1. itself indicates that (apart from Na, K and Mg) hydration has not significantly affected the concentrations of most elements in pumice.

II.2. COMPOSITIONAL VARIATIONS AMONG ANALYSED SAMPLES.

With the exceptions of Si, Al, Fe, Mn, V and to a lesser extent La, Ce and Ta, appreciable variations in element abundances are apparent through the series. In recent years, the use of normalised ("spider") diagrams in studying compositional variations among igneous rock suites has become established in the literature (e.g. Thompson et al., 1982). Such diagrams have the advantage

over the more conventional variation diagrams that each plot presents the complete geochemical signature of a sample on one diagram, and they are employed here to study variations within and between the members of the pumice series. In constructing Fig. 2.3, the concentration of an element in a sample was divided by its concentration in sample AF3 (the trachyandesitic mafic portion of pumice fall A), as this sample is considerably less evolved in composition (CaO = 4.69%) than any other analysed sample (CaO $\leqslant$1%), and thus serves as a convenient reference point. Elements were then plotted in decreasing order of the ratio from left to right. Thus, the compositional contrasts between firstly, trachyandesite and phonolite, and secondly, different phonolites, are presented. Representative samples from each deposit are plotted in Fig. 2.3.

II.2.i. Behaviour of elements in the pumice series.

Ba and Sr are strongly depleted in the phonolitic pumices with respect to trachyandesite. The top of fall E, the bases of A & G, and fall J are anomalously rich in Ba and Sr.

Ca, Ti and P are depleted in the phonolites to a lesser degree than Ba and Sr and show progressive depletion with phonolite evolution, behaving as a more or less coherent group.

Eu exhibits marked variation, its concentration varying by a factor of 7. In the least-evolved phonolites, its abundance approaches that in trachyandesite; however it is then progressively depleted, following the elements above.

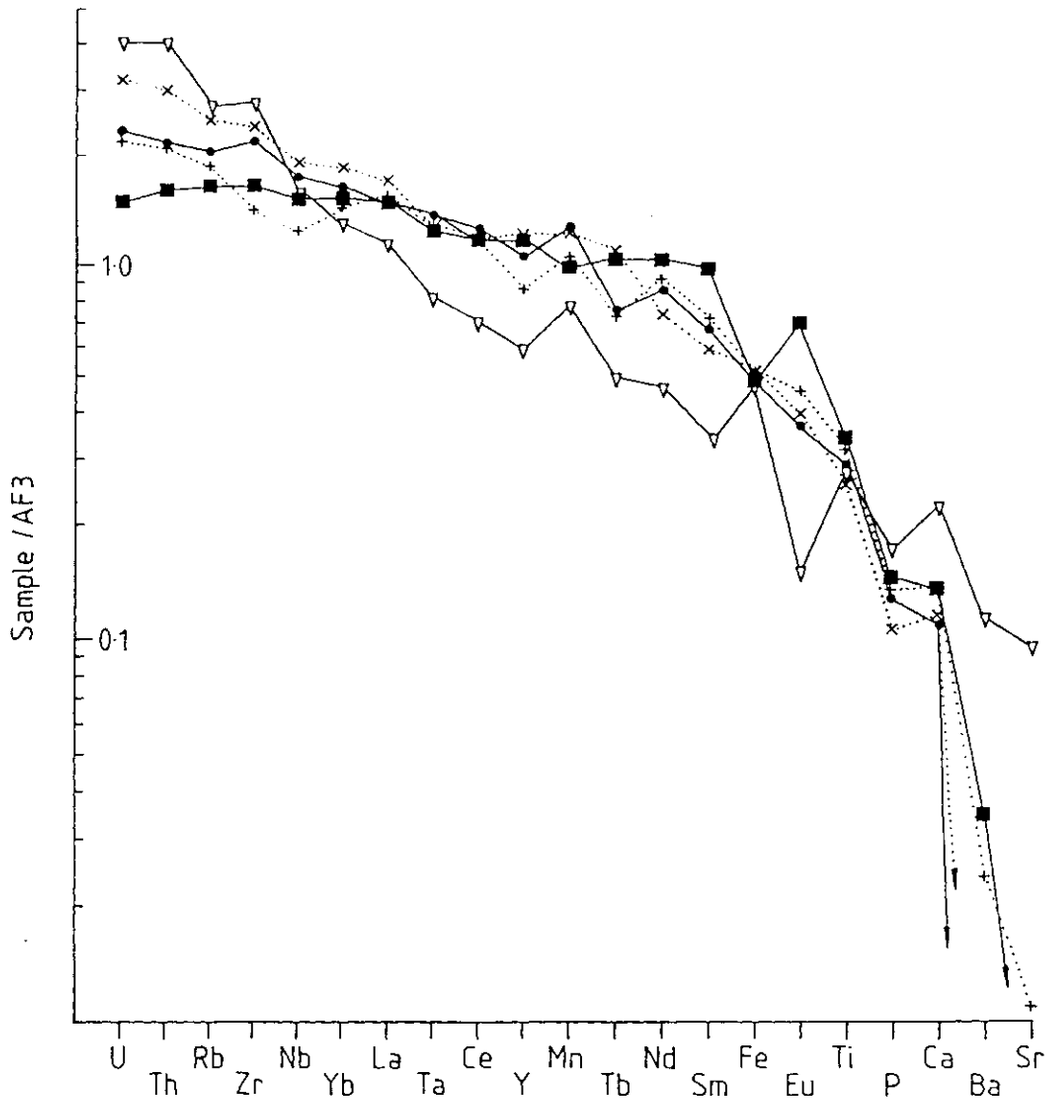

Fig. 2.3 Normalised (to trachyandesitic pumice AF3) element diagram for DF1 (small solid circles), EF2 (filled squares), GF8 (diagonal crosses), GF13 (vertical crosses) and JF5 (inverted triangles). Note that GF8 is enriched in the more incompatible elements, and depleted in the more compatible elements, with respect to GF13.

The normalised value of Fe is virtually constant at about 0.5 in phonolitic pumice.

Nd, Sm and Tb behave in a similar fashion to Eu, but less markedly. The apparent behaviour of Tb is not always consistent with that of Nd and Sm, probably a reflection of the poorer analytical precision for this element is due to a large Th interference (Appendix A).

Mn and Y are variable around a normalised value of 1. Both elements are relatively depleted in pumice fall J.

Si and Al are slighly more abundant in phonolite than in trachyandesite, but show little significant variation within the phonolites.

La, Ce and Ta are slightly enriched in most of the phonolitic pumices with respect to trachyandesite, but show no variation through most of the series within analytical precision. The phonolitic part of A, and fall J are unusually depleted in these elements.

U, Th, Rb, Zr, Nb and Yb are almost always enriched in phonolite, with U and Th having normalised values of up to 4 (in fall J). These elements vary in the opposite sense to that of Nd, Sm, Tb, Ca, Ti and P throughout the series.

Mg, Na and K are considered to be susceptible to alteration as discussed above and will not be treated further.

II.2.ii Features of individual deposits.

Fall A consists of phonolitic pumice overlain by mafic trachandesitic pumice; as discussed in Chap. I, there is no evidence for any break in eruption between emplacement of the two layers. Compared to most of the other deposits, the phonolitic portion is relatively poor in La, Ta, Le, Tb, Nd, Sm and Eu, and enriched in Ba and Sr.

Fall D is remarkable for its internal chemical homogeneity; there is no variation within analytical error. D is generally chemically similar to G.

Fall E is closer in composition to the trachyandesitic portion of A than any of the other deposits. It exhibits internal variation, with upward enrichment in Ba, Ca, Ti, P and upward depletion in Th, Zr, Nb and Rb. However a sample taken from the base (EF1) is markedly depleted in Zr, Nb and Y relative to other elements.

Fall G has been sampled in detail and also exhibits marked internal variation. The base and top of the deposit, and the overlying ignimbrite, are depleted in U, Th, Rb, Zr, Nb, Yb and enriched in Ca, Ti, P, Sm and Nd relative to a central portion (Fig. 2.2). In addition, the bottommost tephra is especially rich in Ba and Sr, and an anomaly, possessing chemical affinities with the basal zone, exists at the 6m level at the sampling locality. The anomaly excepted, gradation from base to middle to top is generally smooth (Fig. 2.2).

Fall J is strongly enriched in U, Th, Rb and Zr in comparison with other deposits, and depleted in most other

II.2.iii Variation in rare-earth elements (REE)

The REE all exist solely in the +3 state (except Eu) in magmas, and exhibit gradual change along the group in ionic radius (the lanthanide contraction), resulting in subtle differences in geochemical properties progressing from La to Lu. This, combined with the ability of Eu to exist in the +2 or +3 valence state and thus exhibit markedly different behaviour, makes the REE extremely useful as petrogenetic indicators.

Chondrite-normalised REE diagrams are, with the exception of the Fall A trachyandesite, markedly concave-upwards (Figs 2.4 to 2.8). When abundances are normalised to fall A trachyandesite, a distinctive and unusual pattern of REE variation more clearly emerges (Fig. 2.9), with strong depletion in Sm and Nd, and a developing negative europium anomaly as Yb increases, with La and Ce remaining approximately constant. This variation may be identified on the scale of a single deposit (Fig. 2.9b and Fig. 2.2).

II.2.iv. Variation in Nb/Ta ratio.

Niobium and tantalum are normally considered to be geochemically inseparable elements, due to their identical charges and atomic radii. In a given magmatic series, the ratio Nb/Ta should be constant. Fig. 2.3 clearly indicates that the ratio varies considerably within the Tenerife pumice series, and even within a single pumice fall deposit (compare Nb and Ta profiles within fall G, Fig. 2.2). The variation is greater than can be accounted for by analytical error, and is regular when compared with

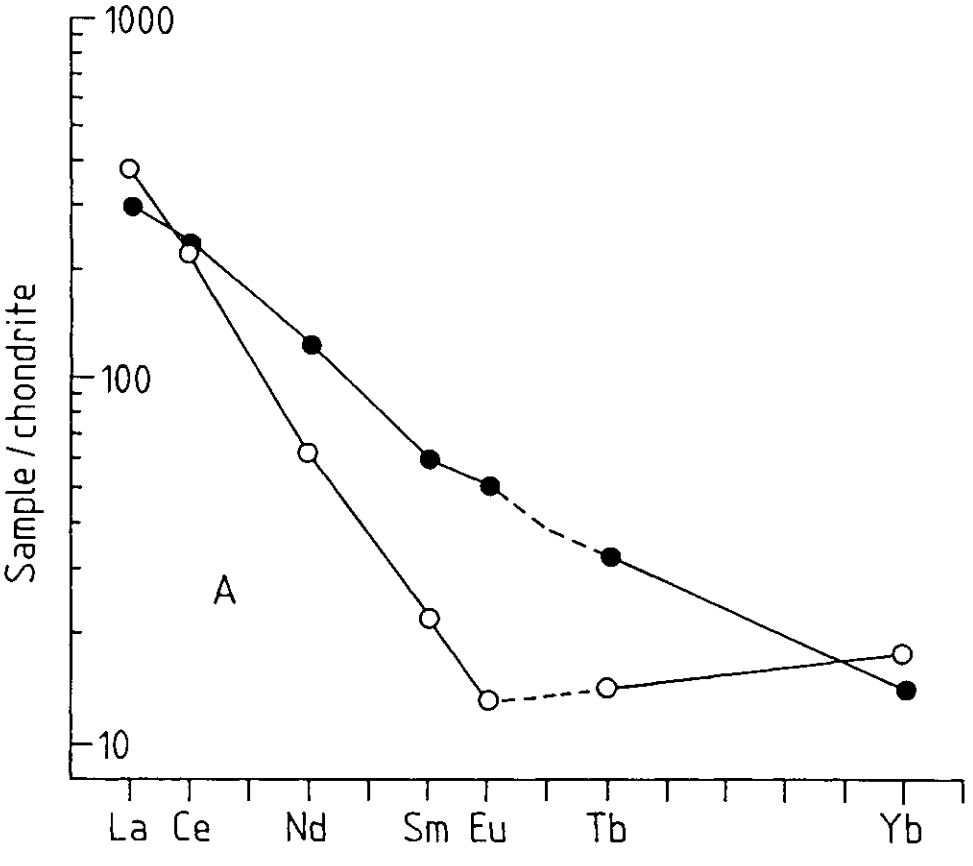

Fig. 2.4 Chondrite-normalised REE plots for the phonolitic (open circles, AF1) and trachyandesitic (filled circles, AF3) portions of pumice fall A. Note strong depletion of middle REE in the phonolitic pumice. Chondritic values from Haskin et al. (1966).

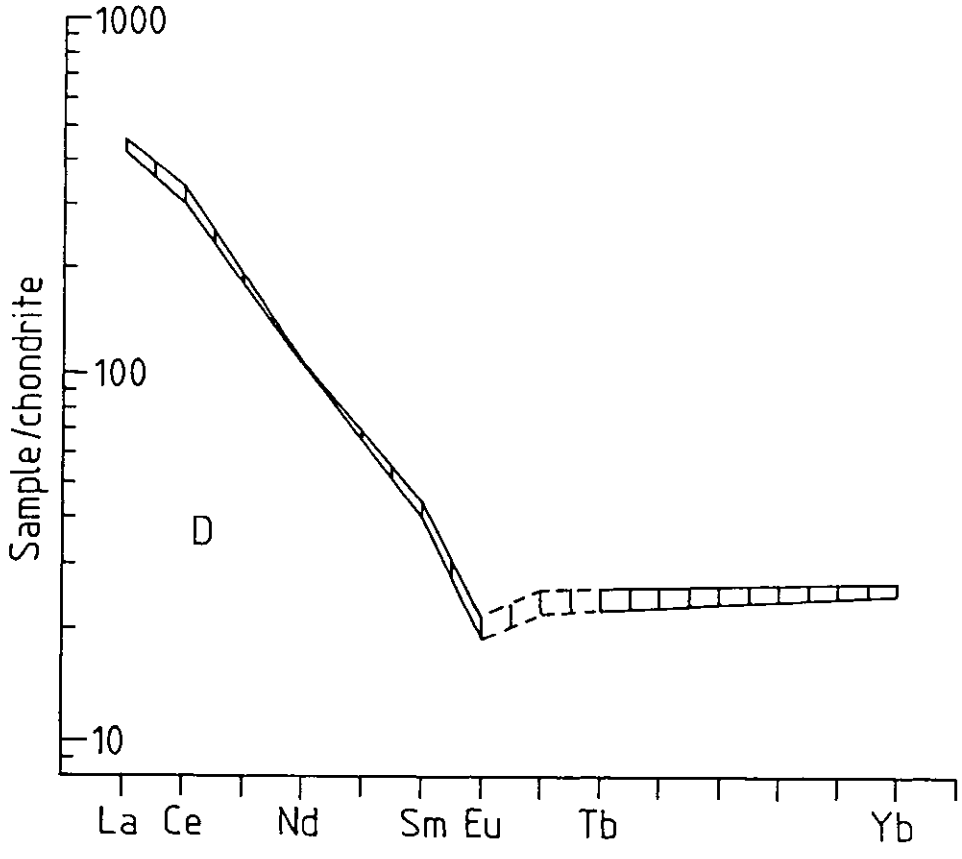

Fig. 2.5 Range of REE contents in pumice fall D (3 samples). Chondritic values from Haskin et al. (1966).

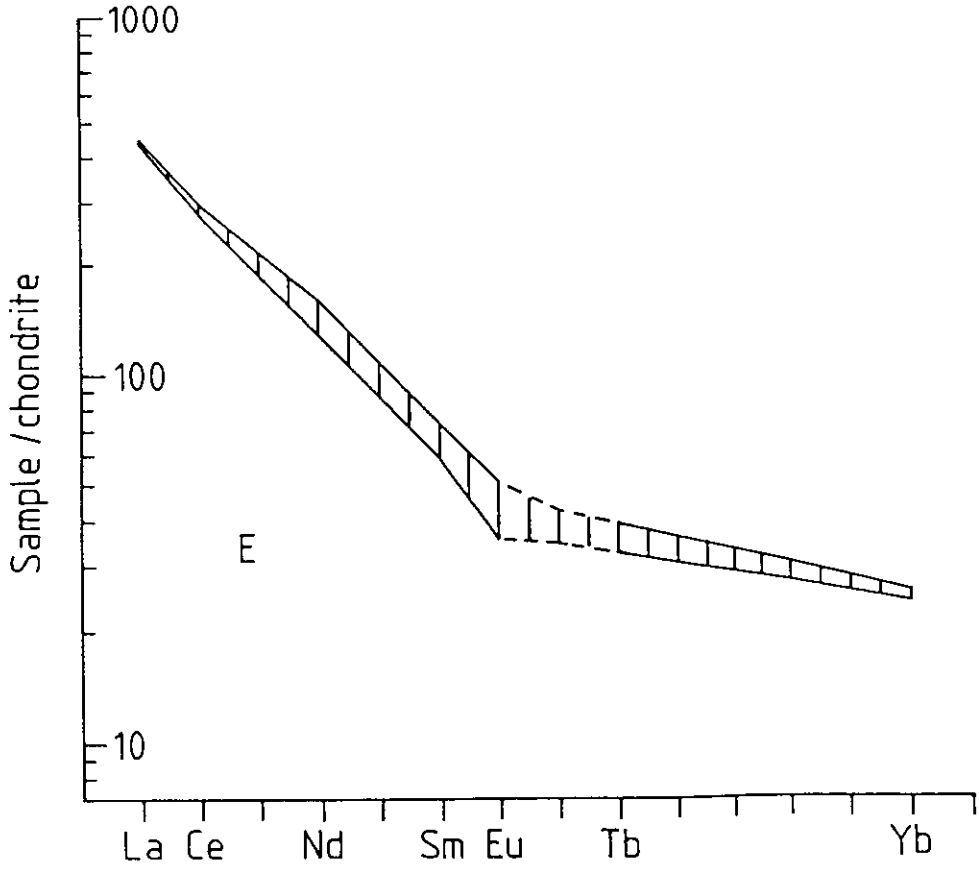

Fig. 2.6 As Fig. 2.5, for pumice fall E (4 samples).

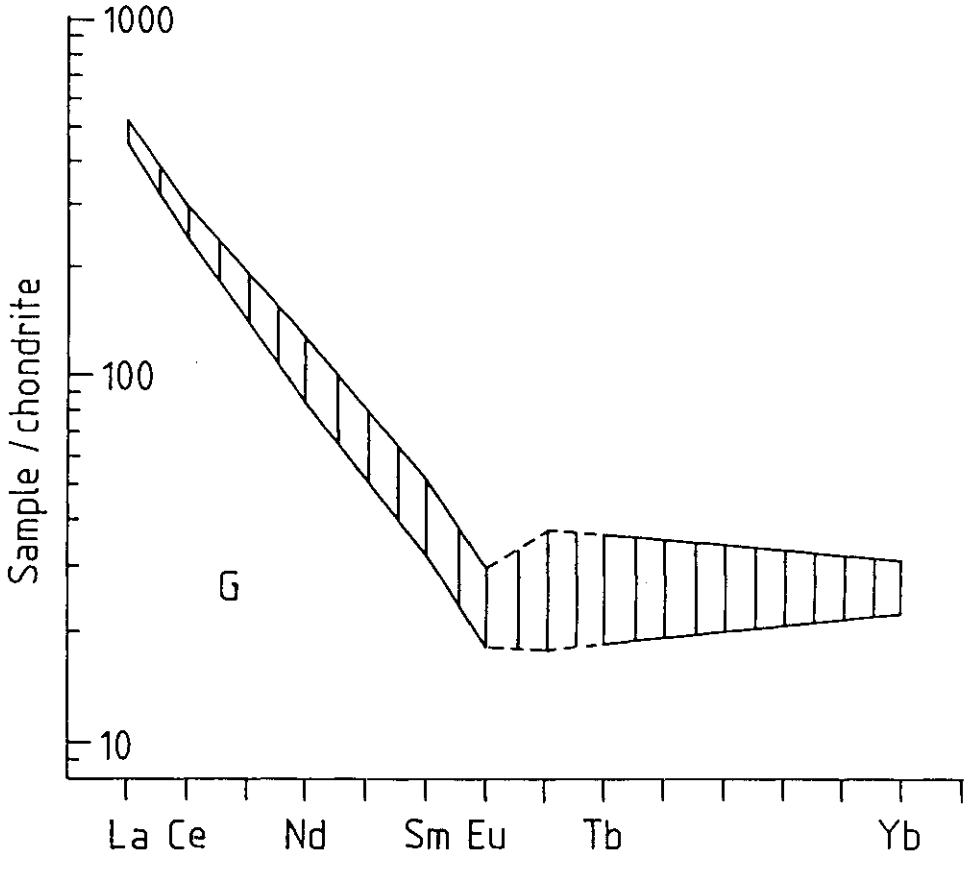

Fig. 2.7 As Fig. 2.5, for pumice fall and ignimbrite G (14 samples).

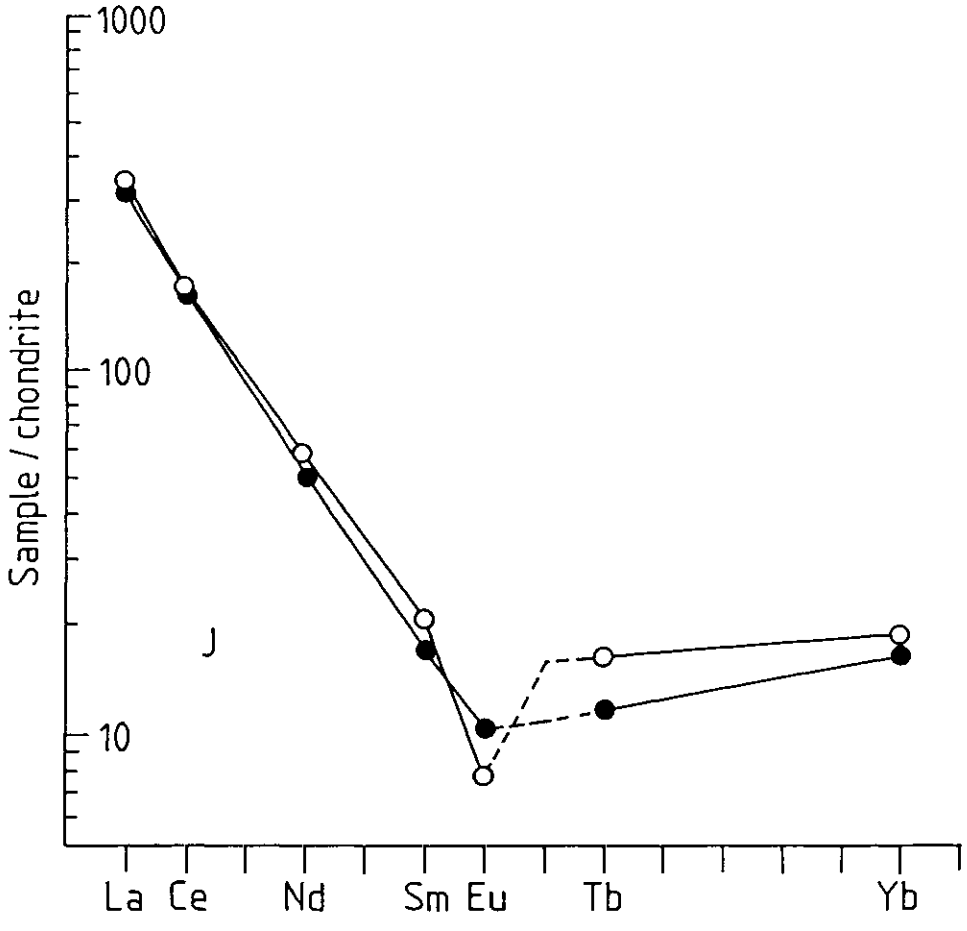

Fig. 2.8 Chondrite-normalised REE plots for JF1 (open circles) and JF5 (filled circles). Chondritic values from Haskin et al. (1966).

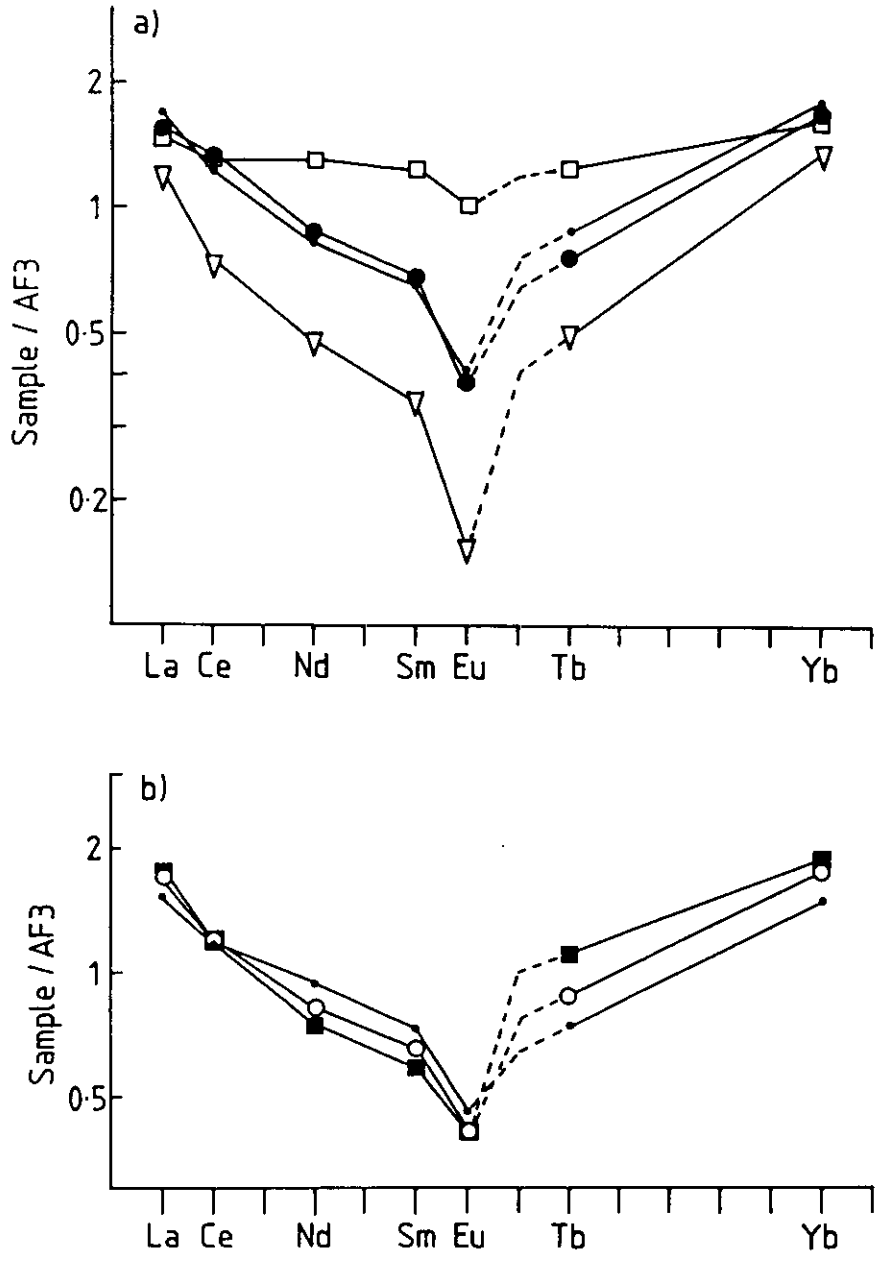

Fig. 2.9 Normalised (to trachyandesitic pumice AF3) REE plots for: a) DF1 (filled circles), EF4 (open squares), GF10 (dots) and JF5 (inverted triangles), and b) GF8 (filled squares), GF10 (open circles) and GF13 (dots).

other chemical trends within the series. Of the two elements, Nb is the more variable. The maximum variation in the ratio through the whole series is by a factor of 3.

II.3. DISCUSSION.

II.3.i. Differentiation mechanisms.

All previous workers on Tenerife have considered the phonolites to be the products of differentiation of, ultimately, primitive alkali basalt. The overall smoothness of chemical trends in the lavas, and the continuously undersaturated nature of the series support this conclusion (Ridley, 1970b, Borley, 1974). Ridley (1970a) showed that all the evolved magmas of Tenerife (trachybasalt, trachyandesite, phonolite) could be produced by successive fractionation of observed phenocryst assemblages. The existence of a compositional ("Daly") gap in the intermediate range does not preclude the derivation of phonolite by crystal fractionation (Chap. III., Ridley, 1970a).

The ultimate origin of phonolitic magma is not the principal subject of this chapter and the crystal fractionation process is accepted. Rather it is desired to account for variation within the pumice series itself. Unusual behaviour of REE and other trace elements led Hildreth (1979) and Mahood (1981) to reject crystal fractionation as a method of producing compositional variation in rhyolitic magma of the Bishop Tuff, California and La Primavera Volcano, Mexico respectively. Instead, these authors appealed to a mechanism of thermogravitional diffusion whereby geochemical fractionation takes place essentially

in the liquid state without the participation of solid phases. At first sight it may seem that the unusual behaviour of REE, Nb and Ta in the Tenerife pumices may require a similar explanation. However, given that magmas crystallise with cooling and that crystals and magma are capable of segregation, it is first necessary to absolutely rule out crystal fractionation as a mechanism for producing chemical variation before appealing to other processes.

Mahood and Hildreth largely rest their respective cases on the following points:-

1) Rejection of crystal settling (my underlining) as a viable mechanism, largely on the basis of physical constraints.

2) Inability of fractionation of observed phenocryst phases in their modal proportions to account for the chemical variation.

3) "Compatible" behaviour of LREE (light rare earth elements La, Ce, Nd) and "incompatible" behaviour of MREE and HREE (middle and heavy rare earth elements, Sm, Tb, Dy, Yb, Lu), the opposite to that observed during the crystal fractionation of most magmas.

The following criticisms may be levelled at these points in order:-

1) Crystal fractionation does not imply that crystal settling is the process by which it occurred. Substantial settling is indeed improbable in many magmas (McBirney + Noyes, 1979). Recent studies have shown that other more efficient mechanisms of effecting crystal-liquid segregation may operate in crystallising magma bodies, particularly sidewall crystallisation and boundary layer transfer

(McBirney, 1980; Turner and Gustafson, 1981; see Chap. III). The improbability of settling by no means rules out the role of crystal fractionation in producing compositional variation in magmas.

2) Removal of phenocrysts from magma in the proportions observed modally is unlikely to occur by any segregation mechanism, due to differences in sizes and densities of phenocrysts. Furthermore a number of complex dynamic phenomena may occur in magma chambers (Turner and Gustafson, 1981), which may involve crystal fractionation, magma mixing, remelting of precipitated crystals, and the establishment of chemically-isolated convecting layers; added to this, the transport and eruption of magma may substantially modify the distribution of phenocrysts within magma. It is thus unlikely that the modal proportions of phenocrysts in a volcanic rock will accurately represent the proportions crystallising to produce any observed fractionation trend.

3) The role of accessory, rare-metal-bearing and, in particular, REE-bearing phases in producing REE variation has not been fully appreciated by Hildreth (1979) and Mahood (1981). Mittlefehldt and Miller (1983) have shown that precipitation of monazite and/or allanite, into which LREE preferentially partition, can produce REE behaviour similar to that observed in the Bishop Tuff. The Bishop Tuff contains allanite (Hildreth, 1979) which preferentially incorporates LREE (La/Lu=100, Mahood and Hildreth, 1983). Furthermore Michael (1983) has modelled the chemical variation in the Bishop Tuff by extraction of the observed phenocryst phases, with some manipulation of the observed modal proportions, using the same data set as

Hildreth (1979). With regard to the La Primavera case (Mahood, 1981), the effect of accessory phases has been similarly overlooked. Clough (1981) identified the mineral chevkinite (a REE-rich titansilicate) in two of the lavas of La Primavera volcano, and inspection of an ignimbrite sample (from the Tala Tuff of Mahood, 1981) collected by J.V. Wright revealed microphenocrysts of allanite. Neither mineral is listed by Mahood (1981) as present in any La Primavera sample.

It must be concluded that the case against crystal fractionation in producing the chemical variation observed in the Bishop Tuff and at La Primavera can at best be regarded as "non-proven". Crystal fractionation must therefore remain as the premier hypothesis to explain chemical variation in evolved magmas.

II.3.ii. Behaviour of REE in Tenerife pumices.

As noted in II.2, the REE exhibit considerable variation in behaviour along the group. La and Ce show little variation, Nd, Sm and Eu exhibit compatible behaviour, while Yb is incompatible. If crystal fractionation is responsible for the geochemical variation, then the segregating phase assemblage must preferentially incorporate the MREE. Fractionation of the MREE appears largely confined to the phonolites, since fall E, the closest in composition to trachyandesite with respect to other trace elements, is also undepleted in MREE. The phenocryst assemblage of the samples concerned is alkali feldspar + sodalite (s.l.) + augite biotite + sphene + Fe-Tioxides $\pm$ amphibole $\pm$ nepheline. Of these minerals, sphene preferentially incorporates Sm and Nd (Hellman & Green, 1979, shown in Fig. 2.10) and progressive removal

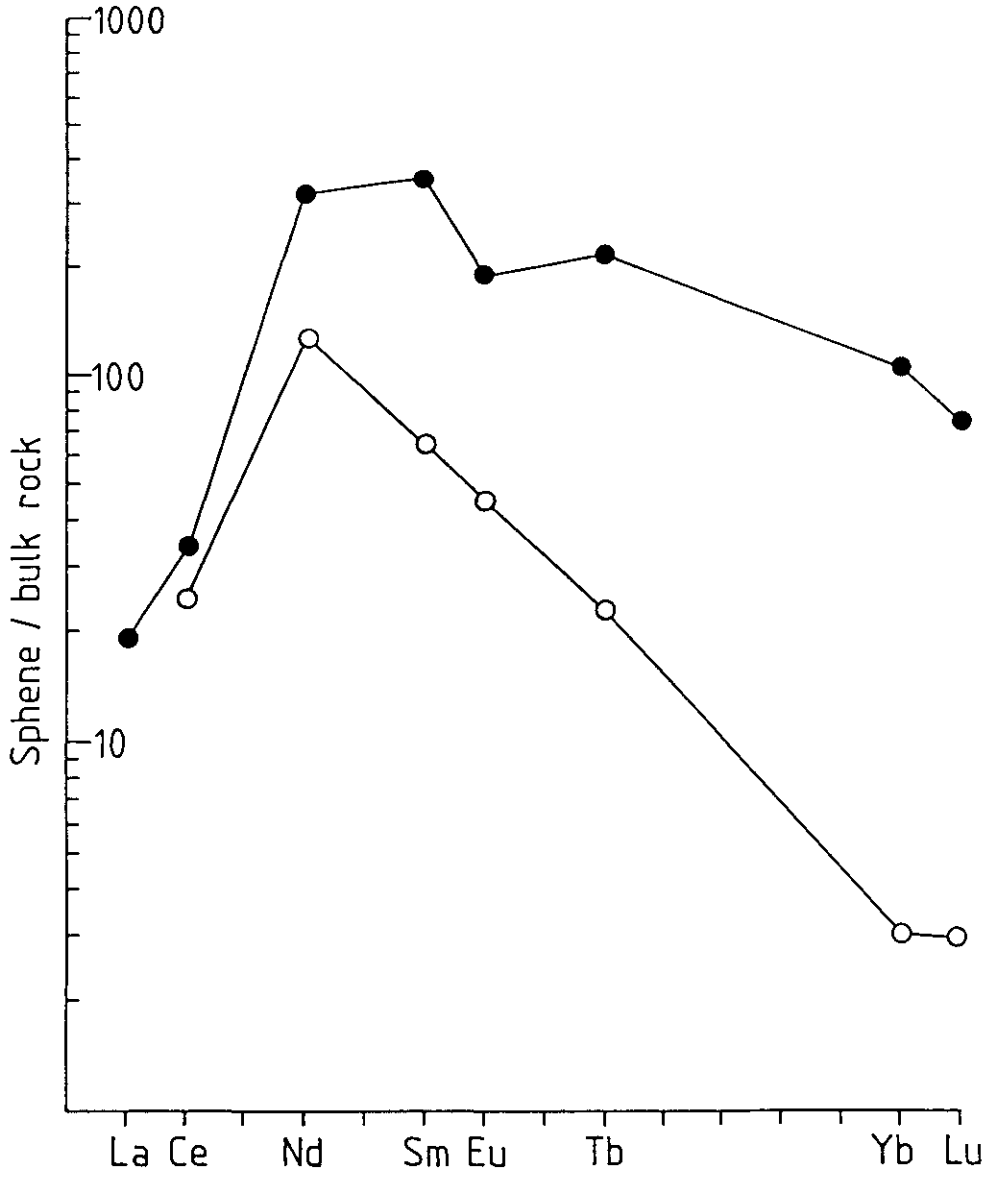

Fig. 2.10 REE distribution coefficients between two sphenes and bulk rock for a trondjemite, from Hellman and Green (1979).

of sphene would thus preferentially deplete a magma in Sm and Nd, producing concave-upward REE patterns (Fig. 2.9). Appreciable REE were qualitatively detected by microprobe in sphenes from the pumice series, thus only small quantities of the mineral need be fractionated in order to produce the required variation.

It may be noted that the correspondence between observed REE variation and mineralogy seen on Tenerife (removal of MREE in the presence of sphene) and the Bishop Tuff and La Primavera (removal of LREE in the presence of allanite) would be a remarkable coincidence were crystal fractionation not the mechanism responsible.

II.3.iii. Behaviour of Nb and Ta.

Nb behaves as an incompatible element through most of the series, though not to the same extent as U and Th. In contrast, Ta shows little variation; in most samples it is slightly enriched relative to trachyandesite, but is depleted in J and the phonolitic part of A, which on other criteria are the most fractionated members of the series. Nb/Ta varies from 8 to 24, and shows smooth variation when plotted against the abundance of Th (Fig. 2.11), the most incompatible element determined with reasonable reliability. Nb/Ta thus appears to be a function of fractionation. Nb was qualitatively detected in sphenes with the microprobe (Chap. III), and thus this variation may also be controlled by sphene fractionation. In the Nb, REE-rich perovskites in the nepheline syenites, Nb/Ta (determined by microprobe) is around 5(Chap. V). Thus the variation in the ratio through the whole of the salic suite on Tenerife and their constituent minerals is at least by a factor of 5, with Ta as the more compatible

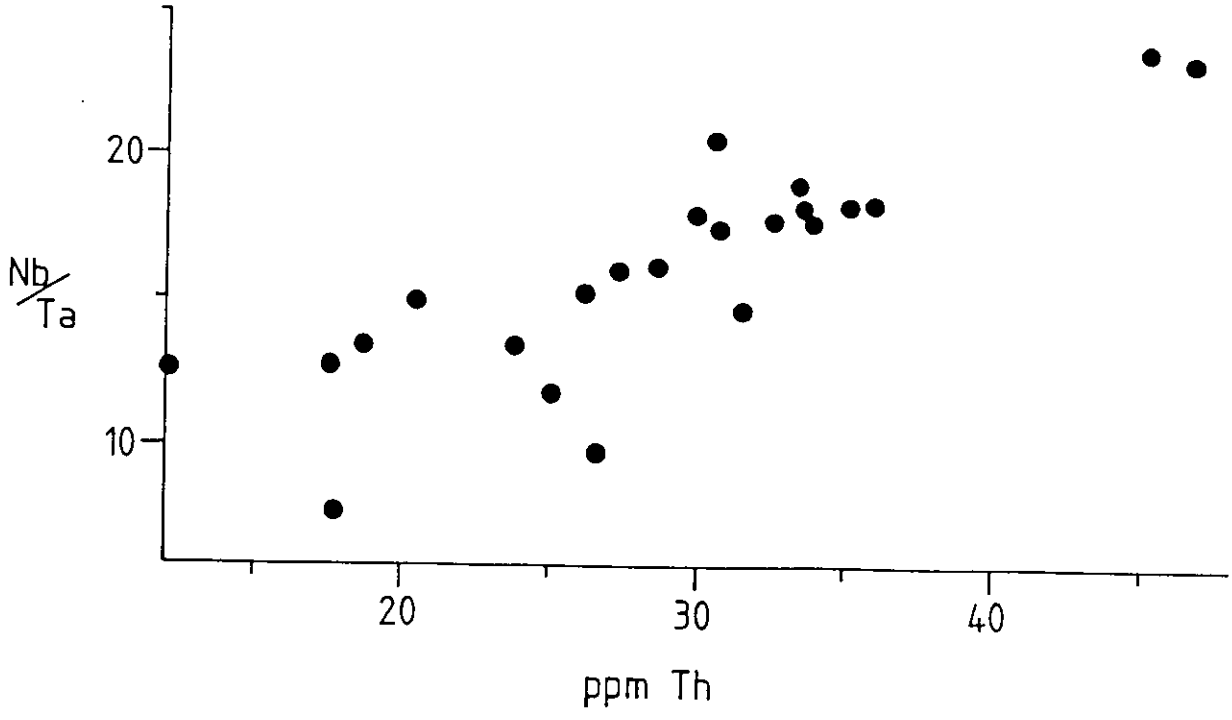

Fig. 2.11 Nb/Ta vs. Th content for all analysed pumice samples.

element of the two. This is remarkable for a pair of elements usually considered to be geochemically identical, but has been reported recently by other workers (A.D. Saunders, pers. comm., R.N. Thompson, pers. comm.). Perhaps one of the two partly or wholly exists in an oxidation state other than +5 under certain conditions.

II.3.iv. Relationship of phonolite to trachyandesite.

Inspection of Fig. 2.3 allows the qualitative evaluation of crystal fractionation processes responsible for the generation of phonolite from a slightly less evolved precursor, assuming that the trachandesitic portion of fall A is representative of those magmas immediately parental to the other members of the series.

The dominant influence of feldspar fractionation is apparent in the extreme depletion of Ba and Sr in the phonolites. The greater depletion of Sr as compared to Ba and Eu in pumice fall E suggests that plagioclase fractionation is important initially, succeeded by alkali feldspar to produce depletion in Ba and progressive depletion in Eu.

Depletion of all phonolites in Fe indicates that Fe-Ti oxides are also important in the derivation of phonolite. Fe is virtually constant within the phonolites, while Ti continues to decrease with fractionation, indicating that sphene removal operates once phonolitic compositions are reached (Ti-bearing biotite, present in the phenocryst assemblages, is unlikely to be responsible for Ti removal as this would then be accompanied by further depletion in Fe). The greater depletion in Ca than Ti probably reflects the operation of apatite fractionation,

indicated by the depletion in P in the phonolites. Mn is not depleted in most phonolites, suggesting that the Fe-Tioxides precipitating from trachyandesite magma were Mn-poor, consistent with microprobe data (Chap. III). The roles of augite and amphibole in the change from trachyandesite to phonolite are difficult to assess as their effects are qualitatively duplicated by other phases; however, had they been very extensively removed, greater depletion in Ca would be expected.

II.3.v. Variation within individual deposits.

The marked zonation in pumice fall A is discussed in Chap. III; this sub-section is primarily concerned with elucidating vertical compositional variations within purely phonolitic deposits.

Pumice fall D appears to be completely homogeneous, and is not discussed further.

Pumice fall E exhibits a fractionation trend with the least-evolved pumice found at the top (EF2→EF4 upwards). However the very basal pumice is depleted in Zr, Nb and Y, but not in other incompatible elements (Fig. 2.12). The least-evolved pumice in fall G exhibits a similar-shaped pattern, but less strongly developed (Fig. 2.3). Possibly trachyandesite magmas of more than one composition are parental to the pumice series.

Pumice fall G exhibits marked internal variation (Fig. 2.2), the central portion being the most evolved. The relationship of the upper part to the centre is one of simple fractionation, the upper part being richer in the compatible elements Eu, Ca, Sm, Nd, Ti, P, Sr and Ba,

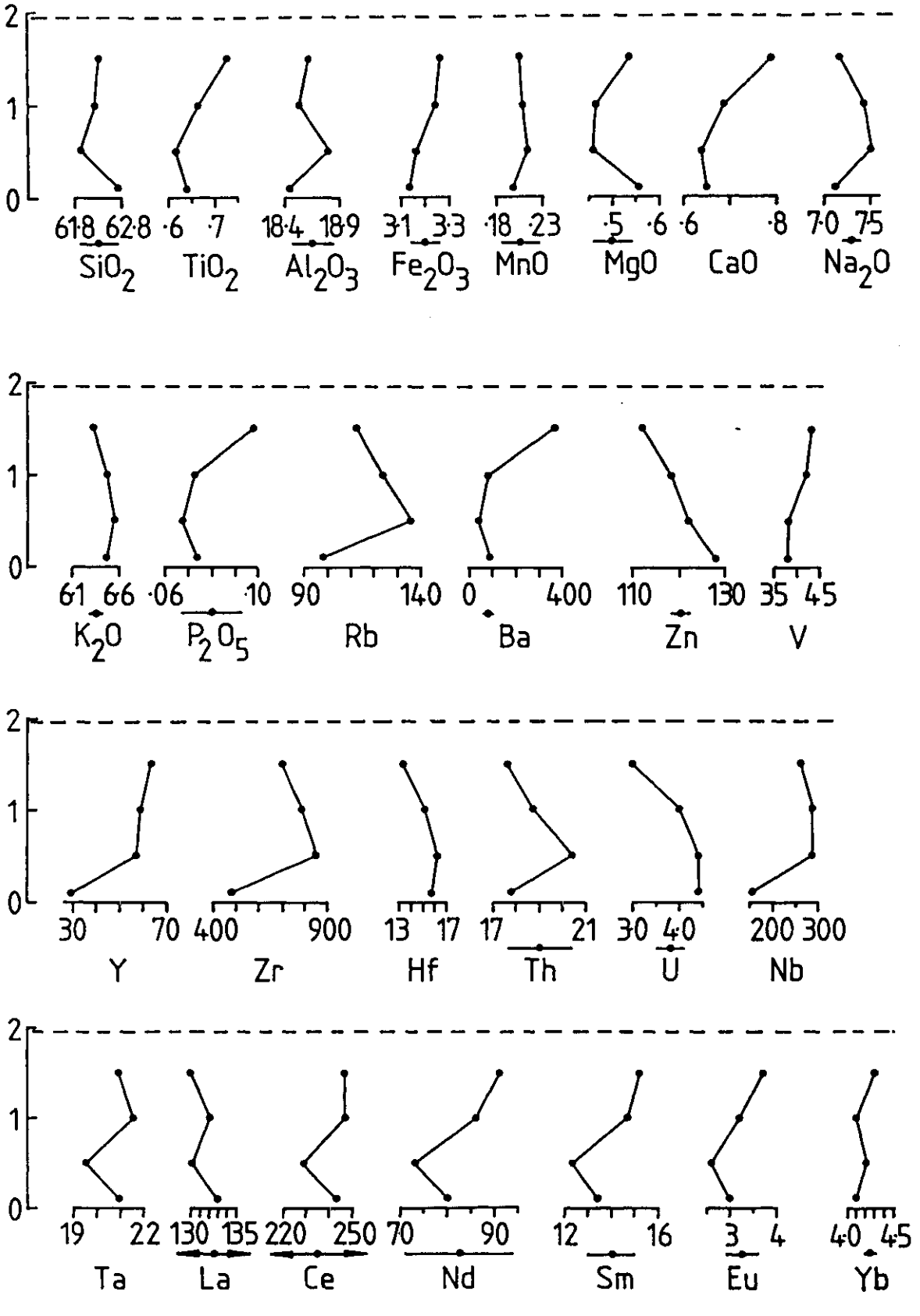

Fig. 2.12 Variation in all analysed elements with height (left-hand scale in m) in pumice fall E. Details of section given in Chap. I and Fig. 1.18. Dotted line marks top of deposit.

and poorer in the incompatible elements Zr, Nb, Tb, U, Hf, Th, Y, Rb, Yb. The base (GF1) is almost identical in composition to the top (GF13), but is additionally enriched in Eu, Ca, P, Sr and Ba, as shown by comparison of base/middle and top/middle element ratios (Fig. 2.13). The uppermost flow unit of the overlying ignimbrite has a composition more evolved than that of the uppermost pumice fall/base of the ignimbrite; and an anomalous sample at the 6m level (GF11) possesses the geochemical characteristics of the base.

Variation within the fall is generally smooth with height, probably due to magma extraction effects discussed in Chap. I. No attempt is made here to model "layers" of magma in the G chamber using the equations of Blake (1981), as this model is very sensitive to assumptions of chamber morphology and variation in magma properties. Nonetheless, if the internal composition stratigraphy of fall G qualitatively represents an inverted magma chamber stratigraphy, then the very top of the chamber appears to have been fractionating less efficiently than magma at a lower level. Below this zone, the bulk of the fall indicates a gradual downward change in the chamber from highly fractionated to less-evolved magma, as documented in ignimbrite sheets from the western U.S.A. (Smith, 1979) and other areas.

The enrichment of the base of G in Eu, Ca, P and especially Sr and Ba cannot be explained by lack of fractionation alone, which should simply produce a composition similar to that at the top of the fall. The contrast in Sr and Ba contents between intermediate and phonolitic magmas on Tenerife is much greater than for any

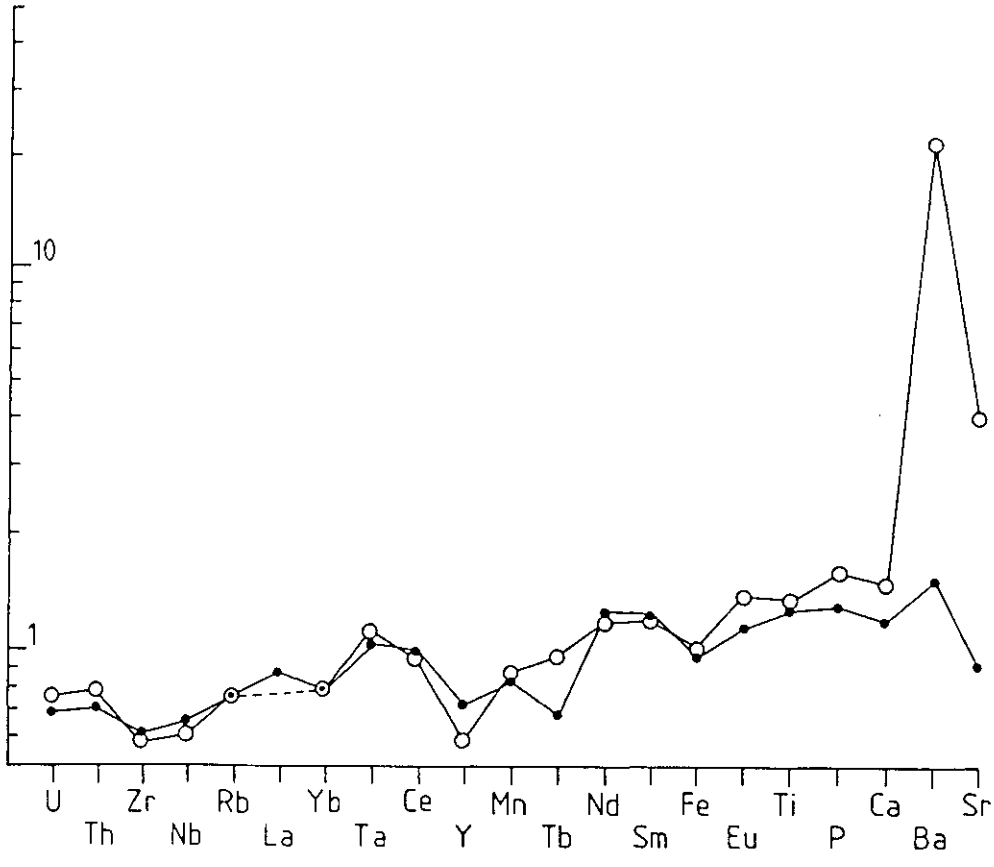

Fig. 2.13 Ratio of element abundances in basal tephra of pumice fall G (GF1) to central portion (GF7) shown by open circles; that of topmost airfall pumice (GF13) to central portion (GF8) shown by small filled circles. Samples from central portion chosen to be in the same NAA runs as GF1 and GF13 respectively, to maximise precision. Ba in GF8 is recorded as <20 ppm (detection limit) and so the value of 20 ppm from GF7 was used for the Ba top/centre point.

other element, these elements being ca. 100 times more abundant in trachyandesite than phonolite (Fig. 2.3). Thus one means of enriching phonolite in these elements without otherwise greatly affecting the composition is to introduce a small proportion of intermediate material into the phonolite, by magma mixing or contamination with country rock of appropriate composition. The base of fall G bears small lithics of trachyandesite with a juvenile coating, indicating that they were immersed in magma. Partly disaggregated fragments of this material are occasionally seen within pumice clasts. Although every attempt was made to exclude this material from the analysed sample, it thus appears to have made a contribution to the composition of the basal G pumice. The material may have been incorporated into the magma whilst residing in the chamber, or possibly during uprise of the first-erupted portion of magma through an opening fissure or conduit (see Chap. III for further discussion). Contamination with this material also appears to have affected the 6m sample.

It is impossible at present to do more than speculate on the significance of the return from less evolved to more evolved compositions at the close of the G eruption, as shown by the sample from the uppermost ignimbrite flow unit (Gig 6). Mixing of magmas derived from different portions of the chamber, non-regular compositional stratification in the chamber, or non-duplication of the eruption order by ignimbrite stratigraphy could all produce this effect.

In terms of U, Th, Rb and Zr abundances, fall J is the most fractionated deposit analysed. It is especially de-

pleted in Nd, Sm and Eu, and, compared to other deposits, in La, Ta, Ce, Y, and Tb. Removal of a larger than usual quantity of sphene, coupled with extensive fractionation of alkali feldspar, is capable of explaining this difference. J is however richer in Ca, Ba and Sr than is usual. As noted in Chapters I and III, J is a mixed-magma deposit bearing a small proportion of trachybasaltic material throughout, and the enrichment in these elements is ascribed to this cause.

II.3.vi. Concluding remarks.

The phonolitic lavas of Las Cañadas analysed by Ridley have less-evolved compositions than several samples studied here. Lava volumes are orders of magnitude smaller than those of individual pumice deposits and thus give a less representative sample of the (presumed) sub-surface magma body. The composition of the base of pumice fall G, the most completely sectioned and fully sampled deposit, may be significant in this regard. Lavas might be expected only to sample the very uppermost magma in an underlying chamber; if the arguments presented in II.3.v. are correct, then lava compositions would be expected to be less evolved (and perhaps contaminated with more basic country-rock) than those of the more-representative pyroclastics. This point is further discussed in Chap. III.

Most of the conclusions reached in this section are somewhat speculative, partly because a very much more comprehensive sampling programme would be needed for their confirmation. The data do, however, indicate that there is scope for further very valuable geochemical work on these deposits, with two principal objectives in mind:-

1) Detailed study of traee-element variations, especially the REE, Nb and Ta; mineral separation and analysis would be invaluable in this regard.

2) Internal chemical variation within individual deposits. It is recommended that in future complete sampling profiles (as opposed to sampling at vertical height intervals) through the larger-volume pumice falls be attempted, in order to obtain a more detailed picture of internal variation and, hopefully, gain a fuller insight into magma chamber compositional structure.

CHAPTER III

PUMICE MINERALOGY AND MAGMA MIXING

III.1 GENERAL PETROGRAPHY AND MINERALOGY

In Chapter I it was noted that several of the pumice deposits contain a minor mafic component, often in intimate association with salic material in individual pumice clasts. In thin section it becomes apparent that this association is due to fluid mixing of phonolitic with intermediate and/or basaltic magma. Because of magma mixing, the pumice series contains phenocrysts representative of the entire magmatic range on the island; in some cases this range is found within the products of a single eruption. Pumice mineralogy is thus unusually diverse and complex.

Each major pumice deposit was examined petrographically, and five mixed-magma units were the subject of an electron microprobe study. The sampling bias towards mixed-magma pumice should be borne in mind when reading this Chapter; phonolitic material accounts for over 99% of the entire volume of the Granadilla and Fasnia series and thus intermediate and basaltic phenocrysts and glasses form only a very minor component. However, optical evidence suggests that mineral compositions in the phonolitic components of mixed samples are representative of the rest of the series, and thus the true mineralogical range has been encompassed by the present data.

With a few exceptions, phenocryst contents are very low. The accurate determination of modal abundances in very poorly phyric pyroclastics is a laborious procedure (Lipman, 1967), and was not attempted in this study. In purely phonolitic pumice, total crystal content is always <5%, of which 90% consists of alkaline feldspar (visual estimates). Other phases, dealt with in turn below, in phonolite are sodalite, nepheline, augite, aegirine-augite, biotite, sphene, magnetite and ilmenite. In mixed-magma deposits, which are typically more crystal-rich, plagioclase, hauyne, magnesian olivine, titanaugite and kaersutite may also be found, together with Mg-rich Fe-Ti oxides.

Two departures from the phenocryst mineralogy of the lavas and minor intrusions, studied by Ridley (1968, 1970), and Scott (1970, 1976) may be noted. Although early workers described alkali feldspars in the phonolites as sanidines, Jeremine (1933) and Hausen (1956) recognised anorthoclase as the dominant alkali feldspar in the phonolite lavas. Ridley (1968) describes all alkali feldspars as anorthoclase although some of his samples possess a structural state (derived from x-ray data) very close to sanidine. Both phases occur in the pumices, sometimes within a single deposit. Secondly, melanite garnet has not been found, although Scott (1970) states that melanite phenocyrsts are restricted to phonolite dykes intruded into the Ancient Series basalts of Anaga and Teno.

Thin sections were prepared in the normal fashion for a few comparatively phyric specimens; in most cases it was first necessary to obtain a reasonable concentration of crystals from the near-aphyric pumice. This was done by crushing up to 1 kg of pumice

to a maximum grain size of a few mm to liberate crystals, which were then concentrated by a crude water flotation/panning method. The concentrates were sealed in epoxy blocks ("floaters") to yield a sample for slide-mounting.

Phenocryst occurrences for each deposit are given in Table 3.1.

III.1.i Feldspar

Alkali feldspar is the dominant phenocryst mineral. Anorthoclase forms tabular euhedra up to 5 mm long, but is more commonly <2 mm. Characteristically it displays fine lamellar or cross-hatch twinning. Sanidine, usually in grains <2 mm long, is distinguished optically by its simple (001) twins and small 2V. Zoning is insignificant (Figure 3.12). Evidence for slight to moderate resorption, in the form of rounded corners and occasional embayments, is seen in mixed-magma samples; otherwise completely formed euhedra or broken fragments are found. Analysed compositions range continuously from anorthoclase $An_3Ab_{77}Or_{20}$ and $An_9Ab_{74}Or_{17}$, to sanidine $An_1Ab_{50}Or_{49}$ (Figure 3.1). The most potassic feldspar described from the lavas is Or_{37} (Ridley, 1968).

Plagioclase is restricted to mixed-magma samples. The majority of analyses fall into two groups: oligoclase-sodic labradorite and calcic labradorite-bytownite (Figure 3.1).

Oligoclases and andesines thought to have precipitated from originally intermediate magmas (by analogy with feldspar compositions in the lavas, Ridley, 1968) - are K-rich with up to 11% Or. Normal, reversed and oscillatory zoning, sometimes spanning a considerable compositional range (Figure 3.13), occurs in most cases. Carlsbad

	Afsp	Olig-and-Na-lab	Ca-lab -byt	Hauyne/Sodalite	Nepheline	Titan-augite	Green augite	Olivine	Amph-ibole	Biotite	Sphene	Opaque
Aphon)	X	X		X			X		X	X	X	
)												
At-and)		X					X		X			X
D	X									X	X	X
E ^{o}	X	X		?			X		X	X	X	
F	X	X		X			X			X		X
G	X	X*		X		X*	X	X*	X	X	X	X
Tajao^{oo}	X	X	X	X	X	X	X	X	X	X	X	X
J ^{oo}	X	X		X	X	X	X	X	X	X	X	X
K^{o}	X	X		X			X		X	X	X	X
L	X	X*		X		X*	X		X	X	?	X
M^{oo}	X	X	X	X		X	X	X	X	X	X	X
N	X	X*					X	X	X*	X(*)	X	X
O^{oo}	X	X	X	X	X	X	X		X	X		X
Adeje$^{(o)}$	X		X				X			X		X
B.d.T.	X						X			X		X

Table 3.1. Mineralogy of the pumice series. ? indicates doubtful identification, one small grain only found. * indicates xenolithic material, distinguished by adhering crystalline groundmass; where this occurs, it is a very minor component of the whole deposit. Aphon = phonolitic layer in A; At-and = trachyandesitic layer in A(1.3). Deposits showing phonolitic-intermediate mixing are labelled^{o}; those showing phonolitic-intermediate-basaltic mixing are labelled oo. The Adeje ignimbrite displays phonolitic-basaltic mixing. Hauyne and sodalite are distinguished only where analysed.

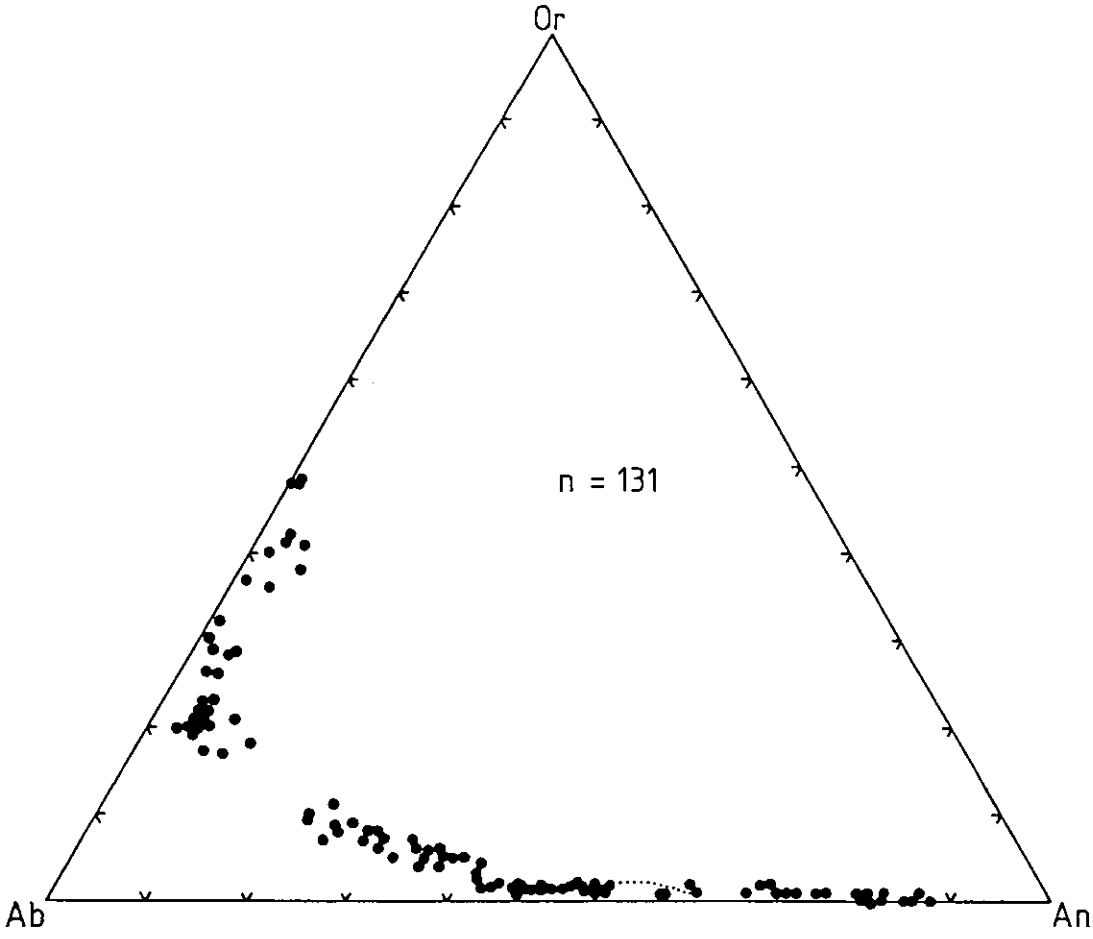

Fig. 3.1 Feldspar compositions analysed from mixed pumices. Dotted line joins extreme compositions in a zoned cyrstal from pumice fall J.

and/or albite twinning is typical. Resorption varies from zero to almost total, where the only indication of an original crystal is adjacent rounded fragments in approximate optical continuity (the detailed form of these, with vesicular glass separating the fragments, indicates that the pre-eruptive configuration has been preserved; this is possible if the magma foam possesses a yield strength, since volumes of zero shear may form during magma transport).

Calcic plagioclases are always resorbed to some extent and are often sieved with black glass blebs. Zoning is less extensive than in the intermediate feldspars (Figure 3.12). Bytownite occurs in the Tajao and Adeje ignimbrites and in ignimbrite O. Plagioclase more calcic than An_{70} (Ridley, 1968) has not previously been described from Tenerife and these occurrences, albeit in unusual magmatic settings, of more "primitive" feldspars is thus of some interest. In some cases compositions may have been modified by resorption; the four analyses in the range An_{85-88} (Figure 3.1) are from heavily resorbed crystals in the Adeje and O ignimbrites. However, in the Tajao ignimbrite, small pristine inclusions of An_{71-81} are found in unresorbed titanaugite and are thus completely insulated from changes in the magmatic environment surrounding the pyroxene crystal. This indicates that bytownite precipitated from the original basaltic liquid component of this ignimbrite (III.2.i). The mere presence of the feldspar is unusual, since plagioclase rarely forms a phenocryst phase in Tenerife alkali basalts which carry titaniferous augite and magnesian olivine (Ridley, 1968; Scott, 1970). Thus the type of basaltic magma available for mixing with more evolved liquid in the centre of the Tenerife volcano appears to be almost unrepresented among Recent lavas on the flanks of the island (although

the author has observed an extensive plagioclase-phyric flow in W. Tenerife).

In summary, the pumice succession affords feldspar samples which extend the previously-known compositional range on Tenerife; this range is duplicated in single eruptive units, and even in single pumice clasts (III.2-III.4).

III.1.ii Feldspathoids

Euhedral nephelines occur in a few deposits. Only one analysed sample, from the Tajao ignimbrite, contains the mineral; its composition is $Ne_{72}Ks_{11}Q_{17}$. Nepheline however is a near-ubiquitous phase in the syenite blocks, and its chemistry is considered in more detail in Chapter V.

More commonly, the feldspathoid present is sodalite/nosean (usually in phonolite) or haüyne (usually in intermediates), although this distinction is based on the few cases where analytical data are available. Haüynes are typically bright blue, the colouring also being apparent in thin section, whereas sodalite is greyish, pale blue or colourless. The appearance of a sodalite-group mineral before nepheline in the crystallisation sequence is compatible with textural evidence from the syenites (Chapter V) and with theoretical considerations of respective mineral stabilities (Stormer and Carmichael, 1971).

Some alkali content variation in the hauynes is apparent. Limited variable substitution of K for Na is apparent; the total alkali content also varies by some 30%. Taylor (1967) proposes two

types of Ca substitution in the hauyne-nosean solid solution series:

$$Ca^{2+}\square \rightleftharpoons Na^{+}_{2}$$

$$\text{and } Ca^{2+}_{2}(SO_4)^{2-} \rightleftharpoons Na^{+}_{2}$$

Neither mechanism explains the observed variation, rather it appears that alkali content varies independently of a near-constant Ca content (appendix B). Present data are too scanty for a full evaluation, although the low totals indicate appreciable water contents of some samples, some of which may be present as H_3O^+. Comparison of haüyne with sodalite/nosean from the Tajao ignimbrite indicates that the first substitution is important in producing large variations.

III.1.iii Pyroxene

Pyroxenes in Tenerife lavas have been studied in detail by Scott (1970, 1976). The principal trend, with evolving magma composition, in the lavas is from titanaugite with up to 10% (by weight) Al_2O_3 in the ankaramites and alkali basalts, through the augites with minor Ti, Al and Na in the intermediate and phonolitic rocks, with some Na enrichment in the most highly evolved lavas. Fe/Mg increases only slightly through the series as a whole, although individual crystals may exhibit appreciable Fe/Mg zonation. Colour varies from pale purple, pink or buff coloured titanaugite to pale or medium green augite. Scott distinguishes normal, reversed, irregular, oscillatory and hourglass zoning forms, and notes the special nature of "green-core" zoning, where green augite is rimmed by pink titanaugite. "Green-core" pyroxenes are known from basic alkaline rocks world-wide (Brooks and Printzlau, 1978, and references cited therein).

Pyroxenes in the pumices exhibit all these features. A colour change, from buff-pink to green, occurs when the TiO_2 content falls below approximately 2% and Al_2O_3 below 5%. Wilkinson (1974) notes that the term "titanaugite" is not precisely chemically defined. One usage (Yagi and Onuma, 1967) places the lower limit of TiO_2 in titanaugite at 2% by weight, and, for convenience, this is adopted here to denote the buff-pink pyroxene. Aegirine-augite has been analysed only from the Tajao ignimbrite; all other analysed pyroxenes are referred to as augite.

Titanaugite occurs only in the Tajao and O ignimbrites, and in pumice fall J; it is inferred to be derived from original alkali basalt magma. Oscillatory and overall normal zoning (Figure 3.2) are common; reversed and hourglass zoning also occur. Two or more zoning patterns may be superimposed within a single crystal (Figure 3.2). A "green-core" pyroxene with titanaugite rim (Figure 3.3) occurs in the Tajao ignimbrite; its basaltic provenance is indicated by the rim composition.

Decreasing Al and Ti in titanaugite is accompanied by an increase in Mg (Figure 3.3). Ti in titanaugite is due to the presence of the molecule $CaTiAl_2O_6$ (Yagi and Onuma, 1967). The excess of Al over 2Ti in the Tenerife pyroxenes (Appendix B5, Scott, 1976) indicates the presence of other Tschermak's molecules; calculation of pyroxene end-members by the method of Cawthorn and Collerson (1974) indicates 3-7% of CaAlAlSiO6 in the titanaugites. The incorporation of $CaTiAl_2O_6$ and $CaAl_2SiO6$ into clinopyroxene may be simply understood as follows. Consider an alkali basalt in which augite and plagioclase are co-precipitating. We may write

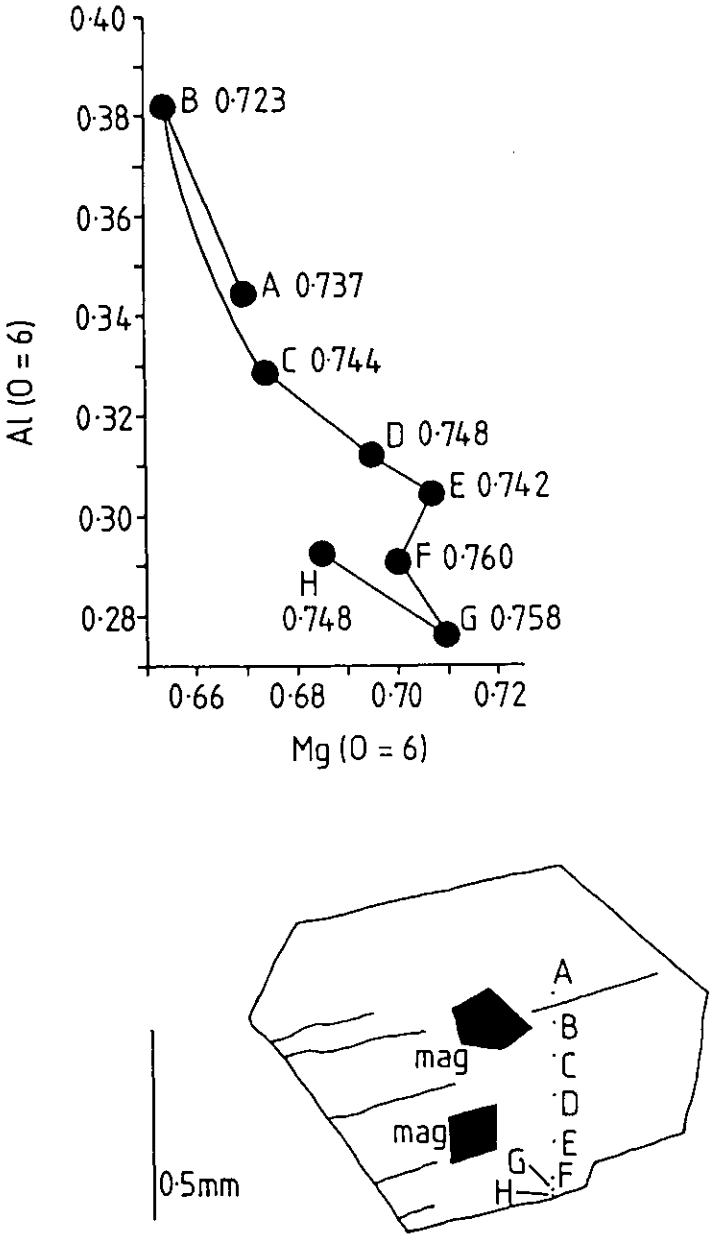

Fig. 3.2 Plots of Al vs. Mg (cations calculated on the basis of 6 oxygen atoms per mineral formula) for 8 points in a zoned titanaugite from the Tajao ignimbrite, shown in accompanying sketch. Numbers against lettered points are Mg/(Mg + Fe). Analysis B is considered to be a core composition. Note minor ozcillation of zoning near rim of crystal.

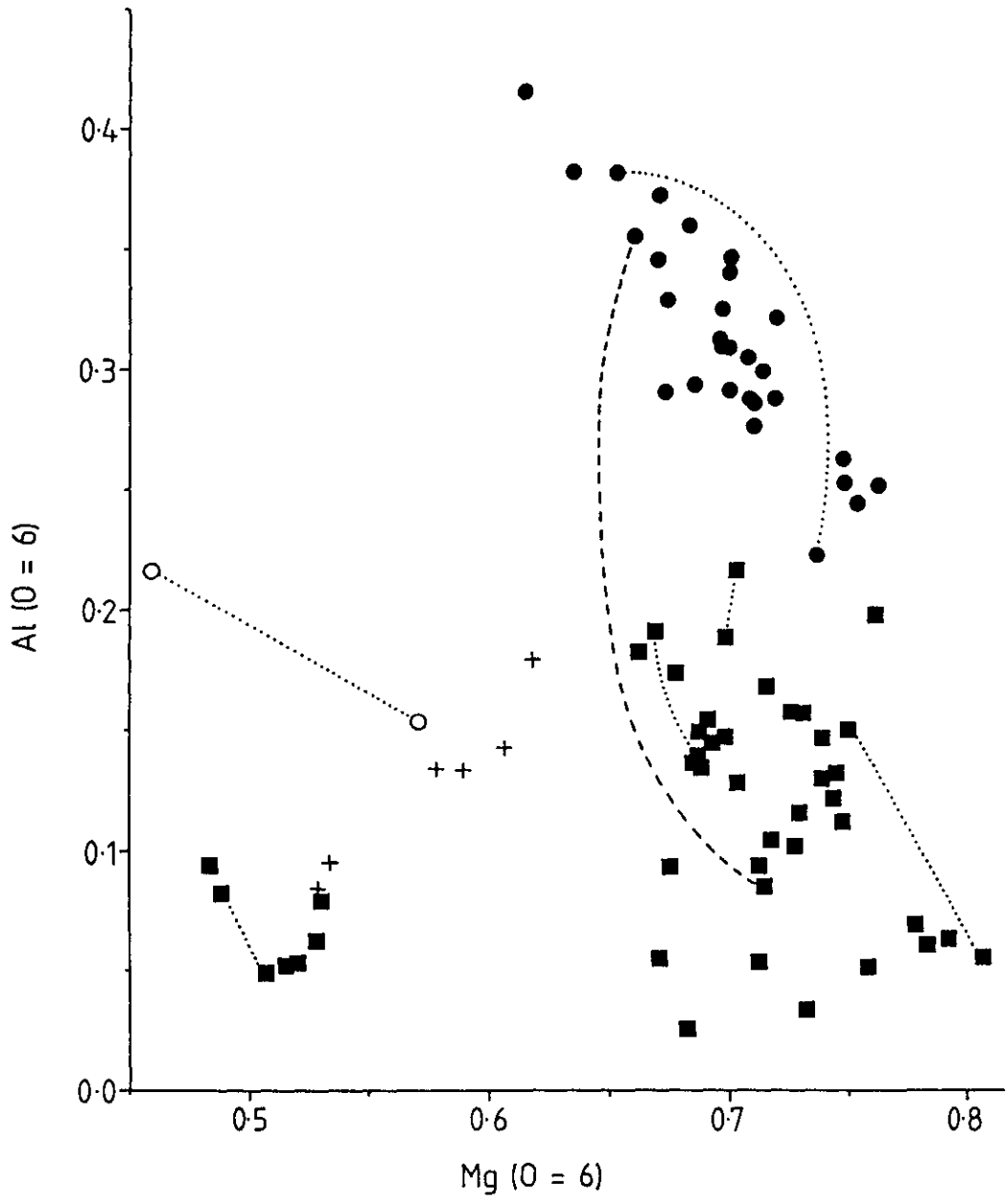

Fig. 3.3 Plot of Al vs Mg (on the basis of 6 oxygen atoms) for all analysed pyroxenes in mixed pumice samples. Filled circles: buff-pink titanaugites; filled squares: green augites; crosses: selected Al-poor augites from Medano xenoliths; open circles: core and rim of a euhedral pyroxene from haüyne-phonolite intrusion, Teneguia, La Palma. Dotted lines link extreme compositions in zoned crystals; dashed line links core (square) and rim (circle) of a "green-core" pyroxene from the Tajao ignimbrite. The squares plotting in the lower left-hand corner are all of deep green aegirine-augite from the Tajao ignimbrite. Were aegirines from the nepheline syenites to be included, they would plot at Al = 0.05, Mg=0-0.3, indicating a trend of decreasing Mg once Al drops below ~0.1 atoms per formula. Note then the anomalous positions of (possibly metasomatic) compositions (Chap. V) from Medano xenoliths, and of the unrelated La Palma sample.

$$CaAl_2Si_2O_8 + TiO_2 \rightarrow CaTiAl_2O_6 + 2SiO_2$$

plagioclase liquid pyroxene liquid

and $$CaAl_2Si_2O_8 \rightarrow CaAl_2SiO_6 + SiO_2$$

plagioclase pyroxene liquid

Alkali basalt liquids have high a_{TiO_2} and low a_{SiO_2} and thus their pyroxenes are comparatively Al and Ti-rich. If, as during the normal course of magmatic evolution, a_{TiO_2} and the anorthite content of plagioclase fall, and/or a_{SiO_2} rises, then pyroxenes become progressively impoverished in the Tschermak's components. This is fully consistent with observed Al content variation (Figures 3.3, 3.13, 3.28; Scott, 1970). Thus the increase in Mg with falling Al is partly due to the increasing proportion of other pyroxene components as the Tschermak's-molecule content falls. However, when individual zoned crystals are examined (Figure 3.2), a small but progressive increase in $Mg/(Mg+Fe^{2+})$ with decreasing Al becomes evident; this relationship is partly obscured by the greater scatter when all samples are considered together. The same relationship is found in individual zoned crystals analysed by Scott (1970). The low degree of Fe enrichment in pyroxene through most of the series has already been noted; if the previous remarks about falling Al content hold true, then it appears that $Mg/(Mg+Fe^{2+})$ actually increases slightly for small increments of pyroxene evolution. The relative availability of Mg and Fe^{2+} in the magma governs the $Mg/(Mg+Fe^{2+})$ ratio of any ferromagnesian mineral. Petrographic evidence indicates that the pumice titanaugites crystallised in the absence or near-absence of olivine, but in the presence of titanomagnetite with an $Mg/(Mg+Fe^{2+})$ ratio of ca. 0.25 (Figure 3.16). Clearly if sufficient titanomagnetite is co-precipitating, the relative abundance of Mg in the liquid may increase. The changing ferric/ferrous ratio of the evolving magma will also limit the availability of Fe^{2+}. Fe^{3+}/Fe^{2+}

increases with decreasing Fe_{total}, Mg and temperature, and with increasing Na, K and fO_2 (Sack et al., 1980). Therefore Fe^{2+} in magma falls faster than the total iron content with evolution, tending to increase $Mg/(Mg+Fe^{2+})$. The importance of T-fO_2 variation during differentiation in controlling overall Tenerife pyroxene trends has been discussed by Scott (1976). The possible role of water in producing the Mg/Mg+Fe variation is discussed in III.5.

Pale green augite is found in mixed-magma pumice as part of an intermediate assemblage, and in phonolitic tephra. The latter is usually slightly richer in sodium. To examine the behaviour of Na in the pyroxenes, compositions have been plotted in $Mg-(Fe^{2+}+Mn)-Na$ (Figure 3.4). Fe^{2+} was calculated by assuming that all Na is in acmite i.e. $Fe^{2+} = Fe_{total} - Na$. This is at variance with the recommended scheme of Cawthorn and Collerson (1974) which minimises the significance of the unreported Fe^{3+} in microprobe analyses, and thus in theory allows rigorous comparison with end-member concentration. In this scheme Al is first allotted to jadeite ($NaAlSi_2O_6$) any residual Na being allotted to acmite ($NaFe^{3+}Si_2O_6$). Ti is allotted to $CaTiAl_2O_6$, any remaining Al being used to form $CaAl_2SiO_6$. This method is suitable for the titanaugites where Al >> Na; for the Al-poor augites it typically results in the calculation of negative quantities of $CaAl_2SiO_6$. Worse, where Na > Al, Ti cannot be allocated (Na-Ti pyroxene members have only been considered as components of aegirine from the nepheline syenites, Chapter V). Therefore, the scheme of Cawthorn and Collerson (1974) is rejected for the Al-poor pyroxenes in favour of calculating all Na as acmite, and thus $Fe^{3+} = Na$. This procedure was adopted by Scott (1970, 1976) and seems intuitively reasonable for pyroxenes crystallising at low pressure from alkaline magma. For comparative purposes, titanaugites have been plotted in

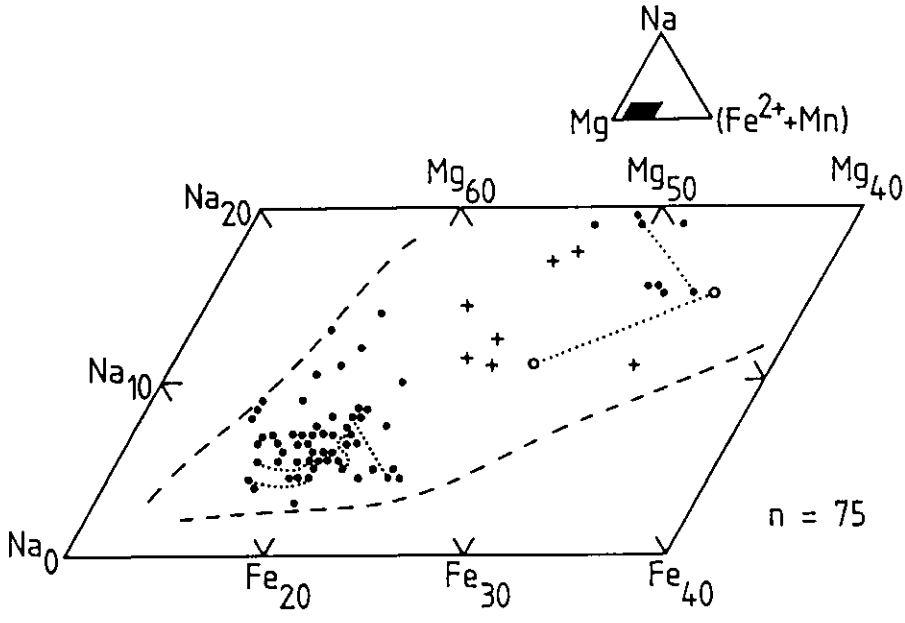

Fig. 3.4 Plot of Mg - (Fe^{2+} + Mn) - Na for pyroxenes. n = 75 refers to pyroxenes from mixed pumices (dots). Other symbols as Fig. 3.4, except dashed lines which delimit the field of Tenerife pyroxene compositions reported by Scott (1970, 1976).

Figure 3.4 on the same basis, although their low Na contents have an insignificant effect on the Mg/Fe^{2+} ratios.

Some features of Figure 3.4 deserve comment. Firstly, all analyses plot within the spread of values found by Scott (1970, 1976) for all available Tenerife pyroxene analyses. The maximum concentration of points (around $Mg_{73}(Fe+Mn)_{20}Na_7$) represents pyroxenes derived from basaltic and intermediate magmas in mixed-magma units; most phonolitic augites plot on the Na-rich side of this cluster, and a few have Na > 10. Secondly, individual zoned crystals may show enrichment trends towards either hedenbergite or acmite, probably a reflection of how fO_2 varied with falling temperature during crystal growth (Scott, 1976). Thirdly, aegirine-augites from one ignimbrite (points around $Mg_{52}Fe_{31}Na_{17}$) are considerably more Fe- and Na-rich than any others, and are at the limit of Na-Fe enrichment found by Scott for lava pyroxenes. The reality of the compositional gap is uncertain; Scott's data also suggest a gap, although much smaller, in the same region of the diagram. The gap is occupied by some compositions from the Medano syenites, although these may be partly metasomatic in origin (Chapter V); their anomalous compositions are apparent in Figure 3.3.

Overall, compositional variations in the pumice pyroxenes show less scatter than those found by Scott (1970), who records, for example, occasional titanaugites from phonolite and trachyandesite lavas, and crystals displaying irregular zoning patterns encompassing both Al-rich and Al-poor varieties. In the mixed-magma pumices, pyroxene is always the mineral least affected by resorption, and it can thus be envisaged that pyroxenes may survive as recorders of

magma mixing events after complete homogenisation and re-equilibration of other minerals and magma. The large scatter in pyroxene compositions from similar lavas may indicate that some of these are mixed-magma rocks; groundmass crystallisation tends to obscure evidence for magma mixing (Anderson, 1976).

III.1.iv Olivine

Forsteritic olivine rarely occurs in the pumice series; it is recorded from falls J, M and the Tajao ignimbrite. In all three it is a very minor component; a few crystals occur in concentrates of J and M but were not analysed. Three colourless and featureless rounded grains in a Tajao section were analysed; the composition between and within grains is constant at Fo_{79} with minor Ca and Mn.

III.1.v Amphibole

Fresh euhedra of a strongly pleochroic (pale brown-medium red-brown-dark brown) amphibole, thought to have precipitated originally from trachybasalt/trachyandesite magmas, are found in mixed-magma pumice. The mineral is Ti-rich ($TiO_2 > 5\%$) and Si-poor ($SiO_2 \simeq 40\%$) and is classified as kaersutite. Compositions are closely similar to those analysed by Scott (1970) from lavas, and are remarkably uniform (Appendix B). The small sympathetic variation in alkali versus silica content (Figure 3.5) suggests limited substitution of the $(Na, K)Si \rightleftharpoons M^{2+}Al$ type common in alkali amphiboles (e.g. Powell, 1978). In many cases Na+K is less than 1.00 cations per 23 oxygen atoms in the recalculated formula, indicating an incompletely filled A site. In the most alkali- and silica-poor samples, Si+Al is less than 8.00, suggesting the entry of Fe^{3+} into the tetrahedral (Z) site. Ridley (1970) found that Fe^{3+} in a kaersutite megacryst from Tenerife accounted for 36% of

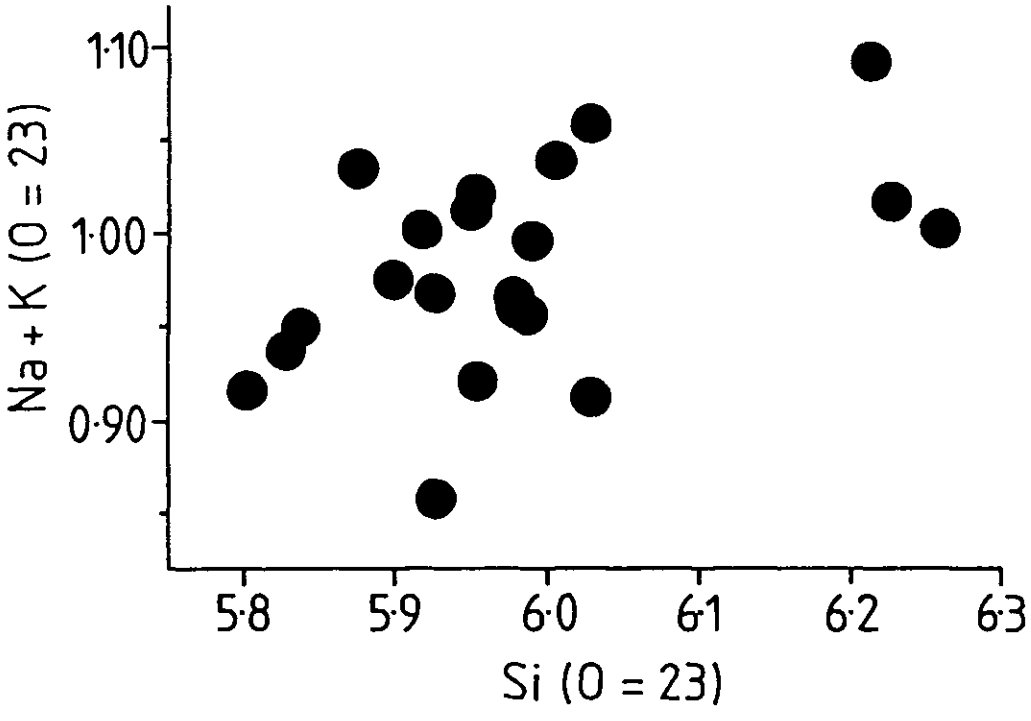

Fig. 3.5 Na + K vs. Si per mineral formula recalculated on the basis of 23 oyxgen atoms, for amphiboles from mixed pumices. Note that analytical error (App. B) is a sufficiently large fraction of the small compositional range to account for the scatter.

total iron; if this is typical, it may explain the non-systematic Mg/Fe variation observed in the present examples (Appendix B).

In many of the lava samples studied by Scott (1970) the kaersutite is heavily altered to, and sometimes completely pseudomorphed by, a fine-grained mass of pyroxene and Fe-Ti oxides. Scott attributed this to amphibole instability consequent on P_{H_2O} reduction accompanying surface extrusion. The invariably fresh nature of kaersutite in the pumice samples, where P_{H_2O} and T dropped from magmatic to atmospheric values very rapidly during explosive eruption thus quenching hydrous phases, supports Scott's hypothesis. A more problematic aspect of the occurrence of hydrous phenocrysts in lavas is that substantial volatile loss must have occurred shortly before eruption, otherwise either the mineral could not have precipitated in the first place, or else the magma would have been erupted explosively, not as a lava. Magmatic volatile separation and relationships between spatially-associated lavas and pyroclastics are discussed in III.5.

III.1.vi Biotite

Biotite is a minor component of all studied deposits. Crystals almost always appear fresh (cf. amphiboles above) and show intense pleochroism (light brown/golden yellow-very dark brown or near-black) typical of Ti-rich biotites (Borley, pers. comm.). Chemical and optical zoning are absent. Analysed biotites are Mg-rich; several have Mg/(Mg+Fe) greater than 0.67 (Figure 3.6) and thus may be termed phlogopites (Deer et al., 1966).

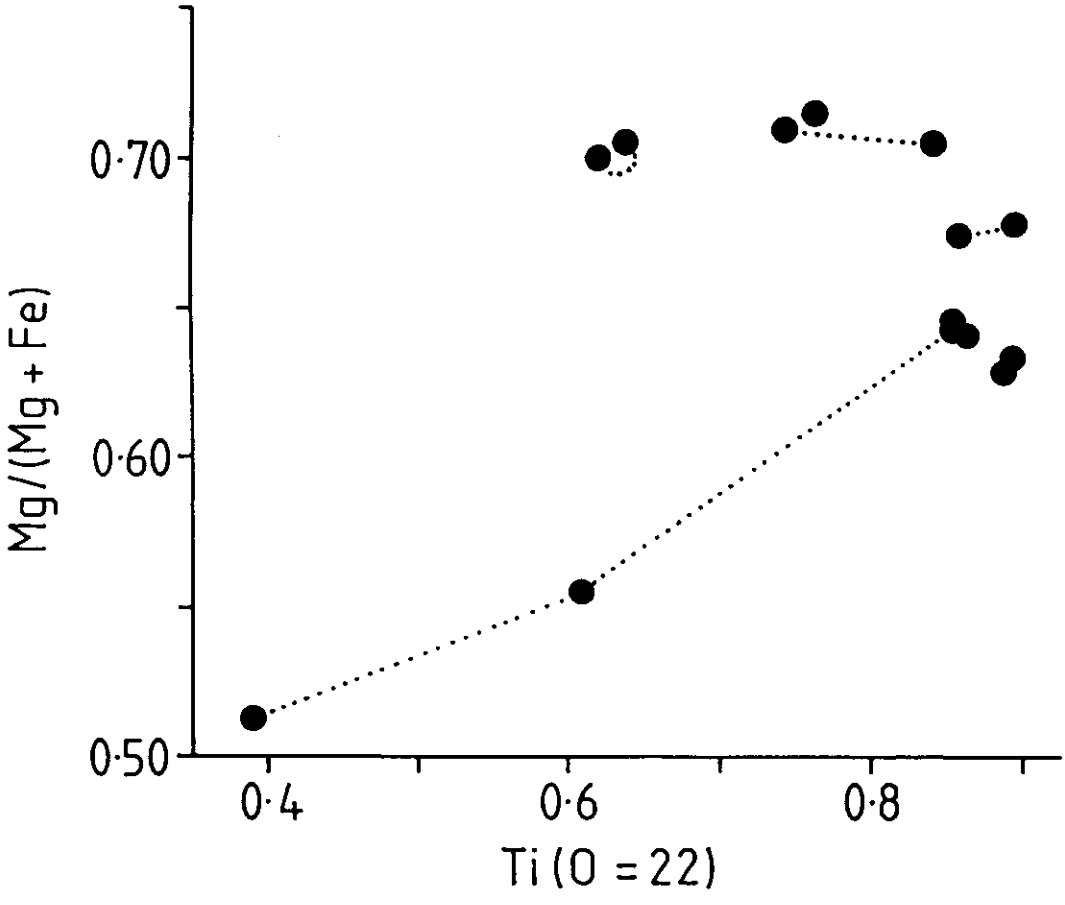

Fig. 3.6 Mg/(Mg+Fe) vs. Ti per mineral formula recalculated on the basis of 22 oxygens, for biotite from mixed pumices. Grains from the same deposit either overlap or are joined by dotted lines; the five points so indicated are all from the Tajao ignimbrite.

The biotites are notable for their high Ti contents ($TiO_2 \leqslant 8.5\%$). All analysed crystals possess a tetrahedral site deficiency (mean Si+Al = 7.80, σ = 0.07). Carmichael (1967a) and Scott (1970) analysed closely similar specimens, and suggested that Ti^{4+} was capable of entering the tetrahedral site in biotite, thus explaining the apparent correlation of high Ti with low Si. A plot of Si versus Ti for Ti-rich biotites (Figure 3.7a) indeed shows an apparent 1:1 replacement of Si by Ti. However, the large degree of scatter (r = 0.77), and the distinct trend of some Azorean biotites, indicate that the actual substitution is more complex than simple Ti $\rightleftharpoons$ Si exchange. Furthermore, there is no correlation between Si + Al and Ti (Figure 3.7b), which refutes the suggestion that Ti enters the tetrahedral site in biotite.

Holdaway (1980) has studied the compositions of biotites from pelitic metamorphic rocks (mean Ti content = 0.281 per 22 oxygens) and proposes that Ti entry is governed by the substitution

1. $(M^{2+})^{oct}\ Al^{oct}_{0.67} \rightleftharpoons Ti^{oct}\ \square^{oct}_{0.67}$ where $\square$ = vacancy

Holdaway further proposes the substitution

2. $(M^{2+})^{oct}\ Si^{tet} \rightleftharpoons Al^{oct}\ Al^{tet}$,

and thus the possibility of an antithetic relation between Ti and Si arises

3. $(M^{2+})^{oct}_{2}\ Si^{tet} \rightleftharpoons Ti^{oct}\ Al^{oct}_{0.33}\ \square^{oct}_{0.67}\ Al^{tet}$

These substitutions require the presence of Al in the octahedral site, which seems unlikely where there is a tetrahedral site deficiency. Another possible means of incorporating Ti into biotite is analogous to its entry into clinopyroxene:

$$(M^{2+})^{oct}\ Si^{tet}_{2} \rightleftharpoons Ti^{oct}\ Al^{tet}_{2} \qquad 4.$$

Ti+Al versus M^{2+} + Si shows an excellent correlation (Figure 3.8), but with a slope inconsistent with (4). An appropriate simple substitution mechanism for Ti in biotite is

$$(M^{2+})^{oct}_{2}\ Si^{tet} \rightleftharpoons Ti_{1.25}\ Al^{tet}\ \square^{oct}_{0.75} \qquad 5.$$

Note that this substitution has a slope closely similar to that of (3) and thus would be virtually indistinguishable at the comparatively low Ti levels of Holdaway's (1980) samples. However it should be emphasised that, until an exhaustive study of chemical variation in Ti-rich biotites is made, the proposed substitution (5) can only be considered tentative.

If stoichiometry of 16 cations + vacancies per 22 oxygens in the recalculated biotite formula is assumed, then the Fe^{3+} content can be estimated. Calculation using either substitution (3) or (5) indicates negligible Fe^{3+}, consistent with the unoxidised appearance in thin section.

Storey (1981) finds a systematic decrease in biotite Ti content with decreasing Mg/(Mg+Fe) for successive stages in the crystallisation of a single trachytic magma body periodically tapped by pumice eruptions at Agua de Pau volcano, Sao Miguel, Azores. This relationship has only been found within one eruptive unit on Tenerife (Figure 3.6), suggesting further (Chapter II) that no such simple genetic inter-relation exists between the major pumice deposits.

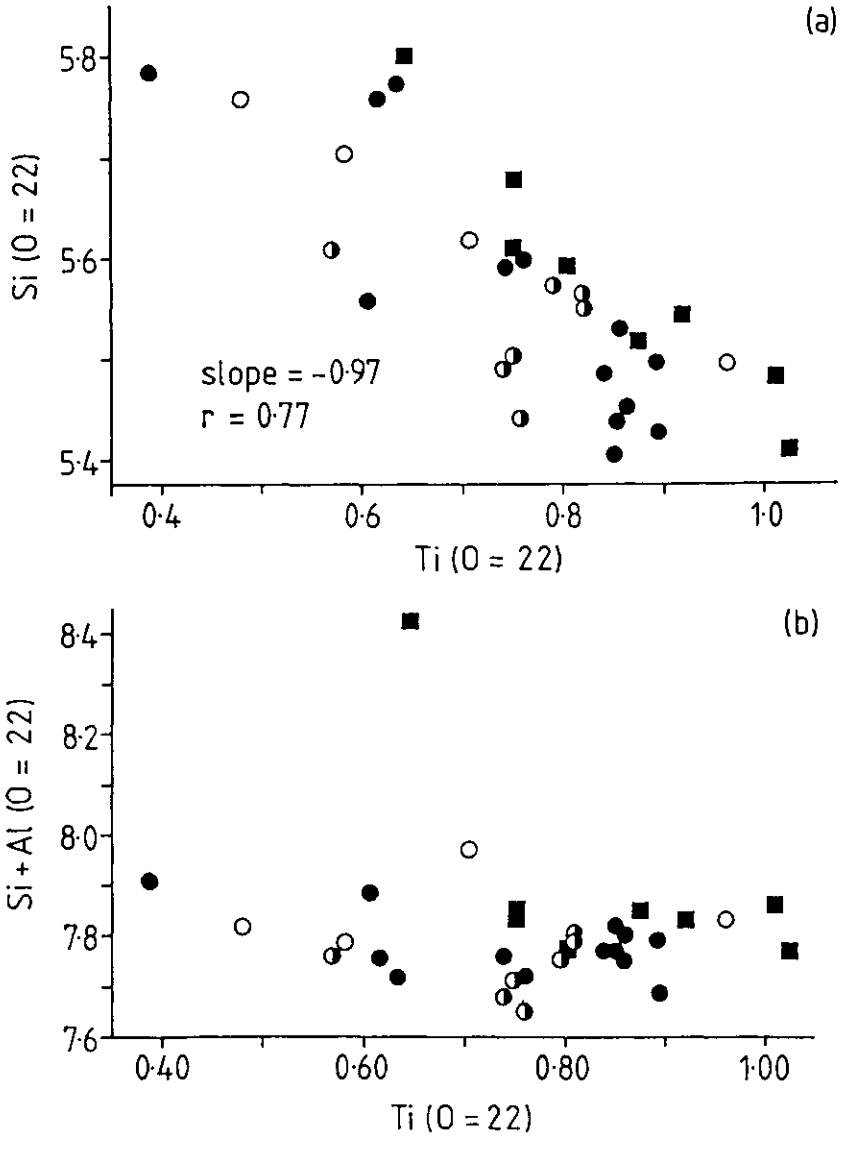

Fig. 3.7 Compositional relations in Ti-rich biotite (cations on basis of 22 oxygens). Filled circles: Tenerife pumices; open circles. Tenerife syenites; half-filled circles: Tenerife biotites analysed by Scott (1970) and Carmichael (1967); filled squares: biotites from trachytic pumices, Sao Miguel, Azores (Storey, 1981). (a) Si vs. Ti. (b) (Si + Al) vs. Ti.

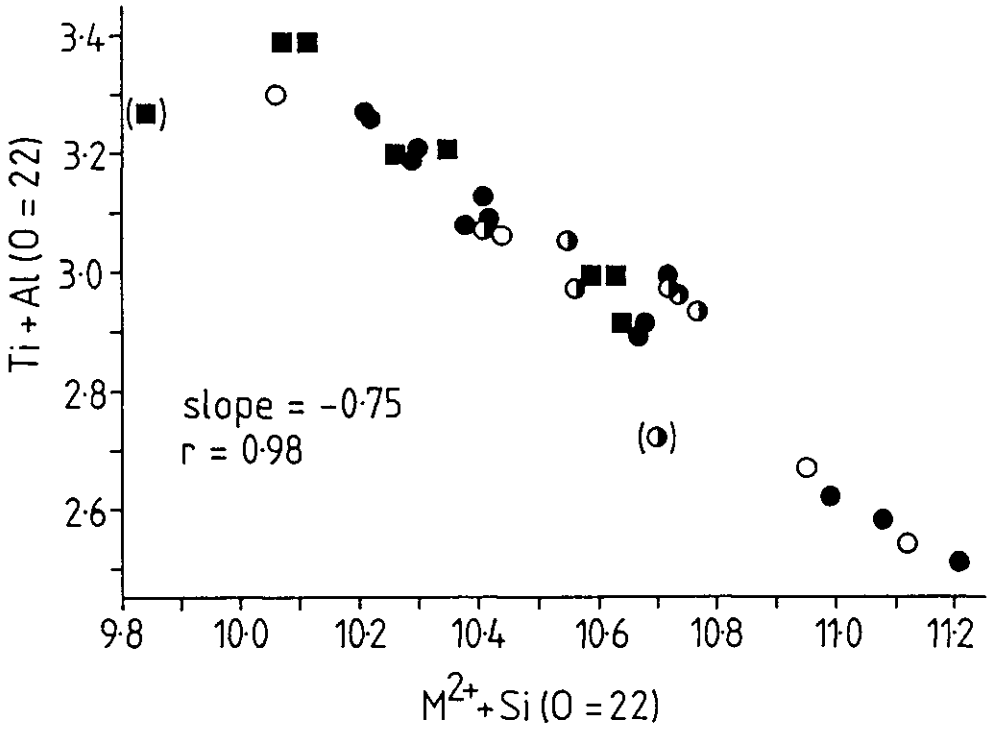

Fig. 3.8 (Ti + Al) vs M^{2+} (Fe + Mn + Mg) + Si in biotites on basis of 22 oxygens, same symbols as Fig. 3.7. Small quantities of Co are included in M^{2+} for some Azores samples. Bracketed points were omitted from regression.

III.1.vii Sphene

Small golden-yellow sphenes occur in several deposits. Partial analysis of a grain in the Tajao ignimbrite reveals minor quantities of Na, Al and Fe. Appreciable Nb was qualitatively detected, consistent with the occurrence of Zr, Nb and REE in sphenes from the Medano xenoliths (Chapter V).

III.1.viii Fe-Ti oxides

At least one Fe-Ti oxide is always present; titanomagnetite is more common and often forms perfect octahedra. Co-existing ilmenite is usually subordinate and sometimes absent from phonolites. Both minerals are present as free crystals up to several hundred microns in diameter, but are especially common as inclusions in silicate phases, particularly pyroxene. Considerable chemical variation is apparent. Ulvöspinel content in titanomagnetite varies between 25% and 50%, whereas ilmenite contains 10-20% of the hematite component. In both minerals, the titanium content falls with magmatic evolution. Mg, Mn, Ca, Al, Cr and Si have been detected, Mg and Mn (and Al in titanomagnetite) being particularly abundant. Mg decreases with the ulvöspinel content of titanomagnetite (Figure 3.9); Al and Cr also decrease, and Mn increases, with magmatic evolution. The Mg/Mn ratio in both phases, is a sensitive indicator of the magma type from which they originally precipitated, and is thus useful in deciphering relations in mixed-magma deposits (III.2). Carmichael (1967a) finds that Mg/Mn ratios of coexisting magnetite and ilmenite are comparable, with the spinel phase being relatively enriched in Al. This relationship is clearly displayed by all analysed co-existing oxides (e.g. Figure 3.14). Minor element contents, and the use of co-existing Fe-Ti oxides in geothermometry and oxygen barometry is further discussed in Chapter IV.

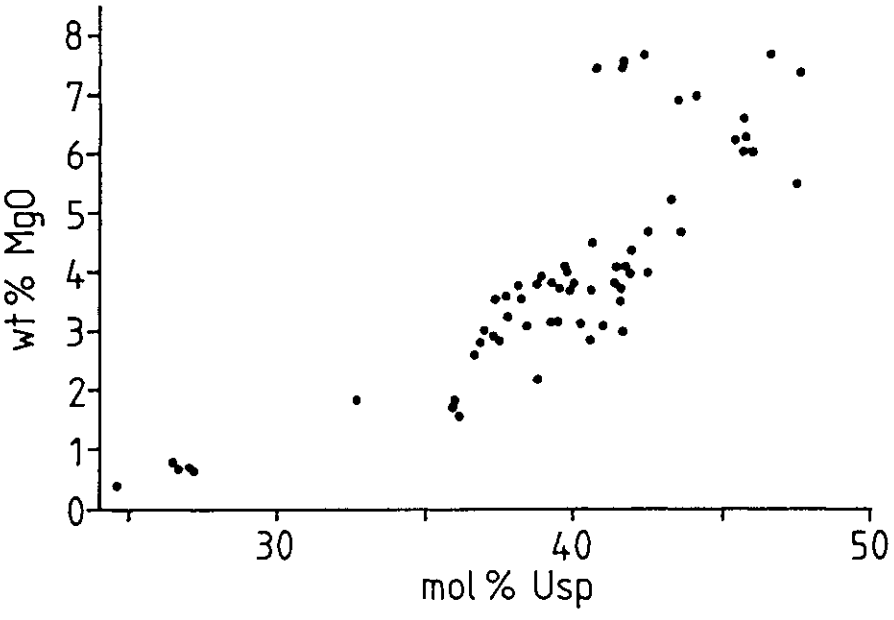

Fig. 3.9 Wt% MgO vs. ulvo spinel content of titanomagnetites from mixed pumices.

Ilmenite is sometimes absent from phonolites, where its place as a host for Ti may be taken by sphene. A plausible representation of this reaction is

$$3CaFeSi_2O_6 + 3FeTiO_3 + O_2 \rightarrow 3CaTiSiO_5 + 2Fe_3O_4 + 3SiO_2$$

pyroxene ilmenite sphene Ti-mag liquid

As a_{SiO_2} falls during phonolite evolution as alkali feldspar precipitation drives the liquid towards more highly ne-normative compositions, the reaction is driven to the left and sphene forms at the expense of ilmenite. The reaction is thus consistent with the presence of composite grains of pyroxene, sphene and magnetite in the phonolite of the Tajao ignimbrite, which has undergone considerable alkali feldspar fractionation. A more complex sphene paragenesis, also dependent on falling a_{SiO_2}, is given by Carmichael et al. (1974, p.110).

III.1.ix Apatite

Apatite is a ubiquitous accessory among the studied samples. It always occurs as inclusions in other minerals, especially Fe-Ti oxides, pyroxene, and amphibole. Free crystals have not been found, suggesting that the mineral has preferentially nucleated on the surfaces of growing silicate or oxide crystals.

The ideal apatite formula is $3Ca_3(PO_4)_2.Ca(OH,F)_2$. Analysis reveals minor quantities of other elements; Fe, Mg and Na, and presumably Ti, substitute for Ca; Si and S substitute for P; Cl substitutes for F. La and Ce were qualitatively detected in phonolite apatites, although a long (500 sec) count on an "intermediate" apatite from pumice J failed to detect any REE. The sum P+Si+S is usually close to 6.00 when (albeit partial) analyses are recalculated on the basis of 25 oxygens as required by stoichiometry; however $\Sigma_M{}^{2+}$ is usually greater than 10.0. A similar excess was noted by Vlasov et al. (1966)

in REE-rich apatites from the Kola peninsula, U.S.S.R.

III.1.x Pyrrhotite

Pyrrhotite has been found in several analysed samples; it probably occurs in other pumice deposits for which polished sections were not available. It occurs in two distinct forms. The dominant form is as rounded inclusions in phenocrysts up to several tens of microns in diameter. These are most often found in Fe-Ti oxides, occasionally in ferromagnesian silicates, and rarely in feldspars. It is uncommon to find more than one or two grains per phenocryst, and they are considered to have precipitated from the magma before inclusion in the host mineral. The other form is as a fine "dusting", individual grains being a few microns or less in diameter, in haüyne phenocrysts. This is thought to have formed as a response of the haüyne to changing conditions after its formation; for example increasing temperature or falling f_{O_2} causing instability of the sulphate radical.

All analysed pyrrhotites have an excess of S over Fe. Excess S is expressed in terms of a solid solution FeS-S_2, and directly reflects the fugacity of sulphur in the environment from which the pyrrhotite crystallised (Toulmin and Barton, 1964; see Chapter IV). Some grains have a minor content of Mn or Cu; Co, detected in sulphides from xenoliths (Chapter V), is absent in the pumice pyrrhotites.

III.1.xi Glass

Glass was originally the principal mineral of the pumice series, but little pristine material has survived. It remains chiefly in poorly- or non-vesiculated samples; curiously, some exceptionally

inflated pumice clasts (density = 0.3-0.5 gcm^{-3}, indicating >80% vesicularity, G.P.L. Walker, pers. comm.) are also composed of glassy material. Examination of hydration rinds in cracked obsidian suggests that most glassy pumice is substantially hydrated, since bubble wall thicknesses are typically less than hydration depth ($\leqslant$ 50 μm).

Most pumice has devitrified to a crypto-crystalline mass appearing structureless in thin section. Comparison of whole-pumice compositions with remnant glassy patches shows that substntial Na loss occurs during devitrification.

Analysed salic glasses are peralkaline phonolites; oxide totals are usually less than 99%, reflecting variable hydration (Appendix B). The peralkalinity is not found among whole-pumice samples, due to their having suffered Na loss, but is in keeping with phonolite lava chemistry (Ridley, 1968). The extent to which hydration alone affects Na content is uncertain; Scott (1971a, b) finds that hydration tends to remove Na from rhyolitic ash. Thus the highest recorded Na content from a given sample should be close to the original; however the glass may have been heterogeneous prior to hydration (III.2-4). It is nonetheless apparent that Na contents in the probed glasses are close to those of the lavas, and thus there is no significant difference in major-element composition between Tenerife lavas and pyroclastics (see III.V for fuller discussion).

Mixed-magma pumice in thin section consists of streaks or bands of colourless or pale yellow glass alternating with dark brown to black glass (Figure 3.10). Banding, often with delicate inter-

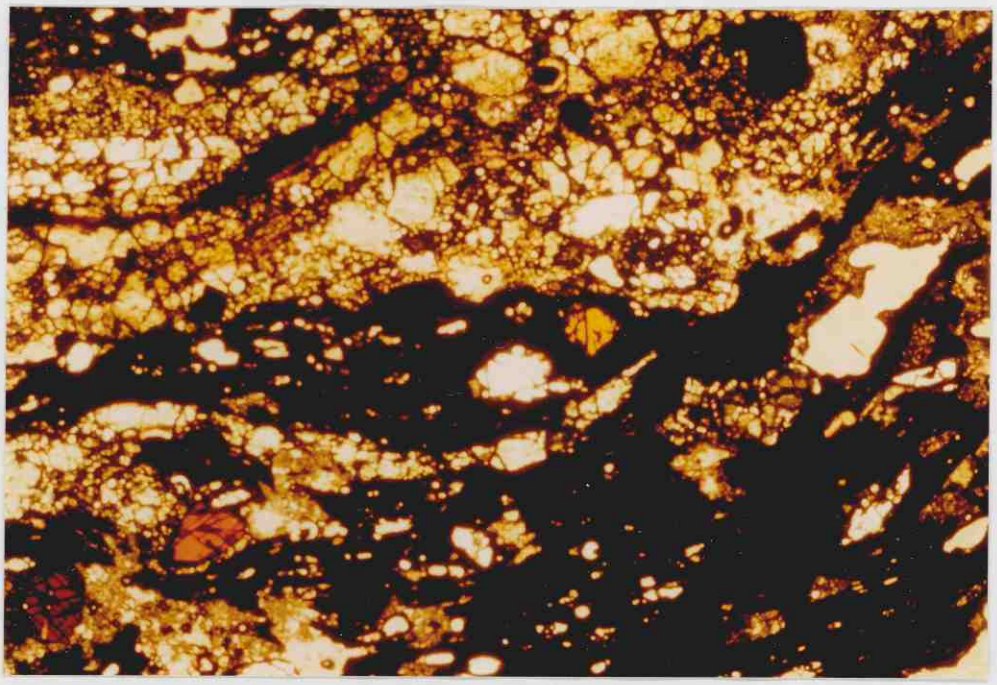

Fig. 3.10a Streaky mixed pumice from the Tajao ignimbrite, in thin section. Note dark glass adhering to amphibole phenocrysts. PPL, x8.

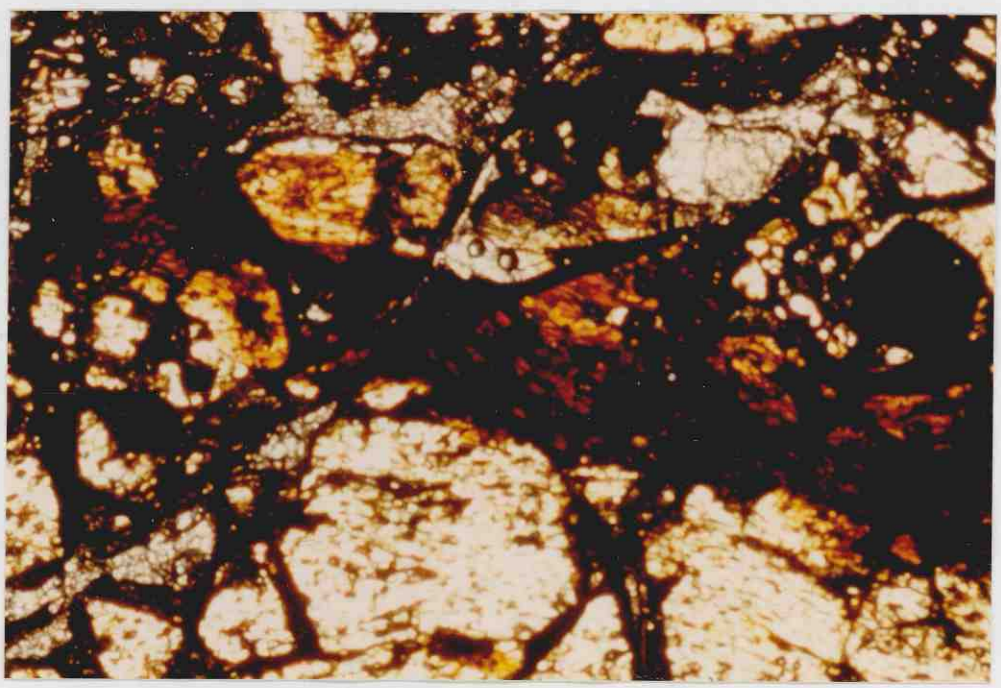

Fig. 3.10b Detail of dark streak in mixed pumice, as above. Note partial homogenisation of brown and pale glasses. PPL, x60.

fingering, is typically on the scale of <1 mm to a few cm. Occasional large blocks (> 10 cm) consisting almost entirely of black pumice also occur in the Tajao and O ignimbrites. Band boundaries may be sharp or gradational and most samples contain a proportion of pale brown glass intermediate in shade between the light and dark varieties. The mafic glass varies in composition from trachyandesitic to phonolitic, and the compositional contrast is considerably less than that suggested by the colour contrast, and by the compositions of associated phenocrysts. Compositional variation within the mafic glass approximates to a straight-line relationship and is ascribed to partial homogenisation of intermediate and phonolitic end-members (III.2,3). Thus the dark colour, presumably inherited from the original mafic magma, is retained until a high dilution of original mafic in original salic component is reached (Figures 3.22, 3.23, 3.30).

The colour banding may be partly explained as follows. The Fe^{3+} cation is the principal colouring agent present in natural glasses. The Fe^{III}/Fe^{II} ratio increases in magmas with decreasing temperature, Fe and Mg concentrations, and with increasing alkali concentration (Sack et al., 1980). Thus evolved liquids such as phonolite commonly have higher Fe^{III}/Fe^{II} ratios than more primitive types, although their low total iron contents result in a low absolute concentration of Fe^{3+} and hence pale colouration. If a more basic liquid, with higher total iron content but lower Fe^{III}/Fe^{II} ratio, is now mixed with the salic magma, the value of the ratio will adjust towards that of the salic magma. This will cause an abnormally high absolute concentration of Fe^{3+} in the more basic component, thus intensifying its colouration. If the mixed magma is quenched before chemical homogenisation occurs,

the colour contrast is preserved in the glass, and streaky or banded pumice is produced. The operation of additional unknown factors in causing colour contrast is indicated by a streaky-pumice ignimbrite from La Primavera, Mexico, in which the two members have identical major-element compositions (Wolff et al., 1980; Wright, 1981).

The compositional variation of glass in one mixed ignimbrite is discussed in detail in III.2.

III.2 THE TAJAO IGNIMBRITE

Field relations of the Tajao ignimbrite are briefly described in Chapter I. In summary, the unit forms the top of the Granadilla Series, has a probable original erupted volume of <0.2 km^3 DRE, is non-welded and contains roughly 20% of dark pumice.

III.2.i Petrography and mineralogy

Combined thin-section and electron microprobe study of streaky pumices from the Tajao ignimbrite has revealed the presence of 18 phenocryst phases together with mafic and salic glass (Figure 3.10) both of which are compositionally variable. On the basis of enclosing relationships and intergrowths in aggregate phenocryst grains, these have been grouped into three mineralogically and compositionally distinct assemblages (Table 3.2). The Fe-Ti oxides were especially useful in constructing these "correlations" due to their frequent occurrence as inclusions in silicate phases. Crystals of assemblages 1 and 2 are normally found in dark glass or, if in salic, are surrounded by a thin envelope of brown glass, although this

is not invariably the case (Figure 3.11). The only mineral not found in aggregate grains is nepheline; however, as this is never found in association with mafic glass and is Ca-poor it may with confidence be assigned to assemblage 3. It should be stressed that all the described relations may be observed within a single thin section.

The lack of remnant cumulate textures (as distinct from aggregate grains), of finely crystalline material adhering to assemblage 1 and 2 phenocrysts, and the association with optically and compositionally variable ass demonstrates that the more basic material has not been introduced by xenolithic contamination. Plutonic lithics are absent from this ignimbrite, and basaltic lithics lack any juvenile coating, nor do they exhibit partial disaggregation as seen in the basal fall unit of pumice G, or other occurrences of undoubted xenolithic contamination (Chapters I and II, Table 3.1). It is difficult to envisage any mechanism which could allow the retention of basaltic phenocrysts by the late differentiate of a single magma batch. The preservation of crystals in gross disequilibrium with their environment indicates that they entered that environment a very short geological time before quenching (eruption). Therefore, it is concluded that the observed relations in the Tajao ignimbrite, and others like it, are the result of magma mixing shortly before eruption. Of course, this conclusion alone places few constraints on the spatial and chemical relationships of the magmas before mixing.

Associations in aggregate grains	Inferred assemblage
Buff-pink pyx - bytownite - high Mg magnetite; Buff-pink pyx - high Mg ilmenite; Olivine - high Mg magnetite	Olivine - buff-pink pyx - bytownite - high Mg magnetite - high Mg ilmenite. (Assemblage 1).
Andesine - pale green pyx - medium Mg ilmenite - medium Mg magnetite; Andesine - amphibole - medium Mg magnetite; Andesine - amphibole - hauyne	Andesine - pale green pyx - amphibole - medium Mg magnetite - medium Mg ilmenite - hauyne. (Assemblage 2).
Alkali fsp - biotite - low Mg magnetite; Deep green pyx - sphene - low Mg magnetite; Alkali fsp - deep green pyx; Alkali fsp - sodalite; (nepheline)	Alkali fsp - deep green pyx - low Mg magnetite - biotite - sphene - sodalite - nepheline. (Assemblage 3).

Table 3.2. Summary of correlations of phenocryst phases in the Tajao ignimbrite.

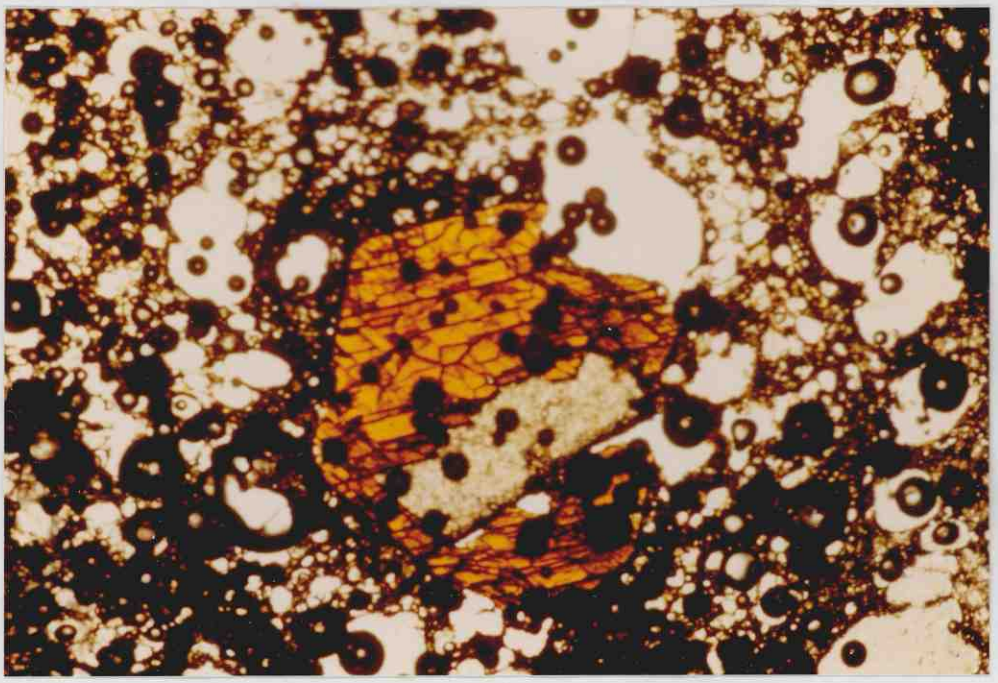

Fig. 3.11 Assemblage 2 (intermediate) amphibole in salic pumiceous glass, thin section from Tajao ignimbrite clast. The crystal has been stripped of its envelope of brown glass. Note that, were the two glasses not colour-contrasted (Fig. 3.10), this crystal would not in itself appear unusual. If this kind of relative crystal-magma movement is normal during eruptions, then the value of attaching precise significance to phenocryst-matrix trace-element distributions in heterogeneous volcanic rocks (e.g. Mahood, 1981; Mahood & Hildreth, 1983) should perhaps be questioned. Photomicrograph taken in PPL, x50. Apparent inclusion is actually a pluck-mark.

The mineralogy conforms to that described in III.1. Minerals common to all three assemblages (feldspar, pyroxene, FeTi oxides) fall into widely-spaced compositional groups (Figures 3.12, 3.13, 3.14). It is notable that the range of zoning in a single crystal often encompasses almost the full compositional range for a particular group (e.g. assemblage 2 feldspars, assemblage 1 and 2 pyroxenes), further emphasising the distinct identity of each assemblage. The chemical contrast between minerals of each assemblage is summarised in Figure 3.15.

Resorption varies between assemblages and minerals. Among the feldspars, calcic plagioclase is always resorbed to some extent and several grains are heavily sieved with black glass blebs (Figure 3.16). These blebs could only be analysed with some difficulty, since they are generally too small to allow a defocussed or scanning microprobe beam to be used, and spot analysis is unsuitable for glasses (Appendix B). Satisfactory analyses indicate a composition atypical of groundmass mafic glass; the significance is discussed below. Resorption of oligoclase-andesine (Figure 3.17) is highly variable, from very slight to almost complete dissolution, whereas resorption of sanidine is generally confined to rounding of crystal corners. All other assemblage 3 phases appear unresorbed (Figure 3.18), as does amphibole in assemblage 2 and pyroxene in assemblages 2 and 3. Fe-Ti oxides frequently show rounded contacts with glass, (Figure 3.19), although this is not invariably the case (Figure 3.20). Olivine of assemblage 1 is also rounded; the glass within a few tens of microns of one olivine grain is anomalously Mg-rich, indicating that resorption was actively taking place at the time of quenching.

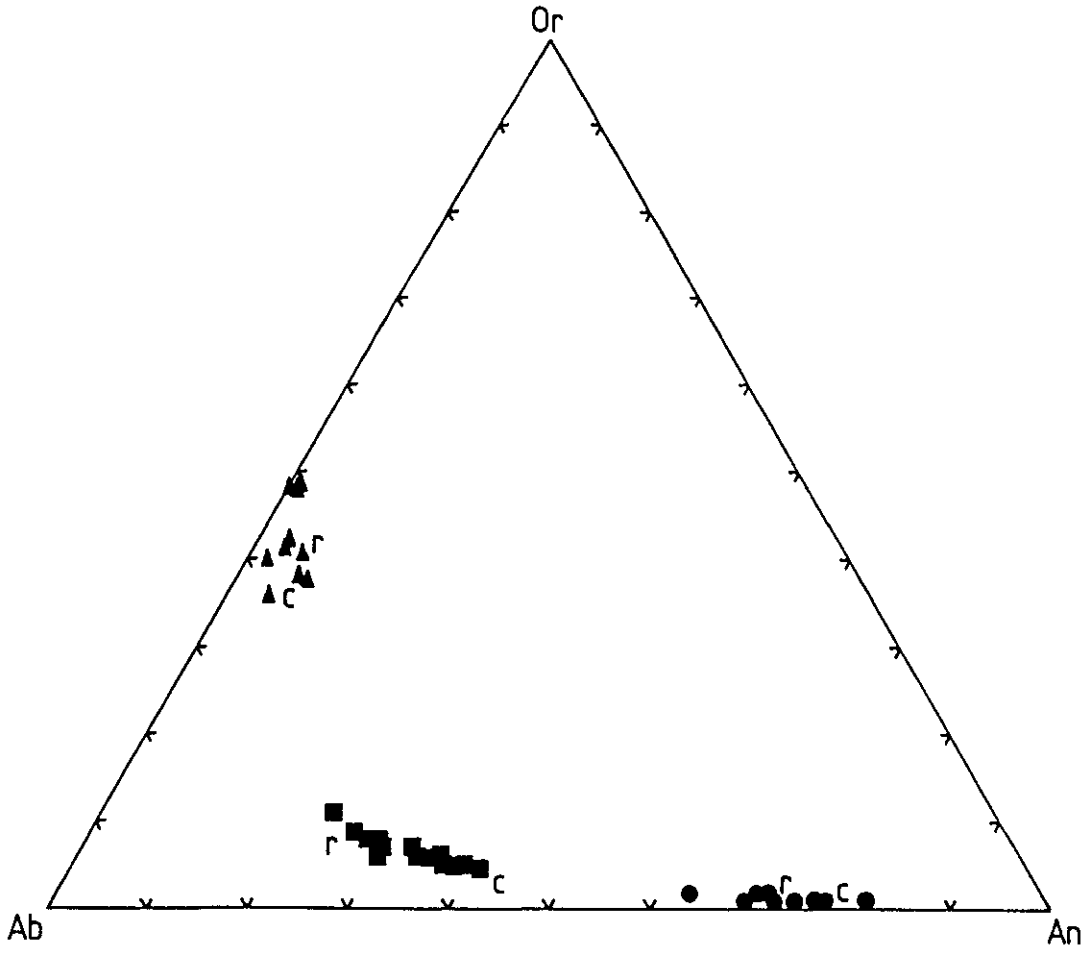

Fig. 3.12 Feldspar compositions in the Tajao ignimbrite. Circles: assemblage 1; squares: assemblage 2; triangles: assemblage 3. r and c indicate rim and core compositions respectively of most intensely zoned cyrstals found.

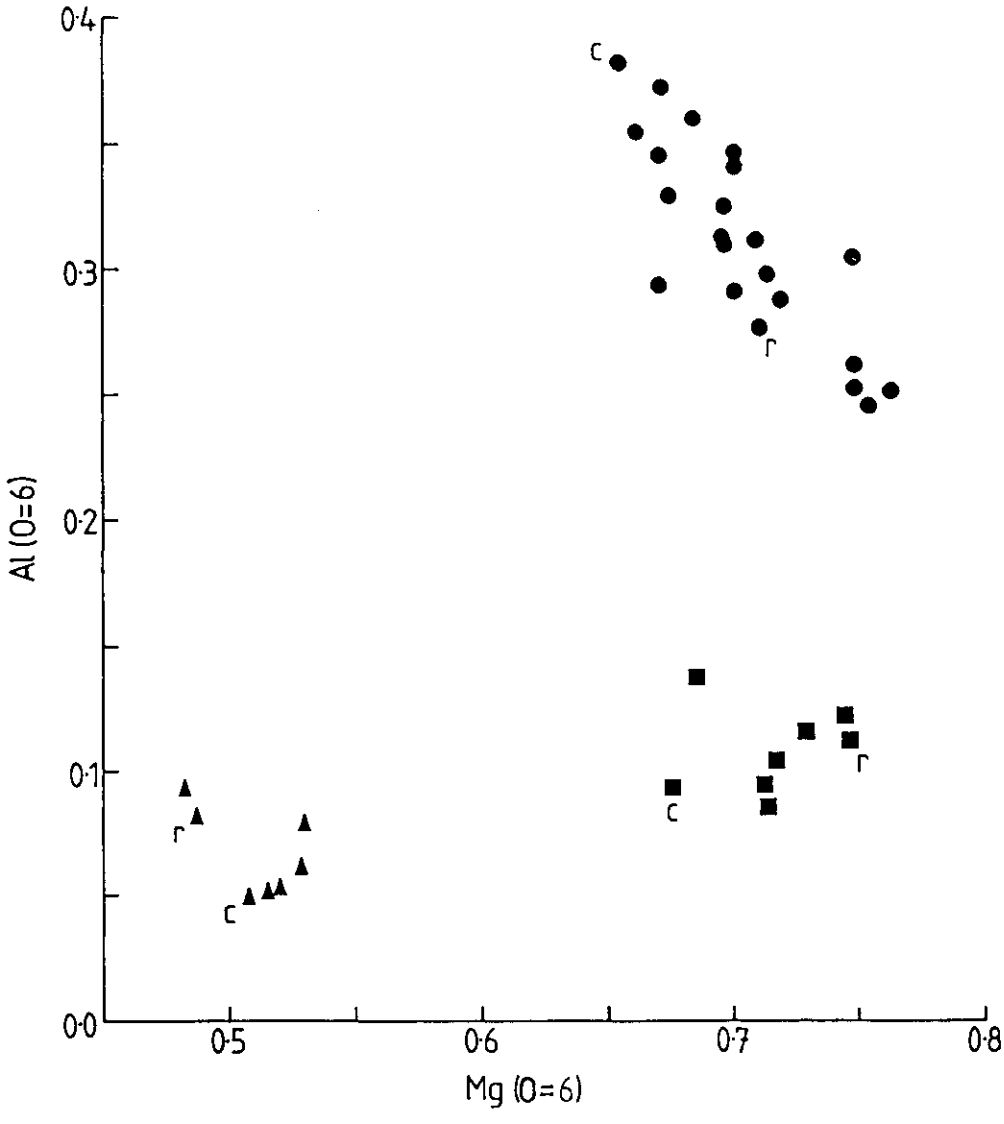

Fig. 3.13 Pyroxenes from the Tajao ignimbrite on a plot of Al vs. Mg per 6 oxygens. Symbols as Fig. 3.12.

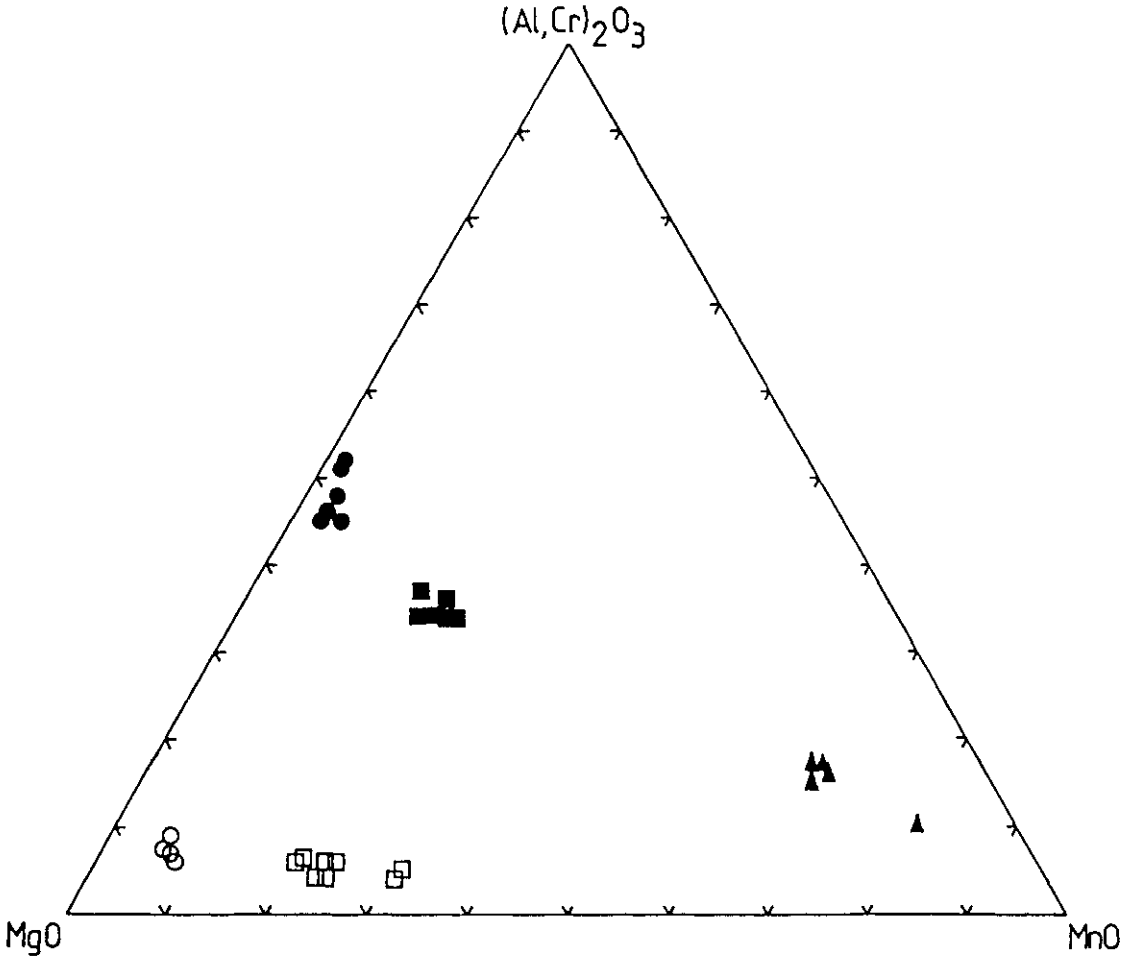

Fig. 3.14 Minor element (oxide wt%) variation in Fe-Ti oxides from the Tajao ignimbrite. Filled symbols: titanomagnetites; open symbols: ilmenites; otherwise as Fig. 3.12.

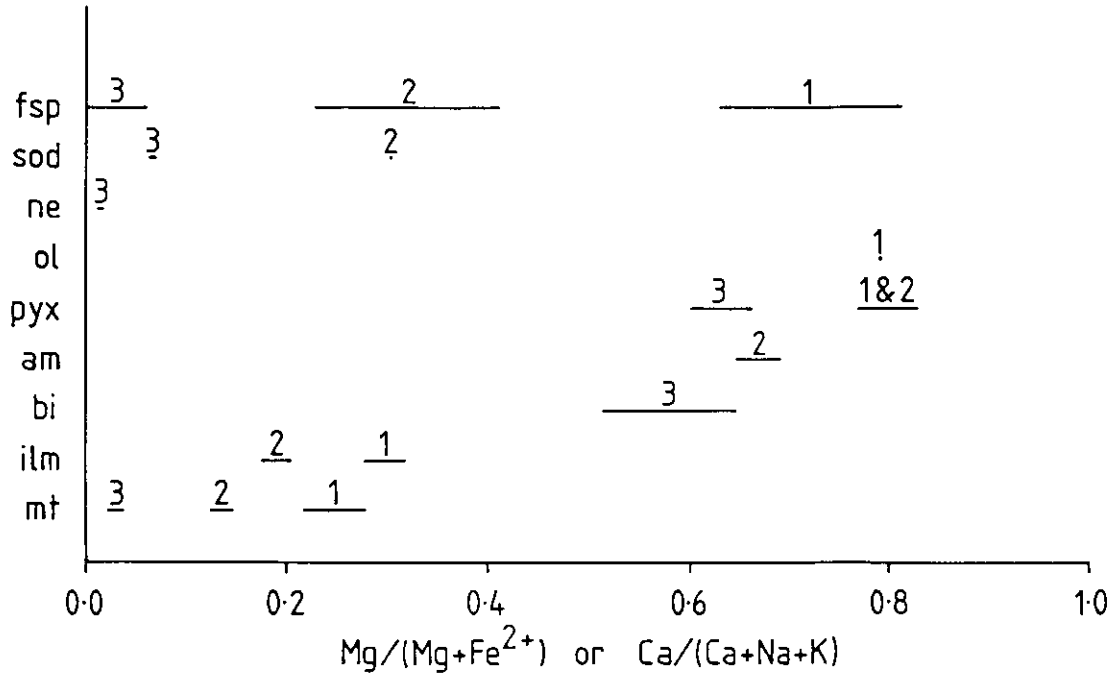

Fig. 3.15 Ca/(Ca+Na+K) for feldspar, sodalite and hauyne, and $Mg/(Mg+Fe^{2+})$ for other minerals, for principal phenocryst species in the Tajao ignimbrite.

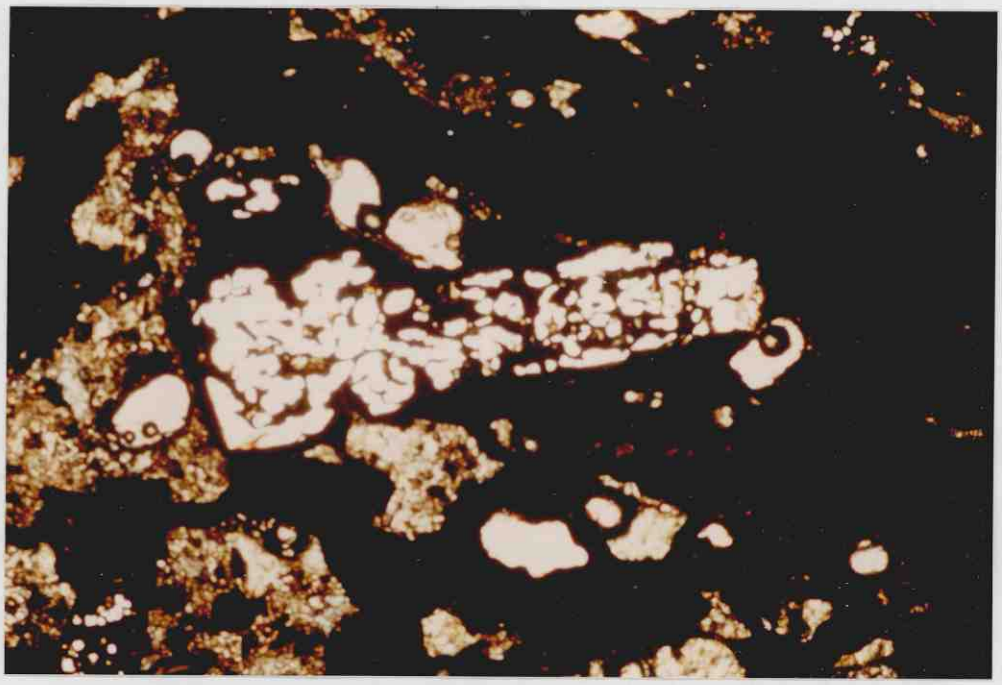

Fig. 3.16 Partly resorbed assemblage 1 bytownite crystal, Tajao ignimbrite. The composition of the black glass seiving the crystal is discussed in the text. PPL, x70.

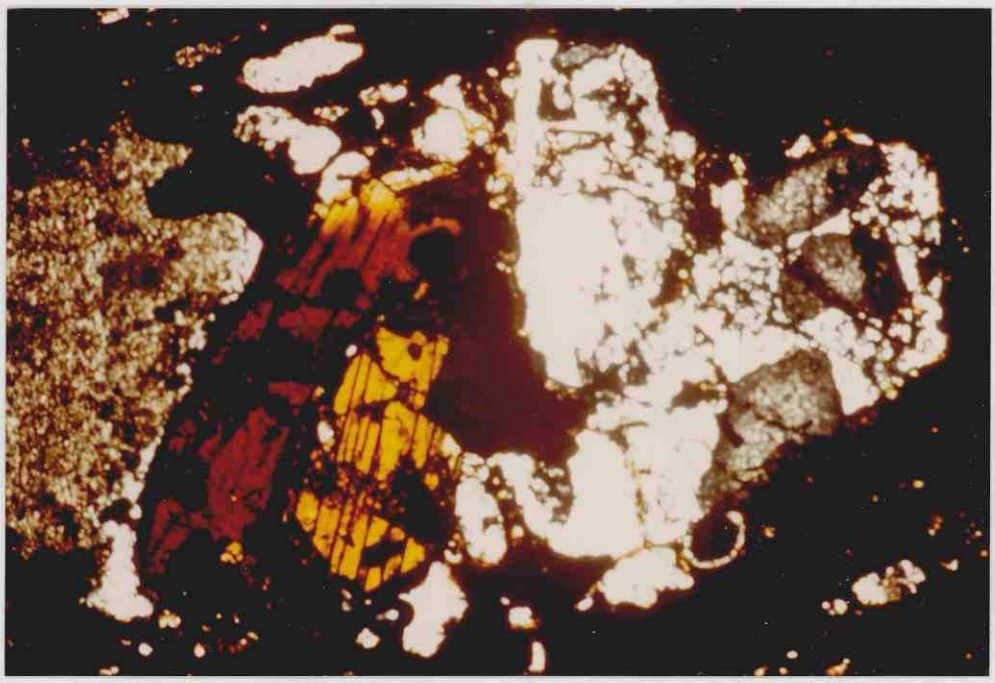

Fig. 3.17 Assemblage 2 aggregate grain of amphibole-plagioclase-Fe-Ti oxides surrounded by mafic glass, Tajao ignimbrite. Note partial resorbtion of feldspar. PPL, x50.

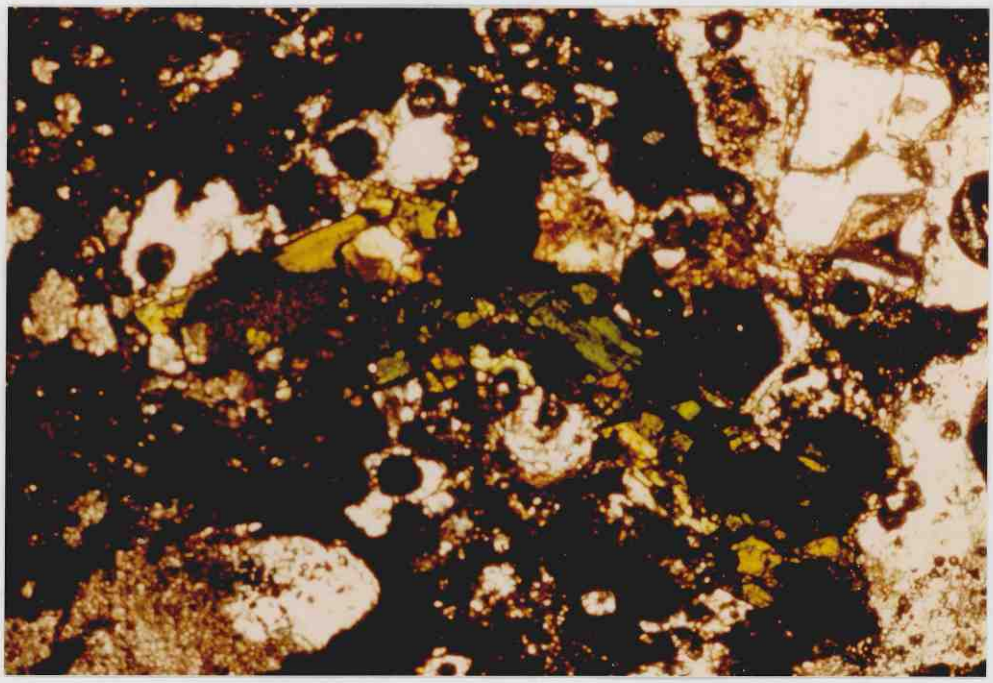

Fig. 3.18 Assemblage 3 aggregate grain of aegirine-augite with magnetite and sphene, Tajao ignimbrite. Colourless mineral to top right is nepheline. PPL, x50.

Fig. 3.19 Assemblage 1 olivine and titanomagnetite (rounded opaque grain to right), Tajao ignimbrite. Partly crossed polars, x50.

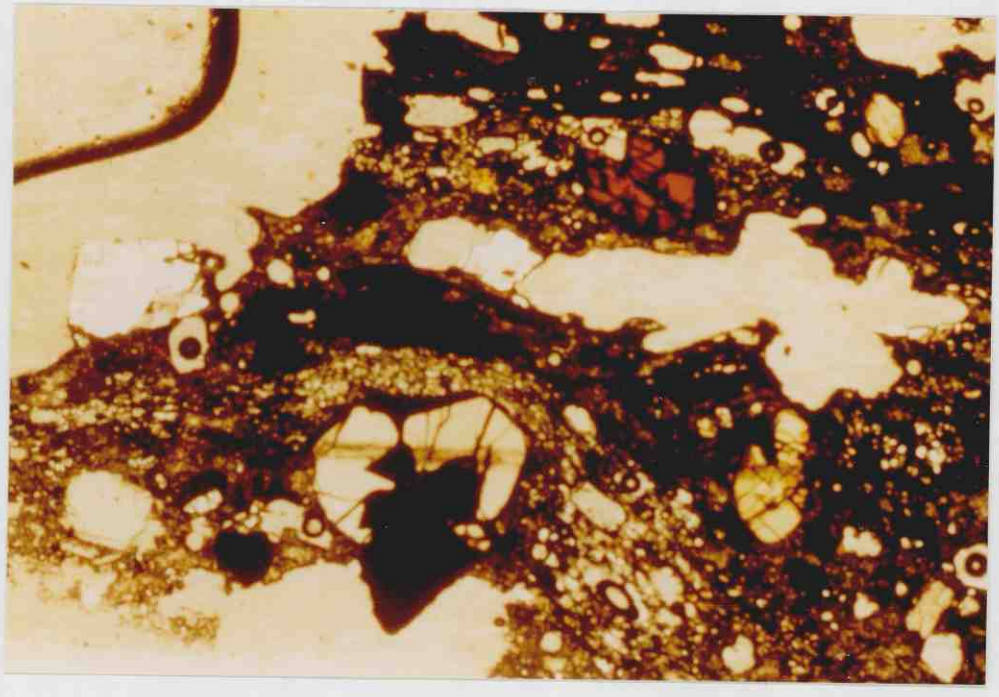

Fig. 3.20 Assemblage 1 pyroxene-FeTi oxide aggregate grain in streaky pumice, Tajao ignimbrite. Contrast crystal outlines with those of Fig. 3.19. Note adhesion of mafic glass in a surface depression of the aggregate grain, and nearby assemblage 2 augite and amphibole (right and upper right) and assemblage 3 alkali feldspar (left). PPL, x10.

III.2.ii Glasses

Analysed glasses in streaky pumices range in composition from trachyandesite to phonolite (Figure 3.21). This restricted range is rather surprising in view of the diverse phenocryst mineralogy, and indicates that homogenisation of the original magmas was near completion at the time of quenching.

Compositional variation of the two glasses (Figures 3.22, 3.23) has been examined in terms of deviation from a simple straight-line mixing trend, by calculating the correlation coefficient of the best-fit straight line through all possible major-element oxide pair combinations for 22 glass analyses. The analyses were selected to give a statistically-significant number spanning the entire observed range; those from glass included in, or in proximity to, a phenocryst were rejected. Totals, originally in the range 95% to 99%, were recalculated before performing the regressions. Results are shown in Table 3.3. Regressions between CaO, FeO, MgO and TiO_2 show a low degree of scatter and these oxides appear to have mixed in a straight-line fashion. The agreement is less good for SiO_2, and poor for Al_2O_3, Na_2O and K_2O. Three causes of scatter have been identified: analytical error, post-eruptive chemical alteration, and mixing of initially heterogeneous end-members. Analytical error is an appreciable fraction of the small variation in Al_2O_3 content, and less so for SiO_2 and MgO (Table 3.4). For all other elements, errors should not greatly affect the correlation quality. Within the group CaO, FeO, MgO and TiO_2, the slightly greater scatter of MgO and TiO_2 compared to CaO and FeO (Table 3.3) is predicted by consideration of analytical errors (Table 3.4).

	SiO_2	TiO_2	Al_2O_3	$FeO_{tot.}$	MgO	CaO	Na_2O	K_2O
K_2O	+0.66	-0.61	+0.14	-0.67	-0.64	-0.68	+0.15	(+1)
Na_2O	+0.18	-0.21	+0.47	-0.64	-.63	-0.46	(+1)	
CaO	-0.82	+0.93	-0.59	+0.97	+0.96	(+1)		
MgO	-0.75	+0.88	-0.60	+0.91	(+1)			
FeO_{tot}	-0.79	+0.93	-0.57	(+1)		n=22		
Al_2O_3	+0.29	-0.77	(+1)					
TiO_2	-0.76	(+1)						
SiO_2	(+1)							

Table 3.3. Correlation matrix for major element oxides in microprobe analyses of glasses from streaky pumice clasts in the Tajao ignimbrite.

	SiO_2	TiO_2	Al_2O_3	FeO_{tot}	MgO^+	CaO	Na_2O	$K_2O^{\ddagger}$
Max. concentration (wt%)	60.64	2.33	21.08	6.31	1.90	5.50	5.50	7.80
Min. concentration (wt%)	53.38	0.38	18.27	2.47	0.17	0.79	10.55	4.45
Range (wt%)	7.26	1.95	2.81	3.84	1.73	4.71	5.05	3.35
Middle of range (wt%)	57.01	1.36	19.67	4.39	1.04	3.15	7.80	6.12
σ^*	3.9%	2.2%	9.8%	2.3%	0.3%	0.6%	1.4%	10.2%

σ^* one analytical standard deviation, determined from precision of replicate amphibole analyses (App. B1), at the middle of the composition range divided by that range. ^+MgO σ^* valve is misleading since analysed quantities of MgO are very much less than those used to construct precision estimate; σ^*= 2.9% for 0 = 5% as a rough guide. $^{\ddagger}K_2O$ σ^* value misleading as analysed quantities of K_2O are much greater than those used in precision estimate; errors in K_2O analysis are comparable to those in CaO. Note that analytical error is an appreciable fraction of Al_2O_3 range.

Table 3.4. Analytical error as a fraction of compositional range in microprobe analyses of glasses from streaky pumice clasts in the Tajao ignimbrite.

The poor correlations of Na_2O and K_2O with other elements are due to post-eruptive processes. Although only fresh looking glass was selected for analysis, some hydration, evidenced by the low analysis totals, has evidently occurred. As noted in III.1, this has affected Na_2O concentrations. Although the inverse Na-K relations found by Scott (1971) to accompany glass hydration are not observed, K_2O may also have been affected.

From Figure 3.22, it is evident that the phonolitic glass is itself heterogeneous; this particularly affects the quality of the regressions between SiO_2 and the other oxides. This variation is distinct from the principal (mixing) trend, with TiO_2, FeO, MgO and CaO varying positively with SiO_2. Trends of this type are typical of phonolites which are fractionating an alkali feldspar together with small quantities of ferromagnesian minerals; the last liquid becomes progressively impoverished in SiO_2 with differentiation. Ignoring the presence of sodalite, the variation in the phonolitic glass may be accounted for by approximately 50% crystallisation of a solid assemblage consisting of 90% salic sanidine, 4.5% pyroxene, 3% biotite, 2% sphene and 0.5% magnetite of the observed compositions, based on SiO_2, TiO_2, MgO, CaO and FeO. Although the poorly phyric-nature of the salic glass precludes direct comparison, this is consistent with the massive dominance of alkali feldspar in the mode of assemblage 3.(Table 3.5). Since the variation is encountered on the mm scale, bulk removal of crystals from magma on the whole-magma scale is not implied, although vertical zonation of the phonolite magma could equally give rise to these relations (I.2). It may be noted that a fractionation trend in the salic endmember magma would be far less obvious in, say a calc-alkaline association, since fractionation would tend to duplicate the mixing trend.

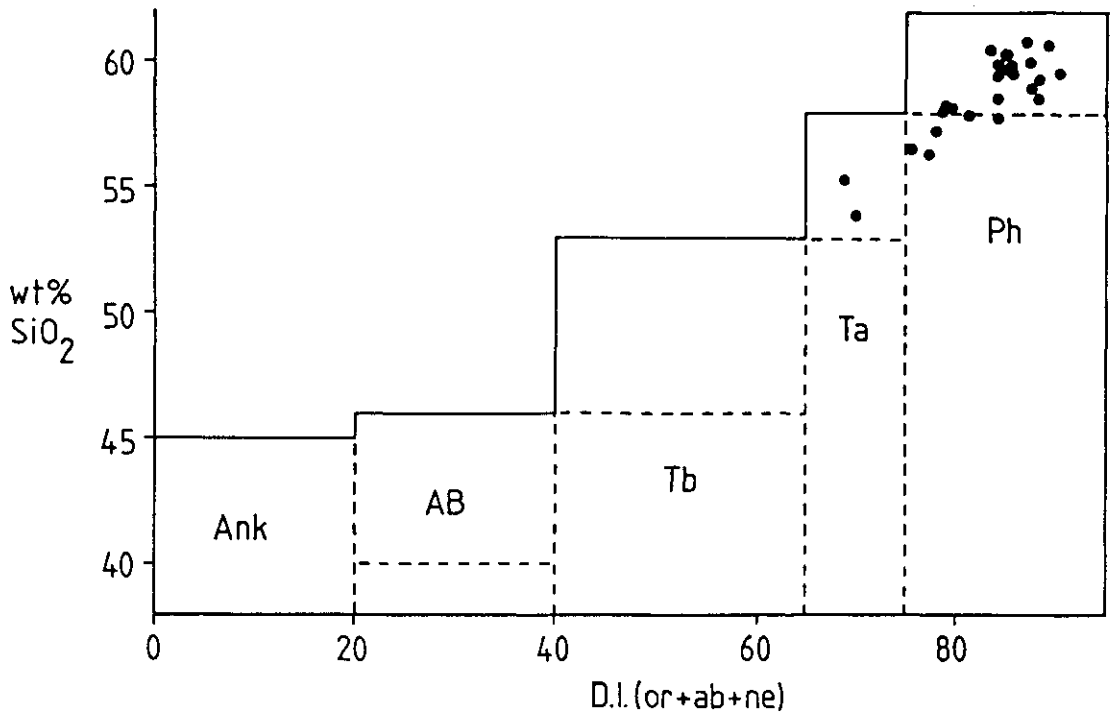

Fig. 3.21 Streaky pumice glasses from the Tajao ignimbrite plotted on the classification of Borley (1974).

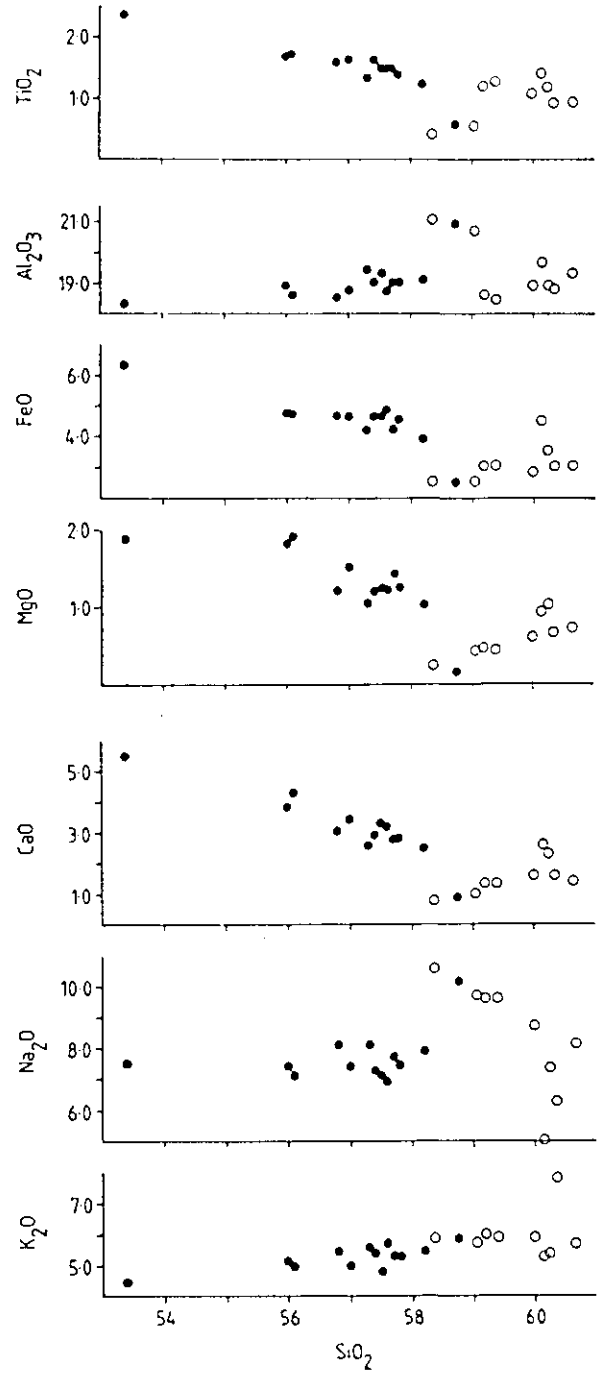

Fig. 3.22 Variation diagrams vs. SiO_2 for streaky pumice glasses from the Tajao ignimbrite. Filled circles: mafic glass; open circles: salic glass.

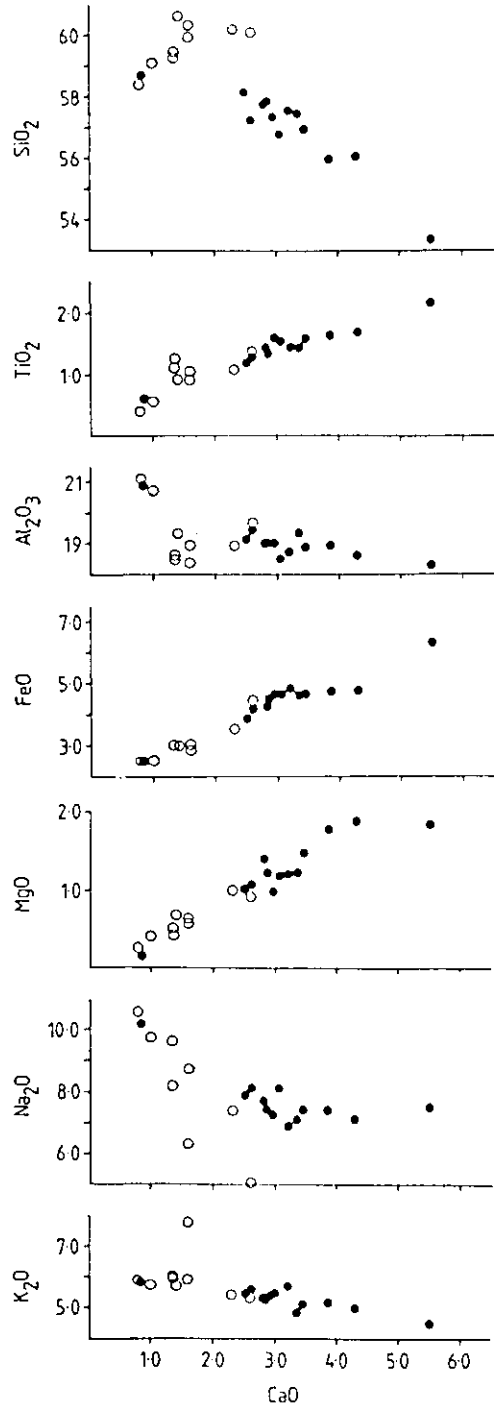

Fig. 3.23 Variation diagrams vs. CaO for streaky pumice glasses from the Tajao ignimbrite. Symbols as Fig. 3.22.

In contrast with the pre-mixing phonolite magma, the mafic liquid appears to have been homogeneous, despite its two phenocryst populations. Thus it appears that two distinct mixing events have occurred; the first, between the "assemblage 1 magma" (basalt) and the "assemblage 2 magma" (intermediate) proceeded to the liquid homogenisation stage before the second, between the mixed mafic and phonolite magmas took place.

III.2.iii Estimation of original magma compositions

Within assemblage 1, the resorption characteristics of plagioclase are distinctive. Fe-Ti oxides, olivine, and pyroxene all show simple rounding (very slight in the case of pyroxene), whereas feldspar resorption appears to proceed mainly by the formation of pits and embayments, with only minor rounding, giving a "perforated" appearance in thin section (Figure 3.16). Assemblage 2 andesines exhibit similar features. If resorption commenced while the crystal was still surrounded by an envelope of "its own magma" (possibly by rapid equilibration of P_{H_2O} with the exterior liquid), then the original composition of this envelope may be preserved in the embayments. The infilling glass has a composition which lies well off the extrapolated mixing trend in the groundmass glass (Figure 3.24), and is considerably more basic than any other analysed glass. In what follows it is assumed that this material is representative of the original basalt liquid which carried the assemblage 1 phenocrysts. Undoubtedly its composition will have been modified by feldspar resorption and diffusive mixing with the exterior liquid. However, it will emerge that enrichment of the liquid in the anorthite molecule or a proportion of original intermediate liquid does not qualitatively affect the arguments presented. For convenience, this liquid is

referred to as "basaltic" in the argument developed below in order to distinguish it from the intermediate liquid. In reality its composition is rather more evolved than implied by the use of this term; the MgO content (Table 3.6) indicates a basic trachybasalt.

If a few further (and reasonable) assumptions are made, the initial magma compositions may be estimated as follows. The procedure is illustrated for two oxides in Figure 3.24. A regression line is drawn for the main mixing trend for each oxide in the streaky pumice glass (for the sake of completeness, all oxides have been calculated; however little significance can be attached to results for Na_2O, K_2O and Al_2O_3). Assuming that the composition of the liquid which mixed with the phonolite magma lies on this extrapolated line, then the initial composition of the intermediate liquid (before mixing with basalt) lies on the low FeO, MgO, CaO, TiO_2 and high SiO_2 extrapolation of the line joining this point with the assumed initial basalt composition. In this particular case, the required intermediate liquid composition can be quite closely constrained by the geometry of the construction and analogy with analysed Tenerife lavas and pyroclastics (Ridley, 1968; Scott, 1970; this study) which precipitate assemblage 2-type minerals. For example, assumption of 3% FeO_{total} in the initial intermediate liquid in Figure 3.24 implies only 0.3% MgO, which is unreasonably low for trachyandesite. A roughly 2:5 mix of the initial basaltic to initial intermediate material is indicated; estimated compositions are given in Table 3.6. Comparison of this ratio with modal abundances of all phenocrysts and glasses (Table 3.5) allows calculation of the initial modal abundances, and thence bulk compositions of the mixing magmas (Table 3.6), assuming that the salic glass is pure unmixed phonolite (Figures 3.22, 3.23).

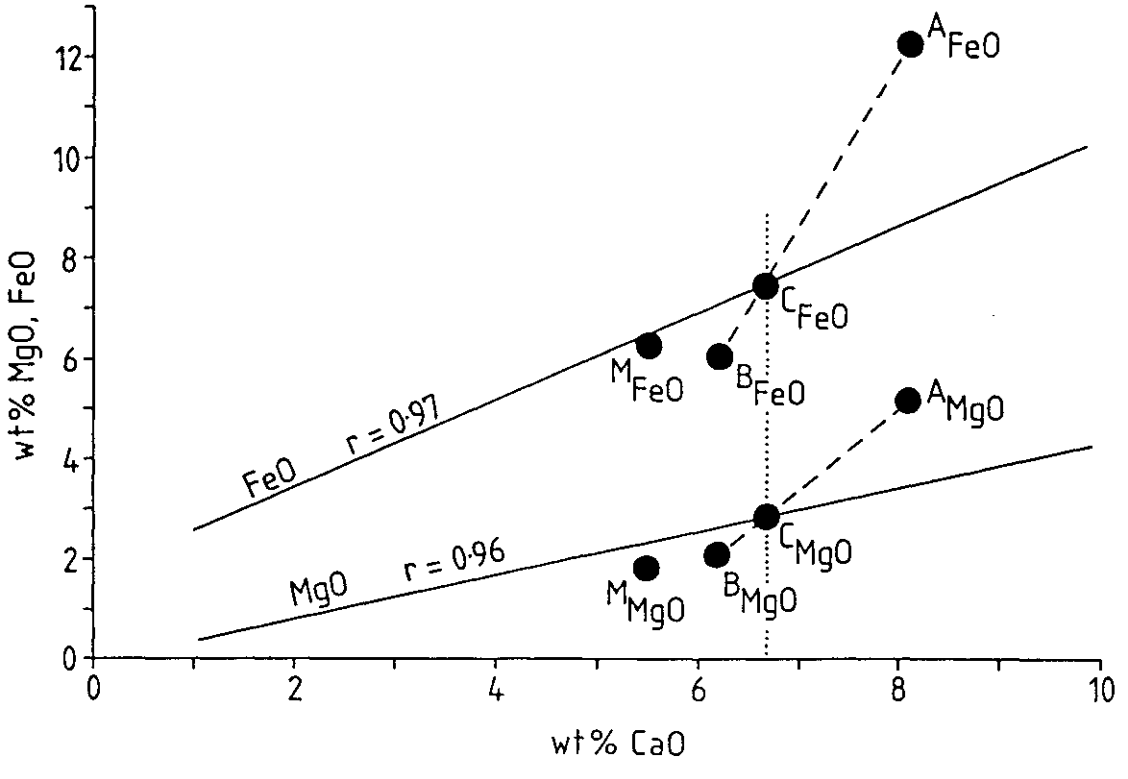

Fig. 3.24 Calculation of initial liquid compositions for two magmas and their mixed product for CaO, MgO and FeO, Tajao ignimbrite. Solid lines are regressions through CaO vs FeO and MgO respectively for analysed glasses, where r is the correlation coefficient. A = composition of initial "basalt" liquid, from analysis of dark glass associated with calcic feldspars (Fig. 3.16). B = best estimate of initial intermediate liquid composition (see text). C = Resultant mix of A & B, assuming straight line mixing. Proportions are 73% B, 27%A. M = most basic analysed glass composition.

Phase	Total mode%	Salic + ass. 3 mode %	Mafic + ass. 1 & 2 mode %
Salic glass	36.6	92.4	-
Mafic glass	54.6	-	90.5
Feldspar (Ass 1)	3.0	-	5.0
"(Ass 2)	1.4	-	2.2
"(Ass 3)	2.8	7.1	-
Pyroxene (Ass 1)	0.3	-	0.5
"(Ass 2)	0.6	-	1.0
Amph (Ass 2)	0.5	-	0.8
Biotite (Ass 3)	0.2	0.5	-

All other minerals listed in Table 3.3 present in trace quantities.

Table 3.5. Modal analysis of streaky pumice from the Tajao ignimbrite.

	1	2	3	4	5	6	7	8	9	10
SiO_2	59.71	58.50	60.31	57.05	46.5	54.8	52.9	60.12	54.7	48.6
TiO_2	0.97	0.39	1.16	1.47	4.2	2.5	3.0	0.94	2.4	2.5
Al_2O_3	19.32	21.13	18.90	19.03	13.2	16.0	15.3	19.28	16.1	20.1
FeO_{tot}	3.08	2.50	3.49	4.48	12.3	6.1	7.8	2.92	5.9	7.6
MgO	0.62	0.24	1.02	1.28	5.1	2.1	2.9	0.65	2.7	3.5
CaO	1.56	0.80	2.31	3.18	8.1	6.2	6.7	1.48	7.2	11.4
Na_2O	8.19	10.58	7.37	7.70	5.2	7.7	7.0	8.01	7.1	4.3
K_2O	5.95	5.87	5.43	5.28	3.5	4.5	4.2	6.05	3.8	2.1

(1) = Mean composition of salic glass. (2) & (3) = Extreme compositions of analysed salic glass. (4) = Mean composition of mafic glass. (5) = Mean composition of glass associated with resorbing calcic feldspars, assumed equal to the original "basalt" liquid composition. (6) Estimated composition of original intermediate liquid. (7) = Composition of intermediate liquid after mixing with basalt (27% (5), 73% (6)). (8) = Mean bulk composition of phonolite (significant mode = 92.4% liquid, 7.1% alkali feldspar, 0.5% biotite). (9) = Bulk composition of original intermediate magma (significant mode = 83% liquid, 9% plagioclase, 3.5% amphibole, 4.5% pyroxene). (10) = Bulk composition of original basalt magma (significant mode = 57% liquid, 39% Ca-plagioclase, 4% pyroxene). All compositions are given volatile-free; Mn and P are present in minor quantities but have been ignored. Calculation of compositions explained in the text.

Table 3.6. Compositions of magmas before mixing for the Tajao ignimbrite.

Fig. 3.25 Flow-unit in pahoehoe plagioclase-phyric basalt, Chio, W Tenerife. Note strong accumulation of feldspars at top of flow-unit, demonstrating flotation accumulation. Diameter of lens cap is 3.5cm.

Several features of these results deserve comment. Firstly, the indicated compositions are agreeably close to respective typical Tenerife magma types, even for the alkalis. The calculated "basalt" composition would be in equilibrium with the analysed olivine Fo_{79} (Roeder and Emslie, 1970) if approximately 4.5% Fe_2O_3 were present. This is consistent with the Fe_2O_3 contents of basalts analysed by Ridley (1968), and with the generally relatively oxidised nature of alkali basalt liquids (Sack et al., 1980). Secondly, the very high modal plagioclase in the initial basalt is in keeping with the Ca and Al-poor, and Fe-rich nature of its associated liquid; the basalt magma has precipitated calcic plagioclase in unusually large quantities. Such basalts are rare on Tenerife although an extensive pahoehoe flow occurs in the west of the island; the source is unknown but it can be traced from Chio to the coast (G.P.L. Walker, pers. comm.). The flow is rich in large plagioclases which have very rapidly accumulated by flotation at the tops of individual pahoehoe flow units (Figure 3.25). Comparison of the proposed initial basalt composition with average alkali basalts suggests that it, too, may be accumulative; removal of approximately half of the observed modal plagioclase from the analysis would give a typical composition transitional between alkali basalt and trachybasalt. Finally, the mafic pumice glass has a mean composition of 71% phonolite, 21% initial intermediate, and 8% initial basalt. Thus the ignimbrite as a whole is very much more phonolite-rich than suggested by hand-specimen examination; if the proportion of dark material observed in the field is typical of the whole, then the ignimbrite consists of roughly 94% phonolite, 4% intermediate, and 2% basalt. In III.5 it is suggested that phonolite-intermediate mixing occurs during eruption as magma is drawn up the conduit. If so, liquid homogenisation proceeds at a considerably faster rate than is suggested by consideration

of cation diffusion rates alone (e.g. Sparks et al., 1977).

III.2.iv Summary

Compositions and inter-relations of phenocrysts in the Tajao ignimbrite indicate the participation of three chemically discrete magmas in its eruption. Glass chemistry suggests that basaltic magma first mixed with a greater volume of intermediate magma, which then mixed with a very much greater quantity of phonolite magma. The second mixing event had not gone to completion (liquid homogenisation) when the eruption products were quenched. Original magmatic compositions are calculated on the basis of a few assumptions on glass compositional variation. The initial basalt was an unusual plagioclase-rich variety, suggesting an unusually hydrous mafic magma (III.5).

III.3 IGNIMBRITE O

The field aspects of ignimbrite O are closely similar to those of the Tajao ignimbrite, from which it is only distinguished by stratigraphic position.

III.3.i Petrography and mineralogy

Petrographically this ignimbrite is virtually identical to the Tajao ignimbrite. The only differences apparent in thin section are that olivine is absent, and that occasional plagioclases are unresorbed. Analysis of phenocrysts and glasses however demonstrates that the two ignimbrites are not directly comparable. Whereas the Tajao ignimbrite is the product of mixing of three magmas whose

distinct chemical identities are directly reflected in their phenocryst compositions, no such sharp separation is found in O. Feldspar, Fe-Ti oxide and pyroxene compositions (Figures 3.26, 3.27, 3.28) occupy continua stretching from compositions typical of basalt to those typical of phonolite, although magnetite and pyroxene do not seem to have attained such evolved compositions. Mg/Mn relations in Fe-Ti oxides are consistent with those found in the Tajao ignimbrite in terms of associated silicate phases (Figure 3.27), but any division into sub-assemblages as above is a near-arbitrary procedure. Ilmenite is restricted to the medium MgO content range, where it appears to fall into two compositional groupings, unlike co-existing magnetite (Figure 3.27). These two groups give temperatures of 940° (higher-Mg) and 915° (lower-Mg) respectively (Chapter IV). An assemblage alkali feldspar-sodalite-biotite-low Mg magnetite can be correlated with the phonolitic member, and titanaugite-bytownite-high Mg magnetite forms a clear basalt-derived association, but the spread in "intermediate" compositions is considerable, and must reflect either a very heterogeneous initial intermediate component, or else the participation of two (or more) intermediate magmas, for example a trachybasalt and a trachyandesite.

The order of mixing is likewise difficult to determine. The freshest plagioclases have a limited range of composition around An_{52}, whereas alkali feldspars may show substantial resorption.

By contrast, glass chemistry appears to vary in a more straight-forward fashion than in the Tajao ignimbrite (Figure 3.29). Compositions of both mafic and salic glasses plot along the same trend,

although variation in the salic glass is comparatively restricted. Possible explanations are: (i) the salic glass has fractionated as in the Tajao ignimbrite, but the trend duplicates that of mixing; (ii) the salic glass has fractionated, but the resulting trend makes a too acute angle to the mixing trend for the two to be distinguished within analytical precision; (iii) the salic magma was originally homogeneous, but the dark colour is absent for high dilution of the original mafic in the salic component. Explanation (i) can be dismissed as the salic glass is SiO_2 - undersaturated, and thus fractionation of alkali feldspar should produce a trend similar to that in the Tajao ignimbrite. (ii) is unlikely as the trend duplication is exact for FeO (versus SiO_2), which is the most abundant element of the group TiO_2, FeO, MgO and CaO and has the least error. Thus explanation (iii) is considered the most probable; the minimum indicated degree of dilution is ca. 85% (this introduces an insignificant error into the calculation of initial modal abundances in III.2 above).

The overall compositional range of the glasses is similar to that in the Tajao ignimbrite, and, by analogy, the most basic composition found here may be close to an original intermediate. A search was made for original "basaltic" glass to provide a compositional intercept as in III.2 above, but satisfactory analyses could not be obtained from glass blebs in resorbing bytownite due to their small size.

Ignimbrite O, the product of a single eruption, contains phenocyrsts representative of the entire magmatic range on Tenerife, without the sharp compositional breaks found in other similar deposits (III.2.ii, III.2.iv). Further work on this deposit could therefore prove very fruitful.

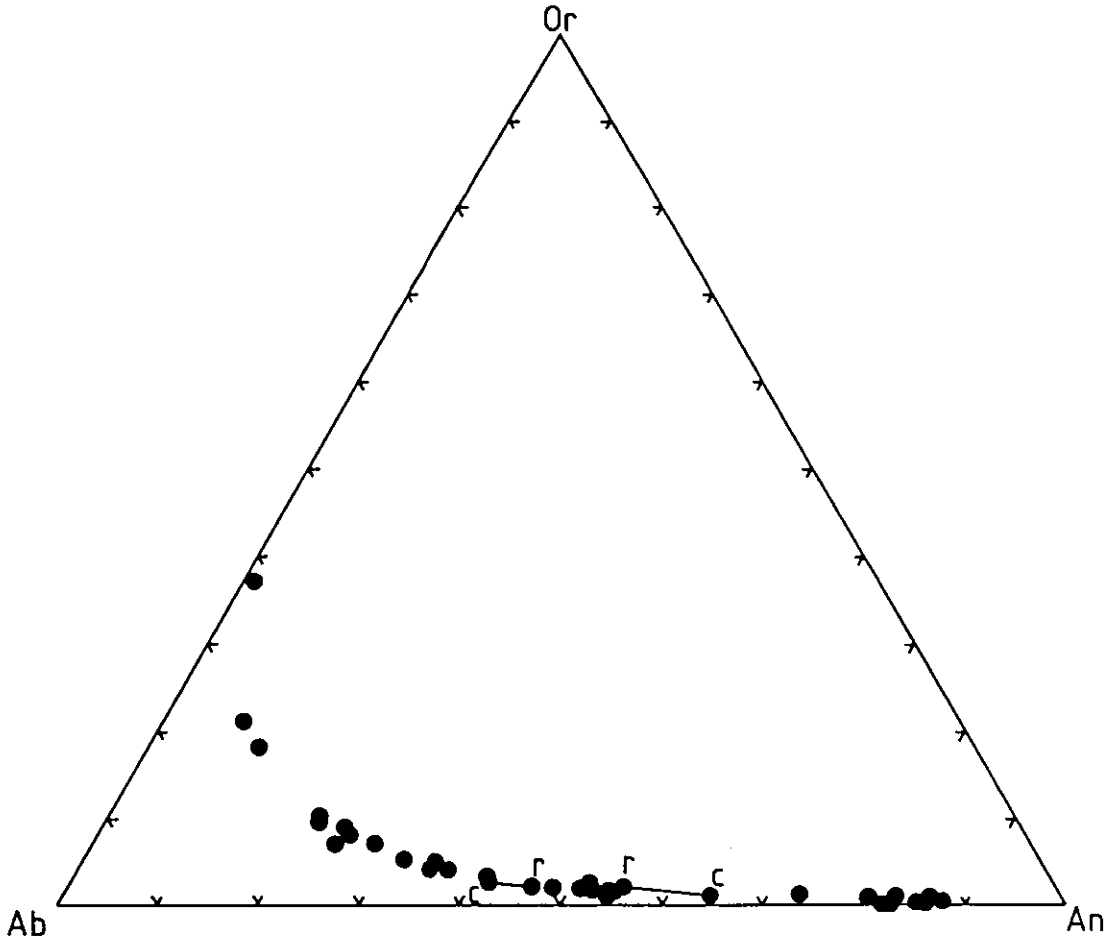

Fig. 3.26 Feldspar compositions in ignimbrite C. r and c as Fig. 3.12.

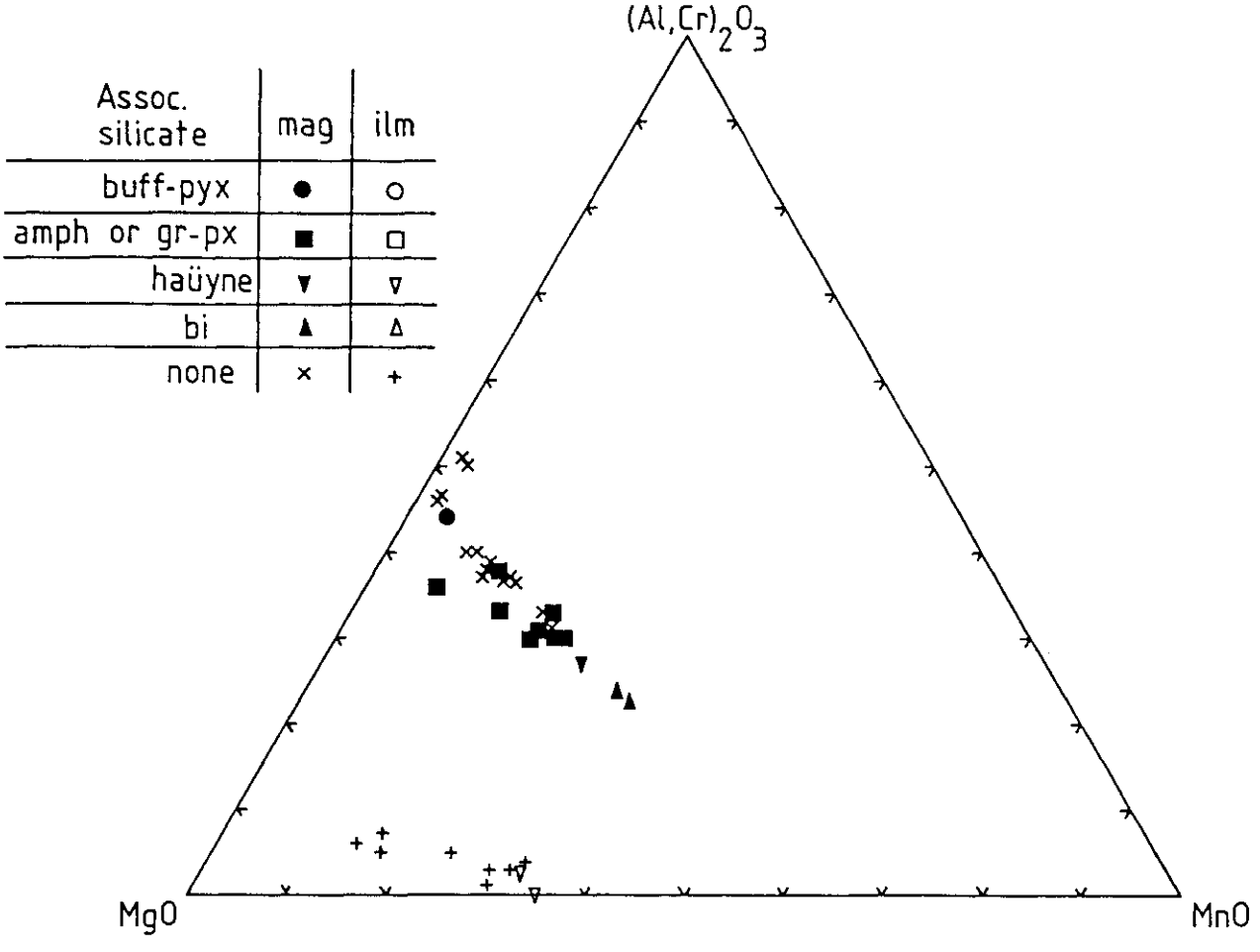

Fig. 3.27 Minor element (oxide wt%) variation in Fe-Ti oxides from ignimbrite O.

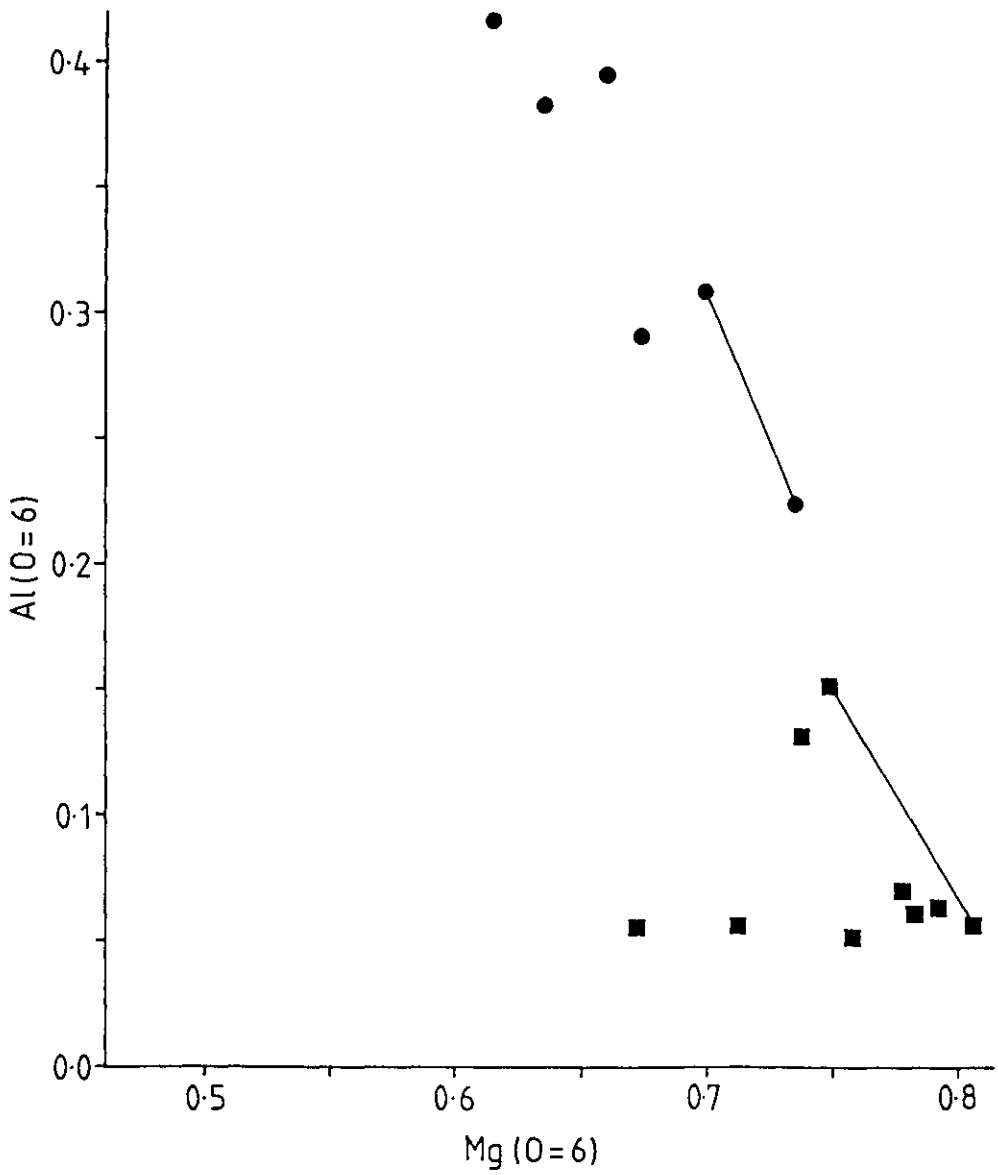

Fig. 3.28 Al vs. Mg per 6 oxygen atoms for pyroxenes from ignimbrite O. Filled circles: buff pink titanaugites; filled squares: green augites.

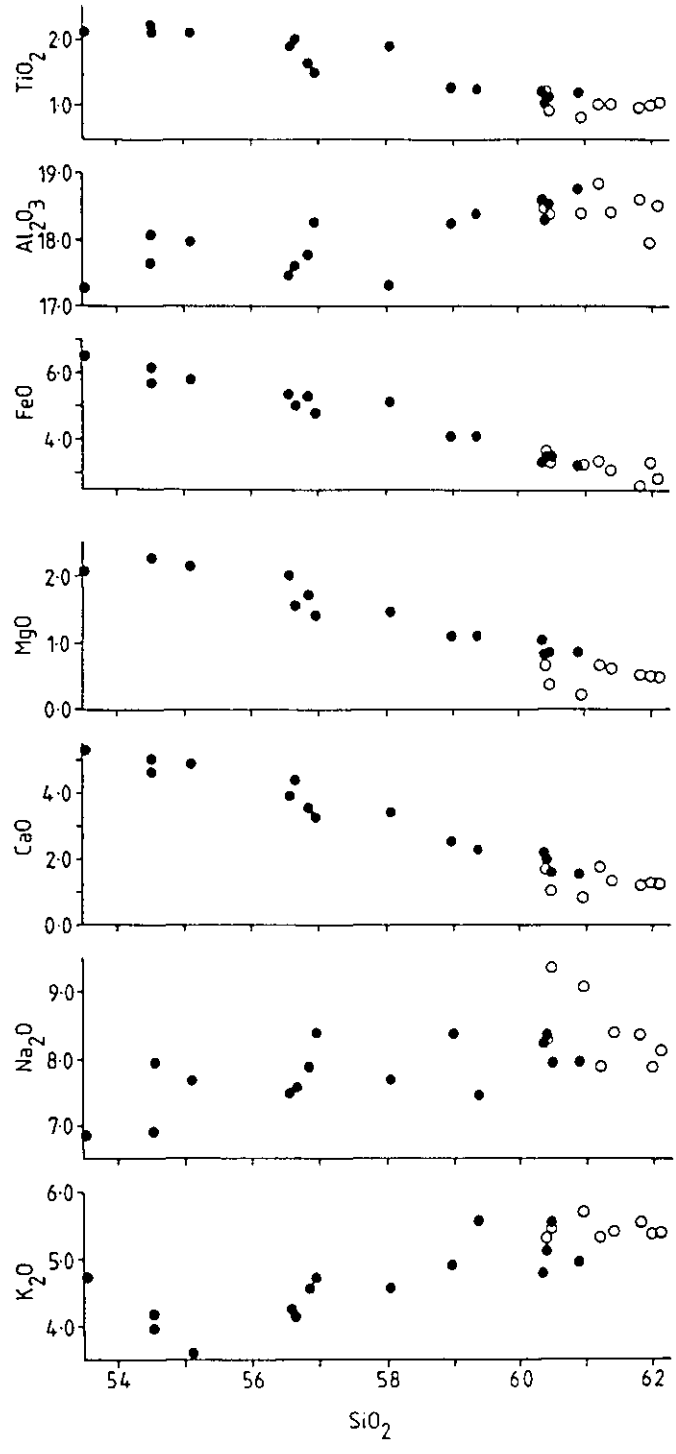

Fig. 3.29 Variation diagrams vs. SiO_2 for streaky pumice glasses from ignimbrite O. Filled circles: mafic glass; open circles: salic glass.

III.4 OTHER DEPOSITS

iii.4.i Airfall and ignimbrite E

Airfall E is one of the group of very voluminous deposits on Tenerife (with D, G and J), which are close to the normally-observed size limit of plinian deposits (Walker, 1980). At the very top, rare clasts of streaky pumice are found. Locally the fall is capped by an ignimbrite or ignimbrite veneer deposit (Chapter I) formed during the same eruption. Clasts of streaky and dark pumice are relatively abundant in this ignimbrite. Sampled material is highly inflated and unaltered material difficult to find, but four glass analyses have been made, indicating that the mafic and salic components are of similar relative compositions to those in the Tajao and O ignimbrites (Figure 3.30); the apparent lack of partly homogenised glass is probably a reflection of the scantiness of the data.

No phenocrysts of "basaltic" provenance have been found in E (Table 3.2), but an intermediate assemblage oligoclase/andesine - pyroxene-amphibole - high-Mg Fe-Ti oxides has been identified. Other Fe-Ti oxides, correlated with the phonolitic component, are much richer in Mn (Figure 3.31).

The almost exact coincidence of the appearance of mafic and streaky pumice among the eruption products and the onset of column collapse suggests that magmatic heterogeneity may influence the style and course of an explosive eruption. A similar change is seen in airfall and ignmibrite O, although there is some doubt about the airfall-ignimbrite correlation in this case (Chapter I). Among zoned airfalls, the appearance of mafic pumice heralds the end of the eruption (A, K and several minor deposits, Chapter I). Thus

the eruption of mafic material tends to either cause the eruption to become less explosively violent, or to cease altogether. Wolff et al. (1980) suggest that lower volatile contents of the mafic components are responsible for these effects. In the case of E, this seems a likely explanation, as the phonolitic component was extremely water-rich (III.3), and a considerable drop in eruption column gas content, with consequent collapse, may have attended the inclusion of the intermediate magma in the column.

III.4.ii The Adeje red ignimbrite

This is an unusual deposit in many respects. Firstly, it is one of only three welded ignimbrites found on the lower slopes of Tenerife (Chapters I, II). Secondly, it has an unusual glass chemistry. Thirdly, it contains a high proportion of non-vesicular juvenile material (discussed in Chapter VI). Finally, it provides the only example of mixing between a phonolitic and a basaltic magma without evidence of intermediate liquid being involved.

Chemically, Adeje glasses are characterised by low Al_2O_3 and high FeO (Figure 3.30). SiO_2 varies over a small range; the only "trends" are decreasing Na_2O accompanying increasing K_2O; this is probably a hydration effect (Scott, 1971). The low Al_2O_3 compared to most Tenerife phonolites results in correspondingly higher peralkalinity (Na+K/Al $\simeq$ 1.4) and, in the most Na-rich analyses, persodicity. Together with the high FeO content, the composition is thus more reminiscent of an iron-rich peralkaline phonolite from the E. African Rift Valley than of the Tenerife pumice series. The liquid could have been generated through extensive fractionation of

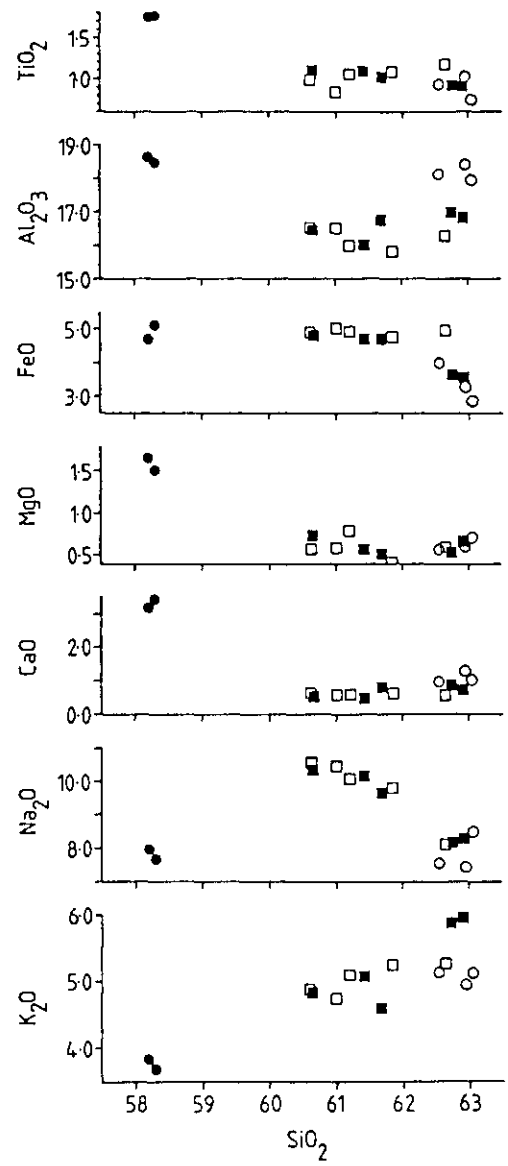

Fig. 3.30 Variation diagrams vs. SiO_2 for streaky glasses from pumice fall/ ignimbrite E and the Adeje ignimbrite. Circles: E; squares: Adeje. Filled symbols: mafic glass; open symbols: salic glass.

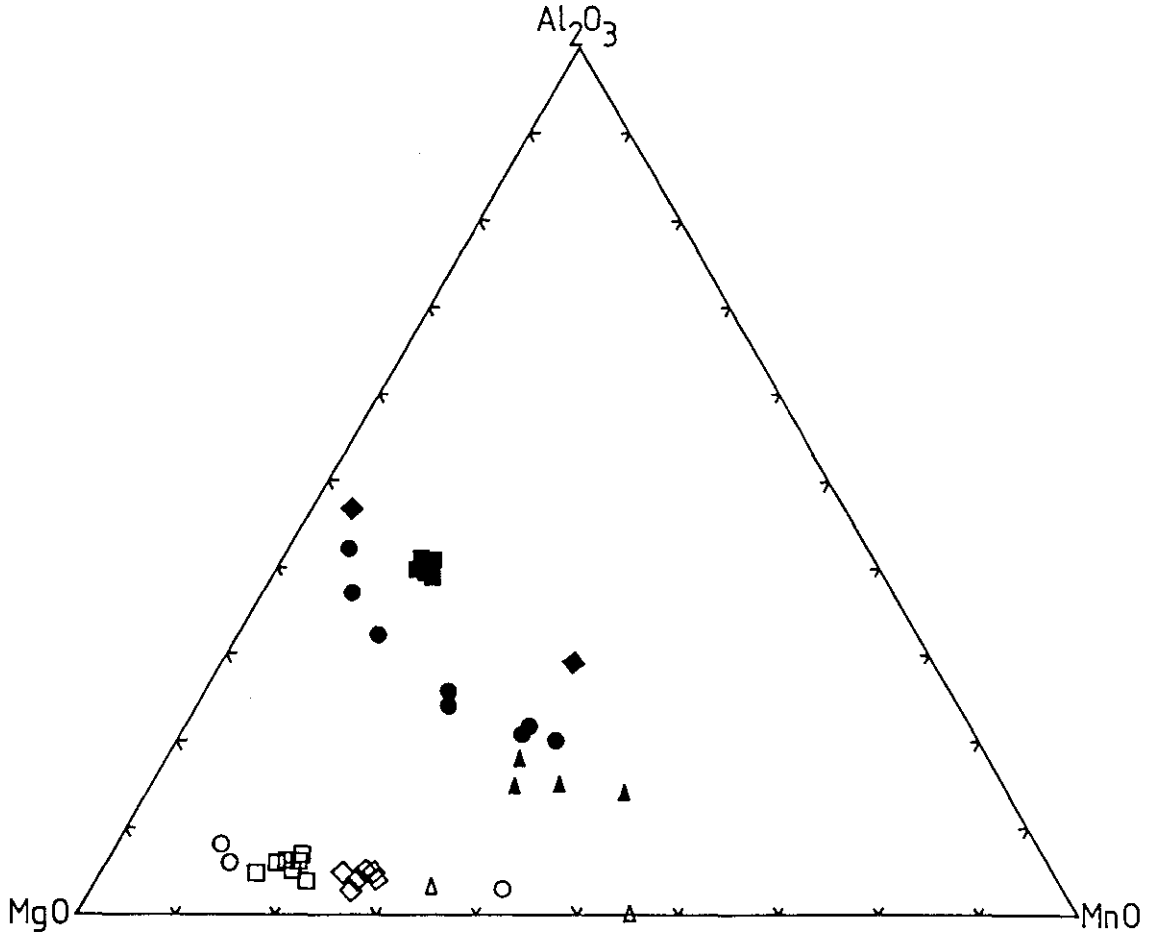

Fig. 3.31 Minor element (oxide wt%) variation in Fe - Ti oxides from pumices E, J and the Adeje ignimbrite. Filled symbols: magnetite; open symbols, ilmenite. Circles: E; diamonds: J, squares: accumulative intermediate fragment in J; triangles, Adeje.

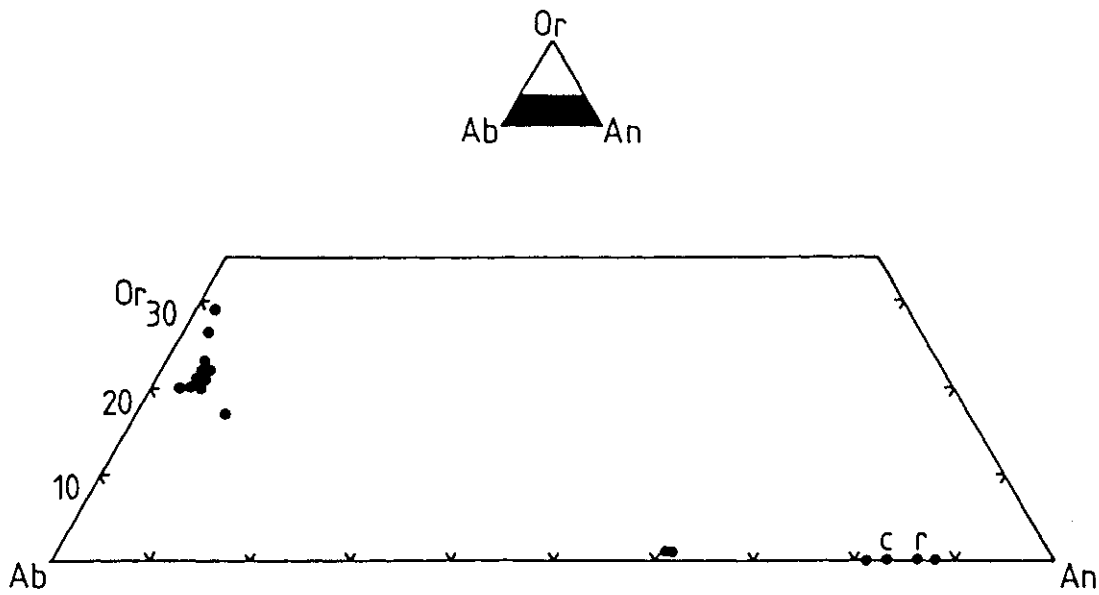

Fig. 3.32 Feldspar compositions in the Adeje ignimbrite.

alkali feldspar and small quantities of other minerals from a "normal" Tenerife phonolite, or may possibly represent the end stage of evolution from an initially Al-poor parent. Trace-element data are required to elucidate this point.

Glass chemistry affords no evidence of mixing and although both pale yellow and brown varieties are present there is no systematic compositional relationship (Figure 3.30). The principal (phonolitic) phenocryst assemblage is alkali feldspar-green augite-biotite-Fe Ti oxides. Oxide minor elements show some variation (Figure 3.31); only the more Mn-rich grains are found associated with the other phases. Also present are occasional calcic feldspars (Figure 3.32) surrounded by a thin envelope of dark glass into which they appear to be resorbing; they bear a close resemblance to basaltic plagioclases in the Tajao and O ignimbrites. The mafic envelope has the same composition as the surrounding clear glass. These plagioclases thus supply the only evidence of "magma mixing" in this ignimbrite, although their petrographic relations to the host material are closely similar to those seen in undoubted mixed tephra. A possible reason for their presence is given in III.5.

III.4.iii Pumice fall J

Fall deposit J is also volcanologically and petrologically unusual. It contains several small ignimbrites, and the only known widespread pyroclastic surge on the island, as intra-plinian deposits. It is the most evolved of the main pumices (Chapter II), and the only one to bear hauyne as a constituent of a phonolitic assemblage. Streaky and mafic pumice is most abundant in the basal fall units, in marked contrast to all other mixed pumice deposits on the island. Streaky pumice also occurs in small quantities

Three phenocryst assemblages are present; olivine-titanaugite-magnetite; plagioclase (An_{42-55})-augite-amphibole-magnetite-ilmenite; alkali feldspar-haüyne-biotite-sphene-magnetite. Titanomagnetite chemistry corresponds well to these straightforward correlations, although ilmenite minor-element abundances do not (Figure 3.31). The present data are not exhaustive and only the intermediate assemblage has been well characterised, from a large (5 x 2 cm) mafic fragment bearing 70% crystals in a highly vesicular groundmass of alkali feldspar, amphibole and residual glass. The presence of glass and the correspondence of phenocryst compositions with those from the rest of the deposit, indicate that this is not a xenolith but rather an accumulative fragment of a constituent magma of the tephra.

Plagioclase compositions and minor-element abundances in Fe-Ti oxides suggest a relatively basic composition for the intermediate magma, consistent with the relatively high temperature derived from geothermometry (III.3).

III.4.iv Remaining deposits

Other deposits were not subjected to microprobe study. Of mixed pumice, M is the most noteworthy; it clearly bears phonolitic, intermediate and basaltic phenocrysts in streaky pumice and closely petrographically resembles the Tajao and O ignimbrites. All other mixed deposits appear to contain only phonolitic and intermediate material. F bears a sodic plagioclase and G and L magmatic amphibole, but both these phases may crystallise from phonolitic magma (Ridley, 1968; Scott, 1970) and their presence alone is therefore not diagnostic of mixing.

Several apparently "pure magma" units contain a very small proportion of partly-assimilated xenolithic material of alkali basaltic or intermediate composition; where this occurs in larger quantities, pumice chemistry may be modified (Chapter II).

III.5 DISCUSSION

One-third of all (major and minor) pumice deposits distinguished by Booth and Walker (in prep.) on Tenerife are, on field, petrographic and/or chemical evidence, magmatically heterogeneous (Chapter I for full list). This is remarkable for the recent products of a relatively well-studied volcano from which magma mixing has not previously been noted. The remainder of this section is an attempt to explain these and other features of the Tenerife pyroclastic series.

Answers to questions concerning the petrological character of evolved magmas erupted from established volcanic centres are normally sought in hypothetical underlying magma chambers. Geological evidence for such chambers has always been abundant in the roots of old eroded volcanoes; in recent years, direct geophysical evidence for their existence has become available (e.g. Ryall and Ryall, 1981). It is not the intention of this author to deviate from this time-honoured practice; there is considerable circumstantial evidence for the existence of a large magma chamber under the central part of Tenerife during its recent history (Ridley, 1968, 1970b; Booth, 1973; Booth and Walker, in prep; this study, Chapter I).

Several constraints can be placed on the behaviour of substantial magma bodies by consideration of basic physical properties; the most important of these in the present context is the density of the magma. Densities of five compositions for a range of water contents are shown in Figure 3.33. Although primary water contents cannot be estimated for the basalt and intermediate components of mixed-magma eruptions, it would seem reasonable that in any single magmatic system (i.e. for a given volcano) that basalt will always be "drier" than associated intermediate melts, and will thus be denser by a minimum of 0.15 g cm^{-3} (Figure 3.33). Put simply, a compositional difference implies a melt density difference (this is not always the case for very primitive compositions; Sparks et al., 1980). Phonolite magmas have especially low densities; their high water contents (Chapter IV) imply values around 2.1 g cm^{-3}.

The maximum vertical thickness a magma body can attain before eruption must occur is controlled by the buoyant force the body exerts on its surroundings; if this exceeds the lithostatic load plus the tensile strength of the country rock, then the buoyant magma will erupt through fractures in the chamber roof. Rock tensile strengths (typically less than a few hundred bars) are insignificant compared to lithostatic pressures and thus the maximum thickness (h) a magma layer can attain is approximately given by

$$h = \frac{Pc}{Pc-Pm} D,$$

where Pc, Pm are the densities of country rock and magma respectively, and D is the depth to the roof of the magma chamber. Consider a salic magma body which is just water-saturated at the roof, which is situated at 5 km depth in country rock of density 3.0 g cm^{-3}. Then the lithostatic pressure is approximately 1.5 kb, the water

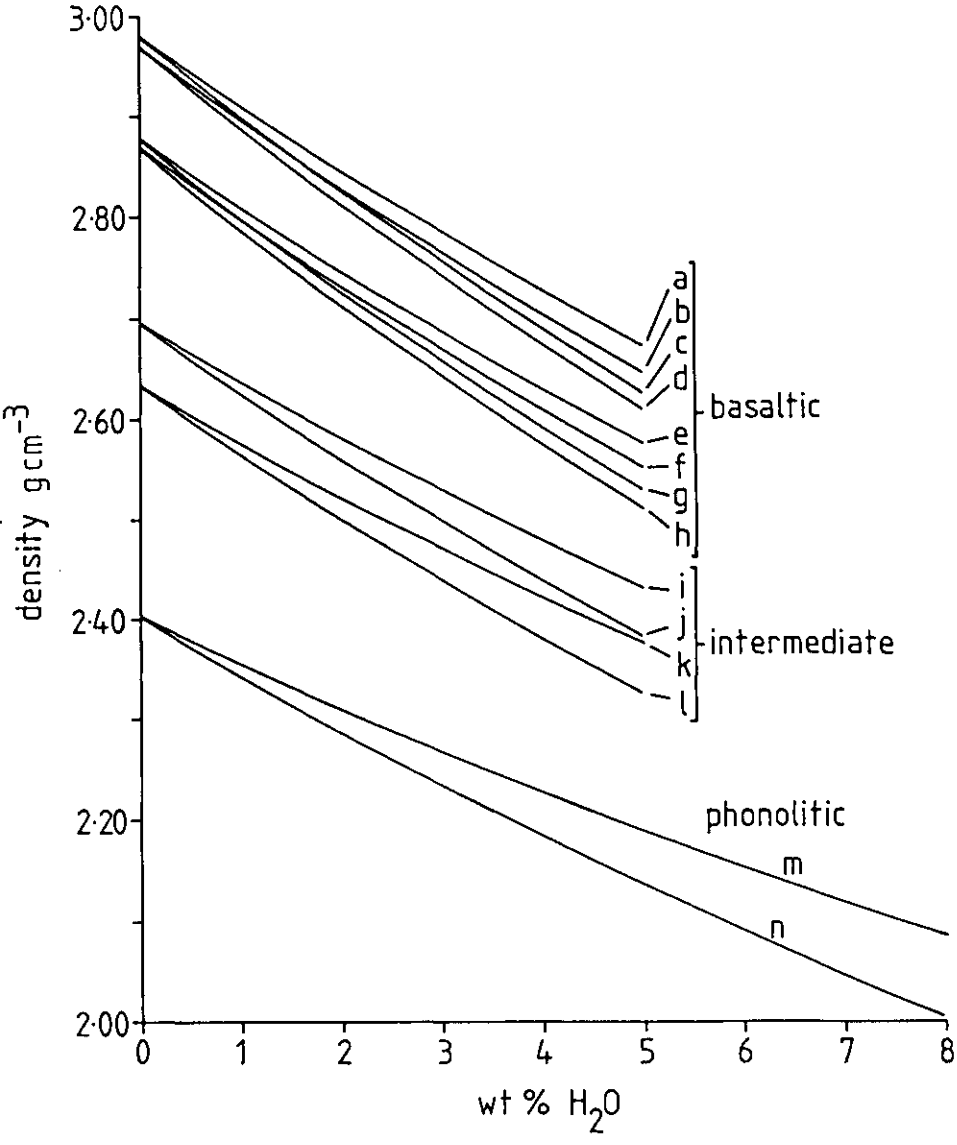

Fig. 3.33 Densities of 5 typical Tenerife magmas, calculated for varying water contents, from partial molar volume data of Bottinga and Weill (1970) and Nelson and Carmichael (1979). a-d: average of 5 alkali basalts from the Vilaflor Series, Ridley, 1967. e-h: initial liquid composition of basaltic component of Tajao ignimbrite. a & e: 10 kb, 1000°C; b & f: 10 kb, 1300°C; c & g: 1000°C; d & h: 1 kb, 1300°C. i-l: intermediate magmas, at 900°C. i,j: Average of four trachybasalts from Portillo and Tauce escarpments, Ridley, 1968. k,l: most basic analysed glass (= M in Fig. 3.24) in Tajao ignimbrite. i,k: 10 kb; j, l: 1 kb. m,n: most evolved phonolite glass analysed from Tajao ignimbrite at 800°C. m: 10 kb; n: 1 kb. Note that the effects of changing temperature and pressure on melt density are insignificant compared with that of chemical composition.

content 5% (from functions given by Wilson and Head, 1981), and the magma density 2.15 g cm^{-3}. Neglecting the minor dependence of magma density on temperature and pressure (Figure 3.33), and assuming a constant distribution of water throughout the homogeneous magma, then the maximum thickness of magma which can form is 18 km. For a crustal density of 3.5 g cm^{-3}, this decreases to 13 km. Unrestricted eruption from wide magma bodies having these depths would produce tephra volumes of the order of a few thousand km^3 (Blake, 1981). This is the order of the maximum known volumes of large ignimbrites (Smith, 1979) suggesting that buoyant forces may cause the largest caldera-forming eruptions. Clearly, however, in the majority of salic eruptions, other factors predominate in triggering the event. Buoyancy is nevertheless a critical factor in determining the behaviour of different magmas when these come into contact, and may thus indirectly influence the eruption of mixed magmas. The data in Figure 3.33 indicate that different members of the Tenerife magma series will rapidly stratify when they come into contact, with the most evolved liquid at the top. A proposed mixing mechanism must account for the apparent ease with which the various magmas overcome their density contrasts and mix to near-homogeneity before and/or during eruption.

III.5.i Qualitative model for the genesis of Tenerife pumice deposits

Any model for the genesis of the phonolitic and mixed pumices (and their associated lavas) must account for, or at least be capable of accommodating, the followng observations:

1. All mappable deposits of both pure phonolitic and mixed types have source vents located in the caldera (Chapter I).

2. Both ordered, i.e zoned pumice deposits, e.g. A (Figure 1.16) and chaotic (streaky and banded pumices) arrangements of phonolitic and intermediate magmas occur, although the quantity of streaky pumice may increase towards the end of an eruption.

3. On a geological time scale, virtually simultaneous mixing of at least three contrasted magmas has occurred on four separate occasions.

4. Differences between phonolitic pumices and lavas. These are (i) differences in mineralogy, e.g. the absence of sanidine from the lavas; (ii) differences in trace-element chemistry, lavas generally having less evolved compositions (Chapter II); (iii) the greater abundance of mixed-magma features in the pumices.

5. Subtle chemical variations within individual deposits, and the lack of any clear relations between successive deposits.

6. The distribution of rock types in the Las Canadas caldera, basalt/trachybasalt in the west, and phonolite in the east (Chapter I). Note that this applies to the caldera wall successions and to younger cone-building volcanism within the caldera (Viejo, Teide and their flank vents, and scattered cinder and spatter cones).

7. Four out of five mixed-magma pumices which bear a basaltic component contain calcic plagioclase (bytownite) as a phenocryst of that component, yet plagioclase-bearing basalts are rare on the surface of Tenerife.

8. Occasional deviations from the typical magma-mixing pattern, such as the concentration of streaky pumice in the basal part of fall J.

For the phonolitic and intermediate magmas, observations 1, 2 and 3 point to their coexistence within a single magma chamber located under the Las Canadas caldera. Repeated mixing of more than two magmas requires that two co-exist, unless a formidable coincidence has occurred. Other explanations, such as each magma type having a different chamber connected via conduits with others, seem unnecessarily complicated, and inconsistent with repeated mixed-magma eruptions. Density relations noted above require that the phonolitic magma forms a layer above the intermediate liquid. The form of the pumice deposit erupted from such a system is dependent on chamber morphology; a high-aspect ratio chamber (tall narrow pipe) will tend to erupt a zoned deposit, whereas a wide, flat-roofed configuration favours the formation of streaky pumice (Figure 1.4), although the first-erupted material may be free of the intermediate component (see Chapter I for full discussion).

How do the phonolite and intermediate liquids attain their relative positions? Previous workers (Ridley, 1969, 1970b; Borley, 1974) have favoured an origin for the Tenerife phonolites by high-level crystal fractionation of trachybasalt/trachyandesite. The present data do not conflict with this hypothesis (Chapter II) and it is not questioned here; rather the physical details of the differentiation process are under consideration. Phonolite may be generated in situ to form a zoned magma chamber as a thermal response of intermediate magma to emplacement in cool country rock. Consider an intermediate magma chilled against walls and roof.

Crystals of plagioclase, amphibole, pyroxene and Fe-Ti oxides nucleate and grow on the chill; as they do so the magma which is precipitating then becomes steadily more phonolitic in composition. Even quite vigorous convection will leave a stationary boundary layer and thus the evolving part of the liquid is not all re-mixed with the main body. This liquid is less dense than its parent, and evolved melt generated at the chamber walls will bouyantly ascend to join that forming at the roof (Figure 3.34), eventually forming a phonolite layer. Analogous processes have been observed in the laboratory by Turner (1980) and Turner and Gustafson (1981). Continuing accumulation of the phonolite layer is mainly by further border-facies crystallisation of the intermediate liquid and resultant boundary layer ascent of the differentiate. The accumulative intermediate fragment found in pumice J (III.4.iii) is believed to be from this incompletely-solidified border facies.

Turner and Gustafson (1981) state that this boundary layer uprise mechanism is common to all magma-chamber analogue systems yet studied in the laboratory, and that given sufficient time, a fine stratification of independently convecting layers develops throughout the bulk of the liquid. This latter fluid structure has also been treated by Rice (1981); however, its formation is not inevitable as implied by Rice, but is preceeded by a period in which a discrete layer of differentiated liquid builds up above the initially homogeneous less-evolved region (see sequence of shadowgraphs in Figure 5, Turner and Gustafson, 1981). If the chamber contents are erupted at this stage, two compositionally well-defined magmas with relatively little internal variation will be erupted, as in the Tajao ignimbrite (ignoring the basaltic component). However, if the system is allowed to develop to the finely stratified stage, a

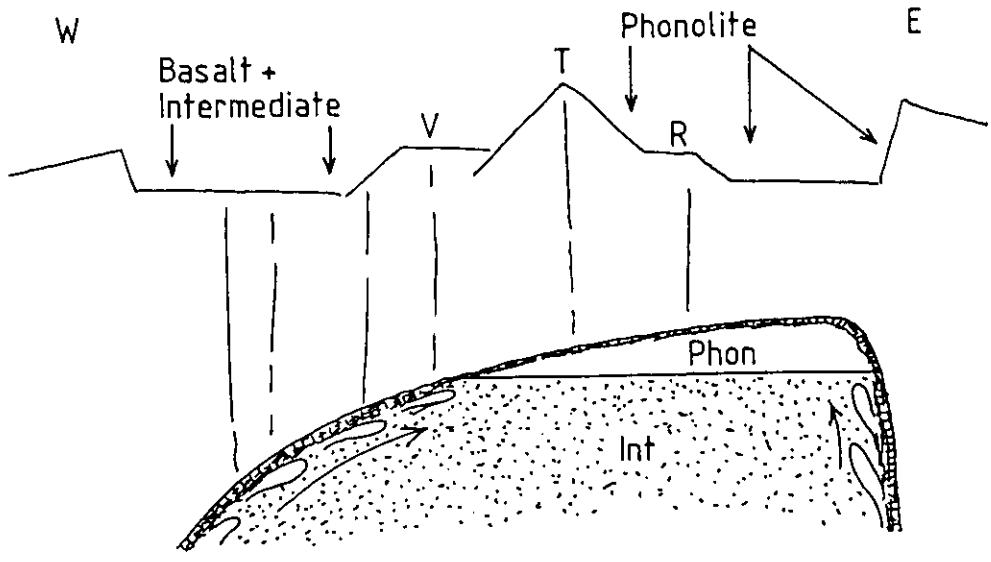

Fig. 3.34 Cartoon of proposed magma chamber and relationship to Las Canadas. V = viejo (intermediate and phonolitic lavas); T = Teide; R = Mta. Rajada (Phonolite lavas and pyroclastics). To the west of Viejo is the Sandiago volcanic field, which has erupted principally mafic lavas with very occasional phonolites. In the magma chamber, crystallisation of intermediate melt at the walls leaves a residual phonolitic liquid, which bouyantly ascends up the wall to the roof zone. The roof is postulated to lie under the E. sector of Las Canadas, in view of the overwhelming dominance of phonolites in that region. Small quantities of magma slowly ascen through conduits to form lavas of the central volcanoes; more catastrophic eruptions result in widespread pumice deposits. If a conduit or pipe is open to the magma chamber, it may partly fill with phonolite; eruption from this "chamber" geometry would favour the formation of a zoned deposit as opposed to streaky pumice (see I.2iii). Note that the proposed mechanism of phonolite generation requires vertical or inward-sloping chamber walls.

compositional continuuum will be approached among the erupted products, as is found in ignimbrite O. The observation of Booth and Walker (unpub.) that repose periods in the Fasnia Series are generally longer than those in the Granadilla Series may be significant in this regard.

The phonolite layer, with an upper solid boundary and a lower boundary with hotter magma, possesses a thermal gradient and conditions are favourable for the development of an accompanying chemical gradient (temperature data (Chapter IV) and evidence from the nepheline syenites (Chapter V) indicate a substantial melting range for the Tenerife phonolitic liquids). Processes within the phonolite layer will be controlled by several factors, but the low thermal expansion of magma coupled with the drastic effect of water on melt density (Figure 3.33) makes it likely that the convective tendency will be overcome by a gradient in water content, particularly as the continually-accumulating phonolite is unlikely to be identical in composition, and that the layer will thus stagnate. Crystal settling within the layer (if permitted by magma rheology) then generates internal heterogeneity. Slight support for a volatile gradient within phonolite is provided by the plinian fall-ignimbrite sequence which is frequently encountered among erupted products, and is consistent with decreasing magma gas content as the eruption proceeds, but could equally well result from changing vent radius. More direct evidence is provided by variation in biotite composition in the Tajao ignimbrite; unfortunately the phase assemblage does not permit direct calculation of P_{H_2O} in this case (Chapter IV).

Eruption has a catastrophic effect on this system, particularly if the magma chamber has a low aspect ratio; the conduit simultaneously samples a large portion of the phonolite layer and part of the underlying intermediate, resulting in the formation of streaky pumice in which both glasses are of variable composition as mixing is superimposed on a pre-existing chemical trend. If the phonolite layer is very thick, the eruption may substantially deplete it without sampling the underlying mafic liquid. If a wide, flat-roofed chamber morphology is assumed, then the minimum thickness of the phonolite layer for purely phonolitic deposits can be calculated from the expression of Blake (1981):

$$V = \frac{2}{9} \pi r^3$$

where V is the total erupted volume (D.R.E.) and r is the maximum depth tapped by the eruption. The maximum volume of purely phonolitic pumice ejected in any eruption is 24 km^3 in the case of J (Chapter I), or approximately 5 km^3 D.R.E., giving an estimate of 1.9 km for phonolite layer depth. In other cases, the layer was very much thinner; approximately 500 m is indicated for O (it should be mentioned that the method of deriving the tephra volumes is independent of the grain-size distribution of the fine fraction (Chapter I) and is thus unaffected by the findings of a recent study (Brazier et al., 1983) that the proportion of fine ash released during explosive eruptions is much greater than previously thought).

After eruption, irrespective of whether the volume deficit is made good by caldera collapse or replenishment with new magma, drastic mixing of the contents is likely. A new phonolite layer, the detailed composition of which cannot be simply related to the pre-eruption layer, forms as the process begins again.

The close spatial association of intermediate and phonolitic rocks in Las Canadas, but with each showing a preference for a certain part of the caldera, can be accommodated in the model if the magma chamber is assumed to be slightly assymetric, with the shallowest portion lying under the eastern section (Figure 3.34). The proposed zoned magma chamber is an attractive way of explaining the "Daly Gap" which has been demonstrated to be a volumetric reality on Tenerife (Ridley, 1970a); if the volume data of Booth and Walker (in prep.) are included, the compositional bimodality is intensified. If intermediate magma normally only exists under a phonolite "cap", it will be prevented from reaching the surface by the density contrast, unless the phonolite is first removed. Extensive pyroclastic deposits of intermediate composition, erupted after phonolitic pumice, are unlikely to form due to the lower volatile content of the intermediate magma; the mafic portions of zoned deposits are volumetrically negligible in the whole pumice series.

Phonolite lavas are abundant in central Tenerife, and their derivation from a different magma chamber seems implausible. Relationships to major explosive eruptions (Sparks et al., 1973) cannot be determined but many, for example those of Teide, appear to be associated with only minor or no pyroclastic activity. Volumes are insignificant compared to the pumice deposits, and it is reasonable that they represent small quantities of magma occasionally bled from the top of the magma chamber. Conditions adjacent to the chamber roof are not representative of the whole phonolite layer and thus differences in lava and pumice chemistry are to be expected. In Chapter II it is shown that one pumice fall deposit (G) was erupted from a magma chamber which had a roof zone of anomalous, in this case less evolved, composition. It is therefore plausible that

anorthoclase-bearing lavas could be erupted from a phonolite body which, in bulk, is precipitating sanidine. Such small-volume tappings are unlikely to affect the underlying intermediate liquid, and thus mixing will rarely be manifested in lavas. The generally less evolved trace-element abundances in lavas, consistent with the chemistry of pumice G (Chapter II), may be further affected by the different mechanisms of lava and pumice eruption. As previously noted, several lavas bear more or less resorbed phenocrysts of hydrous minerals which demonstrate that almost total loss of volatiles must have occurred between phenocryst equilibration and eruption (III.1). Some lavas bear biotite of similar composition to that in the pumices, implying crystallisation under similar P_{H_2O} conditions, say, around 1 kb (Chapter IV). At saturation this corresponds to roughly 4% water content by weight; for implausibly high pressures (10 kb) this decreases to 2%. Wilson and Head (1981) find that some explosive activity should accompany the terrestrial eruption of any magma with an initial gas content greater than 0.1%. A magma with 2% water is fully capable of plinian eruption (Sparks and Wilson, 1976). This problem does not arise with basalts, due to their lower water contents and viscosities which permit easy separation of exsolved gas in rising bubbles (basalts which rise too rapidly to lose gas via bubble separation can also form lavas; they erupt as fire-fountains to form fluid agglutinates which rapidly transform into lava flows (Wilson and Head, 1981; this thesis, Chapter VI). The analogous eruptive style for a salic magma is plinian or ignimbrite-forming. It is impossible for volatile segregation by bubble rise alone to fully deplete a salic magma in volatiles. The Stokesian rise velocity of typical bubbles forming at depth in salic magma (of the order of 100 μm diameter, Sparks, 1978) is a few mm per year; even for a 1 cm bubble at atmospheric pressure in a magma of viscosity

10^6 poise - favourable bubble-rise conditions which are unlikely to occur in nature - the rise rate is approximately 10 cm/day. Stokesian velocities are generally over-estimates of real velocities, due to the effects of neighbouring particles. A vertical conduit full of magma would have to be stationary for a very long period before loss of all volatiles occurred, and in all probability would solidify before the process was complete. Possibly bubble coalescence by shearing during uprise may allow more rapid degassing. In any case, slow rise rates would seem to be necessary for salic lava formation, and is consistent with their evidently low mass eruption rates. Appreciable chemical modification may take place during this slow rise. The magma, in all probability in a narrow vertical conduit with a large surface area, is in intimate contact with the country rock. Substantial assimilation may occur, or material be exchanged with the surroundings. The demonstrable effect of xenolithic contamination on pumice fall G has been to accentuate the less-evolved compositions among the first-erupted tephra, representing that portion of the magma which "did the donkey work" of breaking through to the surface. It can easily be visualised that this type of contamination would be very common among small-volume salic lavas; furthermore direct evidence of contamination could be obscured during their slow rise, slow eruption and slow cooling. It may also be noted that slow rise rates would permit full homogenisation of mixed-magma lavas, in view of the well-advanced homogenisation observed in rapidly-ejected banded pumice (III.2).

An alternative, and equally plausible, explanation of the differences between lava and pumice compositions is that lava extrusion/dyke intrusion may be episodic and related to major eruptions.

After a major explosive event, caldera collapse (or an increment thereof, see Chapter I) is probable, in which case the sunken block is likely to be disrupted to some extent. The first batch of newly-formed phonolite liquid arriving at the top of the residual magma from renewed boundary-layer fractionation may then be intruded into the old cracked roof as a dyke network, and its composition and properties modified by processes discussed above. The degassed magma in those dykes which succeed in breaking through to the surface then forms lavas rather than pumice. Eventual plugging of cracks permits the accumulation of a new phonolite reservoir under the roof. Age data on salic lavas within the pumice series are required as a first step towards testing this hypothesis.

Thus far the only "magma mixing" proposed has been that caused by eruption as stratified magma is drawn into the conduit. The presence of mixed basaltic and intermediate components at a more advanced stage of homogenisation in the mafic glass of four deposits argues that thorough mixing of two magmas can occur in the presence of, but not involving a third liquid, and points to a cause-and-effect relation with the eruption itself.

Sparks et al. (1977) presented a mechanism for the triggering of acid explosive eruptions by the input, at the base of the chamber, of basaltic magma. It was envisaged that forced convection of the acid magma, following the sudden thermal input, entrained and distributed clots of basalt throughout the chamber and led to volatile super-saturation and hence explosive eruption. Although the details of this mechanism seem, on theoretical grounds (Sparks et al., 1980) and from laboratory experiments (Huppert et al., 1982b) to be incorrect (the basalt is more likely to firmly stratify at the

base of the chamber), the essential connection, between the mixing and eruptive events, is plausible and supported by the present petrological evidence. A major problem is nonetheless how the density contrast between, in these cases, basaltic and intermediate magma is overcome. Eichelberger (1979, 1980) has proposed that basalt coming into contact with silicic magma chills and partially crystallises to the point where the residual liquid becomes water-saturated. Vesiculation, due to the specific volume of water being greater than its partial volume in silicate liquid solution under given conditions (Burnham et al., 1969a, b) causes the chilled basalt to become bouyant in the rhyolite and mixing is thus allowed. This mechanism is applicable to low-pressure situations, which are necessary unless unreasonably high basalt magma water contents are postulated (Figure 3.35). However, the Tenerife mixed-magma pumices provide no textural evidence for the operation of the process; in particular, chilled microcrystalline mafic fragments are absent, despite the presence of well-preserved phenocrysts.

In the model adopted for the Tenerife magma chamber, there are three ways in which basalt could mix with the intermediate layer. The most straightforward is intersection of the chamber by a laterally-propogating basalt intrusion; if the basalt debouches into the chamber well above the base, then mixing can occur as it sinks through the less dense intermediate liquid. This is considered an unlikely event for two reasons. Firstly, laterally-moving magma would tend to migrate to the lower-pressure regions on the flanks of the volcano, and secondly, the rarity of this basalt type on Tenerife suggests that it does not normally move through lateral fissures at a high structural level. The second mechanism is illustrated in Figure 3.36;

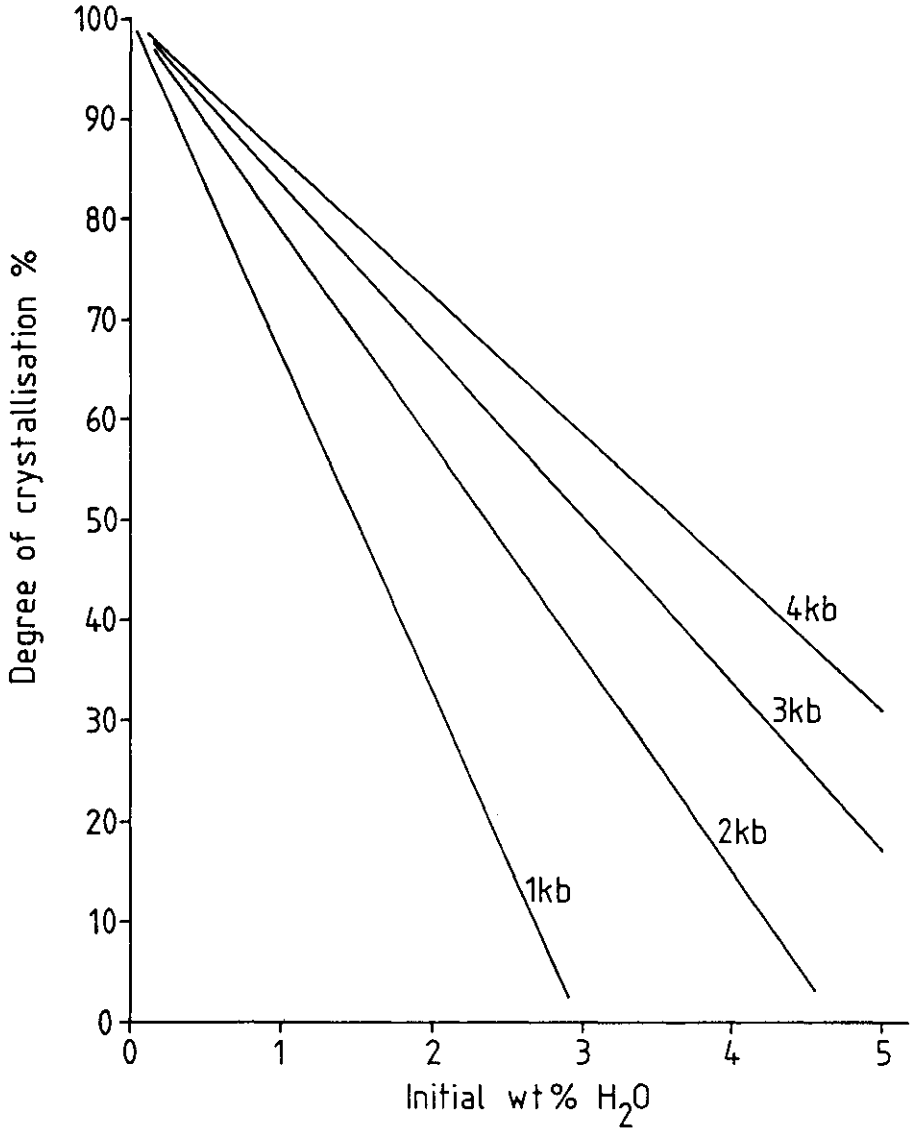

Fig. 3.35 Required degree of crystallisation for saturation of basalt with water at 1100°C as a function of total pressure and initial water content of melt, estimated from solubility data of Burnham (1975).

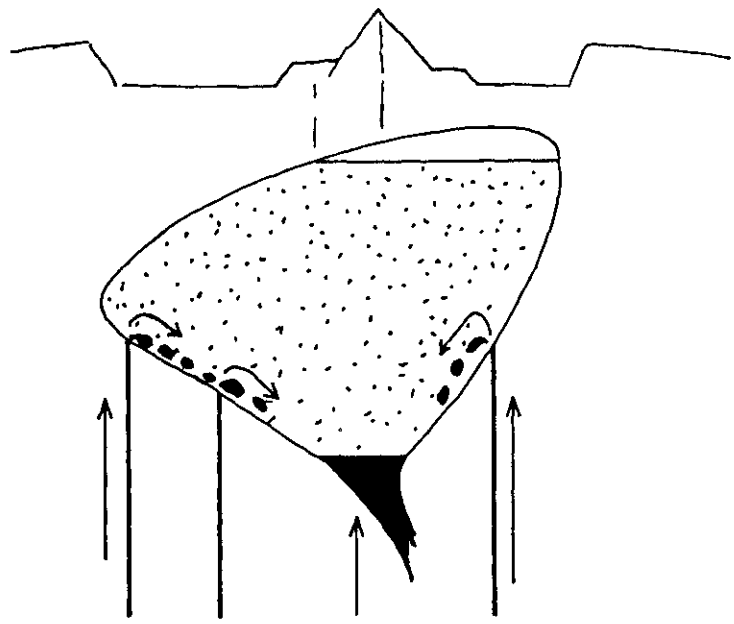

Fig. 3.36 Possible mechanism for mixing of dense basalt (black) with intermediate magma (stipple). Degree of mixing as basalt descends chamber walls is uncertain; note also the rather contrived geometry necessary for generation of phonolite layer as in Fig. 3.34.

the essential element is a funnel-shaped magma chamber, which can thus intercept rising basalt to give the same end result as previously. A corrollary is that basalt rising in the centre of the volcano, but intercepted by the evolved magma body before reaching the surface, is different from that erupted on the flanks. By this mechanism, eruption could be triggered simply by the increased stress on the chamber roof consequent on the volume influx. A problem with this model is that thorough stirring of the mixed magma must occur before eruption; in the case of the Tajao ignimbrite, where the mafic portion represents a mixed intermediate/basalt body of unknown volume, the quantity of basalt is a substantial fraction of the original intermediate (2:5, III.2). It is just as probable, where initial volumes of the mixing components are of a similar order, that the invading basalt would simply run down the chamber walls and pond at the base.

The third means of mixing intruding basalt into the less dense liquid is to have the basalt made bouyant by exsolution of volatile constituents. The most abundant magmatic volatile species is water. The unusually calcic nature of the plagioclase phenocrysts in the mixing basalts (III.1.i) strongly suggests that these magmas were more water-rich than those represented by presently-exposed lavas on Tenerife. The quantitative effect of magma water content on the composition of precipitating plagioclase is poorly known; Thompson and Humphris (1980) have reviewed the available evidence and suggest that small increases in P_{H_2O} (of the order of 100 bars) may increase plagioclase An content by 10-20%, although the presence of other volatile species may also affect plagioclase - P_{H_2O} relations (Yoder, 1969).

The consequences of hydrous basaltic magma ponding beneath cooler, lighter intermediate magma are now considered. Huppert and Sparks (1980) have modelled the fluid dynamics of a similar system involving basic/ultrabasic magma layering. They showed that turbulent convection in the layers resulted in rapid cooling and partial solidification in the lower, denser, more basic layer. For turbulent convection in a liquid body, the Rayleigh number (R) should exceed $\sim 10^8$, where

$$R = \frac{\alpha g \Delta\theta d^3}{K\nu}$$

where α = coefficient of thermal expansion, $\Delta\theta$ is the vertical temperature difference across the layer, d is its depth, K is the thermal conductivity, and ν the kinematic viscosity. For the range of conditions examined below, the condition $R > 10^8$ is met, and thus the turbulent convection model of Huppert and Sparks (1980) can be applied to the present problem.

The initial cooling rate of the hydrous basalt is given by rewriting equations (9) and (10) of Huppert and Sparks (1980) in the form

$$T = \left(\frac{\alpha^7 g K^2 (\Delta T)^{10}}{\nu} \right)^{1/3} \cdot \frac{0.16}{h(\Delta p)^2}$$

where K = thermal diffusivity, ΔT is the temperature contrast between layers, h is the thickness of the lower layer, and Δp is the density contrast between layers. Results for cases of interest (magma viscosity = 100-10000 poise, h = 10-1000 m, ΔT = 50-200°C) are given in Figure 3.37. It may be noted that cooling rates are lower than for the example given by Huppert and Sparks (1980), due to the dependence of T on Δp and ν, although this is to some extent

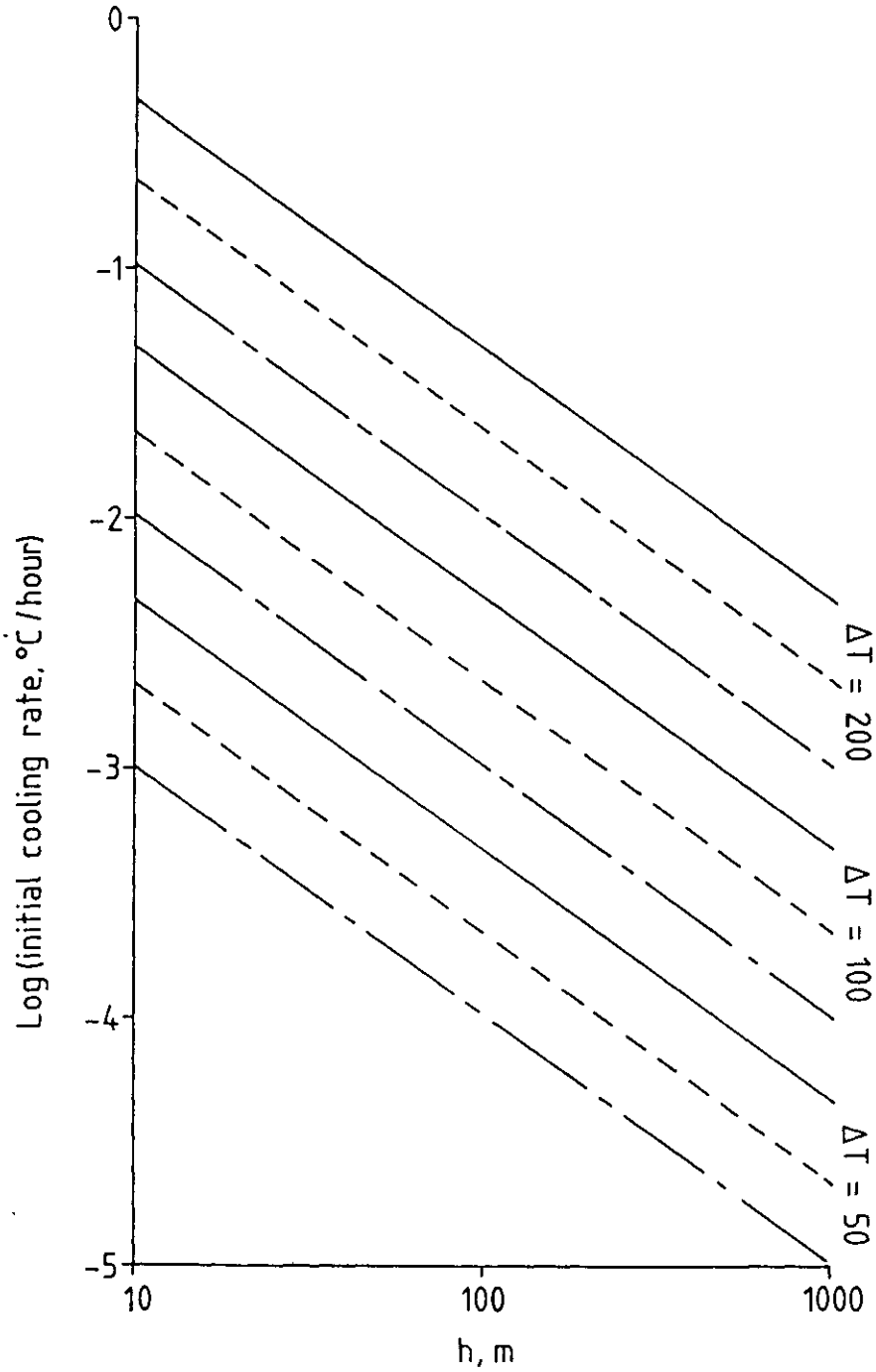

Fig. 3.37 Variation of initial cooling rate of the lower magma layer with layer depth (h) in the two-layer turbulent convection model of Huppert and Sparks (1980), for an alkali basalt-intermediate layer system. T = initial temperature contrast between layers; solid, dashed and chain-dot lines are for magma viscosities of 10, 100 and 10,000 poise respectively. Note that initial cooling rates are maxima in the cooling history of the lower layer (Huppert & Sparks, 1980).

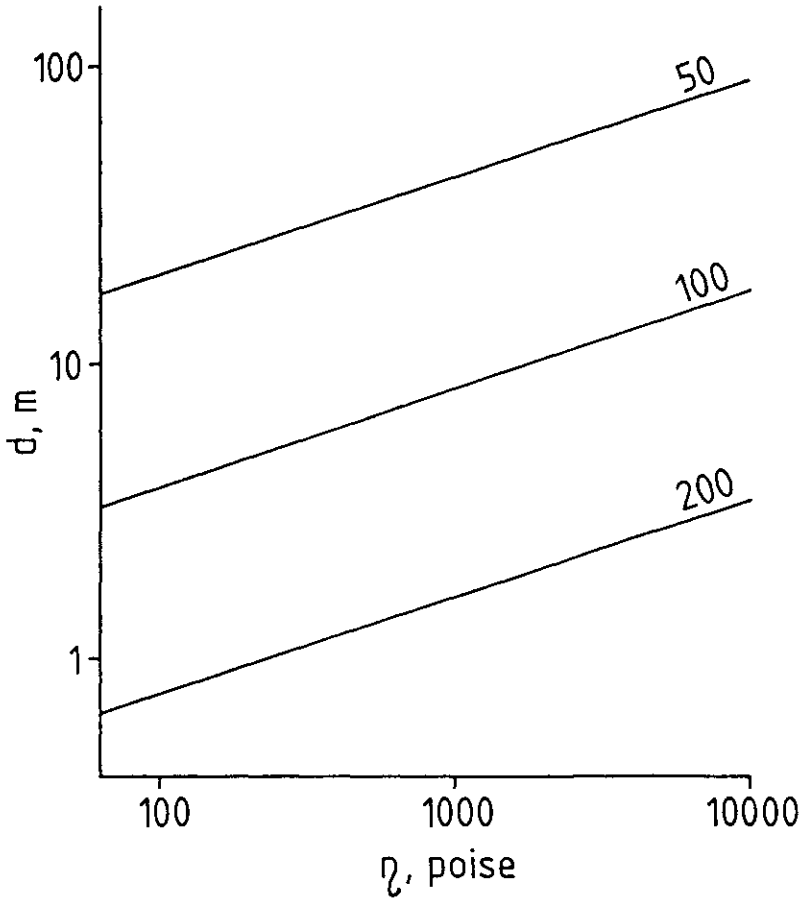

Fig. 3.38 Variation of stable interface thickness (d) in the two-layer turbulent convection model of Huppert and Sparks (1980), as a function of magma viscosity (η) and temperature difference between layers (°C, numbers on curves).

offset by the greater thermal expansivity of hydrous alkali basalt magma ($1.475 \times 10^{-4} K^{-1}$, calculated from data of Nelson and Carmichael (1980) and Burnham et al. (1969a) for Table 3.7, composition 5 + 2 wt% H_2O).

The low cooling rates are reflected in the greater thickness of the non-turbulent interface between the two layers, given by

$$\text{Interface thickness} = 3.125\ (\Delta p)^2 \left(\frac{K\nu}{g(\alpha\Delta T)^7} \right)^{1/3}$$

(modified from equation (13) of Huppert and Sparks, 1980). Results (Figure 3.38) indicate that the stable interface thickness is likely to be of the order of several m. The time required for a diffusional wave to cross this distance may be crudely estimated from

$$x = \sqrt{Dt}$$

where x is distance, D is the diffusion coefficient and t is time. For water, probably the most rapidly diffusing chemical species in basalt magma ($D = 10^{-5} - 10^{-6}\ cm^2 s^{-1}$, Sparks, 1978) t varies from $10-10^5$ years. In this time the bulk of the magma will have substantially cooled, due to the much greater molecular diffusivity of heat. Thus chemical interchanges are negligible in comparison to thermal effects; this is important in what follows.

Cooling the hydrous alkali basalt results in crystallisation of anhydrous phases and thus concentration of water in the residual melt, water being unable to diffuse out through the interface with overlying magma sufficiently rapidly. Increasing P_{H_2O} in the melt will tend to increase f_{O_2}, consistent with the reversed Fe/Mg zoning pattern in pyroxene discussed in III.1.iii. Eventually the residual melt becomes water-saturated and vesiculation occurs. At a high structural level, excessive crystallisation is not required;

for example, at 1 kb, 30% crystallisation of a basalt melt initially containing 2 wt% water will result in vesiculation (Figure 3.35). When the bulk density of the froth drops below that of the overlying non-vesicular magma, bouyant mixing occurs. It is improbable that the entire volume of basalt will bouyantly mix into the overlying magma. After the onset of vesiculation, the whole magma and crystals and bubbles system will not be bouyant until the bubbles have atained a certain volume fraction. Despite the turbulent convection, there will be an overall tendency for these bubbles to migrate upwards and become concentrated in the stagnant interface zone, which may thus become bouyant before the whole basalt layer. Plagioclase crystals will also tend to accumulate by flotation in this region (density $An_{75} \simeq 2.72$, cf. curves a-h, Figure 3.33), perhaps accounting for the apparent plagioclase-rich nature of the mixing basalt in the Tajao ignimbrite (Tables 3.5, 3.6).

Clearly the bouyant mixing will occur as soon as the bulk density of vesicular basic magma falls below that of the intermediate liquid, which is itself substantially denser than the uppermost layer of phonolite (Figure 3.33). Thus the bouyant basalt is unlikely to penetrate the phonolite layer, giving the two-stage mixing (basic-intermediate followed by basic + intermediate - phonolite) shown by petrographic relations.

This model has several attractions. Firstly, it is physically plausible. Secondly, it is consistent with petrological evidence from the Tajao ignimbrite, the basaltic component of which is deduced to have been highly phyric and bears Ca-rich plagioclase

and clinopyroxenes showing normal Al, Ti-zoning and reversed Fe/Mg zoning (although it must be noted that settling and flotation of crystals may have modified bulk crystal distribution within the basaltic layer; furthermore the small proportion of basaltic component in the samples studied may not be representative). Thirdly, the envisaged process is likely to be associated with eruption triggering, thus producing the short time gap between mixing and quenching required for the preservation of the disequilibrium textures. A schematic model for the mixing and eruption events in the Tajao and O ignimbrites is presented in Figure 3.39. The volume increase consequent on vesiculation implies expansion of the magma chamber; whether super-saturation and vesiculation exert increased pressure and cause chamber roof fracturing, or whether the near-saturated nature of the magma makes it sensitive to chamber volume modifications due to external influences (e.g. earthquakes), is of course unknown for a given case.

The drawback of the model is that it requires a relatively high basalt magma water content. This requirement may however be more apparent than real. Thus far it has only proved possible to calculate an initial "basalt" component composition for the Tajao ignimbrite; it was noted in III.2.iii that this magma is in reality considerably evolved in terms of its MgO content, which is appropriate to a trachybasalt rather than an alkali basalt sensu stricto. The data of Ridley (1968) indicate that up to 50% crystallisation of Tenerife alkali basalt magma is required to produce liquids having this MgO content. Thus a minimum water content of around 1% is required in the parental basalt, similar to values found in alkali basalts erupted onto the ocean floor (Carmichael

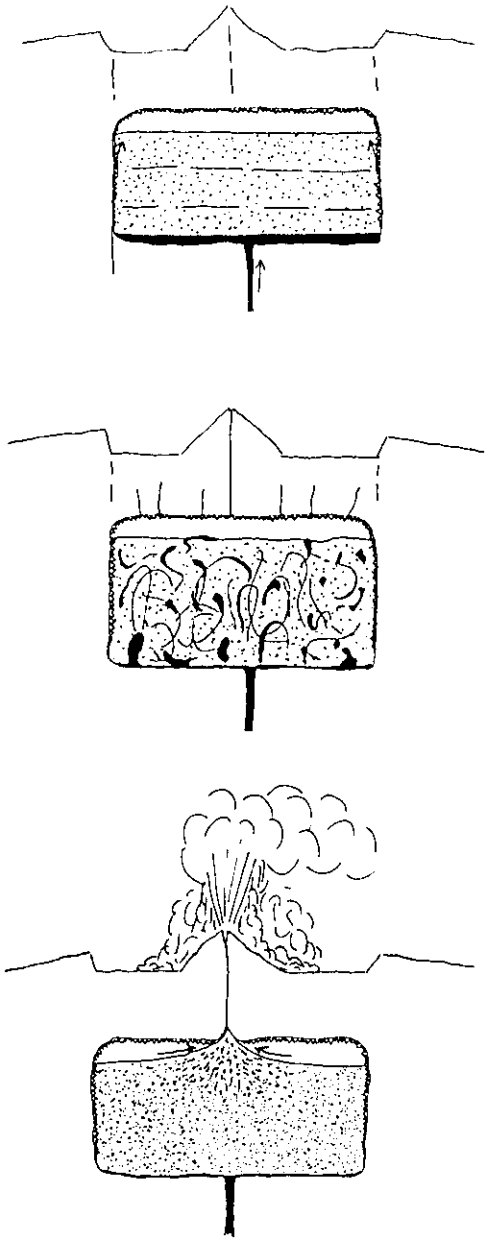

Fig. 3.39 Suggested schematic model for the ~~genesis~~ of pumice deposits in which the full range of magmas is represented. a. Initial magma chamber chamber contents are assumed for the sake of simplicity to be homogeneous alkaline intermediate magma. Wall crystallisation of intermediate (stipple) results in the accumulation of a capping phonolite layer (unornamented). With time, convective layers may develop throughout the liquid (dashed lines); this may be relevant to the compositional continuum found in ignimbrite O (see text). Chamber depicted at the moment of input of alkali basalt magma (black), which ponds at the base. b. Crystallisation and volatile exsolution causes buoyant mixing of basalt into intermediate magma. Vesicular basalt is too dense to mix with capping phonolite layer. PV increase accompanying vesiculation fractures roof-rock and opens a line of weakness in the volcanic edifice. c. Eruption. The mixed basalt/intermediate magma (dense stipple) and phonolite are simultaneously drawn into the conduit and erupted.

et al., 1974, p.322), where eruptive degassing does not occur. Nonetheless, although the required H_2O contents are not unreasonable, they appear not to be attained by the majority of basalts on Tenerife, or else these lose their water at some stage during ascent.

The basalt/trachybasalt magma under discussion is an obvious candidate for material parental to more evolved magmas. If vesiculation did not occur, for example if P_{total} were too high, then the lower basalt layer would continue to evolve by crystallisation towards the composition of the overlying magma, thus replenishing the envisaged reservoir of intermediate (and ultimately phonolitic) liquid. The evidence discussed here suggests that crystallisation paths of the differentiating liquid may be unique to the situation, in other words they are not followed by the basalt magmas which erupt to form the Tenerife lava pile. Geochemical studies on evolved volcanic suites which have differentiated from basalt magma normally assume that exposed lavas are representative of the various stages of magmatic evolution. This study suggests that this assumption should perhaps be questioned.

Finally, consider a vesicular liquid which is not bouyant in overlying magma. The volatile phase passes upwards through the whole system as bubbles, and the accompanying disruption of all liquids results in a degree of mixing. Rising bubbles carry with them an envelope of liquid (bubble film transport) as a form of boundary layer, and as they pass upwards through the magma chamber envisaged (Figure 3.40) will carry basic magma to the top of the chamber. This could account for the occasional bitownite crystals

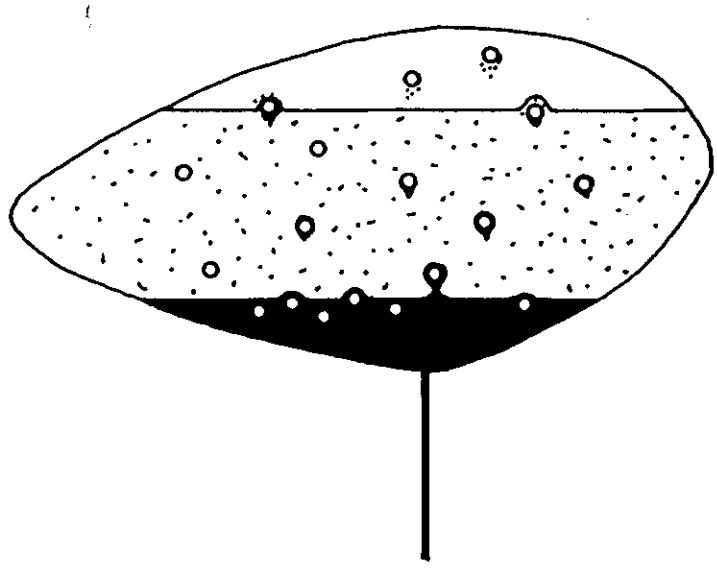

Fig. 3.40 Effect of bubble rise through successive magma layers in a zoned chamber. Small quantities of basic magma are entrained by bubbles and rise into the intermediate and phonolitic layers. Ornament as Figs. 3.34 and 3.36.

in the Adeje ignimbrite, andfor the concentration of mixed material among the first-erupted portion of fall J.

III.5.ii Suggestions for further study

The suggested magma-chamber model has a more than purely local significance, as none of the processes involved are controlled by local conditions, except perhaps the proposal that some of the basaltic magmas are H_2O-rich. Zoned and heterogeneous pumice deposits, where the major component is highly evolved, are common world-wide (Wolff et al., 1980). A major remaining problem is the spatial arrangement of basalt, and generation of the intermediate liquid, in the chamber. It seems likely that the intermediates are generated in situ from underplating basalt, in view of relations in the "three-magma" pumices. Future research should address the following problems:

(a) A more precise characterisation of plagioclase-bearing basalts on Tenerife, both as mixed and unmixed eruptives. Extensive sampling of the most highly mafic material in the Tajao and O ignimbrites, and more detailed study of falls J and M, may discover un- or partly-homogenised initial basalt liquid. Trace-element studies on this and other material from these deposits would be particularly valuable. This should be complemented by detailed field and laboratory study of basalts (especially plagioclase-bearing varieties) contemporaneous with the pumice series.

(b) Detailed field and petrological study of recent eruptives within Las Canadas. The model predicts that mixed lavas should occur in the Viejo region. Mapping and location of lava source vents,

tied to chemistry, would enable the intra-caldera compositional variation to be more precisely defined. A more complete study of phonolite lava geochemistry and petrography particularly as regards their precise chemical relationship to the salic pumices, would furthermore enable critical evaluation of the value of lavas as true representatives of the local salic magma.

(c) Re-mapping of the caldera wall succession in the light of recent volcanological theory, with the intention of more closely locating source vents, and determining the time relations of caldera formation and eruption of the pumice series; this would necessitate correlation with the south-eastern pumice deposits, which should be possible with the present detailed geochemical data.

(d) More extensive age data for both lavas and pumices should be acquired; the value of the proposed model would be greatly increased were it temporally constrained.

(e) Present configuration of the sub-volcanic complex, and location of any liquid magma bodies, using geophysical methods; the model predicts that the magma body roof lies at a shallower depth under the eastern part of Las Canadas than the western.

(f) Experimental studies of model magma systems where exsolution of poorly soluble volatiles is taken into account, using presently-available experimental methods (Huppert and Turner, 1981; Huppert et al., 1982b, Turner and Gustafson, 1981). In particular, the capacity of violent mixing of mafic magmas confined to a low level in the chamber to trigger an eruption from the roof should be assessed;

petrographic data indicates a close temporal association (III.2-4) between mixing and eruption.

(g) Disequilibrium experiments which simulate the magma mixing process, in particular the behaviour of common phenocryst species in foreign magma under a range of T-P-P_{H_2O} conditions, are urgently required; it is intuitively felt that the varying behaviour of phenocrysts during mixing evident from this and other studies (e.g. overgrowth versus resorption; mode and degree of resorption of different species) could be valuable guides to conditions under which mixing occurred in any given case.

Addendum

A recent paper (Huppert et al., 1982a), published shortly after the preparation of this account, gives a more rigorous theoretical treatment (for calc-alkaline magmas) of the crystallisation of hydrous basic magma and consequent bouyant mixing in a layered magma chamber similar in principle to that considered here. The conclusions of Huppert et al. (1982a), based mainly on theoretical considerations, are not significantly different from the model suggested here on the basis of petrological evidence. Such models may therefore have applications to the evolution and eruption of magmas of widely different types in a range of volcano-tectonic settings.

CHAPTER IV

TEMPERATURES AND VOLATILE COMPONENTS OF THE PUMICE-FORMING MAGMAS

A knowledge of the compositions of the constituent minerals of igneous rocks can provide information on their conditions of formation and crystallisation history, and may shed light on the genesis of their magmas. This is particularly true of phenocrysts in young volcanic rocks, since these have usually been unaffected by processes occurring during and after eruption. Analysis of volcanic groundmass material can also yield valuable information. Accordingly, some of the pyroclastic units in the Tenerife succession were selected for an electron microprobe study with two principal aims: firstly, to investigate the nature of visibly heterogeneous tephra such as streaky pumice (Chapter III) and secondly, to deduce conditions prevailing in the magma before eruption, particularly with reference to magmatic volatile contents.

This chapter is in three parts. In the first, a brief resumé of thermodynamic theory is given. The second part discusses the various geothermometers potentially applicable to the mineral assemblages encountered here. The third section deals with the estimation of pre-eruptive magmatic volatile abundances for some welded and non-welded pumice deposits.

IV.1 THERMODYNAMIC BACKGROUND

The principles of equilibrium thermodynamics are very widely employed by petrologists, often with the aim of determining the P-T formation conditions of igneous and metamorphic rocks. This thesis, in common with the majority of such studies, uses thermodynamic data which has been manipulated into the most readily usable form, such as geothermometers and geobarometers. A brief summary of basic thermodynamic theory and method used in these formulations follows. No attempt is made to provide a detiled account of the application of thermodynamics to petrological problems as there are several excellent texts currently available; the reader is particularly referred to Wood and Fraser (1976) and Powell (1978).

For any chemical reaction, we have at equilibrium

$$\Delta G^{O} = -RT\ln K \qquad 1$$

where ΔG^{O} is the standard free energy for the reaction, K is the equilibrium constant, R is the universal gas constant and T is the temperature. Consider the equilibrium

$$\underset{w}{aA} + \underset{x}{bB} \rightleftharpoons \underset{y}{cC} + \underset{z}{dD} \qquad 2$$

where a, b, c, d refer to the number of moles of components A, B, C, D in phases w, x, y, z involved in the reaction. In this case K is given by

$$K = \frac{(a^{y}_{C})^{c}.(a^{z}_{D})^{d}}{(a^{w}_{A})^{a}.(a^{x}_{B})^{b}} \qquad 3$$

where a^{y}_{C} is the activity of component C in phase y, etc.
K is found from a knowledge of phase compositions and activity-composition relations for each phase (see below).

ΔG is found by evaluating the free energy for each component from the relation

$$G = H - TS \qquad 4$$

where H is the enthalpy and S is the entropy of the component under consideration. Enthalpy and entropy vary as a function of temperature and pressure. The relationship between enthalpy and temperature is

$$dH = CpdT \qquad 5$$

where Cp is the heat capacity of the phase of interest. Thus if H is known at temperature T_o, it may be found at any temperature T from

$$\int_{T_o}^{T} dH = \int_{T_o}^{T} Cp\, dT \qquad 6$$

Cp is itself a function of temperature:

$$Cp = a + bT + c/T^2 \qquad 7$$

where a, b, c are constants for the phase of interest.

The temperature dependence of entropy may be expressed in a similar form

$$dS = \frac{CpdT}{T} \qquad 8$$

and thus

$$\int_{T_o}^{T} dS = \int_{T_o}^{T} \frac{CpdT}{T} \qquad 9$$

The effect of changing pressure on G (at constant temperature) is given by

$$\left(\frac{\partial G}{\partial P}\right)_T = V \qquad 10$$

where V is the molar volume of the phase of interest. Thus for a reaction involving a volume change ΔV

$$\left(\frac{\partial \Delta G}{\partial P}\right)_T = \Delta V \qquad 11$$

The free energy change of a reaction at any temperature and pressure may be calculated by combining equations (6), (9) and (11) in the relationship of (4). Thermodynamic data is usually tabulated at a reference temperature and pressure of 298K and 1 bar. Therefore the overall expression is most conveniently written in the form

$$(\Delta G)_{P,T} = \Delta H_{1\ bar,298} + \int_{298}^{T} \Delta C_p dT - T\left(\Delta S_{298} + \int_{298}^{T} \frac{\Delta C_p dT}{T}\right)$$

$$+ \int_{1\ bar}^{P} \Delta V\, dP \qquad 12$$

From equation (1), lnK for a given reaction is thus a function of P and T, or, in other words, a given value of K (as found, for example, by analysis of the phases concerned in a rock sample) defines a curve in P-T space. This is the basis of geothermometry and geobarometry. Potential geothermometers are those reactions in which the value of K is strongly temperature dependent, but is little affected by pressure. Inspection of equation (12) shows that this requires a large value for ΔC_p, resulting in large $\Delta H_{1\ bar,\ T}$. Potential geobarometers require a strong dependence of K on pressure, and thus a large value of ΔV. For most solid-solid reactions, ΔV is small, which accounts for the paucity of geobarometers applicable to igneous mineral assemblages. Indeed the only means of estimating P_{Total} applicable to volcanic rocks involves liquid components (Nicholls et al., 1971; Carmichael et al., 1977). In contrast, several equilibria have been proposed as geothermometers, with varying degrees of success. Thermometers

considered in this thesis, whose individual merits are discussed below (III.1.ii) are: titanomagnetite-ilmenite (Buddington and Lindsley, 1964); alkali feldspar-plagioclase (Stormer, 1975; Powell and Powell, 1977a); nepheline-alkali feldspar (Perchuk and Ryabchikov, 1968; Powell and Powell, 1977b); olivine-clinopyroxene (Powell and Powell, 1974); clinopyroxene-ilmenite (Bishop, 1980).

If it is wished to investigate the activity of a particular component of the equilibrium, fixing the activities of all other components defines a surface in P-T-a space. If T is known and the P dependence of the reaction is small (or vice-versa), or alternatively if some reasonable value of P can be chosen, then the activity of the component can be defined. This approach is commonly employed to determine the activities of such magmatic components as SiO_2, and fugitive species such as H_2O (Wones and Eugster, 1965). The estimation of magmatic volatile components is treated more fully in III.3.

The determination of the equilibrium constant is the business of the petrologist wishing to apply these methods to a particular mineral assemblage. In some cases it is merely necessary to recast mineral analyses into the appropriate end-members, and then to insert these values into, say, the geothermometer expression, which includes the activity-composition relations. In others, the activities of the relevant species must be calculated from a knowledge of composition and activity-composition relations. For most solid solutions of geological interest, these relations may be approximated by one of a few simple models. The simplest is the ideal solution, in which

$$X_A = a_A$$

where X_A is the mole fraction of component A in its host phase, and a_A is its activity. Where there is more than one site per formula unit, then the activity of the component is clearly equal to the mole fraction raised to the power of the number of sites, e.g. for olivine solid-solution

$$a^{ol}_{Fe_2SiO_4} = X^2_{Fe} \quad \text{where } X_{Fe} = \frac{Fe}{Fe+Mg}$$

Many solid solutions, however, are strongly non-ideal. For these we write

$$a_A = \gamma_A X_A$$

for the single-site case, where γ_A is the activity coefficient. Activity coefficients may be complex functions of temperature, pressure and composition. The simplest model which describes the variation of γ_A is the symmetrical regular solution model, in which

$$RT\ln \gamma_A = W_G(1-X_A)^2$$

for a binary solution, where W_G is an experimentally determined interaction parameter. In ternary and more complex solutions, γ_A is a more complicated function of composition. The assymetric regular solution model is slightly more complex in that each end-member has its own interaction parameter. The activity coefficient of one component (γ_A) in a binary solid solution is then given by

$$RT\ln \gamma_A = (2W^B_G - W^A_B)\, X^2_B + 2(W^A_G - W^B_G)X^3_B$$

where X_B is the mole fraction of the other component, and W^A_G, W^B_G are the experimentally determined interaction parameters for each end-member. This model is used for high-temperature alkali feldspars, following Thompson and Waldbaum (1969).

Where data on the mixing properties of solutions are unavailable, it is common practice to assume ideality. In certain cases, this may not lead to large errors even when several of the phases concerned are markedly non-ideal, since activity coefficients for most silicate solid solutions have comparable values and thus tend to cancel out in the equilibrium expression (e.g. Wood and Banno, 1973). This considerably simplifies calculations. Conversely, if site occupancies in a complex non-ideal solution are strongly temperature (or pressure) dependent, it may be necessary to employ a lengthy iterative procedure in order to find temperature, pressure, or the activity of a given component (Powell and Powell, 1977b).

Finally, it may be noted that some geothermometers rely on direct experimental calibration, by means of analysing the products of experimental runs under known conditions, rather than using these data to derive thermodynamic data. This approach was employed by Buddington and Lindsley (1964) for coexisting titanomagnetite-ilmenite pairs, and by Hamilton (1961) for the temperature dependence of nepheline composition.

IV.2 GEOTHERMOMETERS

Reactions with a large ΔH show a strong dependence of K on temperature, and thus make good geothermometers. It is of considerable importance to reliably estimate the temperature at which the phenocryst assemblage of a volcanic rock last equilibrated, both as a piece of valuable petrological information and because further thermodynamic calculations, using data from the same assemblage, such as the estimation of the activities of magmatic components, require a knowledge of temperature.

IV.2.i Iron-titanium oxides geothermometer

The titanomagnetite-ilmenite geothermomemter and oxygen barometer, calibrated by Buddington and Lindsley (1964) has been widely employed in the study of igneous rocks. Titanomagnetite composition may be expressed as a solid solution between ulvöspinel (Fe_2TiO_4) and magnetite (Fe_3O_4), and ilmenite composition as a solid solution between ilmenite ($FeTiO_3$) and hematite (Fe_2O_3). Two reactions may be written between these components:

$$Fe_2O_3 + Fe_2TiO_4 \rightleftharpoons Fe_3O_4 + FeTiO_3 \qquad 1$$

$$6Fe_2TiO_4 + O_2 \rightleftharpoons 2Fe_3O_4 + 6FeTiO_3 \qquad 2$$

Reaction (1) is used as a geothermometer, and reaction (2) as an oxygen barometer. Thus a knowledge of the compositions of coexisting titanomagnetite and ilmenite solid solutions allows simultaneous determination of T and f_{O_2} (oxygen fugacity). Buddington and Lindsley (1964) present their calibration graphically. Powell and Powell (1977c) reformulated the geothermometer and oxygen barometer on a thermodynamic basis using the experimental data of Buddington and Lindsley, enabling calculation of T and f_{O_2} from the mineral data. The two methods are nearly equivalent for phases whose compositions lie wholly in the system TiO_2-FeO-Fe_2O_3. Since microprobe analysis does not differentiate between FeO and Fe_2O_3, it is first necessary to recast the analyses of both phases to include Fe_2O_3, both to check analytical quality (as indicated by the analysis wt % oxide totals, which will obviously be too low if substantial amounts of Fe_2O_3 are reported as FeO) and in order to calculate end-member proportions. Procedures for doing this have been given by Carmichael (1967a), Anderson (1968) and Lipman (1971). The effect of oxide components other than FeO, TiO_2 and Fe_2O_3 on estimated values of T and f_{O_2} has been the subject of some discussion, particularly as to how these components are best dealt with in the recalculation. Commonly present are SiO_2,

Al_2O_3, V_2O_3, Cr_2O_3, MnO, MgO, CaO and ZnO; in the samples analysed here, only Al_2O_3, MnO and MgO are present in significant quantities (Appendix B). Buddington and Lindsley (1964) suggested that minor components be discarded, although most of the data available to them was in the form of major constituent (FeO, TiO_2, Fe_2O_3) analyses. The scheme of Carmichael (1967a), designed specifically for application to microprobe analyses, is probably the most widely used, and, for reasons to be given, was used in this study. This scheme is as follows: for titanomagnetite, all the MnO, MgO, CaO and ZnO and sufficient FeO equivalent to twice the value of (TiO_2+SiO_2) is alloted to the molecular proportions of (TiO_2+SiO_2); FeO is then allotted in the ratio 1:1 to the molecular proportions of Al_2O_3, Cr_2O_3 and V_2O_3 and the remaining FeO is recalculated to equivalent magnetite. The weight % Fe_2O_3 may then be calculated and the analysis corrected accordingly. For ilmenite, all the MnO, CaO, MgO and ZnO is combined with the molecular proportions of (TiO_2+SiO_2), sufficient FeO then being added to make the ratio 1:1. The excess FeO is then converted to Fe_2O_3 (hematite).

The essential features of Carmichael's procedure, the assigning of divalent cations to $R_2^{2+}TiO_4$ and $R^{2+}TiO_3$ molecules in titanomagnetite and ilmenite respectively, are endorsed by Anderson (1968) and Lipman (1971), although the former first allocates a proportion of Mg to $(Mg,Fe)Al_2O_4$ in order to "use up" the Al content of the spinel phase. Spiedel (1970) has experimentally shown that the effect of MgO on the geothermometer-oxygen barometer is to slightly raise f_{O_2} at a fixed temperature, but that this error is minimised if Mg is assigned to Mg_2TiO_4 and $MgTiO_3$ molecules in titanomagnetite and ilmenite respectively, thus supporting Carmichael's method. Powell and Powell (1977c) reject the above procedures, and instead propose that the

greatest possible theoretical variation in each emdmember be found by assigning minor oxides first to one molecule, then to the other, for each phase. The maximum and minimum values of endmembers so found are then combined in the most unfavourable way to get the maximum uncertainty in calculated T and f_{O_2}. However, Hildreth (1979) considers that the recalculation method of Carmichael (1967a) is fully vindicated by experimental results obtained by D.H. Lindsley and associates (Mazzulo et al., 1975; Pinckney and Lindsley, 1976) on the effect of Mn and Mg in iron-titanium oxides on the apparent T and f_{O_2} values yielded by the calibration curves of Buddington and Lindsley (1964). Lindsley (pers. comm. cited by Hildreth, 1979) recommended several recalculation schemes, each appropriate over a certain T-f_{O_2}-composition range, which best reflect his experimental run conditions. Hildreth (1979) compared these with the method of Carmichael (1967a) as applied to co-existing Fe-Ti oxides from the Bishop Tuff, California, and reports a negligible discrepancy between T and f_{O_2} values yielded by the two methods.

Fe-Ti oxides in the pumice deposits of Tenerife contain considerable quantities of minor elements (typically 4-8% by weight $MgO+MnO+Al_2O_3$, although spinels from basaltic assemblages in mixed-magma deposits may contain as much as 17% by weight $Al_2O_3+Cr_2O_3+MnO+MgO$; see Chapter III), and the errors in estimated T and fo_2 values due to this cause are therefore considered in some detail.

The errors suggested by Powell and Powell (1977c) completely invalidate the use of Fe-Ti oxides with these minor element contents in geothermometry and oxygen barometry, but they are the theoretical maximum errors that can apply to the impure phases. If it can be shown that these maximum errors are overestimates, then the impure

phases can still be used. One way of doing this is to compare the error boxes in T-f_{O_2} space given by Powell and Powell's method with constraining data from the same equilibrium mineral assemblage. In three of the pumice deposits selected for microprobe analysis, titanomagnetite and ilmenite coexist with sanidine and biotite, and thus f_{H_2O} can be calculated from a knowledge of T and f_{O_2} (see section IV.3 for a full account of the method). Conversely, if a geologically reasonable range of f_{H_2O} is chosen, limits can be placed on the possible range of T and fo_2 from the same data. 5 kb was chosen as a maximum value of fH_2O; this corresponds to approximately 10% by weight H_2O in the magma (Burnham, 1975) at saturation, and the Tenerife phonolites are unlikely to have resided in a magma chamber at great depth (Chapters I and III). Water contents are thought unlikely to have been less than 2% by weight; this corresponds to roughly 0.3 kb water pressure at saturation. In the case of fall deposit E, which has a very wide dispersal of coarse pumice (I.3) testifying to the extreme violence of the eruption, field evidence is incompatible with a magmatic water content of less than 4% as deduced by the volcanological methods of Wilson (1976, 1980), corresponding to 1 kb water pressure at saturation. Even using these very wide ranges of f_{H_2O}, Figures 4.1-4.3 show that the errors calculated by the Powell and Powell method are considerably over-estimated, especially as regards f_{O_2} determination. In one case (E fall, Figure 4.2) the mean value given by the Powell and Powell method is geologically unreasonable. In contrast, values calculated by using the scheme of Carmichael (1967a) in conjunction with the curves of Buddington and Lindsley (1964) always plot well within the geologically reasonable range (Figures 4.1-4.3).

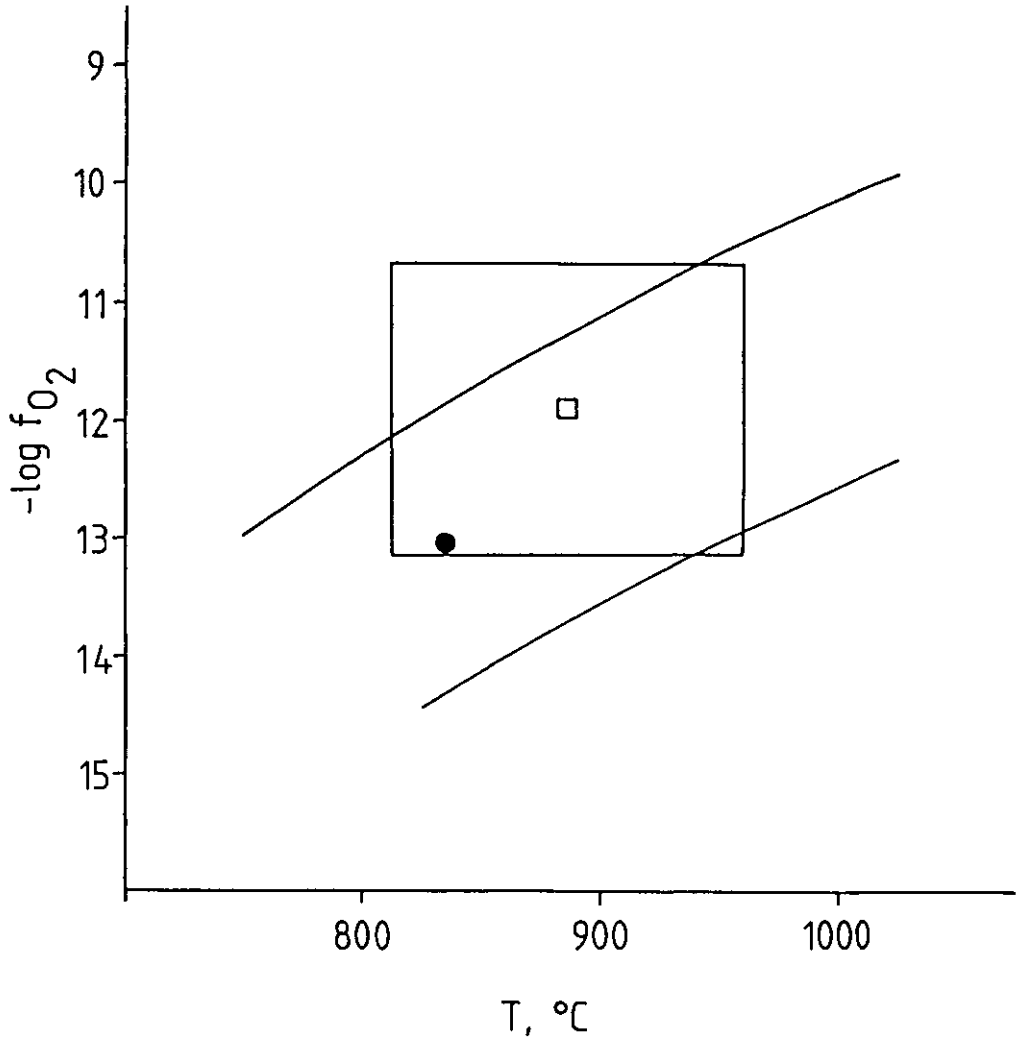

Fig. 4.1 T-f_{O_2} diagram for Fe-Ti oxide equilibration in the Boca de Tauce welded air-fall tuff. Solid circle given by the recalculation method of Carmichael (1967) applied to the data of Buddington and Lindsley (1964); open square and large rectangle are point and error limits respectively calculated by the method of Powell and Powell (1977). Curves are T-fO_2 limits imposed by the composition of co-existing biotite, as discussed in the text.

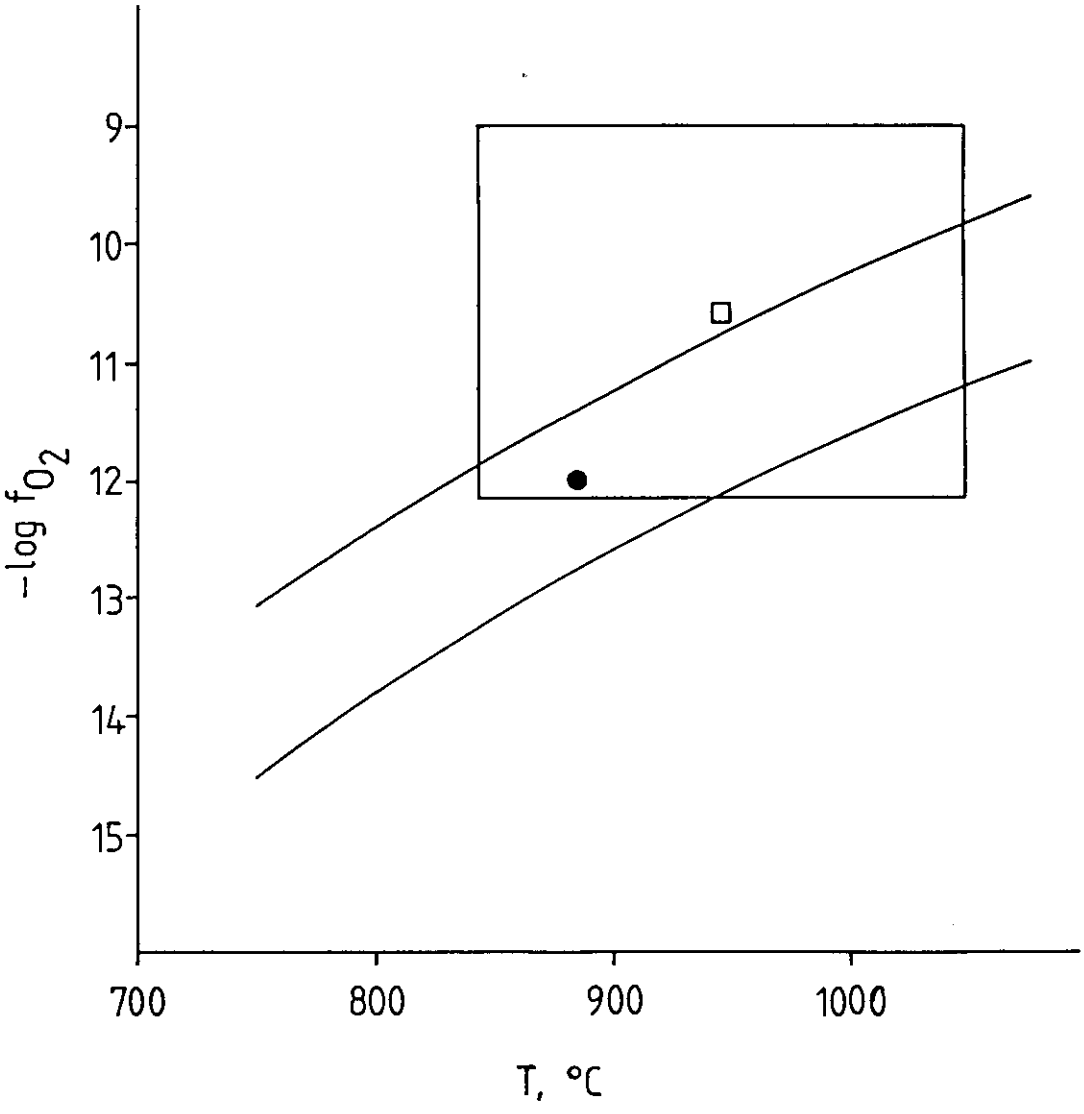

Fig. 4.2 T-f_{O_2} diagram for Fe-Ti oxide equilibration in pumice deposit E; notation as Fig. 4.1.

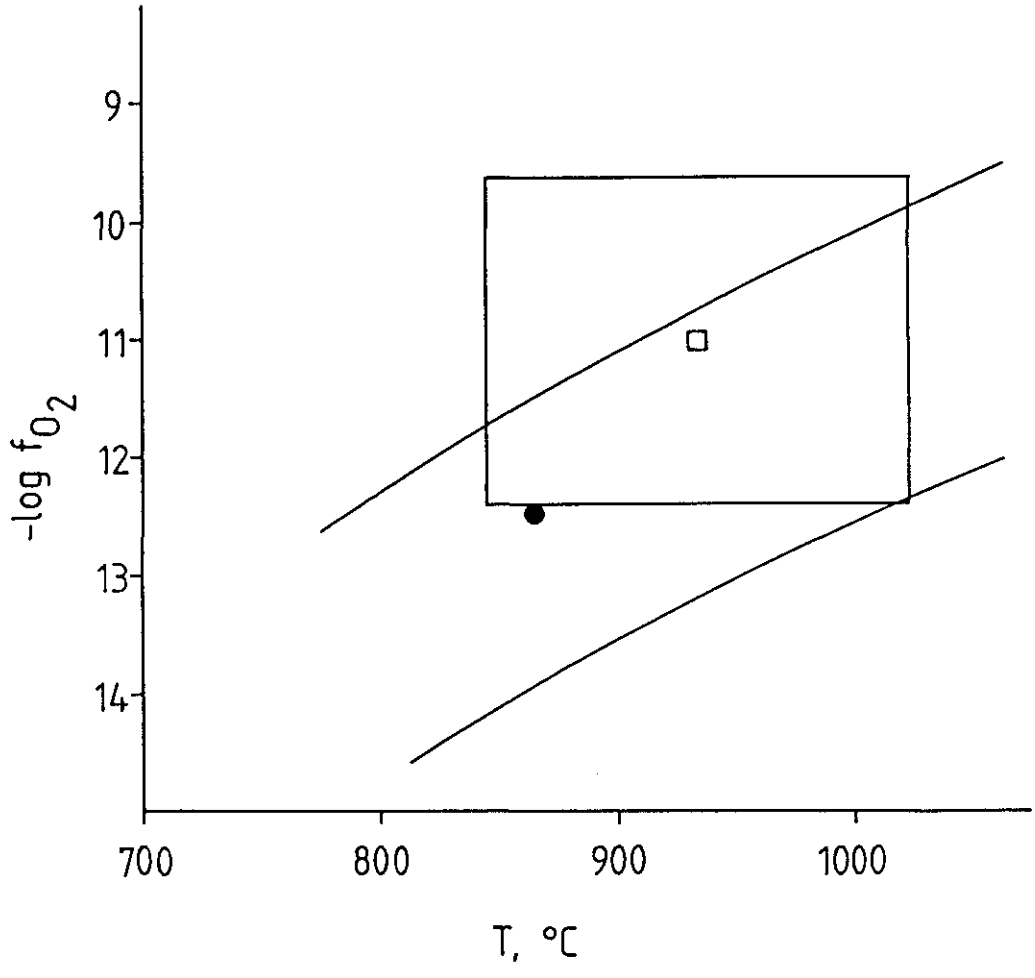

Fig. 4.3 T-f_{O_2} diagram for Fe-Ti oxide equilibration in the Adeje Red Ignimbrite; notation as Fig. 4.1.

Temperatures obtained by the Carmichael procedure are vindicated by an independent geothermometer, the clinopyroxene-ilmenite geothermometer of Bishop (1980). Agreement between the two is good, and is much better than would be expected from the errors proposed by Powell and Powell (Table 4.1).

The original T-f_{O_2} data determined by Carmichael for a wide range of salic magmas, also militate against very large errors applying to the determinations. Carmichael found that most of his samples plotted along three curves in T-f_{O_2} space, one of which was the quartz-magnetite-fayalite oxygen buffer. Each curve indicated a different ferromagnesian silicate mineral assemblage associated with the Fe-Ti oxides. The curves have since been vindicated by several studies as illustrating the oxygen-buffering effect of ferromagnesian silicate minerals in salic magmas (Ewart et al., 1971; Lipman, 1971; Heming and Carmichael, 1973; Rutherford and Heming, 1978). Carmichael's analyses of oxides show a considerable range in minor element content, from a few tenths of one percent to 7.75% by weight. The error boxes deduced from the Powell and Powell method cut across all of these buffer curves for some determinations, and yet minor-element-rich mineral pairs yield T-f_{O_2} values that plot as closely to the curves as those determined from almost pure FeO-TiO_2-Fe_2O_3 phases. Were the errors of Powell and Powell applicable, a considerable degree of scatter would be expected. It must be concluded that the errors suggested by Powell and Powell (1977c) are very much greater than those obtaining in practice.

Table 4.1. Comparison of temperatures obtained by applying the Fe-Ti oxides geothermometer (Buddington & Lindsley, 1964) to analyses recast by the method of Carmichael (1967), with those given by the clinopyroxene-ilmenite geothermometer (Bishop, 1980), for those deposits whre titanomagnetite, ilmenite and augite coexist.

Eruptive unit	Temperature (°C) from Fe-Ti oxides	Temperature (°C) from cpx-ilm
[a]Ignimbrite 0(i), Tenerife	940	980
[a]Ignimbrite 0(ii), Tenerife	915	923
Boca de Tauce welded air-fall tuff, Tenerife	835	810
Tajao ignimbrite, Tenerife	915	907
Adeje red Tenerife	865	833

[a]Mixed-magma eruption: temperatures are given for two of the magmas represented in the pumice deposit (see Chap. III).

In view of the available evidence, particularly that given by Hildreth (1979), it is concluded that the recalculation procedure of Carmichael (1967a), when used in conjunction with the curves of Buddington and Lindsley (1964), offers the most accurage and straightforward currently available means of estimating T-f_{O_2} conditions from equilibrium mineral pairs of impure Fe-Ti oxides.

It remains to estimate the magnitude of the errors associated with applying this method to the present study. Errors inherent in analysis and from slight variations in mineral compositions (Appendix B) do not cause inaccuracies worse than $\pm 10^{o}C$ and ± 0.25 log units f_{O_2}. Buddington and Lindsley (1964) suggested calibration errors of $\pm 30^{o}C$ and ± 1 log unit f_{O_2}. However, there is evidence that the accuracy may be better than this. Helz (1973) analysed Fe-Ti oxide pairs from experimental charges and found results within $10^{o}C$ and 0.2 log units f_{O_2} of actual run conditions. Hildreth (1979) gives further evidence of accuracy superior to that suggested by Buddington and Lindsley (1964). The effect of minor elements is estimated at $\pm 5^{o}C$ and ± 0.15 log units f_{O_2} by Hildreth for his Bishop Tuff samples, none of which appear to have in excess of 5% by weight minor oxides. Carmichael (1967a) does not indicate the errors involved in his determinations from phases containing up to 8% by weight minor oxides. Lipman (1971) appears to have deduced values of T and f_{O_2} from phases as rich as 10% in MnO. The agreement with clinopyroxene-ilmenite geothermometry deteriorates where the oxides have $>8\%$ minor components (Table 4.1), although this could be due to the increasing unsuitability of pyroxene compositions (see below). Certainly Fe-Ti oxides from alkali basalts, typically with 15% $MgO+Al_2O_3$ in the case of the spinel, do not give acceptable results (ca. $950^{o}C$ for the phenocryst assemblage). Hildreth considers an overall accuracy of $\pm 10^{o}C$

and $\pm$0.25 log units fo_2 to be appropriate for his samples with their low minor element contents. It is suggested that errors of $\pm 30^{o}C$ and ± 1 log units f_{O_2} are reasonable for the Tenerife samples.

Fe-Ti oxide geothermometry and oxygen barometry is here applied to pumice samples (IV.3), welded tuff samples (Chapter VI) and plutonic xenoliths from Tenerife (Chapter V).

IV.2.ii Clinopyroxene-ilmenite geothermometer

Bishop (1980) has experimentally investigated the distribution of Fe^{2+} and Mg between clinopyroxene and ilmenite as a function of temperature, pressure and composition. Bishop found that both $FeTiO_3$-$MgTiO_3$ and $CaMgSi_2O_6$-$CaFeSi_2O_6$ solid solutions are non-ideal, and incorporated corrections for non-ideality into his geothermometer equation. The clinopyroxene-ilmenite geothermometer is

$$T(K) = \frac{748 + 2745\ (Mg/(Mg+Fe^{2+}))_{cpx} + 817(2(Fe^{2+}/(Fe^{2+}+Mg))_{ilm}-1)}{\ln K_D}$$

For high pressures, a correction of $+0.0106P/\ln K_D$ is made; this is typically a few degrees per kilobar.

There are a number of limitations to the use of this thermometer. The pyroxene compositions used by Bishop (1980) were slightly sub-calcic with a moderate ($\sim$2%) TiO_2 content. The presence of other pyroxene components (e.g. acmite, Tschermak's molecules) may cause deviations from the determined activity-composition relations, although their effect is negligible at small concentrations. With the exception of Na-rich and Ti, Al-rich

varities, pyroxenes studied here are closely similar to those of Bishop, particularly the "intermediate" pyroxenes found in some pumice-fall deposits. The most serious problem of pyroxene composition lies in determining the Fe^{3+} content from microprobe analyses. Following the scheme employed for all pyroxenes (except aegirines) in this thesis, Na is assigned to acmite rather than jadeite, and thus Fe^{3+}=Na on an atomic basis.

Ilmenites used by Bishop (1980) were poor in Fe_2O_3 ($\leqslant 5.5\%$ $Fe_2O_3/(Fe_2O_3+FeTiO_3)$). Bishop states that his results were not significantly altered by this hematite content, but expresses reservations about applying the thermometer to ilmenites having 25-30% hematite. Tenerife ilmenites to which the thermomemter has been applied contain up to 15% hematite, and thus some uncertainty attaches to the deduced temperatures. Bishop considers that errors of $\pm 10^{o}C$ arise from experimental uncertainty, and another $\pm 10^{o}C$ from analyses of the mineral pairs in his calibration. Adding another $\pm 10^{o}C$ for mineral analysis, the deduced temperatures are correct to $\pm 30^{o}C$ if the possible error due to hematite is neglected. The exact agreement with Fe-Ti oxide temperatures from the same samples within the error range of both thermometers, independently calibrated, is evidence for their accuracy when applied to the phases studied here (Table 4.1).

IV.2.iii Olivine-clinopyroxene geothermometer

Powell and Powell (1974) proposed a geothermometer based on Fe^{2+}-Mg exchange between olivine and clinopyroxene, calibrated by temperatures derived from coexisting Fe-Ti oxides in mutual equilibrium with olivine-clinopyroxene pairs in the groundmasses of eight lavas. This thermometer has been criticised by Wood (1976)

on several grounds; in particular the assumed free energy of hedenbergite, the paucity of calibration data, and unreasonably large deduced mixing parameters for calcium-rich pyroxenes. To this it may be added that the use of an existing geothermometer to calibrate another via natural rock samples is an unsatisfactory approach (Wood and Frazer, 1976). However, Powell (1978) claims that the thermometer may be usefully applied to olivine and clinopyroxene compositions within the calibration range, and finds geologically reasonable temperatures for cumulus crystallisation of some augite and nepheline syenites whose olivine-clinopyroxene pairs fulfil this condition. All but two of the nineteen results listed by Powell (1978) fall into the range 930-980°C (two samples yielding 900 and 905°C respectively). Wood (1976) has shown that the form of the geothermometer expression presented by Powell and Powell (1974) is such that almost all 1 bar temperature estimates are constrained to fall within the range 915-1060°C, irrespective of compositions, and thus the thermometer inevitably gives apparently reasonable results for samples whose actual crystallisation temperatures lie within this range. The agreement with experimental data cited by Powell (1978) is therefore no evidence for the general validity of the thermometer. Seen in this light the exact agreement between clinopyroxene-olivine and Fe-Ti oxides temperatures for a pantellerite sample (Chapter VI) is also unremarkable. The author therefore endorses the conclusion of Wood (1976) that this thermometer "is not applicable in its present form". However, some of the results presented by Powell and Powell (1974, Table 6) indicate that the thermometer may have some qualitative value, and is thus capable of indicating a low or high crystallisation temperature for a particular sample. The thermometer has therefore been applied to olivine-clinopyroxene pairs in an augite syenite xenolith (Chapter V).

IV.2.iv Plagioclase-alkali feldspar geothermometer

Stormer (1975) developed a geothermometer based on the distribution of the albite molecule between sanidine and plagioclase. Subsequently Powell and Powell (1977a) modified the Stormer formulation to take into account the effect of small amounts of Ca in the sanidine; the two expressions are exactly equivalent for Ca-free alkali feldspar. The geothermometer is applied to perthites in nepheline syenite xenoliths in Chapter V.

IV.2.v Nepheline-alkali feldspar geothermometers

Perchuk and Ryabchikov (1968) and Powell and Powell (1977b) have proposed geotherometers based on the thermodynamics of an Na-K exchange reaction between nepheline and alkali feldspar; the latter takes into account the effect of excess silica in the nepheline. Both geothermometers are extremely composition-sensitive over the composition range of alkali feldspar found in Tenerife volcanic and plutonic rocks, and therefore cannot be usefully applied.

IV.2.vi Nepheline geothermometer

A semi-quantitative estimate of nepheline crystallisation temperature may be obtained from Hamilton's (1961) experimental study of the temperature dependence of the excess silica content of nepheline-kalsilite solid solutions. Considerable interpolation of Hamilton's curves between 775°C and 1068°C is required. This method is not suitable for slowly-cooled nephelines (Hamilton, 1961; see also discussion of nepheline composition in Chapter V).

IV.3 THE PRE-ERUPTIVE VOLATILE COMPONENT OF THE PUMICE-FORMING MAGMAS

The magmatic volatile component may be defined as those species which are normally gaseous at magmatic temperatures and atmospheric pressure, and are thus largely released from the magma upon eruption. The volatile component is the essence of explosive volcanism, yet little is known of the pre-eruptive abundances of volatile constituents in pumice-forming magmas. The fugitive nature of these constituents necessitates that pre-eruptive abundances be determined from information preserved in the final pumice deposit, assuming that data from the actual eruption are not available. The most satisfactory method is to directly analyse samples of pre-eruptive magma preserved as glass inclusions in tephra phenocrysts (Sommer, 1977). A more generally applicable approach, using mineral chemistry data obtained during the course of routine petrological investigation, is to employ thermodynamic methods to deduce the fugacities of volatile species in equilibrium with the phenocryst assemblage before eruption. This approach has been demonstrated by Rutherford and Heming (1978), who determined species in the system H-O-S in dacitic and rhyolitic pyroclastics from New Zealand. However, very few similar studies appear to have been made. This section is concerned with the application of these methods to some of the Tenerife pumice deposits, and discusses the significance of the results obtained.

IV.3.i Estimation of temperature and oxygen fugacity

Temperatures and oxygen fugacities have been obtained from the compositions of equilibrium mineral pairs of Fe-Ti oxides, discussed in detail in IV.2.i. Temperatures are corroborated by another

geothermometer (Table 4.1). T-f_{O_2} values are shown in Figure 4.4; the very low degree of scatter about a straight line is remarkable, and probably reflects the operation of mineral and/or liquid component oxygen buffers. Several workers (Carmichael, 1967a) Ewart et al., 1971; Lipman, 1971; Heming and Carmichael, 1973; Rutherford and Heming, 1978) have found that natural rhyolitic and dacitic liquids tend to plot on one of four curves in T-f_{O_2} space, each curve corresponding to the buffering of O_2 by the ferromagnesian minerals found in association with the Fe-Ti oxides (Figure 4.4). Clearly the opx and opx-amph buffers cannot apply to alkaline magmas. All of the studied samples contain biotite and/or amphibole, yet lie well below the bi-amph curve. Thus it seems that either the mineral buffers found in acidic magmas do not operate in phonolitic and trachytic liquids, or else their effects are substantially modified by overall magma composition. Plausible reactions may be written for the mineral assemblages observed, but none are applicable over the entire range. As the assemblages do not permit an estimation of f_{H_2O} which is independent of the f_{O_2} determination, the possibility that the dissociation of water controls f_{O_2} cannot be tested. It must be concluded that magma type exerts a considerable influence on f_{O_2}, but that the effect by which this operates remains open to question.

IV.3.ii Estimation of water fugacity and concentration

The compositions of co-existing biotite, sanidine and magnetite may be used to estimate the fugacity of water, by means of the reaction

$$KFe_3AlSi_3O_{10}(OH)_2 + \tfrac{1}{2}O_2 \rightleftharpoons KAlSi_3O_8 + Fe_3O_4 + H_2O$$

biotite sanidine magnetite

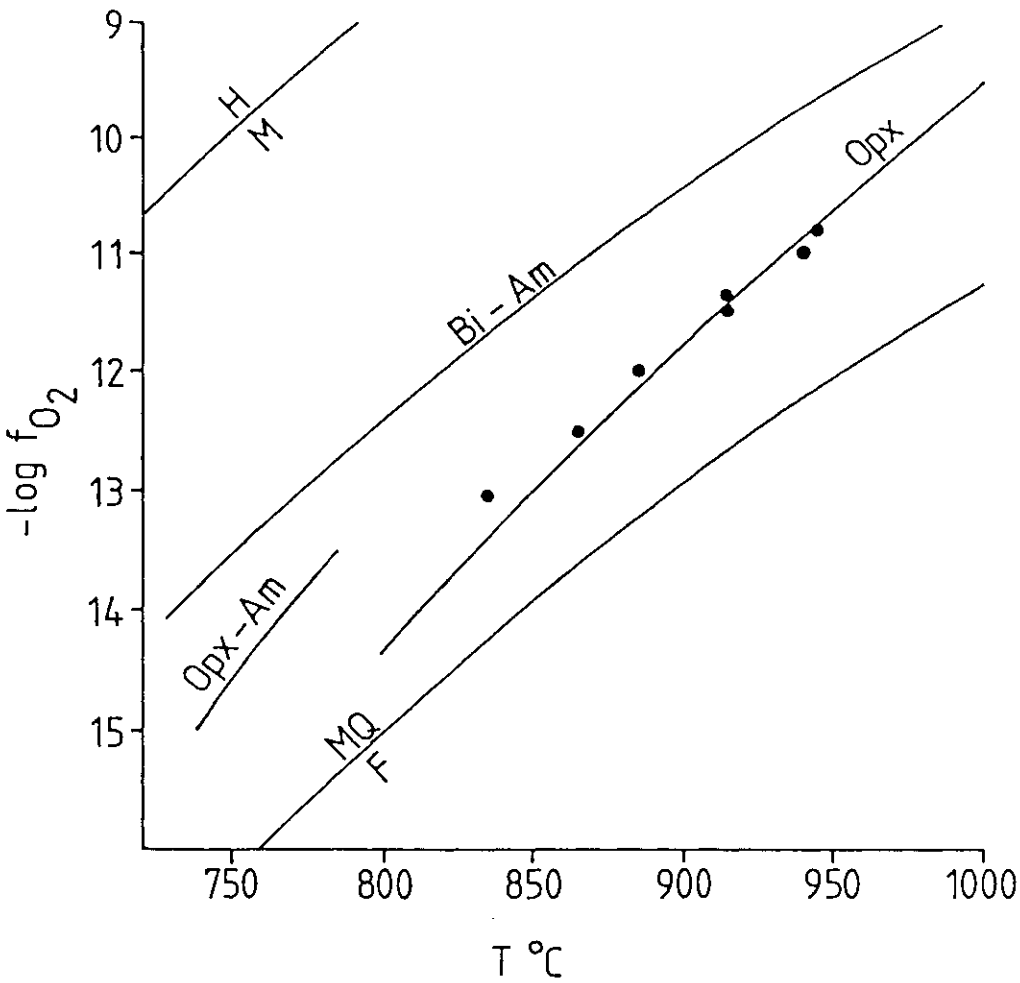

Fig. 4.4 T, f_{O_2} data for Tenerife pumices. HM = hematite - magnetite buffer; MQF = magnetite - quartz - fayalite buffer. Other curves explained in the text.

for which free-energy data are given by Wones and Eugster (1965), who adopted a regular solution model for biotite in the system annite-phlogopite-oxyannite. However, Mueller (1972) and Wones (1972) have shown that mixing on the biotite octahedral site is approximately ideal, where the Fe^{3+} content of this site is small. Charge balance calculations show that the Fe^{3+} content of the biotites is negligible, and therefore the activity of annite in the biotites is equal to $(X_{Fe}^{oct})^3$, where X_{Fe}^{oct} is the octahedral site occupancy of Fe^{2+} in biotite. Appreciable substitution of Na for K and of F for OH may also occur, and the activity expression should therefore be modified by factors of K/(K+Na) and $(OH/(OH+F))^2$, assuming ideal mixing on both of these sites. However, the OH/(OH+F) ratio is very susceptible to post-eruptive change due to hydration, and this change may not be petrographically apparent. Therefore, it is assumed that the biotites are fluorine-free, and thus the calculated values of f_{H_2O} are maxima. The expression used for the activity of the annite component is therefore

$$a_{ann}^{bi} = K/(K+Na).(X_{Fe}^{oct})^3.$$

The activity of $KAlSi_3O_8$ in sanidine is calculated from the assymetric regular solution treatment of Thompson and Waldbaum (1969), who give the following expressions for the interaction parameters:

$$W_G^{ab} = 6326.7 + 0.0925P - 4.6321T$$

$$W_G^{or} = 7671.8 + 0.1121P - 3.8565T$$

Inserting these into the activity coefficient expression (III.1.i) gives

$$RT\ln\gamma_{or} = (5055.3-5.4077T)X_{ab}^2 + (2729.4+1.5512T)X_{ab}^3$$

for a total pressure of 1 Kb (it may be seen that the effect of pressure on the values of W_G^{ab} and W_G^{or} is in any case small). Magnetite solid solutions are assumed to be ideal, following Nicholls et al. (1971) and Carmichael et al. (1977), and thus

$$a_{mag}^{Timag} = X_{mag}^{Timag}$$

Results are given in Table 4.2 for three deposits which bear the appropriate mineral assemblage.

Burnham et al. (1969a) have determined the fugacity coefficient of water over a wide range of temperatures and pressures, and thus P_{H_2O} can be found for a given f_{H_2O} and temperature. If P_{Total} is known, the mole fraction of water in the magma (X_{H_2O}) can be calculated from the relationship given by Spera in Ewart et al. (1975). As P_{Total} is not known, it is assumed that the magmas were water-saturated and X_{H_2O} is therefore equal to the solubility of water in the magma. If the overall magma composition is known, X_{H_2O} is readily converted into a primary wt % magmatic water content. The water contents so found (Table 4.2) are maximum values, because of the assumptions of saturation and of fluorine-free biotite. Although the values found seem high, a similar treatment of samples from Sao Miguel (Wolff and Storey, 1983) yields comparable values that are in good agreement with volatile contents deduced by the methods of Wilson (1976, 1980) from field data on tephra dispersal (Booth et al., 1978).

IV.3.iii Estimation of hydrogen fugacity

The fugacity of hydrogen may also be estimated from biotite composition:

$$KFe_3AlSi_3O_{10}(OH)_2 \rightleftharpoons KAlSi_3O_8 + Fe_3O_4 + H_2$$

biotite sanidine magnetite

This reaction was used by Rutherford and Heming (1978) to estimate f_{H_2}. However, the expression for f_{H_1} which they used assumes a regular solution model for biotite, which is inconsistent with the assumption of biotite ideality in the expression used to find f_{H_2O} from the same mineral data. Unreasonably high f_{H_2} values (several hundred bars) were derived by using the thermodynamic data of Wones and Eugster (1965) and assuming biotite ideality. An alternative means of estimating f_{H_2} is by using the water formation reaction

$$H_2 + \tfrac{1}{2}O_2 \rightleftharpoons H_2O$$

Thermodynamic data for this reaction are given in the JANAF thermochemical tables (Stull and Prophet, 1971), in the form of tabulated values of logK at 100°C intervals. To obtain the temperature dependence of the equilibrium constant, logK values were regressed against 1/T for the temperature range 300-2000K, giving

$$\log K = \frac{12811}{T} - 2.79 \qquad r = 1.000$$

where r is the correlation coefficient of the regression. f_{H_1} is then given by

$$\log f_{H_2} = \log f_{H_2O} - \tfrac{1}{2}\log f_{O_2} - \log K$$

Values for f_{H_1} are shown in Figure 4.6.

IV.3.iv Estimation of sulphur fugacity

The composition of pyrrhotite, found in a number of samples as inclusions in oxide and silicate phases (Chapter III) may be used to define the fugacity of sulphur (f_{S_2}) in the environment from which it crystallised (Toulmin and Barton, 1964). Pyrrhotite composition may be expressed as a solid solution FeS-S_2; the mole fraction of FeS in this solution (N_{FeS}) varies between 0.899 and 1.00

Table 4.2. Estimated magmatic water contents

Pumice Deposit	a^{bi}_{ann}	a^{san}_{or}	log fH_2O	P_{H_2O}	X_{H_2O}	wt% H_2O[a]	Total water[b]
Pumice fall E Tenerife	0.0129	0.373	3.39	2800	0.22	7.1	0.78
Adeje red ignim-brite, Tenerife	0.0117	0.391	3.20	1900	0.18	5.6	0.006
Boca de Tauce welded air-fall tuff, Tenerife	0.0152	0.480	3.11	1500	0.14	4.2	-

[a] Calculated assuming water saturation of magma.

[b] Total volume of water (calculated as liquid in Km^3) released from the magma during the eruption. Ad ignimbrite estimate is a minimum, based on present extent of deposit.

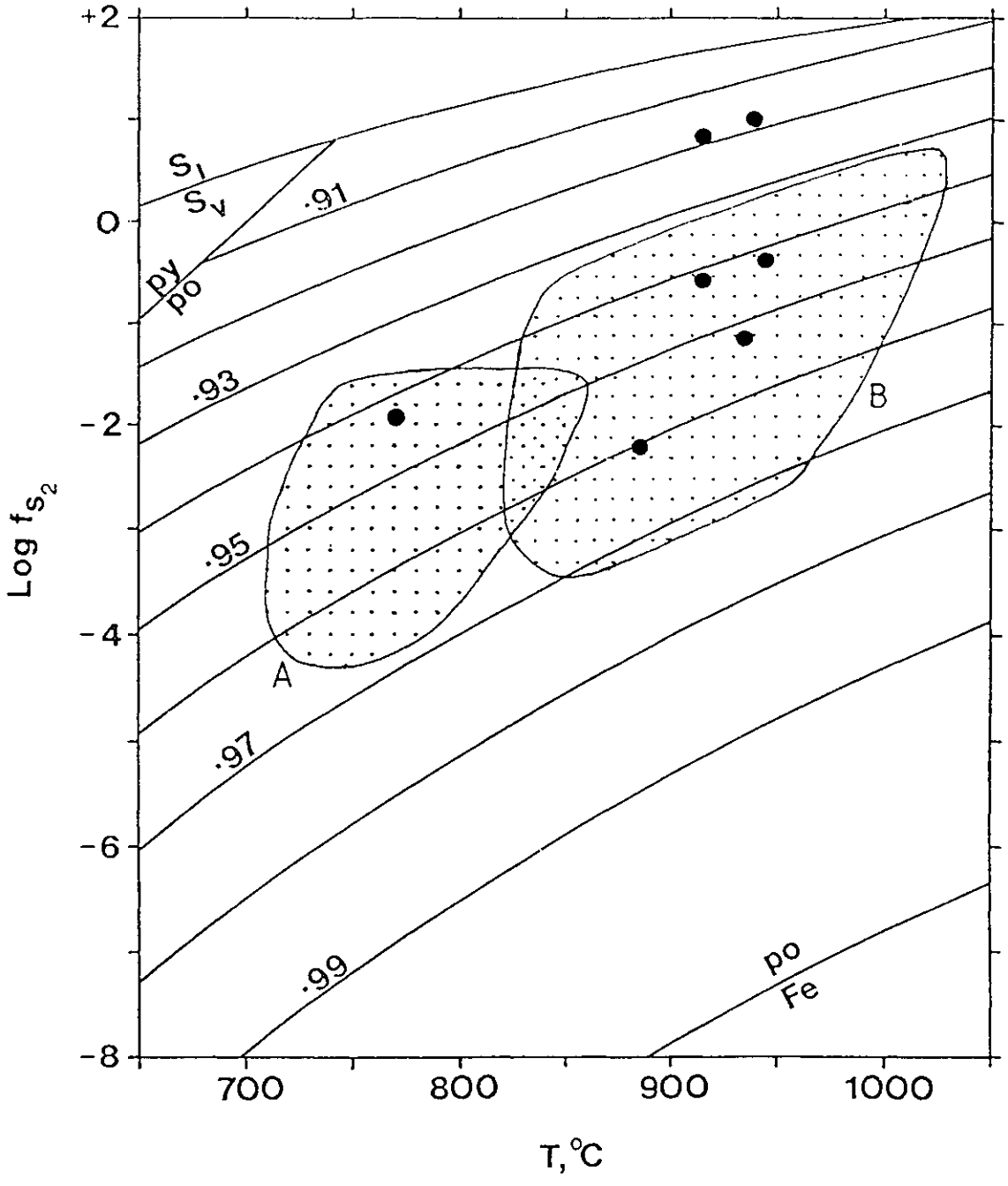

Fig. 4.5 f_{S_2} data for pumices. Stippled fields: A = New Zealand ignimbrites (Rutherford and Heming, 1978); B = pumices from Rabaul, New Guinea (Heming and Carmichael, 1973).

Sulphur fugacity is directly related to N_{FeS} by

$$\log f_{S_2} = (70.03-85.83N_{FeS})(1000/T-1)+39.30(1-0.9981N_{FeS})^{0.5}-11.91$$

(Toulmin and Barton, 1964). This relationship is shown graphically in Figure 4.5. The analysed pyrrhotites contain small quantities of other divalent elements, most commonly Mn (Appendix B). Following Heming and Carmichael (1973), these have been included in the FeS end-member. Pyrrhotite grains ceased to be in equilibrium with the magma upon inclusion in other phases, and therefore their composition records sulphur fugacity at, presumably, slightly higher temperatures than those indicated by present Fe-Ti compositions. Fe-Ti oxide temperatures are used here in the absence of data on the enclosure temperatures of the pyrrhotite grains. Values of f_{S_2} show a similar degree of variation (Figure 4.5) and are comparable to, those found for dacitic and rhyolitic magmas (Heming and Carmichael, 1973; Rutherford and Heming, 1978).

IV.3.v Estimation of f_{H_2S}, f_{SO_2}, f_{SO_3}

With a knowledge of f_{S_2}, f_{H_2} and f_{O_2}, the fugacities of three sulphur compounds may be estimated from the formation reactions:

$$H_2S \rightleftharpoons H_2 + \tfrac{1}{2}S_2$$

$$SO_2 \rightleftharpoons \tfrac{1}{2}S_2 + O_2$$

$$SO_3 \rightleftharpoons \tfrac{1}{2}S_2 + 1\tfrac{1}{2}O_2$$

LogK for each reaction was obtained from the JANAF thermochemical tables in the same manner as for the water formation reaction (IV.3.iii). Therefore we have:

For H_2S:

$$H_2 + \tfrac{1}{2}S_2 \rightleftharpoons H_2S$$

$$\therefore \log f_{H_2S} = \log K + \log fH_2 + \tfrac{1}{2}\log fS_2$$

$$\text{where } \log K = \frac{1286}{T} - 0.67 \qquad r = 0.960$$

For SO_2:

$$\tfrac{1}{2}S_2 + O_2 \rightleftharpoons SO_2$$

$$\therefore \log fSO_2 = \log K + \tfrac{1}{2}\log fS_2 + \log fO_2$$

$$\text{where } \log K = \frac{17453}{T} - 2.74 \qquad r = 0.999$$

For SO_3:

$$\tfrac{1}{2}S_2 + \tfrac{3}{2}O_2 \rightleftharpoons SO_3$$

$$\therefore \log fSO_3 = \log K + \tfrac{1}{2}\log fS_2 + \tfrac{3}{2}\log fO_2$$

$$\text{where } \log K = \frac{21711}{T} - 6.84 \qquad r = 0.999$$

Results are shown in Figure 4.6. For SO_2 and SO_3, results are closely similar to those from dacitic and rhyolitic pyroclastics (Heming and Carmichael, 1973; Rutherford and Heming, 1978).

IV.3.vi Discussion

Accuracy

Errors in the f_{O_2} determination have been discussed (III.1.ii). The distribution of T-f_{O_2} values, however, suggest that the precision associated with this set of results is rather better than $\pm 30^{\circ}C$ and $\pm$ 1 log unit f_{O_2}. The error introduced into the f_{H_2O} determination by the f_{O_2} value is thus less than ± 0.5 log units. The geologically reasonable values of wt % H_2O derived, although these are maxima, suggests that the overall error in the f_{H_2O} determination is much less than one order of magnitude. The calculation of N_{FeS} for

pyrrhotites is critically dependent on the iron analysis; replicate analyses of pyrrhotites indicate an appreciable error here (Appendix B), approaching one order of magnitude for f_{S_2} when combined with the error in the temperature determinations. Errors in f_{H_2S}, f_{SO_2} and f_{SO_3} are therefore probably worse than one order of magnitude, since these values are derived from f_{O_2}, f_{S_2} and f_{H_2O}.

General limitations

There are four main limitations to the accuracy of the data and the general applicability of this approach:

1. Errors arising from errors in (a) mineral analyses and (b) thermodynamic data. (b) does not apply if results obtained by using the same calculation procedures are being compared, but errors from both sources are compounded when gas reactions are used (e.g. to find fSO_2, fSO_3) where the input data are fugacities already estimated from mineral data. In these cases the minimum error is approximately ± 1 log unit fugacity.

2. Errors due to assumptions made. These can usually be assessed with a degree of confidence, e.g. the assumption of fluorine-free biotite results in the calculation of maximum f_{H_2O} values.

3. Pumice deposits often have very low phenocryst contents, and, if aggregate mineral grains are rare or absent, it may be difficult to establish equilibrium between phenocryst phases.

4. The required mineral phases may not be present. It is noteworthy that of the erupted magmas dealt with here, only one (E fall phonolite) bears the assemblage titomagnetite-ilmenite-

pyrrhotite-biotite-sanidine necessary for the determination of all species in the system H-O-S. Many lack ilmenite and thus no determinations at all can be made, except f_{S_2} if pyrrhotite coexists with another geothermometer assemblage. Alternatively, the Fe-Ti oxides may be too rich in minor elements to be of use in geothermometry/oxygen barometry. More seriously, none of the samples studied here - in common with the vast majority of erupted magmas - bear a mineral assemblage which permits the determination of the important volatile species CO_2, CO, HF and HCl.

Despite these problems, the approach is a powerful one, as it allows the rapid calculation of the composition of part of the volatile component of a range of salic magma types.

Comparison with other magma types

The calculated fugacities for each species bear little resemblance to the composition of Kilauea gas (Figure 4.6). SO_2 and SO_3 are in general agreement, but this may be fortuitous. The data bear a much closer similarity to that obtained by Heming and Carmichael (1973) and Rutherford and Heming (1978) for Quaternary pumice-forming magmas from Rabaul, New Guinea and North Island, New Zealand respectively (Figure 4.7). The New Zealand results are typically lower for each species than those for the Tenerife and Rabaul pumices; this is principally a reflection of their lower equilibration temperatures (729-810°C). f_{S_2} is on average slightly higher, at a given temperature, in the Tenerife magmas.

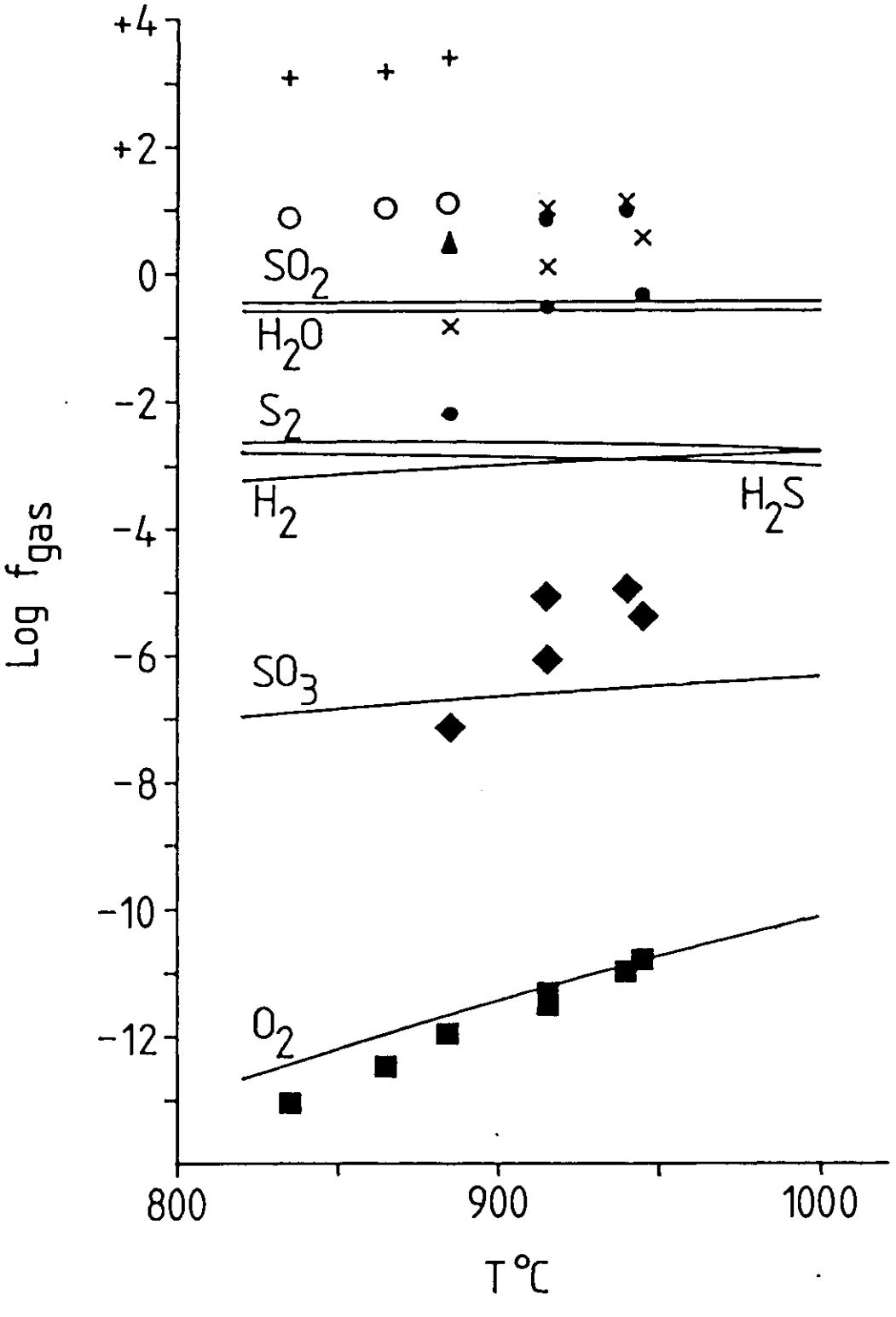

Fig. 4.6 Fugacity data for all determined volatile components in Tenerife pyroclastics. Vertical crosses: H_2O; open circles: H_2; filled triangles: H_2S; diagonal crosses: SO_2, dots: S_2; filled diamonds: SO_3; filled squares: O_2. Labelled curves are estimates for Kilauea gas (Nordlie, 1971).

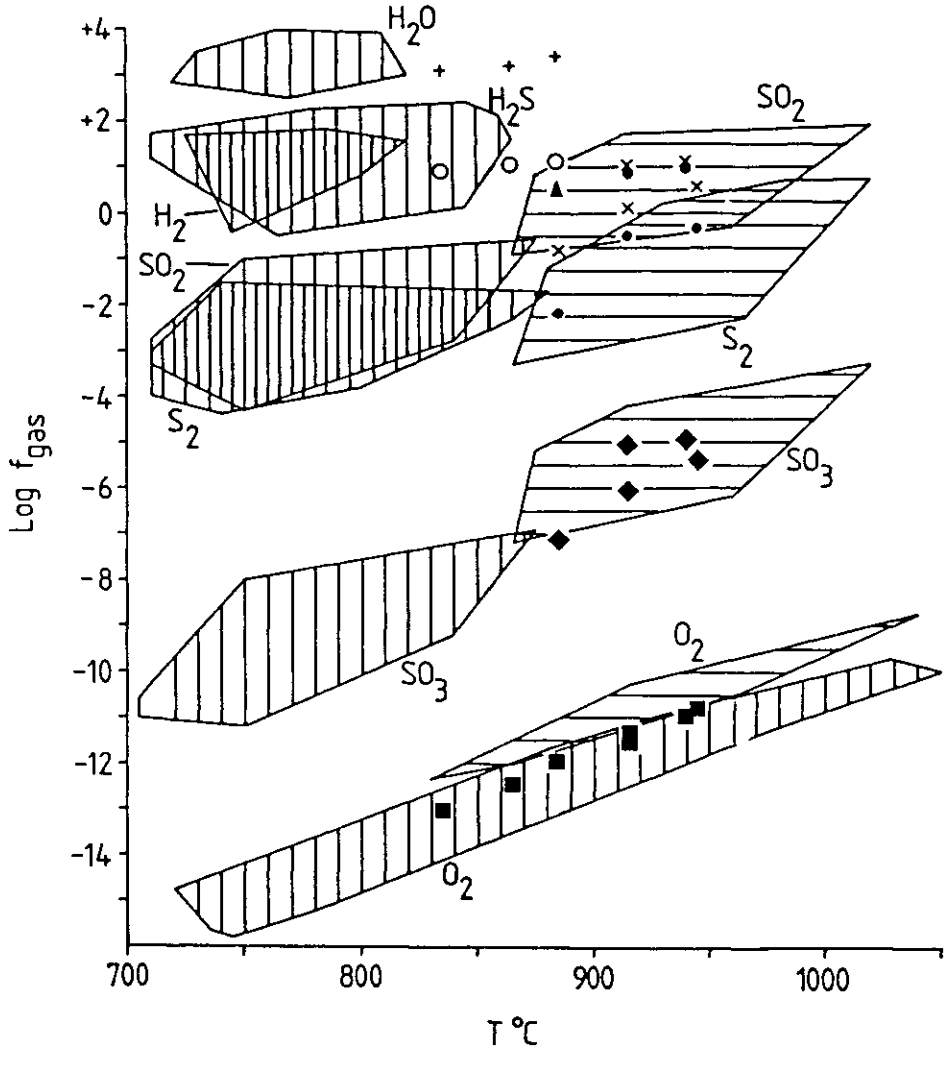

Fig. 4.7 Symbols as Fig. 4.6, with the addition of: vertical rule, fugacity data for each species in the system H-O-S found in New Zealand ignimbrite magmas (Rutherford and Heming, 1978; horizontal rule, range of f_{S_2}, f_{O_2}, f_{SO_2}, f_{SO_3} values in New Guinea pumice magmas (Heming and Carmichael, 1973).

Table 4.3. Molar abundances, as a percentage of total abundance of the five major species in the system H-O-S, for two cases[a]

	Pumice fall deposit E, Tenerife	Average New Zealand ignimbrite[b]
H_2O	99.4%	99%
H_2	0.5%	0.5%
H_2S	0.1%	0.5%
SO_2	(0.005%)	(0.0002%)
S_2	(0.0002%)	(0.0001%)

[a] Calculated using fugacity coefficients tabulated by Ryzhenko & Volkov (1971) and assuming ideal mixing

[b] From data of Rutherford & Heming (1978).

Fugacities may be converted to abundances if it is assumed that volatile species mix ideally with each other and with magma, and if fugacity coefficients are known for each volatile species. When this is done for the five principal species in H-O-S, the similarity between the rhyolite and phonolite data becomes even more apparent (Table 4.3). The general similarity in relative abundances is presumably a consequence of the relative stabilities of the various gas species under magmatic conditions; for example SO_2 will always predominate over SO_3 at the oxygen fugacities usually encountered in magmas. Thus it may be concluded that the magmatic volatile component has a similar composition (at least in H-O-S) in a wide variety of pumice-forming salic melts. This is borne out by the abundances of H-O-S species in pumice-forming trachyte magmas from the Azores, which fall into the same range for each species as do the Tenerife, New Zealand and Rabaul pumices (Wolff and Storey, 1983).

Rough estimation of f_{H_2O} for non-biotite bearing samples

The five principal species in the system H-O-S are related by the equilibrium

$$S_2 + 2H_2O \rightleftharpoons H_2S + SO_2 + H_2$$

Taking data as before from the JANAF tables (Stull and Prophet, 1971) we find

$$\log K = \frac{-6883}{T} + 2.17.$$

If the variation with temperature of H_2S, SO_2 and H_2 is established by regression for a suite of samples, then f_{H_2O} can be found as a function of f_{S_2} and temperature. Although this procedure is at best semi-quantitative owing to the substantial errors involved (particularly in the values of f_{H_2S}, f_{SO_2} and f_{H_2} which form input

data for the calculation), the results (Figure 4.8) receive some support from other evidence: Ignimbrite O (ii) should be more water-rich than O (i), since it is derived from a cooler, more fractionated part of the same magma chamber (Chapter III).

Magmatic water contents

Water is the most abundant volatile constituent in the great majority of magmas, and a knowledge of magmatic water content is essential to the estimation of such parameters as the viscosity and density of magma before eruption. Rutherford and Heming (1978) considered the water contents of New Zealand ignimbrite magmas to be unusually high, and ascribed this to an origin by anatexis of water-rich basement greywackes (for which there is a considerable body of evidence; see Carmichael et al., 1974, and references cited therein). The mean water content of the values tabulated by Rutherford and Heming corresponds to approximately 6.5% by weight, closely similar to the values obtained here. Sommer (1977) found volatile contents of up to 7% (average 5.4%) for the Bandelier Tuff, New Mexico, rhyolite magma; 92% of this consisted of H_2O, the remainder being mostly CO and CO_2. Thus, when compared to other pumice-forming magmas, the New Zealand examples cannot be considered particularly water-rich.

Wolff and Storey (1983) calculated primary wt % magmatic water contents for Fogo pumice fall deposits A, B and C using the methods described here. Detailed field data on tephra dispersal exists for these deposits (Booth et al., 1978) and these were used to calculate muzzle velocities for the three eruptions using the method of Wilson (1976) described in Chapter VI. Eruption muzzle

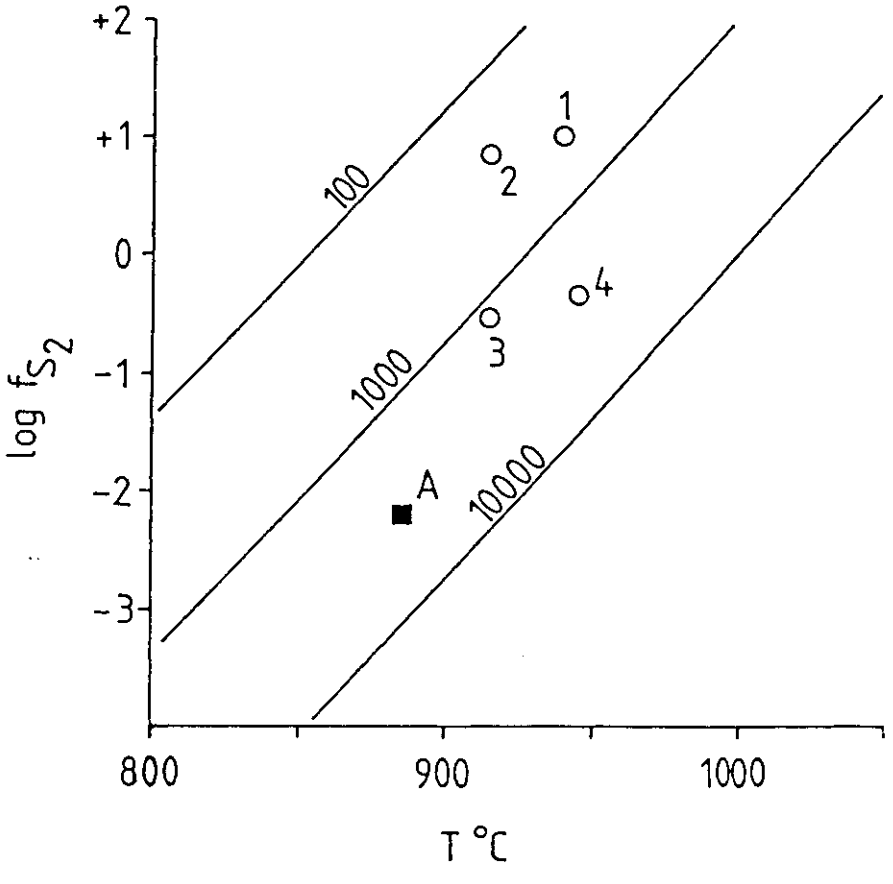

Fig. 4.8 Relationship between f_{S_2} and temperature for three values of f_{H_2O} in bars (see text). A = Tenerife deposit E, for which an f_{H_2O} of 2.5 kb is given by biotite composition. 1 = ignimbrite O (i), 2 = Tajao ignimbrite; 3 = Ignimbrite O (ii); 4 = pumice fall J.

velocity is directly dependent on magmatic volatile content (Wilson, 1980), assumed to be entirely water (it is further assumed that the gas released during plinian eruptions is derived entirely from the magma). Magmatic water contents have thus been estimated from the muzzle velocity - gas content data of Wilson (1980). Wolff and Storey find good agreement between results from the two methods. It may be expected that the 'petrological' method would yield higher results than the 'volcanological' approach, since the former are maximum values, and no account is taken of energy losses occurring during magma disruption in the latter estimates (Wilson, 1980).

Widely dispersed plinian pumice fall deposits, similar to those studied here, are a common manifestation of salic volcanism, yet few estimates of their magmatic volatile contents exist. The data discussed here suggest that natural salic liquids commonly have water contents in excess of 5% by weight.

Some volcanological implications

1. Physical models of explosive eruptive processes often assume that the magmatic volatile component consists entirely of water. This appears to be a valid approximation for most salic magma types (for volatiles in the system H-O-S).

2. The density of released magmatic gas affects the behaviour of a plinian eruption column. Dense columns tend to collapse to form ignimbrites (Sparks and Wilson, 1976), whereas lighter columns more readily undergo convective uprise to form an eruption cloud some tends of kilometres high, fall-out from which produces a plinian

pumice fall deposit (see section I.2). The data discussed here indicate that variations in the density of released gas, due to compositional variations in the system H-O-S, are unlikely to be great enough to significantly affect eruption column dynamics.

3. Appreciable quantities of combustible gases (H_2, S_2, H_2S) are present in salic magmas and will be released upon explosive eruption. The oxidation of these in the eruption cloud will contribute to the thermal energy budget of the eruption. Simple calculations using maximum mole percent abundances of each of H_2, S_2 and H_2S and the appropriate heats of combustion for each gas indicate that this contribution is unlikely to exceed 5% of the total energy released during eruption. This has a very small effect on overall eruption dynamics; for example, the height of a 50 km high plinian eruption column is increased by approximately 0.5 km by this proportion of added energy (Wilson et al., 1978).

4. Large quantities of water are released during pumice eruptions (Table 4). If it is assumed that a large proportion of released water fallsas rain during or soon after eruption, then the formation of mudflows by remobilisation of the newly-deposited tephra is a virtually inevitable consequence of any such eruption. Mudflows are very common associates of all types of pumice deposit.

CHAPTER V

SYENITE XENOLITHS FROM THE PYROCLASTIC SERIES

V.1 INTRODUCTION

Xenoliths of plutonic origin are a locally common feature of the Tenerife volcanics. They occur at all stratigraphic levels, from the Ancient Series to Viejo (Fuster et al., 1968). The lithological range is equally broad. Dunites, pyroxenites, monomineralic kaersutite rocks, pyroxene-amphibole cumulates, alkali gabbros and rocks with sphene and apatite as significant cumulus phases are among the ultramafic and mafic types represented. Borley et al. (1971) have described such xenoliths included in the Ancient Series basalts, and conclude that the majority are cumulates precipitated from alkali basaltic magmas; however they note a cataclastic texture in a dunite from Teno. Dunite fragments, now completely iddingsitised, are abundant in several Teno flows, and sheared dunites occur in Recent scoria on the adjacent island of La Palma (author's observations); it is tempting to regard these as evidence of direct ascent of the host basalt from the upper mantle, whereas the other mafic xenolith types probably formed in magma chambers located at the base of the crust, or within the oceanic crust or overlying volcanic edifice (Borley et al., 1971).

More evolved and extreme types range through augite syenites to aegirine-bearing nepheline syenites, and Le Bas (pers. comm.) reports a carbonatite fragment from a Las Canadas lava. Only nepheline syenites are found within the pumice series, and a description and discussion of their mineralogy and petrology forms the principal subject of this chapter. A brief account of some alkali gabbroic and intermediate

blocks from a surtseyan tuff-ring at Medano, which pre-dates the pumice series, is also given (V.3).

V.1.i General aspects of the nepheline syenite xenoliths

There is a very large body of literature on the mineralogy and petrology of nepheline syenites (see Sørensen, 1974, for a bibliography up to that date; more important recent studies include Powell, 1978; Larsen, 1976, 1981; Stephenson and Upton, 1982; Nielsen, 1979; Jones and Peckett, 1980; Mitchell and Platt, 1982) and some justification for undertaking yet another study in similar vein may be required. The Tenerife syenites are of particular interest for a number of reasons. The bulk of existing data deals with syenite bodies exposed in continental, often Precambrian shield, areas whereas the Tenerife rocks are from a youthful oceanic setting. They are present at an active stage of the volcanism, rather than as exposed plutons with little surviving evidence for associated surface volcanism. Their occurrence as xenoliths allows the possibility of quenching and preservation of textures which may be obscured during cooling to the ambient regional geotherm; in one case a sample has been quenched just above the solidus and the last liquid preserved as a glass of extreme composition (V.2). Finally, some rare-metal minerals (e.g. lavenite, loparite) occur as interstitial phases.

The two principal sources of syenite xenoliths in the succession are both in the Fasnia Series; they are one of the intraplinian ignimbrites in J and the topmost ignimbrite/mudflow with associated gravels, probably equivalent to member O (Chapter I). Those from J are heavily altered and were not studied closely. Although altered blocks are likewise common in O, several fresh specimens were collected. A single 30 cm block of relatively fresh syenite (sample S4)

was also collected from the Adeje Red ignimbrite. Heavily altered fragments also occur in pumice fall G, but were not studied.

The nepheline syenites presumably represent bodies of phonolite magma which, for one reason or another, did not erupt but solidified at (probably shallow, see V.2) depth. The occurrence of an incompletely crystallised xenolith in the youngest member of the pumice series indicates approximate comtemporaneity of volcanic and plutonic processes, and, taken with the heavy post-magmatic alteration of syenite in older eruptive units, strongly suggests more than one episode, or at least a single long-lived episode, of syenite formation. Exact relations between syenite and pumice forming magmas are unknown. One possibility is that the syenite blocks are derived from a crystallised roof-zone of the phonolite magma chamber, although the restricted stratigraphic occurrence of the xenoliths does not support this suggestion.

V.i.ii Petrography of the nepheline syenites

The usual mineralogy of the fresh nepheline syenites is alkali feldspar + nepheline + sodalite + pyroxene (aegirine-augite to aegirine) + amphibole + ilmenite + loparite $\pm$ biotite $\pm$ lavenite $\pm$ sphene. Representative modal analyses are given in Table 5.1. Departures are found in samples S4, which lacks nepheline, and SX3, which contains a pale yellow glass. In the following account, the word "cumulus" is used to indicate those crystals which from textural evidence formed at the magmatic stage. No implication of crystal settling is intended.

Sample	S1/1	S1/2	S1/4	S3/2	S4	SX3
No. of counts	3068	2546	2831	2680	3479	2109
Feldspar	64.5%	61.0%	56.1%	51.4%	79.9%	57.7%
Nepheline	16.1%	23.4%	28.8%	34.1%	abs	19.1%
Sodalite	10.9%	7.6%	5.4%	9.4%	1.9%	8.6%
Pyroxene	7.6%	5.0%	6.5%	3.9%	8.4%	8.4%
Amphibole	0.5%	1.6%	2.2%	0.8%	3.0%	1.5%
Ilmenite	tr	0.4%	tr	tr	1.2%	0.8%
Lavenite	abs	tr.	0.4%	tr	abs	abs
Sphene	tr	0.6%	tr	tr	abs	tr
Other*	abs	abs	abs	abs	5.5%	3.8%

* glass in SX3, unidentified phase in S4.

Table 5.1. Modal analyses of selected nepheline syenite xenoliths, established by point counting. Results of fewer than 10 counts (< 0.5% of mode) are recorded as trace quantities. Loparite is always present in trace quantities; traces of biotite occur in S1/2, S1/4 and SX3, and of ramsayite in S1/1. Ramsayite and eudialyte/eucolite are also present in an uncounted sample S3/4, otherwise similar to those listed here.

Alkali feldspar is always dominant and is the principal cumulus phase, forming euhedral laths up to 5 mm long. Unmixing to give patch perthites is common, and where well developed the exsolved albite phase shows lamellar twinning (Figure 5.1). Albite also occurs as overgrowths on crystal margins (Figure 5.2) with or without perthite development in the same crystal. Sericitisation of varying intensity is common.

Nepheline always bears an interstitial relationship to feldspar, but the large size ($\leq$5 mm) of some grains, and a general lack of poikilitically-enclosed feldspars, suggest that it was probably a cumulus mineral which continued to grow from the interstitial liquid, consistent with its occasional occurrence as a phenocryst phase in the phonolite pumices (Chapter III) and lavas (Ridley, 1968). Typically, it is homogeneous and free from inclusions. The mineral is usually less altered than coexisting feldspar, where this is partly sericitised.

Sodalite is a common cumulus phase. In contrast to nepheline, it is often finely dusted with inclusions. Morphology varies from euhedral to highly irregular, and some crystals have clear overgrowths on dusty euhedral cores.

Feldspar, nepheline and sodalite also occur as small, usually anhedral interstitial grains in their own right as well as overgrowths on cumulus grains.

Mafic minerals constitute less than 12% of most specimens (Table 5.1) and are mainly interstitial, although, as with nepheline, the size of some pyroxene aggregates suggests an initial cumulus origin, the initial pyroxene composition perhaps being modified by later

Fig. 5.1 Exsolved albite, showing lamellar twinning, in a perthite grain from a nepheline syenite xenolith (S1/1). x125, crossed polars.

Fig. 5.2 Development of albite (first order yellow) at the margins of an alkali feldspar grain, nepheline syenite block S3/2. x125, crossed polars.

reaction with trapped liquid (V.2.iii). Biotite and sphene sometimes occur as inclusions in feldspar laths and are thus also considered to have crystallised at the magmatic stage. The remaining minerals, blue-green amphibole, ilmenite, lavenite and loparite, are of late-stage origin; relations between interstitial minerals are discussed in V.2.

Finally, it should be noted that all of the textural features displayed in the nepheline syenites, with the exception of lavenite growth, albite development and sericitisation are displayed by the glass-bearing sample SX3, thus establishing that the rocks attained their essential character through crystallisation from a silicate liquid.

V.2 MINERALOGY OF THE NEPHELINE SYENITES

V.2.i Feldspar

Alkali feldspar forms more than 50% of all of the studied samples (Table 5.1). Perthite exsolution texture is variably developed, and is completely absent from SX3, which was quenched above the liquidus. Sample S4 shows incipient perthite development only. In other specimens numerous unmixed and homogeneous grains coexist. Homogeneous crystals have compositions between $Ab_{49}Or_{51}$ and $Ab_{64}Or_{36}$, similar to sanidine phenocrysts in the pumice series (Figure 3.1). They are almost always Ca-free (Appendix B). The host feldspar in perthite grains is more potassic at $Ab_{35}Or_{65}$ to $Ab_{44}Or_{56}$ (exsolved phase compositions are $Ab_{93}Or_{7}$ to $Ab_{99}Or_{1}$). The K-enriched host compositions suggest that unmixing was roughly isochemical for each grain; this is borne out by crude estimation of

the proportions of exsolved phase within grains (ca. 20%). Temperatures of unmixing are considered in V.2.vi. Overgrowth of albite, on both exsolved and unexsolved crystals, is observed in some specimens. Compositional relations of this mode of albite growth to the perthites is well shown in S3/2. In this rock, perthite host compositions fall between $Ab_{38}Or_{62}$ and $Ab_{43}Or_{57}$, while the composition of homogeneous unexsolved grains is $Ab_{51}Or_{48}$ to $Ab_{54}Or_{46}$. An otherwise homogeneous feldspar of $Ab_{53}Or_{47}$ has a sharply defined rim of $Ab_{97}Or_{3}$. Although this is identical in composition to the albite in exsolved grains, the crystal has clearly undergone a net gain of Na; the simplest way of reconciling this with the optical evidence is to postulate a late albitic growth on pre-existing feldspars.

V.2.ii Nepheline and sodalite

Nepheline occurs in all of the fresh syenites except S4, where it may have been replaced by an unidentified alteration product (V.2.v). The morphology of many grains suggests that initially cumulus crystals continued to grow in the interstitial environment (V.i.ii).

Nepheline is a difficult mineral to analyse by electron microprobe, due to its high content of sodium which easily "burns off" under the electron beam. Although a low beam curent and scanning rather than spot analysis were used to minimise Na loss (Appendix B) it was felt necessary to employ a means of checking analytical quality. Based on nepheline crystal chemistry, Bannister and Hey (1931) and Dollase and Thomas (1978) recommend that (Si+Al+Fe) in acceptable nepheline analyses should sum to 16 per 32 oxygen formula, and then that (K+Na+2Ca) must equal (Al+Fe). Dollase and Thomas (1978)

consider that analyses which show a difference between (K+Na+2Ca) and (Al+Fe) of greater than 0.25 valence units per 32 oxygen formula should be rejected; this criterion was employed in the present study. All acceptable nepheline analyses are plotted in Figure 5.3.

Nephelines in the syenites are homogeneous within analytical error. Some variation in the proportion of excess silica, apparent in Figure 5.3, is however found between specimens and among different crystals from the same specimen. The ratio of sodium to potassium is virtually constant, although more K-rich nepheline occurs in samples of different petrography (Figure 5.3).

The compositions of natural nephelines are very strongly controlled by crystal chemical factors (Barth, 1963; Dollase and Thomas, 1978). Two types of alkali metal ion site exist in the nepheline structure. The smaller type exhibits a very strong preference for Na^+ ions, and accounts for 75% of the total alkali sites. The remaining 25% accept K^+ ions or remain vacant, charge balance being maintained by one substitution of Si for Al in the tetrahedral site per vacancy. Nepheline compositions in $NaAlSiO_4$-$KAlSiO_4$-SiO_2 thus tend to plot on the line shown in Figure 5.3, the projection of the "natural nepheline composition plane" of Barth (1963) onto this figure. Substantial deviations can however be artificially produced, for example by exchange in molten NaCl at 800°C (Dollase and Thomas, 1978) which gives a composition very close to the $NaAlSiO_4$-SiO_2 join. Dollase and Thomas compiled 42 natural nepheline analyses and found that most plotted on the $NaAlSiO_4$ side of the ideal compositional line, microprobe analyses tending to plot closer to the line than wet chemical analyses. They ascribed this difference to the possible

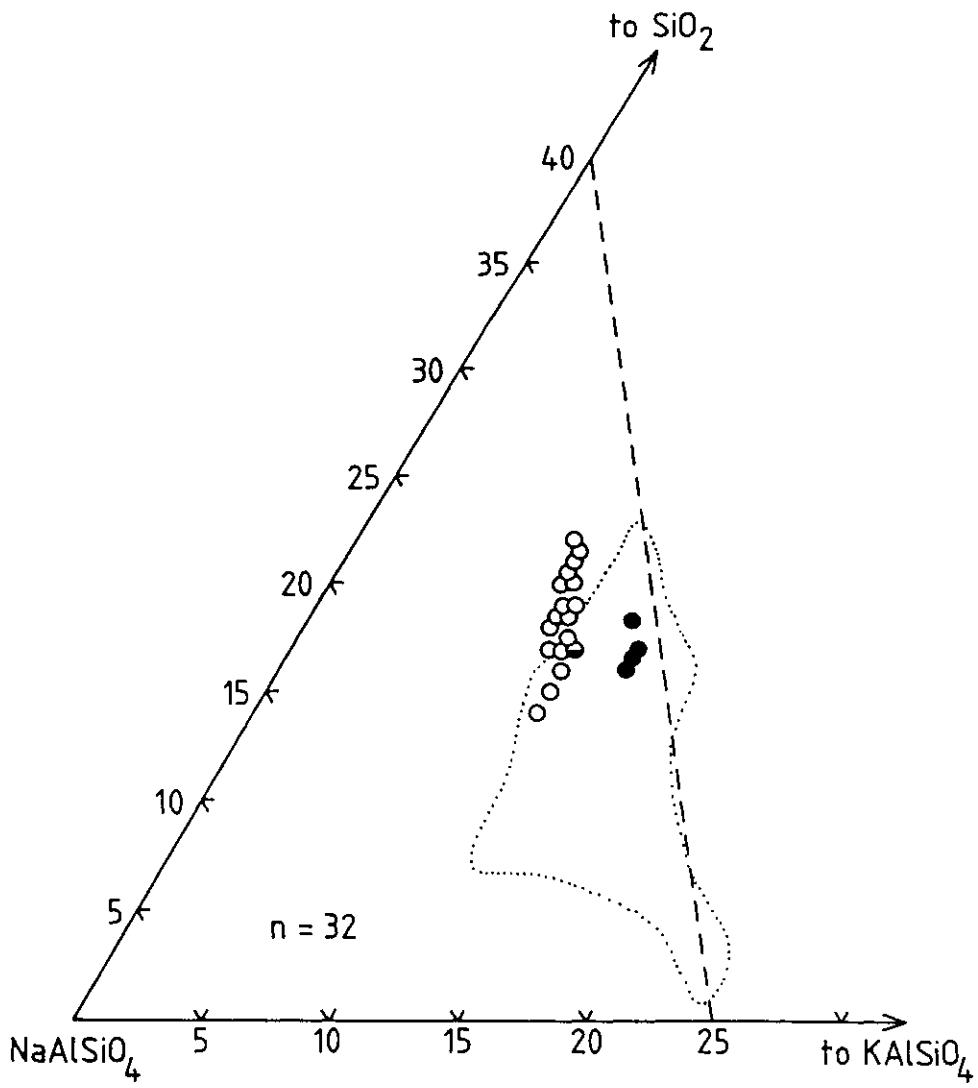

Fig. 5.3 All nepheline analyses acceptable by the criteria of Dollase & Thomas (1978), plotted in $NaAlSiO_4$ - $KAlSiO_4$ - SiO_2. Open circles: nephelines from the nepheline syenite xenoliths in the pumice series; filled circles: nephelines from the Medano xenoliths; half-filled circle: nepheline from the phonolitic component of the Tajao ignimbrite (Chap. III). The dotted line outlines the field of natural nepheline compositions compiled by Dollase & Thomas (1978), with exception of an unusually silica-rich sample reported by Nash et al. (1969), which plots at $Ne_{60}Ks_5Q_{35}$. Dashed line is the projection of the "natural nepheline composition plane" of Barth(1963).

inclusion of altered material in the wet-chemically analysed samples. The present data are significant in this regard, as they plot at some distance from the ideal line, with the wet chemical analyses. The data were obtained over several analytical sessions during each of which the analysed Na level in a standard jadeite was periodically checked (Appendix B) and the tendency of the nepheline analyses to cluster in a narrow field, well away from the ideal line, is thus not considered to be an analytical artefact. Furthermore, analyses of nephelines from samples of contrasting petrography plot in a different field, close to the ideal line.

The tendency of the nephelines to thus plot on the $NaAlSiO_4$ side of the compositional field compiled by Dollase and Thomas (1978) may reflect their crystallisation from the highly sodic evolved Tenerife liquids. Possibly they have equilibrated directly at a late stage with a NaCl-rich fluid phase, although the nephelines in SX3 are identical in composition. Among the volcanics, phenocrystal nepheline has only been analysed from the phonolitic component of the Tajao ignimbrite (Chapter III), but is equally Na-rich (Figure 5.3). Probably, therefore, nephelines have not been affected by late-stage exchange with alkali-halide-rich fluids, but retain their "igneous" compositions; this finding is however hardly conclusive, due to the paucity of nepheline analyses from the volcanics. Further work may prove fruitful in this regard.

In Chapter VI it is suggested that iron (as Fe^{3+}) enrichment in alkali feldspars crystallising from silica-rich alkaline liquids is governed by the reaction

$$NaFeSi_2O_6 + SiO_2 \rightleftharpoons NaFeSi_3O_8$$

pyroxene liquid feldspar

If so, alkali feldspars in nepheline-bearing rocks should be generally poorer in Fe than those from comendites and pantellerites, for equal activities of $NaFeSi_2O_6$ in pyroxene; this is found to be the case for the Tenerife phonolites and syenites compared to oversaturated rocks from Gran Canaria and Pantelleria (see Appendix B). An analagous reaction

$$NaFeSiO_4 + SiO_2 \rightleftharpoons NaFeSi_2O6$$

nepheline liquid pyroxene

may be envisaged for rocks which contain nepheline and an acmitic pyroxene, the iron content of nepheline increasing with falling a_{SiO_2}. The role of this reaction in controlling nepheline iron content cannot be examined as was done for feldspar (Figure 6.30), since both a_{SiO_2} (buffered by the coexistence of alkali feldspar and nepheline) and pyroxene compositions are similar in all the nepheline syenites. Nephelines are however richer in Fe than feldspar (Appendix B).

Sodalite occurs as both euhedral crystals up to 2 mm in diameter and as anhedral, generally smaller grains restricted to interstitial patches. The euhedral grains are sometimes poikilitically enclosed by nepheline and, occasionally, are partly included in feldspar laths and are thus interpreted as cumulus crystals. Often they are finely dusted; use of the microprobe beam indicates that this dust is an iron sulphide (pyrrhotite?) but grains are too small for quantitative analysis (cf. pyrrhotite parageneses considered in Chapter III). Crystals are unzoned, and all those within a given specimen have identical compositions. Some variability between specimens is apparent, especially in replacement of chloride by sulphate (Appendix B); restricted variable substitution of K for Na is also apparent.

V.2.iii Aegirine-augite and aegirine

Pyroxene in the nepheline syenites occurs in two distinct forms. The dominant type is as single or aggregate crystals up to a few millimetres across consisting of euhedral to anhedral members, the boundaries of an aggregate usually being determined by surrounding cumulus phases. Textural relationships with amphibole are complex (V.2.iv). The other, more clearly interstitial, mode of occurrence is as radial or stellate clusters of acicular crystals; this growth pattern is common among the late-stage pyroxenes of nepheline syenites (e.g. Vlasov et al., 1966).

Compositionally the former type vary from aegirine-augite to almost pure acmite, while the stellate clusters are always close to acmite. Additional substituents are Ti, Mn, Al and occasionally, Zr. A significant body of recent literature has focussed on aegirine chemistry, especially the substitution mechanisms governing the entry of Ti and Zr into the mineral formula and the associated excess of Na over Fe_{total} (Ferguson, 1977; Jones and Peckett, 1980; Larsen, 1981; Nielsen, 1979; Scott, 1976, 1977). It is now clear that Ti and Zr are incorporated into aegirine in the molecules $Na(Ti,Zr)AlSiO^{6}$ and $Na(Fe^{2+}, Mg)_{0.5}(Ti,Zr)_{0.5}Si_2O_6$ (Nielsen, 1979; Jones and Peckett, 1980) with the tetravalent ions always occupying an octahedral site. However, there is no generally agreed, or indeed unique, method of recasting titanian aegirine analyses into end-members.

Larsen (1981) uses a procedure based on the stoichiometric assumption of 4 cations to 6 oxygen atoms in the pyroxene formula, as statistically demonstrated by Cawthorn and Collerson (1974) for less exotic compositions. This procedure would be acceptable were it not for the considerable error involved in the SiO_2 determination, the

absolute magnitude of which is comparable to the abundance of minor components, and may seriously affect the estimation of Fe^{3+}. More satisfactory is the scheme of Jones and Peckett (1980), where end-members are progressively calculated and some indication of analytical quality can be gained from the amount of residual Si, expressed as total percentage of cations assigned. This method, modified to assign equal weighting to Ti and Zr in their competition for the appropriate molecules, is adopted here. (Zr+Ti) is assigned to $Na(Zr,Ti)SiAlO_6$; excess (Zr+Ti) is then assigned to $Na(Zr,Ti)_{0.5}(Fe,Mg)_{0.5}Si_2O_6$, or residual Al is assigned to $NaAlSi_2O_6$. Remaining Na is used to form $NaFeSi_2O_6$, which is assumed to contain all the Fe^{3+} present. Mn and remaining (Fe^{2+} + Mg) are assigned to $CaM^{2+}Si_2O_6$; residual (Fe^{2+} + Mg) is calculated as $(Fe,Mg)_2Si_2O_6$, or excess Ca as $Ca_2Si_2O_6$. The ratios $Mg/(Fe^{2+} + Mg)$ and Ti/(Ti + Zr) are assumed to be equal in all the molecules in which they occur, and individual end-members are then calculated as mole %. Note that $NaAlSi_2O_6$ and $Na(Ti,Zr)_{0.5}(Fe,Mg)_{0.5}$ $-Si_2O_6$ are mutually exclusive in this scheme. Another drawback is the usual excess of Si when all other cations have been assigned, suggesting that $Na(Ti,Zr)AlSiO_6$ has been overestimated. For present purposes, these are not serious problems as (Ti,Zr) endmembers are considered together in the following discussion (see caption to Figure 5.4), and Al is in most cases a minor constituent.

Aegirines in Tenerife syenites have previously been examined by Scott (1970), 1976) who presented 14 analyses and noted the general compositional trend from aegirine-augite to aegirine with limited Fe^{2+} enrichment. The present data confirm this trend. When plotted in Di-Hed-Ac (Figure 5.4a), the trend extends from the evolved end of the volcanic pyroxene compositional field to near-pure acmite, with very limited curvature towards the hedenbergite corner, in marked contrast to Gardar Province syenite complexes (Figure 5.4 and also see

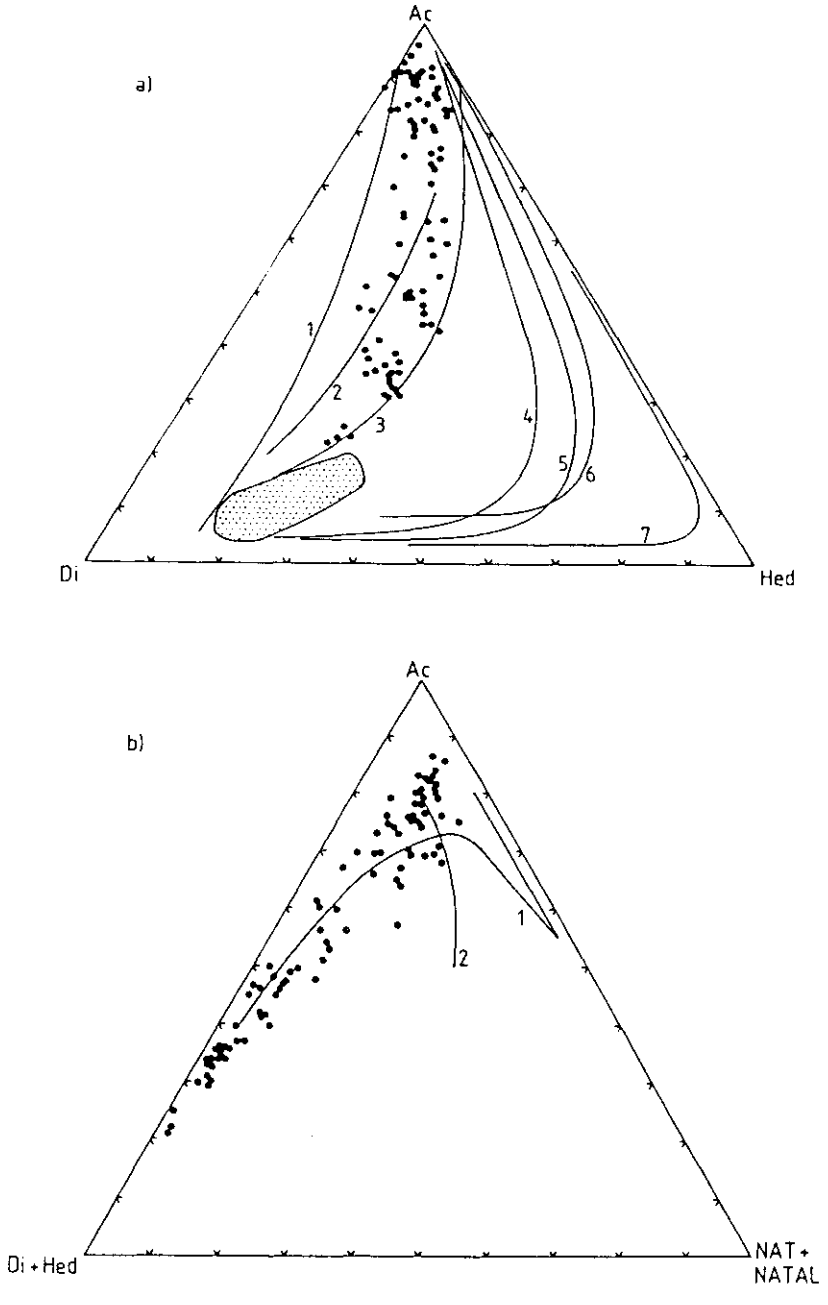

Fig. 5.4 Compositional variation among all analysed aegirines and aegirine-augites, from nepheline syenite xenoliths in the pumice series. a) Diopside (Di) - hedenbergite (Hed) - acmite (Ac) plot. Stippled field: pyroxene phenocrysts from pumices (Chap. III). Labelled curves are generalised trends from: 1. Gardiner Complex, E. Greenland (Nielsen, 1979); 2. Auvergne (Varet, 1969); 3. Itapirapua, Brazil (Gomes et al., 1970); 4-7 from Gardar alkaline province, S.W. Greenland: 4. S. Qoroq (Stephenson, 1972); 5 & 6, two units of the Motzfeldt Centre (Jones and Peckett, 1980); 7. Ilimaussaq (Larsen, 1976). b) Acmite-Diopside + Hedenbergite - Ti (Zr) pyroxene (NAT + NATAL, defined in text) plot. Labelled curves: 1. Gardiner (Nielsen, op. cit.); 2. Zr-rich aegirines, Motzfeldt (Jones and Peckett, op. cit.).

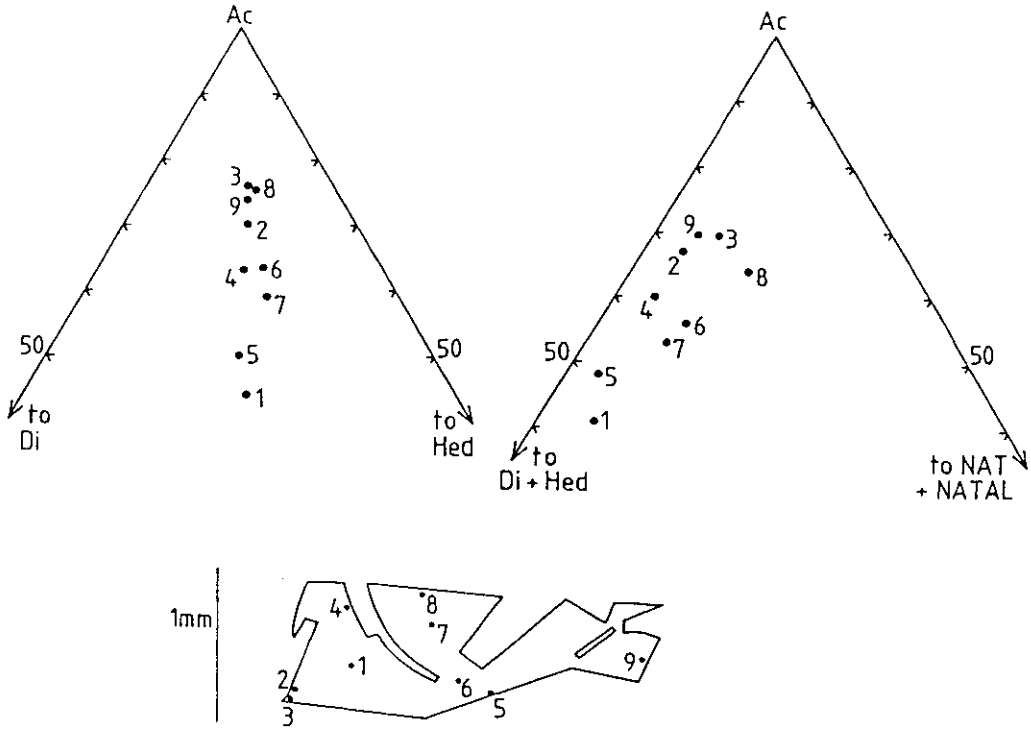

Fig. 5.5 Zoning in an interstitial pyroxene bounded by cummulus feldspars, nepheline syenite block S1/2. Numbered spots were located using the microprobe optical system and thus their positions as marked on the sketch are only approximate.

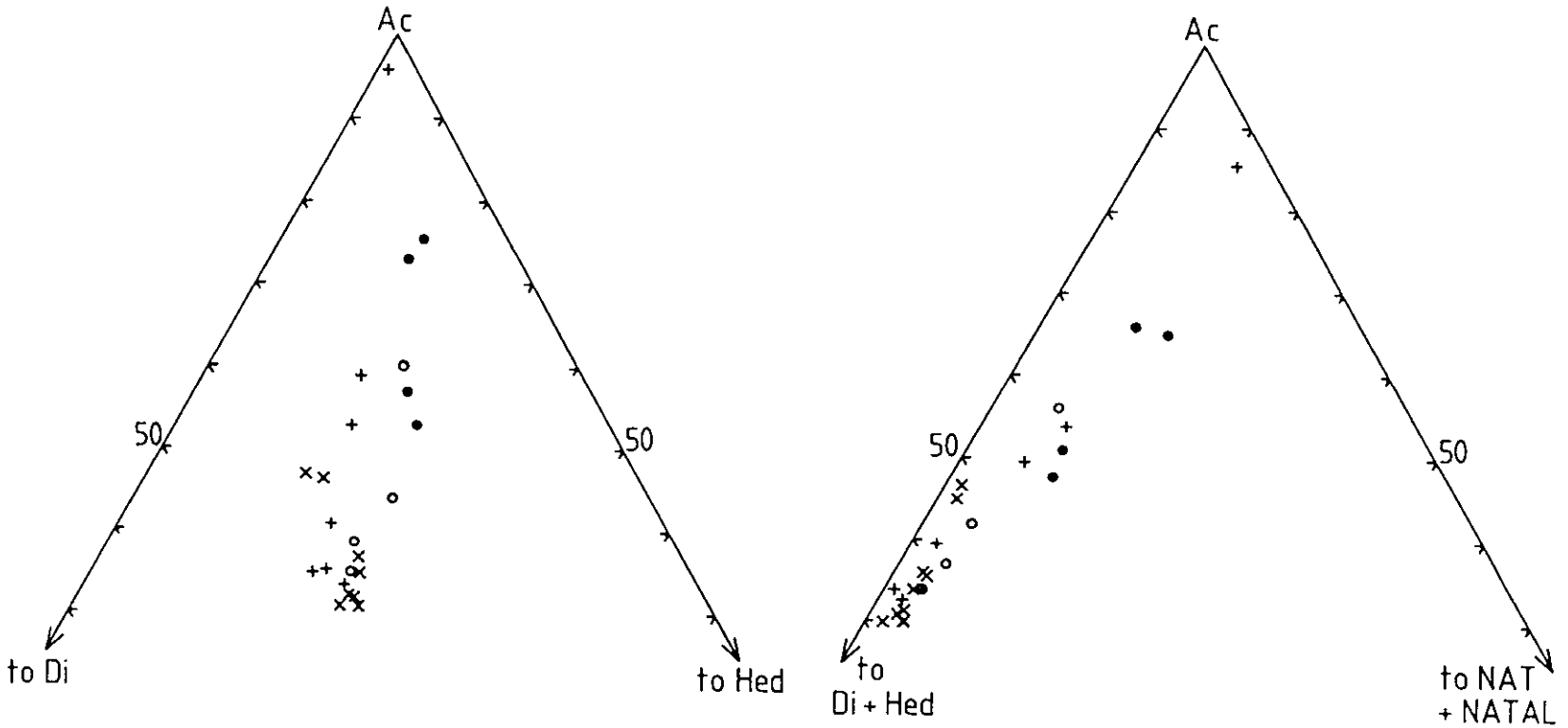

Fig. 5.6 Zoning in four interstitial pyroxenes from xenolith S1/2, each crystal having a different symbol. For any one crystal, the least and most acmite-rich points are the core and rim compositions respectively.

Mitchell and Platt, 1982, for a recent compilation of sodic pyroxene trends). The Tenerife trend is, however, similar to some from other areas. Mitchell and Platt (1982) state that " . . . strong FeO-enrichment along a diopside-hedenbergite trend is characteristic of the early stages of pyroxene evolution in feldspar-bearing alkaline rocks . ." and suggest that Na_2O-Fe_2O_3 enrichment trends are limited to pyroxenes from feldspar-free rocks. Clearly these generalisations do not apply to the Tenerife syenites. No two alkaline centres yet described have yielded identical pyroxene trends in Di-Hed-Ac, and alkali pyroxene evolution is therefore probably a complex function of very many variables.

The acmite enrichment trend is accompanied by (Ti,Zr)-enrichment (Figure 5.4b); considerable scatter about both trends is apparent. It could be argued that this is due to derivation of xenoliths from different plutons, as is found for different units of the Motzfeldt Centre, Greenland (Jones and Peckett, 1980). However, the same degree of scatter is apparent among pyroxenes from the same thin section (Figures 5.5, 5.6). Comparison of individual analyses from a single crystal (Figure 5.5) reveals a possible origin for the compositional scatter, principally due to variations in Mg, Fe^{2+} and Ti content. Two distinct compositional trends are found in different portions of this crystal. Both are characterised by normal zoning from relatively (Fe^{2+}, Mg)-rich cores to acmite-rich rims, but one trend is enriched in NAT+NATAL and (slightly) in hedenbergite (Figure 5.5). Larsen (1981) has given a detailed description of sector zoning in aegirines from Ilimaussaq, and optically identified three other occurrences. Aegirine sector zoning is characterised by variable

enrichment in Ca and Fe^{2+}(001), Al (010), Ti (110) or Fe^{3+}(100), and a normal zoning pattern is typically superimposed. It should be noted that Larsen's aegirine samples are Mg-free and thus, it could be argued, atypical. An optical reconnaissance revealed sector zoning in Mg-bearing aegirines in Tenerife samples S3/2 and S4 (Figure 5.7), supporting the general significance of Larsen's observations. Sector zoning may however be difficult to detect optically, depending on the orientation of the crystal (Larsen, 1981), or in certain sections may be mistaken for normal or reversed zoning (e.g. 001 sectors will appear as concentric "cores" in crystals cut perpendicular to the c axis). No optical evidence for sector zoning is apparent in the crystal in Figure 5.5, but the Ti-rich nature of the central portion is highly suggestive of its presence. Following Larsen's sector enrichment schemes, this portion may have been incorporated into the crystal via an advancing (110) crystal face. The data also suggest a slight sector distinction between Mg and Fe^{2+}, undocumented by Larsen. Further work on aegirine sector zoning should prove fruitful.

Individual crystals show highly variable degrees of normal zoning (Figures 5.5, 5.6, 5.8). Some crystals show only limited acmite enrichment towards the rim, while others in the same specimen have rims of near-pure aegirine (Figures 5.6, 5.8). This may reflect variable intercumulus crystallisation conditions, or, more probably, cessation of growth of some crystals along the plane of section before exhaustion of the interstitial liquid, consistent with the localised distribution of quenched liquid in SX3.

Fig. 5.7 Hourglass sector zoning in an aegirine crystal, nepheline syenite block S3/2. Top left are some acicular aegirines; grey crystals to left and lower centre are alkali amphiboles.

The most extreme zoning has been found in a pyroxene from SX3, in that the core composition is less evolved (Figure 5.8). Generally, syenite pyroxenes contrast markedly with the comparitively unevolved volcanic phenocrysts (e.g. Figure 5.4). Scott (1970) considers this to be due to the instability of acmite at magmatic temperatures (Bailey, 1969). Nonetheless the presence of acmite-poor pyroxene phenocrysts in phonolite magmas of similar bulk composition suggests that the initial cumulus pyroxene compositions should fall in the "volcanic" field of Figure 5.4. If the syenites are the plutonic equivalents of the phonolites, then pyroxene compositions have changed during cooling. The comparatively unevolved core composition of SX3 pyroxene is consistent with modification of initial pyroxenes by continuous in situ reaction with interstitial liquid, which in this sample was interrupted by quenching above the solidus.

Late-stage acicular aegirines in stellate clusters are always close to acmite in composition (Figure 5.9). Their presence in SX3 shows that they can form in the presence of silicate liquid, although later subsolidus growth cannot be ruled out. Zoning is limited and follows no simple pattern, although variable zoning in Ti suggests that a sector control may operate in the needles as well as larger crystals (Figure 5.9).

V.2.iv Amphibole

Blue-green alkali amphibole, close to Mg-rich arfvedsonite in composition, occurs as an intercumulus mineral in all fresh samples studied. In one sample (S4) the amphibole is brown but of similar composition. Usual associates are pyroxene and lavenite. Amphibole-pyroxene textural relations are highly variable, even within the same specimen. Thus amphibole may replace, or be replaced by, aegirine-

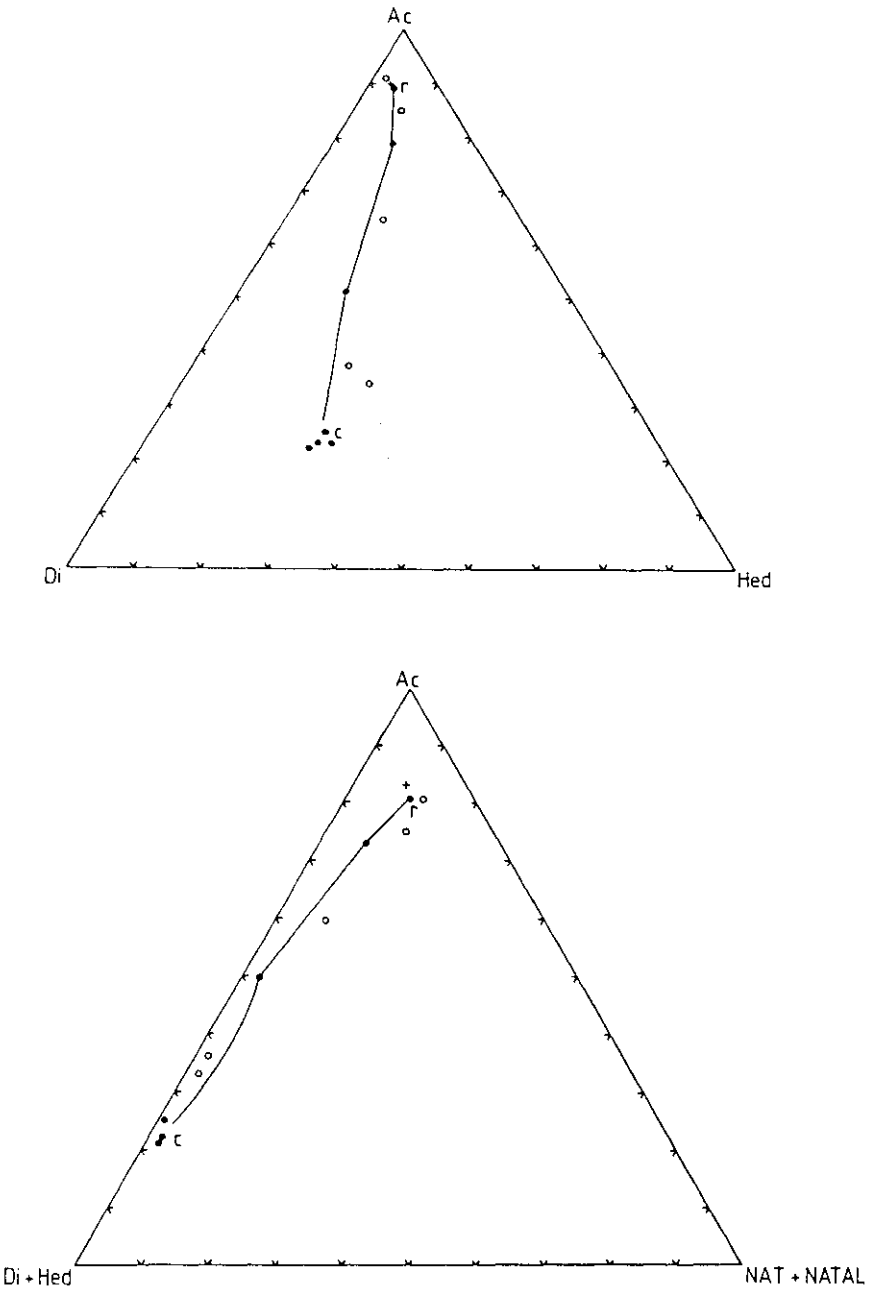

Fig. 5.8 Pyroxenes in glass-bearing sample SX3. Filled circles: single strongly zoned crystal, c = core, r = rim. Note that core analyses plot close to the field of volcanic phenocrysts in Fig. 5.4a. Open circles: other interstitial grains. Cross: late-stage acicular aegirine in a stellate cluster.

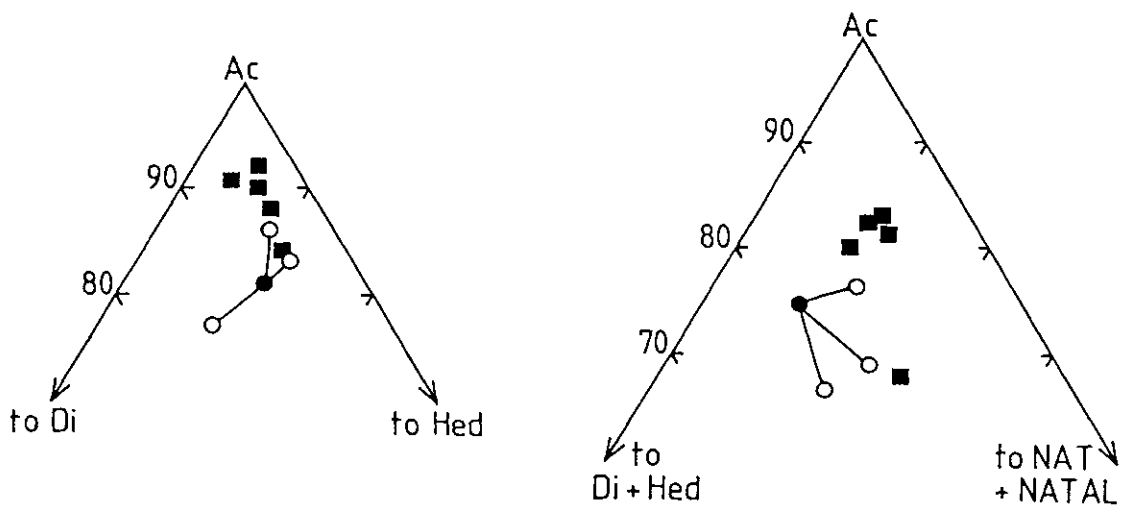

Fig. 5.9 Late-stage acicular aegirines in sample S1/2. Filled circle: centre of a stellate cluster. Open circles: ends of individual needles in the same cluster. Filled squares: other crystals.

augite, or both may coexist without any obvious reaction relationship. Only one textural style is seen within any one interstitial patch, suggesting that individual intercumulus microenvironments may follow different crystallisation paths when communication through the interstitial liquid ceases. Amphibole also occurs as fringes around the rare biotites found in the syenites. In S1/4, small biotites partly enclosed in feldspar are seen in all stages of replacement by amphibole, which ultimately completely pseudomorphs the original biotite in the feldspar cavities. This provides a ready explanation of the near-absence of biotite from the syenites, in distinct contrast to the phonolitic volcanics. The composition of the residual glass in sample SX3 shows that peralkalinity and Na/K increase to extreme levels during interstitial crystallisation; both these factors will favour the biotite $\rightarrow$ arfvedsonite reaction. Thus the distribution of amphibole in the nepheline syenites may be partly controlled by the abundance of biotite in the initial cumulates (it should be noted that there is no contradiction between the postulated cumulus biotite and the final interstitial amphibole; the large size of the cumulus feldspars dictates intercumulus cavity geometry and other cumulus minerals may take up "interstitial" positions during cumulate formation). Stephenson and Upton (1982) note a similar (riebeckitic) amphibole paragenesis in the Kungnat Fjeld alkaline complex, South Greenland.

Compositionally the amphiboles show little variation. Stephenson and Upton (1982) suggest that amphiboles in peralkaline undersaturated rocks normally show an alkali enrichment trend with or without an initial increase in Fe/Mg (Figure 5.10), while those in their over-saturated counterparts show slight alkali depletion, with a return to Na-rich compositions at a very late stage. Amphiboles in the

appear to show Fe/Mg variation at near constant alkali contents (Figure 5.10). Amphiboles from single samples do however show a slight increase in alkali content with Fe/Mg. The Fe/Mg ratio of around 1 mirrors that of hed/di maintained by the pyroxenes during the greater part of their evolution. Similarity between coexisting sodic amphibole and pyroxene trends also occurs in the alkaline complexes of S. Qoroq (Stephenson, 1972) and Ilimaussaq (Larsen, 1976) in the Gardar province (compare trends 1 and 2 in Figure 5.10 with 4 and 7 respectively in Figure 5.4) and is further discussed by Stephenson and Upton (1982).

V.2.v Other minerals

Remaining accessory minerals are present in much smaller quantities and may be entirely absent from some samples (Table 5.1).

Lavenite

Lavenite is an interstitial phase in most samples. It has a variable acicular to anhedral habit and exhibits pale pink-pale yellow-golden yellow pleochroism. It is usually associated with late-stage aegirine (occasional stellate clusters containing both minerals are seen) and/or amphibole. Analyses conform to the general formula $R_4Si_2O_7(O,OH,F)_2$ proposed by Zachariasen (1930) for lavenite-wöhlerite group minerals, where R = Ca, Sr, Na, Mn, Fe, Mg, Zr, Nb, Ta, Ti. A crystal in S1/4 was found to be antithetically zoned in Zr and Ti, with some variation in Fe and Mn (Appendix B). Ferguson (1978) notes considerable variation in Zr, Nb, Ti and Mn among lavenites from a Tenerife nepheline syenite. Lavenite chemistry and substitition schemes are incompletely understood; Zr-Ti relations suggest that these elements compete for the same lattice sites, as in aegirine. Further study is warranted.

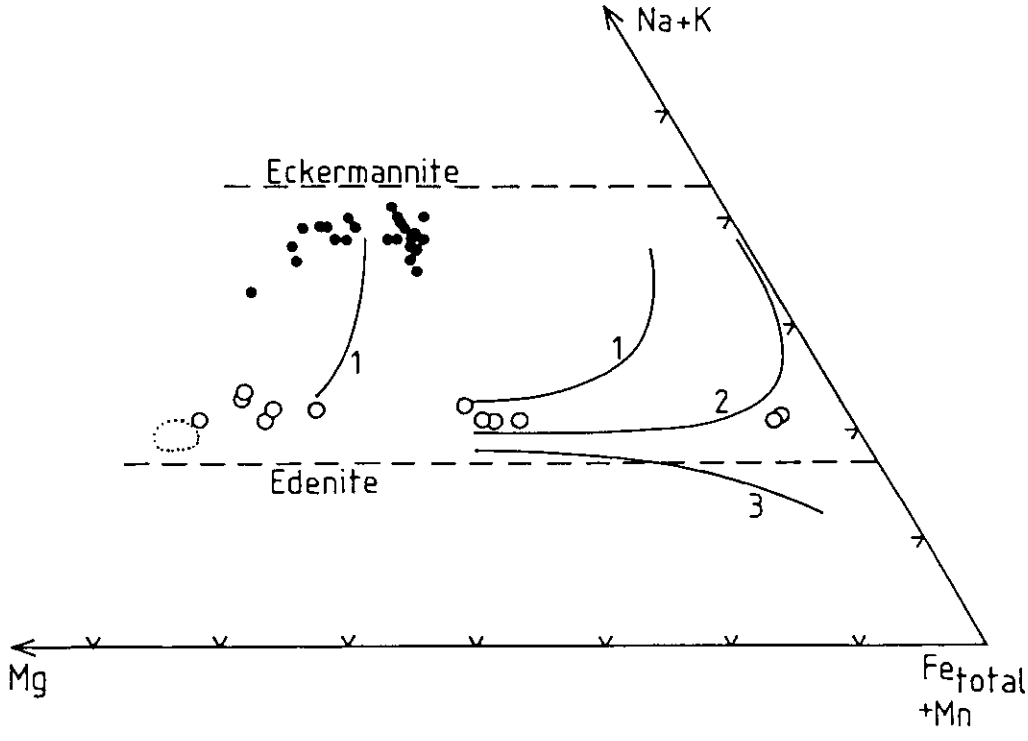

Fig. 5.10 Amphiboles in nepheline syenites (small filled circles) and in the Medano xenoliths (large open circles), plotted in molar Mg - (total Fe + Mn) - (Na + K). Dots outline field of Tenerife volcanic phenocrysts. Labelled curves are amphibole compositional trends from: 1.S. Qoroq (Stephenson, 1972); 2. Ilimaussaq (Larsen, 1976); 3. Nunarssuit (Anderson, 1974). Note that the "eckermannite" line is not comparable with the nepheline syenite amphiboles as their low Al contents indicate considerable substitution of Fe^{3+}.

Sphene

Rhombs and needles of sphene, often corroded, are sparsely distributed through most of the studied specimens. The mineral is absent from aegirine-ilmenite-lavenite interstitial areas and is often seen as inclusions in cumulus feldspars. These textures suggest that sphene precipitated as a cumulus mineral (consistent with its occasional presence as a phenocryst in the pumices, Chapter III), and was unstable in the presence of the residual intercumulus liquid.

Chemically, the sphenes show appreciable substitution of Na and Fe into the basic formula $CaTiSiO_5$ (Appendix B). Nb was invariably qualitatively detected, often with Zr and REE (Appendix B).

Biotite

Rare bioties occur as inclusions in cumulus feldspar crystals. Often they are partly replaced, and occasionally completely pseudomorphed, by blue-green amphiboles (V.2.iv). Compositionally they are similar to the most Ti, Mg-poor biotites found in the phenocryst assemblages of the pumice series, and exhibit the same apparent tetrahedral site deficiency (Chapter III). Biotite may have been more abundant in the original cumulates forming at the magmatic stage, as discussed above (V.2.iv).

Ilmenite

Interstitial ilmenite, associated with aegirine, occurs in all samples; it is especially abundant in S4 (Table 5.1). It is always rich in Mn (10-17% MnO by weight) and, compared to ilmenites from the pumices, poor in Mg. An extended (750 seconds) microprobe count on a grain in S1/4 qualitatively revealed the presence of small amounts of V, Nb and Zn.

Loparite

The rare mineral loparite, a Nb-REE rich member of the perovskite group, occurs in trace quantities as an interstitial mineral in several of the nepheline syenites. It is deep red, has very high relief, and is isotropic. Typically it is found as small cubes or anhedra in association with stellate aegirine. Substantial compositional variation of rare metals is apparent, especially Nb, Ta, Th, and REE (Appendix B). A partly analysed loparite from S4 contains 3.4% BaO (J. Bevan, pers. comm.), undetected in other specimens. Variation across most of the range may be seen within a single specimen (Appendix B), although all analysed individual grains are unzoned. Chondrite-normalised LREE plots of seven loparites are shown in Figures 5.11 and 5.12. Slopes are similar to those of whole-rock phonolitic pumices (Chapter II), and probably reflect relative LREE abundances in the liquids from which the loparites grew.

Ferguson (1978) considered loparite in one Tenerife nepheline syenite sample to be an early crystallising phase out of equilibrium with the residual liquid, and implied co-precipitation with sphene and biotite. There is considerable evidence against this contention. Firstly, in the present samples, loparite always occurs in interstitial areas and frequently appears to have formed after late-stage stellate aegirine, whereas sphene and biotite often occur as inclusions in cumulus feldspar. Secondly, loparite is never found as a phenocryst in the phonolitic volcanics, unlike sphene and biotite. Thirdly, had loparite ever precipitated from any of the pumice-forming magmas, they could not have retained their REE-rich character. Finally, the low silica activities required to stabilise minerals of the perovskite group

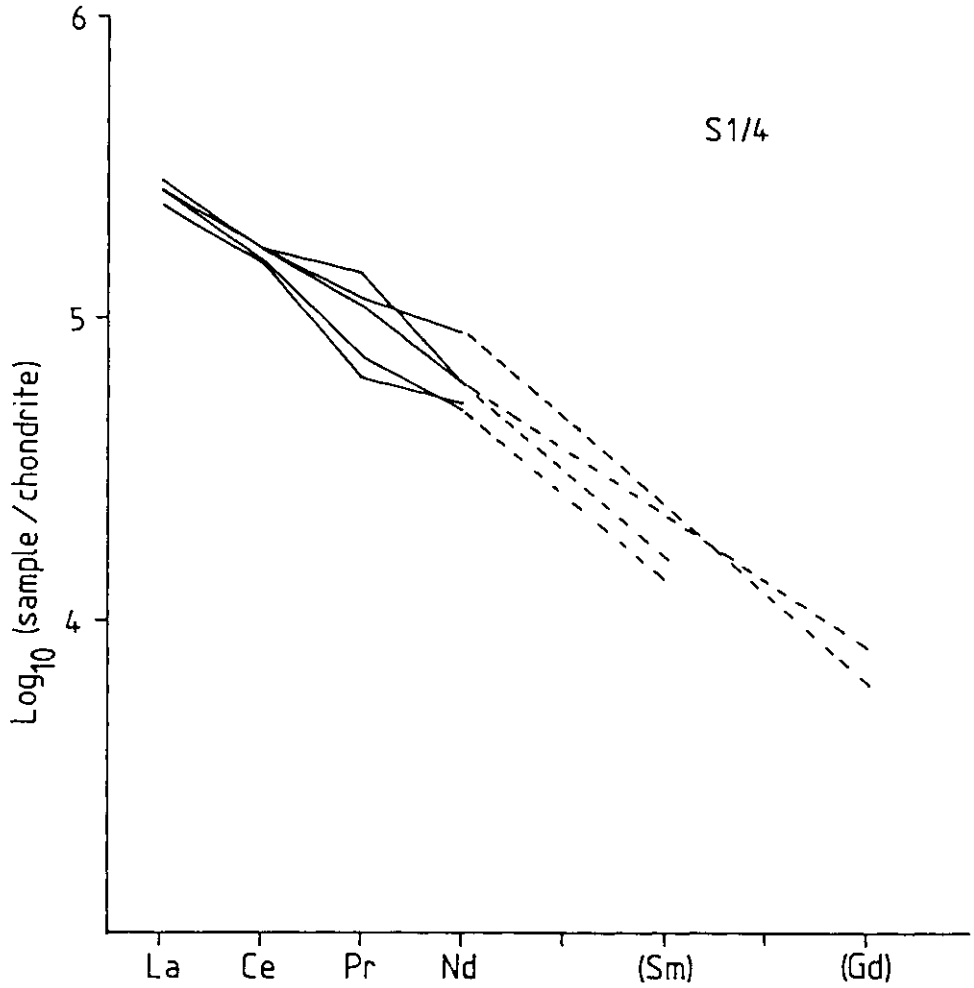

Fig. 5.11 Chondrite-normalised LREE plots for five loparites from nepheline syenite xenolith S1/4. Sm and Gd are order-of-magnitude values, as discussed in Appendix B. Each plot is either a single analysis or the mean of two. Normalising chondrite values taken from Haskin et al. (1966).

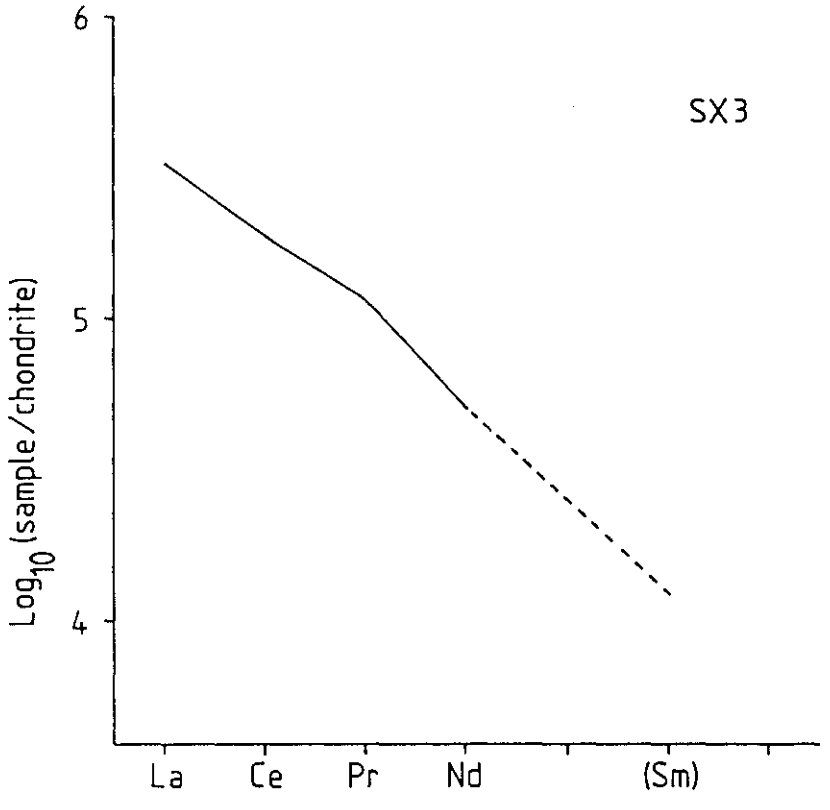

Fig. 5.12 As Fig. 5.11, for a loparite grain from glass-bearing syenite xenolith SX3. Mean of 3 analyses.

are not compatible with the presence of feldspar (Carmichael et al., 1970), and early precipitation of loparite is thus unlikely. All the evidence therefore points to the mineral having grown from the last highly undersaturated, interstitial liquid.

Remaining minerals

Other minerals found in the syenites are restricted to one or two specimens only.

Sample SX3 bears a proportion (3.8%) of interstitial glass, now largely devitrified. Where fresh (although probably hydrated), the glass is pale greenish-yellow in thin section and has about 80% vesicles. Mineral grains, including stellate aegirines, are always euhedral toward it, indicating that the glass is a quenched residual liquid, and not the product of partial melting due to heating resulting from immersion of the block in magma (e.g. Harris and Bell, 1982). The glass composition is extreme and variable.

Hydration may have removed some Na from the glass. Despite this, (Na+K)/Al varies between 2.30 and 2.45, and Na/K between 5.90 and 7.77. Textural relations with solid phases then indicate that the glass represents an extreme differentiate of more normal Tenerife phonolitic liquid. The dominant influence of alkali feldspar crystallisation on the glass composition is apparent in the depletion of Si, Al and K, and enrichment in Na, P, Ti, Fe and Mn compared to pumice whole-rich compositions (which approximate the bulk compositions of the nepheline syenites). The glass composition is consistent with the crystallisation of aegirine (Na, Fe-rich), Mn-ilmenite (Mn, Fe, Ti-rich) and lavenite (Na, Ti, Mn-rich) as interstitial phases. The absence of lavenite from SX3 (Table 5.1) perhaps indicates that the glass

was quenched before key components necessary for the crystallisation of the mineral (Zr, Nb?) had attained sufficient concentrations. The possible significance of the glass occurrence with regard to the compositions of erupted magmas is briefly discussed below.

An unidentified phase, or mixture of phases, is present in S4. It occurs interstitially, is extremely soft (on a polished thin section, the mineral formed hollows below the surface and only very restricted areas took the polish) and very pale yellow with low - moderate relief in thin section. It grows as cryptocrystalline radial masses, often with "maltese cross" extinction and is apparently an alteration product, perhaps after nepheline in view of the lack of this mineral in S4 (Table 5.1). Microprobe analysis indicates that Na, Si and Zr are major constituents, with lesser amounts of Fe, Mn, Ti and S. Possibly more than one mineral may be present in the cryptocrystalline mass.

Two more interstitial minerals occur very rarely. One is found as minute anhedral masses with occasional hexagonal and acicular crystals, usually growing into cavities and often associated with late-stage aegirine. It is pleochroic from pale pink or pinkish-yellow to deep pink/magenta and is weakly birefringent; it is identified as a member of the eucolite-eudialyte group. The other mineral is very pale yellow-brown with barely perceptible pleochroism to a slightly paler shade, has a shagreen surface appearance, good cleavage in one direction and straight extinction, with low first order birefringence. It is probably ramsayite.

V.2.vi Discussion

Conditions of formation

Although four of the geothermometers listed in Chapter IV are potentially applicable to the phase assemblage of the nepheline syenites, quantitative temperature estimates for the various stages of textural development during cooling, after the manner of Powell (1978), cannot be extracted from the data. The climopyroxene-ilmenite Fe^{2+}-Mg exchange geothermometer cannot be used for the interstitial assemblage as these phases are rich in other components ($NaFeSi_2O_6$ in pyroxene, $MnTiO_3$ in ilmenite) putting them well outside the calibration range (Bishop, 1980). Neither can the nepheline-alkali feldspar geothermometers of Perchuk and Ryabchikov (1968) and Powell and Powell (1977b) be usefully applied, as the compositions of feldspar and nepheline in the syenites lie within the most composition-sensitive range of the thermometers; for example, an error of $\pm$1% on the alkali feldspar composition results in an uncertainty of 100°C on the estimated temperature, in addition to the error of 70°-130°C due to uncertainties in the thermodynamic data (Powell and Powell, 1977b).

Nephelines show an appreciable variation in excess silica content, suggesting use of the nepheline composition geothermometer of Hamilton (1961). Estimates range between 710°C and 900°C for all nepheline compositions from the syenites. However, Hamilton (1961) recommends that application of the method be restricted to volcanic rocks, as plutonic nephelines gave erroneous temperatures. This is particularly the case where another feldspathoid is present. The wide range of temperatures given by the present samples supports Hamilton's caution, particularly as nepheline is absent from the phenocryst

assemblage of pumices whose Fe-Ti oxides give temperatures within this range (Chapter IV). Nepheline is present in small amounts in one pumice (the phonolitic component of the Tajao ignimbrite) and gives a temperature of 770°C, which seems reasonable. Only three nephelines from the syenites have a lower excess silica content (Figure 5.3), yielding lower temperatures. Consequently little value is placed on the nepheline temperature estimates.

Nonetheless syenite crystallisation temperatures can to some extent be constrained by experimental data on relevant systems.

Firstly, the presence of a single hypersolvus alkali feldspar in SX3 implies that this sample was quenched at a temperature greater than 640°-670°C, for the compositional range of the feldspar (solvus of Bowen and Tuttle, 1950). Textural and mineralogical similarities with the other samples (which carry perthites) suggest that the solidus was in all cases at a higher temperature. This is consistent with the minimum at 750°C in the undersaturated portion of the system $NaAlSiO_4$-$KAlSiO_4$-SiO_2 at 1Kb P_{H_2O} (Hamilton and MacKenzie, 1965). Wellman (1970) studied the effect of adding an aqueous chloride fluid to the same system, with particular reference to sodalite stability. Wellman found that near the vapour-saturated liquidus in $NaAlSi_3O_8$-$KAlSi_3O_8$-$NaAlSiO_4$-$KAlSiO_4$-NaCl-KCl-H_2O, sodalite-bearing syenite assemblages formed over a wide range of temperature and pressure. Wellman concluded that assemblages like those in the present samples (nepheline-sodalite-one alkali feldspar) crystallise near the vapour-saturated minimum at temperatures greater than 680°C and fluid pressures less than 1.6 kb.

The lowest reliable temperatures obtained from a pumice deposit are 835°C (Fe-Ti oxides) and 810°C (cpx-ilm). Thus the crystallisation of the interstitial assemblage from liquid trapped between cumulus crystals, and the various mineral-liquid and mineral-mineral reactions which modify the phase assemblage from that of the erupted rocks to that of the syenites (see below), appear to take place largely between 800°C and 680°C, assuming that the pumice magmas are representative of those that crystallised to form the nepheline syenites.

The limiting fluid pressure of 1.6 kb is compatible with the P_{H_2O} values found for the pumice magmas if it is assumed that volatiles are allowed to "boil off" from the saturated system as crystallisation proceeds; otherwise it is necessary to postulate relatively dry syenite-forming magmas. The presence of rare biotite among the cumulus assemblage however argues against initially dry magmas. The depth of <5 km implied by the limiting fluid pressure at saturation is consistent with geological evidence for a phonolitic magma body underlying the Las Canadas caldera (Chapters I and III).

Following crystallisation, the syenites underwent subsolidus recrystallisation. In the freshest specimens (except SX3), feldspars show almost the only evidence of this. Perthitic exsolution of near-pure albite from a K-enriched host is common (V.2.i). Albite also appears as overgrowth/replacement rims on pre-existing feldspars. This latter mode of growth is a predictable feature of closed system cooling within a sodalite-nepheline-feldspar assemblage, but requires the presence of an aqueous alkali-chloride-bearing fluid phase (Wellman, 1970). Such a phase is likely to be present at the initial stages after full crystallisation of the melt; the high vesicularity of the

glass in SX3 indicates that solidification would have released a fluid phase. Compositional relations between fringing albite and perthite patches in the same grain (Described in V.2.i) suggests that unmixing of the feldspar was an isochemical process unaffected by albite development at the rim. Application of the Stormer (1975) geothermometer to albite-host pairs in perthites implies temperatures between 558°C and 603°C (Table 5.2) for the cessation of exsolution in these grains.

Most of the collected samples have been affected by pervasive metasomatism, causing sericitisation of feldspars and feldspathoids, growth of zeolites and calcite, and hematisation of ferromagnesian phases. Aegirine is usually the last-affected phase, although occasionally nepheline and/or feldspar survive in the presence of completely pseudomorphed pyroxene. Weathering of blocks after incorporation into the host ignimbrite is unlikely to be responsible as both fully altered and completely fresh specimens were collected from a single locality; in situ weathering is likewise a very remote possibility as there are, at present, no plutonics exposed on Tenerife and the chief syenite-bearing ignimbrite/mudflow is the youngest widespread eruptive unit on the island. The nature of the alteration is typical of interaction between cooling rock and hydrothermal fluids. The occurrence of the xenoliths in volcanics erupted from the summit area of the island implies the existence of an unknown thickness of plutonic rocks above liquid magma; in such circumstances it is highly probable that an extensive hydrothermal system would develop within the upper crystalline zone.

Sample	Host	Exsolved phase	T°C
S1/2	$Ab_{48}Or_{52}$	$Ab_{98}Or_{2}$	573
"	$Ab_{39}Or_{61}$	$Ab_{95}Or_{5}$	579
"	$Ab_{62}Or_{38}$	$Ab_{93}Or_{7}$	603
"	$Ab_{38}Or_{62}$	$Ab_{95}Or_{5}$	576
"	$Ab_{40}Or_{60}$	$Ab_{99}Or_{1}$	560
"	$Ab_{42}Or_{58}$	$Ab_{98}Or_{2}$	569
"	$Ab_{43}Or_{57}$	$Ab_{98}Or_{2}$	570
"	$Ab_{37}Or_{63}$	$Ab_{98}Or_{2}$	558
S1/4	$Ab_{39}Or_{61}$	$Ab_{97}Or_{3}$	568
"	$Ab_{37}Or_{63}$	$Ab_{98}Or_{2}$	558
"	$Ab_{38}Or_{62}$	$Ab_{95}Or_{5}$	576
"	$Ab_{40}Or_{60}$	$Ab_{98}Or_{2}$	565
"	$Ab_{38}Or_{62}$	$Ab_{97}Or_{3}$	566
"	$Ab_{37}Or_{63}$	$Ab_{97}Or_{3}$	563
"	$Ab_{39}Or_{61}$	$Ab_{95}Or_{5}$	579
"	$Ab_{40}Or_{60}$	$Ab_{96}Or_{4}$	576
S3/2	$Ab_{39}Or_{61}$	$Ab_{97}Or_{3}$	568
"	$Ab_{43}Or_{57}$	$Ab_{98}Or_{2}$	570
"	$Ab_{53}Or_{47}$	$Ab_{98}Or_{2}$	569
"	$Ab_{38}Or_{62}$	$Ab_{98}Or_{2}$	561

Table 5.2 Temperatures of cessation of exsolution in perthite grains from three samples, using the geothermometer of Stormer (1975), in the modified form given by Powell & Powell (1977a). Exsolution lamellae occur rarely in sample S4, but are too fine to analyse satisfactorily with the microprobe beam.

Comparison with the mineralogy of the phonolites

There is no direct evidence that the magmas which erupted to form the phonolitic pumice series are representative of those which crystallised to form the nepheline syenites. Nevertheless their similarity in bulk rock compositions, in the presence and compositions of several constituent minerals, and the close association in space and time make such an assumption reasonable. It then becomes necessary to account for the mineralogical discrepancies between co-magmatic eruptives and plutonics. These are the absence of magnetite, and the near-absence of biotite, from the syenites, and the contrasting pyroxene and ilmenite compositions.

The problem of biotite is discussed above (V.2.iv). It is suggested that biotite initially formed a cumulus phase, but was later replaced by arfvedsonitic amphibole due to increasing peralkalinity and Na/K ratio in the interstitial liquid.

In V.2.iii a case was made for the modification of cumulus augite to aegirine-augite and aegirine, since Bailey (1969) considers that acmite-rich pyroxenes are unstable at magmatic temperatures. The mechanism for this change may be linked to the absence of magnetite within the syenites. In peralkaline liquids the reaction

$$6SiO_2 + 2Fe_3O_4 + 3Na_2Si_2O_5 + \tfrac{1}{2}O_2 \rightarrow 6NaFeSi_2O_6$$

liquid magnetite liquid pyroxene

operates to produce acmite at the expense of magnetite. In the interstitial environment of the nepheline syenites, a_{SiO_2} may be held approximately constant by the nepheline-albite buffer reaction. However $a_{Na_2Si_2O_5}$ will increase as peralkalinity increases; eventual extreme peralkalinity is demonstrated by the composition of the interstitial

glass in SX3. Thus the reaction will run to the right, using up a postulated initial cumulus magnetite component. As the process is dependent on the gradual increase in $a_{NaSi_2O_5}$, a smooth zoning is produced in the pyroxene, rather than, for example, distinct acmite overgrowths on augite crystals.

Finally the Mn-rich ilmenite in the syenites is considered to be unrelated to the ilmenite forming at the magmatic stage, which may react in response to falling a_{SiO_2} (Chapter III) to produce sphene. The manganoilmenite in the syenites is a late-stage interstitial phase; it perhaps forms as a response to increasing levels of Mn, Ti and Fe during the final evolution of the trapped liquid, as evidenced by glass compositions in sample SX3.

General considerations

Features of the Tenerife nepheline syenites are generally typical of similar sodic rocks found throughout the world. Their textures, mineral assemblages and mineral compositional trends approximate to those of well-documented nepheline syenites in, for example, the Precambrian Gardar alkaline province of SW Greenland. Although different in detail, there are certainly no features of mineralogy or petrology which could be ascribed to formation in a different tectonic setting. This is simply due to the fact that magmas of similar general major element composition emplaced at similar crustal levels are constrained to follow predictable crystallisation paths. Volcanoes such as Tenerife may thus serve as models for surface activity contemporaneous with the formation of ancient alkaline centres.

The pumices are the most voluminous eruptives of similar bulk composition to the syenites and are likely representatives of syenite-forming magma. The glass compositions recorded from sample SX3 then demonstrate that these liquids were capable of fractionating to extreme compositions. The members of the pumice series are, however, strikingly uniform and much less extreme in composition (Chapter II). The larger pumice deposits have DRE volumes of several km^3 (Chapter I). Fractionation of such phonolite bodies to the extent seen in SX3 (4% residual glass) would result in 0.1-0.2 km^3 DRE of compositionally extreme magma, capable of forming pumice deposits having vesiculated volumes > 0.5 km^3. Such eruptives should be detected in the field, if they existed, particularly as their compositions would favour the formation of distinctive welded deposits (see Chapter VI). Possibly they exist in the near-vent region of the Las Canadas wall, but the welded tuffs found there are more likely to be equivalents of the major deposits of S. Tenerife (see Chapters I and VI). It seems more probable that efficient segregation of crystals and liquid, by whatever mechanism, does not take place after a certain stage of magmatic evolution is reached. Perhaps the magma develops a yield strength great enough to prevent the operation of crystal settling and/or boundary layer transfer mechanisms.

V.3 THE MEDANO XENOLITHS

V.3.i Occurrence

At Medano (Figure 1.15) there is a well-preserved basaltic surtseyan tuff-ring, now partly eroded by the sea. It is fine-grained, fully lithified, and contains numerous base-surge horizons typical of phreatomagmatic tuffs (Walker, 1973). The ring pre-dates the Granadilla Series, and is probably ca. 10^5 years old (G.P.L. Walker, pers. comm.). It is partly infilled by an ignimbrite flow unit (possibly G), which has "slopped" over the inland rim and ponded in the centre. The stratigraphically highest parts of the tuff bear blocks up to 20 cm in diameter of coarse-grained plutonic rocks, while xenoliths of volcanic origin are common throughout the thickness. Lack of a juvenile basalt coating on the blocks suggests that they were incorporated into the erupting mixture above the explosion level in the crater/conduit system. Their situation in a phreatomagmatic host rock thus suggests that the parent rock body presently underlies surface volcanics in the Medano region at no great depth.

V.3.ii Petrography

Only five samples (TF161-5 inc.) were examined in thin section, but are sufficient to show the less evolved and more variable nature of this suite as compared to the nepheline syenites. Cumulus plagioclase is ubiquitous (Table 5.3); other cumulus phases are titanaugite, kaersutite, olivine, Fe-Ti oxides, sphene and apatite with interstitial nepheline, although in most cases the interstitial assemblage has been obscured by alteration. One specimen (TF 165) possesses an igneous lamination picked out by plagioclase and

Sample	Plagioclase	Nepheline	Sodalite	Pyroxene	Amphibole	Olivine	FeTi oxides	Biotite	Sphene	Apatite
TF161	X	X		tr.	X		X		X	X
TF162	X			X	X		X	X		X
TF163	X	X	tr.	X	X		X		X	X
TF164	X	X		X	X		X		X	X
TF165	X			X	X	X	X	tr.		X

Table 5.3. Assemblages of Medano xenoliths TF161 - TF165.

Fig. 5.13 Parallel arrangement of titanaugite (pink) and plagioclase laths, Medano xenolith TF165. x10, ppl.

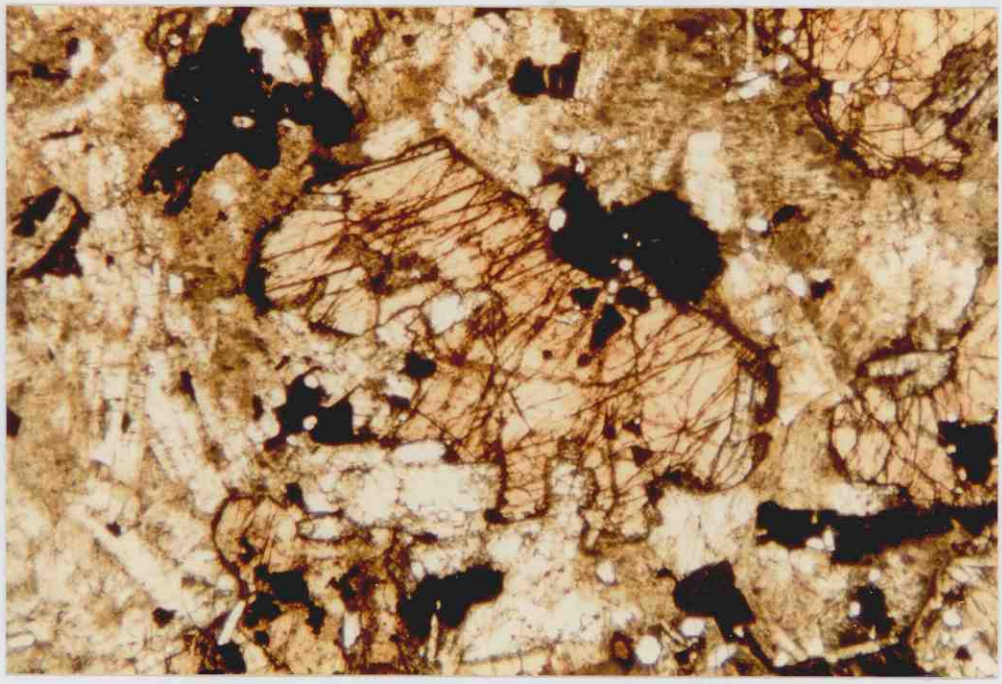

Fig. 5.14 Titanaugite partly enclosing plagioclase, Medano xenolith TF162. x10, ppl.

titanaugite laths up to 5 mm long (Figure 5.13); in others, plagioclase laths are poikilitically enclosed by titanaugite in a sub-ophitic relationship (Figure 5.14). Abundant evidence for subsolidus recrystallisation is seen in the replacement of titanaugite by amphibole (Figure 5.13) and exsolution textures in feldspars and Fe-Ti oxides. Furthermore Fe-Ti oxides are often rimmed with biotite, amphiboles have oxidised margins, and the edges of deep pink titanaugites are altered to green aegirine-augite, perhaps evidence for the passage of brines through the rock at subsolidus temperatures. Plagioclase and nepheline are frequently heavily sericitised.

Assemblages in TF161-5 are recorded in Table 5.3.

V.3.iii Plagioclase

Plagioclase varies considerably in composition even within the single specimens and zoned crystals (Figure 5.15). Although reversed zoning is found in some crystals, normal zoning predominates and the most anorthite-rich compositions within a given sample are found at crystal cores. These range from An_{58} to An_{14}, however the greater part of this range is represented within most individual samples (Figure 5.15). The most albitic grains have ternary compositions with up to 7% Or, and have exsolved near-pure potassium feldspar in an antiperthitic relationship. The exsolution lamellae are of dimensions comparable to the microprobe beam widths and are consequently difficult to analyse; the most K-rich composition obtained was Or_{94}.

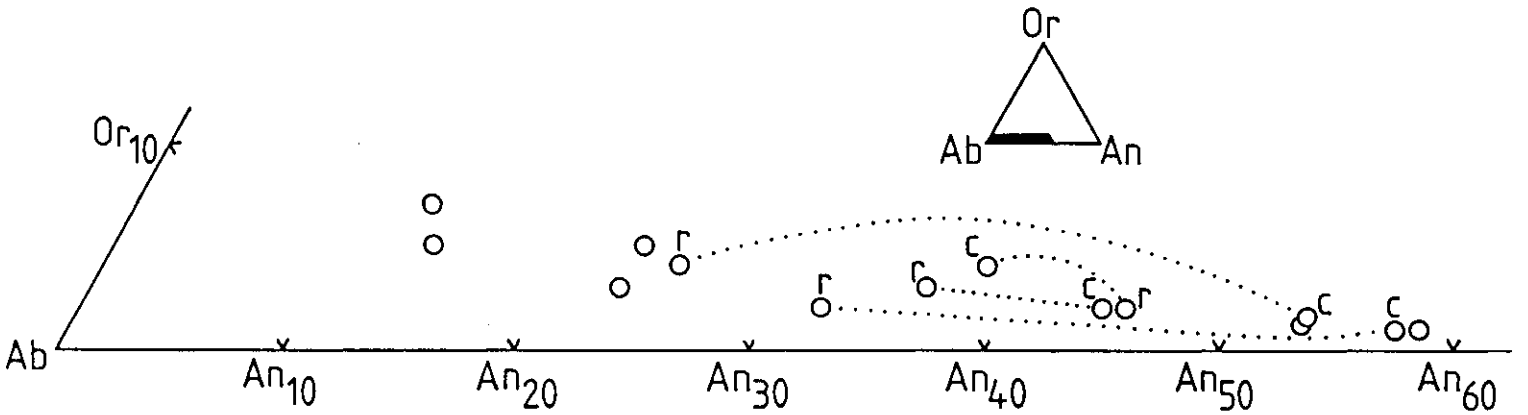

Fig. 5.15 Plagioclase compositions from the Medano xenoliths. C and r are respectively the core and rim compositions of zoned crystals, joined by dotted lines.

V.3.iv Feldspathoids

Nepheline occurs as an interstitial phase. An interesting textural relationship is seen in TF161, where the mineral forms large (1-1.5 cm) grains with a high proportion (up to 50%) of poikilitically-enclosed euhedral plagioclase and amphibole crystals. The nepheline is relatively fresh, as are the enclosed feldspars, in contrast to feldspar in the rest of the rock which is almost completely altered (Figure 5.16). Enclosed amphiboles have likewise suffered less rim oxidation than those outside of the nepheline patches (Figure 5.16). The margins of the nepheline are usually strongly altered to a depth of up to 1 mm, and alteration also penetrates cracks in the nepheline. It seems that nepheline has formed large protective "capsules" which the agent of alteration was unable to penetrate. Possibly this is a grain size effect; the short dimension of feldspar grains in TF161 is usually < 1 mm, an order of magnitude less than the size of the nephelines, and comparable to the thickness of the altered margins around nepheline. If so, alteration of TF161 by means of fluids which pervasively penetrated grain boundaries within the rock is implied.

Compositionally the Medano nephelines are richer in K and Ca than those in the nepheline syenites, but have similar levels of excess silica. Despite the large size of some grains, zoning is absent.

Sodalite occurs as rare euhedral grains poikilitically enclosed by nepheline in only one sample (TF163), which has the most Na-rich feldspars. It is chemically near-pure end-member sodalite, closely similar to sodalites in the nepheline syenites.

Fig. 5.16 Fresh plagioclase (high birefringence due to abnormally thick section) and amphibole (brown) enclosed in nepheline (grey), contrasting with heavily altered plagioclase exterior to nepheline. Also note dark rim around amphibole grain largely exterior to nepheline (left). Medano xenolith TF161, x10, crossed polars.

V.3.v Mafic phases

Olivine occurs as a cumulus phase in one sample only (TF165). It is frequently partly hematised. Individual fresh crystals are unzoned, although a very slight variation in composition between grains (Fo_{56-58}) is apparent. Most grains have the composition $Fo_{57}Fa_{41}Tp_2$.

Pyroxenes are purple to pale buff or pale green, often with deeper green rims. Most core compositions are similar to those of pyroxenes derived from the intermediate magmas represented in the pumice series. The green rims are however atypical of these (see Figure 3.3), in that the Mg content is lower, for a given Al content, than that of the volcanic pyroxenes. The green colouration is most usually found inside completely altered rims, and, occasionally, bordering cracks in pyroxene and is thus probably metasomatic in origin. However, some crystals have pale green, partly Mg-depleted, cores with more evolved rim compositions. More data on pyroxene compositional variation within these samples are required.

Pyroxene is always replaced to some degree by amphibole (pleochroic yellow-brown - red-brown - dark brown), which also occurs as a cumulus phase. In most respects the amphibole is similar to that recorded from the intermediate members of the pumice series, although Fe/(Fe+Mg) is highly variable (Figure 5.10). Cumulus amphibole cores have similar Fe/(Fe+Mg) ratios to volcanic amphiboles; however rims are always more Fe-rich (Fe/(Fe+Mg) up to 0.93). In TF163, rims have identical compositions to the amphibole which is replacing pyroxene.

Biotite occurs as haloes around Fe-Ti oxides in TF162 and 165 and as an interstitial phase in TF162. It is generally heavily oxidised and otherwise altered. Fresh parts of grains yield compositions very similar to the Ti-rich biotites of the pumice series.

V.3.vi Other phases

Fe-Ti oxides are present in all samples and show evidence of subsolidus exsolution in the form of broad lamellae. Compositions of lamellae/host pairs are relatively pure ilmenite and magnetite respectively in terms of $FeO-Fe_2O_3-TiO_2$ (although the ilmenite often has a high MnO content), indicating that exsolution ceased at fairly low temperatures. The MnO contents of ilmenite (up to 12.6% by weight) preclude geothermometric calculations in most cases; a temperature of 615°C was obtained for an exsolved grain in TF162 with about 4% total minor element content, and of 500°C and 530°C respectively for two lamellar grains in TF 165, with similar minor element contents. These temperatures are similar to those obtained for exsolved Fe-Ti oxides in similar rocks by Powell (1978).

Sphene occurs in three samples (Table 5.3), and is a prominent cumulus phase in TF 163. A large (1.5 mm) grain in this sample was found to be antithetically zoned in Zr and Ce, with the rim enriched in Zr. Nb is also present in appreciable quantities (Appendix B).

Apatite is found as inclusions in other phases in all specimens. Apatites from TF 163 and TF 165 were quantitatively analysed for REE with the microprobe and found to contain variable quantities of

La, Ce and Nd, with TF 163 apatites being richer in REE, consistent with the generally more evolved nature of this sample.

Pyrrhotite occurs rarely as inclusions in other phases in TF 163 and TF 165. A complex sulphide grain (with magnetite) occurs in TF 165; it appears to have unmixed into a near-pure pyrrhotite and one enriched in copper (2.6 wt. % Cu), with small amounts of Co (Appendix B).

Minute grains of zircon and a pure Zr-phase (Baddelyite?) occur in amphibole which forms a halo around a pyroxene grain in TF 162. Zircon is usually absent from silica-undersaturated igneous rocks; however, it has been previously reported as an accessory alteration product due to pyroxene breakdown in alkaline rocks from Lovozero, U.S.S.R. (Vlasov, et al., 1966).

V.3.vii Discussion

The data reported here are of a reconnaissance nature only; the Medano xenoliths await a more detailed investigation. Nonetheless some preliminary conclusions may be drawn.

Field evidence (V.3.i) suggests that the parent intrusion is present at a shallow depth under the Medano tuff-ring. The same arguments may be used to deduce that the xenoliths are all derived from within a relatively small volume, that of the upper conduit-vent system during the surtseyan eruption. It is thus tempting to suggest that the studied rocks are derived from a single pluton, though this cannot be substantiated at present. It is clear however that intrusive activity has taken place well away from the main volcanic focus. Few constraints can be imposed on the age of the intrusion(s), beyond

that it had evidently cooled substantially before formation of the tuff-ring, and is thus considerably older than the pumice series. Southern Tenerife is underlain by Ancient Series basalts (Cahpter I), into which the intrusion(s) may have been emplaced.

Core compositions of plagioclases, pyroxenes and amphiboles in the less-evolved specimens suggest precipitation from an alkaline intermediate, perhaps trachybasaltic, magma. Little quantitative information on conditions of cumulus crystallisation is forthcoming, largely as a result of the substantial subsolidus recrystallisation and alteration. The co-precipitation of olivine and magnetite (in TF 165) does not imply T-f_{O_2} conditions near the quartz-fayalite-magnetite (QFM) buffer curve in undersaturated liquids (Powell, 1978), but rather that f_{O_2} was probably some way below QFM. The olivine composition in TF 165 would be in equilibrium with a liquid having $Mg/Fe^{2+} \simeq 0.5$ (using the olivine-liquid compositional relations determined by Roeder and Emslie, 1970), again suggestive of a trachybasaltic magma. Application of the Powell and Powell (1974) geothermometer to olivine and clinopyroxene in TF 165 gives a temperature of 1010°C; this is in the upper part of the calibration range of this thermometer and probably in reality indicates a somewhat higher temperature of equilibration, as discussed in Chapter IV.

Mineral compositional trends in the suite are distinct from those displayed among the volcanics in the nepheline syenites, particularly amphiboles (Figure 5.10) and pyroxenes (Figure 3.3), although the degree to which post-magmatic processes have affected trends is uncertain. Furthermore, associations not seen elsewhere are found, for example the co-existence of nepheline with plagioclase and amphibole.

It is likely that the Medano intrusion(s) is not directly related to the other rocks studied in this thesis. Further work on the Medano samples is desirable.

CHAPTER VI

THE WELDING OF ALKALINE PYROCLASTIC DEPOSITS

VI.1 INTRODUCTION

Welded tuffs, by reason of their widespread occurrence throughout the geological record, are among the most familiar of all pyroclastic rocks. The Canary Islands have an important place in the history of our recognition and understanding of these rocks; over a century ago, Fritsch and Reiss (1868) coined the term "eutaxite" to describe indurated pyroclastic deposits with a crude foliar structure on Tenerife, and noted the presence of similar rocks on neighbouring Gran Canaria. Over the next 90 years, concepts of pyroclastic flow and welding mechanisms were gradually developed until the publication of the classic texts by Smith (1960a, b) and Ross and Smith (1961). Since then, most workers have concentrated their attention on large-volume (up to 3,000 km^3, Smith, 1979) rhyolitic welded ignimbrites in the western U.S.A.

Although the term "eutaxitic" has been retained to describe the texture first noted by Fritsch and Reiss the pyroclastic geology of the Canaries was virtually ignored until the work of Ridley (1967) and Schmincke and Swanson (1967a, b). This latter and several subsequent studies (e.g. Schmincke, 1970, 1974: Villari, 1969, 1974; Gibson, 1970; Hay et al., 1979; Wallace et al., 1980) have established that considerable textural and structural differences exist between some welded tuffs of alkaline composition and their calc-alkaline counterparts. Peralkaline ignimbrites, especially those of silica-

oversaturated composition, commonly show a degree of welding comparable to, or greater than, rhyolitic and dacitic deposits several orders of magnitude thicker and more voluminous. Some examples exhibit structures indicative of post-compactional mass flowage, rare among calc-alkaline welded tuffs. Explanations advanced to account for the evident differences in tephra viscosity include the relatively low viscosities of alkaline magmas, their generally high eruption temperatures, and differences in the nature and abundance of the volatile component (Schmincke, 1974). Sparks et al. (1978) have suggested that the dense welding of peralkaline ignimbrites is primarily due to low magmatic gas contents, resulting in the formation and emplacement of dense pyroclastic flows which efficiently retain heat. However, the correlation between alkalinity and welding extends to air-fall tuffs: for example, 6 km^2 is the maximum areal extent of welding found by Sparks and Wright (1979) among dacitic and rhyolitic air-fall deposits, whereas the strongly peralkaline Green Tuff of Pantelleria is densely welded over at least 85 km^2 (Wright, 1980). The pyroclastic horizon of peralkaline phonolitic composition, described by Hay et al. (1979) from Mt. Suswa, Kenya, which from the field description would appear to be an air-fall tuff (VI.5.ii), is welded over an area of 300 km^2, yet its maximum thickness is only 2.5 m. These observations suggest that the cause of dense welding of alkaline pyroclastics lies primarily in the chemical composition (and perhaps temperature) of the ejecta, and is only partly influenced by the emplacement mechanism.

Welded tuffs on Tenerife (undersaturated, mildly to strongly peralkaline compositions) are of infrequent occurrence but include both ignimbrite and air-fall types. They are normally only welded in part, rarely show evidence of post-depositional flowage, are of limited areal extent and are sparsely distributed through the succession. In contrast, the welded ignimbrites of Gran Canaria (oversaturated, moderately to strongly peralkaline) are welded virtually throughout their thickness, form a single sequence, and display abundant laminar viscous flowage structures. A comparative study was therefore initiated to investigate factors affecting welding in these examples. Fieldwork on Gran Canaria led the author to an interpretation of the viscous flowage structures in the ignimbrites at variance with that of Schmincke and Swanson (1967a), and a detailed investigation and analysis of these structures was therefore undertaken. Several of the features displayed by the Gran Canaria ignimbrites are duplicated in the Green Tuff of Pantelleria, a densely welded air-fall tuff of comparable composition, for which field data are available (Wright, 1980) and the study was extended to include this unit. The possible role of impact agglutination in the compaction of welded air-fall tuffs, as implied by Booth (1979) and Mahood and Hildreth (1980) is theoretically investigated in section VI.5 and found to be probably negligible in most cases; based on these findings and existing literature on deformation processes during welding a thermal facies model for air-fall tuffs is tentatively proposed.

In this chapter, then, aspects of the physical structure and petrology of welded ignimbrites and air-fall tuffs from Tenerife, Gran Canaria and Pantelleria are described and discussed with particular reference to their post-emplacement compaction, flowage and eventual solidification.

VI.2 WELDED TUFFS ON TENERIFE

VI.2.i Ignimbrites

Three occurrences of welded ignimbrites are known in Tenerife: the Arico-Abona ignimbrite (unit F of Booth and Walker, in prep.); the thick (> 30 m) densely welded cooling unit at San Juan de la Rambla on the northern coast, which possibly correlates with the Arico flow, and the prominent Adeje red ignimbrite in south-western Tenerife. The field characteristics, stratigraphic positions, and classification of these deposits have been discussed in Chapter I. Pertinent aspects are summarised here.

A distinctive feature of all three occurrences is the abundance of poorly- or non-vesiculated juvenile clasts up to 50 cm in diameter, which account for roughly 10% of all material in the Adeje red ignimbrite. Their proportion in the other two units is difficult to ascertain due to the denser welding and alteration, and flow density sorting, but rounded obsidian blocks are abundant in the basal 1 m of the Arico ignimbrite (Figure 1.19), and in associated mudflow and flood deposits, while the San Juan ignimbrite contains a flow unit rich in 30 cm poorly vesiculated clasts. No such juvenile material is found in significant quantity in the non-welded ignimbrites, despite abundant evidence, such as 50 cm lithic fragments, that the flows were fully capable of supporting large obsidian blocks. Their occurrence therefore suggests that the welded ignimbrite magmas were less thoroughly vesiculated than usual.

Neither the Adeje nor Arico ignimbrites are underlain by a preceding plinian deposit (the base of the San Juan unit is unexposed) such as is common among the non-welded flows; the brief pyroclastic-fall phase represented by the bimodal ash parting between the two main flow units of the Adeje red ignimbrite (Chapter I) cannot be compared to the voluminous precursors of non-welded ignimbrites E, G, J, K and O. The overall explosivity of the welded-tuff-forming eruptions was therefore less than those which produced non-welded ignimbrites.

Welded and non-welded flows show similar internal features such as coarse-tail grading and basal layer development, and are designated as type 2 in the classification of Wilson (1980). Generally, however, internal structures are rather better developed in the non-welded ignimbrites (Chapter I), suggesting that higher fluidising gas-flow rates are appropriate to their emplacement (Wilson, 1980). Sparks (1978b) has shown that the velocity of the fluidizing gas through the pyroclastic flow is dependent on the original magmatic gas content.

Field evidence, therefore, suggests that the welded ignimbrites were formed by magmas with unusually low gas contents compared with most of the Tenerife tephra deposits, and thus supports the deduction of Sparks et al. (1978) that welding is favoured by a low abundance of magmatic volatiles. It shall emerge however that this evidence is of a rather equivocal nature.

Petrology of the Adeje red ignimbrite

This unit was selected for petrological study as its phenocrysts appear unaffected by post-eruptive processes which have substantially altered the Arico and San Juan ignimbrites; this may be a consequence of its lower emplacement temperature (Chapter I and below).

The ignimbrite shows evidence for magma mixing, and its petrography and mineral chemistry have therefore been discussed in Chapter III; a brief resume is given here.

Glass is compositionally variable but shows no petrographic evidence for alteration. The general composition is peralkaline phonolite which has high Na and Fe, and low Al compared to the main pumice succession. It is the most peralkaline tuff unit found on Tenerife. The dominant phenocryst phase is alkali feldspar ($Ab_{70}Or_{25}An_5$) with biotite, augite, titanomagnetite, ilmenite and heavily resorbed plagioclase of variable composition (An_{60}-An_{88}). Equilibrium mineral pairs of Fe-Ti oxides and cpx-ilm (Buddington and Lindsley, 1964; Bishop, 1980) yield temperatures of 865°C and 833°C respectively. The mineralogy permits the estimation of f_{H_2O} prevailing at the time of equilibration; a maximum estimate is 1900 bars (Chapter IV). If it is assumed that the magma was water-saturated, then the primary concentration of H_2O can be estimated; a value of roughly 5.6% by weight is obtained (Chapter IV).

Discussion

The value of 5.6% for the magmatic water content in the Adeje ignimbrite is at variance with field evidence for low gas contents. This figure probably represents a maximum value, due to the nature of the assumptions involved in the calculation, of which perhaps the least justifiable is that the biotite composition on which the calculation is based contained no fluorine at equilibrium (see Chapter IV for a full discussion of uncertainties involved in the thermodynamic estimation of magmatic water contents). However, let us now re-examine the field evidence. Firstly, lack of a preceding plinian fall phase is, in itself, not evidence for low magmatic gas content; large vent radius or low muzzle velocity may also be responsible. The thin fall deposit between the two main flow units indicates that the magma was not so gas-poor as to be inherently incapable of plinian eruption, and a variable vent radius may account for the presence of this layer (Chapter I). Secondly, the variation in gas-flow rate required to produce the observed range of internal fluidization structures is very small (Wilson, 1980) and may simply be a function of flow thickness (Sparks, 1978b) or the proportion of gas derived from external sources (Wilson, 1980). Finally, the occurrence of unvesiculated material is a problem in itself which cannot be simply a consequence of total volatile content. Sparks (1978a) has shown that bubble nucleation in magma occurs at volatile super-saturation pressures of less than 10 bars; thus, if both obsidian and pumice are present in the same eruptive unit, then the magma must be heterogeneous with respect to some factor affecting bubble nucleation rate, since otherwise a thousand-fold variation in water fugacity within a small ($\sim$0.1 km^3) magma volume must be postulated. A possible cause is heterogeneous distribution of surface-active

components (e.g. sulphur) in the magma; the concentration of these is crucial to bubble nucleation rates (Sparks, 1978a).

It will now be shown that the Adeje ignimbrite could have been derived from gas-rich magma. The welded nature of the cooling unit, and yet the very rare development of eutaxitic texture, indicates that it was emplaced at close to the minimum welding temperature of its constituent glass shards. For rhyolitic pumice, this is 625°C (Smith, 1960a). The modelling of Sparks et al. (1978) shows that an ignimbrite with a magmatic water content of 5% will be emplaced at a temperature at least 300°C below the initial magmatic temperature. If the temperature of approximately 850°C, indicated by geothermometry, is taken as the initial eruption temperature, it is therefore required that the minimum welding temperature of Adeje glass is of the order of 100°C lower than that of rhyolitic pumice. Although calculated magmatic viscosities cannot be quantitatively extrapolated to such low temperatures (Shaw, 1972) this is consistent with the relative viscosities of Adeje and rhyolitic liquids, which are respectively 10^6 and 10^8 poise at 1000°C. Thus the welding in the Adeje ignimbrite could simply be a consequence of its major-element composition.

It must be concluded, however, that the Adeje ignimbrite offers no unequivocal evidence for the relative importance of the various factors affecting the development of welding. Inability to rigorously assess the available evidence is due principally to our ignorance of the physical and chemical behaviour of magma-gas systems before and during explosive eruption.

VI.2.ii Welded air-fall tuffs

Air-fall pumice can weld to form a coherent rock provided the viscosity of the accumulating tephra is sufficiently low (Walker, 1973). Welded air-fall tuffs may be distinguished from welded ignimbrites by their grain-size characteristics, mantling of topography and irregular compaction profiles (Sparks and Wright, 1979). Conditions required for the welding of air-fall pumice favour its development in the near-vent region of the deposit. A number of thick welded air-fall tuffs occur high on the rim of Las Canadas (Booth and Walker, in prep.) and at least one unconformably mantles the caldera wall. Ridley (1968) describes some welded "breccia and ash flows" from this area which display the characteristics of air-fall deposits. It is probable that these tuffs have non-welded equivalents in the pumice succession of south-eastern Tenerife (Booth and Walker, pers. comm.) but the scarcity of exposures in the intervening region renders correlation difficult.

The Boca de Tauce tuff

A prominent welded air-fall tuff occurs at Boca de Tauce (Figure 6.1). Both the phenocryst assemblage, Afsp-bi-cpx-ilm-mag, and the mineral and glass chemistry (Appendix B) are similar to the south-eastern pumices but a distinct correlation with any one deposit cannot be established. Fe-Ti oxides give a magmatic temperature of 835°C, cpx-ilm yields 810°C. Primary water content, calculated as before, is roughly 4.2% (Chapter IV). Therefore the magma which produced this tuff had no chemical or physical properites to distinguish it from the non-welded pumice deposits of Tenerife. Every pumice deposit described by Boothand Walker has a deduced source in the Las Canadas area. In this case, therefore, the welding is solely

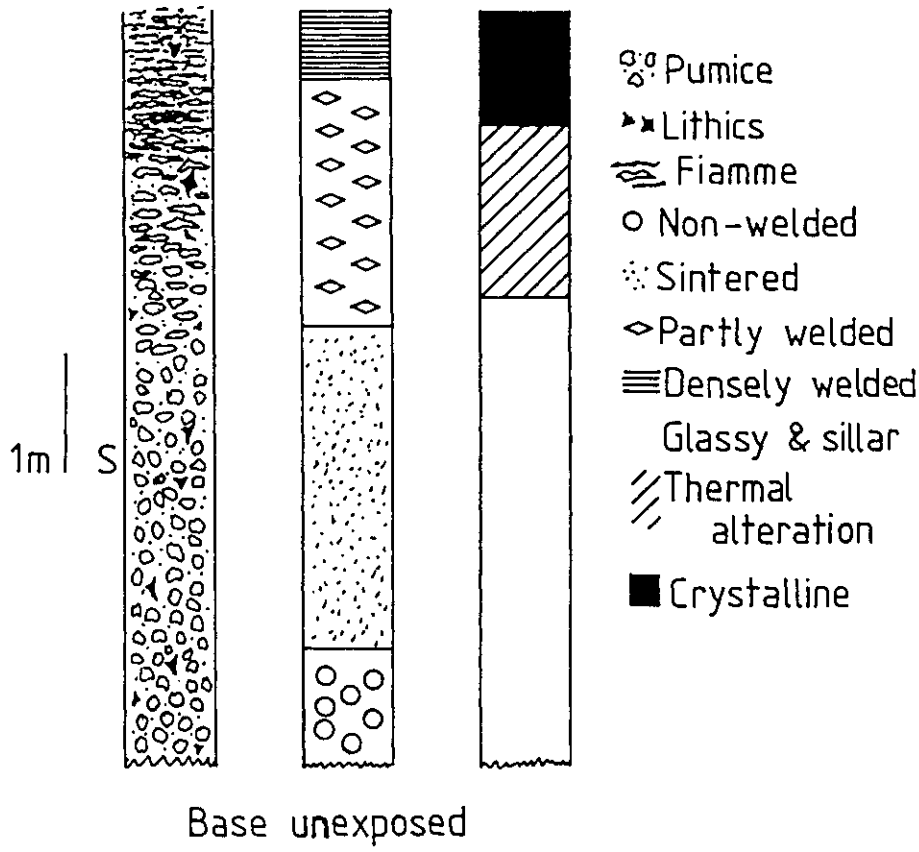

Fig. 6.1 Section through welded air-fall tuff at Boca de Tauce. 10 m of densely welded tuff overlies the section shown. S marks zone of dense glassy pumice sampled.

a consequence of the physical circumstances of the eruption, and the Boca de Tauce tuff is simply a near-vent welded facies of a plinian deposit.

VI.3 THE WELDED IGNIMBRITES OF SOUTH-WESTERN GRAN CANARIA

Gran Canaria has an impressive development of welded tuffs in the south western part of the island. The general geology, structure and petrology of these rocks have been described by Schmincke (1970, 1974) and Schmincke and Swanson (1967a). The tuffs are notable for their comenditic to pantelleritic composition, dense welding even where thin (10 m), and internal viscous flowage structures. Flow structures typically include lineations, folds and tension cracks defining a movement direction sensibly parallel to the dip of the underlying surface and clearly indicate flowage as a coherent viscous mass occurring after the particulate fluidized flow episode. This would seem to require low glass viscosities during deposition and cooling. Closely similar structures have been described from many other peralkaline silicic welded tuffs (Gibson, 1970; Villari, 1969, 1974; Noble, 1968; Walker and Swanson, 1968; Parker, 1972) and very occasionally, from calc-alkaline tuffs (Chapin and Lowell, 1979; limited development in the Askja 1875 welded air-fall tuff, H. Sigurdsson, pers. comm.). Other workers have constantly debated whether these structures were generated after compaction and welding and are therefore secondary features (Rittmann, 1958, 1962; Rutten and Van Everdingen, 1961; Lock, 1972) or represent compaction during the final stages of the primary flowage of ignimbrites (Schmincke and Swanson, 1967a; Noble, 1968; Walker and Swanson, 1968; Parker, 1972; Deal, 1972; Chapin and Lowell, 1979). Recently, Wolff and

Wright (1981a) have suggested that, in the absence of unequivocal evidence for a primary origin, all such cases should be treated as the result of secondary flow, and proposed the term "rheomorphic welded tuff" for the final rock body.

VI.3.i General field characteristics

The tuff sequence described corresponds to the Upper Mogan Formation of Schmincke (1970) and was erupted at 13.5 $\pm$ 0.25 m.y. ago (McDougall and Schmincke, 1977) from vents in the central part of Gran Canaria. The sequence outcrops over a wide area (Figure 6.2) but is particularly well exposed in coastal cliffs and roadcuts between Playa de Mogan and Arguineguin, and in deep barrancos leading inland. Key sections are shown in Figure 6.3. All the welded tuffs in this area are identified as ignimbrites, for the following reasons:

(a) Infilling of underlying topography, well-seen locally (Figure 6.4);

(b) Poor sorting chacteristics; where uncompacted or poorly compacted tuff is found, large (10-75 cm) pumice clasts are invariably seen to be dispersed in a matrix of fine ash;

(c) A fine-grained layer is present at the base of each cooling unit. The layer is generally unwelded, although instances of welding are seen (Figure 6.5), and tends to infill the underlying relief on the cm scale; comparatively thick accumulations are found in small depressions (Figure 6.5). The presence of such a layer is diagnostic of a pyroclastic flow origin (Walker, 1971; Sparks, 1976; Wright et al., 1980).

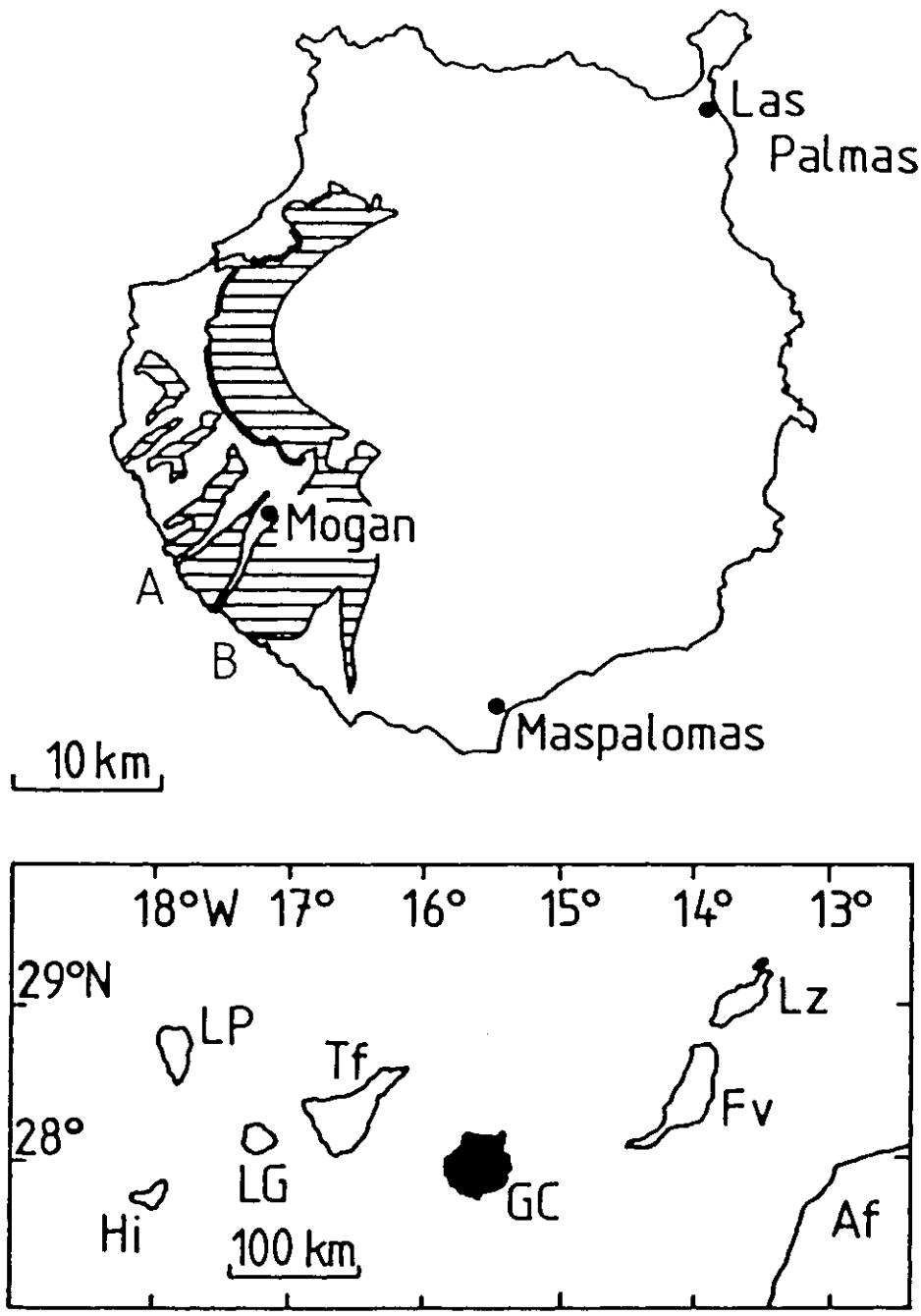

Fig. 6.2 Distribution of late Miocene - early Pliocene ignimbrite sequence on Gran Canaria (after Schmincke and Swanson, 1967). Horizontal rule: welded ignimbrites; thick line: caldera fault; A-B; coastal section studied and described here. Inset shows location of Gran Canaria.

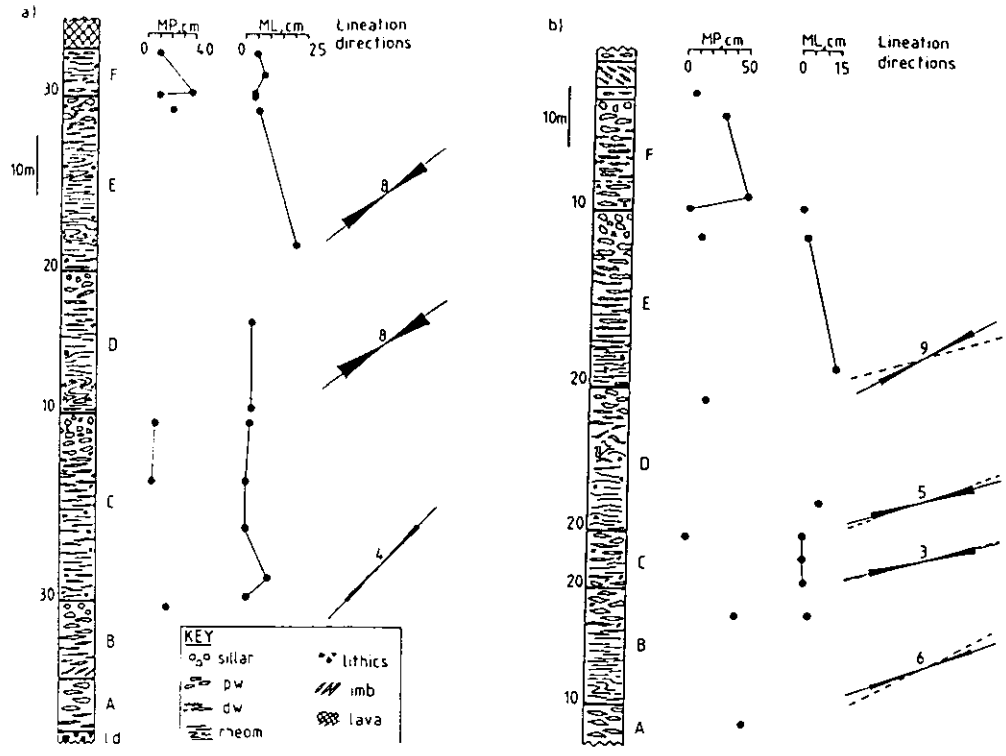

Fig. 6.3 Key sections through ignimbrite sequence, south-west Gran Canaria. MP = average of three largest pumice clasts at given stratigraphic level; ML = as MP for lithic clasts. Lineation directions show range of orientations found, mean orientation (solid line), slope direction of paleosurface (dashed line) where measured, and no. of measurements made. Numbers to left of columns refer to the maximum thickness of basal vitrophyre for each ignimbrite in cm. Capital letters are stratigraphic notation. l.d. = lava debris flow, pw = partly welded tuff, dw = densely welded tuff, rheom = rheomorphic welded tuff, imb = imbricate structure. a) Section in cliffs near mouth of Bco. de Mogan, 1 km NE of Playa de Morgan. b) Western wall of Bco. Medio Almud, 3 km E of Playa de Mogan. Dotted line in F is the only undoubted flow unit boundary found inside a cooling unit in these sections. Note sharp boundary between rheomorphic and densely welded tuff in ignimbrites B (b), D and E (a).

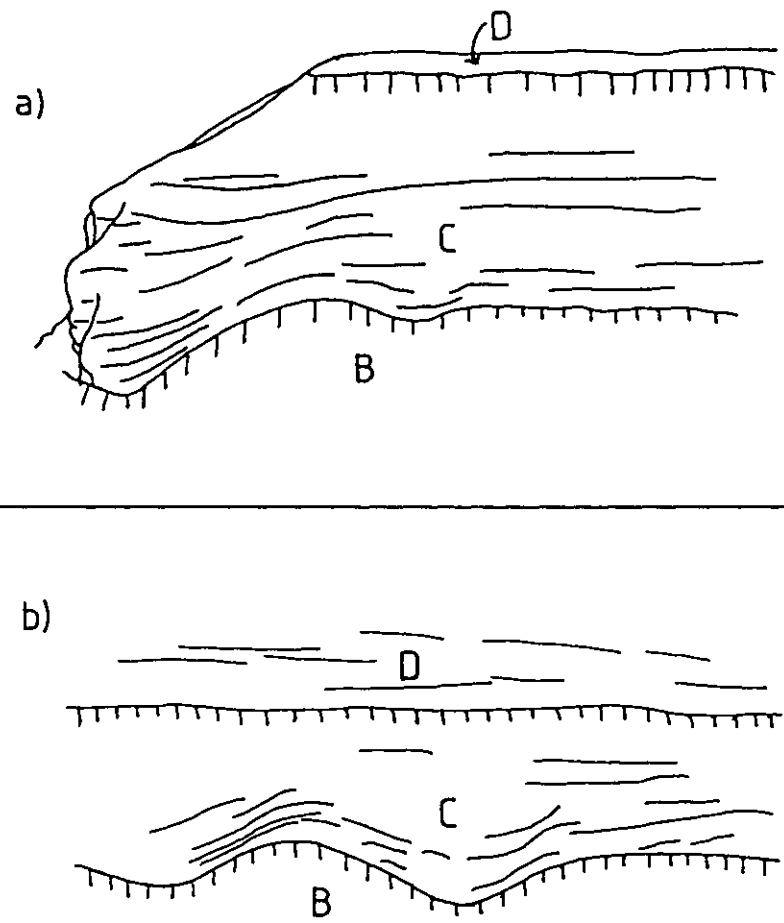

Fig. 6.4 Infilling of hollows in underlying topography by ignimbrite C, Bco. de Medio Almud. Note that foliation has been gently folded by compaction of tuff into hollows. Vertical hatch indicates weathered surfaces of ignimbrites. Letters are stratigraphic notation. a) E. wall of Bco. Medio Almud, 3 km E of Playa de Mogan; b) 100 m N of a). Ignimbrite C is ~10 m thick in a) and b).

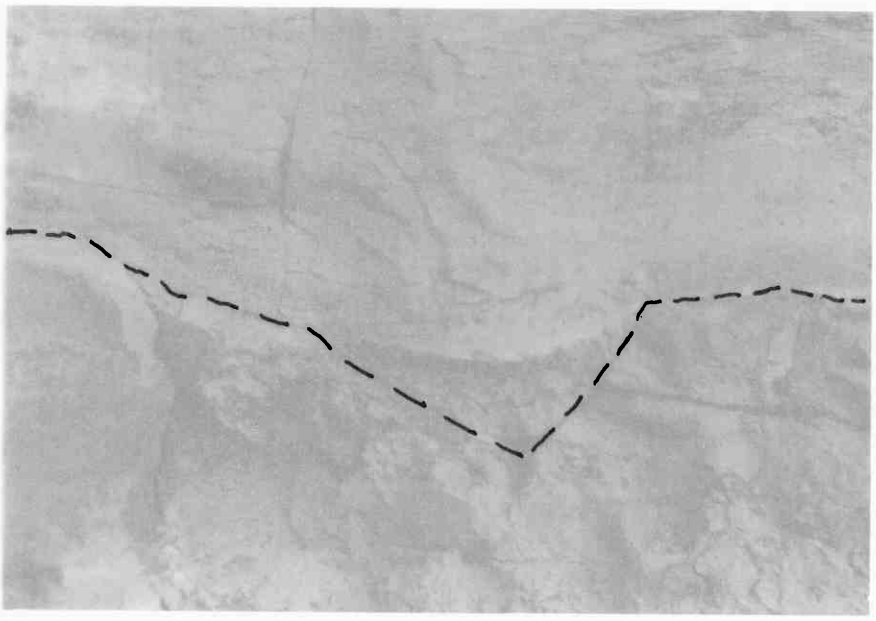

Fig. 6.5 Thick development of fine-grained basal layer in small hollow in paleosurface, base of ignimbrite C. Note welding of upper part of basal layer, and imbrication of fiamme immediately above. Dashed line on overlay marks paleosurface. Diameter of lens cap is 3.5cm.

Fig. 6.5 Thick development of fine-grained basal layer in small hollow in paleosurface, base of ignimbrite C. Note welding of upper part of basal layer, and imbrication of fiamme immediately above. Dashed line on overlay marks paleosurface. Diameter of lens cap is 3.5cm.

Tuff A, the lowest ignimbrite exposed in the area (Figure 6.3), rests on a hot-debris-flow deposit and is characterised by 2 m of green eutaxitic tuff grading upwards into a partly welded orange groundmass containing distinctive black fiammé. There is a locally well-developed fine-grained basal layer.

The remaining welded tuffs, B to F, are closely similar to each other and a general description is given here. Each ignimbrite forms a single cooling unit with only minor deviations from the simple pattern (Smith, 1960b) although, in favourable cases, individual flow units can be distinguished. Up to 20 cm of friable yellow material, interpreted as original non-welded pumice, normally marks the base of each cooling unit. A fine-grained lithic-free basal layer may be distinguished within this (Figure 6.5). The layer is best developed in small hollows in the pre-existing surface (Figure 6.5), and is extremely thin or absent where the underlying ground was smooth and flat. At such localities tuff may be welded to the very base, the lowest welded zone being a dark green to black vitrophyre. This is rarely more than 20 cm thick and passes upwards into eutaxitic welded tuff with imbricated fiammé (Figures 6.6, 6.7). This zone rapidly grades into densely foliated pale green or pink rheomorphic tuff which accounts for 25%-75% of an entire cooling unit. Lineations, tension cracks, flow folds and other flowage structures are developed in this zone; these are described in detail below. Alternate pink and green banding, which where undisturbed by folding is parallel to the palaeosurface, is developed in the crystalline matrix.

A sharp boundary with overlying partly welded tuff is commonly observed (Figure 6.3). Heavily oxidised deep brown or orange sillar forms the top of each cooling unit. Crude columnar jointing is

seen within the rheomorphic and upper partly-welded zones; in the former the joints are commonly lined with amorphous silica. Very rarely they deform the pre-existing structure (Figure 6.8).

Original pumice grain-size variations have largely been obscured by welding and viscous flow. The portions of each flow unit are sometimes richer in large pumice clasts than the bulk; for example the sillar of tuff B is rich in large pumice clasts up to 75 cm in diameter at one locality. Lithics are generally small (Figure 6.3), but in some cases (tuffs C, E) the largest are noticeably concentrated towards the base of flow units (Figure 6.3). Occasional large blocks of weathered sillar are thought to have been picked up from the paleosurface during flow. The ignimbrites therefore fall into the Type 2 class (Wilson, 1980) of moderate gass flow rates, and were fluidised to a similar degree to the Tenerife flows. The small and generally uniform lithic sizes (Figure 6.3) suggests that these ignimbrites are at some distance from their source vents: this agrees with the mapping of Schmincke (1970).

VI.3.ii Petrology of ignimbrite E

A petrological description of these rocks has been given by Schmincke (1970) and Schmincke and Swanson (1967a) who emphasised their peralkaline composition and simple phenocryst mineralogy (anorthoclase and amphibole, with minor amounts of augite, biotite, sphene and Fe-Ti oxides in some units). Some cooling units are heterogeneous, with upward increase in the amount of Fe-Ti oxides and augite. The groundmass consists chiefly of alkali feldspar, aegirine, and quartz. The results of an electron microprobe study of E, the most strongly welded and rheomorphic of the ignimbrites, are presented here.

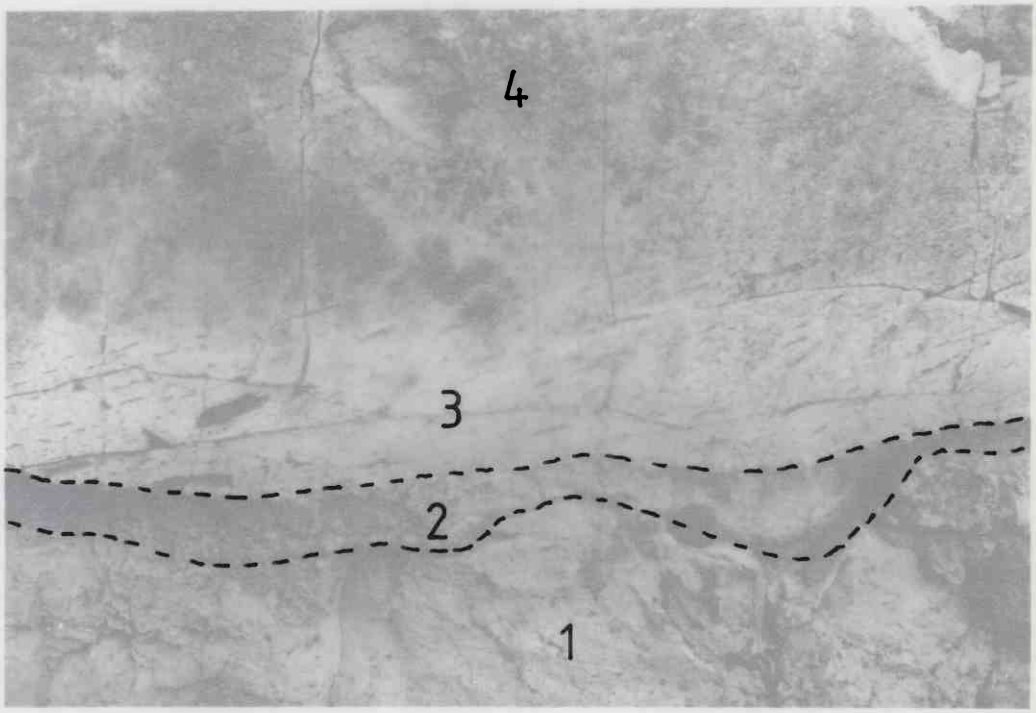

Fig. 6.6 Imbrication of fiamme in basal part of ignimbrite D. On overlay, 1: underlying ignimbrite; 2: basal non-welded zone; 3: imbricate structure; 4: foliated densely welded tuff. Diameter of lens cap is 3.5cm. The primary pyroclastic flow moved from left to right in the photograph.

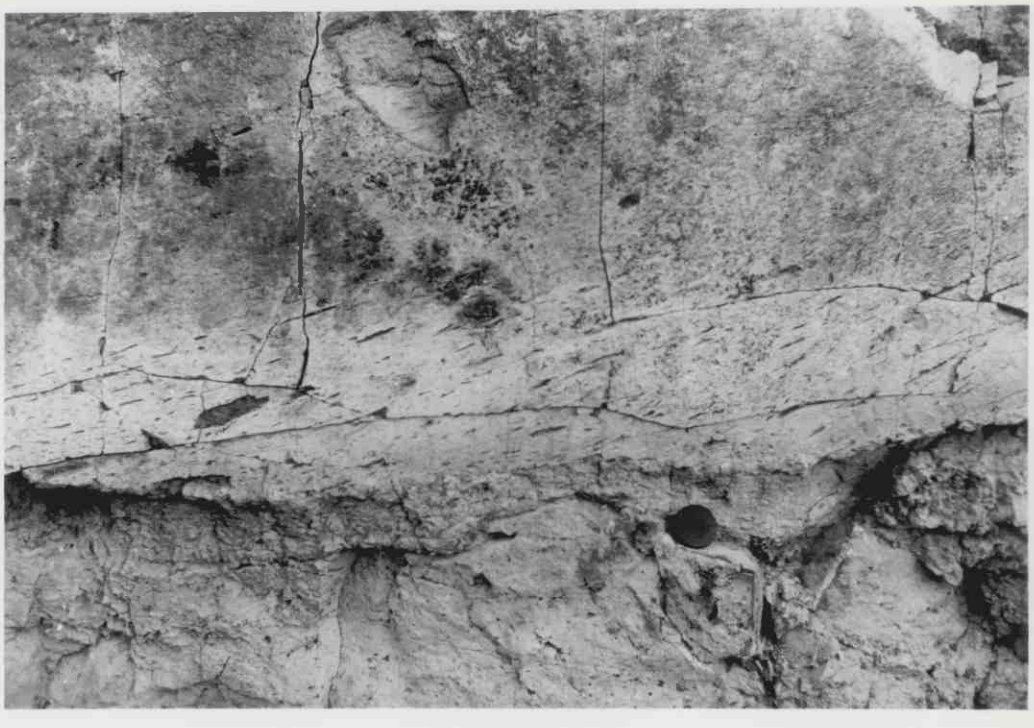

Fig. 6.6 Imbrication of fiamme in basal part of ignimbrite D. On overlay, 1: underlying ignimbrite; 2: basal non-welded zone; 3: imbricate structure; 4: foliated densely welded tuff. Diameter of lens cap is 3.5cm. The primary pyroclastic flow moved from left to right in the photograph.

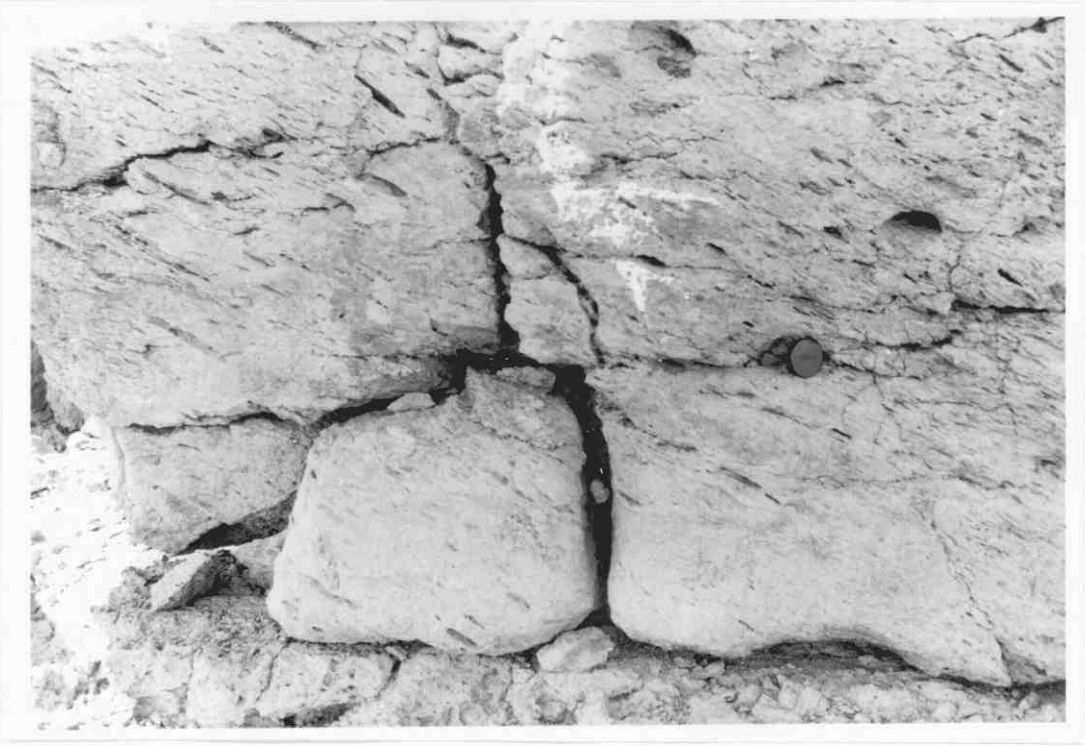

Fig. 6.7 Strongly imbricated fiamme, undesignated ignimbrite above unit F, W side of Bco. Medio Almud, 3km E of Playa de Mogan.

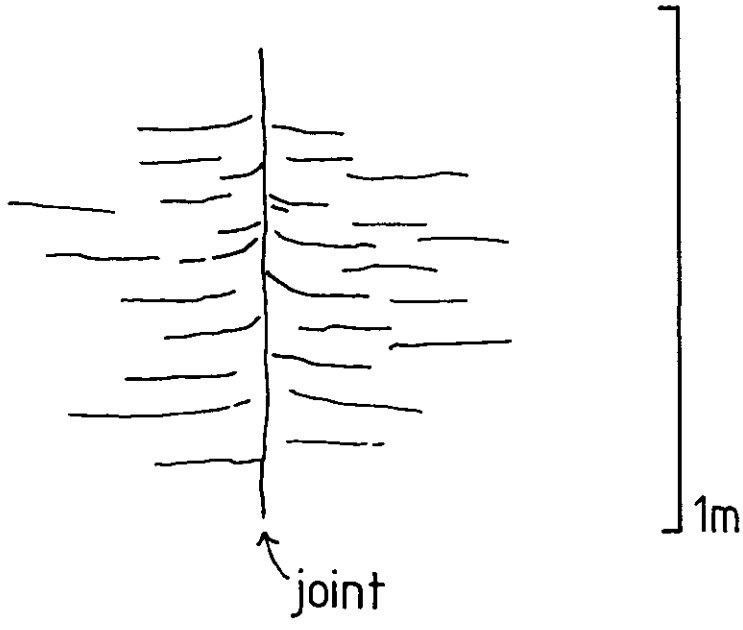

Fig. 6.8 Deformation of foliar fabric around cooling joint, ignimbrite E, location as Fig. 6.3b). Joint is filled with vitreous silica.

Phenocrysts

The large ($\leqslant$ 1 cm) tabular anorthoclase crystals are virtually constant in composition at Or_{29-30}.

Two amphiboles, green and brown, are present. The green type shows varying amounts of (Na+K) substitution for Ca in the X site, and Si for Al in the Z site (richterite-edenite solid solution), while the brown variety is closer to kataphorite in composition (Figure 6.9). No systematic variation in amphibole composition with height above the base of the cooling unit was found.

Three Fe-Ti oxides are present: titanomagnetite (Usp_{30}), ilmenite (Ilm_{85}) and, rarely, a manganiferous ilmenite similar in composition to the late-stage Mn-ilmenites in the Tenerife syenites (Chapter V). Magnetite grains have suffered some post-eruptive oxidation at their margins but the cores appear unaffected. Ilmenites are homogeneous and also apparently unoxidised. Ilmenite-magnetite pairs are found in petrographic equilibrium and their minor element abundances show similar equilibrium relationships as those discussed in Chapter III; the manganiferous ilmenite presumably therefore was not in equilibrium with the other oxides. Mineral pairs yield a temperature of 840°C and an oxygen fugacity of $10^{-12.5}$ bars.

Groundmass phases

The groundmass in the samples studied consists of aegirine, feldspar and quartz together with small amounts of sub-microscopic iron oxides in the samples of pink tuff. The aegirine displays the same enrichment in Ti and excess of Na over Fe as is found in the late pyroxenes of the Tenerife syenites (Chapter V), but to a

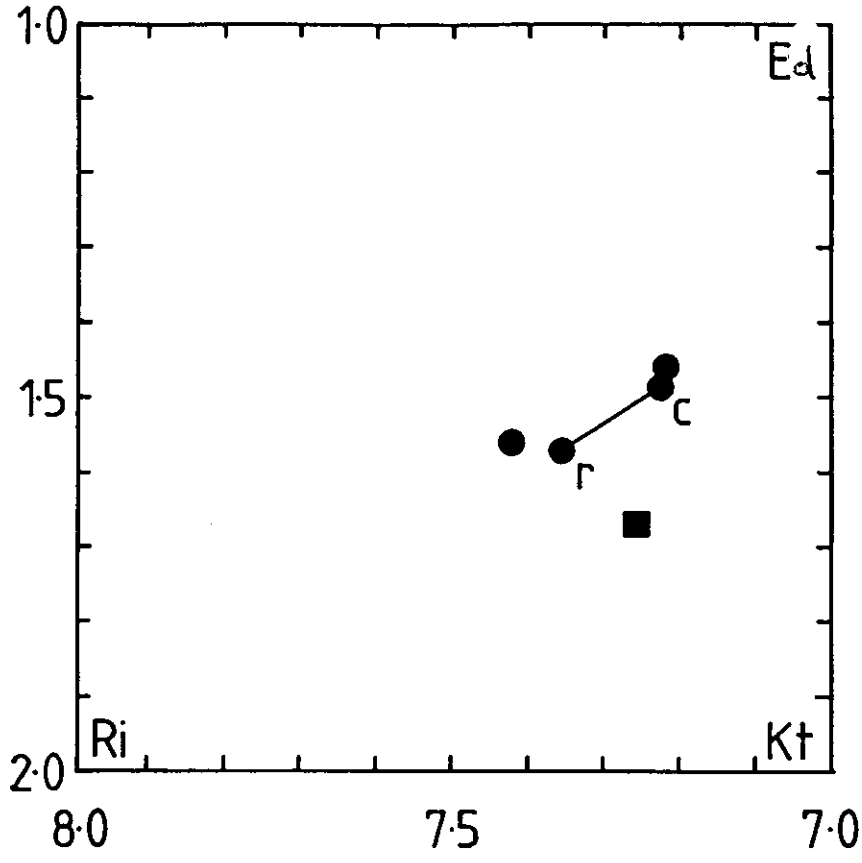

Fig. 6.9 Si vs. (Na+K), cations per 23 oxygen atoms, for amphiboles in ignimbrite E. c = core, r = rim of one zoned crystal. Ed = edenite, Kt = kataphorite, Ri = richterite. Circles = green amphibole, square = brown amphibole.

greater degree. In this case the NAT endmember (Grapes et al., 1979, Nielsen, 1979) also accounts for the observed composition more satisfactorily than the molecules proposed by Scott (1976, 1977) and Ferguson (1977), with only 3% of the Na remaining unassigned after the calculation of endmember proportions. The pyroxene is very nearly a binary solid solution between NAT and acmite in the proportions 40:60 (anal 705), close to the maximum NAT content of Ti-aegirines found by Nielsen (1979).

The other mineralogical peculiarity of the matrix assemblage is the iron content of the feldspar; the $(Na,K)Fe^{3+}Si_3O_8$ content of groundmass feldspars is about 8%, compared with 2%-3% among the phenocrysts. Similarly, the groundmass feldspars of the Green Tuff of Pantelleria (VI.4) have an iron-feldspar content of up to 10%. Up to 20% $KFe^{3+}Si_3O_8$ in groundmass sanidine was reported by Carmichael (1967b) in orendites from the Leucite Hills, Wyoming, and ascribed by him to the perpotassic nature of the whole rock. Orendites, however, are low in Na_2O, and the groundmass pyroxene is diopside rather than aegirine. It is difficult to see how simple peralkalinity could directly cause appreciable substitution of Fe^{3+} for Al in feldspar of composition Ab_{60} in the presence of aegirine. Leaving aside the question of increasing Fe^{3+} concentration during cooling, another effect may be responsible. In a rock consisting principally of aegirine, feldspar, and quartz, an equilibrium:

$$\underset{\text{pyx}}{NaFe^{3+}Si_2O_6} + \underset{\text{qz}}{SiO_2} \rightleftharpoons \underset{\text{fsp}}{NaFe^{3+}Si_3O_8}$$ may be envisaged.

Increasing activities of silica and $NaFeSi_2O_6$ will drive the reaction to the right, and thus increase the iron content of the feldspar. The low Fe^{3+} contents of phenocryst feldspars reflect the absence of quartz and pyroxene in the phenocryst assemblage. Similar relationships are seen in the two phenocryst assemblages of the Green Tuff of Pantelleria, where the presence of quartz, and increasing soda content of pyroxene, are accompanied by an increase in Fe content of feldspar (VI.4).

VI.3.iii Flowage Structures

As noted above, ignimbrites B through F display evidence of coherent viscous flowage. Of these, unit C shows only a weak linear fabric and occasional rotation of lithic fragments. Unit E has the greatest abundance of structures and the bulk of the observations below are taken from this horizon, with subsidiary data from ignimbrites B, D and F. Many of the data presented here have been summarised by Wolff and Wright (1981a).

Extensional Structures

Elongation of fiamme imparts a variably-developed linear fabric imposed on the normal eutaxitic foliation. Well-developed lineations take the form of closely-spaced parallel ridges, several mm wide and up to tens of cm long, on the foliation surface (Figure 6.10). Except where folded, the orientation of the linear fabric is virtually constant and closely parallels the dip of the underlying surface (Figure 6.3). The accompanying foliation also parallels slope and is commonly intense, giving the rocks a well-developed layering and a phyllitic appearance in the field. Where best developed, it is associated with intense lineation. Late-stage tension cracks,

oriented normal to the elongation direction, are common in fiammé (Figure 6.11). Their presence demonstrates, at least during the final stages of flowage, a considerable competency contrast between fiamme and matrix; fold styles (see below) supply further evidence. In side elevation, cracked fiammé are separated into discrete boudins which are frequently rotated into the flowage direction (Figure 6.12); this rotation is also seen with lithic clasts. Rarely, rotation is in the opposite sense to regional flowage, indicating local perturbations in the velocity profile of the flow.

Imbricate structure

This is characterised by eutaxitic texture having a consistent upslope dip of 30°; it is commonly found in the basal 1 m of the densely welded zone and persists to the very base (Figures 6.6, 6.7). Where this zone is unusually thin ($<$ 5 m), however, it may persist throughout; it does so in the absence of any other flow structures. Normally, however, it passes upwards into densely foliated rock with decreasing dip and increasing flattening of fiammé. Rarely, where individual flow units can be distinguished, the structure is seen in the basal part of several flows in the same cooling unit. These features indicate that the structure forms rapidly and during the initial stages of welding.

Flow folds

Folds occur sporadically throughout tuffs B, D, E and F; products of intense folding up to 150 m across occur in E, and the bulk of the data below are taken from these. The pockets are associated with local perturbations in the underlying topography, as seen at the principal fold locality 3 km east of Playa de Mogan

Fig. 6.10 Lineations on sub-horizontal foliation surface, ignimbrite B, Bco. Medio Almud. Diameter of lens cap is 3.5cm.

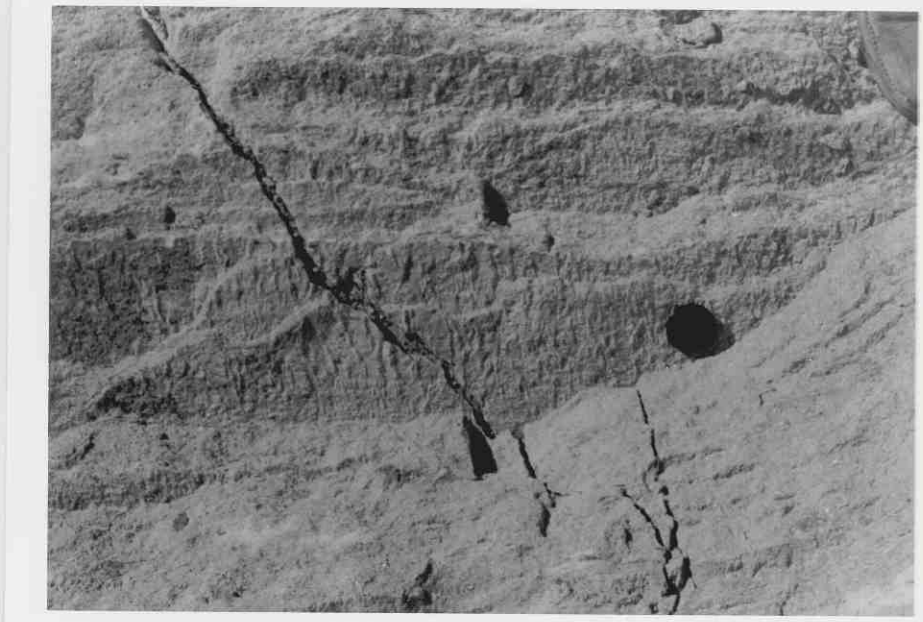

Fig. 6.11 Tension cracks in a stretched pumice lapillus, ignimbite E (note photograph looks down onto sub-horizontal foliation surface). Cracks are nearly normal to movement direction as indicated by lineations. Diameter of lens cap is 3.5cm.

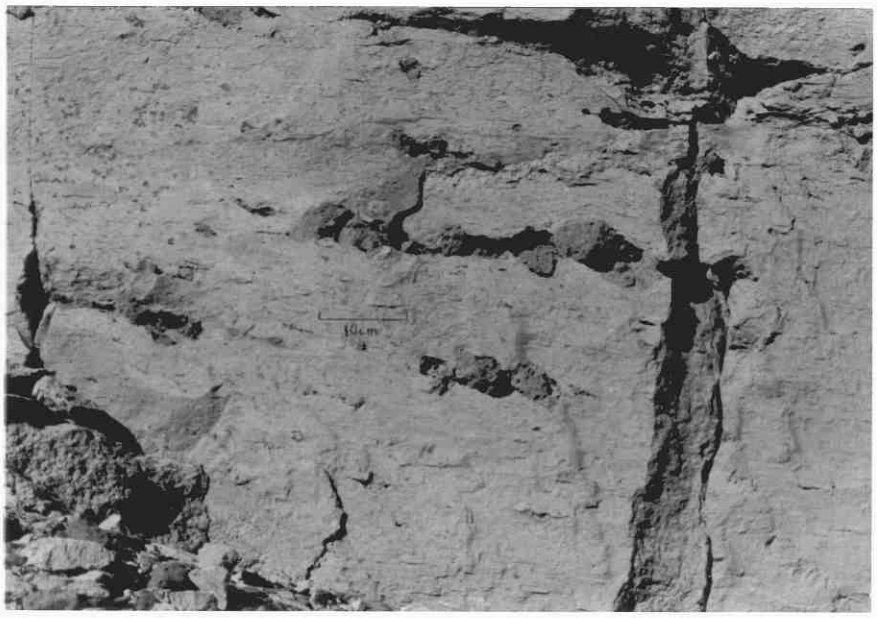

Fig. 6.12 Rotation of fragments of cracked fiamme by laminar flow (shearing) of matrix, ignimbrite E. Flow direction from left to right. Fragments have been rotated by up to 30°. Scale drawn on vertical rock surface in left-centre of photograph.

(Figure 6.2). Folding affects stretched fiamme, foliation, lineation, welding-zone boundaries and colour banding.

The distribution of fold sizes was investigated by measuring wavelength and amplitude of individual folds. Where "full-wavelength" fold units were not present, measurements were taken on "half-wavelength" units and doubled. Where intrafolial fold packets without clearly defined inflexion points were present, the "height" and "width" of the packet were measured (Woodcock, 1976); these measurements were doubled to give wavelength and amplitude respectively. Fold size varies from a few mm to tens of metres, the majority being in the sub-1 m size range; the size frequency distribution (Figure 6.17) is crudely lognormal, as is the case for minor tectonic folds (Hudleston, 1973c) and sedimentary slump folds (Woodcock, 1976).

Over 85% of folds have dimensions less than 1 m, and over 50% are less than 10 cm in size. Fold amplitudes tend to be slightly smaller than wavelengths (Figure 6.13). Within the sub-10 cm size range, the size distribution is much more even than over the whole observed range for both wavelength and amplitude, although the dominant size for each is 2-4 cm (Figure 6.13c, f). Folds of less than 0.5 cm dimensions were not measured, although few of these were observed. The large numbers of sub-10 cm folds reflects the occurrence of discrete small volumes of rheomorphic tuff within which very many small-scale folds are developed. The significance, if any, of the anomalously large number of folds with dimensions between 6 and 8 cm is unknown. The dip of fold axial surface varies from upright to recument. There is a correlation between interlimb angle and fold attitude (Figure 6.14), tighter folds having more gently inclined

axial planes than open folds. This points to the initiation of folds as gentle upright structures in the place of the welded sheet; with progressive deformation, tightening and overturning of the folds towards recumbency occurred (Figure 6.15). Slump folds show an analogous deformation history (Woodcock, 1976).

Fold surface shapes have been classified by Fourier analysis (Hudleston, 1973a). "Quarter wavelength" segments of folds have been fitted (using the computer program of Hudleston, 1969) to a function of the form

$$f(x) = b_1 \sin x + b_3 \sin 3x + \ldots$$

where b_1 and b_3 are constants for a given segment. Each fold segment is represented by a point on a plot of b_1 vs. b_3 calibrated by the "shape" and "amplitude" factors of Hudleston (1973a). The plot reveals a range of shapes between chevron and semi-elliptical folds at low to medium amplitudes with a tendency towards semi-elliptical at high amplitudes (Figure 6.16). Despite the large amplitude variation for a given shape, the general trend of the distribution resembles that found in experimental single-layer buckles (Hudleston, 1973b), metamorphic rocks (Hudleston, 1973c) and slumped sediments (Woodcock, 1976).

Fold layer shapes cover the whole range of Ramsay's (1967) classification; class 1c (Figure 6.17b) and class 2 (Figure 6.17c) are the most common. Class 1a and 1b folds, with strongly convergent dip isogons, are generally restricted to fiammé folded on the cm scale; class 3 folds, with divergent dip isogons, are found in the associated matrix (Figure 6.17a). This shows a competency contrast between fiammé and matrix, the more competent fiammé being comparatively resistant to plastic deformation, although it must be noted that

the reciprocal relationship is occasionally found. Class 2 (similar) folds are most commonly found where the texture, picked out by fiamme and banding, is folded on the scale of tens of cm to a few metres (Figures 6.17c, 6.18).

Interference patterns or refolded folds, are commonly found and may be locally abundant. Type 3 (Ramsay, 1967) is the most common configuration (Figure 6.19); type 2 is also found. Both types are formed when recumbent folds are refolded by new structures with steeply inclined axial surfaces, and their presence is thus consistent with continuous fold initiation and development over a period of time (Figure 6.15). Occasional patterns of great complexity are also seen, suggesting several folding deformations.

Discussion

Compaction and welding of tuff is a simple flattening process giving the classic eutaxitic texture (Ragan and Sheridan, 1972). Viscous flowage imposes a secondary stretching deformation on this, resulting in a variably-developed linear fabric of fiamme elongated in the flowage direction. The development of a linear fabric is hence a necessary consequence of laminar viscous flowage in welded tuffs and is taken as the diagnostic criterion for the recognition of the process. Lineation is developed before any other features except the imbricate structure, which was formed during the final deceleration of the primary flow (see below). In all cases lineation parallels paleoslope dip (Figure 6.3), demonstrating the dominant influence of gravity in controlling the phase of flowage responsible for the generation of the observed structures. However, as each ignimbrite was emplaced on smooth paleotopography, post-depositional flowage

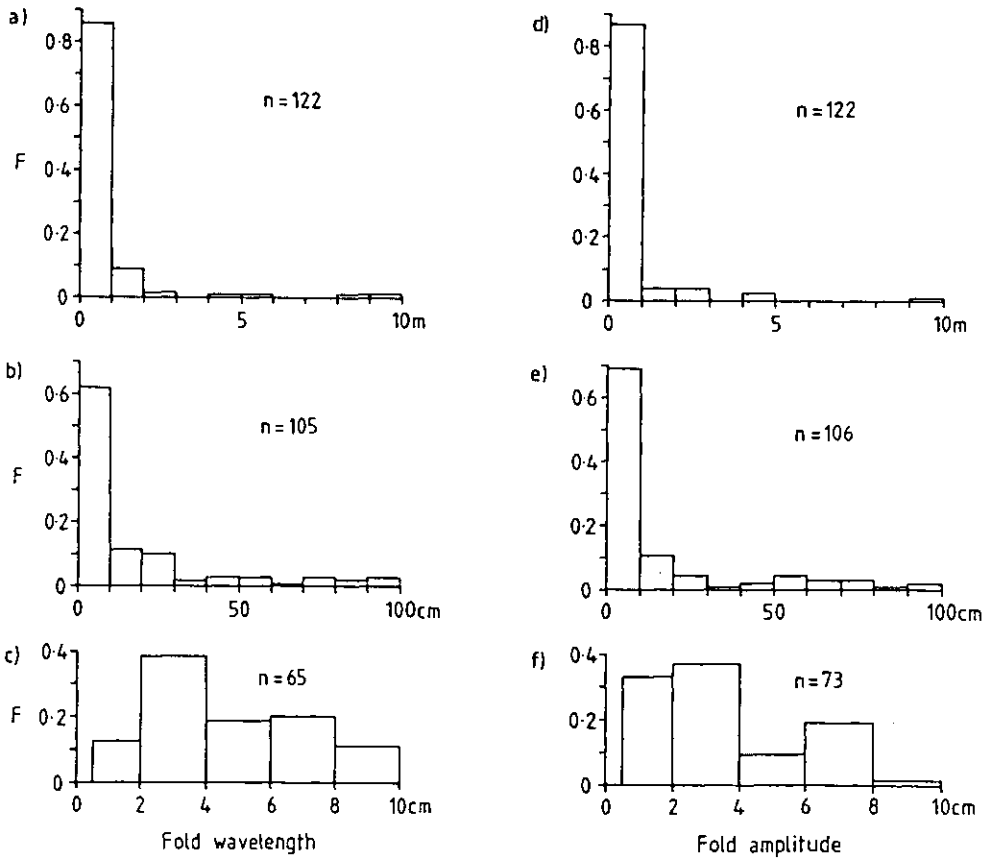

Fig. 6.13 Frequency histograms for wavelength (a,b,c) and amplitude (d, e, f) of folds from ignimbrites B, D, E and F. a) and d) show data for all folds measured; b) and e) for those with dimensions less than 1 m; c) and f) for those with dimensions less than 10 cm. Folds of less than 0.5 cm size were not measured. For clarity, the very large fold illustrated in Fig. 6.20 has been omitted.

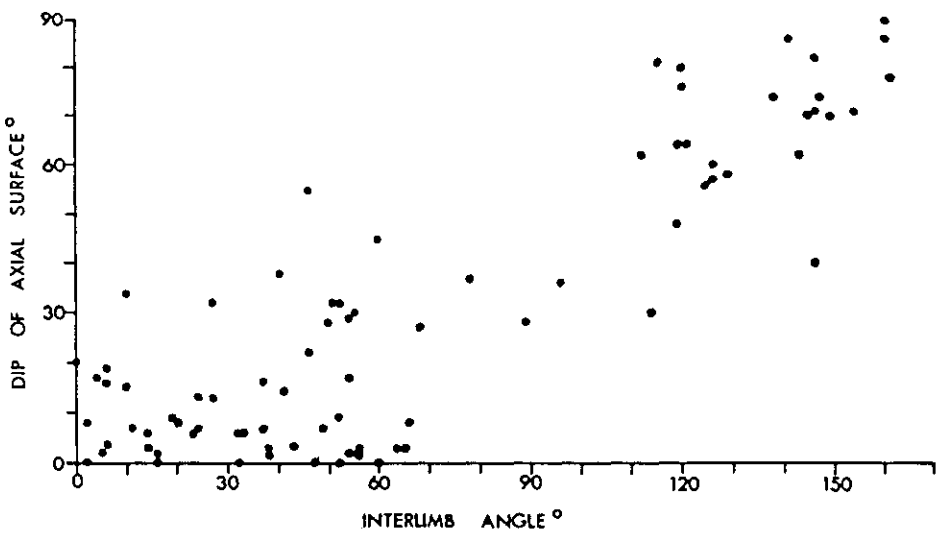

Fig. 6.14 Relation between dip of axial surface and interlimb angle of folds in ignimbrites B, D, E, F.

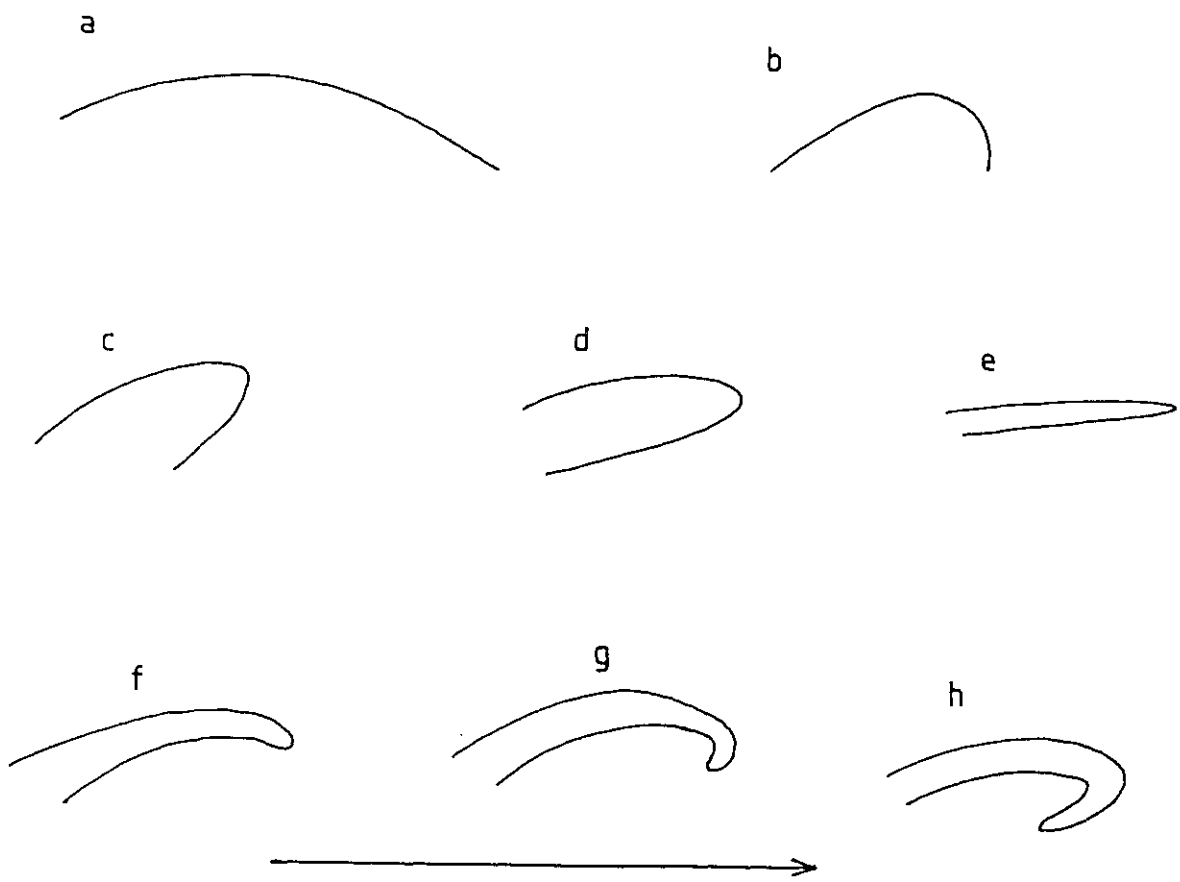

Fig. 6.15 Schematic representation of fold development during viscous flow, a through h. At f, a new fold has been initiated on the axial surface of the pre-existing structure, resulting ultimately in a Type 3 (Ramsay, 1967) interference pattern, h. Arrow nominally represents movement direction, though this is unimportant during early stages a-b (Borradaile, 1972; Sanderson, 1973).

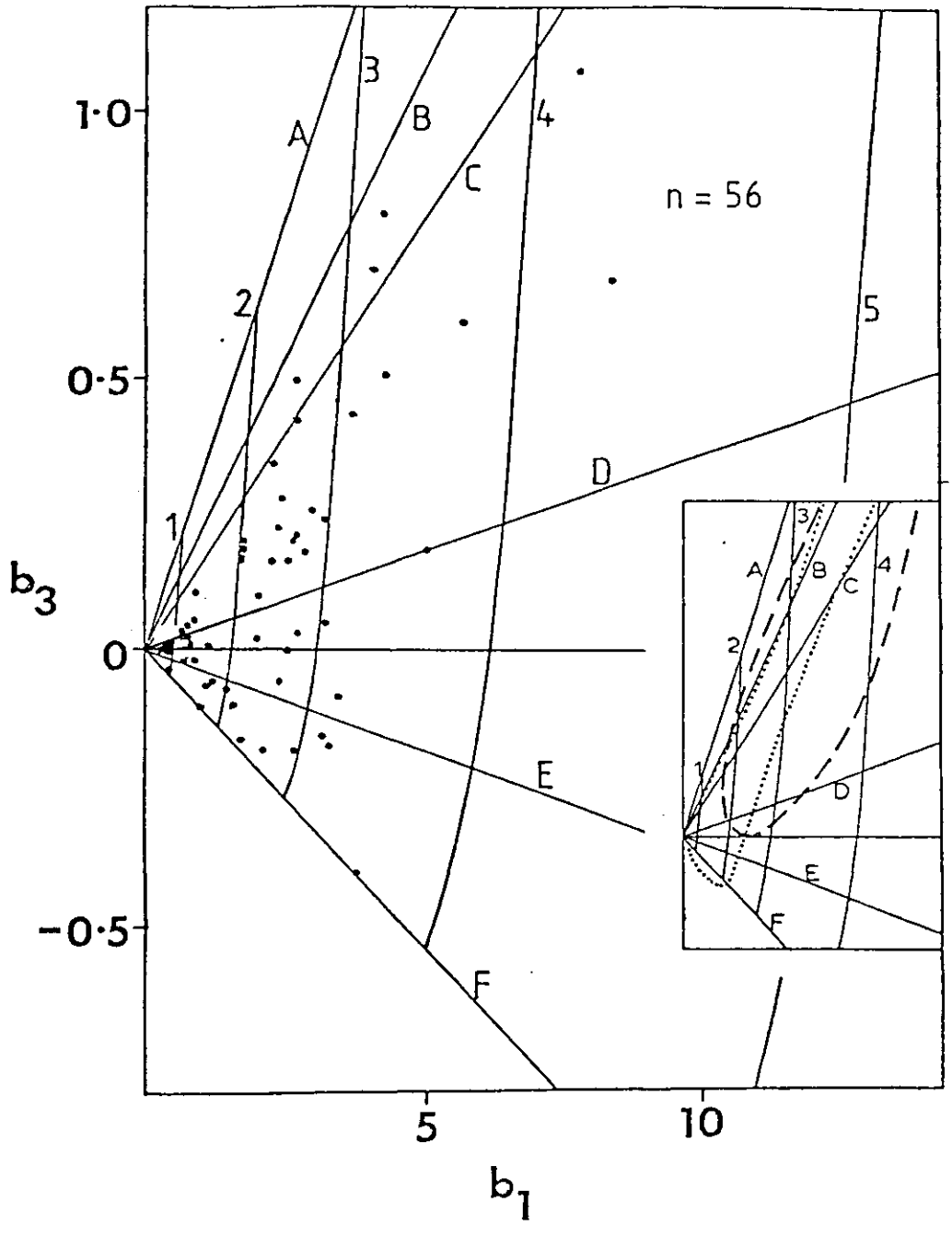

Fig. 6.16 Plot of harmonic coefficients b_1 vs b_3 for flow folds in ignimbrites B, D, E and F. The fold shapes represented by the shape factors A-F of Hudleston (1973a) are: A: box folds; C: semi-ellipses; D: parabolas; b_3 = 0: sine waves; F: chevron folds. Inset: dashed line: field of small scale tectonic folds (Hudleston, 1973c); dotted line, field of sedimentary slump folds (Woodcock, 1976).

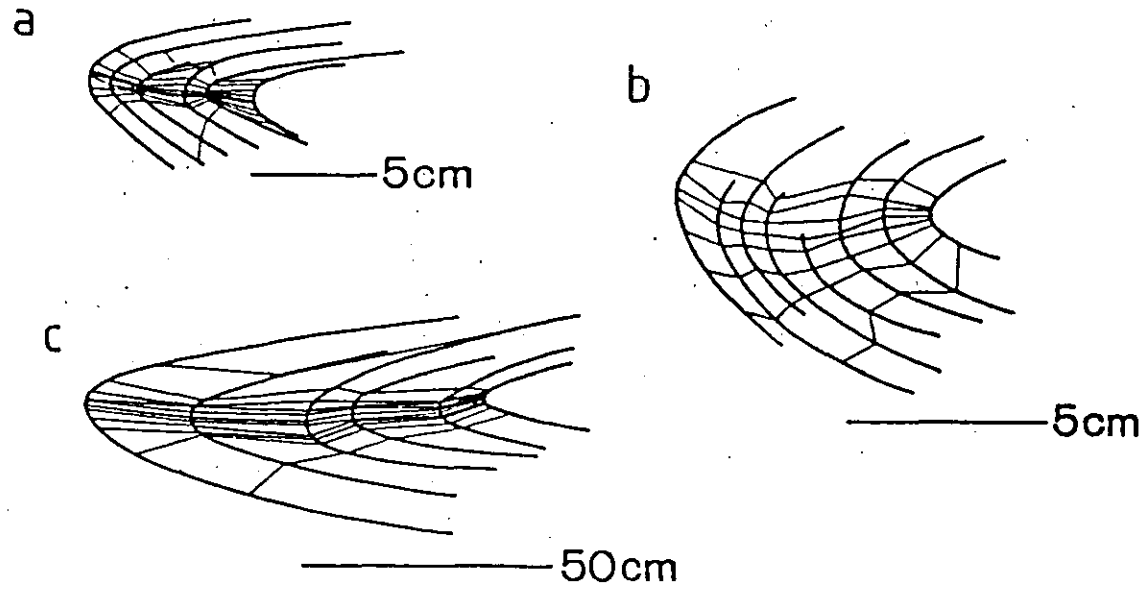

Fig. 6.17 Flow folds in ignimbrite E with dip isogons constructed at 15° intervals. a) Alternating class 3 layers, with convergent dip isogons, and class 1 layers. b) Class 1c fold c) Approximately similar fold (class 2).

Fig. 6.18 Recumbent similar folding in bulk of welded tuff, ignimbrite E. Notebook is approx. 20cm x 12cm.

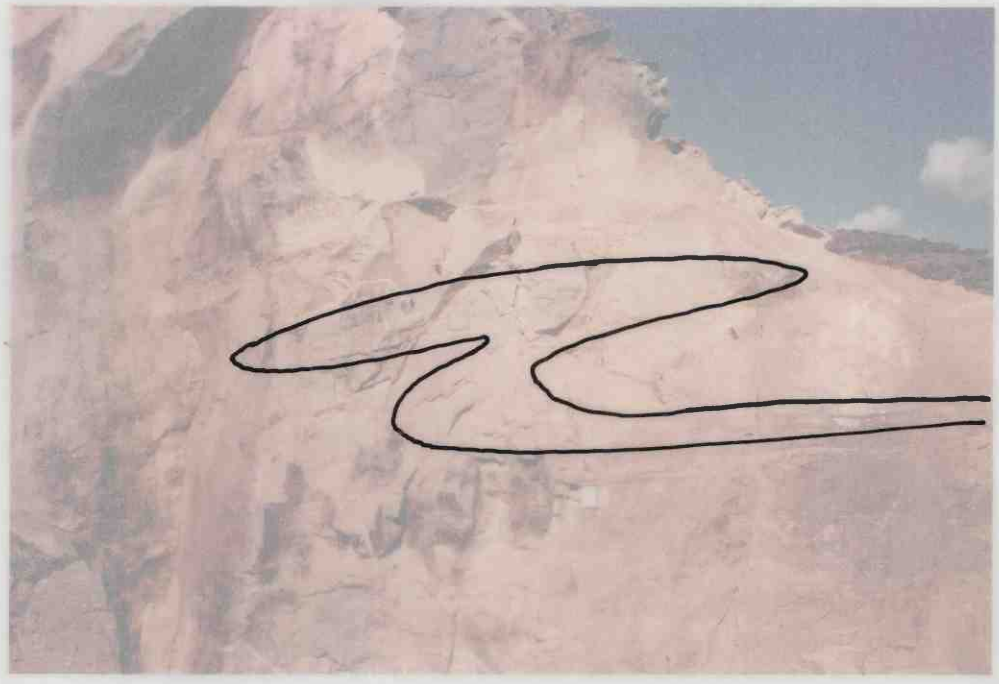

Fig. 6.19 Refolded fold, picked out by colour banding, ignimbrite E. Fold conforms approximately to the Type 3 interference pattern of Ramsay (1967).

Fig. 6.19 Refolded fold, picked out by colour banding, ignimbrite E. Fold conforms approximately to the Type 3 interference pattern of Ramsay (1967).

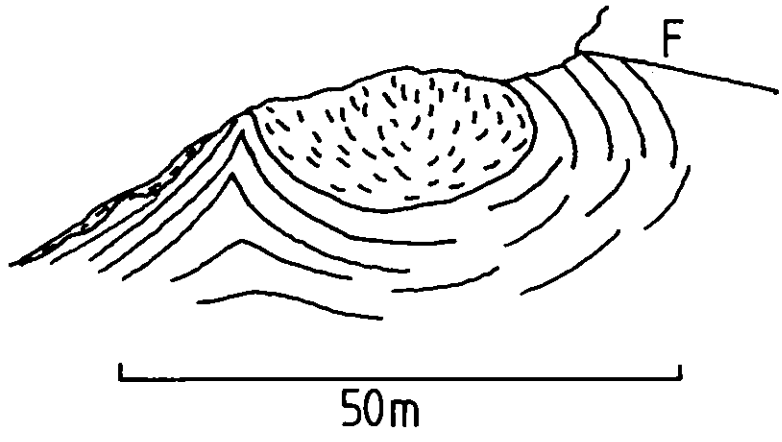

Fig. 6.20 50m wavelength fold deforming boundary between densely-welded and partly-welded zones, ignimbrite E. Dashed ornament indicates orientation of eutaxitic fabric within partly-welded zone; lined ornament indicates rheomorphic fabric in densely-welded zone. F is overlying unit. Coastal road section near point B in Fig. 6.2.

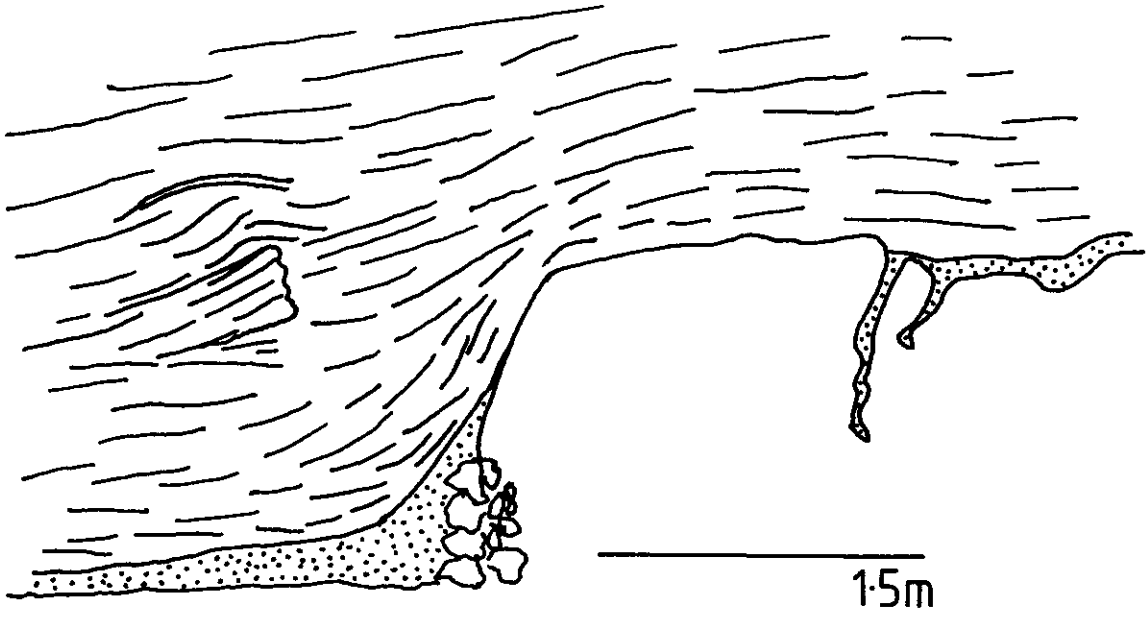

Fig. 6.21 Relations around a 1.5m step in pre-existing surface under ignimbrite E. Blank ornament is underlying ignimbrite D (note weathered rubble of D accumulated at base of step); stipple is the non-welded basal part of E; lined ornament denotes foliation in densely-welded/rheomorphic E. Note penetration of old cracks by non-welded E ash; gentle monoclinal folding of foliation in E; and (left of centre) competent block petrographically indistinguishable from surrounding more fluid material. Road section 0.5km SE of locality in Fig. 6.20.

direction will duplicate that of the primary flow and thus lineation directions alone cannot be used as evidence for either primary or secondary flowage.

The intense foliation is also predominantly the product of viscous flowage. Simple compaction of pumice resulting in loss of pore space does not normally result in axial ratios greater than 20:1 among fiamme (Ross and Smith, 1961); ratios up to 300:1 are observed in ignimbrite E. Foliation has therefore been intensified by the same stretching deformation which produced the linear fabric; lineations are invariably dispersed on the foliation surface (Figure 6.13).

Folds afford the most spectacular evidence of viscous flowage and provide information on the rheological properties of the flow. Fold styles have therefore been examined in some detail. The deformation of welding-zone boundaries (Figure 6.20) and colour banding (Figure 6.19), both of which are post-depositional features, unequivocally shows that at least part of the viscous flowage was rheomorphic in origin.

The association of folding with paleotopographical irregularities suggests that the roughness of the underlying surface plays an important role in fold initiation; this is clearly demonstrated in ignimbrite E at one locality where monoclinal folding has been induced by compaction and flowage over a small vertical step (Figure 6.21). Similar relationships are seen where tuff C folds into hollows in the underlying surface (Figure 6.4); fold-shapes have been produced by compaction around the underlying irregularities.

Small folds may be induced by internal inhomogeneities such as lithic fragments and complex mm-scale folding is found in the pressure shadows of some lithics. Rheological variations in the bulk of the sheet, perhaps the result of varying degrees of groundmass crystallisation, may also initiate folds (Figure 6.21). Once initiated, folds are developed by laminar flow into recumbent isoclinal structures; initiation of new folds at this stage results in interference patterns (Figure 6.15). Assuming that zones of intense folding are induced by topographic steps, rheomorphic movement distances may be estimated from the distance between the step and the furthest "downstream" folds. For ignimbrite E, estimates range from $\sim$1 m for the locality in Figure 6.21 to $>$100 m for the main fold locality 3 km E of Playa de Mogan.

The wide scatter in fold shapes as compared to those found in other media (Figure 6.16) may be a consequence of the high bulk ductility of silicate liquids (compared to materials normally encountered in structural geology) combined with competency contrasts caused by fiamme and other heterogeneities. The development of both similar folds (class 2) as well as more parallel styles (class 1) indicates the operation of both simple shear and flexural slip mechanisms respectively during folding (Ramsay, 1967). Flexural slip has operated where competent layers (e.g. fiammé) have been folded on a small scale such that the layer thickness is an appreciable fraction of the fold size. Despite this evidence for small-scale heterogeneities, the predominance of similar folding on the metre scale indicates that the bulk of the flowing mass may be considered as a homogeneous fluid.

Tension cracking of fiamme and rotation of the resultant fragments shows that the matrix was behaving as a liquid when fiamme had become essentially solid at the prevailing strain rate. Similar contrasts are seen in the body of a sheet (Figure 6.21). Varying rates of groundmass crystallisation may be responsible. Partly crystallised lavas exhibit non-Newtonian rheology (Sparks and Pinkerton, 1978); yield stress increases with increasing degree of crystallisation. Thus there will come a point during the cooling of a flow where the yield stress is greater than the applied gravitational stress; at this point deformation will cease and existing structures will be preserved in the finally solidified rock. Therefore, most fiamme must initially crystallize more rapidly than the matrix, and competent blocks within more fluid welded tuff serve to delineate areas of comparatively rapid crystallisation in the matrix.

Generation of the imbricate structure may be also explained in terms of non-Newtonian rheology. Liquid foams have a Bingham or pseudoplastic rheology, much as do those bearing solids in suspension. Their apparent viscosities are thus strain-rate dependent (Figure 6.22) and are low in high strain-rate situations (and vice versa). Sparks (1976), Wright (1979), Fisher (1979), Wright and Walker (1981) and C.J.N. Wilson (1980) emphasize that pyroclastic flows are emplaced as high-concentration debris flows in many ways analogous to mudflows. Such flows halt rapidly by sudden "freezing", resulting in a high shear stress being momentarily imposed on the constituent clasts. Transient clast strain rates will be high and shearing of clasts results, giving a uniformly oriented fabric. The fabric is preserved at the base of the welded sheet, where cooling is sufficiently rapid to preclude the onset of rheomorphism. The energy required for clast deformation is

the momentum of the primary flow, and this structure is therefore primary in origin.

The relevance of structures described here to paleogeographical reconstructions of ancient deformed volcanic successions where similar rocks occur is worth comment. Lineations are potentially excellent indicators of the movement axis. Analysis of the linear fabric within the Ordovician Pitt's Head ignimbrite of Snowdonia indicates a movement axis (Wolff, 1976) consistent with paleoslope as determined by other criteria (Shackleton, 1959). The sense of rotation of lithics and discrete fragments of tension-cracked fiamme will give the direction of paleoslope when combined with lineation measurements, provided a statistically significant sample is taken. Folds, however, should be approached with caution as there is no criterion of style by which rheomorphic folds may be distinguished from tectonic structures. Large (10-50 m wavelength) rheomorphic folds which deform welding-zone boundaries could easily be misinterpreted as having a tectonic origin.

Origin of structural relations

Wolff and Wright (1981a) have shown that, on simple theoretical grounds, rheomorphism of welded tuffs should be a much more widespread phenomenon than is actually the case. The reasons why it is not are briefly discussed by Wolff and Wright, but the salient point is the (theoretical) ease with which rheomorphism can develop in welded tuffs emplaced on gentle slopes. Therefore it is more satisfactory to treat equivocal evidence for primary vs. secondary viscous flowage as having a secondary origin. It may be noted that previous workers favouring primary viscous flow (e.g. Schmincke and Swanson, 1967a;

Chapin and Lowell, 1979) do not supply appropriate evidence in support of their case.

A reconstruction of events occuring between eruption and lithification may now be attempted.

The primary particulate pyroclastic flow has travelled at least 20 km from its source vent (Schmincke, 1970). Eventually, the gas flow rate within the semi-fluidised mass decreases to the point where the yield stress is less than the movement shear stress, and the flow rapidly halts. As it halts, the soft pumice fragments sinter together and shear to give a partly-welded tuff with a foliation dipping steeply "upstream": the imbricate structure. At this point, the flow may be regarded as a foam whose predominantly glassy framework has a non-Newtonian rheology. Compaction now proceeds, through deformation of the glass itself, generating a eutaxitic foliation which parallels the underlying surface, except at the base where cooling is sufficiently rapid to preserve the primary imbricate structure. Nearer the centre of the sheet, where cooling is negligible (Riehle, 1973) rheomorphic flow is initiated. Lineations, flow folds and lithic rotation structures are generated. At the height in the flow where the yield stress of the foam is equal to the applied gravitational stress, a sharp boundary may develop above which viscous flow cannot occur; this is the boundary between the rheomorphic and upper partly-welded zones (Figure 6.3). The rigid partly-welded zone is then rafted along on top of the rheomorphic flow. (A similar sharp boundary has been described from a rheomorphic welded tuff in Oregon, Walker and Swanson, 1968). As groundmass crystallisation proceeds, rheological inhomogeneities

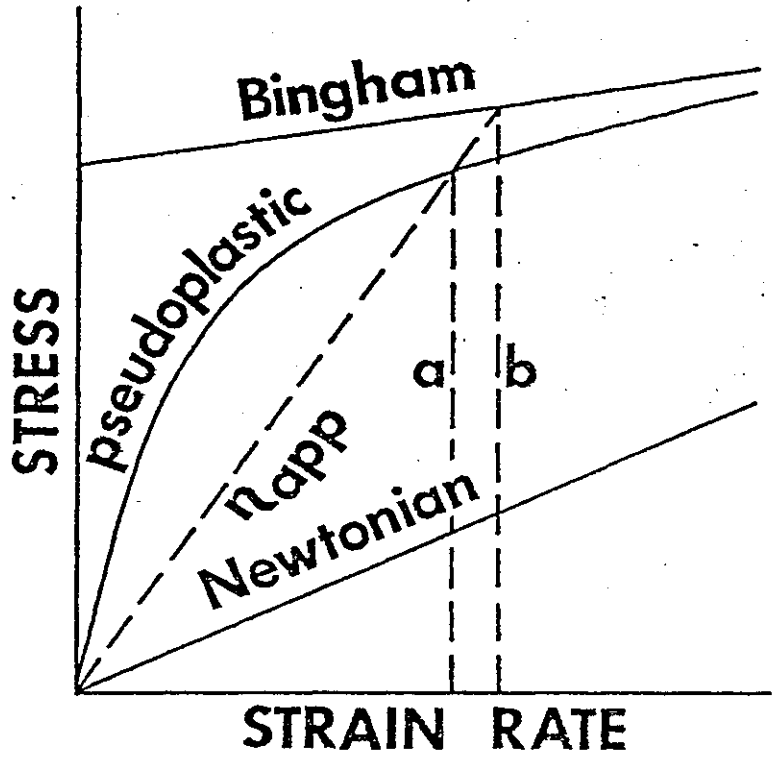

Fig. 6.22 Flow curves for a Bingham, a pseudoplastic, and a Newtonian material (Skelland, 1967); η_{app} is the apparent viscosity of the pseudoplastic material at strain rate a, and of the Bingham material at strain rate b.

develop in the flow and tension cracks form in stretched fiamme. Eventually the yield stress of the flowing mass increases again, due to the increasing proportion of crystals in the glass to the point where flowage ceases. Further cooling and contraction results in jointing, the earliest joints forming before complete solidification (Figure 6.8).

This reconstruction is necessarily tentative, but represents the simplest interpretation of field relations in terms of magma rheology. It is amenable to more rigorous modelling when data on the physical properites of cooling vesicular silicate liquids become available.

VI.3.iv Discussion

The Gran Canaria ignimbrites appear to have been fluidised to a comparable extent to the Tenerife flows, and their initial magmatic temperatures are similar. While noting the danger of making deductions about a poorly-understood process as discussed in VI.2.i, it is possible that a third factor may be responsible for the higher fluidity of ejecta in the Gran Canaria examples: the chemical composition. Calculated viscosities for Gran Canaria magmas are lower than for Tenerife phonolites with the exception of the Adeje red ignimbrite. Two other effects may, however, be important. All the rocks considered here are strongly alkaline, and may have had a high magmatic fluoride content. HF, however, does not partition into the vapour phase as strongly as other volatile species, due to its affinity for silicates. Therefore a fluoride-rich magma will have a higher residual volatile content than a similar water-rich

one, and its post-eruptive glass will be more fluid, especially as F^- in any case acts to lower the viscosity of silicate melts in which it is a component. The kinetics of groundmass crystallisation are critical in determining the extent to which welding and rheomorphism are developed (Wolff and Wright, 1981a). Since heat is efficiently retained for considerable periods by tuff sheets (Riehle, 1973), hot tuff will in general solidify less rapidly than cooler tuff, tending to accentuate the effects of primary gas content of magma.

VI.4 THE GREEN TUFF OF PANTELLERIA

Some of the factors affecting welding development can be more closely assessed if independent data on the physical parameters of the eruption can be obtained. This is possible in the case of the Green Tuff of Pantelleria, an excellently exposed rheomorphic welded air-fall tuff of strongly peralkaline composition. Work on the Green Tuff has been conducted jointly with Dr. J.V. Wright, formerly of Imperial College, who collected the samples and field data. I am extremely grateful to Dr. Wright for permission to freely use these samples and data for the purposes of this thesis. The author alone, however, is responsible for the petrological data and field data analysis presented in VI.4.ii and VI.4.ii. Volcanology of the Green Tuff is considered in more detail than here by Wolff and Wright (1981b).

VI.4.i General field characteristics

This account of the field relations of the Green Tuff is based on descriptions by Villari (1969, 1974) and Wright (1979, 1980).

The Green Tuff is found throughout Pantelleria except where covered by younger rocks, and is usually welded throughout its thickness. Its original distribution covered the entire island (85 km^2). The mean thickness is approximately 5m. An air-fall origin is deduced on the basis of compaction characteristics, grain-size distribution and overall geometry. At most locations a basal vitrophyre passes upwards into revesiculated rheomorphic tuff which constitutes the bulk of the sheet, although an incipiently-welded top and non-welded basal pumice are occasionally found. Rheomorphic structures are ubiquitous and better-developed than in the Gran Canaria examples; at some locations considerable draining of the fluid sheet into valleys is seen. Offshore, the tuff correlates with the widespread deep-sea ash layer Y-6 of Keller et al. (1978) with an age of 45,000 years B.P; the total erupted volume was approximately 20 km^3 (Wolff and Wright, 1981b) or 7 km^3 DRE (dense rock equivalent). The distribution of large lithic clasts indicates that the eruption was of plinian type.

VI.4.ii Petrology

Summary accounts of the petrology of the Green Tuff are given by Korringa and Noble (1972) and Villari (1974).

Petrographically the tuff consists of phenocrysts set in a finely crystalline matrix, although the basal vitrophyre has a groundmass of vesiculated glass. Original pumice lapilli outlines could not be distinguished in the samples studied, a testimony to the peculiarly thorough welding. Hence the total magmatic abundance of phenocrysts cannot be estimated; as plinian deposits are normally enriched in crystals with respect to the magmatic abundance (Walker, 1980), an upper limit of 19% is imposed by the observed modal abundance. Two distinct phenocryst assemblages are present: the bulk of the unit has alkali feldspar + pyroxene + aenigmatite + magnetite + ilmenite + fayalite $\pm$ quartz $\pm$ pyrrhotite, while the basal vitrophyre has feldspar + aenigmatite + pyroxene + quartz + apatite.

Phenocrysts

Quartz is abundant in the vitropyre but rare in the crystallised tuff; in the latter it appears resorbed.

Large tabular crystals of anorthoclase up to 1.3 cm in length are ubiquitous. Occasionally slightly rounded and embayed examples are seen, suggesting a degree of post-eruptive resorption. Crystals are essentially unzoned. Compositions vary between $Ab_{67}Or_{33}$ and $Ab_{65}Or_{35}$ in the crystalline tuff, and $Ab_{64}Or_{36}$ and $Ab_{62}Or_{38}$ in the vitrophyre; the vitrophyre feldspars are richer in iron than those higher in the cooling unit.

The pale to deep green pyroxenes are hedenbergitic with a minor acmite component. Those in the basal vitrophyre have a slightly higher Fe and Na content than those in the bulk of the tuff, although zoned examples are found which span the two compositions (Figure 6.23).

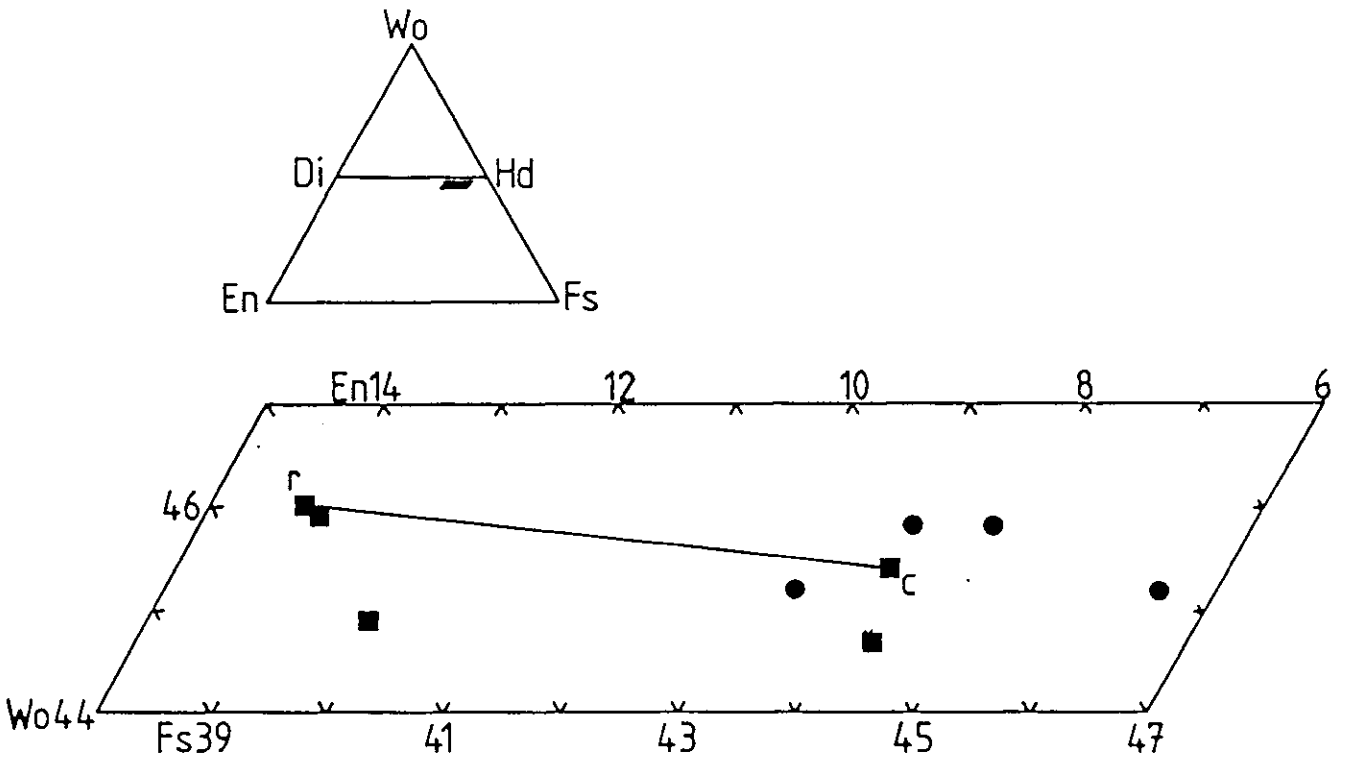

Fig. 6.23 Compositions of pyroxene phenocrysts in the Green Tuff. Squares = phenocrysts in the main part of the tuff; circles = phenocrysts from basal vitrophyre.

Occasional strongly resorbed crystals of olivine are found in the crystalline tuff. No compositional variation is found within the precision limits of the microprobe. The composition is $Fa_{85}Fo_{9}T_{P5}La_{1}$.

Aenigmatite is found throughout the tuff but is especially abundant in the basal vitrophyre. Compositions are closely similar and correspond to those described from other peralkaline rhyolites (Nicholls and Carmichael, 1969).

Fe-Ti oxides are absent from the vitrophyre but occur as microphenocrysts and inclusions in silicate phases throughout the rest of the tuff. Two ilmenites are found; one has a mean hematite content of 4%, the other 2%. Only the former is seen in equilibrium with titanomagnetite, which has a mean ulvospinel content of 71%.

Apatite and rare pyrrhotite occur as inclusions in other phases.

Groundmass phases

The glass of the basal vitrophyre is strongly peralkaline ($Na+K/Al < 2.0$) and contains appreciable Cl and ZrO_2; it is closely similar to that reported by Korringa and Noble (1972). In the main part of the Green Tuff, the groundmass consists of a fine-grained mass of quartz, feldspar, aenigmatite, pyroxene and amphibole. Feldspar is enriched in Fe^{3+}, and pyroxene in Na and hence Fe^{3+}. Feldspar and pyroxene thus show a similar compositional relationship as found in the groundmass

of ignimbrite E, Gran Canaria (VI.3.ii); this is further discussed below. Small, ($\leqslant$ 100 μm), roughly spherical opaque blebs occur dispersed through the rock; they appear to be largely composed of SiO_2 and Fe_2O_3. They may be subsequently oxidised immiscible blebs of iron-rich liquid which separated during cooling of the welded sheet; Philpotts (1966, 1978) has documented similar textures in basaltic rocks. An alternative explanation is that the blebs may be altered representatives of iron sulphide grains formed during groundmass crystallisation.

Discussion

There is considerable evidence for zonation of the Green Tuff magma chamber. The vitrophyre assemblage does not include a geothermometer, but temperature estimates for the bulk of the magma, roughly corresponding to the crystalline tuff, have been obtained from Fe-Ti oxides and ol-cpx (Powell and Powell, 1974). The applicability of the latter thermometer has been discussed in Chapter IV; in this case the temperature yielded, 960°C, is identical to that obtained from Fe-Ti oxides, which also give $f_{O_2} = 10^{-12.1}$ bars. These conditions lie very close to the QFM oxygen buffer curve in T-f_{O_2} space (Figure 6.24), a not unexpected result in view of the phenocryst assemblage. Nicholls and Carmichael (1969) have demonstrated the existence of a "no-oxide" field in T-f_{O_2} space for peralkaline rhyolites within which Fe-Ti oxides are absent and Ti is incorporated into aenigimatite. This field is bounded by the reactions:

1. $4Fe_3O_4 + 6Na_2Si_2O_5 + 12SiO_2 + O_2 \rightleftharpoons 12NaFeSi_2O_6$

mag liquid qz/liquid pyx

2. $Na_2Fe_5TiSi_6O_{20} + Na_2Si_2O_5 + O_2 \rightleftharpoons 4NaFeSi_2O_6 + FeTiO_3$

aenig. liquid pyx ilm

3. $6Fe_2SiO_4 + 6Na_2Si_2O_5 + 6SiO_2 + 3O_2 \rightleftharpoons 12NaFeSi_2O_6$

ol liquid qz/liquid pyx

The position of the "no-oxide" field thus varies with varying activity of $Na_2Si_2O_5$ in the silicate liquid, and, since the appropriate equilibrium assemblages are not found, it cannot be precisely delineated for the Green Tuff magma. However, the absence of Fe-Ti oxides in the basal vitrophyre suggests that the portion of the magma represented by this horizon equilibrated at lower temperature than the phenocrysts found in the crystalline tuff (Figure 6.24). This is corroborated by the presence of abundant quartz and less magnesian pyroxene in the vitrophyre.

Further evidence for the iron content of feldspar being controlled by the reaction

$NaFeSi_2O_6 + SiO_2 \rightleftharpoons NaFeSi_3O_8$

pyx qz/liquid fsp

is found by comparing feldspar compositions from phenocrysts and groundmass. Figure 6.25 shows a correlation between acmite content of pyroxene and Fe content of feldspar for the environments of crystallisation found in the Green Tuff; a_{SiO_2} will also influence the reaction. It is therefore suggested that Fe content of feldspar in sodic rocks is controlled by this reaction, although a quantitative assessment of the reaction must await the arrival of accurate thermodata for $NaFeSi_3O_8$.

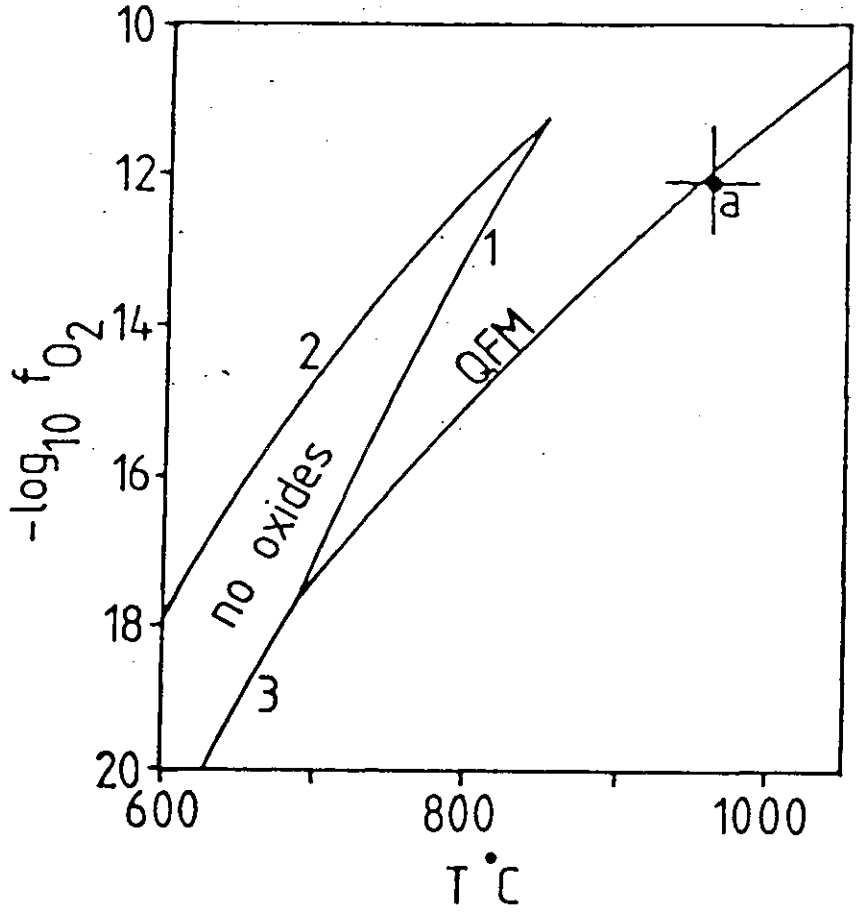

Fig. 6.24 Fugacity of oxygen vs temperature showing the position of the "no-oxide" field for unit activities of acmite and sodium disilicate, after Nicholls and Carmichael (1969). Point a given by Fe-Ti oxide equilibration in the main part of the tuff. Nos 1-3 refer to reactions given in the text.

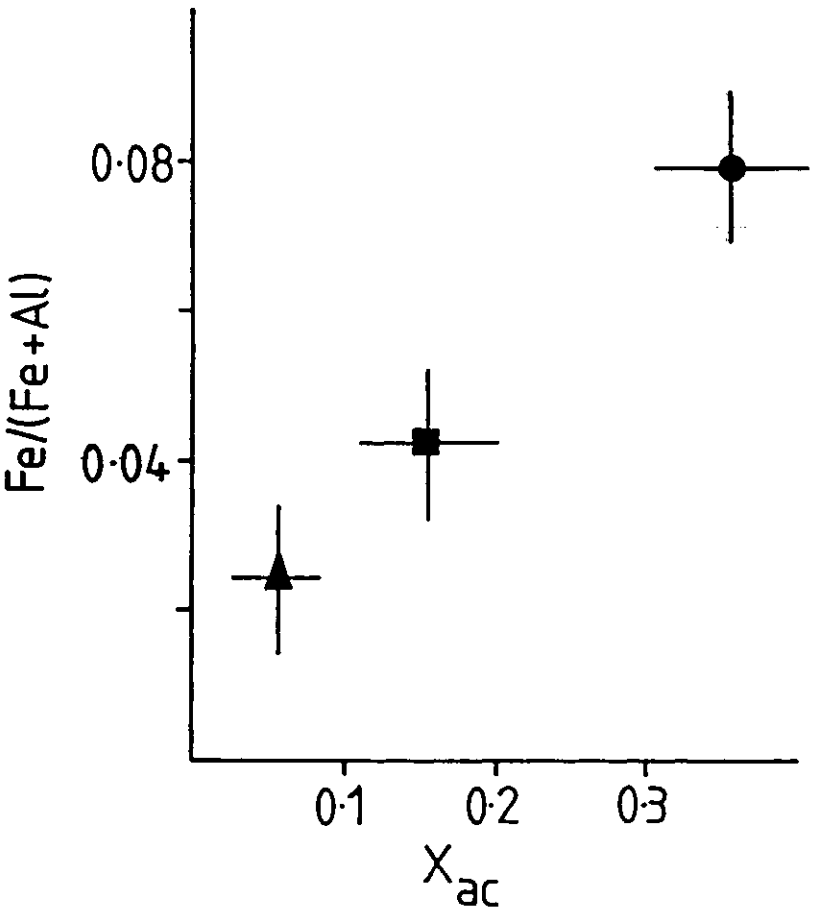

Fig. 6.25 Fe/(Fe+Al) in feldspar vs. mole fraction of $NaFeSi_2O_6$ (X_{ac}) in co-existing pyroxene from the Green Tuff. ▲ = main tuff; ■ vitrophyre; ● = groundmass.

Blake (1981) has modelled the extraction of magma from a flat-roofed magma chamber and shows that the initially-erupted material is taken from a layer nearest the chamber roof. Hence the observed mineralogical variation indicates that the Green Tuff was erupted from a magma chamber the topmost portion of which contained cooler, slightly more fractionated material than the rest. Blake (op. cit.) has further shown that the topmost layer continues to contribute to the extracted products throughout the eruption; a similar process has been invoked in Chapter III to explain the high incidence of banded pumice on Tenerife. Therefore the quartz, and some of the aenigmatite, pyroxene and feldspar found distributed throughout the tuff may also be derived from this upper zone.

VI.4.iii Estimation of physical parameters for the eruption

For any plinian eruption, it is theoretically possible to deduce such physical parameters as muzzle velocity, vent radius and eruption column height from study of the resultant pyroclastic fall deposit (Wilson, 1976; Wilson et al., 1978; Ledbetter and Sparks, 1979). Unfortunately, in the case of the Green Tuff much useful information has been destroyed by the processes of welding and rheomorphism. However, since rheomorphism is very unlikely to have involved bulk movement of welded tuff over distances greater than a few hundred metres (Wolff and Wright, 1981a), the primary lithic size distribution may be considered to have survived largely unchanged, and the average maximum lithic diameter map of Wright (1980) is used as the basis of the following analysis.

Vent position has been inferred from the lithic size distribution, and agrees closely with the field observations of Mahood and Hildreth (1980) that the Cuddia di Mida was the source of the tuff. Average maximum lithic size data from Wright (1980) are plotted against distance from vent; a line drawn along the top of the resulting scatter of points (Figure 6.26) gives the maximum range of fragments for a given size. This line shows an inflexion at about 5 km from source, indicating the maximum range of ballistic clasts (those largely unaffected by wind drift). Similar distributions have been found for several other plinian deposits (Walker and Croasdale, 1971; Booth et al., 1978). Extrapolation of this graph to zero range yields a value of 4.3 m for the maximum diameter of lithics at the vent. This value is corroborated by the existence of 5 m blocks in the tuff in the vent area (Wolff and Wright, 1981b). Using the value of 4.3 m in equation (6) of Wilson (1976) gives a figure of 650 ms^{-1} for the maximum muzzle velocity during the eruption; the average velocity may conveniently be taken as half this value (Wilson, 1976).

The instantaneous mass rate of eruption of material from a vent of radius b_o is $\dot{m}$, where

$$\dot{m} = \frac{100 p_o}{n} \mu_o \pi b_o^2, \text{ where } p_o = \text{gas density}$$

n = % magmatic gas

μ_o = muzzle velocity

(Wilson, 1976).

Figure 6.27 shows the relation between volumetric eruption rate, magma gas content, and vent radius for the Green Tuff eruption. For certain combinations of these variables column collapse to form pyroclastic flows occurs (Sparks and Wilson, 1976). Since the tuff

is air-fall in origin, the "collapse boundary" limits the conditions of formation as shown.

The degree of welding of an air-fall tuff is critically dependent on ejecta accumulation rate (Sparks and Wright, 1979), which is a simple function of eruption rate, total erupted volume and tuff thickness. The primary uncompacted thickness of tuff at maximum observed range on the island was roughly 10 m (Wolff and Wright, 1981b). Using this figure, values of accumulation rate for a given eruption rate are also shown on Figure 6.27.

Little data are available on the critical accumulation rate required to form a welded air-fall tuff. Sparks and Wright (1979) estimate a value of 20 cm/minute for the production of densely welded rhyolitic tuff during the eruption of Askja, 1875. This is an order of magnitude greater than the rates shown on Figure 6.27, and, for the Green Tuff, would require volumetric discharge rates or a vent radius too great to form a plinian eruption column (Wilson et al., 1978). The Green Tuff therefore directly illustrates the role that chemical composition plays in promoting welding; required viscosities are approximately 0.01-0.001 times that of rhyolite, which corresponds to the order of difference of calculated liquidus viscosities for pantellerite and rhyolite (Wolff and Wright, 1981a, b).

VI.4.iv Discussion

The physical analysis of the eruption presented above is at best only a first approximation, however the salient conclusion concerning ejecta viscosity holds even if unreasonably large errors are introduced into the calculation, for example, substitution of non-plinian muzzle velocities into Wilson's (1976) equations.

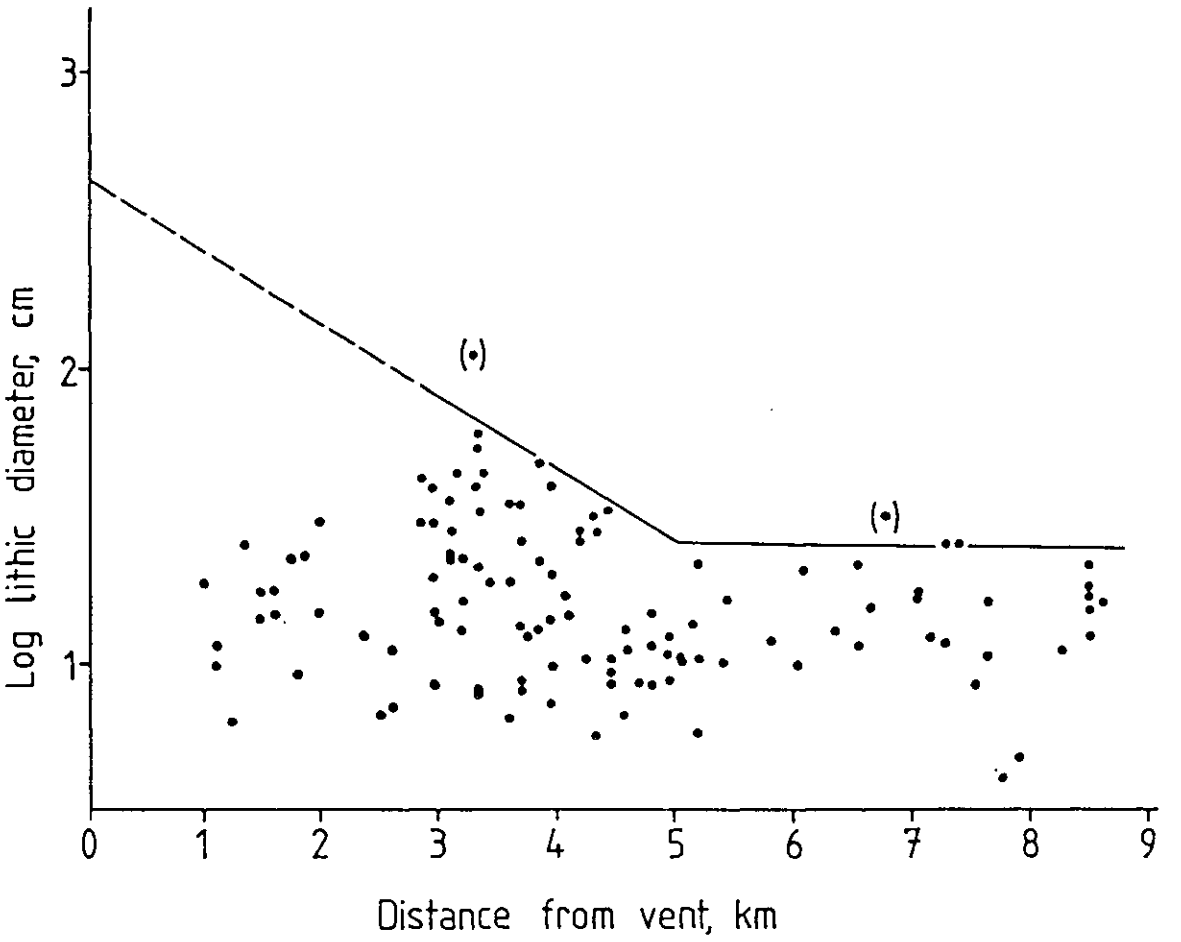

Fig. 6.26 Average maximum lithic size in the Green Tuff vs. distance from vent. Each data point is the average of the five largest lithic clasts from any one locality. Solid and dashed lines explained in text.

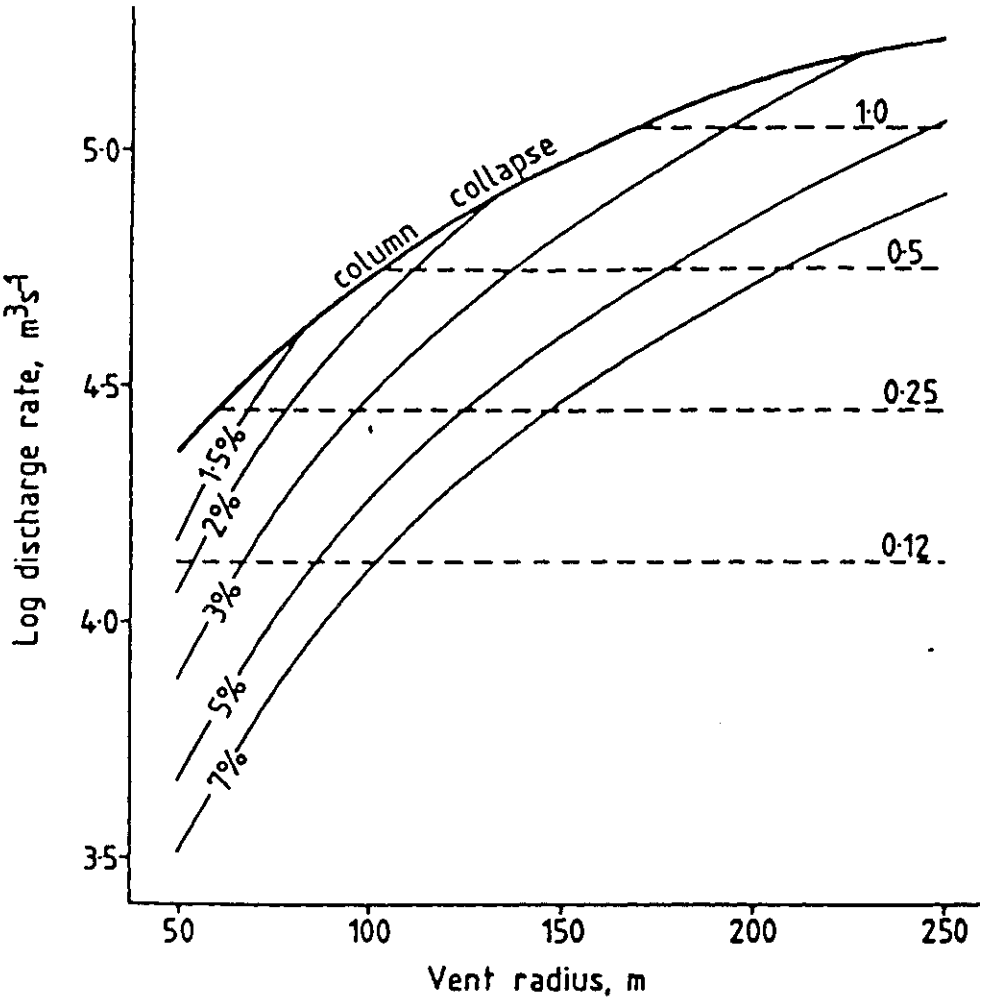

Fig. 6.27 Variation of volumetric discharge rate of tephra as dense rock (density 2.5×10^3 kg m^{-3}) in a plinian eruption column with vent radius for five values of magmatic volatile content in weight% and a muzzle velocity of 250 m s^{-1}, from the model of Wilson (1976). Dashed lines indicate the discharge rates required to accumulate 10m uncompacted tephra (maximum thickness of the Green Tuff at maximum range on Pantelleria) at four values of tephra accumulation rate (in cm/minute) for a total erupted volume of $20km^3$ of vesicular tephra.

At a given accumulation rate, the loss of heat from pyroclasts during atmospheric flight will be closely similar for all plinian eruptions, since particle concentration per unit volume of air is the most important factor affecting heat loss (Sparks and Wright, 1979). Thus the gas content arguments discussed in VI.2 and VI.3 cannot be extended from pyroclastic flows to pyroclastic falls. Thus temperature and chemical composition alone (assuming that temperature-independent groundmass crystallisation factors do not vary greatly from one composition to another) have caused the unusually dense welding of the Green Tuff. The magmatic temperature of the Green Tuff was high (960°C) compared to all other deposits discussed in this chapter, and considerably higher than the eruption temperatures of most rhyolitic tuffs (e.g. Hildreth, 1979; Ewart et al., 1971; Rutherford and Fleming, 1978). It may be concluded that temperature and chemical composition are at least as important as gas content in determining the extent to which welding is developed in pyroclastic rocks. Therefore, the final appearance of salic pyroclastic rocks is determined largely by the physico-chemical state of the magma prior to eruption.

VI.5 AGGLUTINATION OF FLUID TEPHRA

The low viscosity of the Green Tuff ejecta, deduced from field evidence and compositional data, requires an assessment of the possible role of agglutination, commonly observed during basaltic fire-fountaining and strombolian eruptions, in the compaction of hot, strongly peralkaline, Fe-rich tephra. Agglutination, for the purposes of this treatment, is defined as the deformation and sintering of air-fall pyroclasts upon impact onto the accumulating deposit. It

is thus a primary process, caused by the momentum of the falling pyroclasts, as distinct from welding sensu stricto, which occurs under the influence of load pressure imposed by already-accumulated tephra on the underlying, still hot, part of the same deposit. Agglutination is an important process in some basaltic eruptions, leading to the formation of coherent cinder cones, spatter deposits, and clastogenic lavas, such as formed during Hawaiian fire-fountaining eruptions (Richter et al., 1970). Clastogenic lavas may be regarded as an extreme form of rheomorphic tuff, in that the magma was released from the vent as pyroclasts, not a steady effusion.

To the author's knowledge, no attempt has been made to theoretically quantify or assess the general importance of the agglutination process. Agglutination may be envisaged as involving both equal-volume deformation of the liquid or glassy component of the vesicular pyroclasts, and porosity-loss flattening as in load pressure welding. Clearly the void fraction of the undeformed pyroclast is a factor in determining the relative importance of the two mechanisms. A first attempt at modelling agglutination may therefore be made by considering two limiting cases: (i) equal-volume deformation of non-vesicular pyroclasts; (ii) pure porosity-loss compaction of vesicular pyroclasts.

VI.5.i Modelling agglutination processes

The following is primarily designed to estimate ejecta viscosities required to allow agglutination during plinian eruptions for a range of particle sizes. It is not directly applicable to conditions obtaining during those basaltic eruptions in which agglutination is commonly observed, however conclusions pertinent to such eruptions are noted.

Equal-volume deformation of non-vesicular pyroclasts

The following simplifying assumptions are made:

(i) Fall of clasts is vertical; impact surface is horizontal,

(ii) Clasts are homogeneous and isotropic,

(iii) Clasts have Newtonian rheology during the flattening episode,

(iv) Initial clast shape is a sphere radius r_o; final clast shape is an oblate spheroid, vertical (short) axis 2a, horizontal axes 2b,

(v) Force of impact is distributed equally over the whole flattening episode,

(vi) Area of contact of clast with the underlying surface at any one time during the flattening episode is equal to πr^2, where r is the instantaneous value of b. This together with (iv) above, represents the actual deformation, where the clast will rapidly assume a crudely hemispherical shape due to impact on a theoretical mean flat surface (and thus area of contact $\simeq$ horizontal cross-sectional area), as the much simpler deformation to a spheroid; the overall stress-strain relations are assumed to be similar.

For any viscous deformation,

$$\frac{d\varepsilon}{dt} = \frac{\sigma}{\eta}$$

$$\varepsilon = \frac{1}{\eta}\int \sigma \, dt \qquad 1$$

where ε is the strain, η the viscosity, σ the stress, and $\frac{d\varepsilon}{dt}$ the rate of strain. Stress is equal to the total force divided by the area over which the force acts

$$\sigma = \frac{mf}{A} \qquad 2$$

where m is the mass of clast, f is the deceleration from impact velocity to zero velocity through the distance (r_o-a), and A is the area of impact. Substituting for m, f and A in equation (2) gives

$$\sigma = \frac{2r_o^3 du^2}{e(r_o-a)r^2}$$

where d is the clast density and u is the impact velocity. the duration of the flattening episode is given by

$$t = \frac{2(r_o-a)}{u} \qquad 3$$

Therefore, substituting in (1)

$$\varepsilon = \frac{2r_o^3 du^2}{3\eta(r_o-a)} \int_{t=0}^{t=\frac{2(r_o-a)}{u}} \frac{1}{r^2}\, dt \qquad 4$$

Since the volume of the deforming clast is constant,

$$a^1 r^2 = r_o^3$$

where a^1 is the instantaneous value of a. For small degrees of flattening, which are the principal cases of interest here, we may assume $a^1=a$. Therefore from equation (3)

$$r^2 = \frac{2r_o^3}{(2r_o-ut)}$$

and substituting into equation (4)

$$\varepsilon = \frac{du^2}{3\eta(r_o-a)} \int_{t=0}^{t=\frac{2(r_o-a)}{u}} (2r_o-ut)\,dt$$

$$= \frac{2du(r_o+a)}{3\eta} \qquad 5$$

If it is assumed that falling clasts have reached their terminal velocities prior to impact, a likely case for most material released during a plinian eruption (Walker et al., 1971), then the resulting

shape (in terms of axial ratio) of the deformed clast may be calculated from clast viscosity and clast size and density, using values of terminal velocity given by Walker et al. (1971). Results using equation (5) for four values of axial ratio are shown in Figure 6.28.

For non-Newtonian rheologies, the viscosity term in (5) becomes a mean apparent viscosity for the deformation episode. However, if the clasts possess a yield stress, then this stress must be exceeded upon impact if deformation is to occur. The yield stress, σ_y, required to resist deformation to a certain axial ratio defined as appreciable deformation may be approximately estimated from

$$\sigma_y = \frac{2r_o du^2}{3(r_o - a)} \qquad 6$$

Required yield stresses, for two values of axial ratio, are shown in Figure 6.29.

Porosity-loss flattening of vesicular tephra

Porosity-loss compaction is the dominant mechanism during load-pressure welding of pyroclastic fall and flow deposits. It is distinct from equal-volume deformation in that strain is only experienced along the vertical axis of the deforming clast. The process has been theoretically investigated (with reference to load-pressure welding) by Kono and Osima (1971), who give the equation

$$\ln \phi = \ln \phi_o - \frac{3Pt}{4\eta} \qquad 7$$

where ϕ_o, ϕ are the initial and final tuff porosities, P is the load pressure, t is time and η is tephra viscosity. Riehle (1973) gives a similar relationship

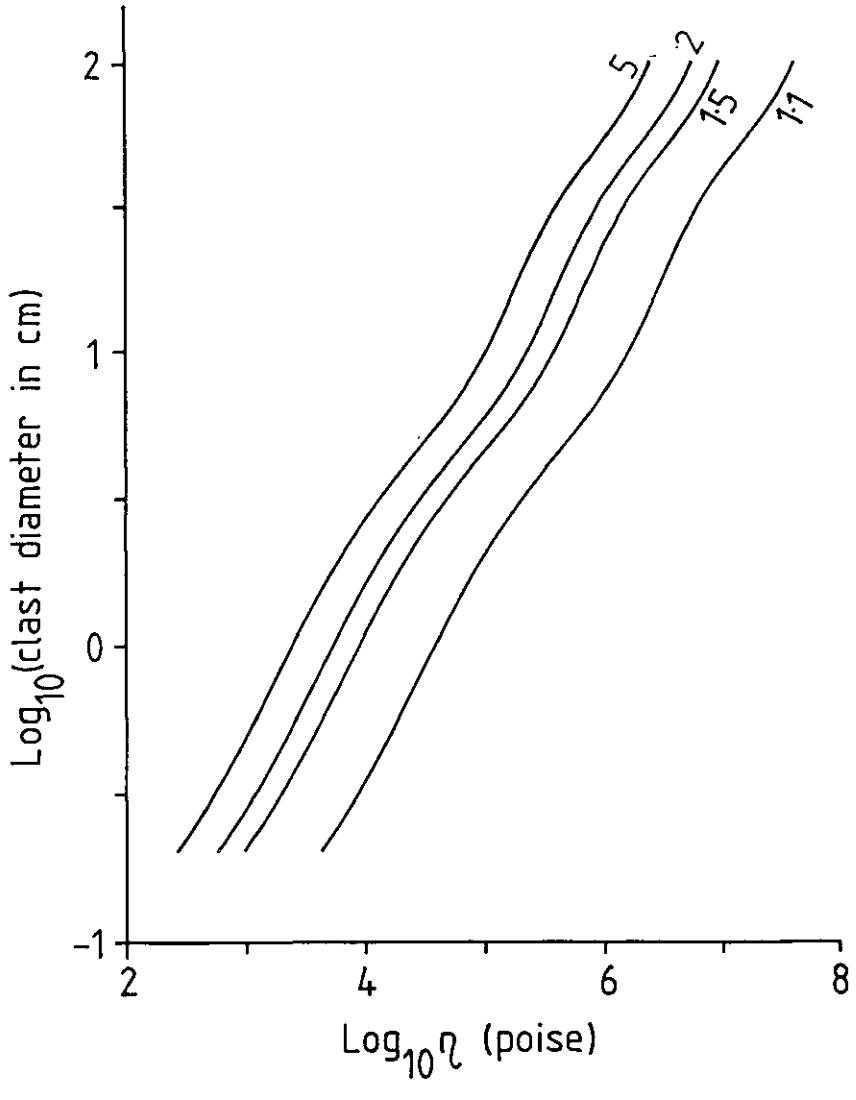

Fig. 6.28 Combinations of clast size and viscosity required to produce axial ratios of 5, 2, 1.5 and 1.1 during agglutination, calculated from equation (5). Clast initially spherical (equal-volume deformation).

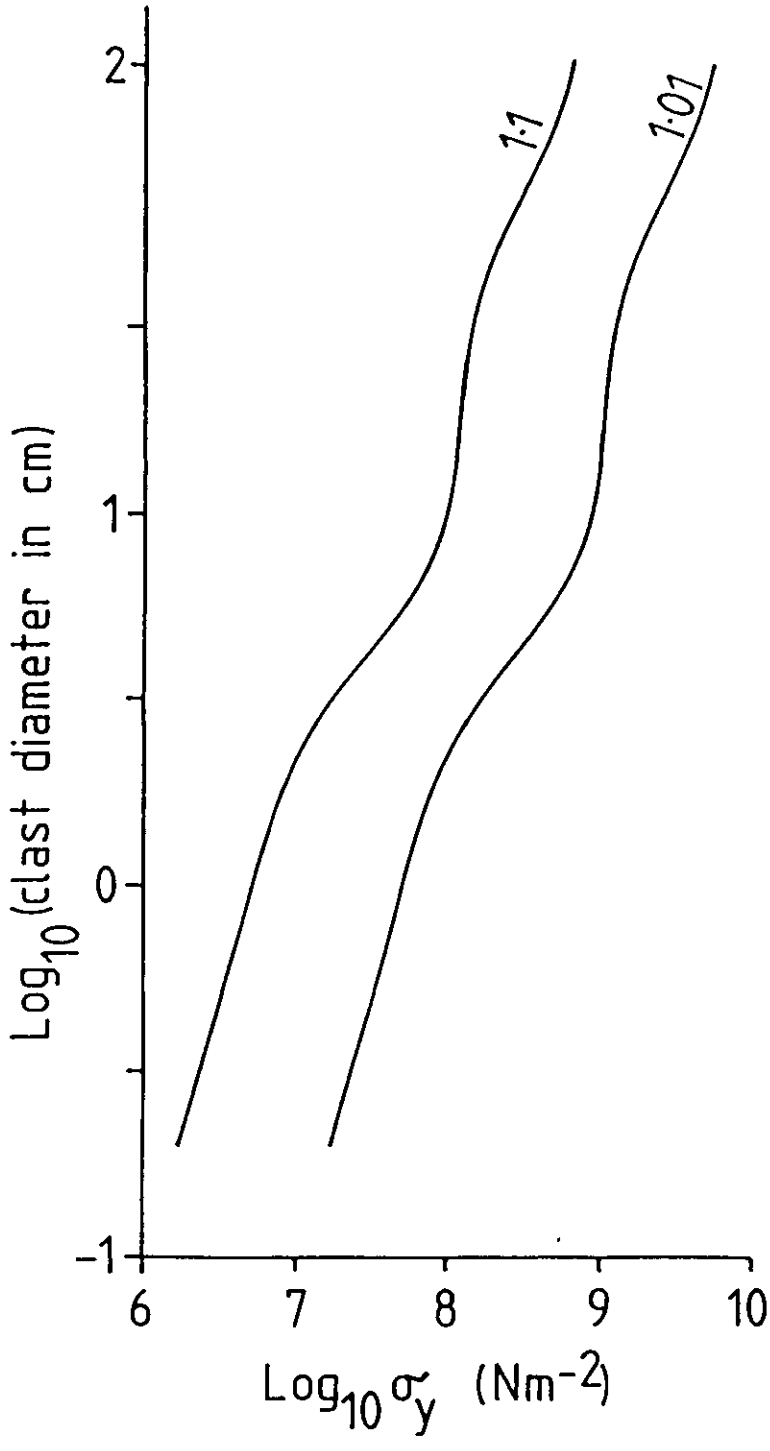

Fig. 6.29 Clast yield stress (σ_y) required to completely resist deformation plotted against clast size, for two axial ratios below which no deformation is considered to have taken place, calculated from equation (6).

$$\beta = \frac{\sigma_z \Delta t}{\ln\left(\frac{P_f - 1}{P_i - 1}\right)} \qquad 8$$

where β is the compaction coefficient, σ_z is the vertical uniaxial stress and P_i, Pf are the tuff porosities before and after time increment Δt respectively. β, values of which were deduced by Riehle from the experimental studies of Friedman et al. (1963), is closely related but not equivalent to, tephra viscosity; for example, it follows from (8) that β is undefined for non-porous material. However, for consistency with the previous section, β is here assumed equivalent to viscosity if only porosity-loss of vesicular tephra is considered. Both equations (7) and (8) assume Newtonian rheology. The two methods yield similar answers when applied to the same data set. Riehle's (1973) equation is used here; its form is such that it may be simply converted to predict axial ratios of deformed clasts, rather than porosities, since

$$\frac{P_f - 1}{P_i - 1} = \frac{r}{a}$$

where r is the radius of the undeformed spherical clast, and 2a is the vertical (short) axis of the deformed clast. Since no strain is experienced in the horizontal plane, r/a is equal to the axial ratio of the final deformed shape. Equation (8) is directly applied to porosity-loss agglutination by expressing the vertical stress as a function of the mass and impact velocity of the clast. Substituting this information into equation (8) gives

$$\ln\left(\frac{r}{a}\right) = \frac{4urd}{3\eta}$$

equating β to η. Note that d is here the overall density of the vesicular clast. In this case assumptions (i), (iii) and (v) above also apply. However, for highly vesicular pyroclasts, which form by the fracturing of bubble walls in the magma and thus have very rough surfaces (Sparks, 1978a), it cannot be assumed that a large

proportion of the clast surface is initially in contact with the underlying surface. This is allowed for by the introduction of a factor x:

$$\ln \left(\frac{r}{a}\right) = \frac{4urd}{3\eta x} \qquad 9$$

where $x = A^1/A$, A^1 is the area of contact of the clast with the underlying surface, and A is the cross-sectional area of the spherical clast radius r. Clearly x will change during the deformation, therefore axial ratios produced by various combinations of η and clast size are given for four different values of x in Figure 6.30.

VI.5.ii Discussion

The rheological properties of pyroclasts as they arrive at the ground surface after eruption and atmospheric transport are a complex function of very many variables, and full investigation is beyond the scope of the present work. The most important factors are temperature (itself a function of initial magmatic temperature, gas release from pyroclasts, volumetric eruption rate, grain size, distance from source, and wind speed) and the chemical composition of the ejecta (including the volatile fraction still dissolved in the glass, which is time-dependent in the first few hours after eruption (Sparks, 1978b). The role of agglutination in the compaction and welding of large pyroclastic deposits cannot therefore be accurately estimated, although existing data permit a crude assessment.

A minimum value for the axial ratio of 1.1 is, somewhat arbitrarily, chosen as indicating that deformation has occurred (the curve a/r=1.04 is also shown in Figure 6.30 as this corresponds to a 1% porosity decrease, another possible choice for a minimum value); very small strains are beyond the resolution of field

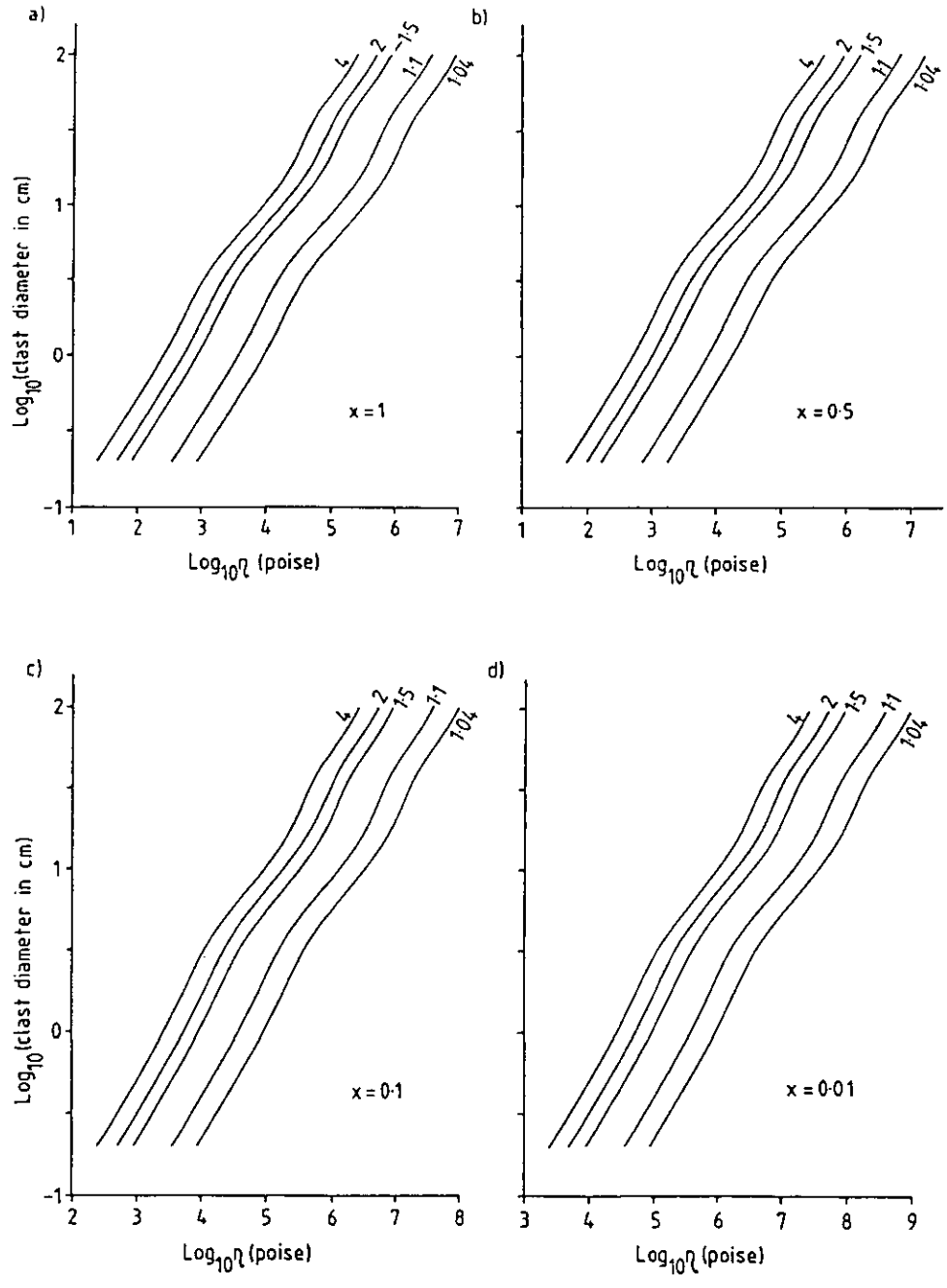

Fig. 6.30 Combinations of clast size and viscosity required to produce axial ratios of 4, 2, 1.5, 1.1 and 1.04 during pure porosity-loss agglutination, for four values of area factor x: a) x = 1; b) x = 0.5; c) x = 0.1; d) x = 0.01, calculated from equation (9). Initial porosity = 75% and therefore 4 is the maximum axial ratio that may result from deformation of a spherical clast; a porosity decrease of 1% corresponds to axial ratio 1.04.

measuring techniques due to initial variations in clast shape, orientation, and viscosity (Sparks and Wright, 1979). Incipient agglutination and/or welding, without noticeable deformation, may be indicated by coherence of tephra, but this may also be the product of post-cooling alteration (Chapter I). Using this criterion, tephra with effective viscosities greater than 10^8-10^9 poise at impact will not agglutiinate (Figures 6.28, 6.30). Riehle (1973) has calculated values of β over a range of temperatures for rhyolitic ash, and finds 10^9-10^{10} poise at 900°C. Thus we may define a minimum agglutination temperature of roughly 900°C for rhyolite tephra (cf. the minimum welding temperature of 625°C for rhyolitic ash given by Smith, 1960a), assuming Newtonian rheology for the pyroclasts (the effect of non-Newtonian behaviour on this figure is discussed below). The eruptive temperatures of rhyolites, particularly rhyolitic pumices, are commonly less than 900°C (Carmichael, 1967; Ewart et al., 1971; Lipman, 1971; Rutherford and Heming, 1978; Hildreth, 1979) and therefore many rhyolitic explosive eruptions are inherently incapable of forming agglutinates, even ignoring cooling during atmospheric transport. No data are available on the rheology of pumice and ash of other compositions. The supraliquidus viscosities of pantellerites are typically two orders of magnitude below rhyolites (Wolff and Wright, 1981a); if these relations can be approximately extended below the liquidus, then a minimum pantellerite agglutination temperature of approximately 600°C-700°C is indicated. Substantial agglutination will require much higher temperatures, since these figures are based on the incipient agglutination of 1 m diameter clasts which acquired terminal velocity before impact. Such a clast will have been falling long

enough for a chilled skin to form, the mechanical strength of which may be sufficient to resist any deformation upon impact. If 10^9 poise is taken as a minimum emplacement viscosity for rhyolitic tephra, the corresponding value for pantellerite is roughly 10^7 poise. Of the range of conditions studied here, only those of Figure 6.30d allow substantial agglutination at this viscosity, however these conditions only occur during the initial contact between clast and underlying surface (see below). Therefore agglutination is only likely to be responsible for a small percentage at most of the compaction of pantellerite air-fall tuffs, and probably does not occur during deposition of pumice of the commonly observed range of salic magmas.

One example of a densely welded, rheomorphic air-fall tuff of evolved composition which may have agglutinated substantially is the "globule" tuff of Mt. Suswa, Kenya. Described as a "froth flow" by Johnson (1966, 1968) this horizon was re-interpreted as an ignimbrite by Schmincke (1972, 1974) and Hay (1975). Hay et al. (1979) while continuing to favour an ignimbrite origin, give a field description suggestive of a welded air-fall tuff; in particular, the sheet mantles topography, is frequently stratified, welded tuff is found interbedded with air-fall pumice in distal exposures and passes upwards into air-fall pumice in the near-vent region, and the overall degree of welding shows a strong dependence on distance from source. Petrological data given by Hay et al. (1979) indicate an unusually fluid magma, an Fe-rich peralkaline phonolite with a temperature (from Fe-Ti oxide phenocrysts) of ca. $1040^{\circ}C$, yielding a volatile-free viscosity of 10^5 poise. Again by analogy

with magmatic viscosities, the emplacement viscosity may have been one or two orders of magnitude less than that of the Green Tuff ($\eta \simeq 10^6$ poise at 1000°C, Wolff and Wright, 1981a), other factors being equal. This would permit substantial agglutination in the near-vent region, where maximum emplacement temperatures are found.

Some assessment of the relative roles of the two deformation mechanisms may be gained by comparing Figures 6.28 and 6.30 (Figure 6.30 has been plotted for an initial clast density of 0.625 g cm^{-3}, corresponding to 75% porosity, a typical value for pumice, Sparks, 1978a; Wilson and Head, 1981); this gives a maximum axial ratio after compaction, i.e. at zero porosity, of 4.0. Maximum axial ratios (n) for other densities and porosities may be readily found from $n=D/d$, where D= glass density, d=density of porous clast. For direct comparison between the two diagrams, the curves in Figure 6.28 plot at 0.9 log units of viscosity less for a density of 0.625 g cm^{-3} and appropriate terminal velocities. The greatest degree of flattening at given clast size and viscosity occurs for vesicular clasts when x=0.01 (Figure 6.30d). As flattening proceeds, x will increase as coalescence occurs at points of contact. At x=0.5 (Figure 6.30b), the strain produced by porosity-loss is approximately equal to that produced by equal-volume deformation, and is less at higher values of x. Thus the deformation history of a clast may be initially dominated by porosity loss, with no expansion of the clast in the horizontal plane, and by equal-volume deformation in the later stages, during which horizontal strain occurs. This pattern will also be produced during the deformation of poorly-vesiculated clasts, where there is residual impact energy after loss of the available pore-space.

The relative importance of agglutination and post-depositional welding may be illustrated by considering the whole deformation history of a 40 cm spherical clast with a viscosity upon emplacement of 10^8 poise and an initial porosity of 75%. From Figure 6.30d, agglutination produces an axial ratio of 1.1, in other words the clast becomes incipiently agglutinated with little loss of pore space. The conditions under which pyroclasts are sufficiently hot to agglutinate and weld after atmospheric transport imply very high ejecta accumulation rates (Sparks and Wright, 1979), and burial of the clast would be sufficiently rapid to preclude significant radiative heat loss. However, let us assume that the clast cools sufficiently before burial to a depth providing full thermal insulation ($<$ 1 m for the time required, Riehle, 1973) to increase viscosity by two orders of magnitude. Compaction to zero porosity occurs in ca. 1 day due to load-pressure welding and conditions are favourable for the initiation of rheomorphism. Thus in most cases agglutination is a subordinate process, except where it produces the bulk of the deformation and no rheomorphic flow ensues, as is the case where the clasts possess a large yield strength (see below). Furthermore agglutination structures in glassy pyroclastic deposits have very low preservation potential, except perhaps at the very top of a deposit, where lack of overburden and rapid cooling prevent the development of load-pressure welding.

Effect of non-Newtonian rheology

Throughout the above discussion it is assumed that clasts have a Newtonian rheology. Evidence from lava flow morphology (Hulme, 1974; Hulme and Fielder, 1977) and field measurements on flowing

lava (Pinkerton and Sparks, 1978) demonstrate that lavas commonly possess a yield strength, and Wolff and Wright (1981a) invoked non-Newtonian behaviour to explain high apparent viscosities during rheomorphism of ignimbrites and welded air-fall tuffs. However, the development of a yield strength appears to be principally due to groundmass crystallisation which occurs as a response to undercooling during eruption (Sparks and Pinkerton, 1978). Although sub-solidus glasses may not be Newtonian, welding itself is evidence that they are deformed by low applied stresses. Thus either the yield strength of such glasses is low, or else they possess pseudoplastic properties (Figure 6.22), or conform to some other model (it is of course possible that Newtonian behaviour closely approximates their actual behaviour) allowing strain at low stresses; the author knows of no relevant experimental data. However, the above analysis is valid if the results are considered as apparent viscosities (Figure 6.22). Apparent viscosities are strain-rate dependent and thus are lower in high strain-rate situations, such as agglutination, than in load-pressure compaction and welding, where strain rates are lower. Thus a greater amount of deformation could occur during agglutination than is indicated by taking apparent viscosities (or compaction coefficients) from load-pressure welding experiments. Therefore the minimum agglutination temperatures given above may be overestimated, and agglutination may be more important than is concluded above. Quantitative rheological data on sub-liquidus and supercooled natural silicate liquids are required for more rigorous investigations.

Application to basaltic eruptions

Explosive basaltic eruptions take two principal forms: fire-fountaining (commonly termed Hawaiian) and strombolian activity. Wilson and Head (1981) have shown that some magma disruption must always occur during subaerial eruptions if the magma contains >0.1 wt % water, although the proportion of erupted lava to pyroclastic material may be high if the magmatic gas content is very low. Steady fire-fountaining occurs if the magma rise speed is greater than 0.5-1 m s^{-1}; at slower rates bubble coalescence in the magma causes intermittent strombolian activity. The greater discharge rate and lower degree of magma fragmentation during fire fountaining (Walker, 1973) favours the development of agglutinates, while the typical product of strombolian activity is a cone and surrounding blanket of loose or weakly sintered scoria. More heavily "welded" strombolian scoria cones are, however, fairly common (G.P.L. Walker, pers. comm.), but whether these are the products of agglutination or load pressure welding is uncertain. Less equivocal are spatter deposits (several excellent examples on Tenerife are illustrated by Ridley, 1968) and clastogenic lavas formed by rapid agglutination, as observed during the 1959-60 eruption of Kilauea (Richter et al., 1970).

An important difference between basaltic and salic explosive eruptions is the quantity of released gas, and degree of resultant undercooling of the ejecta. Basaltic magma is typically undercooled by 50°C (the minimum degree of undercooling produced by 1 wt % gas loss, Sparks and Pinkerton, 1978). By contrast, rhyolitic pumice may be undercooled by several hundred degrees as it leaves the vent. Optimum conditions for crystal nucleation and growth are 50°C-100°C undercooling (Sparks and Pinkerton, 1978); greater cooling causes

inhibition of crystal growth due to slower rates of reaction. This effect is intensified in undercooled salic magmas due to their generally lower initial temperatures and higher viscosities. Thus salic pyroclastics are frequently glassy and groundmass crystallisation is not initiated, if at all, until substantially after eruption. Crystallisation does not therefore interfere in the initial stages with the processes of agglutination and welding, although it may eventually restrict the full development of welding and rheomorphism (Wolff and Wright, 1981a). By contrast, basalts may crystallise substantially within a few minutes of the undercooling event (Sparks and Pinkerton, 1978). The rheological consequence is the rapid development of a yield strength in the erupting magma.

Apparent viscosities of terrestrial basalt magmas are typically 10^3-10^5 poise at 1 bar. Figures 6.28 and 6.30 indicate that some degree of agglutination is inevitable if these viscosities are retained during transport, even allowing for sub-terminal velocity impact speeds. If the agglutinate is Newtonian, a lava flow will rapidly form; this may be the case where gentle fire-fountaining activity causes the rapid accumulation of a spatter pile close to the vent. Under these conditions a clastogenic lava may begin to flow before the magma develops a substantial yield strength, particularly if undercooling is at a minimum, as would be expected for the small amounts of gas released by low fountains (Wilson and Head, 1981). Conversely, very large rheological changes may occur during the transport of large clasts during strombolian eruptions, as evidenced by spindle bombs.

Such bombs must be derived from a magma, which was sufficiently fluid at fragmentation to allow viscous flow-dominated morphologies to form,

yet their yield strengths (or v scosities) upon impact were sufficient to completely resist deformation. Thus a large range in rheologies is exhibited by basaltic pyroclasts.

It was earlier shown that agglutination structures are unlikely to be preserved in glassy deposits, due to the high probability of modification by subsequent load-pressure welding and rheomorphism. This is not necessarily the case in basaltic eruptions where the magma develops an appreciable yield strength during or soon after its emergence from the vent. The critical depth, d_c, required of a lava with a yield strength σ_y flowing under the influence of gravity is

$$d_c = \frac{\sigma_y}{gp\alpha} \qquad 10$$

where p = density, and α = slope angle (Hulme and Fielder, 1977). Critical depths are shown for a range of yield strengths and slope angles in Figure 6.31. Comparison with Figure 6.29 demonstrates that there is a range of yield strengths which are low enough to allow agglutination, but too high to permit a lava flow to form. For thin accumulations ($\sim$5 m), this range is approximately 10^5-10^7 Nm^{-2}. Therefore, if cooling is sufficient to produce an appropriate yield strength, spatter structures will form and be preserved with no lava flow. A corollary is that thick spatter piles cannot form from Newtonian magma. Spatter cones are fairly commonly formed during small basaltic eruptions.

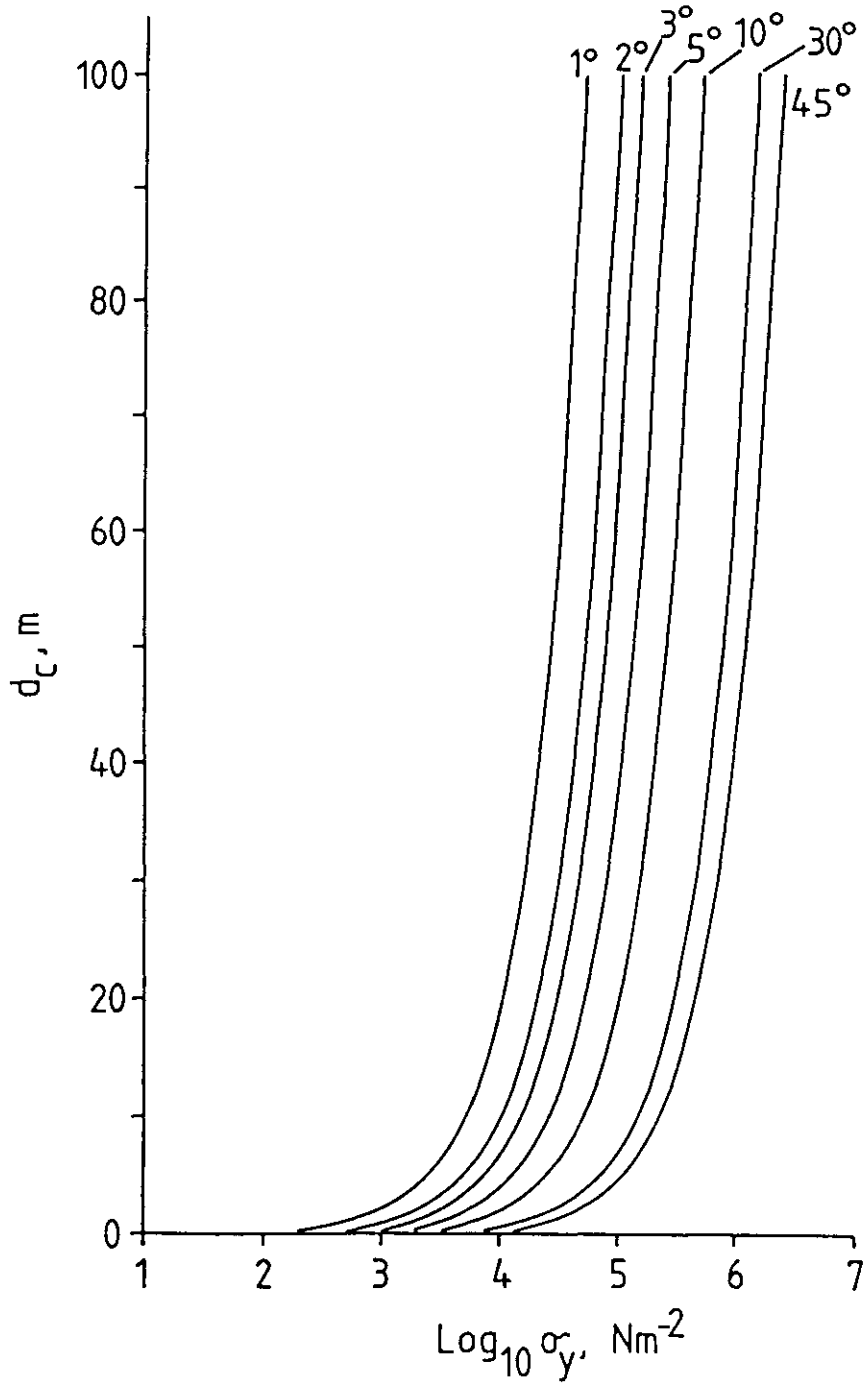

Fig. 6.31 Relationship between critical depth required for flow (d_c) and yield stress (σ_y) of a Bingham lava for seven values of slope angle, calculated from equation (10).

VI.5.iii Suggested thermal facies model for plinian air-fall deposits

The facies concept is an extremely useful tool in geology, but has been little employed in the field of volcanology. Smith's (1960b) welding-zone classification is essentially a facies model, and recently Wright et al. (1980) have proposed a facies model for ignimbrites. The demonstration that agglutination requires more fluid (and therefore, for any one eruption unit, hotter) pumice than load-pressure welding, together with the recognition of conditions necessary for rheomorphism (Wolff and Wright, 1981a) suggests a simple thermal facies model for air-fall deposits. It is emphasised that the proposed scheme is very tentative and is open to modification in the event of further data on welded air-fall tuffs becoming available.

The scheme is summarised in Table 6.1. The lateral changes indicated also occur vertically; most of the examples given display the whole range of facies from the maximum in single vertical sections. Considerable uncertainty attaches to the clastogenic lava facies, since this has never been described from a salic pumice deposit, and indeed is likely to occur only very rarely, among unusually fluid ejecta derived from magmas of extreme composition. The rheomorphic facies is itself rare among air-fall deposits, and at present has only been documented from Pantelleria (Wright, 1980), although its occurrence in other areas of alkaline volcanism seems probable, particularly as incipient rheomorphic structures occur in some rhyolitic Icelandic welded air falls, including the Askja 1875 tuff (H. Sigurdsson, pers. comm.). The remaining welded facies (3+4 in Table 6.1) are relatively common; several examples are listed by Sparks and Wright (1979). It should

be noted that the model cannot be directly applied to basaltic air-fall deposits due to the rheological differences noted previously, and thus the uncertainty regarding the role of load-pressure welding of basaltic scoria.

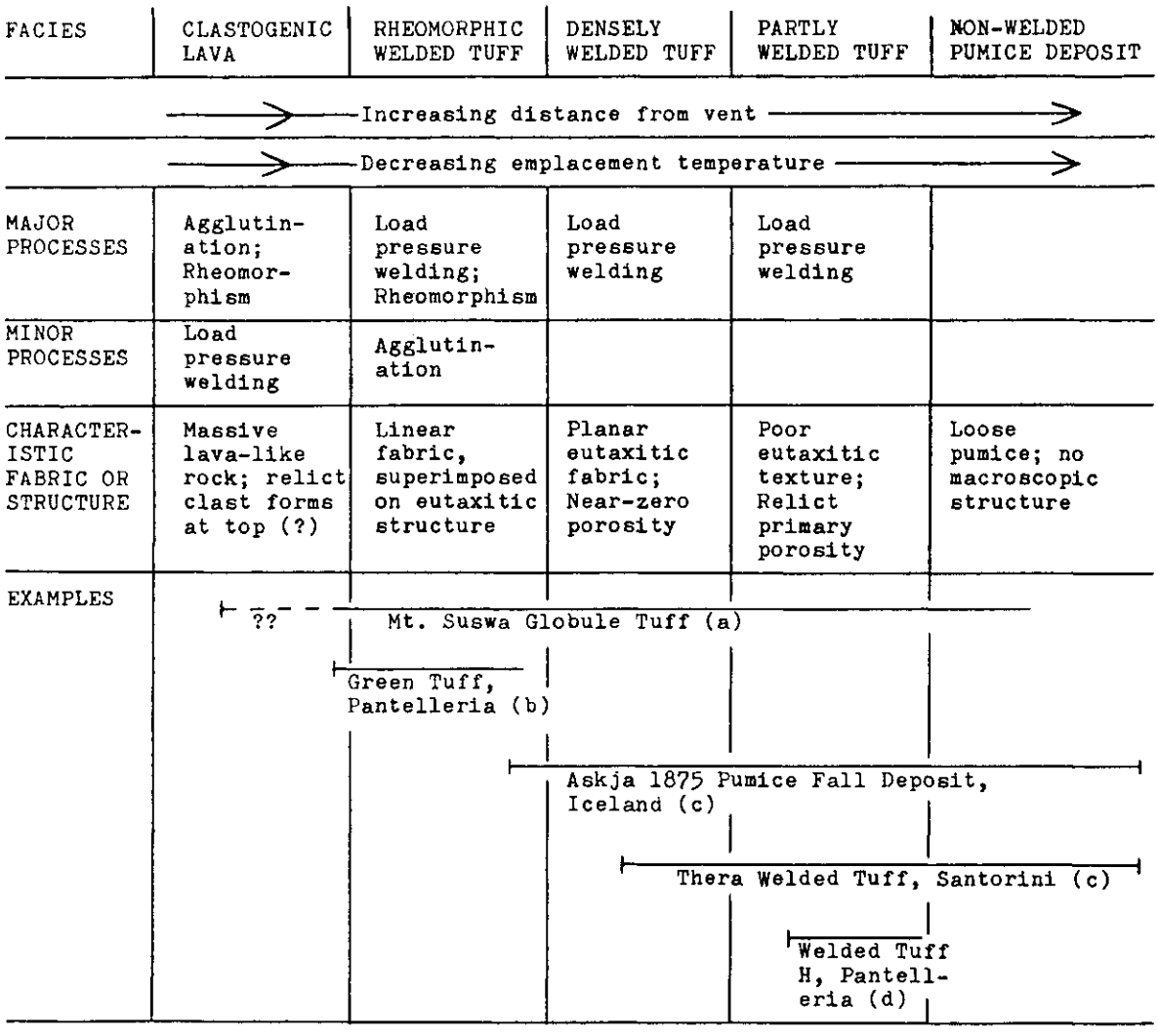

(a) Hay et al. (1979), this work; (b) Wright (1980), Wolff & Wright (1981a,b), this work; (c) Sparks & Wright (1979), H. Sigurdsson (pers. comm.); (d) Wright (1980).

TABLE 6.1 Suggested thermal facies model for plinian air-fall pumice deposits.

REFERENCES

ABDEL-MONEM, A., WATKINS, N.D. & GAST, P.W., 1971. Potassium-argon ages, volcanic stratigraphy, and geomagnetic polarity history of the Canary Islands: Lanzarote, Fuerteventura, Gran Canaria and Gomera. Amer. J. Sci. 271, 490-521.

ABDEL-MONEM, A., WATKINS, N.D. & GAST, P.W., 1972. Potassium-argon ages, volcanic stratigraphy, and geomagnetic polarity history of the Canary Islands: Tenerife, La Palma, Hierro. Amer. J. Sci. 272, 805-825.

ANDERSON, A.T., 1968. The oxygen fugacity of alkaline basalt and related magmas, Tristan da Cunha. Amer. J. Sci. 266, 704-727.

ANDERSON, A.T., 1976. Magma mixing: petrological process and volcanological tool. J. Volcanol. Geotherm. Res. 1, 3-33.

ANDERSON, J.G., 1974. The geology of Alangorssuaq, Northern Nunarssuit Complex, South Greenland. Ph.D. thesis, Univ. of Aberdeen.

ARAMAKI, S. & LIPMAN, P.W., 1965. Possible leaching of Na_2O during hydration of volcanic glasses. Japanese Acad. Proc. 41, 467-470.

BAILEY, D.K., 1969. The stability of acmite in the presence of H_2O. Amer. J. Sci. 267A, 1-18.

BANNISTER, F.A. & HEY, M.H. 1931. A chemical, optical and X-ray study of nepheline and kaliophilite. Mineral. Mag. 22, 569-608.

BARTH, T.F., 1964. The composition of nepheline. Schweiz. Mineral. Petrol. Mitt. 43, 153-164.

BISHOP, F.C., 1980. The distribution of Fe^{2+} and Mg between co-existing ilmenite and pyroxene with applications to geothermometry. Amer. J. Sci. 280, 46-77.

BLAKE, S., 1981. Eruptions from zoned magma chambers. J. Geol. Soc. Lond. 138, 281-287.

BLOOMFIELD, K., SANCHEZ-RUBIO, G. & WILSON, L., 1977. Plinian eruptions of Nevada de Toluca volcano, Mexico. Geol. Rundsch. 66, 120-146.

BOOTH, B., 1973. The Granadilla Pumice Deposit of southern Tenerife, Canary Islands. Proc. Geol. Assoc. 84, 353-370.

BOOTH, B., 1979. Assessing volcanic risk. J. Geol. Soc. Lond. 136, 331-340.

BOOTH, B., CROASDALE, R. & WALKER, G.P.L., 1978. A quantitative study of five thousand years of volcanism on Sao Miguel, Azores. Phil. Trans. R. Soc. A 288, 271-319.

BOOTH, B. & WALKER, G.P.L., in preparation. Products of explosive volcanism on Tenerife, Canary Islands.

BORLEY, G.D., 1974. Aspects of the volcanic history and petrology of the island of Tenerife. Proc. Geol. Assoc. 85, 259-279.

BORLEY, G.D., SUDDABY, P. & SCOTT., P.W., 1971. Some xenoliths from the alkalic rocks of Tenerife, Canary Islands. Contrib. Mineral. Petrol. 31, 102-114.

BORRADAILE, G.J., 1972. Variably orientated co-planar folds. Geol. Mag. 109, 89-98.

BOSSHARD, E., 1969. Crustal studies around the Western Canary Islands. Ph.D. thesis, Univ. of London.

BOSSHARD, E. & MACFARLANE, D.J.,1970. Crustal structure of the western Canary Islands from seismic refraction and gravity data. J. Geophys. Res. 75, 4901-4918.

BOTTINGA, Y. & WEILL, D.F., 1970. Densities of liquid silicate systems calculated from partial molar volumes of oxide components. Amer. J. Sci. 269, 169-182.

BOWEN, N.L. & TUTTLE, O.F., 1950. The system $NaAlSi_3O_8$-$KAlSi_3O_8$-H_2O. J. Geol. 58, 489-511.

BROOKS, C.K. & PRINTZLAU, I., 1978. Magma mixing in mafic alkaline volcanic rocks: the evidence from relict phenocryst phases and other inclusions. J. Volcanol. Geotherm. Res. 4, 315-331.

BUDDINGTON, A.F. & LINDSLEY, D.H., 1964. Iron-titanium oxide minerals and synthetic equivalents. J. Petrol. 5, 310-357.

BURNHAM C.W., 1975. Water and magmas: a mixing model. Geochim. Cosmochim. Acta 39, 1007-1084.

BURNHAM, C.W., HOLLOWAY, J.R. & DAVIES, N.F., 1969a. Thermodynamic properties of water to 1000°C and 10,000 bars. Geol. Soc. Amer. Special Paper 132, 1-96.

BURNHAM, C.W., HOLLOWAY, J.R. & DAVIES, N.F., 1969b. The specific volume of water in the range 1000 to 8900 bars, 20° to 900°C. Amer. J. Sci. 267A, 70-95.

CARMAN, J.H. & TUTTLE, O.F., 1967. Experimental verification of solid solution of excess silica in sanidine from rhyolites. Geol. Soc. Amer. Special Paper 115, 33.

CARMICHAEL, I.S.E., 1967a. The iron-titanium oxides of salic volcanic rocks and their associated ferromagnesian silicates. Contrib. Mineral. Petrol. 14, 36-64.

CARMICHAEL, I.S.E., 1967b. The mineralogy and petrology of the volcanic rocks from the Leucite Hills, Wyoming. Contrib. Mineral. Petrol. 15, 24-66.

CARMICHAEL, I.S.E., NICHOLLS, J. & SMITH, A.L., 1970. Silica activity in igneous rocks. Amer. Mineral. 55, 246-263.

CARMICHAEL, I.S.E., NICHOLLS, J., SPERA, F.J., WOOD, B.J. & NELSON, S., 1977. High-temperature properties of silicate liquids: applications to the equilibration and ascent of basic magma. Phil. Trans. R. Soc. Lond. A 286, 373-431.

CARMICHAEL, I.S.E., TURNER, F.J. & VERHOOGEN, J., 1974. Igneous petrology. McGraw-Hill, 739 pp.

CAWTHORN, R.G. & COLLERSON, K.D., 1974. The recalculation of pyroxene endmember parameters. Amer. Mineral. 59, 1203-1208.

CHAPIN, C.E. & LOWELL, G.R., 1979. Primary and secondary flow structures in ash-flow tuffs of the Gribbles Run paleovalley, central Colorado. In: Chapin, C.E. & Elston, W.E. (Eds.), Ash-flow tuffs. Geol. Soc. Amer. Special Paper 180, 137-154.

CLOUGH, B.J., 1981. The geology of La Primavera volcano, Mexico. Ph.D. thesis, Univ. of London.

DASH, B.P. & BOSSHARD, E., 1969. Seismic & gravity-investigations around the western Canary Islands. Earth Planet. Sci. Lett. 7, 169-177.

DEAL, E.G., 1973. Primary laminar flow structures in the rhyolite ash-flow tuff of A.L. Peak, San Mateo Mountains, New Mexico. Geol. Soc. Amer. Abs. W. Prog. 5, 475.

DEER, W.A., HOWIE, R.A. & ZUSSMAN, J., 1966. An introduction to the rock-forming minerals. Longman, 528 pp.

DOLLASE, W.A. & THOMAS, W.M., 1978. The crystal chemistry of silica-rich, alkali-deficient nepheline. Contrib. Mineral. Petrol. 66, 311-318.

DUFFIELD , W.A., STIELTJES, L. & VARET, J., 1982. Huge landslide blocks in the grouth of Piton de la Fournaise, La Reunion, and Kilauea volcano, Hawaii. J. Volcanol. Geotherm. Res. 12, 147-160.

EICHELBERGER, J.C., 1979. Vapor exsolution in andesitic and bimodal volcanism and an estimate of depth to magma. EOS 60, 410.

EICHELBERGER, J.C., 1980. Vesiculation of mafic magma during replenishment of silicic magma reservoirs. Nature 288, 446-450.

EWART, A., GREEN, D.C., CARMICHAEL, I.S.E. & BROWN, F.H., 1971. Voluminous low temperature rhyolitic magmas in New Zealand. Contrib. Mineral. Petrol. 33, 128-144.

EWART, A., HILDRETH, W. & CARMICHAEL, I.S.E., 1975. Quaternary acid magma in New Zealand. Contrib. Mineral. Petrol. 51, 1-27.

FERGUSON, A.K., 1977. Titanium in aegirines - a comment on: Crystallisation trends of pyroxenes from the alkaline volcanic rocks of Tenerife, Canary Islands, by P.W. Scott. Mineral. Mag. 41, 553-554.

FERGUSON, A.K., 1978. The occurrence of ramsayite, titan-lavenite and a fluorine-rich eucolite in a nepheline-syenite inclusion from Tenerife, Canary Islands. Contrib. Mineral. Petrol. 66, 15-20.

FISHER, R.V., 1979. Models for pyroclastic surges and pyroclastic flows. J. Volcanol. Geotherm. Res. 6, 305-318.

FRANCIS, P.W. & BAKER, M.C.W., 1977. Mobility of pyroclastic flows. Nature 270, 164-165.

FRANCIS, P.W., ROOBOL, M.J., WALKER, G.P.L., COBBOLD, P.R. & COWARD, M.P., 1974. The San Pedro and San Pablo volcanoes of northern Chile and their hot avalanche deposits. Geol. Rundsch. 63, 357-388.

FRIEDMAN, I., LONG, W. & SMITH, R.L., 1963. Viscosity and water content of rhyolite glass. J. Geophys. Res. 68, 6523-6535.

FRITSCH, K. VON & REISS, W., 1868. Geologische Beschreibung der Insel Tenerife. Wurster & Co., Winterthur, 496 pp.

FROGGAT, P.C., WILSON, C.J.N. & WALKER, G.P.L., 1981. Orientation of logs in the Taupo ignimbrite as an indicator of flow direction and vent position. Geology 9, 109-111.

FUSTER, J.M., ARAÑA, V., BRANDLE, J.L., NAVARRO, M., ALONSO, U. & APARICIO, A., 1968. Geology and volcanology of the Canary Islands: Tenerife. Inst. "Lucas Mallada", Madrid, 218 pp.

GIBSON, I.L., 1970. A pantelleritic welded ash-flow from the Ethiopian Rift Valley. Contrib. Mineral. Petrol. 28, 89-111.

GOMES, C. DE B., MORO, S.I. & DUTRA, C.V., 1970. Pyroxenes from the alkaline rocks of Itipirapua, Sao Paolo, Brazil. Amer. Mineral. 55, 224-230.

GRAPES, R., YAGI, K. & OKUMURA, K., 1979. Aenigmatite, sodic pyroxene, arfvedsonite and associated minerals from Morutu, Sakhalin. Contrib. Mineral. Petrol. 69, 97-103.

HAMILTON, D.L., 1961. Nephelines as crystallisation temperature indicators. J. Geol. 69, 321-329.

HAMILTON, D.L. & MACKENZIE, W.S., 1965. Phase-equilibrium studies in the system $NaAlSiO_4$ (nepheline) - $KAlsiO_4$ (Kalsilite) - SiO_2-H_2O. Mineral. Mag. 34, 214-231.

HARRIS, C. & BELL, J.D., 1982. Natural partial melting of syenite blocks from Ascension Island. Contrib. Mineral. Petrol. 79, 107-113.

HASKIN, L.A., FREY, F.A., SCHMITT, R.A. & SMITH, R.H., 1966. Meteoric, solar and terrestrial rare-earth distributions. In: Ahrens, L. (Ed.), Physics and chemistry of the Earth 7, 169-321.

HAUSEN, H., 1956. Contributions to the geology of Tenerife. Soc. Sci. Fennica Comm. Phys. Math. 18, 254 pp.

HAY, R.L., 1975. Globule ignimbrite of Mt. Suswa, Kenya. Geol. Soc. Amer. Abs. Prog. 7, 1104.

HAY, R.L., HILDRETH, W. & LAMBE, R.N., 1979. Globule ignimbrite of Mount Suswa, Kenya. In: Chapin, C.E. & Elston, W.E. (Eds.), Ash-flow tuffs, Geol. Soc. Amer. Special Paper 180, 167-175.

HELLMAN, P.L. & GREEN, T.H., 1979. The role of sphene as an accessory phase in the high-pressure partial melting of hydrous mafic compositions. Earth Planet. Sci. Lett. 42, 191-201.

HELZ, R.T., 1973. Phase relations of basalts in their melting range at P_{H2O} = 5kb as a function of oxygen fugacity. Part I. Mafic phases. J. Petrol. 14, 249-302.

HEMING, R.F. & CARMICHAEL, I.S.E., 1973. High-temperature pumice flows from the Rabaul caldera, Papua New Guinea. Contrib. Mineral. Petrol. 38, 1-20.

HILDRETH, W., 1979. The Bishop Tuff: evidence for the origin of compositional zonation in silicic magma chambers. In: Chapin, C.E. & Elston, W.E. (Eds.)., Ash-flow tuffs, Geol. Soc. Amer. Special Paper 180, 43-75.

HOLDAWAY, M.J., 1980. Chemical formulae and activity models for biotite, muscovite and chlorite applicable to pelitic metamorphic rocks. Amer. Mineral. 65, 711-719.

HUDLESTON, P.J., 1969. The morphology and development of folds. Ph.D. thesis, Univ. of London.

HUDLESTON, P.J., 1973a. Fold morphology and some geometrical implications of theories of fold development. Tectonophysics 16, 1-46.

HUDLESTON, P.J., 1973b. An analysis of single layer folds developed experimentally in viscous media. Tectonophysics 16, 189-214.

HUDLESTON, P.J., 1973c. An analysis and interpretation of minor folds in the Moine rocks of Monar, Scotland. Tectonophysics 17, 89-132.

HULME, G., 1974. The interpretation of lava flow morphology. Geophys. J.R. Astron. Soc. 39, 361-383.

HULME, G. & FIELDER, G., 1977. Effusion rates and rheology of lunar lavas. Phil. Trans. R. Soc. Lond. A 285, 227-234.

HUPPERT, H.E. & SPARKS, R.S.J., 1980. The fluid dynamics of a basaltic magma chamber replenished by influx of hot, dense ultrabasic magma. Contrib. Mineral. Petrol. 75, 279-289.

HUPPERT, H.E., SPARKS, R.S.J. & TURNER, J.S., 1982a. Effects of volatiles on mixing in calc-alkaline magma systems. Nature 297,554-557.

HUPPERT, H.E. & TURNER, J.S., 1981. A laboratory model of a replenished magma chamber. Earth Planet. Sci. Lett. 54, 144-152.

HUPPERT, H.E., TURNER, J.S. & SPARKS, R.S.J., 1982b. Replenished magma chambers: effects of compositional zonation and input rates. Earth Planet. Sci. Lett. 57, 345-357.

JÉRÉMINE, E., 1933. Contribution à l'étude pétrographique de trois îles de l'archipel Canarien, Tenerife, La Palma, Gran Canaria. Bull. Soc. Minéral. France 56, 189-261.

JOHNSON, R.W., 1966. The geology of Mount Suswa, Kenya. Ph.D. thesis, Univ. of London.

JOHNSON, R.W., 1968. Volcanic globule rock from Mount Suswa, Kenya. Geol. Soc. Amer. Bull. 79, 647-651.

JONES, A.P. & PECKETT, A., 1980. Zirconium-bearing aegiri es from Motzfeldt, South Greenland. Contrib. Mineral. Petrol. 75, 251-255.

KELLER, J., RYAN, W.B.F., NINKOVICH, D. & ALTHERR, R., 1978. Explosive volcanic activity in the Mediterranean over the past 200,000 years as recorded in deep sea sediments. Bull. Geol. Soc. Amer. 89, 591-604.

KONO, Y. & OSIMA, Y., 1971. Numerical experiments on the welding process in pyroclastic flow deposits. Bull. Volcanol. Soc. Japan 16, 1-14.

KORRINGA, M.K., & NOBLE, D.C., 1972. Genetic significance of chemical, isotopic, and petrographic features of some peralkaline salic rocks from the island of Pantelleria. Earth Planet. Sci. Lett. 17, 258-262.

KRAMAR, U. & PUCHELT, H., 1982. Reproducibility tests for INAA determinations with AGV-1, BCR-1 and GSP-1 and new data for 17 geochemical reference materials. Geostand. Newslett. 6, 221-227.

KUSHIRO, I. & THOMPSON, R.N. 1972. Origin of some abyssal tholeiites from the Mid-Atlantic Ridge. Carnegie Inst. Washington Yearbook 71, 403-406.

LARSEN, L.M., 1976. Clinopyroxenes and coexisting mafic minerals from the alkaline Ilimaussaq intrusion, S. Greenland. J. Petrol. 17, 258-290.

LARSEN, L.M., 1981. Sector zoned aegirine from the Ilimaussaq alkaline intrusion, South Greenland. Contrib. Mineral. Petrol. 76, 285-291.

LEDBETTER, M.T. & SPARKS, R.S.J., 1979. Duration of large-magnitude explosive eruptions deduced from graded bedding in deep-sea ash layers. Geology 7, 240-244.

LIPMAN, P.W., 1965. Chemical comparison of glassy and crystalline volcanic rocks. U.S. Geol. Survey Bull. 1201-D, 1-24.

LIPMAN, P.W., 1967. Mineral and chemical variations within an ash flow sheet from Aso caldera, southwestern Japan. Contrib. Mineral. Petrol. 16, 300-327.

LIPMAN, P.W., 1971. Iron-titanium oxide phenocrysts in compositionally zoned ash flow sheets from southern Nevada. J. Geol. 79, 438-456.

LIPMAN, P.W., CHRISTIANSEN, R.L. & ALSTINE, R.F., 1969. Retention of alkalies by calc-alkaline rhyolites during crystallisation and hydration. Amer. Mineral. 54, 286-291.

LIRER, L., PESCATORE, T., BOOTH, B. & WALKER, G.P.L., 1973. Two plinian pumice fall deposits from Somma-Vesuvius, Italy. Geol. Soc. Amer. Bull. 84, 759-772.

LOCK, B.E., 1972. A Lower Paleozoic rheo-ignimbrite from White Bay, Newfoundland. Can. J. Earth Sci. 9, 1495-1503.

MCBIRNEY, A.R., 1980. Mixing and unmixing of magmas. J. Volcanol. Geotherm. Res. 7, 357-371.

MCBIRNEY, A.R. & NOYES, R.M., 1979. Crystallisation and layering of the Skaergaard intrusion. J. Petrol. 20, 487-554.

MCDOUGALL, I. & SCHMINCKE, H-U., 1977. Geochronology of Gran Canaria, Canary Islands: age of shield-building volc nism and other magmatic phases. Bull. Volcanol. 40, 57-77.

MACFARLANE, D.J., & RIDLEY, W.I., 1968. An interpretation of gravity data for Tenerife. Earth Planet Sci. Lett. 4, 481-486.

MAHOOD, G.A., 1981. Chemical evolution of a Pleistocene rhyolitic centre: Sierra La Primavera, Jalisco, Mexico. Contrib. Mineral Petrol. 77, 129-149.

MAHOOD, G.A. & HILDRETH, W., 1980. Pantelleria, a new interpretation EOS 61, 1141.

MAHOOD, G.A. & HILDRETH, W., 1983. Large partition coefficients for trace elements in high-silica rhyolites. Geochim. Cosmochim. Acta 47, 11-30.

MAZZULO, L.J., DIXON, S.A. & LINDSLEY, D.H., 1975. T-f_{O2}

relationships in Mn-bearing Fe-Ti oxides. Geol. Soc. Amer. Abs. w. Prog. 7, 1192.

MICHAEL, P.J., 1983. Chemical differentiation of the Bishop Tuff and other high-silica magmas through crystallisation processes. Geology 11, 31-34.

MILLER, T.P. & SMITH, R.L., 1977. Spectacular mobility of ash flows around Aniakchak and Fisher calderas, Alaska. Geology 5, 173-176.

MITCHELL, R.H. & PLATT, R.G., 1982. Mineralogy and petrology of nepheline syenites from the Coldwell Alkaline Complex, Ontario, Canada. J. Petrol. 23, 186-214.

MITCHELL-THOMÉ, R.C., 1976. Geology of the Middle Atlantic Islands. Gebruder Borntraeger, Berlin, 382 pp.

MITCHELL-THOMÉ, R.C., 1981. Vulcanicity of historic times in the Middle Atlantic Islands. Bull. Volcanol. 44, 57-69.

MOORE, J.G. & MELSON, W.G., 1969. Nuées ardentes of the 1968 eruption of Mayon volcano, Phillipines. Bull. Volcanol. 33, 600-620.

MUELLER, R.F., 1972. Stability of biotite: a discussion. Amer. Mineral. 57, 300-316.

NASH, W.P., CARMICHAEL, I.S.E. & JOHNSON, R.W., 1969. The mineralogy and petrology of Mt. Suswa, Kenya. J. Petrol. 10, 409-439.

NELSON, S.A. & CARMICHAEL, I.S.E., 1979. Partial molar volumes of oxide components in silicate liquids. Contrib. Mineral. Petrol. 71, 117-124.

NICHOLLS, J. & CARMICHAEL, I.S.E., 1969. Peralkaline acid liquids: a petrological study. Contrib. Mineral. Petrol. 20, 268-294.

NICHOLLS, J., CARMICHAEL, I.S.E. & STORMER, J.C., 1971. Silica activity and P total in igneous rocks. Contrib. Mineral. Petrol. 33, 1-20.

NIELSEN, T.F.D., 1979. The occurrence and formation of Ti-aegirines in peralkaline syenites. Contrib. Mineral. Petrol. 69, 235-244.

NOBLE, D.C., 1967. Sodium, potassium and ferrous iron contents of some secondarily hydrated natural silicic glasses. Amer. Mineral. 52, 280-286.

NOBLE, D.C., 1968. Laminar viscous flowage structures in ash-flow tuffs from Gran Canaria, Canary Islands: a discussion. J. Geol. 76, 721-723.

NORDLIE, B.E., 1971. The composition of the magmatic gas of Kilauea and its behaviour in the near-surface environment. Amer. J. Sci. 271, 417-463.

NORRISH, K. & HUTTON, J.T., 1969. An accurate X-ray spectrographic method for the analysis of a wide range of geological samples. Geochim. Cosmochim. Acta 33, 431-453.

PARKER, D.F., 1972. Laminar flow in a peralkaline ash-flow sheet, Davis Mountains, Texas. Geol. Soc. Amer. Abs. w. Prog. 4, 288.

PARKER, R.J., 1977. Factors affecting the quality of major element rock analysis by X-ray fluorescence combined with flux-fusion sample preparation. Tech. Report XRF-2B, Dept. Geol., Imperial College, 35pp.

PARKER, R.J., 1979. A computer-based system of XRF analysis and its application to a study of volcanic rocks from Vulsini, Central Italy. Ph.D. thesis, Univ. of London.

PARKER, R.J., 1980. Computer processing and evaluation of XRF analytical data for silicate rock samples. Tech. Report. XRF-4, Dept. Geol, Imperial College.

PERCHUK, I.L. & RYABCHIKOV, I.D., 1968. Mineral equilibria in the system nepheline-alkali feldspar-plagioclase and their petrologic significance. J. Petrol. 9, 123-167.

PHILPOTTS, A.R., 1976. Silicate liquid numiscibility: its probable extent and petrogenetic significance. Amer. J. Sci. 276, 1147-1177.

PHILPOTTS, A.R., 1978. Textural evidence for liquid immiscibility in tholeiites. Mineral. Mag. 42, 417-426.

PINCKNEY, L.R. & LINDSLEY, D.H., 1976. Effects of magnesium on iron-titanium oxides. Geol. Soc. Amer. Abs. w. Prog. 8, 1051.

PINKERTON, H. & SPARKS, R.S.J., 1978. Field measurements on the rheology of lava. Nature 276, 383-385.

POTTS, P.J., THORPE, O.W. & WATSON, J.S., 1981. Determination of the rare-earth element abundances in 29 interrational rock standards by instrumental neutron activation analysis: a critical appraisal of calibration errors. Chem. Geol. 34, 331-352.

POWELL, M., 1978. The crystallisation history of the Igdlerfigssalik nepheline syenite intrusion, Greenland. Lithos 11, 99-120.

POWELL, M. & POWELL, R., 1974. An olivine-clinopyroxene geothermometer. Contrib. Mineral. Petrol. 48, 249-263.

POWELL, M. & POWELL, R., 1977a. Plagioclase - alkali feldspar geothermometry revisited. Mineral. Mag. 41, 253-256.

POWELL, M. & POWELL, R., 1977b. A nepheline - alkali feldspar geothermometer. Contrib. Mineral. Petrol. 62, 193-204.

POWELL, R. & POWELL, M., 1977c. Geothermometry and oxygen barometry using co-existing iron-titanium oxides: a reappraisal. Mineral. Mag. 41, 257-263.

POWELL, R., 1978. Equilibrium thermodynamics in petrology. Harper & Row, London, 284 pp.

RAGAN, D.M. & SHERIDAN, M.F., 1972. Compaction of the Bishop Tuff. Geol. Soc. Amer. Bull. 83, 95-106.

RAMSAY, J.G., 1967. Folding and fracturing of rocks. McGraw-Hill, New York, 568 pp.

RICE, A., 1981. Convective fractionation: a mechanism to provide cryptic zoning (macrosegregation), layering, crescumulates, banded tuffs, and explosive volcanism in igneous processes. J. Geophys. Res. 86, 405-417.

RICHTER, D.H., EATON, J.P., MURATA, K.J., AULT, W.V. & KRIVOY, H.L., 1970. Chronological narrative of the 1959-1960 eruption of Kilauea volcano, Hawaii. U.S. Geol. Survey Prof. Paper 537E, 73pp.

RIDLEY, W.I., 1967. Volcaniclastic rocks in Tenerife. Nature 213, 55-57.

RIDLEY, W.I. 1968. The geology of the Las Canadas area, Tenerife. Ph.D. thesis, Univ. of London.

RIDLEY, W.I. 1970a. The abundance of rock types on Tenerife, Canary Islands, and its petrogenetic significance. Bull. Volcanol. 34, 196-204.

RIDLEY, W.I., 1970b. The petrology of the Las Canadas volcanoes, Tenerife, Canary Islands. Contrib. Mineral. Petrol. 26, 124-160.

RIDLEY, W.I., 1970c. Morphology of Quaternary phonolite lavas from Tenerife, Canary Islands. Geol. Mag. 107, 559-560.

RIDLEY, W.I., 1971a. The field relations of the Canadas volcanoes, Tenerife, Canary Islands. Bull. Volcanol. 35, 318-335.

RIDLEY, W.I., 1971b. The origin of some collapse structures in the Canary Islands. Geol. Mag. 108, 477-484.

RIEHLE, J.R., 1973. Calculated compaction profiles of rhyolitic ash-flow tuffs. Geol. Soc. Amer. Bull. 84, 2193-2216.

RITTMAN, A., 1958. Cenni sulle colate di ignimbriti. Catania Acad. Gioenia di Sci., Nat. Boll., Ser. 4 4, 524-533.

RITTMAN, A., 1962. Volcanoes and their activity. Wiley-Interscience, New York, 305 pp.

ROEDER, P.L. & EMSLIE, R.F., 1970. Olivine-liquid equilibrium. Contrib. Mineral. Petrol. 29, 275-289.

ROSS, C.S. & SMITH, R.L., 1961. Ash-flow tuffs: their origin, geologic relations, and identification. U.S. Geol. Survey Prof. Paper 366, 81 pp.

RUTHERFORD, N.F. & HEMING, R.F., 1978. The volatile component of Quaternary ignimbrite magmas from the North Island, New Zealand.

Contrib. Mineral. Petrol. 65, 401-411.

RUTTEN, M.G., & VAN EVERDINGEN, R.O., 1961. Rheo-ignimbrites of the Ramnes volcano, Permian, Oslo Graben. Geol. Mijnbouw 40, 49-57.

RYALL, F. & RYALL, A., 1981. Attenuation of P and S waves in a magma chamber in Long Valley Caldera, California. Geophys. Res. Lett. 8, 557-560.

RYZHENKO, B.N. & VOLKOV, V.P., 1971. Fugacity coefficients of some gases in a broad range of temperatures and pressures. Geochem. Int. 8, 468-481.

SACK, R.O., CARMICHAEL, I.S.E., RIVERS, M. & GHIORSO, M.S., 1980. Ferric-ferrous equilibria in natural silicate liquids at 1 bar. Contrib. Mineral. Petrol. 75, 369-376.

SANDERSON, D.J., 1973. The development of fold axes oblique to the regional trend. Tectonophysics 16, 55-70.

SCHEIDEGGER, K.F., JEZEK, P.A. & NINKOVICH, D., 1978. Chemical and optical studies of glass shards in Pleistocene and Pliocene ash layers from DSDP site 192, north-west Pacific Ocean. J. Volcan. Geotherm. Res. 4, 99-116.

SCHMINCKE, H-U. 1970. Ignimbrite sequence on Gran Canaria. Bull. Volcanol. 33, 119-1219.

SCHMINCKE, H-U., 1972. Froth flows and globule flows in Kenya. Die Naturwiss. 11, 1-2.

SCHMINCKE, H-U., 1974. Volcanological aspects of peralkaline silicic welded ash-flow tuffs. Bull. Volcanol. 38, 594-636.

SCHMINCKE, H-U & SWANSON, D.A., 1967a. Laminar viscous flowage structures in ash-flow tuffs from Gran Canaria, Canary Islands. J. Geol. 75, 641-664.

SCHMINCKE, H-U & SWANSON, D.A., 1967b. Ignimbrite origin of eutaxites from Tenerife, Canary Islands. Neues Jahrbuch Geol. Pal. Mitt. 11, 700-703.

SCOTT, P.W., 1970. Ferromagnesian minerals from the volcanic suite of Tenerife, Canary Islands. Ph.D. thesis, Univ. of London.

SCOTT, P.W., 1976. Crystallisation trends of pyroxenes from the alkaline volcanic rocks of Tenerife, Canary Islands. Mineral. Mag. 40, 805-816.

SCOTT, P.W., 1977. Titanium in aegirines - a reply. Mineral. Mag. 41, 554-555.

SCOTT, R.B., 1966. Origin of chemical variations within ignimbrite cooling units. Amer. J. Sci. 264, 273-288.

SCOTT, R.B., 1969. Chemical variations in fine dust interstitial to glass shards of ignimbrite cooling units. Geol. Soc. Am. Abs. 4, 73.

SCOTT, R.B., 1971a. Chemical variations in glass shards and interstitial dust of ignimbrite cooling units. Amer. J. Sci. 270, 116-173.

SCOTT, R.B., 1971b. Alkali exchange during devitrification and hydration of glasses in ignimbrite cooling units. J. Geol. 79, 100-110.

SELF, S., 1973. Recent volcanism on Terceira, Azores. Ph.D. thesis, Univ. of London.

SELF, S., 1976. The Recent volcanology of Terceira, Azores. J. Geol. Soc. Lond. 132, 645-666.

SHACKLETON, R.M., 1959. The stratigraphy of the Meol Hebog district between Snowdon and Tremadoc. Liverpool & Manchester Geol. J. 2, 216-252.

SHAW, H.R., 1972. Viscosities of magmatic silicate liquids: an empirical method of prediction. Amer. J. Sci. 272, 870-893.

SHERIDAN, M.F., 1979. Emplacement of pyroclastic flows: a review. In: Chapin, C.E. & Elston, W.E. (Eds.), Ash-flow tuffs, Geol. Soc. Amer. Special Paper 180, 125-136.

SHIMOZURU, D., 1978. Dynamics of magma in a volcanic conduit-special emphasis on viscosity of magma with bubbles. Bull. Volcanol, 41, 333-340.

SIGURDSSON, H & SPARKS, R.S.J., 1981. Petrology of rhyolitic and mixed magma ejecta from the 1875 eruption of Askja, Iceland.

J. Petrol. 22, 41-84.

SKELLAND, A.H.P., 1967. Non-Newtonian flow and heat transfer. Wiley-Interscience, New York, 432 pp.

SMITH, R.L., 1960a. Ash flows. Bull. Geol. Soc. Amer 71, 795-842.

SMITH, R.L., 1960b. Zones and zonal variations in welded ash-flows. U.S. Geol. Survey Prof. Paper 354F, 149-159.

SMITH, R.L., 1979. Ash-flow magmatism. In: Chapin, C.E. & Elston, W.E. (Eds.), Ash-flow tuffs, Geol. Soc. Amer. Special Paper 180, 5-27.

SOMMER, M.A., 1977. Volatiles H_2O,CO_2 and CO in silicate melt inclusions in quartz phenocrysts from the rhyolitic Bandelier air-fall and ash-flow tuff, New Mexico. J. Geol. 85, 423-432.

SØRENSEN, H. (Ed.), 1974. The alkaline rocks. Wiley-Interscience, New York, 622 pp.

SPARKS, R.S.J., 1974. The products of ignimbrite eruptions. Ph.D. thesis, Univ. of London.

SPARKS, R.S.J., 1976. Grain size variations in ignimbrites and implications for the transport of pyroclastic flows. Sedimentology 23, 147-188.

SPARKS, R.S.J., 1978a. The dynamics of bubble formation and growth in magmas: a review and analysis. J. Volcanol. Geotherm. Res. 3. 1-37.

SPARKS, R.S.J., 1978b. Gas release rates from pyroclastic flows: an assessment of the role of fluidisation in their emplacement. Bull. Volcanol. 41, 1-9.

SPARKS, R.S.J., MEYER, P. & SIGURDSSON, H., 1980. Density variation amongst mid-ocean ridge basalts: implications for magma mixing and the scarcity of primitive lavas. Earth Planet. Sci. Lett. 46, 419-430.

SPARKS, R.S.J. & PINKERTON, H., 1978. Effect of degassing on rheology of basaltic lava. Nature 276, 385-386.

SPARKS, R.S.J., SELF, S. & WALKER, G.P.L., 1973. Products of ignimbrite eruptions. Geology 1, 115-118.

SPARKS, R.S.J., SIGURDSSON, H & WILSON, L., 1977. Magma mixing: a mechanism for triggering acid explosive eruptions. Nature 267, 315-318.

SPARKS, R.S.J., & WALKER, G.P.L., 1973. The ground surge deposit: a third type of pyroclastic rock. Nature 241, 62-64.

SPARKS, R.S.J., & WALKER, G.P.L., 1977. The significance of vitric-enriched air-fall ashes associated with crystal-enriched ignimbrites. J. Volcan. Geotherm. Res. 2, 329-341.

SPARKS, R.S.J. & WILSON, L., 1976. Model for ignimbrite formation by gravitational column collapse. J. Geol. Soc. Lond. 132, 441-451.

SPARKS, R.S.J., WILSON, L. & HULME, G., 1978. Theoretical modelling of the generation, movement and emplacement of pyroclastic flows by column collapse. J. Geophys. Res. 83, 1727-1739.

SPARKS, R.S.J. & WRIGHT, J.V., 1979. Welded air-fall tuffs. In: Chapin, C.E. & Elston, W.E. (Eds.), Ash-flow tuffs. Geol. Soc. Amer. Special Paper 180, 155-166.

SPEIDEL, D.H., 1970. Effect of magnesium on the iron-titanium oxides. Amer. J. Sci. 268, 341-353.

STEPHENSON, D., 1972. Alkali pyroxenes from the South Qoroq centre, South Greenland. Lithos 5, 187-201.

STEPHENSON, D. & UPTON, B.G.J., 1982. Ferromagnesian silicates in a differentiated alkaline complex: Kungnat Fjeld, South Greenland. Mineral. Mag. 46, 283-300.

STOREY, M., 1981. Trachytic pyroclastics from Agua de Pau volcano, Sao Miguel, Azores: evolution of a magma body over 4,000 years. Contrib. Mineral. Petrol. 78, 423-432.

STORMER, J.C., 1975. A practical two-feldspar geothermometer. Amer. Mineral. 60, 667-674.

STORMER, J.C., & CARMICHAEL, I.S.E., 1971. The free-energy of sodalite and the behaviour of chloride, fluoride and sulphate in silicate magmas. Amer. Mineral. 56, 292-306.

STULL, D.R. & PROPHET, H., 1971. Joint Army, Navy, Air Force thermochemical tables, 2nd. edition. Washington D.C., U.S. Govt. Printing Office.

TAYLOR, D., 1967. The sodalite group of minerals. Contrib. Mineral. Petrol. 16, 172-188.

THOMPSON, J.B. & WALDBAUM, D.R., 1969. Mixing properties of sanidine crystalline solutions, III. Calculations based on two-phase data. Amer. Mineral. 54, 811-838.

THOMPSON, R.N., DICKIN, A.P., GIBSON, I.L. & MORRISON, M.A., 1982. Elemental fingerprints of isotopic contamination of Hebridean Palaeocene mantle-derived magmas by Archean sial. Contrib. Mineral. Petrol. 79, 159-168.

THOMPSON, R.N. & HUMPHRIS, S.E. 1980. Silicate mineralogy of basalts from the East Pacific Rise, OCP Ridge, and Siqueiros fracture zone: Deep Sea Drilling Project Leg 54. In: Rosendahl, B.R., Hekinian, R. et al., Init. Rep DSDP 54, 651-669

TOULMIN, P. & BARTON, P.B., 1964. A thermodynamic study of pyrite and pyrrhotite. Geochim. Cosmochim. Acta 28, 641-671.

TSONG, I.S.T., HOUSER, C.A., YUSEF, N.A., MESSIER, R.F. & WHITE, W.B., 1978. Obsidian hydration profiles by sputter-induced optical emission. Science 201, 339-341.

TURNER, J.S., 1980. A fluid-dynamical model of differentiation and layering in magma chambers. Nature 285, 213-215.

TURNER, J.S. & GUSTAFSON, L.B., 1981. Fluid motions and compositional gradients produced by crystallisation or melting at vertical boundaries. J. Volcan. Geotherm. Res. 11, 93-125.

VARET, J., 1969. Les pyroxènes des phonolite du Cantal (Auvergne, France). Neues Jahrbuch Mineral. Mitt. 4, 1974-1984.

VILLARI, L., 1969. On particular ignimbrites of the island of Pantelleria (Channel of Sicily). Bull. Volcanol. 33, 828-839.

VILLARI, L., 1974. The island of Pantelleria. Bull. Volcanol. 38, 680-724.

VLASOV, K.A., KUZMENKO, M.V. & ESKOVA, E.M., 1966. The Lovozero alkali massif. Oliver + Boyd, London, ..., 627 pp.

WALKER, G.P.L., 1971. Grain-size characteristics of pyroclastic deposits. J. Geol. 79, 696-714.

WALKER, G.P.L., 1972. Crystal concentration in ignimbrites. Contrib. Mineral. Petrol. 36, 135-146.

WALKER, G.P.L., 1973. Explosive volcanic eruptions - a new classification scheme. Geol. Rundsch. 62, 431-446.

WALKER, G.P.L., 1980. The Taupo Pumice: product of the most powerful known (ultraplinian) eruption? J. Volcanol. Geotherm. Res. 8, 69-94.

WALKER, G.P.L., 1981. The Waimihia and Hatepe plinian deposits from the rhyolitic Taupo Volcanic Centre. N.Z. J. Geol. Geophys. 24, 305-324.

WALKER, G.P.L. & CROASDALE, R., 1971. Two plinian-type eruptions in the Azores. J. Geol. Soc. Lond. 127, 17-55.

WALKER, G.P.L., HEMING, R.F. & WILSON, C.J.N., 1980. Low-aspect ratio ignimbrites. Nature 283, 286-287.

WALKER, G.P.L., WILDON, C.J.N. & FROGGATT, P.C., 1981. An ignimbrite veneer deposit: the trail - marker of a pyroclastic flow. J. Volcanol. Geotherm. Res. 9, 409-422.

WALKER, G.P.L., WILSON, L. & BOWELL, E.L.G., 1971. Explosive volcanic eruptions, I. The rate of fall of pyroclasts. Geophys. J.R. Astron. Soc. 22, 377-383.

WALKER, G.P.L., WRIGHT, J.V., CLOUGH, B.J. & BOOTH, B., 1981. Pyroclastic geology of the rhyolitic volcano of La Primavera, Mexico. Geol. Rundsch. 70, 1100-1118.

WALKER, G.W. & SWANSON, D.A., 1968. Laminar flowage in a Pleistocene soda rhyolite ash-flow tuff, Lake and Harvey Counties, Oregon. U.S. Geol. Survey Prof. Paper 600B, 37-47.

WALLACE, A.B., DREXLER, J.W., GRANT, N.K., & NOBLE, D.C., 1980. Icelandite and aenigmatite-bearing pantellerite from the McDermitt caldera complex, Nevada - Oregon. Geology 8, 380-384.

WALSH, J.N., BUCKLEY, E. & BARKER, J., 1981. The simultaneous determination of the rare-earth elements in rocks using inductively coupled plasma source spectrometry. Chem. Geol. 33, 141-153.

WATKINS, N.D., 1973. Palaeomagnetism of the Canary Islands and Madeira. Geophys. J.R. Astron. Soc. 32, 249-267.

WATKINS, N.D., RICHARDSON, A. & MASON, R.G., 1966. Paleomagnetism of the Macronesian insular region: the Canary Islands. Earth Planet. Sci. Lett. 1, 225-231.

WELLMAN, T.R., 1970. The stability of sodalite in a synthetic and aqueous chloride fluid system. J. Petrol. 11, 48-71.

WILKINSON, J.F.G., 1974. The mineralogy and petrography of alkali basaltic rocks. In: Sørensen, H. (Ed.), The alkaline rocks, Wiley-Interscience, 622 pp.

WILSON, C.J.N., 1980. The role of fluidisation in the emplacement of pyroclastic flows: an experimental approach. J. Volcanol. Geotherm. Res. 8, 231-249.

WILSON, L., 1972. Explosive volcanic eruptions, II. The atmospheric trajectories of pyroclasts. Geophys. J.R. Astron. Soc. 30, 381-392.

WILSON, L., 1976. Explosive volcanic eruptions, III. Plinian eruption columns. Geophys. J.R. Astron. Soc. 45, 543-556.

WILSON, L. 1978. Energetics of the Minoan eruption. In: Doumas, C. (Ed.), Thera and the Aegean World, Proc. 2nd Int. Conf., 221-228.

WILSON, L., 1980. Relationships between pressure, volatile content and ejecta velocity in three types of volcanic explosion. J. Volcanol. Geotherm. Res. 8, 297-313.

WILSON, L. & HEAD, J.W., 1981. Ascent and eruption of basaltic magma on the Earth and Moon. J. Geophys. Res. 86, 2971-3001.

WILSON, L., SPARKS, R.S.J., HUANG, T.C. & WATKINS, N.D., 1978. The control of volcanic column heights by eruption energetics and dynamics. J. Geophys. Res. 83, 1829-1836.

WILSON, L., SPARKS, R.S.J. & WALKER, G.P.L., 1980. Explosive volvanic eruptions, IV. The control of magma properties and conduit geometry on eruption column behaviour. Geophys. J. R. Astron. Soc. 63, 117-148.

WOHLETZ, K.H. & SHERIDAN, M.F., 1979. A model of pyroclastic surge. In: Chapin, C.E. & Elston, W.E. (Eds.), Ash-flow tuffs, Geol. Soc. Am. Special Paper 180, 177-194.

WOLFF, J.A., 1976. The geology of an area south-west of Snowdon, North Wales, with particular reference to the acid volcanics. B.Sc. dissertation, Univ. of Leeds.

WOLFF, J.A. & STOREY, M., 1983. The volatile component of some pumice-forming alkaline magmas from the Azores and Canary Islands. Contrib. Mineral. Petrol. 82, 66-74.

WOLFF, J.A. & STOREY, M., in press. The use of tephra studies to determine volatile release during large explosive volcanic eruptions. In: Tech. Reports Planet. Volatiles Conf., Lunar & Planet. Inst., 1982.

WOLFF , J.A. & WRIGHT, J.V., 1981a. Rheomorphism of welded tuffs. J. Volcanol. Geotherm. Res. 10, 13-34.

WOLFF, J.A. & WRIGHT, J.V., 1981b. Formation of the Green Tuff, Pantelleria. Bull. Volcanol. 44, 681-690.

WOLFF, J.A., WRIGHT, J.V., SMITH, A.L., CLOUGH, B.J., ROOBOL, M.J. & SELF, S., 1980. Mixed pumice eruptions: field characteristics. Trans. IX Carib. Geol. Conf. 1, 355-365.

WONES, D.R., 1972. Stability of biotite: a reply. Amer. Mineral. 57, 316-317.

WONES, D.R. & EUGSTER, H.P., 1965. Stability of biotite: experiment, theory and application. Amer. Mineral. 50, 1228-1272.

WOOD, B.J., 1976. An olivine-clinopyroxene geothermometer - a discussion. Contrib. Mineral. Petrol. 56, 297-303.

WOOD, B.J. & BANNO, S., 1973. Garnet-orthopyroxene and orthopyroxene-clinopyroxene relationships in simple and complex systems. Contrib. Mineral. Petrol. 42, 109-124.

WOOD, B.J. & FRASER, D.G., 1976. Elementary thermodynamics for geologists. Oxford Univ. Press, 303 pp.

WOODCOCK, N.H., 1976. Structural style in slump sheets: Ludlow Series, Powys, Wales. J. Geol. Soc. Lond. 132, 399-415.

WRIGHT, J.V., 1979. Formation, transport and deposition of ignimbrites and welded tuffs. Ph.D. thesis, Univ. of London.

WRIGHT, J.V., 1980. Stratigraphy and geology of the welded air-fall tuffs of Pantelleria, Italy. Geol. Rundsch. 69, 263-291.

WRIGHT, J.V., 1981. The Rio Caliente ignimbrite: analysis of a compound intraplinian ignimbrite from a major late Quaternary Mexican eruption. Bull. Volcanol. 44, 189-212.

WRIGHT, J.V., SELF, S. & FISHER, R.V., in press. Towards a facies model for ignimbrite-forming eruptions. In: Self, S. & Sparks, R.S.J. (Eds.), Tephra studies as a tool in Quaternary research, NATO ASI, Iceland, 1980.

WRIGHT, J.V., SMITH, A.L. & SELF, S., 1980. A working terminology of pyroclastic deposits. J. Volcanol. Geotherm. Res. 8, 315-336.

WRIGHT, J.V. & WALKER, G.P.L., 1977. The ignimbrite source problem: significance of a co-ignimbrite lag-fall deposit. Geology 5, 729-732.

WRIGHT, J.V. & WALKER, G.P.L., 1981. Eruption, transport and deposition of ignimbrite: a case study from Mexico. J. Volcanol Geotherm. Res. 9, 111-133.

YAGI, K. & ONUMA, K., 1967. The join $CaMgSi_2O_6$ - $CaTiAl_2O_6$ and its bearing on the titanaugites. J. Fac. Sci. Hokkaido Univ. Ser. IV 13, 463-483.

YODER, H.S., 1969. Calcalkaline andesites: experimental data bearing on the origin of their assumed characteristics. In: McBirney, A.R. (Ed.), Proc. Andesite Conf., Oregon Dept. Geol. Mineral. Ind. Bull. 65, 77-89.

ZACHARIASEN, W.H., 1930. The chemical formula of the "zircon pyroxenes" and "zircon pectolites". Norsk. Geol. Tidsskr. 11, 216-218.

ZIELINSKI, R.A., LIPMAN, P.W. & MILLARD, M.T., 1977. Minor-element abundances in obsidian, perlite, and felsite of calc-alkalic rhyolites. Amer. Mineral. 62, 426-437.

Addenda

BRAZIER, S., SPARKS, R.S.J. + WILSON, L., 1983. The 1979 explosive eruption of the Soufrière volcano, St. Vincent. (abs). J. Geol. Soc. London 140, 325.

MITTLEFEHLDT, D.W. + MILLER, C.F., 1983. Geochemistry of the Sweetwater Wash Pluton, California: implications for "anomalous" trace element behaviour during differentiation of felsic magmas. Geochim. Cosmochim. Acta 47, 109-124.

APPENDIX A.

WHOLE-ROCK CHEMICAL ANALYSIS.

Sample preparation.

Following the guidelines laid down in I.2, the largest clasts from each sample (typically in the 4 - 32cm size range) were taken and cleaned of adhering material on a revolving carborundum lap. Each entire sample thus cleaned was then passed through a jaw crusher to give a maximum grain size of 2 mm. Care was taken to catch all of each sample passing through the crusher, apart from a small proportion which was used to "pre-contaminate" the crusher with identical material; this was discarded. However some unavoidable loss of fine vitric dust occurred during crushing. Samples were then crushed to 400 # in a tungsten carbide tema mill; it was found that grinding times of 15-20s were sufficient for pumice. Powders were stored in glass bottles.

Powders were weighed, dried at 110°C overnight, and reweighed to determine H_2O^-. Some ignition trials were carried out to establish an optimum ignition temperature for the LOI (loss on ignition) determination. Ignition of four representative powders at 750°C for 30 minutes resulted in the development of a yellow-brown biscuit colour in the powders, which retained their loose particulate nature. At 850°C, the colour deepened to bright brick-orange, red, or brown indicating more complete oxidation of Fe. Powders ignited at this temperature were found to be very lightly sintered coherent masses, which could easily be broken up with a spatula. Ignition at 900°C resulted in complete welding of powders to glassy masses (cf welded tuffs, Chap. VI), and pitting damage to porcelain crucibles. 850°C was therefore chosen as the optimum ignition temperature. Reweighing after ignition establishes LOI.

Samples were originally prepared for major element analysis

by X-ray fluorescence (XRF) using the PLTB (pressed lithium tetraborate briquette) method. The preparation procedure in this method is fusion of ignited rock powder with pure lithium tetraborate (sample: flux ratio 1:7), quenching of usions, crushing of resultant glass by tema mill, and pressing of the powder into a briquette using an internal PVC solution binder. At all stages, samples are kept dry by dessicator storage. The success rate (of analyses yielding acceptable oxide weight percentage totals in the range 98.7% - 100.7%) using this preparation method was 50%, which was felt to be unacceptable. A detailed study by Parker (1977) concluded that briquette quality was over-sensitive to several factors of the preparation, and thus that the PLTB method is unsuitable for routine analysis (this was shown by Parker to be particularly the case for salic rock samples).

PLTB results were therefore discarded and samples re-prepared according to the method of Norrish & Hutton (1969), in which the fusion melt is cast directly as a glass disc for presentation to the XRF spectrometer. This method is advantageous for several reasons, particularly that data processing involves fewer matrix corrections, results are more satisfactory, and sample preparation is simpler and more rapid (Parker, 1977). The success rate using this method was 97%. Clough (1981) gives further details of a comparitive study of the two methods, and shows that accuracy and precision of results from the Norrish & Hutton method are superior.

For trace element analysis, approximately 5g of dried (unignited) rock powder was pressed into a briquette (using an internal binder), with a boric acid backing. No dilution with flux is used.

For analysis of the rare earth elements (REE), U, Th, Ta (and Hf in a few samples), 0.1g of dried rock powder was weighed into a polythene capsule and heat-sealed. A nitrate solution containing known concentrations of the required elements (supplied by N.W.

Rogers) was used to make standards. 100µl aliquots were pipetted onto 5 mm diameter filter papers, which were dried and sealed into sample capsules in sealed lead pots after removal from the reactor.

Analysis

Norrish discs and pressed-rock-powder briquettes were analysed on the Phillips 1212 XRF spectrometer in the Geology Department at Imperial College. Discs were analysed for the major and minor elements Si, Ti, Al, Fe, Mn, Mg, Ca, K, and P; briquettes for the trace elements Cu, Ni, Cr, V, Ba, Rb, Sr, Th, Y, Nb, Zr and Zn. Standard procedures given by Parker (1978) were employed. Raw data were processed into concentrations using computer programs detailed by Parker (1980). Calibrations were provided by analysing international rock standards during the course of a run. Na data, obtained by wet chemistry (fusion of rock powder with lithium metaborate, followed by acid digestion of the resultant bead and flame photometric analysis) were incorporated into the data, along with drying and LOI measurements, during processing.

Neutron-irradiated samples were analysed for La and Sc on a lithium-drifted germanium solid-state detector, and for Ce, Nd, Sm, Eu, Gd, Tb, Tm, Ho, Yb and Lu on a pure germanium detector, at ULRC. Both detectors are connected to a Link Systems Ltd. analyser which output the data in the form of counts, in effect a numerical representation of the gamma-ray spectrum emitted by the irradiated samples. The analyser was pre-set before counting only to output regions of interest in the spectrum. Live counting times were around 5000s per sample. The area under each required peak of the spectrum was integrated using a computer graphics program (written by N.W. Rogers) which fitted a polynomial curve to the background data on either side of the peak, in order to interpolate the "background" under the peak itself. Peak integrals were then corrected for radioactive decay during counting and any neutron flux gradient along the sample tube (after correcting some

peaks for interferences), and ratioed to the standard data to yield concentrations.

Results, and their quality.

Whole-rock analytical data for 26 samples from five deposits are collected in Table A.1. As a major aim of the chemical study was to detect subtle differences among samples from the same deposit, an estimation of precision is vital. In Table A.2. are listed precision values, expressed as twice the relative standard deviation, for major element oxides from a set of 9 replicate preparations of a single sample from pumice fall E. Since the total compositional range (with the exception of AF3) of the sample set is very small, the quoted relative errors may be considered an accurate reflection of analytical precision for the whole set. Several replicate preparations of one sample were not made for XRF trace element or neutron activation analysis; instead in Tables A.3 and A.4 respectively are listed maximum relative discrepancies between duplicate samples for each element. Table A.5 confirms that the absolute accuracy of the neutron activation analyses is acceptable.

It was found that results for Gd, Ho, Tm and Lu were of unacceptably poor quality and were rejected. Cr and Sc were not quantitatively detected in any sample (except for 5 ppm Sc in AF3) and these elements are not listed. Ni is also present in amounts close to or below the detection limit (2-3 ppm) in most samples and little significance is attached to quoted values.

Sample locations and positions are detailed in Chapter I, and presentation of results explained in the notes to Table A.1.

Table A1.

	AF1	AF2	AF3	DF1	DF2	DF4	EF1	EF2	EF3	EF4	GF1	GF3	GF4	GF5	GF6	GF7	GF8
SiO_2	57.98	57.36	54.43	58.10	57.70	58.14	58.57	57.62	58.56	58.80	56.46	56.85	56.35	55.90	56.27	55.62	56.55
TiO_2	0.39	0.52	1.75	0.50	0.49	0.49	0.60	0.57	0.62	0.68	0.58	0.52	0.50	0.46	0.43	0.43	0.43
Al_2O_3	18.27	18.16	18.33	17.39	17.38	17.31	17.22	17.56	17.45	17.60	18.16	18.46	18.26	18.22	18.38	18.35	18.45
Fe_2O_3	2.61	2.79	6.29	3.12	3.08	3.12	2.93	2.94	3.05	3.08	3.18	3.18	3.14	3.17	3.12	3.25	3.21
MnO	0.22	0.22	0.21	0.22	0.22	0.20	0.18	0.20	0.20	0.19	0.20	0.23	0.22	0.23	0.25	0.23	0.25
MgO	0.24	0.51	1.71	0.35	0.40	0.63	0.52	0.43	0.44	0.51	0.29	0.40	0.35	0.39	0.39	0.39	0.26
CaO	0.72	1.11	4.69	0.50	0.50	0.51	0.61	0.60	0.65	0.75	0.81	0.70	0.68	0.60	0.54	0.55	0.52
Na_2O	4.68	4.63	5.08	6.81	6.53	6.46	6.66	6.99	7.01	6.77	7.03	7.60	7.52	7.61	7.12	6.60	6.91
K_2O	6.71	6.06	3.45	6.02	5.93	5.88	6.04	6.09	6.09	5.88	5.26	5.43	5.31	5.48	5.63	5.65	5.47
P_2O_5	0.05	0.09	0.44	0.06	0.05	0.05	0.07	0.06	0.07	0.09	0.08	0.06	0.06	0.05	0.05	0.05	0.05
LOI	6.15	6.23	3.36	5.69	5.56	5.44	5.58	5.56	4.68	4.62	5.52	5.18	5.27	5.52	6.16	6.18	5.81
H_2O^-	1.99	1.89	0.53	1.22	1.29	1.23	1.26	1.13	0.68	0.42	1.80	0.84	1.54	1.71	1.75	1.82	1.88
Total	100.01	99.75	100.27	99.98	99.12	99.46	100.24	99.76	99.49	99.39	99.37	99.45	99.20	99.34	100.09	99.12	99.79
Rb	200	n.d.	85	170	169	166	98	135	123	112	137	177	172	175	188	181	203
Sr	69	n.d.	935	4	6	6	5	6	5	13	52	40	42	21	14	13	11
Ba	142	n.d.	1220	-	-	-	87	42	83	364	429	206	259	102	35	20	-
Cu	11	n.d.	16	3	5	4	17	28	31	21	18	16	19	7	8	6	9
Ni	5	n.d.	37	4	4	4	4	5	3	4	6	2	4	3	4	3	5
Zn	126	n.d.	109	131	131	129	128	122	118	112	152	141	153	155	156	151	148
V	23	n.d.	105	39	35	36	38	38	42	43	41	37	36	32	30	30	31
Y	37	n.d.	50	52	54	57	29	57	59	64	33	58	53	57	58	57	59
La	113	n.d.	89	137	135	126	133	130	132	130	n.d.	n.d.	n.d.	n.d.	n.d.	n.d.	153
Ce	186	n.d.	195	254	277	282	243	229	247	247	216	225	211	220	219	227	233
Nd	36	n.d.	71	62	62	62	80	73	86	91	65	64	60	56	58	55	53
Sm	4.5	n.d.	12.4	8.5	8.8	9.2	13.4	12.3	14.7	15.2	9.0	8.6	8.0	7.8	7.5	7.6	7.4
Eu	0.86	n.d.	3.7	1.4	1.4	1.6	3.0	2.6	3.2	3.7	2.0	1.8	1.7	1.6	1.5	1.5	1.5
Tb	0.7	n.d.	1.6	1.2	1.3	1.1	1.8	1.6	1.7	1.9	1.1	1.1	1.1	1.1	1.2	1.2	1.8
Yb	3.5	n.d.	2.8	4.5	4.4	4.2	4.1	4.2	4.1	4.3	4.0	4.6	4.6	4.9	5.3	5.0	5.1
Zr	1140	n.d.	531	1130	1130	1130	484	848	790	698	720	1130	1150	1230	1280	1240	1220
Hf	n.d.	n.d.	n.d.	n.d.	n.d.	n.d.	15.8	16.3	15.2	13.4	18	24	23	27	27	28	27
Th	30.5	n.d.	12.1	27.3	26.1	31.4	17.8	20.4	18.7	17.6	26.6	30.7	32.5	33.5	33.4	33.9	36.0
U	7.3	n.d.	3.0	6.9	7.7	7.0	4.4	4.4	4.0	3.0	6.7	7.3	7.6	8.5	8.4	8.9	9.6
Nb	286	n.d.	199	340	342	344	161	290	288	265	225	368	368	381	389	373	368
Ta	13.9	n.d.	15.8	21.2	22.6	23.5	20.9	19.5	21.5	20.9	23.1	21.1	20.8	21.0	20.6	21.2	20.1

	GF9	GF10	GF11	GF12	GF13	Gig 1	Gig 6	JF1	JF5
SiO_2	56.27	56.44	57.12	56.95	57.03	57.09	57.58	54.60	55.05
TiO_2	0.45	0.48	0.56	0.51	0.55	0.58	0.61	0.48	0.48
Al_2O_3	18.38	18.37	17.94	18.35	18.05	17.89	18.01	19.84	19.84
Fe_2O_3	3.21	3.22	3.10	3.19	3.06	3.04	3.08	2.80	2.89
MnO	0.24	0.23	0.21	0.22	0.21	0.22	0.18	0.17	0.16
MgO	0.23	0.25	0.36	0.30	0.34	0.49	0.43	0.37	0.32
CaO	0.56	0.57	0.72	0.59	0.61	0.68	0.72	1.08	1.05
Na_2O	6.83	7.13	7.01	6.55	6.18	6.17	6.30	8.18	8.28
K_2O	5.25	5.51	5.62	5.77	6.07	6.30	5.98	5.88	6.05
P_2O_5	0.05	0.05	0.06	0.06	0.06	0.07	0.07	0.06	0.07
LOI	6.02	5.87	5.15	5.28	5.37	5.56	5.26	4.60	4.42
H_2O^-	1.81	1.36	1.24	1.42	1.34	1.31	1.13	0.88	0.66
Total	99.30	99.48	99.09	99.19	98.87	99.40	99.35	98.94	99.27
Rb	194	184	155	166	154	141	163	227	229
Sr	17	12	30	11	10	16	16	59	89
Ba	40	30	215	25	30	60	45	80	140
Cu	31	34	23	27	32	23	29	35	53
Ni	3	3	3	2	3	4	5	5	6
Zn	146	148	132	142	120	118	134	117	115
V	33	34	38	37	36	42	34	28	30
Y	61	57	54	53	42	50	50	25	29
La	143	150	131	144	136	132	136	94	102
Ce	199	235	213	237	227	245	226	139	143
Nd	49	58	59	62	67	73	61	29	33
Sm	6.8	8.2	8.6	8.4	9.1	10.8	8.3	3.6	4.3
Eu	1.3	1.5	1.8	1.7	1.7	2.2	1.8	0.8	0.6
Tb	0.9	1.4	1.1	1.4	1.2	1.5	1.4	0.6	0.8
Yb	4.9	4.7	4.0	4.5	4.0	3.8	4.3	3.2	3.6
Zr	1200	1210	1000	1120	740	790	960	1340	1460
Hf	n.d.	23	n.d.	23	19	n.d.	n.d.	n.d.	n.d.
Th	32.7	35.2	24.8	29.9	25.0	23.8	28.6	45.2	46.7
U	7.3	8.5	5.7	7.9	6.5	6.9	8.3	11.9	12.1
Nb	362	384	334	369	241	293	306	270	301
Ta	n.d.	21.1	n.d.	20.6	20.6	22.0	19.0	11.4	12.9

Table A1 Major- and trace-element contents of whole pumice samples from deposits A, D, E, G and J. The deposit is given by the first letter of each alphanumeric sample code, while the following letter(s) indicates the type of deposit (F is fall, ig is ignimbrite). Samples are arranges in ascending order through each deposit. Major-element abundances expressed as oxide weight %, trace-elements in parts per million. Total iron is reported as Fe_2O_3.

SiO_2	0.64
TiO_2	1.04
Al_2O_3	0.92
Fe_2O_3	1.96
MnO	10.2
MgO	7.58
CaO	1.28
K_2O	1.04
P_2O_5	17.4

Table A2 Precision (relative 2x standard deviation as percentage) of major-element XRF determinations.

Rb	1.3
Sr	1.0
Ba	23
Cu	9.9
Ni	36
Zn	1.6
V	1.9
Y	1.6
Zr	1.4
Th	4.8
Nb	2.3

Table A3 Maximum discrepancy between sample duplicates analysed for trace-elements, expressed as a percentage of the mean of the duplicate. Note that precision of the Ba determination is probably much better than the listed value for those samples with Ba >100ppm (Parker, 1979); the level of Ba in most of the samples considered here is close to the detection limit (ca. 20ppm).

La	3.5
Ce	12.9
Nd	15.2
Sm	7.7
Eu	12.1
Tb	72
Yb	1.4
Th	12.3
U	7.6

Table A4 Maximum discrepancy between sample duplicates analysed for REE and other elements by neutron activation, expressed as a percentage of the mean of the duplicate. Note poor precision of Tb determination; this is due to a substantial correction for Th interference.

	(i)	(ii)	(iii)	(iv)
G-2				
Ce	164.0	163	153	155
Nd	53.4	58	65.5	53.5
Sm	7.0	6.9	7.0	7.2
Eu	1.38	1.35	1.38	1.34
Tb	0.58	0.53	-	0.5
Yb	0.78	0.75	0.84	0.84
Th	25.6	23.1	-	26.2
U	-	1.92	-	1.8
GSP-1				
Ce	440.8	411	423	427
Nd	202.5	209	234	201
Sm	25.1	26.5	27	26.0
Eu	2.30	2.2	2.51	2.22
Tb	1.63	1.4	-	1.3
Yb	1.77	1.73	1.81	1.72
Th	114.6	103	-	110
U	-	2.15	-	2.0
AGV-1				
Ce	70.2	66.9	66.7	68.5
Nd	32.7	32.3	39	33.4
Sm	5.84	6.06	5.9	5.9
Eu	1.63	1.62	1.66	1.64
Tb	0.69	0.68	-	0.7
Yb	1.67	1.65	1.74	1.65
Th	6.44	5.8	-	6.3
U	-	1.92	-	1.7

Table A5 Comparison of Ce, Nd, Sm, Eu, Tb, Yb, Th and U cocentrations measured in U.S.G.S. standard rocks analysed as samples during neutron activation analysis, with some recent recommended values determined by neutron activation (columns (i) and (ii)) and inductively-coupled plasma source spectrometry (column (iii)). (i) Data of Potts et al. (1981); (ii) data of Kramar & Puchelt (1982); (iii) data of Walsh et al. (1981); (iv) this work.

APPENDIX B

ELECTRON MICROPROBE ANALYSES

Procedure

The mineral analyses presented in tables B1-B15 were carried out on polished thin sections using the Cambridge Instruments Ltd. Microscan V with EDS attachment installation in the Geology Department at Imperial College. Energy spectra were automatically processed and output at the instrument by a Link Systems Ltd. minicomputer. Output was in the form of oxide weight percentage concentrations and element molar ratios, the latter conveniently calculated to the appropriate mineral formula. A standard live count time of 100s was used (standardised on Co), at an accelerating voltage of 15 Kv and specimen currents of 10, 4 or 3.5 nA. The smaller specimen currents were found to be necessary for routine analyses of alkali feldspars, feldspathoids and glasses, as Na loss under the beam occurred at the higher value. For feldspathoids and glasses, the additional precaution against Na loss of using a focussed beam in scanning (raster) mode was taken. This greatly decreased the time during which any one point of the specimen was under the beam, while keeping the standard 100s livetime.

Quality of analyses

The quality of individual analyses was monitored by means of the oxide weight percent totals, and, where possible, mineral stoichiometry. Except where stated in the notes to individual tables, totals outside the range 98.5% to 101.5% were rejected. The great majority of totals (for non -OH, F- bearing phases) fall between 99% and 101%. Stoichiometric requirements are given in the notes to individual tables.

The precision obtaining during a single analytical session (one during which the electron beam is not switched off) was found by taking 10 analyses, each on a different spot, of a homogeneous amphibole grain in the cummulate fragment from pumice fall J. Results are given in table B.i. Note that the high standard deviation for K is due to the low concentration in the amphibole; the counting statistics for K are normally similar to those for Ca at similar levels. With this exception, precision during a single normal analytical session is generally good.

Precision and accuracy for the whole data set were assessed by comparison of analyses of a standard jadeite and a standard olivine obtained during each analytical session. Histograms and statistics are given in Figs. B.1 and B.2.

The data

A total of 777 microprobe analyses are presented in tables B1 - B15, each mineral group being listed in

a separate table. The analyses are given in the rough order felsic minerals, mafic silicates, glasses, non-silicates (see Contents). Analysis numbers are keyed to samples in the notes to individual tables. Suffixes C and r denote core and rim of individual crystals, any intervening analyses being from between the core and rim of the same crystal in sequence. Thus, for example, 1407c - 1410r would denote that analyses 1407, 1408, 1409 and 1410, in that order, form a progressive core to rim sequence from one zoned crystal. With the exception of oxides and nephelines (and amphiboles in some samples) most grains were found to be zoned where two or more analyses from one crystal were taken. The practice of averaging two or more analyses from one crystal was therefore generally avoided (it was not felt desirable to take more than one analysis from a single spot on a specimen). Analyses from homogeneous phases were, however, averaged where desired for special purposes (e.g. for Fe-Ti oxide geothermometry).

OXIDE	Wt.%	σ	σ%
SiO_2	40.30	0.22	0.5
TiO_2	5.80	0.18	3.1
Al_2O_3	12.34	0.17	1.4
FeO_{tot}	10.96	0.22	2.0
MgO	12.25	0.06	0.5
CaO	11.96	0.13	1.1
Na_2O	2.75	0.03	1.1
K_2O	0.90	0.05	5.6
Total	97.26	0.39	0.4

Table B.i. Mean composition and absolute and relative standard deviation of ten replicate analyses of a homogeneous amphibole grain from the cumulate fragment found in pumice J.

Fig. B1 Histograms showing distribution of 38 jadeite analyses obtained over several microprobe sessions. Arrows indicate means. a) Analysis oxide weight percent totals. Analyses having totals outside the range 98.5% - 101.5% were rejected. b) Number of Na atoms in the mineral formula, recalculated on the basis of 6 oxygen atoms. Standard deviation is 2.89%. c) Number of Al atoms per 6 oxygens. Standard deviation is 2.53%. d) Number of Si atoms per 6 oxygens. Standard deviation is 0.37%. e) Sum of all cations in mineral formula. Standard deviation is 0.42%. f) Na + Fe + Ca + Al in mineral formula. Standard deviation is 0.98%.

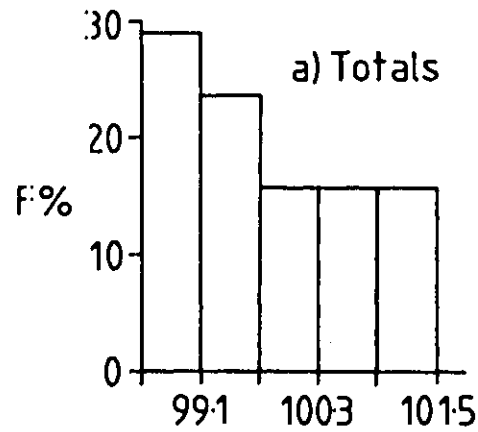
a) Totals
F%
30
20
10
0
99·1
100·3
101·5

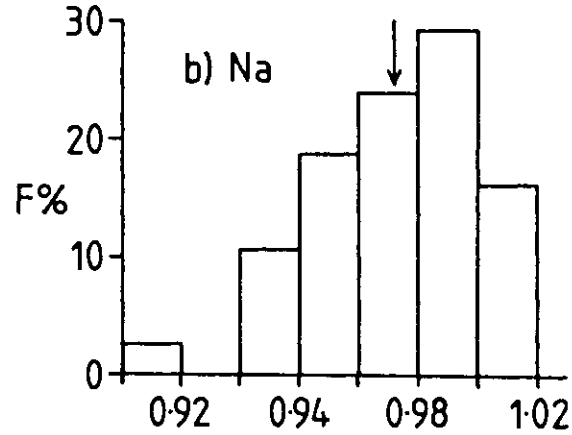
b) Na
F%
30
20
10
0
0·92
0·94
0·98
1·02

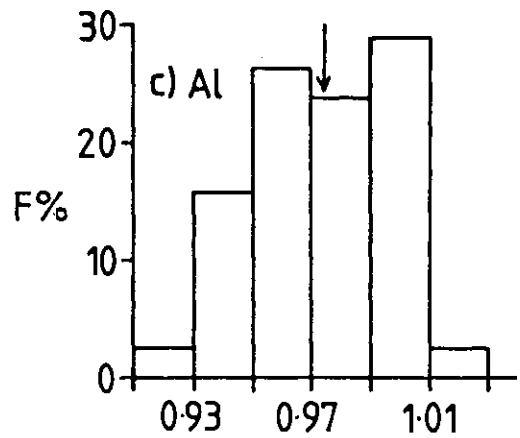
c) Al
F%
30
20
10
0
0·93
0·97
1·01

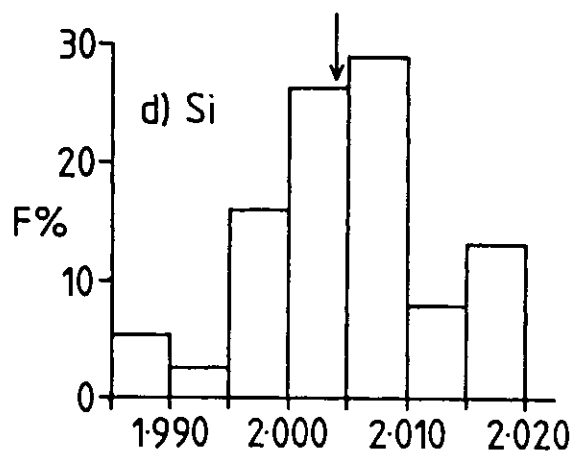
d) Si
F%
30
20
10
0
1·990
2·000
2·010
2·020

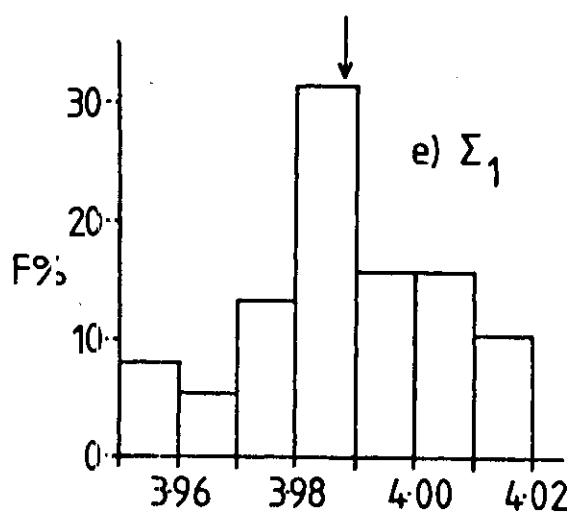
e) Σ1
F%
30
20
10
0
3·96
3·98
4·00
4·02

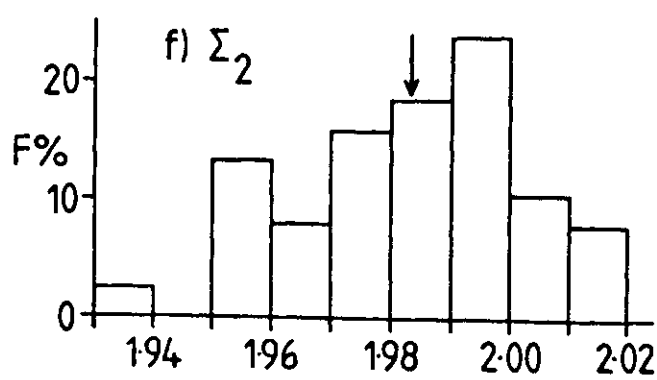
f) Σ2
F%
20
10
0
1·94
1·96
1·98
2·00
2·02

Fig. B2 Histograms showing distribution of 37 standard olivine analyses obtained over several microprobe sessions. Arrows indicate means. a) As Fig. B1. b) Number of Mg atoms in mineral formula recalculated on the basis of 4 oxygen atoms. Standard deviation is 1.18%. c) As Fig. B1e. Standard deviation is 0.55%. d) Mg + Fe + Mn + Ni + Ca in mineral formula. Standard deviation is 0.93%. e) Number of Si atoms per 4 oxygens. Standard deviation is 0.84%. f) Number of Fe atoms per 4 oxygens. Standard deviation is 3.26%.

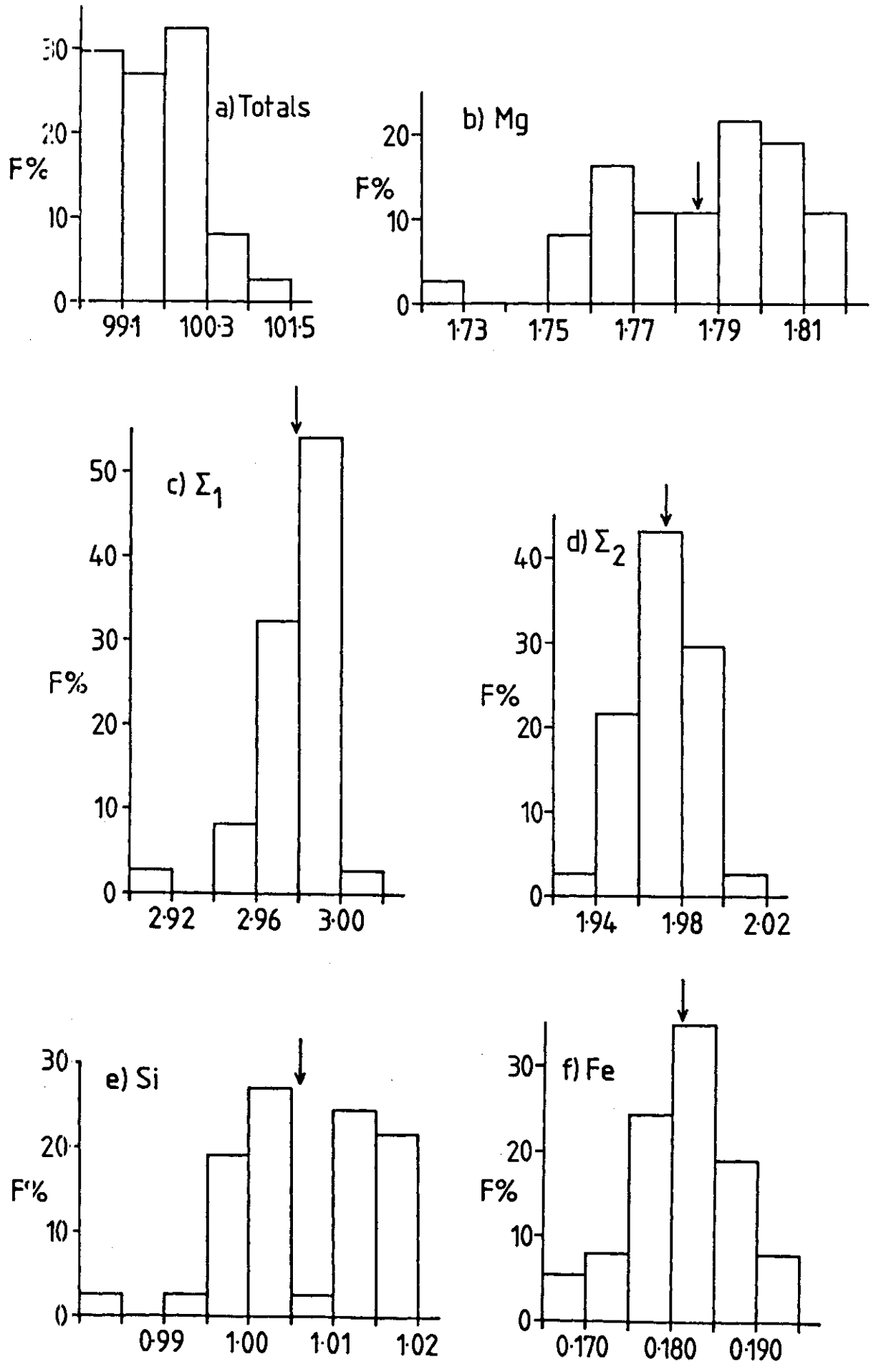
a) Totals
F%
30
20
10
0
99·1
100·3
101·5
b) Mg
F%
20
10
0
1·73
1·75
1·77
1·79
1·81
c) Σ1
F%
50
40
30
20
10
0
2·92
2·96
3·00
d) Σ2
F%
40
30
20
10
0
1·94
1·98
2·02
e) Si
F%
30
20
10
0
0·99
1·00
1·01
1·02
f) Fe
F%
30
20
10
0
0·170
0·180
0·190

B.1 FELDSPARS

In addition to the usual criterion of a satisfactory oxide weight percentage total, the quality of feldspar analyses may be assessed by how closely molecular formulae approximate to stoichiometric requirements, as follows:

$Si + Al + Fe = 4$

$Ca + Na + K = 1$

$(Al + Fe) - 1 = Ca$ for mineral formulae recalculated on the basis of eight oxygen atoms. This criterion is not totally reliable, however, as alkali feldspars at least may exhibit small deviations from stoichiometry (Carman and Tuttle, 1967). 5% variation on individual sites is accepted here. Fe is reported as Fe_2O_3, on the assumption that all Fe in feldspar exists in the trivalent state on tetrahedral lattice sites. Ba was detected in some feldspars from the Adeje Red Ignimbrite; these analyses are reported separately in Table B1b. Suffix h or l on anlayses bearing the same number denote respectively perthite host and lamella compositions from unmixed grains in the nepheline syenites.

Key to Table B1a:-

Tajao ignimbrite:- 632, 636c-637r, 639, 641, 642, 644, 645r-646c, 647r-648c, 649-653, 658, 659, 661r-662c, 663, 667, 1402, 1403r-1404c.

Ignimbrite O:- 760, 763c-765r, 773, 775c-776r, 778-781, 805r-806c, 813, 818, 836, 838-841, 863,866, 867, 873, 886, 890, 891, 912, 913, 915, 916.

Pumice deposit E: 735, 738-740.

Boca de Tauce welded air-fall tuff:- 535r-536c.

Adeje Red ignimbrite:- 33, 367, 368, 370-372, 383, 716.

Cognate mafic cummulate lithic in pumice fall J:- 296-300, 301c-303r, 304c-313r, 360, 287, (phenocrysts); 315, 364 (groundmass).

Welded ignimbrite E, Gran Canaria:- 693, 708 (phenocrysts); 702 (groundmass).

Green Tuff, Pantelleria (main crystalline tuff):- 476, 477, 478c-479r, 513, 515 (phenocrysts); 480-482 (groundmass).

Syenite block S1/2:- 118, 145, 146, 164, 166, 168, 170, 174, 175, 177, 180, 183, 184, 189, 190, 217, 221, 224, 225, 227, 230.

Syenite block S1/4:- 1284, 1286, 1288, 1295, 1301, 1303, 1305, 1307, 1318.

Syenite block S3/2:- 397, 398, 404, 406-410.

Syenite block S4:- 265, 267, 268, 192, 194.

Syenite block SX3:- 1047, 1052, 1059, 1068-1070, 1086, 1317c-1318r, 1321, 1323, 1324r-1325c.

Medano xenolith TF 161:- 1241r-1242c, 1245, 1259c-1261r.

Medano xenolith TF162:- 1190-1192, 1195, 1196.

Medano xenolith TF 163:- 1273, 1274.

Medano xenolith TF 165:- 1220c-1221r.

Key to Table B1.b:-

Adeje Red ignimbrite:- 20, 374c-375r, 377, 379, 381, 382.

Table Bla

	33	118	145	146	1641	164h	1661	166h	1681	168h	170	174h
SiO_2	67.16	67.69	65.77	66.42	67.72	65.63	68.46	65.48	68.04	66.18	66.22	66.33
Al_2O_3	19.07	18.12	18.85	18.55	19.21	18.64	19.16	18.30	19.02	18.73	18.79	18.21
Fe_2O_3	0.39	0.50	0.41	-	-	-	0.29	-	-	0.32	0.33	-
CaO	0.89	-	-	-	-	-	-	-	-	-	-	-
Na_2O	8.17	5.39	6.84	7.17	12.17	5.55	11.27	4.55	11.25	7.29	6.39	5.16
K_2O	3.43	7.99	7.94	6.46	0.33	9.25	0.94	10.84	1.39	6.93	7.79	10.11
Total	99.11	99.69	99.81	98.60	99.43	99.07	100.12	99.17	99.70	99.45	99.52	99.81
Formula per 80 oxygen atoms												
Si	2.955	3.041	2.975	3.007	2.987	2.992	3.001	3.000	2.999	2.988	2.992	3.010
Al	1.003	0.960	1.005	0.991	0.999	1.002	0.990	0.989	0.989	0.997	1.001	0.975
Fe	0.013	0.017	0.015	-	-	-	0.010	-	-	0.011	0.012	-
Ca	0.043	-	-	-	-	-	-	-	-	-	-	-
Na	0.707	0.469	0.600	0.629	1.041	0.491	0.958	0.405	0.962	0.639	0.560	0.455
K	0.196	0.459	0.459	0.374	0.019	0.538	0.053	0.634	0.078	0.400	0.450	0.585

	175h	1771	177h	1801	180h	1831	183h	184h	189	190	217h	221h
SiO_2	65.62	67.59	65.50	68.09	66.78	68.22	65.52	66.24	66.52	66.18	66.30	65.95
Al_2O_3	18.22	19.33	18.25	18.92	18.43	18.97	18.61	18.49	18.81	18.42	18.15	18.45
Fe_2O_3	0.28	0.34	-	0.28	-	0.37	-	0.25	0.42	0.51	-	0.24
CaO	-	-	-	-	-	-	-	-	-	-	-	-
Na_2O	4.50	11.08	4.40	11.96	4.70	12.10	4.83	4.79	6.78	6.13	4.83	3.95
K_2O	10.93	1.02	11.04	0.23	10.67	0.30	10.35	10.04	6.98	7.64	9.78	11.07
Total	99.55	99.36	99.19	99.48	100.58	99.96	99.31	99.81	99.51	98.88	99.06	99.66
Formula per 8 oxygen atoms												
Si	3.000	2.988	3.002	3.000	3.010	2.996	2.992	3.004	2.996	3.006	3.021	3.005
Al	0.982	1.008	0.986	0.983	0.980	0.983	1.002	0.989	0.999	0.987	0.975	0.992
Fe	0.010	0.012	-	0.009	-	0.013	-	0.008	0.015	0.018	-	0.008
Ca	-	-	-	-	-	-	-	-	-	-	-	-
Na	0.399	0.950	0.391	1.022	0.411	1.031	0.428	0.422	0.593	0.540	0.427	0.349
K	0.638	0.058	0.646	0.014	0.614	0.017	0.603	0.581	0.402	0.443	0.569	0.644

	2111	2241	225h	227h	230	2651	265h	267	268	296	297	298
SiO_2	68.48	68.92	66.22	65.16	66.76	68.52	66.55	66.78	67.11	55.81	55.95	55.72
Al_2O_3	19.20	19.11	18.35	18.26	18.76	19.31	18.51	18.85	18.69	26.97	26.68	27.50
Fe_2O_3	0.23	-	0.25	-	0.25	0.29	0.67	0.73	0.67	0.47	0.36	0.43
CaO	-	-	-	0.14	-	-	-	-	-	9.75	9.49	9.71
Na_2O	10.75	10.84	4.10	4.64	6.41	10.15	7.42	7.00	7.82	5.93	5.91	5.99
K_2O	0.37	0.33	11.02	10.48	6.89	2.34	6.04	7.04	6.20	0.29	0.19	0.26
Total	99.03	99.20	99.94	98.68	99.07	100.61	99.19	100.40	100.49	99.22	98.58	99.61
Formula per 8 oxygen atoms												
Si	3.015	3.024	3.009	2.997	3.009	3.000	3.002	2.990	2.995	2.537	2.553	2.522
Al	0.997	0.989	0.983	0.991	0.997	0.997	0.985	0.995	0.984	1.445	1.435	1.468
Fe	0.008	-	0.009	-	0.009	0.009	0.023	0.025	0.023	0.017	0.013	0.015
Ca	-	-	-	0.007	-	-	-	-	-	0.475	0.464	0.471
Na	0.917	0.922	0.362	0.414	0.561	0.862	0.649	0.607	0.676	0.523	0.523	0.526
K	0.021	0.019	0.639	0.615	0.396	0.131	0.348	0.403	0.353	0.017	0.012	0.015

	299	300	301	302	303	304	305	306	307	308	309	310	311
SiO_2	56.29	55.80	54.17	57.02	56.09	53.89	54.27	55.15	55.27	54.88	54.71	56.48	57.40
Al_2O_3	27.22	27.67	28.52	26.98	27.25	28.28	28.16	27.76	27.64	28.04	28.42	26.57	26.47
Fe_2O_3	0.30	0.25	0.35	0.42	0.30	0.39	0.47	0.38	0.38	0.33	0.50	0.44	0.35
CaO	9.27	9.79	11.01	8.74	9.74	11.11	10.79	10.32	9.97	10.91	11.04	9.35	9.06
Na_2O	5.99	5.75	5.10	6.32	5.83	4.98	5.15	5.43	5.48	5.30	4.92	5.91	6.14
K_2O	0.25	0.25	0.20	0.27	0.24	0.22	0.19	0.24	0.21	0.18	0.20	0.25	0.30
Total	99.32	99.51	99.35	99.75	99.45	98.87	99.03	99.28	98.95	99.64	99.79	99.00	99.72
Formula per 8 oxygen atoms													
Si	2.547	2.523	2.464	2.563	2.538	2.465	2.476	2.505	2.515	2.487	2.476	2.565	2.581
Al	1.452	1.475	1.530	1.430	1.454	1.525	1.515	1.487	1.483	1.498	1.516	1.423	1.403
Fe	0.011	0.009	0.012	0.015	0.011	0.014	0.016	0.013	0.014	0.012	0.017	0.016	0.012
Ca	0.450	0.475	0.537	0.421	0.473	0.545	0.528	0.503	0.487	0.530	0.536	0.455	0.437
Na	0.526	0.505	0.450	0.551	0.512	0.442	0.456	0.478	0.484	0.466	0.432	0.521	0.535
K	0.015	0.015	0.012	0.016	0.014	0.013	0.011	0.014	0.013	0.011	0.012	0.015	0.018

	312	313	315	360	364	367	368	370	371	372	383	3971	398h	3981
SiO_2	57.38	56.32	64.79	54.64	66.03	46.85	46.62	52.86	52.78	66.28	47.55	68.08	65.86	67.96
Al_2O_3	26.46	27.13	20.72	28.20	18.62	33.24	33.81	29.07	28.96	19.60	32.93	19.17	18.43	19.23
Fe_2O_3	0.41	0.46	0.41	0.51	0.84	0.67	0.58	0.68	0.74	0.46	0.61	0.21	0.23	0.39
CaO	9.07	9.79	2.05	10.61	0.45	16.76	17.70	12.05	12.24	0.95	16.38	-	-	-
Na_2O	6.34	5.44	8.48	4.90	6.72	1.84	1.62	4.26	4.19	7.86	2.11	11.19	4.43	11.27
K_2O	0.29	0.24	2.81	0.30	6.39	-	-	0.17	0.20	3.59	-	0.45	10.41	0.46
Total	99.95	99.38	99.26	99.16	99.05	99.36	100.33	99.09	99.11	98.74	99.58	99.10	99.36	99.31
Formula per 8 oxygen atoms														
Si	2.581	2.548	2.900	2.483	2.976	2.163	2.136	2.408	2.410	2.954	2.193	2.994	3.000	2.991
Al	1.403	1.447	1.094	1.510	0.989	1.809	1.826	1.561	1.559	1.030	1.790	0.993	0.990	0.998
Fe	0.014	0.016	0.014	0.018	0.029	0.023	0.020	0.023	0.025	0.015	0.021	0.007	0.008	0.013
Ca	0.437	0.475	0.098	0.517	0.022	0.829	0.869	0.588	0.599	0.045	0.809	-	-	-
Na	0.553	0.478	0.736	0.431	0.587	0.165	0.144	0.376	0.371	0.679	0.189	0.954	0.391	0.961
K	0.017	0.014	0.161	0.017	0.368	-	-	0.010	0.012	0.204	-	0.025	0.605	0.026

	3981	3981	398h	4041	404h	406	407	4081	409	4101	410h	454
SiO_2	68.02	68.55	66.37	67.86	66.19	66.17	67.22	69.00	66.48	68.58	66.13	67.36
Al_2O_3	19.19	19.76	18.64	19.06	18.46	18.36	18.89	19.40	18.52	19.40	18.75	18.07
Fe_2O_3	0.24	0.25	0.22	0.30	0.37	0.54	0.67	0.32	0.55	0.27	0.27	1.07
CaO	-	-	-	0.13	-	-	-	-	-	-	-	-
Na_2O	11.25	11.58	4.95	11.24	6.08	5.83	6.14	11.30	5.94	11.21	4.26	7.28
K_2O	0.37	0.29	9.81	0.48	8.15	8.14	7.88	0.43	8.45	0.38	10.72	6.23
Total	99.07	100.43	99.99	99.07	99.25	99.04	100.80	100.45	99.94	99.84	100.13	100.01
Formula per 8 oxygen atoms												
Si	2.997	2.974	2.998	2.998	2.992	3.003	2.999	2.996	2.993	2.995	2.983	3.009
Al	0.997	1.011	0.993	0.993	0.983	0.982	0.994	0.993	0.982	0.998	0.997	0.952
Fe	0.008	0.008	0.008	0.010	0.013	0.019	0.022	0.011	0.019	0.009	0.009	0.036
Ca	-	-	-	0.006	-	-	-	-	-	-	-	-
Na	0.961	0.974	0.434	0.963	0.533	0.513	0.531	0.951	0.518	0.949	0.373	0.631
K	0.021	0.016	0.565	0.027	0.470	0.471	0.448	0.024	0.485	0.021	0.617	0.355

	455	456	476	477	478	479	480	481	482	513	515	535	536	632
SiO_2	67.03	66.93	67.99	67.79	67.80	67.35	68.14	67.36	67.51	67.34	66.82	67.19	66.49	50.27
Al_2O_3	18.02	17.56	18.93	18.52	18.22	18.47	17.63	16.98	16.31	18.02	17.81	18.74	18.79	30.65
Fe_2O_3	1.05	1.28	0.64	0.68	0.97	0.61	1.85	2.30	2.68	1.08	0.95	0.62	0.56	0.63
CaO	-	-	-	0.15	-	-	-	-	-	-	-	0·18	-	14.46
Na_2O	7.24	6.93	7.50	7.54	7.49	7.62	7.13	6.71	6.85	7.44	7.06	7.88	7.39	3.20
K_2O	6.19	6.47	5.92	5.77	6.02	5.91	6.36	6.68	6.57	5.90	5.88	5.28	5.38	0.26
Total	99.53	99.17	100.98	100.45	100.50	99.96	101.11	100.03	99.92	99.78	98.52	99.89	98.61	99.47
Formula per 8 oxygen atoms														
Si	3.008	3.018	2.994	3.012	3.010	3.009	3.012	3.016	3.033	3.009	3.019	2.989	2.990	2.307
Al	0.953	0.933	0.983	0.970	0.953	0.973	0.918	0.897	0.863	0.949	0.948	0.983	0.996	1.658
Fe	0.036	0.043	0.021	0.023	0.033	0.020	0.062	0.077	0.090	0.037	0.032	0.021	0.019	0.022
Ca	-	-	-	0.007	-	-	-	-	-	-	-	0.009	-	0.711
Na	0.631	0.605	0.640	0.650	0.645	0.660	0.612	0.582	0.597	0.645	0.619	0.680	0.644	0.284
K	0.354	0.372	0.333	0.327	0.341	0.337	0.359	0.382	0.377	0.336	0.339	0.300	0.309	0.015

	636	637	638	639	641	642	644	645	646	647	648	649	650
SiO_2	59.07	58.83	66.03	49.35	60.50	61.90	51.51	66.27	66.71	61.70	60.08	63.03	60.72
Al_2O_3	24.61	25.09	19.22	31.50	23.87	23.10	29.94	18.57	19.08	22.66	25.12	21.88	23.87
Fe_2O_3	0.61	0.50	0.30	0.47	0.36	0.46	0.58	0.42	0.24	0.38	0.51	0.49	0.31
CaO	6.98	7.19	0.71	15.38	5.99	4.63	12.89	0.18	0.20	4.68	6.76	3.52	5.78
Na_2O	6.49	6.59	6.81	2.60	6.95	7.36	3.95	5.81	5.79	7.36	6.89	7.11	7.01
K_2O	0.94	0.95	6.19	0.15	1.28	1.80	0.32	8.49	8.28	1.83	1.15	3.00	1.46
Total	98.70	99.15	99.26	99.45	99.95	99.25	99.19	99.74	100.30	98.61	100.51	99.03	99.15
Formula per 8 oxygen atoms													
Si	2.675	2.649	2.970	2.268	2.719	2.767	2.356	2.995	2.987	2.777	2.664	2.830	2.727
Al	1.314	1.332	1.019	1.706	1.264	1.217	1.614	0.989	1.007	1.202	1.313	1.158	1.264
Fe	0.021	0.017	0.010	0.016	0.012	0.015	0.020	0.014	0.008	0.013	0.017	0.017	0.010
Ca	0.331	0.347	0.034	0.757	0.288	0.222	0.632	0.008	0.010	0.226	0.321	0.169	0.278
Na	0.570	0.575	0.594	0.231	0.606	0.638	0.350	0.510	0.503	0.642	0.592	0.619	0.610
K	0.054	0.055	0.355	0.009	0.074	0.103	0.019	0.489	0.473	0.105	0.065	0.172	0.083

	651	652	653	658	659	661	662	663	667	693	702	708	716
SiO_2	63.52	58.31	66.18	50.13	47.98	49.80	48.52	58.27	65.16	67.41	70.25	68.26	66.24
Al_2O_3	21.19	25.66	19.26	30.68	32.45	31.13	32.04	23.35	19.40	18.58	15.31	18.20	18.86
Fe_2O_3	0.50	0.51	0.25	0.97	0.83	0.67	0.63	0.52	0.22	0.71	2.01	0.70	0.58
CaO	2.76	7.58	0.64	14.42	16.25	14.76	15.64	7.54	1.27	0.16	-	-	0.52
Na_2O	7.32	6.49	6.41	3.10	2.02	3.02	2.45	6.34	6.42	7.68	6.23	8.16	8.12
K_2O	3.63	0.91	7.04	0.29	0.12	0.16	0.13	0.88	6.68	5.11	5.96	5.10	4.59
Total	98.92	99.46	99.78	99.59	99.65	99.54	99.41	99.00	99.15	99.65	99.76	100.42	98.91
Formula per 7 oxygen atoms													
Si	2.859	2.621	2.967	2.292	2.211	2.268	2.214	2.596	2.905	3.003	3.119	3.016	2.977
Al	1.124	1.359	1.018	1.653	1.763	1.671	1.723	1.329	1.019	0.975	0.801	0.948	0.999
Fe	0.017	0.017	0.008	0.037	0.032	0.023	0.022	0.017	0.007	0.024	0.067	0.023	0.020
Ca	0.133	0.365	0.031	0.706	0.802	0.720	0.764	0.359	0.061	0.008	-	-	0.025
Na	0.629	0.566	0.558	0.275	0.180	0.267	0.217	0.547	0.554	0.663	0.536	0.699	0.707
K	0.208	0.052	0.403	0.016	0.007	0.009	0.008	0.050	0.380	0.290	0.338	0.288	0.263

	735	738	739	740	760	763	764	765	773	775	776	778	779
SiO_2	66.26	66.09	66.33	66.12	61.42	57.42	57.33	55.88	61.76	54.51	54.60	47.67	48.06
Al_2O_3	20.01	19.13	18.83	19.02	24.04	26.35	26.65	27.76	23.39	28.64	28.85	33.53	33.34
Fe_2O_3	0.47	0.25	0.44	0.36	0.46	0.45	0.50	0.44	0.39	0.61	0.56	0.80	0.72
CaO	1.09	0.89	0.91	0.88	4.95	8.53	8.58	9.74	4.30	11.18	11.18	16.88	16.33
Na_2O	8.45	8.24	7.55	7.79	7.95	6.35	6.44	5.73	7.85	5.13	5.25	1.99	1.96
K_2O	3.70	4.61	4.86	4.95	1.20	0.45	0.53	0.39	1.62	0.24	0.25	-	-
Total	99.98	99.21	98.92	99.12	100.02	99.55	100.23	99.94	99.31	100.31	100.69	100.87	100.41
Formula per 8 oxygen atoms													
Si	2.931	2.961	2.984	2.967	2.722	2.585	2.576	2.511	2.746	2.453	2.442	2.171	2.185
Al	1.043	1.010	0.999	1.006	1.255	1.398	1.407	1.470	1.226	1.519	1.521	1.799	1.787
Fe	0.016	0.008	0.015	0.012	0.015	0.015	0.017	0.017	0.013	0.021	0.019	0.027	0.025
Ca	0.052	0.043	0.044	0.042	0.235	0.412	0.412	0.469	0.205	0.539	0.536	0.824	0.796
Na	0.725	0.716	0.659	0.678	0.683	0.555	0.559	0.499	0.676	0.450	0.456	0.175	0.173
K	0.209	0.264	0.279	0.283	0.068	0.026	0.030	0.022	0.092	0.014	0.014	-	-

	780	781	805	806	813	818	836	838	839	840	841	863	866	867
SiO_2	66.68	49.55	54.24	52.33	55.53	61.25	56.09	46.24	46.63	55.13	45.40	60.60	58.22	54.99
Al_2O_3	19.22	32.10	27.33	29.52	27.84	22.91	26.83	33.51	32.84	27.05	33.31	24.24	25.35	28.05
Fe_2O_3	0.31	0.84	0.66	0.73	0.52	0.39	0.67	0.72	0.84	0.74	0.63	0.70	0.54	0.61
CaO	0.26	15.14	11.32	13.16	10.52	4.88	9.68	17.88	17.33	9.84	18.06	5.56	7.12	10.59
Na_2O	7.18	3.03	4.88	3.97	5.43	7.61	5.97	1.47	1.91	5.69	1.37	7.11	6.80	5.15
K_2O	6.41	0.13	0.27	0.19	0.35	1.48	0.43	0.14	0.21	0.37	0.10	1.08	0.79	0.33
Total	100.06	100.79	98.70	99.90	100.19	99.52	99.67	99.96	99.76	99.82	98.77	99.29	98.82	99.72
Formula per 8 oxygen atoms														
Si	2.976	2.244	2.484	2.379	2.496	2.759	2.536	2.130	2.153	2.511	2.116	2.710	2.632	2.484
Al	1.011	1.713	1.475	1.582	1.474	1.216	1.430	1.820	1.787	1.452	1.834	1.278	1.351	1.494
Fe	0.010	0.029	0.023	0.025	0.017	0.013	0.023	0.025	0.029	0.025	0.022	0.024	0.018	0.021
Ca	0.012	0.734	0.555	0.641	0.507	0.236	0.469	0.882	0.858	0.480	0.904	0.267	0.345	0.513
Na	0.621	0.266	0.433	0.350	0.473	0.665	0.524	0.131	0.171	0.502	0.124	0.617	0.596	0.452
K	0.365	0.008	0.016	0.011	0.020	0.085	0.025	0.008	0.012	0.021	0.006	0.062	0.045	0.019

	873	886	890	891	912	913	915	916	1047	1052	1059	1068	1069
SiO_2	58.10	47.53	64.67	64.97	46.70	47.23	46.13	53.54	67.06	66.79	66.97	66.13	66.97
Al_2O_3	25.75	33.37	21.32	20.41	33.20	33.05	33.47	28.58	17.85	18.07	18.35	18.29	18.51
Fe_2O_3	0.51	0.79	0.50	0.40	0.68	0.79	0.79	0.74	0.67	0.64	0.40	0.54	0.39
CaO	8.73	16.67	2.19	1.60	17.05	16.86	17.31	11.43	-	-	0.20	-	0.17
Na_2O	6.69	2.21	7.89	7.78	1.63	1.98	1.60	5.08	6.47	6.24	6.64	6.55	7.42
K_2O	0.68	0.10	3.12	3.59	-	-	-	0.28	7.25	7.64	6.71	7.09	6.23
Total	99.46	100.67	99.69	98.75	99.26	99.91	99.30	99.65	99.30	99.38	99.27	98.60	99.69
Formula per 8 oxygen atoms													
Si	2.612	2.166	2.867	2.908	2.159	2.171	2.135	2.431	3.028	3.016	3.012	3.006	2.999
Al	1.365	1.792	1.114	1.077	1.810	1.790	1.826	1.530	0.950	0.962	0.973	0.980	0.977
Fe	0.017	0.027	0.017	0.013	0.024	0.027	0.028	0.025	0.023	0.022	0.012	0.019	0.013
Ca	0.373	0.814	0.104	0.076	0.845	0.830	0.858	0.556	-	-	0.010	-	0.008
Na	0.583	0.196	0.678	0.675	0.146	0.176	0.144	0.447	0.567	0.546	0.579	0.577	0.644
K	0.039	0.006	0.176	0.205	-	-	-	0.016	0.418	0.440	0.385	0.411	0.356

	1070	1086	1190	1191	1192	1195	1196	1220	1221	1241	1242	1245	1259c
SiO_2	66.41	67.69	52.36	65.02	53.78	54.45	59.96	58.45	57.35	62.12	54.68	62.38	56.64
Al_2O_3	17.79	18.61	29.50	21.19	28.64	27.61	24.15	25.92	27.11	23.70	28.00	22.89	26.53
Fe_2O_3	0.44	1.14	-	-	0.24	0.24	0.27	0.30	-	-	-	-	-
CaO	-	-	13.37	2.89	11.81	11.10	6.65	8.10	9.51	5.32	11.08	4.77	9.24
Na_2O	5.96	7.18	4.15	10.10	4.59	5.30	7.57	6.85	6.25	8.43	5.26	8.30	6.39
K_2O	8.18	6.69	0.17	0.50	0.11	0.24	0.38	0.67	0.39	0.78	0.25	0.57	0.38
Total	98.78	101.31	99.55	99.70	99.17	98.94	98.98	100.29	100.61	100.35	99.27	98.91	99.18
Formula per oxygen atoms													
Si	3.002	2.992	2.382	2.871	2.441	2.481	2.692	2.607	2.553	2.743	2.477	2.785	2.563
Al	0.954	0.970	1.582	1.103	1.532	1.483	1.278	1.363	1.423	1.233	1.495	1.205	1.415
Fe	0.015	0.038	-	-	0.008	0.008	0.009	0.010	-	-	-	-	-
Ca	-	-	0.652	0.137	0.574	0.542	0.320	0.387	0.454	0.252	0.538	0.228	0.448
Na	0.526	0.615	0.366	0.865	0.404	0.468	0.659	0.592	0.539	0.721	0.462	0.718	0.560
K	0.475	0.377	0.010	0.028	0.007	0.014	0.022	0.038	0.022	0.044	0.015	0.033	0.022

	1261r	1273	1274	1284h	1284L	1286h	12861	1288h	1288L	1295h	1295L
SiO_2	58.56	64.52	64.60	66.01	68.48	65.88	68.76	66.40	68.59	65.58	68.03
Al_2O_3	25.00	21.22	21.22	18.27	18.96	18.11	19.17	18.65	18.87	18.10	18.96
Fe_2O_3	0.27	0.26	0.23	0.34	0.28	0.25	-	-	0.25	-	0.27
CaO	7.41	2.86	2.77	-	-	-	-	-	-	-	-
Na_2O	7.01	9.43	9.35	4.48	11.39	4.41	10.80	4.57	11.35	4.20	11.45
K_2O	0.47	0.85	1.23	10.39	0.66	10.70	0.90	10.84	0.47	10.85	0.45
Total	98.72	99.14	99.40	99.49	99.77	99.35	99.63	100.46	99.53	98.73	99.16
Formula per 8 oxygen atoms											
Si	2.650	2.868	2.870	3.000	2.997	3.009	3.007	2.981	3.013	3.008	3.001
Al	1.333	1.112	1.111	0.979	0.978	0.975	0.988	0.987	0.977	0.978	0.986
Fe	0.009	0.009	0.008	0.012	0.009	0.009	-	-	0.008	-	0.009
Ca	0.359	0.136	0.132	-	-	-	-	-	-	-	-
Na	0.615	0.812	0.806	0.395	0.966	0.391	0.916	0.398	0.967	0.373	0.979
K	0.027	0.048	0.069	0.602	0.037	0.624	0.050	0.621	0.027	0.635	0.025

	1301h	1301L	1303h	1303L	1305h	1305L	1307h	1307L	1317	1318
SiO_2	66.45	68.94	65.94	68.90	65.95	68.22	65.97	68.70	65.87	66.90
Al_2O_3	18.02	19.20	18.30	19.39	18.23	18.95	18.37	19.15	17.80	18.05
Fe_2O_3	0.27	0.31	0.42	0.38	-	0.36	0.50	0.33	0.54	0.54
CaO	-	-	-	-	-	-	-	-	-	-
Na_2O	4.36	11.26	4.57	11.74	4.33	11.26	4.27	11.35	5.88	6.13
K_2O	10.60	0.90	10.47	0.45	10.84	0.56	11.14	0.52	8.83	8.30
Total	99.70	100.61	99.70	100.86	99.35	99.35	100.25	100.05	98.92	99.92
Formula per 8 oxygen atoms										
Si	3.018	3.001	3.001	2.989	3.004	3.007	2.993	3.003	3.010	3.013
Al	0.965	0.985	0.982	0.991	0.979	0.984	0.982	0.986	0.958	0.958
Fe	0.009	0.010	0.015	0.013	-	0.012	0.017	0.011	0.019	0.018
Ca	-	-	-	-	-	-	-	-	-	-
Na	0.384	0.951	0.403	0.988	0.382	0.962	0.375	0.962	0.521	0.536
K	0.614	0.050	0.608	0.025	0.630	0.031	0.645	0.029	0.515	0.477

	1321	1323	1324	1325	1336	1402	1403	1404	1921	192h	194	287
SiO_2	66.62	66.18	66.60	66.11	66.51	66.59	61.68	58.55	67.11	67.09	66.14	55.90
Al_2O_3	18.42	18.33	18.31	18.19	18.23	18.36	23.77	26.54	18.78	18.17	18.54	27.86
Fe_2O_3	0.46	0.39	0.59	0.31	0.64	0.41	0.63	0.59	0.33	0.53	0.59	0.46
CaO	0.14	-	-	-	-	-	5.16	8.28	-	-	-	10.01
Na_2O	6.98	7.33	6.07	5.87	6.36	5.58	7.06	6.05	9.79	7.36	7.84	5.72
K_2O	7.23	6.73	8.25	8.45	8.22	7.95	1.51	0.75	3.53	7.10	5.77	0.23
Total	99.85	98.96	99.82	98.93	99.96	98.89	99.81	100.76	99.54	100.25	98.88	100.18
Formula per 8 oxygen atoms												
Si	2.994	2.994	3.003	3.008	2.997	3.013	2.747	2.597	2.993	3.009	2.993	2.515
Al	0.976	0.977	0.973	0.976	0.968	0.979	1.248	1.388	0.988	0.961	0.989	1.478
Fe	0.016	0.013	0.020	0.011	0.022	0.014	0.021	0.020	0.012	0.018	0.020	0.016
Ca	0.007	-	-	-	-	-	0.246	0.393	-	-	-	0.483
Na	0.608	0.643	0.531	0.518	0.555	0.489	0.610	0.521	0.847	0.640	0.688	0.499
K	0.414	0.388	0.475	0.490	0.472	0.459	0.086	0.043	0.201	0.407	0.334	0.014

Table B1b

	20	374	375	377	379	381	382
SiO_2	66.00	66.37	66.36	65.96	66.48	66.33	66.66
Al_2O_3	19.61	19.55	19.51	19.87	19.33	19.51	19.99
Fe_2O_3	0.39	0.48	0.52	0.41	0.37	0.44	0.37
CaO	0.72	0.94	0.89	1.41	0.78	0.89	1.02
BaO	0.44	0.34	0.39	0.77	0.37	0.49	0.33
Na_2O	8.09	8.24	8.21	8.20	8.07	8.11	8.14
K_2O	3.49	3.60	3.60	3.14	3.62	3.52	3.39
Total	98.74	99.52	99.48	99.76	99.02	99.29	99.90
Formula per 8 oxygen atoms							
Si	2.967	3.964	2.964	2.944	2.979	2.969	2.958
Al	1.039	1.029	1.027	1.045	1.021	1.029	1.046
Fe	0.013	0.016	0.018	0.014	0.013	0.015	0.012
Ca	0.035	0.045	0.043	0.067	0.038	0.042	0.048
Ba	0.008	0.006	0.007	0.013	0.006	0.009	0.006
Na	0.705	0.714	0.711	0.710	0.701	0.704	0.700
K	0.200	0.205	0.205	0.179	0.207	0.201	0.192

B2. Nephelines.

In addition to the requirement of a satisfactory oxide weight sum, nepheline analysis quality was assessed according to stoichiometric requirements, detailed in V.2.ii. Nephelines in sample SX3 were also analysed for Ba, which was not detected.

Key to Table B2:-

Tajao ignimbrite:- 668.

Syenite block S1/4:- 1289c-1292r, 1297 - 1300.

Syenite block S3/2:- 412 - 5, 488, 489.

Syenite block SX3:- 1326 - 8. 1329r - 1333c.

Medano xenolith TF 161:- 1240, 1244c - 1247r.

Medano xenolith TF 163:- 1269

Table B2.

	412	413	414	415	488	489	668	1240	1244	1247	1269	1289	1290	1291	1292	1297	1298	1299
SiO_2	45.90	46.53	46.85	47.12	45.37	47.19	45.52	44.79	45.61	45.25	45.13	46.95	45.22	45.21	46.27	46.98	47.42	47.41
Al_2O_3	31.17	31.36	31.47	31.04	32.06	31.26	31.74	31.92	31.54	31.80	31.83	31.36	31.95	31.57	30.86	30.77	30.70	30.31
Fe_2O_3	1.48	1.51	1.44	1.09	1.59	1.32	0.85	0.31	0.35	0.46	0.68	1.68	0.81	0.94	1.58	1.62	1.52	1.41
CaO	-	-	-	-	-	-	0.36	1.34	1.06	1.38	1.17	-	-	-	-	-	-	-
Na_2O	16.80	17.03	17.19	16.70	17.21	17.33	16.48	15.62	15.80	15.53	15.65	17.62	17.60	17.38	17.08	17.40	16.93	17.08
K_2O	3.79	3.61	3.51	3.28	3.81	3.29	3.86	4.62	4.31	4.53	4.68	3.47	4.08	3.98	3.65	3.50	3.39	3.25
TOTAL	99.14	100.04	100.46	99.23	100.04	100.39	98.81	98.60	98.67	98.95	99.14	101.08	99.66	99.08	99.44	100.27	99.96	99.52

Formula per
32 Oxygen atoms

Si	8.780	8.809	8.817	8.923	8.620	8.886	8.741	8.646	8.760	8.684	8.660	8.800	8.640	8.672	8.840	8.904	8.968	8.992
Al	7.030	6.999	6.980	6.929	7.180	6.938	7.184	7.262	7.140	7.194	7.199	6.928	7.200	7.136	6.952	6.872	6.848	6.792
Fe	0.212	0.215	0.204	0.155	0.228	0.187	0.122	0.046	0.050	0.066	0.098	0.240	0.112	0.136	0.224	0.232	0.216	0.200
Ca	-	-	-	-	-	-	0.074	0.277	0.218	0.284	0.241	-	-	-	-	-	-	-
Na	6.231	6.252	6.274	6.131	6.340	6.327	6.138	5.846	5.886	5.780	5.822	6.400	6.528	6.464	6.328	6.392	6.208	6.280
K	0.923	0.873	0.843	0.791	0.924	0.790	0.945	1.137	1.058	1.110	1.145	0.832	0.992	0.976	0.888	0.848	0.816	0.784

1325	1326	1327	1328	1329	1330	1331	1332	1333
47.15	46.53	46.20	46.11	45.96	45.94	46.82	46.47	46.62
30.63	30.19	30.78	31.26	31.12	30.69	30.22	30.23	30.00
1.69	1.79	1.76	1.87	1.79	1.66	1.91	1.98	1.93
-	-	-	-	-	-	-	-	-
17.02	17.13	17.41	17.16	17.49	17.02	17.07	17.29	17.30
3.32	3.42	3.49	3.78	3.58	3.54	3.38	3.56	3.40
99.78	99.06	99.64	100.18	99.94	98.85	99.40	99.53	99.25

8.936	8.920	8.816	8.752	8.760	8.840	8.960	8.904	8.928
6.836	6.824	6.928	6.992	6.992	6.960	6.816	6.824	6.768
0.240	0.256	0.256	0.264	0.256	0.240	0.272	0.288	0.280
-	-	-	-	-	-	-	-	-
6.256	6.368	6.448	6.312	6.464	6.352	6.336	6.424	6.424
0.804	0.840	0.848	0.912	0.872	0.872	0.824	0.822	0.832

B3. Sodalite-group minerals.

It is difficult to assess the quality of analyses of the sulphur-bearing members of the sodalite group, as some sulphur may be present as S^{2-} rather than in the sulphate radical. Furthermore, sodalites may contain up to a few weight percent of H_2O. Here it is assumed that all sulphur is present as SO_4^{2-}, and that water is absent. Analyses falling outside the range 98.5% - 101.5% oxide sum were rejected. It should be noted that the "success rate" for sodalite analyses was considerably lower than for other phases (ca. 50% as compared to >90%), suggesting that the above assumptions may only have limited validity.

Key to Table B3:-

Tajao ignimbrite:- 671.

Ignimbrite 0:- 761, 762, 848, 860.

Syenite block S1/2:- 157, 158r - 159c, 161.

Syenite block S1/4:- 1025.

Syenite block S3/2:- 429.

Syenite block SX3:- 1082c - 1083r, 1091.

Medano xenolith TF 163:- 1262.

Table B3.

	157	158	159	161	429	671	761	762	848	860	1025	1082	1083	1091	1262
SiO_2	37.41	37.58	37.15	37.59	37.70	34.37	37.47	34.68	33.36	33.84	37.45	37.24	36.98	37.87	37.61
Al_2O_3	30.23	30.49	30.03	30.34	31.11	28.03	27.28	28.35	25.96	27.90	30.12	26.86	30.00	29.97	30.50
Fe_2O_3	0.64	0.60	0.76	0.76	0.69	0.23	0.58	0.34	0.75	0.48	0.62	0.68	0.84	1.28	0.30
CaO	-	-	-	-	-	10.00	8.27	9.03	8.82	10.00	-	-	-	-	0.13
Na_2O	25.56	25.83	25.51	25.53	23.93	12.54	11.46	12.32	16.11	13.01	24.06	25.55	24.60	25.46	25.54
K_2O	0.31	0.38	0.33	0.35	0.56	0.22	1.30	0.44	0.67	0.38	0.53	0.69	0.76	0.68	0.11
Cl	6.73	6.69	6.66	6.56	5.85	n.d.	n.d.	n.d.	0.22	0.22	6.82	6.80	6.66	6.94	6.94
SO_3	0.43	0.59	0.34	0.52	2.11	13.67	12.19	13.82	13.12	13.75	0.72	0.50	0.85	0.63	0.37
TOTAL	101.31	102.16	100.80	101.65	101.95	99.06	98.55	98.98	99.01	99.58	100.32	101.32	100.69	102.83	101.50
Less O=Cl	1.52	1.51	1.51	1.48	1.32	-	-	-	0.05	0.05	1.54	1.53	1.50	1.56	1.56
TOTAL	99.79	100.65	99.29	100.17	100.63	99.06	98.55	98.98	98.96	99.53	98.78	99.79	99.19	101.27	99.94
Formula per 25 Oxygen atoms															
Si	6.084	6.069	6.074	6.089	5.910	4.978	5.416	5.009	4.932	4.895	6.084	6.030	5.996	6.043	6.054
Al	5.796	5.805	5.789	5.793	5.748	4.785	4.649	4.826	4.525	4.756	5.767	5.701	5.733	5.635	5.788
Fe	0.077	0.073	0.093	0.092	0.080	0.025	0.062	0.036	0.083	0.052	0.076	0.083	0.103	0.154	0.036
Ca	-	-	-	-	-	1.553	1.282	1.398	1.397	1.550	-	-	-	-	0.023
Na	8.057	8.086	8.084	8.015	7.274	3.525	3.211	3.449	4.618	3.650	7.577	8.021	7.734	7.875	7.972
K	0.065	0.078	0.069	0.073	0.112	0.040	0.241	0.081	0.127	0.069	0.110	0.142	0.157	0.139	0.023
Cl	1.855	1.831	1.850	1.800	1.556	n.d.	n.d.	n.d.	0.055	0.054	1.878	1.866	1.830	1.877	1.893
S	0.052	0.072	0.042	0.064	0.248	0.485	0.323	1.498	1.456	1.493	0.088	0.061	0.103	0.075	0.045

B. 4. PYROXENES.

Pyroxene analyses are tabulated in two groups; in Table B. 4a are reported analyses of Na-poor clinopyroxenes from the pumice series, the Medano xenoliths, and the Green Tuff, Pantelleria (a single analysis of a groundmass aegirine-augite from the Green Tuff is included with the other pyroxenes from this rock). In Table B.b are reported analyses of aeginine-augites and aegirines from the Tenerife nepheline syenites, and a single groundmass crystal from the Green Tuff, Pantelleria. In the former group, All Fe is reported as FeO, while for the sodic pyroxenes in B.4b, Fe_2O_3 contents have been estimated as part of the calculation procedure described in V.2.iii. Cr was not detected in any of the pyroxenes listed in B.4a.

Key to Table B.4a:-

Tajao ignimbrite:- 1, 2, 554c - 555r, 556 - 8, 560 - 3, 564r - 565c, 566r - 567c, 568, 569c - 571r, 572c - 573r, 574c - 581r, 690, 691, 692c - 693r, 694, 695, 696c - 697r, 698.

Ignimbrite 0:- 798, 804, 807, 811, 827, 835, 854, 871r - 872c, 879r - 880c, 884r - 885c.

Pumice fall J:- 35, 36c - 39r, 40 - 45.

Cognate mafic cumulate block in pumice fall J:- 357 - 9, 362, 363, 366.

Adeje Red ignimbrite:- 713

Boca de Tauce welded air-fall tuff:- 541

Green Tuff, Pantelleria (vitrophyre):- 447c - 448r, 449, 450.

Green Tuff, Pantelleria (main crystalline tuff):- 467 (groundmass), 468c - 469r, 471, 498c - 499r, 550.

Medano xenolith TF 162:- 1198, 1206r - 1211c.

Medano xenolith TF 163:- 1263, 1267, 1277c - 1278r.

Medano xenolith TF 165:- 1227, 1229c - 1230r.

Table B.4a

	1	2	35	36	39	40	41	42	43	44	45	357	358	359	362	363	366
SiO_2	49.41	47.03	52.27	50.54	50.67	50.35	49.66	50.53	50.77	50.22	49.59	50.48	48.42	49.22	49.46	50.60	49.85
TiO_2	1.84	2-60	1.10	1.31	1.52	1.65	2.00	1.48	1.43	1.88	2.05	1.44	2.21	1.65	1.49	1.34	1.48
Al_2O_3	4.51	6.48	2.30	2.88	3.06	3.50	4.31	3.11	3.41	3.94	4.13	3.32	4.90	4.28	3.54	3.01	3.79
FeO	7.08	7.03	7.75	8.32	8.45	8.66	8.61	8.45	8.57	8.43	8.57	7.07	7.79	7.91	7.87	7.27	8.01
MnO	0.21	-	0.41	0.41	0.29	0.43	0.34	0.44	0.42	0.34	0.37	0.27	0.24	0.38	0.31	0.21	0.22
MgO	13.68	12.82	13.18	12.50	12.27	12.43	11.99	12.22	12.35	12.17	11.84	13.30	12.62	12.50	12.50	13.36	12.86
CaO	22.93	22.80	22.83	22.45	22.44	22.63	22.36	22.52	22.50	22.67	22.56	23.05	23.27	23.07	22.73	22.96	23.25
Na_2O	0.40	0.56	0.84	0.89	1.07	1.06	1.11	0.60	1.07	0.62	0.95	0.92	0.80	1.05	0.93	0.88	0.94
TOTAL	100.06	99.32	100.68	99.30	99.77	100.71	100.38	99.35	100.52	100.27	100.06	99.85	100.25	100.06	99.25	99.63	100.40

Formula per
6 Oxygen atoms

Si	1.841	1.770	1.933	1.907	1.903	1.876	1.857	1.904	1.893	1.875	1.861	1.877	1.809	1.842	1.863	1.891	1.861
Ti	0.052	0.074	0.031	0.038	0.044	0.047	0.057	0.042	0.040	0.053	0.058	0.040	0.062	0.046	0.042	0.038	0.041
Al	0.198	0.288	0.101	0.128	0.136	0.154	0.191	0.139	0.150	0.174	0.183	0.146	0.216	0.189	0.157	0.132	0.167
Fe	0.220	7.03	0.239	0.262	0.265	0.269	0.268	0.266	0.266	0.262	0.268	0.220	0.243	0.248	0.248	0.227	0.250
Mn	0.007	-	0.013	0.014	0.009	0.014	0.011	0.015	0.014	0.011	0.012	0.009	0.008	0.012	0.010	0.007	0.007
Mg	0.760	0.719	0.727	0.703	0.687	0.690	0.669	0.686	0.687	0.677	0.662	0.738	0.703	0.697	0.725	0.744	0.715
Ca	0.916	0.920	0.905	0.908	0.903	0.904	0.869	0.910	0.899	0.907	0.907	0.918	0.932	0.925	0.917	0.919	0.930
Na	0.030	0.041	0.060	0.065	0.078	0.076	0.081	0.044	0.077	0.045	0.070	0.066	0.058	0.076	0.068	0.063	0.068

	447	448	449	450	467[a]	468	469	471	498	499	500	541	554	555	556
SiO_2	49.76	49.63	49.28	49.40	49.49	50.12	50.08	50.52	49.25	49.22	49.33	52.68	45.66	45.66	47.53
TiO_2	0.18	0.41	0.25	0.43	1.58	0.45	0.53	0.48	0.38	0.53	0.31	0.58	2.82	3.21	2.05
Al_2O_3	-	-	-	0.25	0.30	-	0.30	-	-	-	-	0.56	7.76	8.15	5.65
FeO	26.04	26.32	27.16	26.38	26.71	26.32	23.02	26.51	23.59	23.44	26.67	9.61	6.82	7.09	6.57
MnO	1.47	1.36	1.46	1.49	1.22	1.35	1.50	1.52	1.43	1.38	1.54	1.19	-	-	-
MgO	3.05	2.73	2.23	2.55	1.74	3.04	4.67	2.94	4.58	4.56	2.99	12.25	12.42	12.22	13.56
CaO	16.88	17.19	17.06	17.26	12.17	18.24	19.64	16.60	18.85	19.22	16.96	20.48	22.85	22.74	22.82
Na_2O	2.27	2.20	2.03	2.20	5.27	1.55	0.95	2.72	0.92	1.11	2.21	2.01	0.58	0.73	0.62
TOTAL	99.65	99.84	99.47	99.96	98.48	101.07	100.69	101.49	99.00	99.46	100.01	99.36	98.91	99.80	98.80
Formula per 6 Oxygen atoms															
Si	2.022	2.012	2.019	2.007	2.026	2.005	1.990	2.010	1.991	1.982	1.998	1.995	1.727	1.712	1.793
Ti	0.006	0.013	0.008	0.013	0.049	0.014	0.016	0.014	0.011	0.016	0.010	0.017	0.080	0.090	0.058
Al	-	-	-	0.012	0.015	-	0.014	-	-	-	-	0.025	0.346	0.360	0.251
Fe	0.885	0.892	0.931	0.896	0.914	0.881	0.765	0.882	0.797	0.790	0.904	0.304	0.126	0.222	0.207
Mn	0.051	0.047	0.051	0.051	0.042	0.046	0.050	0.051	0.049	0.047	0.053	0.038	-	-	-
Mg	0.185	0.165	0.136	0.154	0.106	0.181	0.277	0.175	0.276	0.274	0.181	0.692	0.700	0.683	0.762
Ca	0.735	0.747	0.749	0.751	0.534	0.782	0.836	0.716	0.816	0.829	0.736	0.831	0.926	0.913	0.922
Na	0.179	0.173	0.161	0.173	0.419	0.121	0.073	0.210	0.072	0.086	0.174	0.147	0.042	0.053	0.045

[a] Total = 99.84% if Fe_2O_3 is calculated; FeO = 14.48%; Fe_2O_3 = 13.59%.

	557	558	560	561	562	563	564	565	566	567	568	569	570	571	572
SiO_2	47.81	46.61	50.20	45.99	50.62	51.08	45.59	47.44	45.80	47.56	50.75	51.15	51.42	50.70	51.16
TiO_2	2.46	2.64	1.83	2.95	0.86	0.47	3.25	2.16	2.91	2.09	1.17	0.47	0.54	0.65	0.48
Al_2O_3	5.50	6.70	3.11	6.93	2.06	1.16	7.40	5.78	6.97	5.90	2.59	1.08	1.72	1.84	1.36
FeO	6.50	6.77	8.50	7.20	13.96	12.86	7.19	6.49	7.33	6.82	7.96	13.60	12.63	13.25	13.01
MnO	-	-	0.56	0.20	1.23	1.47	-	-	-	-	0.44	1.46	1.29	1.29	1.47
MgO	13.43	12.69	12.25	12.33	8.43	8.91	12.54	13.57	12.55	13.34	13.02	8.86	9.23	8.62	9.22
CaO	22.70	22.97	22.38	22.81	20.38	20.73	22.62	22.82	22.60	22.78	22.43	21.03	20.94	20.19	21.09
Na_2O	0.55	0.68	1.45	0.71	2.48	2.03	0.60	0.61	0.68	0.75	1.20	1.99	2.47	2.46	2.10
TOTAL	98.95	99.06	100.28	99.12	100.02	98.71	99.19	98.87	98.84	99.24	99.56	99.64	100.24	99.00	99.89

Formula per
6 Oxygen atoms

Si	1.798	1.758	1.883	1.742	1.947	1.983	1.699	1.754	1.736	1.789	1.906	1.965	1.980	1.925	1.965
Ti	0.069	0.075	0.052	0.084	0.025	0.014	0.091	0.060	0.083	0.059	0.033	0.014	0.016	0.019	0.014
Al	0.244	0.298	0.137	0.309	0.093	0.053	0.325	0.252	0.311	0.262	0.115	0.049		0.082	0.062
Fe	0.204	0.214	0.267	0.228	0.449	0.418	0.224	0.201	0.232	0.215	0.250	0.437	0.407	0.421	0.418
Mn	-	-	0.018	0.006	0.040	0.048	-	-	-	-	0.014	0.048	0.042	0.042	0.048
Mg	0.753	0.713	0.685	0.696	0.483	0.515	0.696	0.748	0.709	0.748	0.729	0.507	0.530	0.488	0.528
Ca	0.915	0.928	0.900	0.926	0.840	0.862	0.903	0.904	0.918	0.918	0.903	0.866	0.864	0.821	0.868
Na	0.040	0.050	0.105	0.052	0.185	0.153	0.043	0.044	0.050	0.055	0.088	0.148	0.184	0.181	0.156

	573	574	575	576	577	578	579	580	581	690	691	692	693	694	695
SiO	51.43	45.21	44.22	45.68		46.35	46.25	47.05	46.03	46.19	46.54	50.48	44.26	45.20	51.06
TiO_2	0.39	3.14	3.56	3.05	2.90	2.79	2.85	2.81	2.79	2.77	2.82	1.04	3.49	2.84	1.00
Al_2O_3	1.17	7.84	8.61	7.47	7.09	6.83	6.64	6.29	6.72	6.40	6.44	1.89	7.89	7.62	2.35
FeO	13.23	7.67	7.99	7.44	7.51	7.77	7.11	7.28	7.45	7.43	7.40	8.52	7.78	7.23	7.92
MnO	1.34	-	-	-	-	0.20	0.24	-	-	0.21	-	0.54	0.24	-	0.45
MgO	9.08	12.04	11.66	12.12	12.51	12.53	12.61	12.79	12.42	12.55	12.57	12.59	11.62	12.39	12.79
CaO	21.09	22.81	22.66	22.83	22.83	23.01	22.36	22.36	22.31	22.66	22.66	22.76	22.92	23.11	23.03
Na_2O	1.97	0.65	0.88	0.77	0.67	0.80	0.72	0.74	0.82	0.70	0.83	1.13	0.65	0.82	0.92
TOTAL	99.70	99.36	99.58	99.36	99.31	100.28	99.33	99.32	98.54	98.91	99.26	98.95	98.85	99.21	99.52
Formula per 6 Oxygen atoms															
Si	1.974	1.688	1.664	1.706	1.708	1.754	1.721	1.750	1.703	1.753	1.757	1.920	1.689	1.713	1.921
Ti	0.011	0.088	0.101	0.086	0.081	0.079	0.080	0.079	0.077	0.079	0.080	0.030	0.100	0.081	0.028
Al	0.053	0.345	0.382	0.330	0.312	0.304	0.291	0.276	0.293	0.286	0.287	0.085	0.355	0.340	0.104
Fe	0.424	0.239	0.251	0.232	0.234	0.246	0.221	0.227	0.231	0.236	0.234	0.271	0.248	0.229	0.249
Mn	0.044	-	-	-	-	0.007	0.008	-	-	0.007	0.005	0.017	0.008	-	0.014
Mg	0.520	0.670	0.654	0.674	0.695	0.707	0.700	0.710	0.685	0.710	0.708	0.714	0.661	0.700	0.717
Ca	0.867	0.912	0.914	0.913	0.912	0.933	0.913	0.891	0.884	0.922	0.917	0.928	0.937	0.938	0.928
Na	0.147	0.047	0.064	0.056	0.048	0.058	0.052	0.053	0.059	0.052	0.061	0.084	0.048	0.060	0.067

	696	697	698	713	798	804	807	811	827	835	854	871	872	879	880
SiO	51.02	50.41	50.82	52.86	52.39	52.48	51.83	43.43	46.40	43.83	50.98	50.34	52.12	46.06	47.93
TiO_2	0.89	1.27	0.98	0.66	0.73	0.68	0.91	4.30	2.81	4.47	1.40	1.54	0.54	3.05	2.25
Al_2O_3	2.08	2.75	2.08	0.75	1.14	1.24	1.56	9.30	6.49	8.54	2.94	3.41	1.26	6.98	5.04
FeO	8.49	7.61	9.03	8.87	7.37	9.13	6.86	7.77	7.57	7.50	7.02	7.53	7.13	7.58	7.73
MnO	0.55	0.41	0.51	1.02	0.56	0.88	0.75	-	-	-	0.42	0.46	0.68	-	0.23
MgO	12.63	13.21	12.01	13.16	13.49	11.91	13.86	10.89	11.92	11.21	13.25	13.46	14.45	12.51	13.11
CaO	22.39	22.46	22.80	21.14	22.01	21.45	22.10	23.44	23.16	22.94	22.66	22.46	22.43	23.46	22.69
Na_2O	1.08	0.98	1.60	1.84	0.93	1.35	0.97	0.60	0.70	0.76	0.80	0.97	0.97	0.88	0.73
TOTAL	99.13	99.10	99.83	100.30	98.62	99.12	98.84	99.73	99.05	99.25	99.47	100.17	99.58	100.52	99.71

Formula per
6 Oxygen atoms

Si	1.930	1.901	1.916	1.974	1.974	1.985	1.950	1.646	1.759	1.665	1.905	1.878	1.950	1.726	1.803
Ti	0.025	0.036	0.028	0.019	0.021	0.019	0.026	0.122	0.080	0.128	0.039	0.043	0.015	0.086	0.064
Al	0.093	0.122	0.093	0.033	0.051	0.055	0.069	0.416	0.290	0.382	0.130	0.150	0.056	0.308	0.223
Fe	0.269	0.240	0.285	0.277	0.232	0.289	0.216	0.246	0.240	0.238	0.219	0.235	0.223	0.238	0.243
Mn	0.018	0.013	0.016	0.032	0.018	0.028	0.024	-	-	-	0.013	0.014	0.022	-	0.007
Mg	0.712	0.743	0.675	0.732	0.758	0.671	0.777	0.615	0.673	0.635	0.738	0.749	0.806	0.699	0.735
Ca	0.908	0.908	0.921	0.846	0.889	0.869	0.891	0.952	0.940	0.934	0.907	0.898	0.899	0.942	0.915
Na	0.079	0.072	0.117	0.134	0.068	0.099	0.071	0.044	0.051	0.056	0.058	0.070	0.070	0.064	0.053

	884	885	1198	1206	1211	1227	1229	1230	1263	1267	1277	1278
SiO	52.75	52.66	48.31	51.38	49.98	49.63	50.35	50.96	50.68	50.76	48.90	49.25
TiO_2	0.71	0.83	2.97	-	1.79	2.00	1.70	1.61	1.30	1.27	2.28	1.50
Al_2O_3	1.44	1.39	5.28	1.87	3.22	3.78	3.24	2.76	3.02	3.03	4.02	3.18
FeO	7.10	7.26	7.69	12.84	7.40	7.90	7.84	7.60	10.13	10.31	8.56	9.93
MnO	0.62	0.77	-	0.57	-	-	0.22	-	0.74	0.66	0.30	0.65
MgO	14.30	14.15	11.84	9.27	12.92	11.73	12.18	12.44	10.48	10.34	10.91	10.60
CaO	22.23	22.19	22.58	21.25	22.62	22.61	22.42	22.60	22.60	22.78	22.25	22.37
Na_2O	1.12	1.26	0.74	2.25	0.58	0.92	0.86	1.12	1.35	1.81	1.80	1.44
TOTAL	100.27	100.51	99.41	99.43	98.51	98.57	98.81	99.09	100.30	100.96	99.02	98.92
Formula per 6 Oxygen atoms												
Si	1.956	1.951	1.811	1.965	1.885	1.875	1.900	1.913	1.911	1.903	1.858	1.887
Ti	0.020	0.023	0.084	-	0.051	0.057	0.048	0.045	0.037	0.036	0.065	0.043
Al	0.063	0.061	0.233	0.084	0.143	0.168	0.144	0.122	0.134	0.134	0.180	0.143
Fe	0.220	0.225	0.241	0.410	0.233	0.250	0.248	0.239	0.319	0.323	0.272	0.318
Mn	0.019	0.024	-	0.018	-	-	0.007	-	0.024	0.021	0.010	0.021
Mg	0.791	0.782	0.662	0.529	0.727	0.661	0.685	0.696	0.589	0.578	0.618	0.606
Ca	0.883	0.881	0.907	0.871	0.914	0.915	0.906	0.909	0.913	0.915	0.906	0.919
Na	0.080	0.090	0.054	0.167	0.042	0.068	0.063	0.081	0.099	0.132	0.132	0.107

Key to Table B.4b:-

Syenite block S1/2:- 67 - 72, 73, 74c - 75r, 76, 77, 78c - 79r, 80 - 90*, 91 - 100*, 101, 102 - 105*, 106, 119, 120r - 126c, 136r-142c, 143, 163, 201 - 204.

Syenite block S1/4:- 1028, 1032.

Syenite block S3/2:- 416, 419r-420c, 422, 423, 426.

Syenite block S4:- 209c - 213r, 214c-216r, 273.

Syenite block SX3:- 1073, 1075c-1079r, 1085, 1087, 1089c - 1090r, 1098.

Green Tuff, Pantelleria (groundmass):- 705.

* From single crystal.

Table B.4b.

	67	68	69	70	71	72	73	74	75	76	77	78	79	80	81	82	83
SiO_2	52.06	51.40	51.89	52.37	51.72	52.23	51.73	52.20	51.85	52.20	53.62	53.91	52.58	51.56	51.32	50.91	52.17
TiO_2	1.21	1.97	1.61	0.59	3.64	1.86	2.62	2.42	2.29	3.14	2.40	2.52	2.16	2.06	2.00	1.76	1.56
ZrO_2	-	-	-	-	-	-	-	-	-	-	-	-	-	n.d.	-	-	n.d.
Al_2O_3	1.10	1.11	1.08	1.03	1.13	0.98	1.14	1.01	0.98	1.13	1.01	1.00	0.90	1.11	1.25	1.12	1.01
Fe_2O_3	11.14	17.46	13.34	12.09	17.87	23.79	14.95	16.43	20.91	20.47	26.33	25.49	25.41	12.45	13.05	13.87	21.74
FeO	7.99	6.95	8.28	8.14	7.10	4.45	8.08	6.88	5.14	5.73	2.64	2.95	3.62	9.42	8.50	7.85	4.60
MnO	1.18	0.95	1.13	1.02	0.67	0.52	1.06	1.07	0.59	0.62	0.41	0.43	0.57	1.04	1.08	1.11	0.64
MgO	5.89	3.40	4.67	5.88	2.14	1.71	3.73	3.28	2.37	1.90	1.03	1.00	1.00	4.52	4.42	4.34	2.33
CaO	14.79	8.82	12.74	14.16	5.96	4.21	9.96	9.53	5.83	5.17	1.96	1.97	2.98	12.35	12.53	12.36	6.94
Na_2O	4.97	7.60	5.82	5.30	9.03	10.06	7.10	7.59	9.29	9.67	11.41	11.21	10.94	5.74	5.84	6.04	9.01
TOTAL	100.33	99.66	100.56	100.58	99.26	99.81	100.37	100.28	99.20	100.02	100.81	100.47	100.16	100.27	99.99	99.36	100.27
Formula per 6 Oxygen atoms																	
Si	1.979	1.975	1.976	1.988	1.987	1.995	1.973	1.984	1.991	1.988	2.012	2.025	2.000	1.973	1.968	1.965	1.989
Ti	0.035	0.057	0.046	0.017	0.105	0.054	0.075	0.069	0.066	0.090	0.068	0.071	0.062	0.060	0.058	0.051	0.045
Zr	-	-	-	-	-	-	-	-	-	-	-	-	-	n.d.	-	-	n.d.
Al	0.050	0.051	0.049	0.047	0.052	0.044	0.052	0.046	0.043	0.051	0.045	0.044	0.041	0.050	0.057	0.051	0.045
Fe^{3+}	0.317	0.502	0.381	0.344	0.514	0.681	0.427	0.469	0.601	0.584	0.789	0.717	0.724	0.357	0.375	0.401	0.621
Fe^{2+}	0.253	0.222	0.262	0.257	0.227	0.141	0.257	0.218	0.164	0.182	0.088	0.092	0.115	0.300	0.271	0.252	0.146
Mn	0.039	0.032	0.037	0.033	0.022	0.017	0.035	0.035	0.020	0.020	0.013	0.014	0.019	0.034	0.036	0.037	0.021
Mg	0.334	0.195	0.265	0.333	0.123	0.098	0.212	0.186	0.136	0.108	0.058	0.056	0.057	0.258	0.253	0.250	0.133
Ca	0.603	0.363	0.520	0.576	0.246	0.173	0.408	0.389	0.240	0.211	0.079	0.079	0.122	0.506	0.515	0.511	0.284
Na	0.367	0.566	0.430	0.390	0.673	0.744	0.526	0.561	0.692	0.713	0.830	0.816	0.806	0.426	0.434	0.452	0.703

	84	85	86	87	88	89	90	91	92[a]	93[b]	94	95	96	97	98	99	100
SiO_2	52.36	51.69	51.87	51.67	51.37	51.93	52.67	51.95	53.10	53.14	52.01	51.87	51.74	51.46	51.22	51.78	51.90
TiO_2	2.10	1.62	2.45	1.31	2.29	3.13	1.77	1.05	0.47	0.54	1.10	1.24	1.30	0.52	0.90	1.08	1.09
ZrO_2	n.d.	-	-	-	-	-	-	-	-	-	-	-	-	-	-	-	-
Al_2O_3	0.93	1.00	0.97	1.08	0.89	0.92	1.15	1.05	1.00	0.85	1.22	1.24	1.21	0.82	1.08	1.27	1.26
Fe_2O_3	22.71	19.10	17.91	14.90	16.93	21.10	22.46	10.14	13.90	13.40	11.04	9.41	9.52	9.66	9.79	10.73	11.32
FeO	3.92	6.12	6.47	7.89	7.60	4.90	4.68	8.57	5.62	6.84	8.28	9.11	8.75	8.36	8.78	8.40	8.74
MnO	0.56	0.95	0.93	0.84	0.96	0.62	0.60	1.21	1.31	1.37	1.03	1.18	1.08	1.27	1.18	1.19	1.01
MgO	1.93	3.12	2.59	4.39	3.06	1.98	2.25	6.30	6.62	6.71	5.78	6.12	5.93	6.55	6.24	5.84	6.01
CaO	5.51	8.58	8.04	11.03	8.90	5.41	6.07	15.83	11.89	11.97	13.93	15.57	15.45	16.12	15.48	14.88	14.31
Na_2O	9.84	8.02	8.22	6.42	7.77	10.00	9.37	4.57	5.84	5.53	5.01	4.38	4.42	4.24	4.44	4.92	5.14
TOTAL	99.84	100.19	99.45	99.52	99.77	99.98	101.02	100.66	99.96	100.59	99.39	100.11	99.40	98.99	99.10	100.09	100.78
Formula per 6 Oxygen atoms																	
Si	1.995	1.977	1.992	1.985	1.977	1.980	1.987	1.973	2.009	2.004	1.992	1.979	1.985	1.987	1.976	1.976	1.970
Ti	0.060	0.047	0.071	0.039	0.066	0.089	0.050	0.030	0.014	0.015	0.032	0.036	0.038	0.016	0.026	0.031	0.031
Zr	n.d.	-	-	-	-	-	-	-	-	-	-	-	-	-	-	-	-
Al	0.042	0.046	0.044	0.049	0.041	0.042	0.051	0.048	0.045	0.038	0.055	0.056	0.056	0.038	0.050	0.057	0.056
Fe^{3+}	0.648	0.547	0.515	0.429	0.488	0.603	0.635	0.289	0.394	0.379	0.316	0.269	0.274	0.279	0.283	0.307	0.322
Fe^{2+}	0.124	0.195	0.207	0.253	0.242	0.156	0.147	0.271	0.117	0.215	0.264	0.289	0.279	0.269	0.282	0.267	0.276
Mn	0.018	0.031	0.031	0.028	0.032	0.021	0.020	0.039	0.043	0.045	0.034	0.038	0.035	0.042	0.039	0.039	0.033
Mg	0.110	0.178	0.149	0.252	0.176	0.113	0.127	0.357	0.374	0.378	0.330	0.348	0.339	0.377	0.259	0.333	0.341
Ca	0.225	0.352	0.331	0.454	0.367	0.221	0.245	0.644	0.482	0.484	0.572	0.637	0.635	0.667	0.641	0.609	0.582
Na	0.727	0.595	0.613	0.478	0.579	0.740	0.686	0.337	0.429	0.405	0.372	0.325	0.329	0.317	0.333	0.364	0.379

[a]Total includes 0.21% K_2O [b]Total includes 0.24% K_2O

	101	102	103	104	105	106	119	120	121	122	123	124	125	126	136	137	138
SiO_2	52.57	52.41	52.09	52.06	52.62	53.03	51.21	50.60	50.79	50.46	50.79	50.33	50.42	50.35	51.60	50.32	50.63
TiO_2	3.55	2.58	1.89	3.28	2.94	3.75	2.57	1.40	0.82	1.87	2.00	1.88	1.91	1.88	2.47	2.39	2.14
ZrO_2	-	-	-	-	-	-	n.d.	-	0.17	-	-	-	-	-	-	-	-
Al_2O_3	1.04	1.04	0.92	0.86	1.05	1.09	0.80	1.41	0.81	1.12	1.14	1.05	1.24	1.23	0.89	1.18	1.34
Fe_2O_3	21.90	23.82	25.18	22.25	21.07	21.14	25.67	20.13	15.00	15.81	15.74	15.40	15.38	16.29	28.19	17.79	16.41
FeO	5.11	4.31	4.09	4.80	5.04	6.39	2.36	4.27	7.69	6.47	6.57	6.85	6.50	5.50	0.64	4.74	5.23
MnO	0.54	0.61	0.44	0.51	0.60	0.59	0.67	0.86	1.25	1.04	0.99	1.04	1.15	1.08	0.50	1.00	1.01
MgO	1.08	1.36	1.57	1.13	1.83	1.42	1.65	3.39	4.28	4.41	4.30	4.29	4.35	4.33	0.77	3.76	4.33
CaO	3.32	3.18	4.29	3.71	4.86	3.25	3.56	9.49	12.75	12.09	12.19	12.27	12.18	12.10	2.16	10.16	11.37
Na_2O	10.58	10.56	9.98	10.62	9.78	10.42	11.42	8.63	6.29	6.87	6.93	6.77	6.70	7.05	12.26	8.01	7.18
TOTAL	99.69	99.87	98.70	99.21	99.79	101.10	99.92	100.17	99.85	100.15	100.65	100.10	99.82	99.81	99.48	99.33	99.65
Formula per 6 Oxygen atoms																	
Si	2.003	1.996	1.995	1.997	2.002	1.997	1.959	1.938	1.963	1.938	1.939	1.938	1.941	1.935	1.974	1.939	1.942
Ti	0.102	0.074	0.055	0.095	0.085	0.106	0.074	0.041	0.024	0.054	0.058	0.055	0.056	0.055	0.071	0.069	0.061
Zr	-	-	-	-	-	-	n.d.	-	0.003	-	-	-	-	-	-	-	-
Al	0.047	0.047	0.042	0.040	0.047	0.048	0.037	0.064	0.038	0.051	0.052	0.048	0.057	0.057	0.041	0.054	0.061
Fe^{3+}	0.625	0.680	0.673	0.640	0.600	0.597	0.736	0.578	0.435	0.455	0.450	0.444	0.443	0.469	0.808	0.514	0.472
Fe^{2+}	0.162	0.137	0.130	0.153	0.160	0.211	0.075	0.136	0.248	0.207	0.209	0.220	0.208	0.176	0.021	0.152	0.167
Mn	0.018	0.020	0.015	0.017	0.020	0.019	0.023	0.029	0.041	0.035	0.033	0.035	0.038	0.036	0.017	0.034	0.034
Mg	0.062	0.077	0.089	0.064	0.104	0.080	0.095	0.194	0.247	0.253	0.244	0.247	0.250	0.248	0.045	0.216	0.248
Ca	0.137	0.130	0.176	0.152	0.199	0.132	0.146	0.390	0.528	0.497	0.494	0.507	0.503	0.499	0.089	0.420	0.468
Na	0.782	0.780	0.741	0.790	0.722	0.761	0.848	0.642	0.472	0.512	0.514	0.506	0.500	0.526	0.908	0.598	0.534

	139	140	141	142	143	163	201	202	203	204	209	210	211	212	213
SiO_2	51.05	51.05	50.76	50.98	51.53	50.42	50.90	52.21	51.96	50.80	51.73	51.53	51.74	51.32	51.79
TiO_2	0.89	0.79	1.31	0.47	2.17	1.25	1.23	0.55	0.56	1.93	2.15	3.03	1.59	2.33	1.99
ZrO_2	-	-	-	-	-	-	-	-	-	-	-	-	0.17	-	0.35
Al_2O_3	1.08	1.22	1.28	1.01	0.86	1.33	1.15	1.03	0.97	1.15	0.73	1.00	0.87	0.85	0.63
Fe_2O_3	12.98	10.44	11.13	11.18	27.11	12.22	9.64	10.98	11.76	14.78	24.67	22.97	26.14	23.63	26.02
FeO	6.60	8.30	2.27	7.11	1.26	6.33	8.62	8.55	7.93	7.63	3.19	4.47	1.06	3.00	1.87
MnO	1.08	1.14	1.22	1.14	0.46	1.18	1.63	1.07	1.22	1.06	0.45	0.51	0.72	0.65	0.58
MgO	5.81	6.21	6.29	6.68	1.09	6.15	6.40	6.49	6.29	4.39	1.83	1.77	2.24	2.47	2.10
CaO	12.20	15.41	15.71	15.92	3.13	14.99	16.59	15.21	15.37	12.12	4.24	4.31	3.99	4.29	3.77
Na_2O	5.67	4.77	5.08	4.94	11.64	5.53	4.42	4.87	5.13	6.52	10.74	10.61	10.91	10.42	11.39
TOTAL	99.36	99.34	100.05	99.43	99.25	99.41	100.57	100.95	101.19	100.43	99.74	100.20	99.50	98.97	100.51
Formula per 6 Oxygen atoms															
Si	1.958	1.958	1.943	1.961	1.977	1.939	1.946	1.977	1.968	1.946	1.979	1.965	1.977	1.973	1.967
Ti	0.026	0.023	0.038	0.014	0.063	0.037	0.036	0.016	0.017	0.056	0.062	0.087	0.046	0.068	0.057
Zr	-	-	-	-	-	-	-	-	-	-	-	-	0.004	-	0.007
Al	0.049	0.056	0.058	0.047	0.039	0.060	0.052	0.047	0.044	0.052	0.034	0.045	0.039	0.040	0.029
Fe^{3+}	0.374	0.301	0.319	0.322	0.779	0.352	0.276	0.312	0.333	0.424	0.707	0.656	0.748	0.681	0.740
Fe^{2+}	0.211	0.266	0.232	0.228	0.040	0.203	0.275	0.270	0.250	0.245	0.102	0.142	0.034	0.096	0.059
Mn	0.036	0.038	0.040	0.038	0.015	0.039	0.053	0.035	0.040	0.035	0.015	0.017	0.023	0.022	0.020
Mg	0.333	0.257	0.359	0.283	0.063	0.353	0.365	0.367	0.356	0.251	0.104	0.101	0.128	0.141	0.119
Ca	0.586	0.637	0.644	0.657	0.129	0.618	0.680	0.618	0.624	0.498	0.174	0.177	0.164	0.177	0.154
Na	0.423	0.357	0.378	0.269	0.865	0.413	0.328	0.358	0.377	0.484	0.797	0.785	0.808	0.777	0.839

	214	215	216	273	416	419	420	422	423	426	1028	1032	1073	1075	1076	1077	1078
SiO_2	50.86	51.57	51.48	52.21	52.41	52.55	52.17	52.18	52.12	51.78	52.08	52.31	52.68	51.84	52.04	51.79	51.96
TiO_2	1.67	1.72	1.53	2.21	3.19	2.35	3.28	2.21	1.70	2.16	1.89	2.29	0.46	0.50	0.62	0.63	0.83
ZrO_2	0.66	0.54	-	-	n.d.	0.41	0.51	1.04	1.21	1.01	n.d.	n.d.	-	-	-	-	-
Al_2O_3	0.73	0.51	0.53	0.54	1.24	0.88	0.98	1.01	0.99	0.95	0.64	0.76	1.05	0.72	0.94	1.13	1.15
Fe_2O_3	22.91	25.98	25.12	24.39	23.15	26.41	23.65	26.69	26.47	25.01	28.39	27.45	8.15	7.08	7.14	7.21	15.99
FeO	3.98	2.06	2.43	1.38	2.56	0.30	2.93	0.00	0.00	2.68	0.56	0.39	7.68	7.80	7.55	8.16	4.55
MnO	0.58	0.70	0.64	0.83	0.73	0.89	0.66	1.08	0.53	0.71	0.66	0.84	1.17	1.26	1.31	1.31	1.32
MgO	1.96	1.92	2.16	2.20	2.03	1.79	1.50	1.63	1.82	1.39	1.04	1.66	7.95	8.67	8.87	7.90	5.13
CaO	5.52	3.27	4.45	5.90	5.36	4.08	4.19	2.75	3.87	3.72	2.81	3.57	18.17	19.58	19.21	18.42	12.45
Na_2O	10.05	11.33	10.58	10.81	10.70	11.79	11.41	12.19	11.77	11.40	12.09	11.97	3.80	3.19	3.36	3.49	6.90
TOTAL	99.05	99.60	98.99	100.46	101.39	101.45	101.26	100.80	100.46	100.80	100.16	101.24	101.10	100.66	101.02	100.05	100.28
Formula per 6 Oxygen atoms																	
Si	1.971	1.979	1.983	1.978	1.966	1.973	1.971	0.974	1.975	1.974	1.971	1.955	1.980	1.962	1.960	1.971	1.970
Ti	0.049	0.050	0.045	0.067	0.090	0.067	0.093	0.063	0.049	0.062	0.054	0.065	0.013	0.015	0.018	0.018	0.023
Zr	0.013	0.010	-	-	n.d.	0.008	0.010	0.022	0.025	0.022	n.d	n.d	-	-	-	-	-
Al	0.034	0.023	0.024	0.025	0.055	0.038	0.043	0.045	0.044	0.042	0.029	0.034	0.046	0.032	0.042	0.051	0.051
Fe^{3+}	0.665	0.746	0.724	0.692	0.653	0.746	0.672	0.760	0.755	0.717	0.808	0.772	0.230	0.202	0.203	0.206	0.456
Fe^{2+}	0.128	0.066	0.078	0.043	0.076	0.009	0.093	0.000	0.000	0.091	0.018	0.012	0.241	0.247	0.238	0.259	0.144
Mn	0.024	0.022	0.023	0.027	0.024	0.028	0.022	0.035	0.017	0.023	0.021	0.026	0.037	0.040	0.041	0.042	0.042
Mg	0.113	0.111	0.124	0.124	0.113	0.100	0.085	0.092	0.103	0.079	0.059	0.093	0.445	0.490	0.498	0.448	0.290
Ca	0.230	0.135	0.184	0.239	0.216	0.164	0.169	0.111	0.156	0.151	0.114	0.143	0.732	0.794	0.776	0.751	0.506
Na	0.756	0.843	0.790	0.793	0.778	0.858	0.836	0.895	0.865	0.842	0.887	0.867	0.277	0.234	0.245	0.257	0.507

	1079	1085	1087	1089	1090	1098	705
SiO_2	52.39	51.14	51.85	51.50	51.72	52.27	52.10
TiO_2	1.70	0.54	1.89	0.68	2.60	1.90	6.53
ZrO_2	n.d.	n.d.	n.d.	n.d.	n.d.	n.d.	n.d.
Al_2O_3	0.67	0.59	0.76	0.73	0.76	0.74	-
Fe_2O_3	24.39	10.66	20.18	11.98	24 98	27.31	19.93
FeO	2.83	8.05	4.08	6.82	2.41	0.98	5.45
MnO	0.71	1.50	0.99	1.52	0.78	0.56	1.12
MgO	2.03	6.08	3.28	6.41	1.61	1.35	0.23
CaO	6.25	16.05	9.33	16.19	4.22	3.72	1.26
Na_2O	10.38	4.50	8.85	5.10	1.24	11.63	13.20
TOTAL	101.35	99.10	101.20	100.91	100.31	100.46	99.82
Formula per 6 Oxygen atoms							
Si	1.964	1.968	1.953	1.948	1.953	1.967	1.997
Ti	0.048	0.016	0.053	0.019	0.073	0.054	0.188
Zr	n.d.	n.d.	n.d.	n.d.	n.d.	n.d.	n.d.
Al	0.030	0.026	0.033	0.033	0.034	0.033	-
Fe^{3+}	0.688	0.309	0.572	0.341	0.710	0.773	0.575
Fe^{2+}	0.089	0.259	0.129	0.216	0.076	0.031	0.175
Mn	0.023	0.049	0.031	0.049	0.024	0.018	0.036
Mg	0.114	0.349	0.184	0.361	0.090	0.076	0.013
Ca	0.251	0.662	0.376	0.656	0.171	0.150	0.052
Na	0.754	0.335	0.646	0.374	0.823	0.849	0.981

B5. Amphiboles.

An ideal amphibole analysis should have an oxide weight sum close to 98%. Acceptable analyses therefore have totals in the range 96.5% - 99.5%. However, Al-poor alkali amphiboles (arfvedsonites) have significant quantities of Fe_2O_3 which will result in a lower oxide total if all Fe is reported as FeO. No attempt is made here to estimate Fe_2O_3 contents from mineral stoichiometry, and acceptable Al-poor amphibole analysis totals are therefore adjusted downwards slightly to the range 96% - 99%.

Key to Table B5:-

Tajao ignimbrite:- 9, 674, 675, 677, 678, 715.

Ignimbrite 0:- 769, 783, 831, 833, 859, 876, 903.

Pumice deposit E:- 742, 750.

Cognate mafic cumulate fragment in fall J*:- 320c - 321r, 322, 323.

Syenite block S1/2:- 107, 108c - 110r, 112, 113, 252, 253, 255, 256.

Syenite block S1/4:- 1034.

Syenite block SX3:- 1040, 1049, 1050, 1053, 1081, 1088, 1095.

Syenite block S3/2:- 427, 428.

Syenite block S4:- 196, 249r - 250c, 258 - 261, 262r - 264c,

* Also see 10 analyses of one homogeneous amphibole crystal in the introduction to this Appendix.

Medano xenolith TF 161:- 1249r - 1250c, 1253c - 1254r, 1255r - 1256.

Medano xenolith TF 162:- 1200.

Medano xenolith TF 163:- 1266, 1268, 1279r - 1280c.

Ignimbrite E, Gran Canaria:- 691c - 692r, 695, 699, 707.

Green Tuff, Pantelleria (groundmass):- 529.

Suffixes c - r and r - c denote core to rim and rim to core spot sequences respectively.

Table B5

	9	107	108	109	110	112	113	196	249	250	252	253	255	256	258	259	260	261
SiO_2	39.91	52.83	53.39	52.87	52.97	52.70	52.73	52.80	52.72	52.91	51.96	51.78	51.75	52.22	53.14	52.88	52.99	52.35
TiO_2	5.86	1.53	1.29	1.45	1.21	1.55	1.63	1.60	1.50	1.32	1.37	1.91	1.63	1.24	1.94	1.82	1.74	1.62
Al_2O_3	10.97	1.47	1.50	1.56	1.43	1.69	1.34	1.42	1.05	1.11	1.54	1.49	1.76	1.40	1.28	1.18	1.62	1.59
FeO	12.36	19.38	19.21	19.58	19.36	19.60	19.72	17.09	17.12	16.67	18.84	19.49	18.55	18.71	14.48	14.64	14.83	16.40
MnO	0.35	2.16	2.02	2.04	2.08	1.95	2.18	1.77	1.89	1.87	2.46	2.75	2.75	2.47	1.75	1.75	1.67	1.79
MgO	12.06	8.53	8.96	8.80	8.94	8.61	8.74	10.88	10.81	10.47	9.10	8.30	9.04	9.23	11.80	12.12	11.91	10.82
CaO	12.03	0.72	0.56	0.36	0.60	0.68	0.91	1.46	0.39	0.62	0.49	0.73	1.31	0.49	2.47	2.73	1.46	2.00
Na_2O	2.70	8.54	8.82	8.66	8.81	8.49	8.22	9.76	10.16	10.00	9.69	9.82	9.59	10.07	8.89	8.45	9.58	8.90
K_2O	1.12	1.47	1.43	1.34	1.43	1.39	1.50	1.32	1.18	1.22	1.35	1.50	1.60	1.36	1.04	1.19	1.21	1.17
TOTAL	97.36	96.63	97.15	96.66	96.82	96.66	96.98	98.10	96.82	96.19	96.80	97.78	97.98	97.19	96.78	96.75	97.01	96.62
Formula per 23 Oxygen atoms																		
Si	5.999	8.017	8.037	8.011	8.020	7.990	7.989	7.854	7.934	7.992	7.907	7.856	7.812	7.918	7.897	7.875	7.871	7.868
Ti	0.662	0.174	0.146	0.166	0.138	0.177	0.188	0.179	0.170	0.150	0.158	0.218	0.186	1.142	0.218	0.204	0.195	0.184
Al	1.944	0.263	0.265	0.280	0.256	0.302	0.238	0.249	0.187	0.197	0.276	0.268	0.314	0.251	0.225	0.207	0.284	0.282
Fe	1.547	2.448	2.407	2.470	2.439	2.474	2.488	2.116	2.145	2.095	2.386	2.461	2.331	2.361	1.792	1.815	1.833	2.051
Mn	0.045	0.278	0.258	0.262	0.267	0.251	0.280	0.223	0.241	0.241	0.318	0.354	0.353	0.317	0.220	0.221	0.211	0.228
Mg	2.702	1.930	2.010	1.989	2.016	1.946	1.974	2.412	2.426	2.358	2.063	1.877	2.035	2.086	2.613	2.691	2.636	2.423
Ca	1.938	0.117	0.090	0.058	0.099	0.111	0.149	0.234	0.063	0.102	0.080	0.120	0.212	0.080	0.394	0.435	0.234	0.323
Na	0.787	2.513	2.573	2.542	2.585	2.459	2.415	2.813	2.964	2.928	2.860	2.888	2.805	2.960	2.561	2.440	2.758	2.592
K	0.216	0.286	0.274	0.260	0.277	0.269	0.291	0.251	0.227	0.237	0.262	0.291	0.309	0.264	0.197	0.226	0.229	0.224

	262	263	264	320	321	322	323	427[a]	428[b]	529	674	675	677	678	691	692	695	699
SiO_2	52.71	51.74	53.71	40.49	40.44	40.33	40.35	52.50	52.50	49.50	39.92	40.56	39.97	40.75	49.53	49.93	49.09	50.47
TiO_2	1.53	1.86	1.66	5.71	5.40	5.70	5.84	1.20	1.35	3.29	6.86	6.46	6.28	5.65	2.07	1.74	1.99	1.98
Al_2O_3	1.46	1.75	1.27	12.21	12.32	12.44	12.31	1.42	1.61	0.39	13.23	12.52	12.24	10.53	4.31	3.60	4.16	2.96
FeO	17.49	19.77	15.61	10.79	11.12	10.64	10.79	16.86	16.71	28.78	10.41	11.00	11.70	11.77	10.00	9.74	10.36	10.07
MnO	1.71	1.66	1.78	0.28	0.26	0.23	0.23	3.48	2.54	0.94	-	-	-	0.43	1.33	1.16	1.29	1.31
MgO	10.23	9.06	11.11	12.18	12.17	12.30	12.24	9.08	10.81	2.66	12.85	12.67	11.91	12.05	16.27	16.12	16.01	15.96
CaO	1.19	0.93	1.01	11.93	11.75	11.99	12.18	0.71	1.79	3.15	12.48	12.31	12.16	11.54	8.25	8.07	8.52	7.89
Na_2O	9.60	9.69	9.54	2.94	2.49	2.73	2.78	9.87	9.17	6.54	2.56	2.30	2.84	2.91	4.73	4.85	4.57	4.87
K_2O	1.29	1.21	1.27	1.03	1.00	0.90	0.89	1.37	1.51	1.20	1.06	1.10	0.99	1.34	0.82	0.96	0.83	0.94
TOTAL	97.21	97.67	97.97	97.56	96.94	97.24	96.61	96.87	98.32	96.45	99.37	98.92	98.09	96.97	97.31	96.17	96.82	96.45
Formula per 23 Oxygen atoms																		
Si	7.910	7.816	7.988	6.007	6.031	5.990	5.980	7.966	7.834	7.909	5.804	5.929	5.919	6.132	7.229	7.362	7.215	7.425
Ti	0.173	0.211	0.186	0.638	0.606	0.637	0.652	0.137	0.152	0.395	0.750	0.710	0.700	0.640	0.227	0.193	0.220	0.218
Al	0.258	0.312	0.224	2.136	2.166	2.178	2.152	0.254	0.283	0.073	2.267	2.158	2.136	1.868	0.741	0.625	0.721	0.514
Fe	2.184	2.487	1.933	1.333	1.381	1.316	1.331	2.139	2.085	3.845	1.265	1.344	1.449	1.482	1.220	1.201	1.273	1.238
Mn	0.218	0.213	0.225	0.035	0.033	0.029	0.029	0.447	0.320	0.127	-	-	-	0.055	0.165	0.145	0.160	0.161
Mg	2.288	2.041	2.463	2.694	2.705	2.723	2.705	2.054	2.404	0.634	2.785	2.762	2.628	2.703	3.539	3.544	3.507	3.500
Ca	0.192	0.152	0.162	1.898	1.878	1.909	1.935	0.116	0.287	0.540	1.944	1.928	1.929	1.861	1.290	1.274	1.342	1.242
Na	2.794	2.837	2.751	0.845	0.720	0.785	0.799	2.903	2.652	2.027	0.720	0.652	0.816	0.849	1.337	1.387	1.302	1.388
K	0.248	0.234	0.242	0.196	0.191	0.171	0.169	0.266	0.287	0.245	0.196	0.204	0.188	0.257	0.152	0.180	0.156	0.176

[a] Total includes 0.38% ZrO_2

[b] Total includes 0.33% ZrO_2

	707	715	742	750	769	783	831	833	859	876	903	1034	1040	1049	1050	1053	1081
SiO_2	50.23	39.26	42.09	42.49	39.81	40.22	39.96	40.52	40.04	40.06	40.29	51.89	51.05	51.20	51.63	50.93	51.64
TiO_2	2.58	6.57	5.63	5.62	6.71	6.16	6.08	6.39	6.47	6.09	6.64	1.29	1.97	1.54	1.51	1.56	0.47
Al_2O_3	4.09	12.63	9.56	10.23	12.14	10.86	11.41	12.08	11.52	12.01	12.43	1.85	2.12	1.85	1.93	1.96	2.62
FeO	9.90	10.44	11.20	10.69	11.23	11.98	11.36	10.71	11.77	11.17	10.42	18.78	19.93	20.04	19.29	19.76	13.33
MnO	1.30	-	0.41	0.45	0.35	0.43	0.29	0.23	0.21	0.31	0.23	2.31	1.58	1.59	1.63	1.68	1.60
MgO	15.65	12.74	13.83	13.85	12.55	11.61	12.14	12.72	12.34	12.71	12.49	9.25	8.64	8.67	9.45	8.98	13.18
CaO	8.44	12.19	11.28	11.12	11.75	11.72	12.08	12.13	11.67	12.21	12.29	1.28	1.74	1.44	1.50	1.37	5.61
Na_2O	5.40	2.66	3.28	3.07	3.13	3.18	2.90	3.03	2.99	2.84	2.88	9.15	9.07	8.78	9.22	9.39	6.97
K_2O	0.86	0.90	0.81	0.76	0.84	1.04	0.81	0.81	0.83	0.82	0.85	1.41	1.40	1.39	1.33	1.33	1.60
TOTAL	98.45	97.39	98.09	98.28	98.51	97.20	97.03	98.62	97.84	98.22	98.52	97.21	97.50	96.50	97.49	96.96	97.02

Formula per
23 Oxygen atoms

Si	7.259	5.831	6.216	6.228	5.878	6.035	5.991	5.951	5.954	5.927	5.901	7.865	7.752	7.852	7.799	7.785	7.665
Ti	0.280	0.734	0.625	0.620	0.746	0.696	0.686	0.706	0.723	0.677	0.731	0.147	0.225	0.178	0.171	0.180	0.052
Al	0.696	2.210	1.664	1.766	2.114	1.922	2.016	2.091	2.019	2.094	2.146	0.331	0.379	0.335	0.343	0.353	0.457
Fe	1.196	1.296	1.383	1.310	1.388	1.503	1.425	1.316	1.464	1.381	1.276	2.380	2.531	2.571	2.437	2.526	1.655
Mn	0.159	-	0.051	0.056	0.044	0.054	0.037	0.029	0.027	0.038	0.029	0.296	0.203	0.207	0.209	0.217	0.202
Mg	3.370	2.821	3.046	3.027	2.764	2.597	2.713	2.786	2.736	2.804	2.727	2.090	1.956	1.983	2.128	2.046	2.915
Ca	1.307	1.940	1.786	1.747	1.859	1.884	1.940	1.910	1.859	1.935	1.929	0.208	0.283	0.237	0.242	0.225	0.892
Na	1.513	0.767	0.940	0.873	0.895	0.926	0.842	0.862	0.863	0.816	0.817	2.690	2.670	2.611	2.700	2.784	2.006
K	0.159	0.171	0.152	0.143	0.159	0.200	0.155	0.152	0.158	0.154	0.159	0.273	0.272	0.272	0.256	0.259	0.303

	1088	1095	1200	1249	1250	1253	1254	1255	1256	1266	1268	1279	1280
SiO_2	47.74	49.65	40.34	40.07	39.89	39.26	37.54	37.02	39.50	39.52	41.16	39.59	41.55
TiO_2	2.55	1.78	4.12	6.16	6.46	5.11	3.34	3.30	6.69	1.87	5.10	1.74	4.87
Al_2O	3.85	2.39	10.36	11.38	11.45	10.80	11.03	11.04	11.58	10.49	10.19	10.70	10.07
FeO	19.93	20.42	18.94	14.26	12.86	20.49	28.42	28.54	12.75	21.02	12.57	21.00	12.73
MnO	1.67	1.55	0.36	0.23	0.25	0.48	1.05	0.99	0.20	1.25	0.48	1.20	0.40
MgO	8.53	8.36	6.64	9.21	9.76	5.69	1.18	1.20	10.05	7.21	11.66	7.00	11.47
CaO	3.91	2.11	11.48	11.72	11.90	11.42	10.95	11.00	11.96	11.26	11.62	10.99	11.41
Na_2O	7.70	8.71	2.65	3.01	2.97	2.54	2.51	2.48	2.84	2.93	3.32	2.78	3.50
K_2O	1.42	1.42	1.86	1.13	1.11	1.49	1.91	1.93	1.07	1.75	1.53	1.69	1.47
TOTAL	97.30	96.39	96.75	97.17	96.65	97.28	97.93	97.50	96.64	97.30	97.63	96.69	97.47
Formula per 23 Oxygen atoms													
Si	7.321	7.680	6.266	6.064	6.052	6.129	6.062	6.030	5.991	6.214	6.178	6.241	6.231
Ti	0.294	0.207	0.482	0.701	0.737	0.600	0.405	0.404	0.763	0.221	0.575	0.206	0.549
Al	0.696	0.435	1.896	2.029	2.048	1.988	2.100	2.120	2.07	1.945	1.802	1.987	1.781
Fe	2.556	2.642	2.461	1.805	1.631	2.675	3.838	3.887	1.62	2.764	1.578	2.768	1.596
Mn	0.217	0.203	0.048	0.030	0.032	0.064	0.143	0.137	0.026	0.166	0.062	0.161	0.050
Mg	1.951	1.927	1.536	2.078	2.206	1.323	0.284	0.292	2.273	1.691	2.609	1.645	2.563
Ca	0.642	0.349	1.910	1.901	1.934	1.911	1.895	1.920	1.944	1.897	1.868	1.857	1.834
Na	2.290	2.612	0.797	0.883	0.872	0.768	0.786	0.785	0.835	0.892	0.966	0.851	1.017
K	0.279	0.279	0.368	0.368	0.215	0.297	0.393	0.400	0.208	0.351	0.293	0.340	0.281

B6. Biotites.

In addition to the listed elements, Ca and Cr were analysed for but not detected in any specimens. Because of the (OH,F) anions in the mineral formula, 96% is usually considered the ideal oxide weight sum for Fe-rich biotite. The biotites considered here are Mg-rich, and thus analyses with totals falling in the range 94.00% - 97.00% have been accepted. It may be noted from Table B6 that there is some correlation between iron content and analysis total, presumably due to this molecular weight effect.

Key to Table B6:-

Tajao ignimbrite:- 10, 679-681, 714, 1400

Ignimbrite 0:- 825, 850

Pumice deposit E:- 731, 756

Pumice fall J:- 56

Adeje Red Ignimbrite:- 715

Boca de Tauce welded air-fall tuff:- 537, 538

Syenite SX3:- 1084

Medano xenolith TF162:- 1208, 1209

Table B6.

	10	56	537	538	679	680	681	714	715	731	756	825	850	1084	1208	1209	1400
SiO_2	36.43	36.43	38.48	38.41	36.54	36.65	36.76	36.37	37.92	37.06	37.59	37.08	36.59	36.20	36.93	37.40	37.61
TiO_2	5.22	7.99	5.63	5.47	7.69	7.64	7.71	5.33	6.85	7.55	6.64	7.64	7.92	4.92	8.60	6.25	3.35
Al_2O_3	12.92	13.45	10.99	11.32	13.37	13.37	13.97	13.37	12.22	13.12	12.38	12.63	12.43	11.25	13.33	13.28	11.72
FeO	18.36	14.04	12.35	12.34	13.81	13.67	13.88	18.05	11.60	11.66	11.82	12.60	12.48	20.56	15.06	13.04	19.95
MnO	0.73	0.27	0.48	0.53	0.35	0.52	0.28	0.69	0.42	-	-	0.31	0.38	2.14	0.35	0.33	1.29
MgO	12.80	13.59	16.53	16.21	13.90	14.00	14.03	12.60	16.31	15.72	16.25	14.61	14.80	9.57	11.97	14.16	11.74
Na_2O	0.65	0.93	0.94	1.16	1.03	1.06	1.14	0.74	1.49	1.40	1.05	0.96	1.32	0.85	0.72	-	0.76
K_2O	9.34	9.04	8.66	8.55	8.67	8.85	8.83	8.89	8.47	8.33	8.41	8.61	8.37	8.79	9.09	9.57	9.20
TOTAL	96.45	95.74	94.06	94.00	95.36	95.76	96.60	96.04	95.28	94.84	94.14	94.44	94.29	94.28	96.05	94.03	95.62

Formula per 22 Oxygen atoms																	
Si	5.510	5.425	5.772	5.757	5.448	5.436	5.400	5.505	5.595	5.482	5.588	5.527	5.493	5.704	5.492	5.618	5.784
Ti	0.595	0.894	0.635	0.617	0.862	0.852	0.852	0.607	0.761	0.840	0.742	0.857	0.894	0.583	0.962	0.706	0.388
Al	2.305	2.362	1.944	1.999	2.350	2.338	2.418	2.385	2.125	2.287	2.169	2.219	2.199	2.090	2.337	2.351	2.125
Fe	2.311	1.741	1.550	1.546	1.723	1.695	1.704	2.286	1.431	1.442	1.470	1.571	1.566	2.709	1.906	1.638	2.566
Mn	0.094	0.034	0.060	0.067	0.044	0.065	0.034	0.088	0.052	-	-	0.039	0.049	0.286	0.044	0.042	0.168
Mg	2.885	3.016	3.696	3.622	3.089	3.095	3.073	2.842	3.587	3.467	3.601	3.246	3.312	2.247	2.654	3.171	2.691
Na	0.190	0.268	0.275	0.337	0.297	0.306	0.324	0.218	0.426	0.401	0.303	0.276	0.383	0.260	0.208	0.049	0.225
K	1.803	1.718	1.658	1.635	1.649	1.674	1.655	1.716	1.594	1.571	1.596	1.638	1.602	1.767	1.724	1.834	1.804

B7. Olivines.

Key to Table B7:-

Tajao ignimbrite:- 548r - 549c, 550c - 551r, 552, 553.

Medano xenolith TF 165:- 1212c - 1213r, 1215c - 1216r, 1237.

Green Tuff, Pantelleria:- 463c - 464r, 465c - 466r, 494, 495c - 496r, 497.

Table B7.

	463	464	465	466	494	495	496	497	548	549	550	551	552	553	1212	1213	1215	1216	1237
SiO_2	31.16	30.88	30.87	31.13	29.74	30.47	30.47	30.46	38.93	39.40	39.41	39.27	39.40	39.01	36.86	36.46	36.93	36.51	36.21
FeO	62.14	61.42	60.38	60.29	66.68	61.85	61.54	62.21	19.43	19.53	19.47	19.15	19.92	19.67	34.95	34.11	35.30	35.53	34.75
MnO	3.92	3.87	4.01	3.71	3.27	4.01	3.86	4.18	0.29	0.32	0.39	-	0.36	0.23	1.23	1.24	1.31	1.27	1.37
MgO	2.86	3.06	3.81	3.66	-	3.73	3.42	3.46	41.11	40.74	41.04	40.65	41.13	40.37	27.50	27.37	27.05	27.16	26.50
CaO	0.40	0.48	0.52	0.52	0.20	0.55	0.54	0.34	0.22	0.27	0.28	0.25	0.21	0.24	0.19	0.23	0.31	0.16	0.35
NiO	n.d.	n.d.	n.d.	n.d.	-	-	-	-	-	n.d.	n.d.	n.d.	n.d.	-	-	-	-	-	-
TOTAL	100.48	99.71	99.59	99.31	99.89	100.61	99.83	100.65	99.98	100.26	100.59	99.32	101.02	99.52	100.73	99.41	100.90	100.63	99.18

Formula per
4 Oxygen atoms

Si	1.018	1.009	1.007	1.020	0.996	0.996	1.001	0.993	0.996	1.002	1.001	1.007	0.998	1.003	1.007	1.005	1.010	1.002	1.007
Fe	1.699	1.679	1.648	1.652	1.868	1.691	1.691	1.696	0.416	0.415	0.414	0.410	0.422	0.423	0.799	0.786	0.807	0.815	0.817
Mn	0.108	0.107	0.111	0.103	0.093	0.111	0.107	0.115	0.006	0.007	0.008	-	0.008	0.005	0.028	0.029	0.030	0.029	0.032
Mg	0.140	0.149	0.185	0.179	-	0.182	0.167	0.168	1.568	1.545	1.554	1.553	1.552	1.547	1.120	1.124	1.102	1.111	1.099
Ca	0.014	0.017	0.018	0.018	0.007	0.019	0.019	0.012	0.006	0.007	0.008	0.007	0.006	0.006	0.006	0.007	0.009	0.005	0.010
Ni	n.d.	n.d.	n.d.	n.d.	-	-	-	-	n.d.	n.d.	n.d.	n.d.	n.d.	-	-	-	-	-	-

B8. Lavenites.

Assuming that the specimens analysed here obey the formula $R_4Si_2O_7(O,OH,F)_2$ exactly (see Chapter V), expected oxide totals approximately 96%. The reported totals are therefore acceptable.

Key to table B8:-

Syenite S1/4:- 1348 - 50 core - rim sequence of single zoned crystal.

Table B8.

	1348	1349	1350
SiO_2	31.82	32.06	32.08
TiO_2	10.16	10.91	12.09
FeO	4.08	4.37	4.71
MnO	5.29	5.79	6.45
MgO	0.51	0.42	0.68
CaO	11.45	11.78	11.94
Na_2O	12.30	11.98	11.69
ZrO_2	17.54	15.52	14.10
Nb_2O_5	4.01	4.04	3.71
TOTAL	97.16	96.87	97.45

Formula per 8 Oxygen atoms			
Si	2.012	2.008	1.982
Ti	0.483	0.514	0.562
Fe	0.216	0.229	0.244
Mn	0.283	0.307	0.337
Mg	0.048	0.039	0.063
Ca	0.776	0.791	0.790
Na	1.508	1.456	1.400
Zr	0.622	0.545	0.488
Nb	0.115	0.114	0.104

B9. Aenigmatites.

In addition to the listed elements, all aenigmatites were analysed for K but none was detected.

Key to Table B9:-

Green Tuff, Pantelleria:- 442c - 443r, 451, 483, 492, 493.

Table B9.

	442	443	451	483	492	493
SiO_2	40.73	40.84	40.93	41.38	41.01	39.82
TiO_2	9.10	8.61	9.16	8.96	9.04	8.91
Al_2O_3	0.68	0.47	0.45	0.56	0.74	0.87
FeO	39.74	40.08	39.72	38.43	39.87	40.45
MnO	1.23	1.14	1.03	1.15	1.07	1.103
MgO	1.03	1.19	0.90	1.21	1.11	1.187
CaO	0.53	0.49	0.66	0.66	0.56	0.77
Na_2O	7.29	7.52	7.20	7.17	7.15	6.75
TOTAL	100.33	100.34	100.05	99.52	100.55	99.86

Formula per
20 Oxygen atoms

Si	5.807	5.849	5.863	5.920	5.833	5.750
Ti	0.975	0.927	0.987	0.965	0.967	0.968
Al	0.114	0.079	0.076	0.094	0.124	0.148
Fe	4.738	4.801	4.759	4.599	4.743	4.885
Mn	0.148	0.138	0.125	0.139	0.129	0.135
Mg	0.219	0.253	0.193	0.257	0.236	0.255
Ca	0.080	0.074	0.101	0.101	0.085	0.119
Na	2.015	2.087	1.999	1.989	1.973	1.890

B10. Sphenes.

Sphenes were partially analysed in all samples in which they were found; almost invariably, Zr, Nb and REE were qualitatively detected. Only two analyses, in which Zr, Nb and Ce were quantitatively determined, are reported here. The failure of the analyses to total to near 100% may indicate that the sphene is an (OH,F)-bearing variety (Deer et al., 1966). Na and K were analysed for but not detected.

Key to Table B10:-

Medano xenolith TF 163:- 1360c - 1361r.

Table B10.

	1360	1361
SiO_2	29.64	29.79
TiO_2	35.14	34.70
Al_2O_3	1.36	1.60
FeO	1.36	1.54
MgO	0.18	-
CaO	27.85	28.12
Ce_2O_3	0.41	-
ZrO_2	0.70	1.18
Nb_2O_5	0.60	0.50
TOTAL	97.24	97.43

Formula per 5 Oxygen atoms		
Si	1.006	1.010
Ti	0.897	0.885
Al	0.054	0.064
Fe	0.039	0.044
Mg	0.009	-
Ca	1.013	1.021
Ce	0.006	-
Zr	0.014	0.022
Nb	0.009	0.008

B11. Glasses.

Glass analyses were carried out using a scanning beam at specimen currents of 3.5 - 4nA, to minimise Na loss and avoid surface damage. Under these conditions no surface damage was apparent after 100s live counting time. Because of variable degrees of post-eruptive hydration of glasses, the usual criterion of quality of a total close to 100% cannot be rigorously applied. Here, analyses with totals $\geq$95% have been accepted.

Key to table B11:-

Tajao ignimbrite:- 582, 586 - 602, 604 - 7, 707 - 9, 712, 713, 717.

The following analyses are of glasses intimately associated with phenocrysts, and were not used in the regression analysis in II.2.ii:- 595 - 7, 601, 708, 717.

Ignimbrite 0:- 803, 808, 820, 822, 851, 858, 868 - 70, 875, 892, 893, 898 - 902, 911.

Adeje Red ignimbrite:- 373, 384 - 387, 389, 718 - 721.

Pumice deposit E:- 743, 751, 752, 755.

Boca de Tauce welded airfall tuff:- 539.

Green Tuff, Pantelleria:- 444.

Glass-bearing syenite SX3:- 1039, 1042, 1043, 1060, 1061.

Note that suffix s denotes salic (clear, pale green or pale yellow) glass while suffix m denotes mafic glass (brown or black).

Table B11.

	373s	384m	385m	386m	387s	389s	444s	539s	582m	586s	587m	588m	589s	590m	591s	592m	593s
SiO_2	60.82	60.03	61.44	62.03	59.45	59.70	70.00	61.80	45.25	57.09	56.72	56.72	58.30	56.92	58.25	56.25	57.35
TiO_2	1.12	1.05	0.89	0.88	1.02	1.00	0.48	0.85	3.74	0.38	1.28	0.56	1.16	1.60	1.03	1.57	1.31
Al_2O_3	15.78	15.65	16.59	16.55	15.19	15.54	7.43	16.38	12.98	20.62	19.22	20.16	18.32	18.87	18.35	18.51	18.78
FeO	4.78	4.54	3.55	3.50	4.53	4.77	8.13	4.03	11.36	2.44	4.11	2.39	2.97	4.57	2.71	4.57	4.25
MnO	0.46	0.47	0.24	0.23	0.48	0.36	-	0.21	0.31	0.20	-	0.20	0.30	-	-	0.24	0.29
MgO	0.55	0.55	0.52	0.60	0.40	0.76	-	0.62	4.99	0.23	1.04	-	0.46	1.18	0.59	1.48	0.88
CaO	0.52	0.47	0.83	0.70	0.58	0.53	0.27	0.53	7.26	0.78	2.56	0.84	1.35	2.93	1.56	3.39	2.50
Na_2O	7.91	9.92	8.04	8.21	9.42	9.79	6.53	7.90	4.64	10.33	7.99	9.80	9.48	7.19	8.47	7.28	4.82
K_2O	5.12	5.06	5.77	5.88	5.05	5.07	3.59	5.19	3.85	5.73	5.52	5.63	5.94	5.37	5.74	5.04	5.09
P_2O_5	0.34	0.37	0.40	0.61	0.47	0.42	n.d.	-	1.54	-	-	-	-	0.26	-	-	0.26
S	0.08	-	-	0.08	-	-	0.13	-	0.21	-	-	-	0.08	-	-	0.08	n.d.
Cl	0.33	0.31	0.19	0.17	0.29	0.32	0.93	n.d.	n.d.	n.d.	n.d.	n.d.	n.d.	n.d.	n.d.	n.d.	n.d.
TOTAL	97.82	98.42	98.46	99.44	96.88	98.26	98.06	97.51	96.13	97.60	98.44	96.30	98.17	98.89	96.90	98.43	95.53
less O=S,Cl	0.11	0.07	0.04	0.07	0.05	0.07	0.27	-	0.12	-	-	-	0.04	-	0.10	0.04	-
TOTAL	97.71	98.35	98.42	99.37	96.83	98.19	97.79	97.51	96.01	97.60	98.44	96.30	98.13	98.89	96.80	98.39	95.53
Formula per 10 Oxygen atoms																	
Si	3.592	3.553	3.594	3.585	3.570	3.543	4.079	3.623	2.911	3.391	3.350	3.405	3.450	3.353	3.470	3.339	3.452
Ti	0.050	0.047	0.039	0.038	0.046	0.045	0.021	0.037	0.181	0.017	0.057	0.025	0.052	0.071	0.046	0.070	0.059
Al	1.099	1.092	1.144	1.128	1.075	1.088	0.510	1.132	0.985	1.444	1.338	1.426	1.277	1.210	1.289	1.295	1.332
Fe	0.236	0.225	0.173	0.169	0.228	0.237	0.396	0.198	0.611	0.121	0.203	0.120	0.147	0.225	0.135	0.226	0.214
Mn	0.023	0.023	0.012	0.011	0.024	0.018	-	0.010	0.017	0.010	-	0.010	0.015	-	-	0.013	0.015
Mg	0.049	0.048	0.045	0.052	0.036	0.067	-	0.054	0.479	0.021	0.092	-	0.041	0.104	0.053	0.131	0.079
Ca	0.033	0.030	0.053	0.043	0.037	0.034	0.017	0.033	0.500	0.049	0.162	0.054	0.085	0.185	0.100	0.215	0.161
Na	0.906	1.139	0.913	0.921	1.098	1.127	0.738	0.898	0.579	1.189	0.915	1.141	1.088	0.821	0.979	0.839	0.563
K	0.386	0.382	0.431	0.433	0.387	0.384	0.267	0.388	0.316	0.434	0.416	0.431	0.448	0.404	0.436	0.381	0.391
P	0.017	0.018	0.020	0.030	0.024	0.022	n.d.	-	0.084	-	-	-	-	0.013	-	-	0.013
S	0.009	-	-	0.008	-	-	0.015	-	0.025	-	-	-	0.008	-	0.009	0.010	n.d.
Cl	0.027	0.025	0.015	0.013	0.024	0.027	0.075	n.d.	n.d.	n.d.	n.d.	n.d.	n.d.	n.d.	n.d.	n.d.	n.d.

	594s	595m	596m	597m	598s	599m	600m	601m	602m	604s	605m	606m	607m	707s	708m	709s	712m
SiO_2	58.77	58.88	58.48	58.47	58.46	55.09	51.91	53.30	54.98	58.36	56.91	54.98	55.64	59.35	57.81	57.59	56.59
TiO_2	0.89	2.12	1.63	1.43	1.13	1.68	2.27	1.88	1.64	1.25	1.17	1.51	1.30	0.90	1.44	0.54	1.44
Al_2O_3	18.67	18.45	18.42	18.28	18.32	18.31	17.77	17.43	18.52	18.13	18.66	17.87	18.30	18.53	18.47	20.16	19.03
FeO	2.91	4.42	3.52	3.42	3.39	4.65	6.14	6.21	4.64	2.94	3.76	4.43	4.32	2.93	4.13	2.43	4.51
MnO	0.18	-	-	-	-	0.19	-	-	-	-	0.22	0.32	-	-	-	0.32	-
MgO	0.68	0.66	0.70	0.67	0.99	1.87	1.81	2.93	1.78	0.43	1.00	1.16	1.19	0.64	0.88	0.41	1.21
CaO	1.38	1.15	1.69	1.43	2.24	4.24	5.35	4.49	3.79	1.33	2.46	2.95	2.75	1.59	1.61	0.99	3.28
Na_2O	7.89	7.04	7.83	7.97	7.14	6.95	7.28	6.61	7.25	9.46	7.73	7.95	7.13	6.17	6.42	9.46	7.00
K_2O	5.54	5.90	5.92	6.59	5.27	4.85	4.33	3.87	5.05	5.82	5.32	5.28	5.09	7.67	6.54	5.56	4.76
P_2O_5	-	-	-	-	-	0.38	0.25	0.40	0.43	-	0.38	0.32	0.38	0.33	-	-	-
S	n.d.	n.d.	n.d.	n.d.	n.d.	n.d.	n.d.	n.d.	n.d.	0.09	0.07	n.d.	n.d.	-	-	-	-
Cl	n.d.	n.d.	n.d.	n.d.	n.d.	n.d.	n.d.	n.d.	n.d.	n.d.	n.d.	n.d.	n.d.	n.d.	n.d.	n.d.	n.d.
TOTAL	96.91	98.62	98.19	98.26	96.94	98.21	97.11	97.12	98.08	97.81	97.68	96.77	96.10	98.11	97.30	97.46	97.82
less O=S,Cl	-	-	-	-	-	-	-	-	-	0.05	0.04	-	-	-	-	-	-
TOTAL	96.91	98.62	98.19	98.26	98.94	98.21	97.11	97.12	98.08	97.76	97 64	96.77	96.10	98.11	97.30	97.46	97.82
Formula per 10 Oxygen atoms																	
Si	3.495	3.456	3.454	3.458	3.476	3.297	3.191	3.243	3.292	3.323	3.226	3.113	3.107	3.494	3.445	3.420	3.351
Ti	0.040	0.093	0.072	0.063	0.050	0.076	0.105	0.086	0.074	0.053	0.050	0.064	0.054	0.040	0.065	0.024	0.064
Al	1.309	1.276	1.283	1.274	1.284	1.291	1.287	1.250	1.307	1.217	1.247	1.193	1.205	1.286	1.297	1.411	1.328
Fe	0.145	0.217	0.174	0.169	0.168	0.233	0.316	0.316	0.232	0.140	0.178	0.210	0.202	0.144	0.206	0.121	0.223
Mn	0.009	-	-	-	-	0.009	-	-	-	-	0.011	0.015	-	-	-	0.016	-
Mg	0.060	0.058	0.062	0.059	0.088	0.167	0.166	0.266	0.158	0.037	0.084	0.098	0.099	0.057	0.078	0.036	0.107
Ca	0.088	0.072	0.107	0.090	0.143	0.272	0.353	0.292	0.243	0.081	0.149	0.179	0.165	0.100	0.102	0.063	0.208
Na	0.910	0.802	0.897	0.914	0.824	0.806	0.867	0.780	0.842	1.044	0.850	0.872	0.773	0.704	0.742	1.089	0.804
K	0.420	0.436	0.446	0.497	0.400	0.370	0.340	0.300	0.386	0.423	0.385	0.382	0.363	0.576	0.497	0.421	0.359
P	-	-	-	-	-	0.019	0.013	0.020	0.022	-	0.018	0.015	0.018	0.017	-	-	-
S	n.d.	n.d.	n.d.	n.d.	n.d.	n.d.	n.d.	n.d.	n.d.	0.010	0.008	n.d.	n.d.	-	-	-	-
Cl	n.d.	n.d.	n.d.	n.d.	n.d.	n.d.	n.d.	n.d.	n.d.	n.d.	n.d.	n.d.	n.d.	n.d.	n.d.	n.d.	n.d.

	713m	717s	718m	719s	720m	721s	743m	751m	752s	755s	803m	808s	820s	822s	851m	858m	868m
SiO_2	56.01	59.13	60.17	59.90	59.54	59.44	56.36	57.53	59.17	61.50	57.65	59.48	59.53	59.42	55.22	59.90	58.60
TiO_2	1.41	1.15	0.98	0.81	1.07	0.95	1.69	1.74	0.69	0.91	1.75	1.27	0.79	0.88	1.84	1.15	1.23
Al_2O_3	18.17	19.89	16.31	16.17	16.14	16.16	17.99	18.22	16.80	17.77	17.20	17.32	17.95	18.04	17.05	18.44	18.14
FeO	4.66	3.18	4.56	4.89	4.75	4.77	4.52	5.01	2.67	3.91	5.05	3.46	3.15	3.30	5.18	3.14	4.01
MnO	-	-	0.37	0.30	0.48	0.46	0.25	-	-	0.25	0.21	-	-	-	0.24	0.19	-
MgO	1.19	0.66	0.50	0.56	0.72	0.55	1.59	1.49	0.65	0.55	1.45	0.81	-	0.35	1.94	0.85	1.08
CaO	3.10	1.39	0.78	0.59	0.59	0.61	3.04	3.35	0.95	0.95	3.34	1.25	0.81	0.97	3.79	1.51	2.23
Na_2O	6.73	8.27	9.40	10.27	10.15	10.33	7.69	7.53	7.99	7.42	7.64	7.88	8.85	9.18	7.30	7.83	7.35
K_2O	5.53	5.86	4.49	4.67	4.75	4.77	3.71	3.64	4.81	5.06	4.51	4.86	5.58	5.39	4.15	4.88	5.49
P_2O_5	-	-	n.d.	n.d.	-	-	0.33	0.35	-	-	0.37	-	0.23	0.32	0.51	-	0.27
S	-	-	0.09	0.11	-	-	0.09	-	-	0.09	-	0.09	-	-	-	-	-
Cl	n.d.	n.d.	n.d.	n.d.	0.26	0.33	0.17	0.16	0.22	0.13	0.13	0.15	0.35	0.27	0.11	0.13	0.15
TOTAL	96.80	99.53	97.65	98.27	98.45	98.37	97.41	99.02	95.95	98.54	99.30	96.57	97.24	98.12	97.33	98.02	98.55
less O=S,Cl	-	-	0.04	0.05	0.06	0.07	0.08	0.04	0.05	0.06	0.03	0.08	0.06	0.03	0.03	0.03	0.03
TOTAL	96.80	99.53	97.61	98.22	98.39	98.30	97.33	98.98	95.90	98.48	99.27	96.49	97.16	98.06	97.30	97.99	98.52
Formula per 10 Oxygen atoms																	
Si	3.369	3.424	3.564	3.544	3.527	3.532	3.358	3.366	3.594	3.568	3.396	3.521	3.523	3.501	3.322	3.498	3.445
Ti	0.064	0.050	0.044	0.036	0.047	0.043	0.076	0.077	0.031	0.040	0.078	0.056	0.035	0.039	0.083	0.051	0.054
Al	1.289	1.357	1.139	1.128	1.127	1.132	1.264	1.257	1.202	1.215	1.194	1.209	1.252	1.253	1.209	1.269	1.257
Fe	0.234	0.154	0.226	0.242	0.235	0.237	0.225	0.245	0.135	0.190	0.249	0.171	0.156	0.162	0.261	0.153	0.197
Mn	-	-	0.019	0.015	0.024	0.023	0.013	-	-	0.012	0.010	-	-	-	0.012	0.009	-
Mg	0.106	0.057	0.044	0.050	0.063	0.049	0.141	0.130	0.059	0.048	0.127	0.072	-	0.031	0.174	0.074	0.094
Ca	0.200	0.086	0.049	0.038	0.037	0.039	0.194	0.210	0.062	0.059	0.211	0.079	0.051	0.061	0.244	0.094	0.141
Na	0.785	0.929	1.079	1.179	1.165	1.190	0.889	0.855	0.941	0.835	0.872	0.905	1.016	1.049	0.852	0.887	0.837
K	0.425	0.433	0.339	0.353	0.359	0.362	0.282	0.271	0.373	0.374	0.339	0.367	0.421	0.405	0.318	0.363	0.412
P	-	-	n.d.	n.d.	-	-	0.017	0.017	-	-	0.018	-	0.011	0.016	0.026	-	0.014
S	-	-	0.010	0.012	-	-	0.010	-	-	0.009	-	0.010	-	-	-	-	-
Cl	n.d.	n.d.	n.d.	n.d.	0.022	0.027	0.014	0.013	0.019	0.011	0.010	0.012	0.022	0.022	0.009	0.011	0.012

	869s	870m	875m	892s	893m	898m	899m	900m	901s	902s	911m	1039s	1042s	1043s	1060s	1061s
SiO_2	59.94	54.28	53.15	60.95	55.95	58.03	59.45	59.39	58.80	60.85	56.16	53.19	52.87	52.06	53.10	52.37
TiO_2	0.97	2.10	2.08	1.01	1.44	1.25	1.10	1.01	1.17	0.99	1.60	1.49	1.44	1.24	1.46	1.36
Al_2O_3	18.43	17.98	17.63	18.13	17.94	17.95	18.20	17.97	17.97	18.20	17.54	12.68	12.99	12.93	12.72	12.66
FeO	3.24	6.07	6.40	2.74	4.68	4.00	3.37	3.48	3.47	3.03	5.22	5.57	5.31	5.54	6.47	6.76
MnO	-	0.27	0.36	0.25	-	0.23	-	0.21	0.23	-	0.22	0.93	0.94	0.95	0.96	0.80
MgO	0.64	2.25	2.03	0.47	1.38	1.05	0.85	0.81	0.62	0.59	1.68	0.39	0.48	0.45	0.46	-
CaO	1.34	4.94	5.21	1.17	3.20	2.47	1.55	1.93	1.61	1.30	3.48	0.71	0.75	0.76	0.65	0.66
Na_2O	7.73	6.88	6.80	7.97	8.24	8.24	7.79	8.21	8.09	8.29	7.79	15.78	16.43	17.07	15.19	16.02
K_2O	5.21	3.94	4.67	5.28	4.63	4.84	5.42	5.03	5.16	5.36	4.49	3.71	3.44	3.34	3.91	3.62
P_2O5	-	0.59	0.52	-	-	-	-	-	-	-	0.29	0.63	0.97	0.84	0.93	0.80
S	-	-	0.10	-	0.12	-	0.10	0.08	-	0.13	0.08	-	-	-	-	-
Cl	-	0.15	0.18	n.d.	n.d.	n.d.	n.d.	n.d.	n.d.	n.d.	n.d.	0.31	0.37	0.38	0.38	0.36
TOTAL	97.50	99.45	99.13	97.97	97.58	98.06	97.83	98.12	97.12	98.74	98.55	95.39	95.99	95.56	96.23	95.41
less O.=S,Cl	-	0.03	0.09	-	0.06	-	0.05	0.04	-	0.07	0.04	0.07	0.08	0.09	0.09	0.08
TOTAL	97.50	99.42	99.04	97.97	97.53	98.06	97.78	98.08	97.12	98.67	98.55	95.32	95.91	95.47	96.14	95.33
Formula per 10 Oxygen atoms																
Si	3.515	3.227	3.197	3.558	3.342	3.430	3.488	3.488	3.492	3.527	3.341	3.386	3.344	3.323	3.321	3.307
Ti	0.043	0.094	0.094	0.044	0.065	0.056	0.049	0.044	0.052	0.043	0.072	0.071	0.068	0.060	0.069	0.065
Al	1.274	1.260	1.250	1.248	1.263	1.250	1.259	1.244	1.258	1.243	1.230	0.951	0.968	0.973	0.937	0.942
Fe	0.159	0.302	0.322	0.134	0.234	0.197	0.166	0.171	0.172	0.147	0.260	0.297	0.281	0.296	0.305	0.321
Mn	-	0.013	0.018	0.012	-	0.012	-	0.010	0.012	-	0.011	0.050	0.050	0.052	0.051	0.043
Mg	0.056	0.200	0.182	0.040	0.123	0.093	0.074	0.070	0.055	0.051	0.149	0.037	0.045	0.043	0.043	0.022
Ca	0.084	0.315	0.336	0.073	0.205	0.156	0.098	0.121	0.102	0.080	0.221	0.048	0.051	0.052	0.044	0.044
Na	0.879	0.793	0.793	0.902	0.955	0.945	0.886	0.935	0.931	0.932	0.898	1.947	2.015	2.113	1.842	1.962
K	0.390	0.299	0.358	0.393	0.353	0.365	0.406	0.377	0.391	0.397	0.340	0.302	0.277	0.272	0.312	0.329
P	-	0.030	0.027	-	-	-	-	-	-	-	0.014	0.034	0.052	0.045	0.049	0.043
S	-	-	0.011	-	-	-	0.011	0.009	-	0.014	0.009	-	-	-	-	-
Cl	-	0.012	0.015	n.d.	n.d.	n.d.	n.d.	n.d.	n.d.	n.d.	n.d.	0.027	0.032	0.033	0.033	0.032

B.12 IRON-TITANIUM OXIDES

Titanomagnetite and ilmenite in the studied samples are closely physically and chemically related (Chapters III and IV) and, to faciliate comparison of specimens from individual samples, analyses of both minerals are here tabulated together. Suffice m indicates titonomagnetite analysis, suffice i indicates ilmenite. Fe^{3+} and Fe^{2+} contents, and thence Fe_2O_3 and FeO weight percentages, were estimated using the procedure of Carmichael (1967a) described and discussed in IV.2.i. Reconnaisance work did not reveal measureable quantitites of Ni, V or Zn in any samples, except for an ihmenite in S1/4 in which quantities of V, Nb and Zn below the normal detection limit were revealed by an extended (750s) count. Note that Cr was not determined in all samples; however the presence of measureable quantities of this element appears to be limited to those titanomagnetites with very high MgO and Al_2O_3 contents.

Key to Table B12:-

Tajao ignimbrite:-	11, 609, 610, 612-631, 702-706, 1405, 1406.
Ignimbrite O:-	784, 786, 788-797, 810, 812, 815, 816, 818, 823, 824, 853, 861, 862, 894, 895, 904, 907-910.
Pumic deposit E:-	728, 730, 732, 744-748.

Boca de Tauce welded air-fall tuff:- 542-547.

Adeje Red ignimbrite:- 14, 392, 393, 714, 717, 722.

Pumice fall J:- 46-48, 50-53.

Cognate mg/ic cummulate lithic in pumice fall J:- 279, 281, 326, 328, 331-333, 335-337.

Welded ignimbrite E, Gran Canaria:- 688, 690, 694, 697, 700, 701.

Green Tuff, Pantelleria:- 472, 473, 475, 501, 502, 505-512, 522-526.

Syenite block S1/2:- 239, 240, 242, 243.

Syenite block S1/4:- 1026, 1029

Syenite block S4:- 198, 200, 206, 269

Syenite block SX3:- 1046, 1094.

Medano xenolith TF161:- 1251, 1252, 1257

Medano xenolith TF162:- 1201, 1202, 1204, 1210

Medano xenolith TF 163:- 1264, 1265, 1270, 1271

Medano xenolith TF165:- 1217-1219, 1232.

Table B12

	11m	14m	46m	47m	48i	50i	51i	52i	53i	198i	200i
SiO_2	0.29	0.19	0.16	0.17	-	0.24	0.17	0.23	-	0.29	0.23
TiO_2	16.30	14.77	17.33	11.58	46.14	46.75	46.13	46.86	46.55	51.29	50.88
Al_2O_3	6.80	0.91	6.25	1.53	0.30	0.30	0.25	0.29	0.19	-	-
Cr_2O_3	-	-	-	-	-	-	-	-	-	-	-
Fe_2O_3	33.64	40.72	31.82	46.02	15.92	14.04	15.69	14.63	15.20	2.97	1.67
FeO	36.83	38.50	37.94	37.88	32.62	33.81	32.69	33.62	32.76	33.99	30.79
MnO	0.39	2.21	0.56	1.84	1.47	1.56	1.58	1.67	1.58	11.45	14.68
MgO	7.13	3.00	6.61	1.85	4.26	4.01	4.25	4.10	4.28	0.55	0.29
CaO	-	-	-	-	-	-	-	-	-	-	-
Total	101.38	100.30	100.66	100.87	100.71	100.71	100.75	101.40	100.57	100.54	98.54

Formula per given
no. of oxygen atoms

Si	0.010	0.007	0.006	0.006	-	0.006	0.004	0.006	-	0.007	0.006
Ti	0.417	0.405	0.448	0.318	0.843	0.855	0.842	0.851	0.865	0.960	0.971
Al	0.273	0.039	0.254	0.066	0.009	0.008	0.007	0.008	0.006	-	-
Cr	-	-	-	-	-	-	-	-	-	-	-
Fe^{3+}	0.856	1.112	0.818	1.259	0.291	0.257	0.286	0.266	0.191	0.055	0.032
Fe^{2+}	1.042	1.169	1.089	1.154	0.658	0.683	0.660	0.675	0.765	0.704	0.651
Mn	0.012	0.068	0.016	0.057	0.030	0.032	0.032	0.034	0.033	0.242	0.315
Mg	0.362	0.163	0.339	0.101	0.154	0.145	0.154	0.148	0.158	0.021	0.011
Ca	-	-	-	-	-	-	-	-	-	-	-
O	4.000	4.000	4.000	4.000	3.000	3.000	3.000	3.000	3.000	3.000	3.000

	206i	239i	240i	242i	243i	269i	279m	281i	326m	328i
SiO_2	0.53	0.24	0.14	0.19	0.23	-	0.17	0.16	0.21	0.35
TiO_2	51.91	51.85	52.55	51.33	51.76	50.30	14.27	45.10	14.10	45.10
Al_2O_3	-	-	-	-	-	-	3.50	0.37	3.41	0.29
Cr_2O_3	-	-	-	-	-	-	-	-	-	-
Fe_2O_3	0.78	1.52	1.40	3.08	2.81	5.42	38.20	16.35	38.69	16.93
FeO	34.48	32.88	33.02	31.09	31.26	32.61	37.79	31.18	37.81	30.97
MnO	12.13	14.05	14.39	14.92	15.10	11.75	1.29	1.17	1.22	1.39
MgO	0.39	-	-	0.19	0.23	0.49	3.73	4.85	3.73	4.94
CaO	-	-	-	-	-	-	-	-	-	-
Total	100.22	100.54	101.50	100.80	101.39	100.57	98.95	99.18	99.16	99.97
Si	0.013	0.006	0.003	0.005	0.006	-	0.006	0.005	0.008	0.009
Ti	0.975	0.975	0.979	0.962	0.964	0.945	0.389	0.833	0.384	0.826
Al	-	-	-	-	-	-	0.150	0.011	0.145	0.008
Cr	-	-	-	-	-	-	-	-	-	-
Fe^{3+}	0.014	0.028	0.026	0.057	0.052	0.101	1.036	0.303	1.048	0.310
Fe^{2+}	0.717	0.684	0.681	0.645	0.644	0.677	1.143	0.635	1.141	0.626
Mn	0.257	0.298	0.302	0.315	0.317	0.249	0.039	0.025	0.037	0.029
Mg	0.015	-	-	0.007	0.009	0.019	0.202	0.178	0.201	0.179
Ca	-	-	-	-	-	-	-	-	-	-
O	3.000	3.000	3.000	3.000	3.000	3.000	4.000	3.000	4.000	3.000

	331m	332i	333i	335m	337m	392m	393m	472i	473i	475m	501i
SiO_2	0.19	0.24	0.32	0.25	0.25	0.20	0.31	0.35	0.31	0.33	0.28
TiO_2	14.05	45.03	44.99	14.27	13.91	14.42	14.42	50.92	50.93	25.04	50.48
Al_2O_3	3.40	0.48	0.37	3.43	3.47	0.97	1.19	-	-	0.20	-
Cr_2O_3	-	-	-	-	-	-	-	n.d.	n.d.	n.d.	-
Fe_2O_3	38.77	17.42	15.92	38.27	39.25	41.03	40.85	1.88	1.87	19.42	3.97
FeO	37.69	30.76	31.46	37.89	37.55	37.86	38.15	43.45	43.54	52.59	42.68
MnO	1.16	1.30	1.04	1.19	1.23	2.59	2.26	2.14	2.00	1.67	2.12
MgO	3.77	5.07	4.82	3.83	3.90	2.85	3.07	0.34	0.34	0.24	0.51
CaO	-	-	-	-	-	-	-	-	-	-	-
Total	99.02	100.31	98.92	99.12	99.56	99.92	100.25	99.08	98.99	99.49	100.04
Si	0.007	0.006	0.008	0.009	0.009	0.008	0.011	0.009	0.008	0.012	0.007
Ti	0.383	0.821	0.832	0.388	0.377	0.399	0.396	0.970	0.972	0.706	0.952
Al	0.145	0.014	0.011	0.146	0.147	0.042	0.051	-	-	0.009	0.003
Cr	-	-	-	-	-	-	-	n.d.	n.d.	n.d.	-
Fe^{3+}	1.051	0.320	0.296	1.036	1.057	1.137	1.123	0.036	0.036	0.548	0.075
Fe^{2+}	1.139	0.617	0.641	1.142	1.127	1.166	1.165	0.921	0.924	1.649	0.895
Mn	0.036	0.027	0.022	0.036	0.038	0.081	0.070	0.046	0.043	0.053	0.045
Mg	0.204	0.183	0.177	0.207	0.210	0.157	0.167	0.013	0.013	0.014	0.019
Ca	-	-	-	-	-	-	-	-	-	-	-
O	4.000	3.000	3.000	4.000	4.000	4.000	4.000	3.000	3.000	4.000	3.000

	502i	505i	506i	507i	508i	509m	510m	511i	512i	522m	523m
SiO_2	0.35	0.26	0.32	0.23	0.27	0.41	0.40	-	0.38	0.50	0.35
TiO_2	50.48	51.69	49.43	50.51	51.06	24.41	24.79	50.81	50.30	25.62	24.73
Al_2O_3	-	-	-	-	-	0.24	-	-	-	0.38	-
Cr_2O_3	-	-	-	-	-	-	-	-	-	-	-
Fe_2O_3	3.81	2.88	6.24	3.77	2.91	20.62	20.26	3.63	3.94	18.23	20.64
FeO	43.41	43.94	40.84	42.98	43.64	52.23	52.99	43.30	43.15	53.49	52.45
MnO	1.98	2.18	2.36	2.24	2.00	1.69	1.63	2.37	2.13	1.74	1.79
MgO	0.22	0.36	0.66	0.25	0.32	-	-	-	0.22	0.28	-
CaO	-	-	0.34	-	-	-	-	-	-	-	0.27
Total	100.25	101.31	100.19	100.08	100.20	99.60	100.07	100.11	100.12	100.25	100.22
Si	0.009	0.006	0.008	0.006	0.007	0.015	0.015	-	0.010	0.018	0.013
Ti	0.950	0.964	0.932	0.957	0.961	0.686	0.691	0.960	0.949	0.714	0.692
Al	-	-	-	-	-	0.010	-	-	-	-	-
Fe^{3+}	0.072	0.054	0.109	0.071	0.055	0.580	0.565	0.069	0.074	0.509	0.578
Fe^{2+}	0.909	0.911	0.865	0.906	0.913	1.632	1.643	0.909	0.906	1.658	1.631
Mn	0.042	0.046	0.050	0.048	0.043	0.054	0.051	0.050	0.045	0.055	0.056
Mg	0.008	0.013	0.025	0.009	0.012	-	-	-	0.008	0.016	-
Ca	-	-	0.009	-	-	-	-	-	-	-	0.011
O	3.000	3.000	3.000	3.000	3.000	4.000	4.000	3.000	3.000	4.000	4.000

	524i	525i	526i	542m	543m	544i	545i	546m	547m	609i	610i
SiO_2	0.27	0.45	0.30	0.30	0.29	0.26	0.36	0.30	0.30	0.33	0.32
TiO_2	51.46	51.20	51.04	12.49	12.44	47.21	47.23	12.52	12.32	45.28	45.56
Al_2O_3	-	-	-	0.52	0.56	-	-	0.67	0.61	0.33	0.25
Cr_2O_3	-	-	-	-	-	-	-	-	-	-	-
Fe_2O_3	2.17	2.80	2.33	45.06	44.40	12.31	12.34	44.59	44.25	15.80	16.20
FeO	44.38	43.81	43.73	37.82	37.75	33.32	33.87	37.79	36.92	32.49	32.57
MnO	2.19	2.03	1.93	2.82	2.85	3.97	3.64	2.62	2.78	1.86	1.86
MgO	-	0.40	0.32	1.77	1.57	3.04	3.00	1.86	1.86	3.91	3.97
CaO	-	-	-	-	-	-	-	-	0.12	-	-
Total	100.46	100.69	99.65	100.78	99.86	100.11	100.41	100.35	99.16	100.01	100.73
Si	0.007	0.011	0.008	0.011	0.011	0.006	0.009	0.011	0.011	0.008	0.008
Ti	0.968	0.958	0.968	0.347	0.348	0.877	0.872	0.349	0.347	0.838	0.834
Al	-	-	-	0.023	0.024	-	-	0.029	0.027	0.010	0.007
Cr	-	-	-	-	-	-	-	-	-	-	-
Fe^{3+}	0.045	0.052	0.044	1.253	1.243	0.229	0.228	1.243	1.249	0.298	0.300
Fe^{2+}	0.924	0.912	0.922	1.168	1.174	0.688	0.696	1.171	1.158	0.664	0.659
Mn	0.046	0.043	0.041	0.088	0.090	0.083	0.076	0.082	0.088	0.039	0.038
Mg	-	0.015	0.012	0.097	0.087	0.112	0.110	0.103	0.104	0.143	0.144
Ca	-	-	-	-	-	-	-	-	0.005	-	-
O	3.000	3.000	3.000	4.000	4.000	3.000	3.000	4.000	4.000	3.000	3.000

	612m	613m	614m	615i	616m	617m	618m	619m	620m	621m	622m
SiO_2	0.40	0.20	0.34	0.26	0.26	0.31	0.25	-	0.35	0.34	0.42
TiO_2	15.50	15.47	16.04	45.68	9.11	9.12	9.06	9.26	15.60	13.90	13.29
Al_2O_3	7.87	7.80	7.98	0.28	0.69	0.70	0.70	0.64	7.86	2.33	2.41
Cr_2O_3	0.37	0.52	0.53	-	-	-	-	-	0.65	-	-
Fe_2O_3	31.97	32.87	31.68	16.23	49,46	50.04	50.38	50.21	31.90	40.54	41.53
FeO	35.04	35.22	35.81	31.81	35.84	36.03	35.79	35.39	35.31	38.69	37.69
MnO	0.40	0.29	0.28	1.49	2.74	2.92	2.78	2.91	0.39	1.46	1.46
MgO	7.58	7.48	7.69	4.64	0.65	0.67	0.72	0.78	7.52	3.14	3.26
CaO	-	-	-	-	-	-	0.15	-	-	-	0.26
Total	99.13	99.85	100.35	100.39	98.75	99.79	99.82	99.19	99.58	100.50	100.33
Si	0.014	0.007	0.012	0.006	0.010	0.012	0.009	-	0.012	0.012	0.015
Ti	0.403	0.400	0.411	0.836	0.260	0.259	0.257	0.262	0.404	0.378	0.362
Al	0.321	0.316	0.320	0.008	0.031	0.031	0.031	0.028	0.319	0.100	0.103
Cr	0.010	0.014	0.014	-	-	-	-	-	0.018	-	-
Fe^{3+}	0.833	0.851	0.812	0.302	1.414	1.425	1.426	1.418	0.827	1.107	1.134
Fe^{2+}	1.013	1.013	1.019	0.643	1.137	1.138	1.132	1.124	1.017	1.171	1.142
Mn	0.012	0.008	0.008	0.031	0.088	0.093	0.089	0.093	0.011	0.045	0.045
Mg	0.390	0.384	0.390	0.168	0.037	0.038	0.040	0.044	0.386	0.169	0.176
Ca	-	-	-	-	-	-	0.006	-	-	-	0.010
O	4.000	4.000	4.000	3.000	4.000	4.000	4.000	4.000	4.000	4.000	4.000

	623m	624m	625m	626m	627m	628i	629i	630i	631m	688m	690i
SiO_2	0.27	0.30	0.49	0.24	0.29	0.22	0.28	0.23	0.39	0.29	0.28
TiO_2	13.33	13.51	13.40	17.09	17.13	45.44	45.91	45.53	13.73	10.46	44.82
Al_2O_3	2.57	2.36	2.51	5.62	5.50	0.23	0.37	0.39	2.42	0.31	-
Cr_2O_3	-	-	-	-	-	-	-	-	-	-	-
Fe_2O_3	41.64	41.86	40.84	32.91	32.36	16.21	16.18	16.45	39.79	48.16	15.62
FeO	37.53	38.31	38.11	38.31	38.77	31.82	32.02	32.06	38.10	36.42	32.99
MnO	1.33	1.41	1.43	0.64	0.40	1.46	1.62	1.46	1.54	2.91	4.58
MgO	3.54	3.25	3.09	6.25	6.05	4.48	4.61	4.46	3.14	1.15	1.69
CaO	-	-	0.29	-	-	-	-	-	-	-	-
Total	100.22	101.00	100.16	101.06	100.50	99.87	100.99	100.58	99.11	99.70	99.98
Si	0.010	0.011	0.018	0.008	0.009	0.005	0.007	0.006	0.014	0.011	0.007
Ti	0.363	0.366	0.365	0.418	0.418	0.804	0.826	0.817	0.378	0.295	0.842
Al	0.110	0.100	0.107	0.215	0.211	0.006	0.010	0.011	0.104	0.014	-
Cr	-	-	-	-	-	-	-	-	-	-	-
Fe^{3+}	1.136	1.136	1.114	0.807	0.791	0.291	0.297	0.301	1.098	1.361	0.294
Fe^{2+}	1.137	1.155	1.155	1.042	1.052	0.622	0.635	0.634	1.166	1.143	0.690
Mn	0.041	0.043	0.044	0.017	0.009	0.029	0.033	0.030	0.048	0.092	0.097
Mg	0.191	0.174	0.167	0.303	0.293	0.157	0.165	0.159	0.171	0.064	0.063
Ca	-	-	0.011	-	-	-	-	-	-	-	-
O	4.000	4.000	4.000	4.000	4.000	3.000	3.000	3.000	4.000	4.000	3.000

	694m	697m	700i	701i	702i	703i	704i	705m	706m	714m	717i
SiO_2	0.40	0.39	0.27	0.29	0.36	0.30	0.22	0.28	0.34	0.19	0.21
TiO_2	10.54	10.29	44.66	44.44	48.89	48.62	49.03	16.83	13.67	13.78	47.69
Al_2O_3	0.42	0.53	-	-	0.55	0.58	0.49	7.03	2.81	0.80	0.26
Cr_2O_3	-	-	-	-	-	-	-	-	-	-	-
Fe_2O_3	46.59	49.13	15.60	16.04	11.95	11.81	11.58	31.94	40.44	42.94	12.79
FeO	36.29	36.34	34.48	34.59	31.76	31.82	31.66	37.01	37.72	38.61	32.49
MnO	3.65	3.09	4.24	4.54	0.59	0.49	0.62	0.47	1.27	2.65	2.47
MgO	0.55	1.39	0.96	0.63	6.86	6.83	6.96	7.18	3.51	2.16	4.67
CaO	0.18	-	-	-	-	-	-	-	0.26	-	-
Total	98.62	101.16	100.21	100.53	100.96	100.45	100.57	100.74	100.02	101.14	100.59
Si	0.015	0.014	0.007	0.007	0.009	0.007	0.005	0.010	0.012	0.007	0.005
Ti	0.301	0.284	0.843	0.836	0.875	0.875	0.880	0.435	0.374	0.380	0.869
Al	0.019	0.023	-	-	0.015	0.016	0.014	0.285	0.120	0.034	0.007
Cr	-	-	-	-	-	-	-	-	-	-	-
Fe^{3+}	1.332	1.359	0.295	0.302	0.214	0.213	0.208	0.826	1.107	1.187	0.237
Fe^{2+}	1.151	1.115	0.724	0.724	0.632	0.637	0.632	1.064	1.147	1.185	0.655
Mn	0.117	0.096	0.090	0.096	0.012	0.010	0.018	0.014	0.039	0.082	0.051
Mg	0.031	0.076	0.036	0.023	0.243	0.244	0.248	0.368	0.190	0.118	0.169
Ca	0.007	-	-	-	-	-	-	-	0.010	-	-
O	4.000	4.000	3.000	3.000	3.000	3.000	3.000	4.000	4.000	4.000	3.000

	722i	728m	730m	732i	744i	745i	746m	747m	748m	748m	786m
SiO_2	0.20	0.42	0.28	0.33	0.34	0.18	0.34	0.35	0.40	0.37	0.32
TiO_2	46.47	12.75	12.94	46.21	46.28	45.88	15.74	14.20	15.91	14.09	14.12
Al_2O_3	-	1.46	1.24	-	0.47	0.59	4.22	2.63	3.69	2.36	2.37
Cr_2O_3	-	-	-	-	-	-	-	-	-	-	-
Fe_2O_3	13.05	43.04	43.83	14.65	16.61	16.97	35.79	40.50	36.29	40.01	40.24
FeO	31.47	36.59	37.49	32.06	30.09	29.92	38.17	37.42	37.84	37.45	37.03
MnO	4.25	2.35	2.39	2.88	0.97	0.82	0.66	1.16	0.88	1.74	1.56
MgO	3.51	3.02	2.61	3.91	6.33	6.25	5.26	4.42	5.49	3.76	4.02
CaO	-	-	-	-	-	-	-	-	-	-	0.14
Total	98.94	99.62	100.77	100.04	101.09	100.61	100.18	100.68	100.50	99.77	99.80
Si	0.005	0.016	0.010	0.008	0.008	0.004	0.012	0.013	0.014	0.013	0.012
Ti	0.870	0.352	0.356	0.851	0.830	0.828	0.418	0.382	0.423	0.384	0.384
Al	-	0.063	0.054	-	0.013	0.017	0.176	0.111	0.154	0.101	0.101
Cr	-	-	-	-	-	-	-	-	-	-	-
Fe^{3+}	0.245	1.189	1.210	0.270	0.305	0.315	0.953	1.093	0.966	1.095	1.096
Fe^{2+}	0.655	1.122	1.148	0.656	0.593	0.592	1.129	1.121	1.118	1.130	1.119
Mn	0.090	0.073	0.074	0.060	0.020	0.017	0.020	0.035	0.026	0.054	0.048
Mg	0.130	0.165	0.143	0.143	0.225	0.224	0.277	0.236	0.289	0.203	0.217
Ca	-	-	-	-	-	-	-	-	-	-	0.005
O	3.000	4.000	4.000	3.000	3.000	3.000	4.000	4.000	4.000	4.000	4.000

	788i	789i	790i	791i	792m	793m	794m	795i	797i	810m	812m
SiO_2	0.22	0.34	0.23	0.24	0.40	0.36	0.27	0.24	0.33	0.32	.0.37
TiO_2	45.92	46.62	46.95	46.23	13.54	13.85	14.02	45.26	46.03	16.64	15.34
Al_2O_3	0.20	0.38	-	0.26	1.81	2.47	2.45	-	0.21	7.49	3.03
Cr_2O_3	-	-	-	n.d.	-	n.d.	n.d.	n.d.	-	n.d.	n.d.
Fe_2O_3	15.71	15.17	14.90	15.18	41.67	40.18	40.32	16.57	14.51	31.44	37.99
FeO	31.58	31.93	31 85	31.93	38.03	37.96	37.73	30.52	31.60	37.34	39.53
MnO	2.21	1.68	2.09	2.16	1.72	1.45	1.47	2.41	2.11	0.29	1.10
MgO	4.42	5.03	4.83	4.35	3.12	3.45	3.68	4.50	4.51	7.01	3.97
CaO	-	-	-	-	-	-	-	-	-	-	-
Total	100.26	101.15	100.85	100.35	100.29	99.72	99.94	99.50	99.30	100.54	101.34
Si	0.005	0.008	0.006	0.006	0.015	0.013	0.010	0.006	0.008	0.011	0.013
Ti	0.844	0.842	0.852	0.850	0.371	0.378	0.382	0.837	0.852	0.429	0.410
Al	0.006	0.011	-	0.007	0.078	0.106	0.107	-	0.006	0.302	0.127
Cr	-	-	-	n.d.	-	n.d.	n.d.	n.d.	-	n.d.	n.d.
Fe^{3+}	0.292	0.280	0.272	0.279	1.143	1.099	1.100	0.307	0.269	0.812	1.017
Fe^{2+}	0.642	0.636	0.641	0.653	1.159	1.154	1.144	0.628	0.651	1.070	1.175
Mn	0.046	0.034	0.043	0.045	0.053	0.045	0.045	0.050	0.044	0.008	0.033
Mg	0.161	0.180	0.174	0.159	0.170	0.187	0.199	0.165	0.166	0.358	0.210
Ca	-	-	-	-	-	-	-	-	-	-	-
O	3.000	3.000	3.000	3.000	4.000	4.000	4.000	3.000	3.000	4.000	4.000

	815m	816m	818i	823m	824m	853m	861i	862i	894m	895m	904m
SiO_2	0.21	0.35	-	0.30	-	0.21	0.32	-	-	0.32	0.25
TiO_2	16.32	14.94	46.00	13.14	13.43	14.32	45.61	46.38	15.85	15.92	14.89
Al_2O_3	7.44	2.96	0.21	2.83	1.54	2.62	0.31	0.42	3.64	3.64	3.21
Cr_2O_3	n.d.	n.d.	n.d.	n.d.	n.d.	-	-	-	-	-	-
Fe_2O_3	31.36	38.00	16.52	41.97	42.67	40.10	15.95	15.24	37.15	36.59	39.29
FeO	36.58	38.49	31.19	38.02	37.24	37.55	30.88	31.27	38.77	39.18	38.34
MnO	0.39	1.24	1.94	2.12	2.02	1.24	1.17	0.99	0.69	0.84	1.00
MgO	6.87	4.02	4.69	2.83	2.90	4.13	.36	5.46	4.68	4.72	4.48
CaO	-	-	-	-	-	-	-	-	-	-	-
Total	99.18	100.00	100.55	101.11	99.80	100.17	99.60	99.76	100.78	101.21	101.45
Si	0.007	0.013	-	0.011	-	0.008	0.008	-	-	0.011	0.009
Ti	0.426	0.405	0.841	0.364	0.369	0.389	0.836	0.848	0.421	0.422	0.395
Al	0.304	0.126	0.006	0.062	0.066	0.111	0.009	0.012	0.152	0.151	0.133
Cr	n.d.	n.d.	n.d.	n.d.	n.d.	-	-	-	-	-	-
Fe^{3+}	0.821	1.033	0.306	1.182	1.174	1.091	0.297	0.285	0.989	0.971	1.045
Fe^{2+}	1.063	1.161	0.631	1.150	1.137	1.133	0.625	0.629	1.146	1.155	1.131
Mn	0.011	0.038	0.040	0.066	0.062	0.038	0.024	0.020	0.021	0.025	0.030
Mg	0.356	0.216	0.170	0.156	0.158	0.223	0.195	0.198	0.246	0.248	0.236
Ca	-	-	-	-	-	-	-	-	-	-	-
O	4.000	4.000	3.000	4.000	4.000	4.000	3.000	3.000	4.000	4.000	4.000

	907m	908m	909m	910m	1026i	1029i	1046i	1094i	1201i	1202i	1204m
SiO_2	0.21	0.39	0.29	0.34	0.25	0.26	0.32	0.30	0.23	0.18	0.36
TiO_2	15.06	14.79	17.79	17.41	51.58	52.56	51.18	50.81	46.99	47.28	2.29
Al_2O_3	3.28	3.18	6.62	6.73	-	-	-	-	-	-	0.98
Cr_2O_3	-	-	-	-	-	-	n.d.	n.d.	n.d.	n.d.	n.d.
Fe_2O_3	38.01	37.77	29.39	30.90	3.43	1.02	3.84	2.83	10.78	9.89	61.62
FeO	38.73	38.23	37.11	36.79	30.93	31.69	35.32	34.92	38.08	37.60	33.13
MnO	0.94	1.20	0.34	0.34	14.99	15.49	10.43	10.49	3.20	3.50	0.29
MgO	4.12	4.12	7.37	7.66	0.32	0.34	0.29	0.28	0.68	0.89	-
CaO	-	-	-	-	-	-	-	-	-	-	-
Total	100.35	99.68	98.91	100.17	101.50	101.36	101.38	99.63	99.96	99.34	98.68
Si	0.007	0.014	0.010	0.012	0.006	0.006	0.008	0.008	0.006	0.004	0.014
Ti	0.406	0.401	0.466	0.447	0.958	0.976	0.952	0.964	0.881	0.890	0.066
Al	0.139	0.135	0.271	0.271	-	-	-	-	-	-	0.044
Cr	-	-	-	-	-	-	n.d.	n.d.	n.d.	n.d.	n.d.
Fe^{3+}	1.028	1.027	0.770	0.796	0.064	0.028	0.071	0.054	0.220	0.186	1.767
Fe^{2+}	1.162	1.154	1.080	1.051	0.639	0.646	0.731	0.737	0.794	0.787	1.055
Mn	0.029	0.037	0.010	0.010	0.314	0.324	0.218	0.224	0.068	0.074	0.009
Mg	0.220	0.221	0.382	0.390	0.012	0.012	0.011	0.011	0.025	0.033	-
Ca	-	-	-	-	-	-	-	-	-	-	-
O	4.000	4.000	4.000	4.000	3.000	3.000	3.000	3.000	3.000	3.000	4.000

	1210i	1217m	1218m	1219i	1232i	1251i	1252m	1257i	1264m	1265i	1270m
SiO_2	0.19	0.35	0.31	0.19	0.26	0.23	0.40	0.31	0.37	0.27	0.29
TiO_2	50.23	3.61	6.11	52.82	50.56	50.45	4.68	50.51	3.89	51.05	3.45
Al_2O_3	-	3.15	3.35	-	-	-	1.39	-	1.03	-	1.45
Cr_2O_3	n.d.	n.d.	n.d.	n.d.	n.d.	n.d.	n.d.	n.d.	n.d.	n.d.	n.d.
Fe_2O_3	4.95	57.82	52.70	1.88	3.10	4.02	56.68	3.52	58.73	4.08	59.07
FeO	40.07	34.12	35.77	41.62	42.30	37.40	34.84	37.47	33.78	32.95	33.34
MnO	3.02	-	0.55	2.30	2.19	8.14	1.03	8.22	1.27	12.58	1.17
MgO	1.27	0.83	0.84	2.12	0.56	-	-	-	-	0.30	-
CaO	-	-	-	-	0.20	-	-	-	-	-	-
Total	99.73	99.88	99.63	100.93	99.18	100.24	99.03	100.03	99.07	101.23	98.77
Si	0.005	0.013	0.011	0.005	0.007	0.006	0.015	0.008	0.014	0.007	0.011
Ti	0.939	0.100	0.169	0.970	0.956	0.947	0.132	0.950	0.110	0.944	0.098
Al	-	0.137	0.145	-	-	-	0.062	-	0.046	-	0.065
Cr	n.d.	n.d.	n.d.	n.d.	n.d.	n.d.	n.d.	n.d.	n.d.	n.d.	n.d.
Fe^{3+}	0.093	1.607	1.461	0.034	0.053	0.076	1.601	0.066	1.670	0.076	1.682
Fe^{2+}	0.833	1.052	1.101	0.850	0.895	0.781	1.092	0.784	1.066	0.678	1.054
Mn	0.064	-	0.017	0.048	0.046	0.172	0.033	0.174	0.041	0.262	0.037
Mg	0.047	0.046	0.046	0.077	0.021	-	-	-	-	0.011	-
Ca	-	-	-	-	-	-	-	-	-	-	-
O	3.000	4.000	4.000	3.000	3.000	3.000	4.000	3.0000	4.000	3.000	4.000

	1271i	1405m	1406i
SiO_2	-	0.19	0.27
TiO_2	50.72	8.28	46.31
Al_2O_3	-	0.41	0.39
Cr_2O_3	n.d.	-	-
Fe_2O_3	3.88	52.35	15.57
FeO	34.38	34.90	31.96
MnO	10.07	3.47	1.30
MgO	0.58	0.44	4.88
CaO	-	-	-
Total	99.62	100.04	100.68
Si	-	0.007	0.007
Ti	0.951	0.235	0.843
Al	-	0.018	0.011
Cr	n.d.	-	-
Fe^{3+}	0.073	1.484	0.284
Fe^{2+}	0.717	1.100	0.647
Mn	0.213	0.111	0.027
Mg	0.022	0.024	0.176
Ca	-	-	-
O	3.000	4.000	3.000

B13. Loparites.

Sm and Gd values reported are close to, or slightly below, theoretical detection limits as indicated by the ZAF4 processing program. However they are considered to be accurate to one order of magnitude (N. Wilkinson & G. Cunningham, private discussions), and, when plotted on a logarithmic chondrite-normal-ised REE diagram (Chapter V), are consistent with abundances of the lighter REE. They are reported here in this context only, and should not be taken as exact values.

Key to Table B13:-

Syenite SX3:- 1337.

Syenite S1/4:- 1342 - 6.

Table B13.

	1337	1342	1343	1344	1345	1346
TiO_2	38.61	39.89	37.90	37.37	36.69	37.77
FeO	0.61	-	0.78	0.44	0.44	1.19
CaO	4.44	4.04	3.47	3.23	3.37	3.76
Na_2O	9.18	9.76	10.24	10.94	10.25	9.73
La_2O_3	11.52	10.07	9.44	8.46	9.47	9.39
Ce_2O_3	17.56	15.92	14.72	14.40	16.01	15.92
Pr_2O_3	1.63	1.54	1.05	0.90	1.63	1.96
Nd_2O_3	2.75	4.09	3.39	3.53	3.32	4.04
Sm_2O_3	0.30	0.39	0.33	-	-	-
Gd_2O_3	-	-	0.36	-	0.23	0.22
Y_2O_3	-	-	-	-	-	-
ThO_2	0.46	1.50	1.65	1.66	0.98	1.54
Nb_2O_5	10.98	11.48	15.50	15.44	15.48	12.78
Ta_2O_5	2.28	1.65	2.15	2.75	2.31	1.84
TOTAL	100.32	100.33	100.98	99.12	100.18	100.15
Formula per 3 Oxygen atoms						
Ti	0.853	0.869	0.817	0.816	0.805	0.833
Fe	0.015	-	0.019	0.011	0.011	0.029
Ca	0.140	0.125	0.107	0.100	0.105	0.118
Na	0.523	0.548	0.569	0.616	0.580	0.553
La	0.125	0.108	0.100	0.091	0.102	0.102
Ce	0.199	0.178	0.162	0.161	0.180	0.180
Pr	0.017	0.016	0.011	0.010	0.017	0.021
Nd	0.029	0.042	0.035	0.037	0.035	0.042
Sm	0.003	0.004	0.003	-	-	-
Gd	-	-	0.003	-	0.002	0.002
Y	-	-	-	-	-	-
Th	0.003	0.010	0.011	0.011	0.007	0.010
Nb	0.146	0.150	0.201	0.203	0.204	0.169
Ta	0.018	0.013	0.017	0.022	0.018	0.015

B14. Apatites.

Although apatites from most samples were partially analysed, only those in which La, Ce and Nd were quantitatively determined are reported here. Mn and Ti were analysed for but not detected in the samples in Table B 14.

Key to Table B14:-

Madano xenolith TF 163:- 1357, 1358.

Medano xenolith TF 165:- 1353 - 6.

Table B14.

	1353	1354	1355	1356	1357	1358
SiO_2	1.79	1.59	0.35	0.90	1.78	2.50
FeO	0.58	0.17	-	-	0.55	0.16
MgO	0.16	-	-	-	0.22	-
CaO	53.26	53.98	54.78	54.52	53.44	52.86
Na_2O	0.42	0.33	-	0.29	0.25	0.48
K_2O	0.14	-	-	-	-	-
P_2O_5	40.44	41.11	41.38	41.40	39.35	39.60
La_2O_3	-	-	0.39	-	0.56	0.46
Ce_2O_3	0.38	-	0.51	0.29	0.75	0.79
Nd_2O_3	0.18	-	0.16	0.30	0.18	0.28
SO_3	0.32	0.17	0.18	0.18	0.92	0.38
Cl	0.53	0.47	0.41	0.41	-	-
TOTAL	98.21	97.82	98.15	98.30	98.00	97.51
Formula per 25 Oxygen atoms						
Si	0.300	0.265	0.060	0.150	0.300	0.423
Fe	0.083	0.023	-	-	0.078	0.023
Mg	0.040	-	-	-	0.055	-
Ca	9.560	9.670	9.875	9.778	9.668	9.585
Na	0.135	0.108	-	0.095	0.080	0.155
K	0.030	-	-	-	-	-
P	5.735	5.820	5.895	5.868	5.625	5.673
La	-	-	0.025	-	0.035	0.028
Ce	0.025	-	0.033	0.020	0.050	0.053
Nd	0.010	-	0.010	0.018	0.010	0.018
S	0.040	0.023	0.023	0.023	0.118	0.048
Cl	0.123	0.108	0.095	0.095	-	-

B15. Pyrrhotites.

N_{FeS} is the mole fraction of FeS in the pyrrhotite solid solution Fes-S_2. Mn, Cu, and Co are included with Fe for the purposes of calculating N_{FeS}. Ni and Zn were not detected in any of the analysed pyrrhotites.

Key to Table B15:-

Tajao ignimbrite:- 683, 706, 1401.

Pumice deposit E:- 734.

Ignimbrite 0:- 809, 826, 864, 906.

Pumice deposit J:- 55

Cognate mafic cumulate fragment in fall J:- 341 - 5.

Medano xenolith TF 163:- 1272.

Medano xenolith TF 165:- 1222 - 4.

Syenite block S3/2:- 439.

Green Tuff, Pantelleria:- 460.

Table B15.

	55	341	342	343	344	345	439	460
Fe	60.11	59.70	59.88	59.87	60.23	60.72	60.54	61.45
Mn	-	-	-	-	-	-	-	-
Cu	n.d.	0.47	0.54	-	0.57	0.51	n.d.	n.d.
Co	n.d.	n.d.	n.d.	n.d.	n.d.	n.d.	n.d.	n.d.
S	38.72	38.68	38.74	38.66	38.82	39.00	38.50	40.05
TOTAL	98.83	98.85	99.16	98.53	99.62	100.23	99.04	101.50
N_{FeS}	0.943	0.943	0.944	0.941	0.946	0.948	0.949	0.970

	683	706	734	809	826	864	906	1222
Fe	60.03	60.39	62.55	60.47	60.97	60.85	59.84	59.52
Mn	-	-	-	-	0.27	-	-	-
Cu	n.d.	n.d.	n.d.	n.d.	n.d.	n.d.	n.d.	-
Co	n.d.	n.d.	n.d.	n.d.	n.d.	n.d.	n.d.	-
S	38.99	39.84	38.95	39.31	39.93	39.19	40.50	39.76
TOTAL	99.02	100.23	101.50	99.78	101.17	100.04	100.34	99.28
N_{FeS}	0.938	0.931	0.960	0.938	0.936	0.943	0.918	0.924

	1223	1224	1272	1401
Fe	56.82	59.48	60.02	60.04
Mn	-	-	-	-
Cu	2.58	-	n.d.	n.d.
Co	0.56	0.43	n.d.	n.d.
S	39.34	39.90	39.02	40.45
TOTAL	99.30	99.81	99.04	100.49
N_{FeS}	0.931	0.926	0.938	0.920

ENCLOSURES

Contrib Mineral Petrol (1983) 82:66–74

Contributions to Mineralogy and Petrology
© Springer-Verlag 1983

The Volatile Component of Some Pumice-Forming Alkaline Magmas from the Azores and Canary Islands

J.A. Wolff[1] and M. Storey[2]

[1] Department of Geology, Imperial College, London SW7 2BP, England
[2] Department of Geology, Bedford College, Regent's Park, London NW1 4NS, England

Abstract. The abundances of pre-eruptive magmatic volatile species in the system H-O-S may be determined by application of thermodynamic methods to phenocryst assemblages commonly found in volcanic rocks, as demonstrated by Rutherford and Heming (1978). These methods are applied to alkaline pumice deposits, of airfall and ignimbrite type, from Tenerife (Canary Islands), Sao Miguel and Faial (Azores). It is argued that reliable temperature and fO_2 estimates can be obtained from titanomagnetite-ilmenite pairs containing appreciable quantities of minor elements. fO_2 buffering mechanisms found in rhyolitic magmas appear not to operate in more alkaline liquids. fH_2O is estimated using biotite; the high values found are shown to be compatible with the violently explosive nature of the magmas concerned. fS_2 is estimated from pyrrhotite composition. fH_2, fH_2S, fSO_2, fSO_3 are calculated from gas equilibria. Water fugacity may be very roughly estimated for non-biotite bearing samples from data on the sulphur species. Abundances of these species are similar in alkaline and calc-alkaline salic magmas. Volcanological implications, relating to the release of volatiles during explosive eruptions, are considered.

Introduction

The magmatic volatile component may be defined as those species which are normally gaseous at magmatic temperatures and atmospheric pressure, and are thus largely released from the magma upon eruption. Of particular interest are the volatile contents of pumice-forming magmas, since their very formation is testimony to the presence of appreciable quantities of volatile constituents. The fugitive nature of volatiles necessitates that pre-eruptive abundances be determined from information preserved in the final pumice deposit. The most satisfactory method is to analyse samples of pre-eruptive magma preserved as glass inclusions in tephra phenocrysts (Sommer 1977; Druitt et al. 1982). Suitable inclusions are not ubiquitous and in some areas are uncommon. A more generally applicable approach is to use mineral chemistry data and to employ thermodynamic methods to deduce the fugacities of volatile species in equilibrium with the phenocryst assemblage before eruption. This approach has been demonstrated by Rutherford and Heming (1978), who determined species in the system H-O-S in dacitic and rhyolitic pyroclastics from New Zealand. However, very few similar studies appear to have been made. This paper, therefore, has three principal aims; firstly, to present temperature and volatile data for some phonolitic, trachytic and trachyandesitic pumice deposits from Atlantic islands; secondly, to reaffirm this approach as a rapid means of estimating the composition of the magmatic volatile component; thirdly, to attempt to assess the significance of this information in a volcanological context.

Offprint requests to: J.A. Wolff

Geological Settings

The Canary Islands lie in the Eastern Atlantic on a sea-floor fracture zone extending off the continental slope of North-West Africa (Fig. 1). Tenerife, the largest island, consists of a Tertiary alkali basalt shield capped by younger differentiated volcanics and later basalts (Fuster et al. 1968; Borley 1974). Petrologically the rocks show the evolutionary trend alkali basalt-trachybasalt-trachyandesite-phonolite (Borley 1974). An extensive late Quaternary pyroclastic series of dominantly phonolitic composition is prominent in the south and east of the island. The series has been mapped by Booth (1973) and Booth and Walker (to appear) who distinguish the products of some 40 individual eruptions from vents located in the central caldera of Las Cañadas. The series chiefly consists of non-welded plinian air-fall deposits and ignimbrites[1], although welded examples of both are found. All four types are represented in this study. Several of the deposits consist of mixed-magma pumice (Wolff et al. to appear), as evidenced by variability in glass chemistry and the presence of two or more distinct phenocryst assemblages.

The Azores islands straddle the Mid-Atlantic Ridge (Fig. 1) on a topographic high known as the Azores Platform, those to the east of the Ridge being associated with a seismically active transform fracture zone (Laughton and Whitmarsh 1975). Volcanic rocks from the Azores consist predominantly of alkali basalts and their differentiates which include trachytes and peralkaline types. On some islands, these evolved magmas have been explosively erupted to form extensive pumice deposits. These deposits have been quantitatively studied on Sao Miguel by Walker and Croasdale (1971), Booth et al. (1978) and Storey (1981), on Terceira by Self (1976) and on Faial by Walker and

[1] We adopt the terminology of Wright et al. (1980) when describing the physical characteristics of the rocks studied in this paper

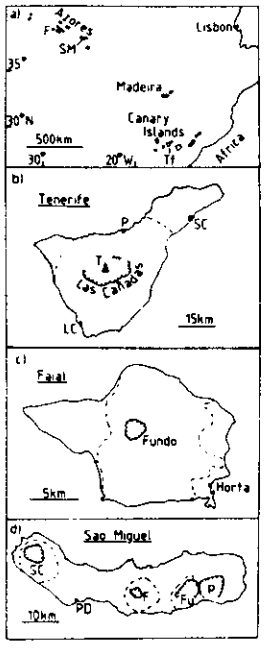

Fig. 1. Location maps. (a) Eastern Atlantic Ocean, showing location of Tenerife (Tf), Sao Miguel (SM) and Faial (F). (b) Tenerife, showing approximate extent of pumice series (dashed lines) erupted from vents in or near Las Cañadas caldera; greatest thicknesses are found south and east of Las Cañadas. T = volcanic peak of Teide. Principal towns: Santa Cruz (SC), Puerto de la Cruz (P), Los Cristianos (LC). (c) Faial, showing approximate extent of pumice series (dashed lines) erupted from the region of Fundo caldera. (d) Sao Miguel, showing the location of calderas associated with the three active volcanoes: Sete Cidades (SC); Fogo (F) caldera of Agua de Pau volcano, and Furnas (Fu). Dashed lines are the 8 m thickness contours for pumice successions erupted from each of the three centres (from Booth et al. 1978), although pumice occurs throughout the island. Also shown are the extinct centre of Povoacao (P) and the principal town, Ponta Delgada (PD)

Croasdale (unpub.). Sao Miguel, the largest island, has three active stratovolcanoes, Sete Cidades, Agua de Pau and Furnas. Faial island consists of a single stratovolcano rising to the peak of Carego Gordo. All four volcanoes possess a central caldera and a long record of explosive activity. Historic eruptions of trachytic pumice occurred from the Fogo caldera of Agua de Pau volcano in AD 1563 and from Furnas in AD 1640. In the last 5,000 years, there have been some 25 explosive trachytic eruptions on Sao Miguel, of which 6 were from the Agua de Pau volcano. As on Tenerife, magmatically heterogeneous pumice deposits are common (Walker and Croasdale 1971; Storey 1981).

Mineralogy and Petrology

The Tenerife deposits consist mainly of mildly peralkaline phonolite with a few modal percent of scattered phenocrysts. Most of the original pumice glass has devitrified to clay minerals, although unhydrated glass is preserved in some of the less vesicular clasts, and is common in welded tuffs. Samples showing evidence of alteration of phenocrysts were rejected. Many of the deposits studied contain a proportion of intermediate (trachyandesitic) tephra introduced by magma mixing shortly before eruption, and banded pumice clasts are common. In such cases detailed petrographic study is required to establish co-existing relationships within two (or more) crystal-magma populations (Wolff to appear). However aggregate phenocryst grains containing several minerals are common, and provide abundant evidence for equilibrium between phases at the time of quenching. Mineral assemblages in the pumice-forming magmas of Tenerife fall into three groups:

(i) Phonolitic:
Afsp + bi + mag ± ilm ± aeg-aug

(ii) Phonolitic:
Afsp + aeg-aug + bi + mag ± sph ± sod ± ne

(iii) Intermediate:
Plag + aug + amph + mag + ilm ± haüyne

Alkali feldspar in assemblages (i) and (ii) is usually sodic sanidine, occasionally anorthoclase. Xenocrysts derived from basaltic magma are common; these include olivine, titanaugite and calcic plagioclase.

The Azores samples are generally similar, except that the groundmass glass is trachytic. The usual phenocryst assemblage is Afsp + cpx + bi + mag ± ilm ± amph, with rare zircon. Basaltic xenocrysts are again common.

Apatite and pyrrhotite grains are found as inclusions in other phenocrysts in samples from both areas.

Analytical Procedure

Phenocryst phases in our samples have been analysed by electron microprobe. Tenerife samples were analysed on the Microscan V/EDS system at Imperial College using an accelerating voltage of 15 KV and a specimen current of 4 nA. Azores samples were analysed on a Microscan V/EDS at University College, London, using an accelerating voltage of 20 KV and a specimen current of 10 nA. The phases used in this study are homogenous within experimental error. Selected analyses for co-existing Fe-Ti oxides are given in Table 1.

Geothermometry

Knowledge of the equilibration temperature of the phenocryst-magma system is a necessary preliminary to determining the fugacities of magmatic volatile components. Nearly all the samples studied contain equilibrium mineral pairs of ilmenite and titanomagnetite, and temperatures have thus been estimated from the geothermometer and oxygen barometer of Buddington and Lindsley (1964), the mineral formulae first being recast in terms of end members by the method of Carmichael (1967). Both oxides contain substantial quantities of minor elements (4%–8% by weight $MgO + MnO + Al_2O_3$, Table 1), in part a consequence of the low silica activities of the magmas from which they precipitated (Carmichael et al. 1970). Powell and Powell (1977) recommend a different recalculation scheme which allows estimation of the maximum errors on the T-fO_2 determination due to the uncertainty involved in assigning minor elements to a particular end-member of the solid solutions. There is, however, evidence that Carmichael's (1967) procedure largely negates the effects of the minor elements. Hildreth (1979) has compared temperatures and oxygen fugacities obtained using Carmichael's method with those obtained by using recalculation procedures based on the actual effect of Mn and Mg components in the oxides (Mazzulo et al. 1975; Pinckney and Lindsley 1976), and finds a negligible discrepancy between results from the two methods. Furthermore, the estimated temperatures for our samples are corroborated by an independently derived geothermometer, the Fe^{2+}-Mg exchange between clinopyroxene and ilmenite (Bishop 1980). Agreement is generally very good (Table 2). We therefore believe that the Fe-Ti oxide

Table 1. Selected Fe-Ti oxide analyses recalculated following the method of Carmichael (1967), see text

	W.A.F.T., Tf[a]	Tajao ig., Tf[b]	Fogo B, S.M.[c]	Fogo C, S.M.[c]	Faial T
Ti mag.					
SiO_2	0.30	0.37	0.44	0.39	0.30
TiO_2	12.44	13.53	17.15	17.66	16.88
Al_2O_3	0.59	2.43	1.11	1.22	3.84
FeO	77.68	75.06	75.18	74.27	70.73
MnO	2.77	1.44	2.02	2.03	0.00
MgO	1.77	3.24	1.39	1.52	4.30
Total	95.55	96.07	97.29	97.09	96.05
FeO	37.57	38.07	43.47	43.66	41.03
Fe_2O_3	44.58	41.05	35.21	33.99	33.04
Recalculation total	100.02	100.13	100.79	100.47	99.39
Mol% usp	36.06	38.42	48.7	50.3	47.0
Ilmenite					
SiO_2	0.31	0.24	0.27	0.50	0.31
TiO_2	47.22	45.63	48.82	49.46	47.37
Al_2O_3	0.00	0.33	0.41	0.24	0.30
FeO	44.69	46.64	44.33	44.64	44.74
MnO	3.81	1.51	2.14	2.60	0.00
MgO	3.02	4.52	2.59	1.85	5.43
Total	99.05	98.87	98.56	99.29	98.15
FeO	33.60	31.97	36.05	38.80	33.27
Fe_2O_3	12.33	16.28	9.20	6.49	12.74
Recalculation total	100.29	100.48	99.48	99.94	99.42
Mol% ilm	88.54	84.52	91.4	93.5	87.8
Temperature (° C)	835	915	910	880	960
fO_2	$10^{-13.1}$	$10^{-11.4}$	$10^{-12.2}$	$10^{-13.2}$	$10^{-11.0}$

[a] W.A.F.T., Tf – Boca de Tauce welded air fall tuff, Tenerife
[b] Tajao ig., Tf – Tajao ignimbrite, Tenerife
[c] S.M. – Sao Miguel

temperatures closely approximate the actual temperatures prevailing at the moment when titanomagnetite-ilmenite-liquid equilibrium was quenched by eruption. Since the oxide phases are in equilibrium with the rest of the phenocryst assemblage in each sample, the temperature estimates apply to the whole assemblage and the associated magma. We have used the Fe-Ti oxide temperatures in the fugacity calculations, rather than temperatures derived from the Bishop (1980) geothermometer, since these phases were also used to find fO_2.

Estimation of fO_2

The composition of co-existing Fe-Ti oxides reflects the fugacity of oxygen as well as the equilibrium temperature (Buddington and Lindsley 1964). Results are shown in Table 1 and Fig. 2. The Tenerife samples show a higher oxygen fugacity for a given temperature than those from the Azores. Also, for individual volcanoes (Tenerife, Agua de Pau) the scatter of points is very small. This probably represents the effect of mineral and/or liquid component oxygen buffers. Several workers, using closely similar or identical Fe-Ti oxide recalculation schemes (Carmichael 1967; Ewart et al. 1971; Lipman 1971; Heming and Carmichael 1973; Rutherford and Heming 1978), have found that natural rhyolitic and dacitic liquids tend to plot on one of four curves in T-fO_2 space, each curve corresponding to the buffering of fO_2 by the ferromagnesian minerals found in association with the Fe-Ti oxides (Fig. 2). Clearly the *opx* and *opx-amph* buffers cannot apply to alkaline magmas. All of the studied samples contain biotite and/or amphibole, yet lie well below the *bi-amph* curve. None of the samples that plot near the QFM buffer curve contain quartz or olivine (with the exception of the Pantelleria sample, which is considerably more oversaturated). Thus it seems that either the mineral buffers found in acidic magmas do not operate in phonolitic and trachytic liquids, or else their effects are substantially modified by overall magma composition. Plausible reactions may be written for the mineral assemblages found in our rocks, but none are applicable over the entire range of assemblages observed.

As the assemblages do not permit an estimation of fH_2O which is independent of the fO_2 determination, we cannot test the possibility that the dissociation of water controls

Table 2. Comparison of temperatures obtained by applying the Fe-Ti oxides geothermometer (Buddington and Lindsley 1964) to analyses recast by the method of Carmichael (1967), with those given by the clinopyroxene-ilmenite geothermometer (Bishop 1980), for those deposits where titanomagnetite, ilmenite and augite coexist

Eruptive unit	Temperature (°C) from Fe-Ti oxides	Temperature (°C) from cpx-ilm
Ignimbrite O(i)*, Tenerife	940	980
Ignimbrite O(ii)*, Tenerife	915	923
Boca de Tauce welded air-fall tuff, Tenerife	835	810
Tajao ignimbrite, Tenerife	915	907
Adeje red ignimbrite, Tenerife	865	833
Fogo A pumice fall deposit, Sao Miguel	960	950
Fogo B pumice fall deposit, Sao Miguel	910	940
Fogo C pumice fall deposit, Sao Miguel	880	800

* Mixed-magma eruption: temperatures are given for two of the magmas represented in the pumice deposit

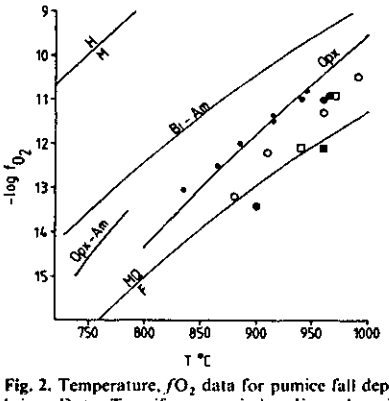

Fig. 2. Temperature, fO_2 data for pumice fall deposits and ignimbrites. Dots: Tenerife; open circles: Fogo deposits, Sao Miguel; filled circles: Faial. Also shown are two basic-intermediate lavas from Sao Miguel (open squares) and the pantelleritic Green Tuff (filled square), product of the largest documented eruption on Pantelleria, Italy (Wolff and Wright 1981). MQF = quartz-magnetite-fayalite buffer; HM = hematite-magnetite buffer. Curves labelled Bi-Am, Opx-Am, and Opx are explained in the text

fO_2. We can only conclude that magma type exerts a considerable effect on fO_2, but that the mechanism by which this effect operates remains open to question.

Estimation of fH_2O, P_{H_2O}, X_{H_2O}

The composition of co-existing biotite, sanidine and magnetite may be used to estimate the fugacity of water, by means of the reaction:

$$KFe_3AlSi_3O_{10}(OH)_2 + \tfrac{1}{2}O_2$$
biotite
$$\rightleftharpoons KAlSi_3O_8 + Fe_3O_4 + H_2O$$
sanidine magnetite

for which free-energy data is given by Wones and Eugster (1965), who adopted a regular solution model for biotite in the system annite-phlogopite-oxyannite. However Mueller (1972) and Wones (1972) have shown that mixing on the biotite octahedral site is approximately ideal, where the Fe^{3+} content of this site is small. Charge balance calculations show that the Fe^{3+} content of our biotites is negligible, and therefore the activity of annite in the biotites is equal to $(X_{Fe}^{oct})^3$, where X_{Fe}^{oct} is the octahedral site occupancy of Fe^{2+} in biotite. Appreciable substitution of Na for K and of F for OH may also occur, and the activity expression should therefore be modified by factors of $K/(K+Na)$ and $[OH/(OH+F)]^2$, assuming ideal mixing on both of these sites. Unfortunately the $OH/(OH+F)$ ratio is very readily changed by post-eruptive processes. We have therefore assumed $OH/(OH+F)=1$, and our calculated values of fH_2O (Table 3) are thus maximum estimates. The effect of fluorine in biotite on the calculated values may be readily assessed by inspection of the above reaction; for example, a fluorine site occupancy of 0.3 results in calculated log fH_2O being in excess by log $(1-0{\cdot}3)^{-2}=0.3$. The activity of $KAlSi_3O_8$ in sanidine is calculated from the assymetric regular solution treatment of Thompson and Waldbaum (1969) and magnetite solid solutions are assumed to be ideal, following Carmichael et al. (1977).

Burnham et al. (1969) have determined the fugacity coefficient of water over a wide range of temperatures and pressures, and thus P_{H_2O} can be found for a given fH_2O and temperature. If P_{total} is known, the mole fraction of water in the magma (X_{H_2O}) can be calculated from the relationship given by Spera in Ewart et al. (1975). As we have no estimate of P_{total}, we have assumed that the magmas were water-saturated. X_{H_2O} may be readily converted into a primary wt% magmatic water content (Table 3). The water contents so found are maximum values, because of the assumptions of saturation and of fluorine-free biotite. Nonetheless they are compatible with the known explosive violence of the pumice eruptions, as evidenced by the wide dispersal of tephra from the source vents (Table 6 and below).

Estimation of fH_2

The fugacity of hydrogen may also be estimated from biotite composition:

$$KFe_3AlSi_3O_{10}(OH)_2$$
biotite
$$\rightleftharpoons KAlSi_3O_8 + Fe_3O_4 + H_2$$
sanidine magnetite

This reaction was used by Rutherford and Heming (1978) to estimate fH_2. However the expression for fH_2 which they used assumes a regular solution model for biotite, which is inconsistent with the assumption of biotite ideality in the expression used to find fH_2O from the same mineral data. We attempted to derive fH_2 values from the thermodynamic data of Wones and Eugster (1965) and assuming biotite ideality, but obtained unreasonably large results (up

Table 3. Estimated magmatic water contents

Pumice deposit	bi a_{ann}	san a_{or}	$\log fH_2O$	P_{H_2O}	X_{H_2O}[a]	wt% H_2O[a]	Total water[b]
Pumice fall E, Tenerife	0.0129	0.373	3.39	2,800	0.22	7.1	0.28
Adeje red ignimbrite, Tenerife	0.0117	0.391	3.20	1,900	0.18	5.6	0.006
Boca de Tauce welded air-fall tuff, Tenerife	0.0152	0.480	3.11	1,500	0.14	4.2	–
Fogo A pumice fall deposit, Sao Miguel	0.0222	0.498	3.47	3,000	0.22	6.6	0.09
Fogo B pumice fall deposit, Sao Miguel	0.0200	0.500	3.36	2,500	0.21	6.5	0.02
Fogo C pumice fall deposit, Sao Miguel	0.0429	0.508	3.30	2,300	0.21	6.5	0.008
Pumice fall deposit B, Faial	0.106	0.433	3.72	5,300	0.23	7.2	–

[a] Calculated assuming water saturation of magma

[b] Total volume of water (calculated as liquid in Km^3) released from the magma during the eruption. Based on total erupted volume of magma, taken from Booth et al. (1978) for Fogo A, B, C, Booth and Walker (in prep.) for Tenerife E, and Wolff (unpublished data) for Adeje, Tenerife. Tenerife volumes, based on present extent of deposits, are minima

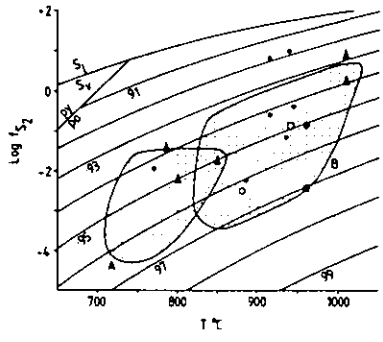

Fig. 3. fS_2 data for pyrrhotite-bearing samples. Numbered contours (calculated from the data of Toulmin and Barton 1964) are the mole fraction of FeS in pyrrhotite solid solution (FeS-S_2). Also shown are the pyrite-pyrrhotite equilibrium curve (py/po) and sulphur liquid-vapour equilibrium curve (S_l/S_v). Legend as Fig. 2, with the addition of sub-volcanic cumulates from Tenerife (filled triangles); sulphur fugacities of these fall within the range found in the Tenerife pumice deposits. Stippled field A is the range of fS_2 found in New Zealand ignimbrite magmas (Rutherford and Heming 1978); stippled field B is the range of fS_2 found for pumice deposits from the Rabaul caldera, Papua New Guinea (Heming and Carmichael 1973)

to 900 bars). We have therefore estimated fH_2 from the water decomposition reaction:

$$H_2O \rightleftharpoons H_2 + \tfrac{1}{2}O_2$$

using data given in the JANAF thermochemical tables (Stull and Prophet 1971). fH_2 data are given in Fig. 4.

Estimation of fS_2

Pyrrhotite occurs in a number of samples as inclusions in Fe-Ti oxides, pyroxene, amphibole, biotite, feldspar and (in the Tenerife pumices) haüyne. That enclosed in haüyne occurs as a fine dust, apparently formed after growth of the including crystal; in all other minerals it is found as blebs up to 100 μ across and is considered to have occurred as discrete grains before and/or during the growth of the principal phases. Pyrrhotite composition defines the fugacity of sulphur (fS_2) in the environment from which it crystallised (Toulmin and Barton 1964). The pyrrhotite grains ceased to be in equilibrium with the magma upon inclusion in other phases, which presumably occurred at slightly higher temperatures than those indicated by the present Fe-Ti oxide compositions. However the Fe-Ti oxide temperatures are used here in the absence of data on the enclosure temperatures of the pyrrhotite grains. Values of fS_2 show a degree of variation (Fig. 3) comparable to those found for dacitic and rhyolitic magmas (Heming and Carmichael 1973; Rutherford and Heming 1978).

Estimation of fH_2S, fSO_2, fSO_3

With a knowledge of fS_2, fH_2 and fO_2, the fugacities of three sulphur compounds may be estimated from the formation reactions:

$$H_2S \rightleftharpoons H_2 + \tfrac{1}{2}S_2$$
$$SO_2 \rightleftharpoons \tfrac{1}{2}S_2 + O_2$$
$$SO_3 \rightleftharpoons \tfrac{1}{2}S_2 + 1\tfrac{1}{2}O_2$$

using data from the JANAF thermochemical tables (Stull and Prophet 1971). Results are shown in Fig. 4.

Limitations

There are four main limitations to the accuracy of the data and the general applicability of this approach.

1. Errors arising from errors in (a) mineral analyses and (b) thermodynamic data. (b) does not apply if results obtained by using the same calculation procedures are being compared, but errors are compounded when gas reactions are used (e.g. to find fSO_2, fSO_3) where the input data are fugacities already estimated from mineral data. Uncertainties in fugacity estimations, calculated by the error propogation method recommended by Powell (1978), are given in Table 4.

2. Errors due to assumptions made. These can usually be assessed with a degree of confidence, e.g. the assumption of fluorine-free biotite results in the calculation of maximum fH_2O values.

3. Pumice deposits often have very low phenocryst contents, and, if aggregate mineral grains are rare or absent, it may be difficult to establish equilibrium between phenocryst phases.

4. The required mineral phases may not be present. We have examined some thirty erupted magmas, of which half bear iron-titanium oxides, and fewer still contain biotite

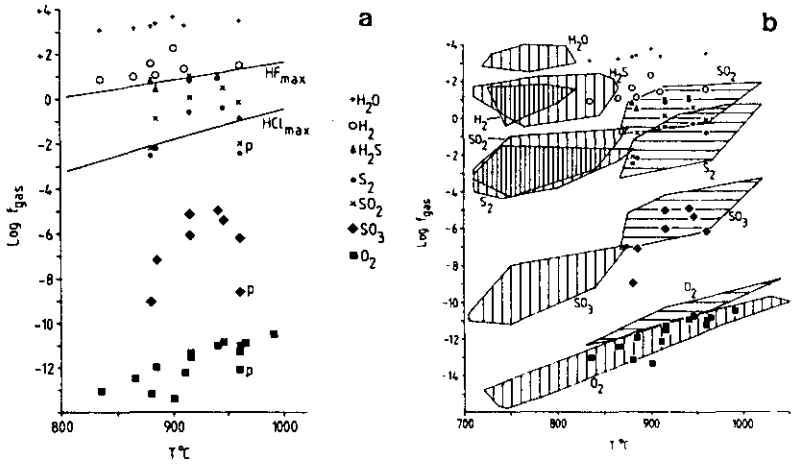

Fig. 4. Fugacity data for all determined volatile constituents in pyroclastics studied. (a) Labelled curves HF_{max}, HCl_{max} are explained in the text; points labelled p are the pantellerite sample. (b) Vertical rule: range of values for each species in H-O-S found in New Zealand ignimbrite magmas (Rutherford and Heming 1978). Horizontal rule: range of fS_2, fSO_2, fSO_3, fO_2 values in New Guinea pumice deposits (Heming and Carmichael 1973). Pantellerite omitted for sake of clarity

Table 4. Uncertainties (±) in calculated fugacity values

$\log fO_2$	0.5	$\log fSO_2$	0.7
$\log fH_2O$	0.3	$\log fSO_3$	0.9
$\log fH_2$	0.4	$\log fH_2S$	0.5
$\log fS_2$	0.5	T	30 °C

and/or pyrrhotite in addition. More seriously, the vast majority of erupted magmas do not bear a mineral assemblage which permits the determination of the important constituents CO_2, CO, HF and HCl.

Despite these problems, the approach is a powerful one, as it allows the rapid calculation of the composition of part of the volatile component of a range of salic magma types.

Discussion

Our data are similar to those obtained by Heming and Carmichael (1973) and Rutherford and Heming (1978) for Quaternary pumice-forming magmas from Rabaul, New Guinea and North Island, New Zealand respectively (Fig. 4b). The New Zealand results are typically lower for each species than those for the Tenerife, Azores and Rabaul pumices; this is principally a reflection of their lower equilibration temperatures (729–810 °C). fS_2 is on average slightly higher, at a given temperature, in the Atlantic magmas.

Fugacities may be converted to abundances if it is assumed that volatile species mix ideally with each other and with magma, and if fugacity co-efficients are known for each volatile species. When this is done for the five principal species in H-O-S, the similarity between the rhyolite, trachyte and phonolite data becomes even more apparent (Table 5). The general similarity in relative abundances is presumably a consequence of the relative stabilities of the various gas species under magmatic conditions; for example SO_2 will always predominate over SO_3 at the oxygen fugacities usually encountered in magmas. Thus we may conclude that the magmatic volatile component has a similar composition (at least in H-O-S) in a wide variety of pumice-forming salic melts, although it must be noted that the single pantellerite sample for which we have data is much poorer in the sulphur species than the alkaline and calcalkaline liquids (Fig. 4).

Table 5. Molar abundances, as a percentage of total abundance of the five major species in the system H-O-S, for three cases[a]

	Pumice fall deposit E, Tenerife	Pumice fall deposit C, Sao Miguel	Average New Zealand ignimbrite[b]
H_2O	99.4%	98.1%	99%
H_2	0.5%	1.6%	0.5%
H_2S	0.1%	0.3%	0.5%
SO_2	(0.005%)	(0.0003%)	(0.0002%)
S_2	(0.0002%)	(0.0001%)	(0.0001%)

[a] Calculated using fugacity coefficients tabulated by Ryzhenko and Volkov (1971) and assuming ideal mixing
[b] From data of Rutherford and Heming (1978)

Rough estimation of fH_2O for non-biotite bearing samples

The five principal species in the system H-O-S are related by the equilibrium:

$$S_2 + 2H_2O \rightleftharpoons H_2S + SO_2 + H_2$$

If the variation with temperature of three of these species can be characterised for a suit of samples, then a simple

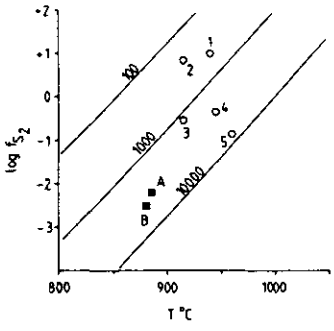

Fig. 5. Relationship between fS_2 and temperature for three values of fH_2O in bars (see text). A = Tenerife deposit E, B = Fogo deposit C, for which independent fH_2O values are available (Table 3). 1 = Tenerife ignimbrite O(i); 2 = Tenerife Tajao ignimbrite; 3 = Tenerife ignimbrite O(ii); 4 = Tenerife deposit J; 5 = Faial deposit T

relationship between the other two is found. We have applied this method to determine fH_2O for non-biotite bearing samples using the data in Fig. 4. Although this procedure is only qualitative owing to the substantial errors involved (particularly in the values of fH_2S, fSO_2 and fH_2 which form input data for this calculation), the results (Fig. 5) are compatible with other evidence; the high fH_2O value found for Faial deposit T is similar to the figure of 5,300 bars for an associated fall deposit (Faial B) which contains biotite; Tenerife ignimbrite O(ii) is very likely to be more water-rich than O(i), since it is derived from a cooler, more fractionated part of the same magma chamber (Wolff, to appear).

Constraints on the Fugacities of Undetermined Constituents

Under conditions of sufficiently high magmatic fCO_2, calcium-bearing minerals break down to form primary igneous calcite, as observed in carbonatites and some magmas of less extreme composition (Scott 1982). The absence of calcite from a given mineral assemblage thus defines an upper limit of fCO_2 for that assemblage. Several reactions between CO_2 and observed major components of solid phases may be written, for example:

$$3CaFeSi_2O_6 + 3CO_2 + \tfrac{1}{2}O_2$$
pyroxene
$$\rightleftharpoons 3CaCO_3 + Fe_3O_4 + 6SiO_2$$
calcite magnetite liquid

and for a sphene-bearing assemblage

$$2CaFeSi_2O_6 + CaTiSiO_5 + 3CO_2$$
pyroxene sphene
$$\rightleftharpoons 3CaCO_3 + Fe_2TiO_4 + 5SiO_2$$
calcite magnetite liquid

Using the thermodynamic data of Helgeson et al. (1978) and typical mineral compositions for our samples, maximum values of fCO_2 lie between 1 and 30 bars. This is in general agreement with the known low solubility of CO_2 in low-pressure, hydrous magmas (Mysen 1977).

The roles of fluoride and chloride species in magmas have been studied by Stormer and Carmichael (1970, 1971). As was done for CO_2, the lack of a fluoride-bearing phase among the mineral assemblage allows approximate calculation of maximum values of fF_2, using the reactions discussed by Stormer and Carmichael (1970) for the formation of fluorite (CaF_2) and villiaumite (NaF). With a knowledge of fH_2O or fH_2, maximum values of fHF, the principal fluorine-bearing volatile species, may be calculated. An overall maximum for fHF in the pumice magmas is plotted in Fig. 4a. Sodalite, the most widespread chloride-bearing igneous mineral occurs as a phenocryst in a few of the Tenerife phonolites; however it is unfortunately restricted to those samples for which no T-fO_2 estimate can be made, prohibiting direct calculation of fCl_2 by the method of Stormer and Carmichael (1971). Instead, maximum fCl_2 and $fHCl$ values for sodalite-free samples were found, and a "ceiling" $fHCl$ curve is given in Fig. 4a.

Thus it appears that CO_2, HCl and HF levels are possibly comparable to the determined minor constituents in H-O-S, but are orders of magnitude less abundant than H_2O.

Magmatic Water Contents

Water is the most abundant volatile constituent in the great majority of magmas, and a knowledge of magmatic water content is essential to the estimation of such parameters as the viscosity and density of magma before eruption. Rutherford and Heming (1978) considered the water contents of New Zealand ignimbrite magmas to be unusually high, and ascribed this to an origin by anatexis of water-rich basement greywackes (for which there is a considerable body of evidence; see Carmichael et al. 1974, and references cited therein). The mean water content of the values tabulated by Rutherford and Heming corresponds to approximately 6.5% by weight, closely similar to the values obtained here. Sommer (1977) found volatile contents of up to 7% (average 5.4%) for the Bandelier Tuff, New Mexico, rhyolite magma; 92% of this consisted of H_2O, the remainder being mostly CO and CO_2. Druitt et al. (1982) found a magmatic water content of 5% in the first erupted portion of the Bishop Tuff, California. Thus, when compared to other *pumice-forming* magmas, the New Zealand examples cannot be considered particularly water-rich.

The deduced water contents are compatible with field evidence for the violently explosive nature of the magmas. The distribution of tephra in a plinian air-fall deposit can be used to estimate various physical parameters of the eruption (Wilson 1976; Wilson et al. 1978). In particular, the dispersal of the largest dense (ballistic) fragments is unaffected by atmospheric transport. Extrapolation of the range dependence of ballistic clast size yields a value for the largest blocks which can be just supported by the eruption column at the vent, and thence maximum muzzle velocity (through a function given by Wilson 1976). Eruption velocity is directly related to the quantity of released gas and the primary magmatic volatile content (Wilson 1980; Wilson et al. 1980). The appropriate field data exist for the Fogo deposits (Booth et al. 1978; Walker and Croasdale 1971) and we have therefore calculated magmatic volatile contents for Fogo A, B and C. Our thermodynamic estimates indicate that other species are greatly subordinate to water, and thus actual water content will approximate

Table 6. Comparison of estimated values of water content with those deduced from field measurements on the dispersal of tephra*

Pumice deposit	wt% H_2O, this paper	wt% H_2O, from field data
Fogo A, Sao Miguel	6.6	6.7
Fogo B, Sao Miguel	6.5	5.7
Fogo C, Sao Miguel	6.5	4.5

* See text for method

total volatile content, permitting comparison with estimates based on the physical model. Agreement between the two approaches is good (Table 6), particularly in view of the uncertainty associated with the fH_2O values (Table 4). Although both methods give maximum estimates of water content, the "petrological" values are expected to be higher, since no account is taken of energy losses occurring during magma disruption in the "volcanological" calculations (Wilson 1980).

Widely dispersed plinian pumice fall deposits, similar to those studied here, are a common manifestation of salic volcanism, yet few estimates of their magmatic volatile contents exist. The data discussed here suggest that natural salic liquids commonly have water contents in excess of 5% by weight.

Some Volcanological Implications

1. Physical models of explosive eruptive processes often assume that the magmatic volatile component consists entirely of water, because of the negligible effect of the presence of small quantities (<10%) of other volatile species on eruption dynamics. Our results indicate that this approximation is valid for alkaline salic magmas. An illustration is provided by the effect of gas density on a plinian eruption column. Dense columns tend to collapse to form ignimbrites (Sparks and Wilson 1976), whereas lighter columns more readily undergo convective uprise to form an eruption cloud some tens of kilometres high, fall-out from which produces a plinian pumice fall deposit (Wilson 1976; Wilson et al. 1978). The data discussed here indicate that variations in the density of released gas, due to compositional variations in the system H-O-S, are unlikely to be great enough to significantly affect eruption column dynamics.

2. Appreciable quantities of combustible gases (H_2, S_2, H_2S) are present in salic magmas and will be released upon explosive eruption. The oxidation of these in the eruption cloud will contribute to the thermal energy budget of the eruption. Enthalpy calculations for the relevant combustion reactions indicate that this contribution is minor compared to the thermal and kinetic energy released, and is unlikely to exceed a few percent of the total eruption energy.

3. Large quantities of water are released during pumice eruptions (Table 3). If it is assumed that a large proportion of released water falls as rain during or soon after eruption, then the formation of mudflows by remobilisation of the newly-deposited tephra is a virtually inevitable consequence of any such eruption. Mudflows are very common associates of all types of pumice deposit.

Acknowledgements. J.A.W. wishes to thank the Natural Environment Research Council of Great Britain for a research studentship at Imperial College, and for funding fieldwork on Tenerife. Part of this work was carried out while M.S. held an Inner London Education Authority research assistantship at South London College, Knight's Hill, London SE27 OTX. M.S. thanks the Dept. of Geology, University College, London for the use of their electron microprobe facility and I.C. Young for analytical assistance. Pumice samples from the Azores were collected by Prof. G.P.L. Walker and Dr. R. Croasdale. Dr. J.V. Wright collected the Pantelleria sample. We are especially grateful to Prof. G.P.L. Walker, Dr. B. Booth and Dr. R. Croasdale for generous access to unpublished data. The original manuscript was substantially improved by the comments of Dr. A.D. Saunders and an anonymous reviewer. Pat Storey kindly typed the final draft.

References

Bishop FC (1980) The distribution of Fe^{2+} and Mg between coexisting ilmenite and pyroxene with applications to geothermometry. Am J Sci 280:46–77

Booth B (1973) The Granadilla pumice deposit of Southern Tenerife, Canary Islands. Proc Geol Assoc 84:353–370

Booth B, Croasdale R, Walker GPL (1978) A quantitative study of five thousand years of volcanism on Sao Miguel, Azores. Philos Trans R Soc London A 288:271–319

Booth B, Walker GPL (to appear) Products of explosive volcanism on Tenerife, Canary Islands

Borley GD (1974) Aspects of the volcanic history and petrology of the island of Tenerife. Proc Geol Assoc 85:259–279

Buddington AF, Lindsley DH (1964) Iron-titanium oxide minerals and synthetic equivalents. J Petrol 5:310–357

Burnham CW, Holloway JR, Davis NF (1969) Thermodynamic properties of water to 1,000° C and 10,000 bars. Geol Soc Am Spec Paper 132:1–96

Carmichael ISE (1967) The iron-titanium oxides of salic volcanic rocks and their associated ferromagnesian silicates. Contrib Mineral Petrol 14:36–64

Carmichael ISE, Nicholls J, Smith AL (1970) Silica activity in igneous rocks. Am Mineral 55:246–263

Carmichael ISE, Nicholls J, Spera FJ, Wood BJ, Nelson S (1977) High-temperature properties of silicate liquids: Applications to the equilibration and ascent of basic magma. Philos Trans R Soc London A 286:373–431

Carmichael ISE, Turner FJ, Verhoogen J (1974) Igneous Petrology. McGraw-Hill, pp 739

Druitt TH, Anderson AT, Nagle F (1982) Water in rhyolitic magma, Bishop, California. Eos 63:451

Ewart A, Green DC, Carmichael ISE, Brown FH (1971) Voluminous low temperature rhyolitic magmas in New Zealand. Contrib Mineral Petrol 33:128–144

Ewart A, Hildreth W, Carmichael ISE (1975) Quaternary acid magma in New Zealand. Contrib Mineral Petrol 51:1–27

Fuster JM, Arana V, Brandle JL, Navarro M, Alonso U, Aparicio A (1968) Geology and volcanology of the Canary Islands: Tenerife. Inst "Lucas Mallada", Madrid 218

Helgeson HC, Delaney JM, Nesbitt HW, Bird DK (1978) Summary and critique of the thermodynamic properties of rock-forming minerals. Am J Sci 278a:pp 229

Heming RF, Carmichael ISE (1973) High-temperature pumice flows from the Rabaul caldera, Papua New Guinea. Contrib Mineral Petrol 38:1–20

Hildreth W (1979) The Bishop Tuff: Evidence for the origin of compositional zonation in silicic magma chambers. Geol Soc Am Spec Paper 180:43–75

Laughton AS, Whitmarsh RB (1975) The Azores-Gibraltar plate boundary. In: Kristjansson L (ed) Geodynamics of Iceland and the North Atlantic area. Riedel, Dordrecht

Lipman PW (1971) Iron-titanium oxide phenocrysts in compositionally zoned ash-flow sheets from Southern Nevada. J Geol 79:438–456

Mazzulo LJ, Dixon SA, Lindsley DH (1975) T-fO_2 relationships

in Mn-bearing Fe-Ti oxides. Geol Soc Am Abstr with Prog 7:1192
Mueller RF (1972) Stability of biotite: a discussion. Am Mineral 57:300–316
Mysen BO (1977) The Solubility of H_2O and CO_2 under predicted magma genesis conditions and some petrological and geophysical implications. Rev Geophys Space Phys 15:351–361
Pinckney CR, Lindsley DH (1976) Effects of magnesium on iron-titanium oxides. Geol Soc Am Abstr with Prog 8:1051
Powell R (1978) Equilibrium thermodynamics in petrology. Harper & Row, London, pp 284
Powell R, Powell M (1977) Geothermometry and oxygen barometry using co-existing iron-titanium oxides: A reappraisal. Mineral Mag 41:257–263
Rutherford NF, Heming RF (1978) The volatile component of Quaternary ignimbrite magmas from the North Island, New Zealand. Contrib Mineral Petrol 65:401–411
Ryzhenko BN, Volkov VP (1971) Fugacity coefficients of some gases in a broad range of temperatures and pressures. Geochem Int 468–481
Scott S (1982) Evidence from Longonot volcano, Central Kenya, lending further support to the argument for a co-existing CO_2-rich vapour in peralkaline magma. Geol Mag 119:215–217
Self S (1976) The Recent volcanology of Terceira, Azores. J Geol Soc London 132:645–666
Sommer MA (1977) Volatiles H_2O, CO_2 and CO in silicate melt inclusions in quartz phenocrysts from the rhyolitic Bandelier air-fall and ash-flow tuff, New Mexico. J Geol 85:423–432
Sparks RSJ, Wilson L (1976) Model for ignimbrite formation by gravitational column collapse. J Geol Soc London 132:441–451
Storey M (1981) Trachytic pyroclastics from Agua de Pau volcano, Sao Miguel, Azores: evolution of a magma body over 4,000 years. Contrib Mineral Petrol 78:423–432
Stormer JC, Carmichael ISE (1970) Villiaumite and the occurrence of fluoride minerals in igneous rocks. Am Mineral 55:126–134
Stormer JC, Carmichael ISE (1971) The free-energy of sodalite and the behaviour of chloride, fluoride and sulphate in silicate magmas. Am Mineral 56:291–306
Stull DR, Prophet H (1971) Joint Army Navy Air Force thermochemical tables. 2nd edn. Washington, DC: US Govt Printing Office
Thompson JB, Waldbaum DR (1969) Mixing properties of sanidine crystalline solutions. III Calculations based on two phase data. Am Mineral 54:811–838
Toulmin P, Barton PB (1964) A thermodynamic study of pyrite and pyrrhotite. Geochim Cosmochim Acta 28:641–671
Walker GPL, Croasdale R (1971) Two plinian-type eruptions in the Azores. J Geol Soc London 127:17–55
Wilson L (1976) Explosive volcanic eruptions, III. Plinian eruption columns. Geoph JR Astron Soc 45:543–556
Wilson L (1980) Relationships between pressure, volatile content and ejecta velocity in three types of volcanic explosion. J Volcanol Geotherm Res 8:297–313
Wilson L, Sparks RSJ, Huang TC, Watkins ND (1978) The control of volcanic column heights by eruption energetics and dynamics. J Geoph Res 83:1829–1836
Wilson L, Sparks RSJ, Walker GPL (1980) Explosive volcanic eruptions, IV. The control of magma properties and conduit geometry on eruption column behaviour. Geoph JR Astron Soc 63:117–148
Wolff JA (to appear) Sampling of an alkaline magma series by individual eruptions of Tenerife, Canary Islands
Wolff JA, Wright JV (1981) Formation of the Green Tuff, Pantelleria. Bull Volcanol 44:681–690
Wolff JA, Wright JV, Smith AL, Clough BJ, Roobol MJ, Self S (to appear) Mixed pumice deposits: field characteristics. Proc IX Carib Conf Santo Domingo, 1980
Wones DR (1972) Stability of biotite: a reply. Am Mineral 57:316–317
Wones DR, Eugster HP (1965) Stability of biotite: experiment, theory and application. Am Mineral 50:1228–1272
Wright JV, Smith AL, Self S (1980) A working terminology of pyroclastic deposits. J Volcanol Geotherm Res 8:315–336

Received in revised from October 23, 1982;
Accepted November 18, 1982

Tech. Rep. Conf. Planetary Volatiles, Lunar Plan. Inst., in press

THE USE OF TEPHRA STUDIES TO DETERMINE VOLATILE RELEASE DURING LARGE EXPLOSIVE VOLCANIC ERUPTIONS. J.A. Wolff, Dept. of Geology, Imperial College, London SW7, U.K. & M. Storey, Geology Dept., Bedford College, Regent's Park, London NW1, U.K.

Outgassing at volcanoes occurs in two principal ways; via fumarolic activity and by direct release of magmatic volatiles during eruptions. Significant quantities of volatiles are released at the earth's surface by large-volume (defined for present purposes as $>10^7 m^3$ magma expressed as dense rock equivalent) explosive eruptions. Such events are characteristic of salic volcanoes in many tectonic situations, but are of infrequent occurrence (typically less than one per century per volcano). Thus in order to estimate the outward volatile flux due to eruptions at a given centre, it is necessary to employ methods applicable to the pyroclastic deposits which have resulted from prehistoric eruptions. This contribution describes a geological/petrological approach to the estimation of volatile output due to plinian eruptions, which produce extensive air-fall pumice deposits (1).

Accurate mapping of individual air-fall tephra blankets, to obtain a value for the total erupted volume of magma, is a necessary preliminary to the determination of total released volatiles. Volumes of air-fall pyroclastic deposits are usually estimated by means of an isopach map. However few deposits, unless erupted very recently, can ever be traced beyond the 10cm isopach, thus allowing no direct means of quantifying the considerable proportions of fine ash released during plinian eruptions to accumulate at considerable distances from source. Walker (2,3) has estimated the total erupted volumes of three large air-fall pumice deposits in New Zealand by a crystal concentration method. These estimates are matched by extrapolating mapped isopachs to a limiting thickness of 1mm, at a thinning rate given by the volume determination, as shown in Fig. 1 for the Taupo deposit. This thinning rate is found to be near-identical for the three New Zealand cases, and provides a method of estimating the volume of any plinian or similar deposit given sufficient near-source isopach data (e.g. ref. 4). This is particularly valuable as the more rigorous crystal concentration method can only be applied to optimum cases. We have therefore taken data on several deposits and plotted them on an area vs. thickness diagram (examples shown in Fig. 1) in order to obtain total erupted magma volume figures which take the fine ash component into account.

For fall deposits it is possible to estimate magmatic volatile contents from field data. Wilson and co-workers (5,6) have shown that the "muzzle velocity" of an explosive eruption depends on the mass eruption rate and magmatic volatile content (Fig. 2). However, dependence on eruption rate is very weak for the range of plinian eruption conditions (p on Fig. 2), and thus volatile content, assumed to be entirely water, can be estimated from muzzle velocity. The error due to variations in the volatile component composition is negligible if H_2O is >80% of the total. Muzzle velocity, μ, is given by (ref. 7): $(8gr_o\sigma_o)/(3C\rho) = \mu^2$ where r_o, σ_o are respectively the radius and density of the largest erupted clast, C is the drag coefficient, and ρ is the effective gas density in the volcanic vent (values of ρ are tabulated by Wilson, ref. 7). The required data,

J.A. WOLFF

the size and density of the largest erupted clast, may be found by extrapolation of the range dependence of clast size. Data on the three largest accessory lithic fragments (for which σ = 2.5 gcm^{-3}) at any one locality exist for several mapped deposits in the literature and an example is given in Fig. 3. The extrapolation is of the largest measured fragments. The proportion of very large fragments in these deposits is often small and thus there is a considerable error on this extrapolation. Experience shows that an error of ± a factor of 4 on the estimated largest clast size is applicable, giving an uncertainty of ± 30% relative on the final deduced volatile content of the magma. Where the field data points are closely spaced, the error is reduced. Results for selected pumice deposits are given in Table 1.

A petrological method of determining pre-eruptive magmatic volatile species in the system H-O-S in equilibrium with the phenocryst assemblage of the pumice has also been used. We have described this method, and presented data for pumice layers on some Atlantic Ocean alkaline volcanoes, elsewhere (8); the essentials are summarised here. T and fO_2 are calculated from coexisting Fe-Ti oxide compositions. fH_2O is estimated from the reaction between biotite, sanidine and magnetite, while pyrrhotite composition yields a value for fS_2. fH_2, fH_2S, fSO_2 and fSO_3 are then found by combining data on the other gas species. Magmatic water content was estimated assuming PH_2O = Ptotal; agreement with values derived from field data is good (8).

The quantitative volcanological data required for calculation of volatile output rates exist for very few salic volcanoes. We have calculated first-approximation magmatic water output rates for three volcanic islands in the Atlantic Ocean (Table 2). A possible correlation between total salic magma output (lavas, essentially water-free at eruption, plus pyroclastics) , water output, and magma composition (specifically, the degree of silica saturation) is apparent. Realisation of the significance of this correlation must await the acquisition of similar data from other centres, but Table 2 gives us a tantalising hint of the fundamental connection between availability of volatiles and the nature and intensity of volcanism.

REFERENCES

(1). Wright, J.V. et al., 1980. J. Volcan. Geotherm. Res. 8, 315-336.
(2). Walker, G.P.L., 1980. J. Volcan. Geotherm. Res. 8, 69-94.
(3). Walker, G.P.L., 1981. N.Z. J. Geol. Geophys. 24, 305-314.
(4). Walker, G.P.L. et al., 1981. Geol. Rundsch. 70, 1100-1118.
(5). Wilson, L., 1980. J. Volcan. Geotherm. Res. 8, 297-313.
(6). Wilson, L. et al., 1980. Geophys. J. R. Astron. Soc. 63, 117-148.
(7). Wilson, L., 1976. Geophys. J. R. Astron. Soc. 45, 543-556.
(8). Wolff, J.A. & Storey, M., in press. Contrib. Mineral. Petrol.
(9). Booth, B. & Walker, G.P.L., in preparation.
(10). Bloomfield, K. et al., 1977. Geol. Rundsch. 66, 120-146.
(11). Self, S., 1976. J. Geol. Soc. Lond. 132, 645-666.
(12). Booth, B. et al., 1978. Phil. Trans. R. Soc. Lond. A288, 271-319.
(13). Walker, G.P.L. & Croasdale, R., 1971. J. Geol. Soc. Lond. 127, 17-55.
(14). Wilson, L., 1978. in Thera and the Aegean World, Proc. 2nd Int. Conf., pp.221-228.

CAPTIONS

Fig. 1. Area vs. thickness plot for pumice fall deposits, the basis of the volume determinations. Taupo line is from Walker (2); distal poritons of other deposits are extrapolated parallel to Taupo. TfE, TfM are from Tenerife, Canary Islands (9); Upper Toluca is from Mexico (10); Terceira B, E, F are from Terceira, Azores (11).

Fig. 2. Relationship between muzzle velocity and mass eruption rate of explosive eruptions for four values of magmatic water content, taken from Wilson et al. (6). p indicates range of plinian mass eruption rates.

Fig. 3. Average of the three largest accessory lithic fragments found at a given locality plotted against distance from source, for a single pumice fall deposit from Sao Miguel, Azores (12). The largest measurements are extrapolated (solid line) to zero range to yield a value for the largest lithic clast which can just be supported by the eruption column at the vent; this forms the basis for the muzzle velocity calculation (7).

Table 1. Magmatic water contents and total water released during eruption for several pumice deposits from Fogo volcano, Sao Miguel and Terceira, Azores (11-13), La Primavera and Toluca, Mexico (4, 10) and the Minoan eruption, Santorini (14). The quoted volume for the Minoan pumice includes ignimbrites and pyroclastic surge deposits formed during the same eruption. Water contents estimated on the basis of field data only.

Table 2. Magma and magmatic water output rates for Tenerife, Canary Islands and Sao Miguel and Terceira, Azores, based on field and petrological data given in refs. 8,9,11,12,13. Figures for Tenerife are approximate.

Fig 1

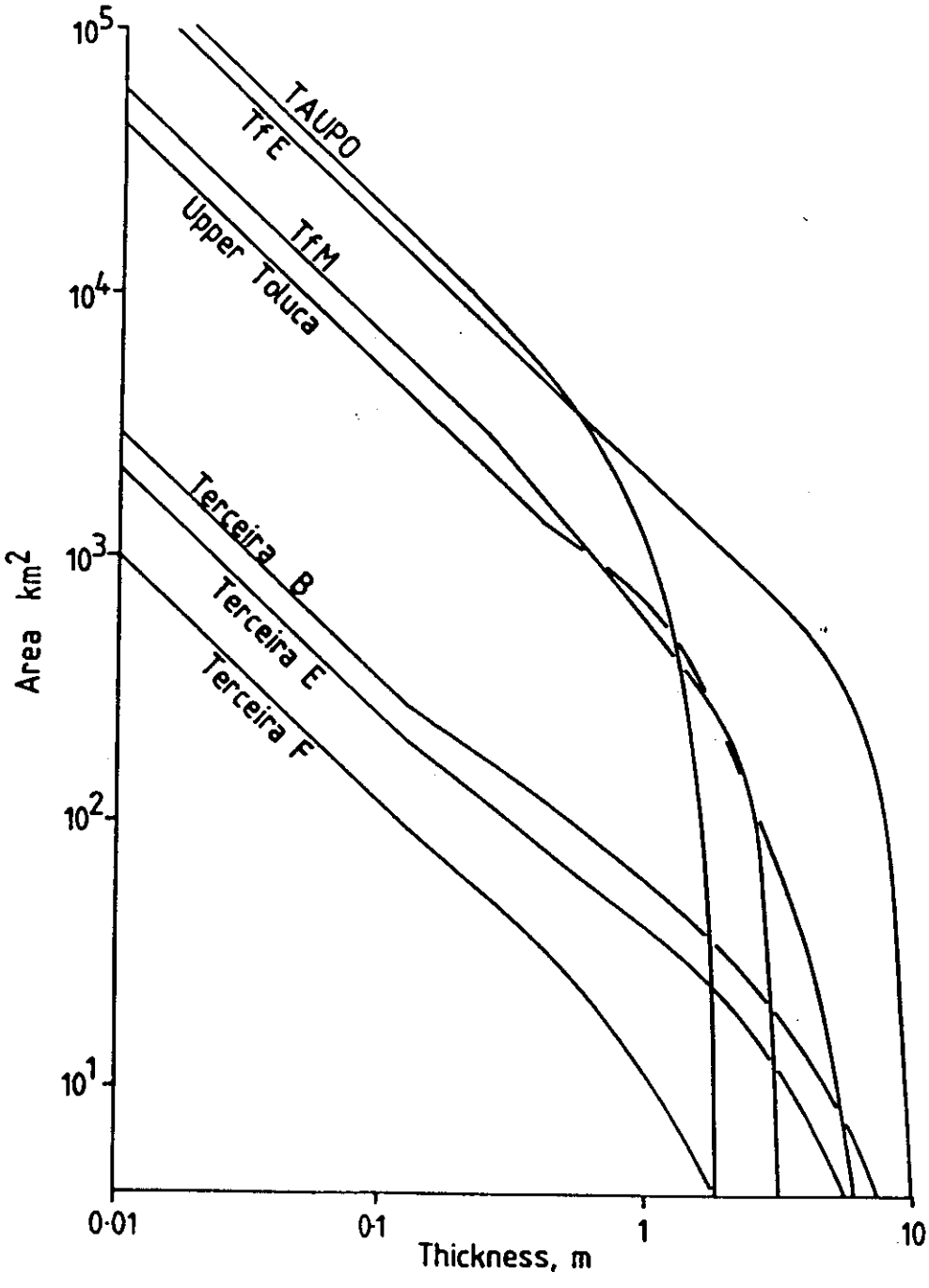
10^5
10^4
10^3
10^2
10^1
Area km^2
TAUPO
TfE
TfM
Upper Toluca
Terceira B
Terceira E
Terceira F
0·01
0·1
1
10
Thickness, m

Fig. 2.

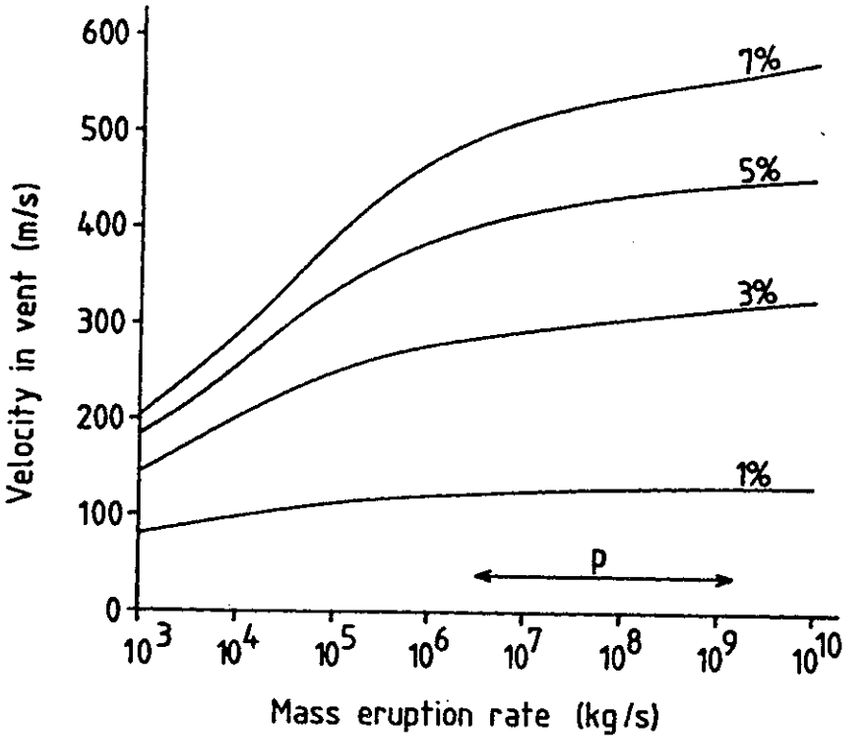
600
500
400
300
200
100
0
Velocity in vent (m/s)
7%
5%
3%
1%
p
10^3
10^4
10^5
10^6
10^7
10^8
10^9
10^{10}
Mass eruption rate (kg/s)

Fig 3

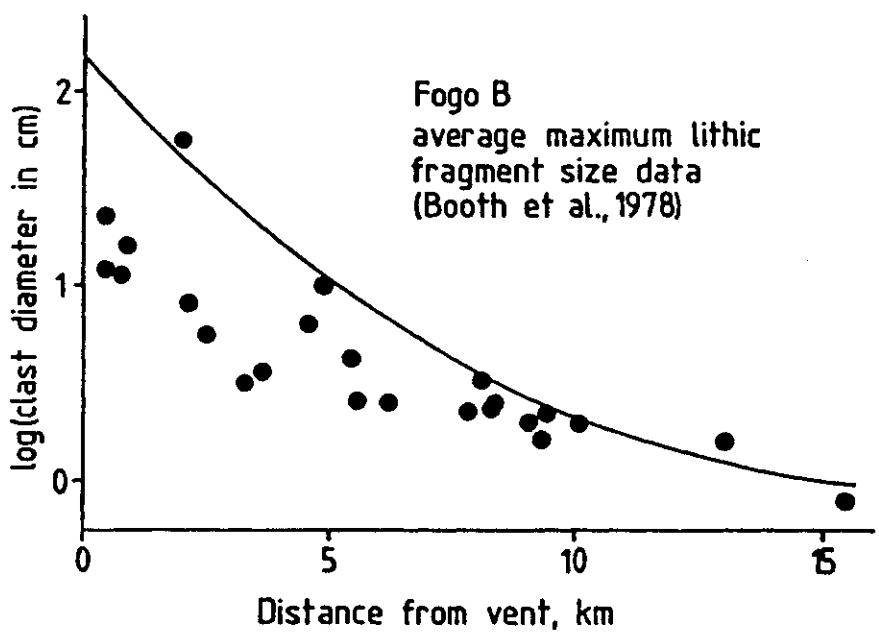
Fogo B
average maximum lithic
fragment size data
(Booth et al., 1978)
log(clast diameter in cm)
2
1
0
0
5
10
15
Distance from vent, km

Deposit	muzzle velocity, m/s	weight % magmatic water	erupted magma volume, km^3	total water released, kg
Fogo A	520	6.5	0.55	8.9×10^{10}
Fogo B	470	5.7	0.14	2.0×10^{10}
Fogo C	400	4.5	0.05	5.6×10^{9}
Fogo 1563	415	4.8	0.14	1.7×10^{10}
Fogo Congro	460	5.5	0.01	1.4×10^{9}
Terceira B	500	6.3	0.27	4.3×10^{10}
Terceira E	460	5.5	0.08	1.1×10^{10}
Terceira F	390	4.3	0.04	4.3×10^{9}
La Primavera B	>340	>3.5	14	$>1.2 \times 10^{12}$
La Primavera D	>250	>2.5	0.6	$>3.8 \times 10^{10}$
La Primavera J	>210	>2.0	3.4	$>1.7 \times 10^{11}$
Upper Toluca	500	6.3	2.7	4.2×10^{11}
Minoan	300	2.9	16	1.0×10^{12}

Table 1

Island	Tenerife	Sao Miguel	Terceira
Salic magma type	Phonolite	Trachyte-comenditic trachyte	Comenditic trachyte-pantellerite
Salic magma output rate, km^3/century	0.13	0.059	0.023
Water output rate, liquid km^3/century	0.017	0.007	0.0007
Volume ratio pyroclastics/(pyroclastics lavas) for salic magma	0.8	0.88	0.23

Table 2

Journal of Volcanology and Geothermal Research, 10 (1981) 13—34
Elsevier Scientific Publishing Company, Amsterdam — Printed in Belgium

RHEOMORPHISM OF WELDED TUFFS

J.A. WOLFF and J.V. WRIGHT*

Department of Geology, Imperial College, London SW7 2BP (Great Britain)

(Received June 5, 1980; revised and accepted September 15, 1980)

ABSTRACT

Wolff, J.A. and Wright, J.V., 1981. Rheomorphism of welded tuffs. J. Volcanol. Geotherm, Res., 10: 13—34.

Peralkaline welded tuffs from the islands of Gran Canaria, Canary Islands, and Pantelleria, Italy, show abundant evidence for post-depositional flow. It is demonstrated that rheomorphism, or secondary mass flowage, can occur in welded tuffs of ignimbrite and air-fall origin. The presence of a linear fabric is taken as the diagnostic criterion for the recognition of the process. Deposition on a slope is an essential condition for the development of rheomorphism after compaction and welding. Internal structures produced during rheomorphic flow can be studied by the methods of structural geology and show similar dispositions to comparable features in sedimentary slump sheets. It is shown that secondary flowage can occur in welded tuffs emplaced on gentle slopes, provided that the apparent viscosity of the magma is sufficiently low. Compositional factors favor the development of rheomorphism in densely welded tuffs of peralkaline type.

INTRODUCTION

Rheomorphism ("flow change") of welded tuff is here defined as secondary mass flowage of a welded tuff body, immediately following deposition, as a coherent viscous fluid. The term *rheoignimbrite* was first introduced by Rittman (1958) to describe welded ignimbrites showing secondary flowage features. Although Rittman's type examples from Tuscany appear to be lava extrusions (G.P.L. Walker, personal communication), the term is valid and rheoignimbrites or similar rocks have been described from a number of areas and geological ages (Rutten and Van Everdingen, 1961; Walker and Swanson, 1968; Villari, 1969; Lock, 1972; Chapin and Lowell, 1979). Herein, welded air-fall tuffs (Sparks and Wright, 1979) showing rheomorphic structures are described, and we therefore prefer to use *rheomorphic welded tuff* as a general lithological description of the rock, with no genetic implications of emplacement mechanism. This distinction is important as it may be difficult in some cases to

*Present address: Department of Geology, University of Puerto Rico, Mayaguez, PR 00708 (U.S.A.).

0377-0273/81/0000—0000/$02.50 © 1981 Elsevier Scientific Publishing Company

distinguish between densely welded ignimbrites and welded air-fall tuffs emplaced on flat terrain, with no geometrical control to distinguish the two (Wright et al., 1980), especially if non-welded or partially welded tephra were not present.

In this paper, rheomorphic structures within welded ignimbrites and welded air-fall tuffs from Gran Canaria and Pantelleria respectively are described and discussed. Rheomorphic welded tuffs are characterized by stretched fiamme which define a lineation parallel to the flowage direction. Flowage is capable of producing folding and other internal flow structures similar to those found in salic lava extrusions (Christiansen and Lipman, 1966). A major thrust of this paper, apparent in our definition, is that rheomorphism is a secondary process. Previous workers have constantly debated whether flowage is secondary (Rittman, 1958, 1962; Rutten and Van Everdingen, 1961; Lock, 1972), or primary (Schmincke and Swanson, 1967, Noble, 1968; Walker and Swanson, 1968; Parker, 1972; Deal, 1973; Chapin and Lowell, 1979). Primary flow can only be applicable to rheoignimbrites as the flowage structures are thought to develop in the last stages of movement as a pyroclastic flow.

GEOLOGICAL SETTING

The late Miocene/early Pliocene peralkaline welded tuffs of southwest Gran Canaria (Fig. 1) have been previously described by Schmincke and Swanson (1967) and Schmincke (1969). They are parts of extensive ignimbrite sheets and show the poor sorting, infilling of underlying topography, and fine-grained basal layers typical of deposition by pyroclastic flows (Sparks et al., 1973; Sparks, 1976). Flowage structures within the welded sheets were described in detail by Schmincke and Swanson (1967), who considered them to be primary features generated at the end stages of pyroclastic flows as they gradually slowed to a halt. With one exception, these structures are here re-interpreted as being due to rheomorphism, and are therefore secondary phenomena. Six major ignimbrite cooling units (Smith, 1960) have been distinguished, five of which are rheomorphic. At least one other thin (4 m) unit also shows rheomorphic structures.

Borsi et al. (1963) first recognized the occurrence of welded tuffs among the strongly peralkaline rocks of Pantelleria, interpreted them as ignimbrites, and noted the presence of rheomorphic structures. Pantelleria contains a plethora of welded tuffs, all of which are now thought to be of air-fall origin, because of their depositional and grain-size characteristics (Sparks and Wright, 1979; Wright, 1980). Seventeen welded tuffs at least have been recognized on the island, five of these being rheomorphic. Most of the data from Pantelleria in this paper comes from the Green tuff (welded tuff B of Wright, 1980, and see also for distribution and location maps) which is the youngest densely welded tuff and the most extensively exposed. This horizon has been previously described by Villari (1969, 1974) who illustrated "turbulent flowage structures".

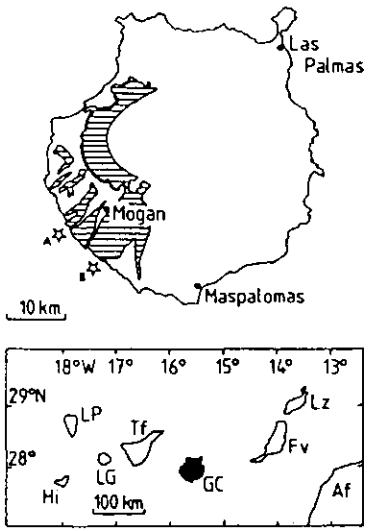

Fig. 1. Distribution map showing late Miocene/early Pliocene ignimbrites of Gran Canaria (taken from Schmincke and Swanson, 1967). Horizontal rule: welded ignimbrites; thick line: caldera fault; *A—B* = coastal section studied and described in this paper (by J.A. Wolff). Inset shows location of Gran Canaria (*GC*); *Af* = Africa, *Lz* = Lanzarote, *Fu* = Fuertaventura; *Tf* = Tenerife; *LG* = La Gomera; *LP* = La Palma; *Hi* = Hierro.

RHEOMORPHIC STRUCTURES

Extensional structures

Compaction and welding of tuff is a simple flattening process giving the classic eutaxitic texture (Ragan and Sheridan, 1972); the resultant strain ellipsoid is oblate with $K \simeq 0$ (Flinn, 1962; Ramsay, 1967, p. 136). Rheomorphism imposes a secondary stretching deformation on this, resulting in a tendency towards prolateness and hence increasing K value (Fig. 2). It is manifested in the field as a variably-developed linear fabric, the presence of which is taken as the essential criterion for the recognition of rheomorphism. The corollary is that deposition on a slope is a necessary condition for rheomorphism, and controls the flowage of the welded sheet (Fig. 3); as will be shown later, slope need only be slight. Slope also exerts a control on thickness (Fig. 4); stretching implies thinning of the original compacted sheet, and rheomorphic welded air-fall tuffs which can be traced over undulating topography show rapid thinning towards steep slopes.

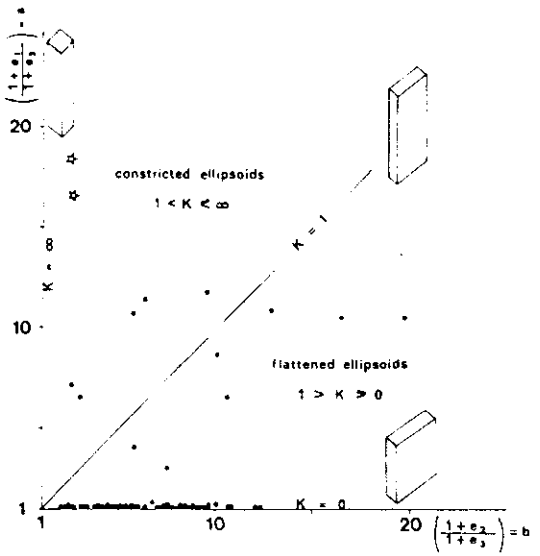

Fig. 2. Finite strain data from the welded air-fall tuffs of Pantelleria. The plot represents ellipsoids in terms of the ratios of principle strain, $(1 + e_1)/(1 + e_2) = a$ and $(1 + e_2)/(1 + e_3) = b$ (after Ramsay, 1967). K is the slope of the line joining the plot of the ellipsoid to the point (1, 1) after Flinn (1962). Closed circles: fiamme having a purely compactional deformation; closed squares: rheomorphic fiamme; stars: vesicles in rheomorphic zones. Vesicles were formed during rheomorphism and only record the later stretching deformation, with no evidence of the earlier compactional deformation.

Well developed lineations approach a "rodding"-type fabric of closely-spaced parallel ridges, a few millimeters wide and tens of centimeters long, on the foliation surface (Fig. 5A). The lineation directions are dispersed within the plane of the welded sheet, the mean orientation being parallel to the maximum slope, and therefore to the movement direction (Fig. 6). In general, stronger developed lineations show less scatter. The accompanying foliation parallels slope (Fig. 6) and is commonly intense, giving the rocks a well-developed layering and a phyllitic appearance in the field.

Late-stage tension cracks (Fig. 5B) occur in both matrix and fiamme; the movement direction indicated by the dilation of these is generally consistent with that measured from slope and lineation (Fig. 7). In side elevation, cracked fiamme are separated into discrete boudins which are frequently rotated into the flow direction; this rotation is also seen with lithic clasts. Such features occurring in rheomorphic tuffs in ancient deformed volcanic terrains could be used as indicators of flowage direction and therefore paleoslope. Rarely, however, rotation is in the opposite sense to regional flowage, indicating local perturbations in the velocity profile of the rheomorphic flow. Internal boudins (Cobbold et al., 1971) observed within the body of a flow indicate appreciable mechanical anisotropy between layers during rheomorphism.

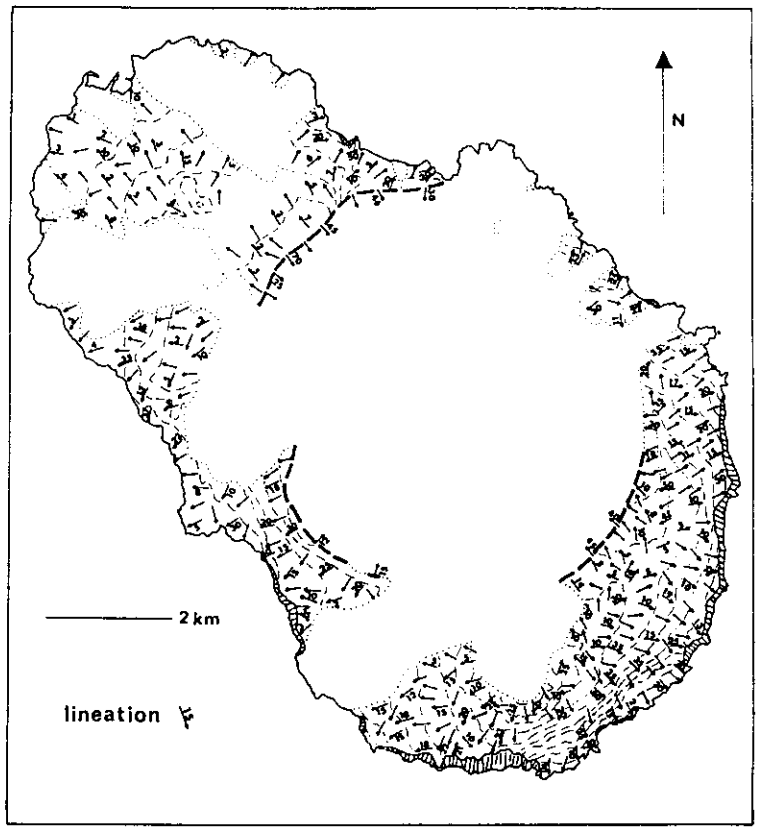

Fig. 3. Generalized lineation map of the Green tuff, Pantelleria, which shows the maximum extension direction of fiamme and indicates the flowage direction; numbers on arrows indicate plunge of lineation. Dashed lines are contours of 50-m intervals. Flowage direction can be seen to be controlled by slope. Unornamented areas are other volcanic rocks (see Wright, 1980, for geological map).

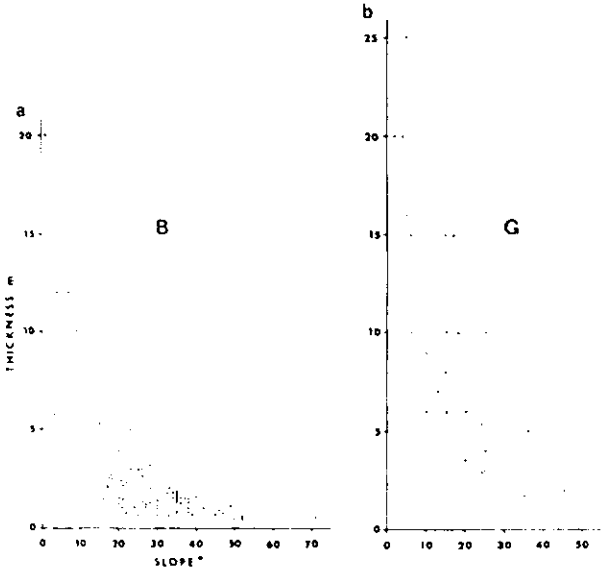

Fig. 4. Relation between thickness and slope of (a) the Green tuff (welded tuff B), Pantelleria, and (b) welded tuff G, Pantelleria (see Wright, 1980, for details of stratigraphy).

Flow folds

Internal folding during flowage is a common feature of salic lavas and high-level intrusions. In the rheomorphic tuffs it is manifested as folding of fiamme (Fig. 8A), foliation (Fig. 8B), lineations, and seen on Gran Canaria *welding-zone boundaries* (Smith, 1960).

The distribution of folds is partly slope-controlled. On Pantelleria, folding is typically found where the welded sheet has flowed into a depression; on Gran Canaria, where the underlying topography is generally smooth, localized "pockets" of folding are found associated with small irregularities in the pre-existing surface. Folds are also found in the pressure shadows of lithic inclusions. Fold size varies from a few millimeters to tens of meters, the majority being in the sub-1 m size range. The size frequency distribution is approximately log-normal (J.A. Wolff, unpublished data; Wright, 1979), as is the case for minor tectonic folds (Huddleston, 1973c) and sedimentary slump folds (Woodcock, 1976). Fold hinges are dispersed in the plane of the welded tuff sheet and are sub-horizontal to gently plunging (Fleuty, 1964) (Fig. 6). The means of the hinge directions are highly oblique to near normal to the movement direction as defined by slope, and the perpendicular to the mean axis thus gives an

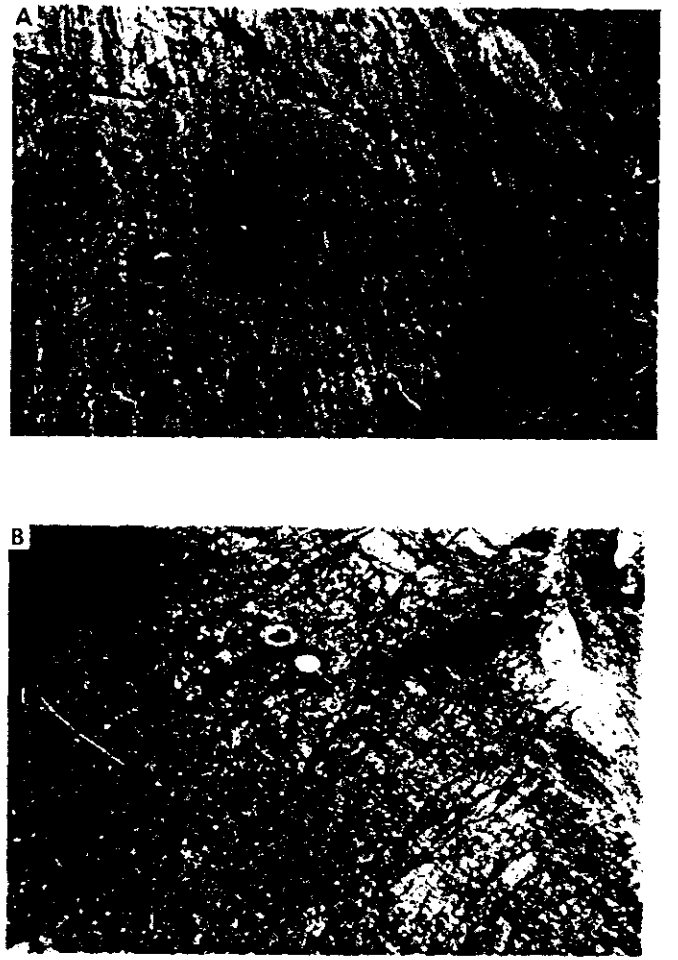

Fig. 5. Extensional structures in rheomorphic welded tuffs. A. Well-developed lineation of stretched fiamme in the Green tuff, Pantelleria. Extended length of compass is 15 cm. B. Late-stage tension cracks in the Green tuff; compass points in the maximum extension direction.

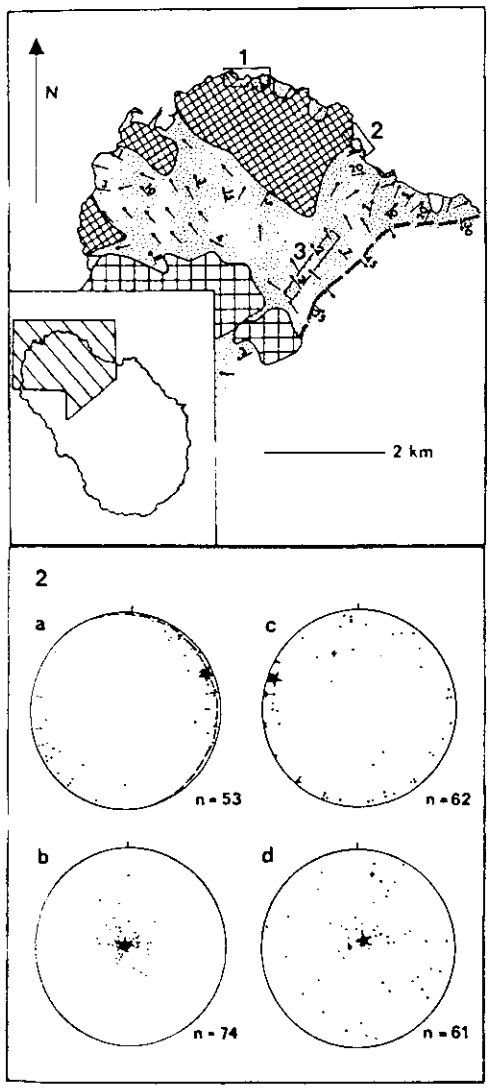

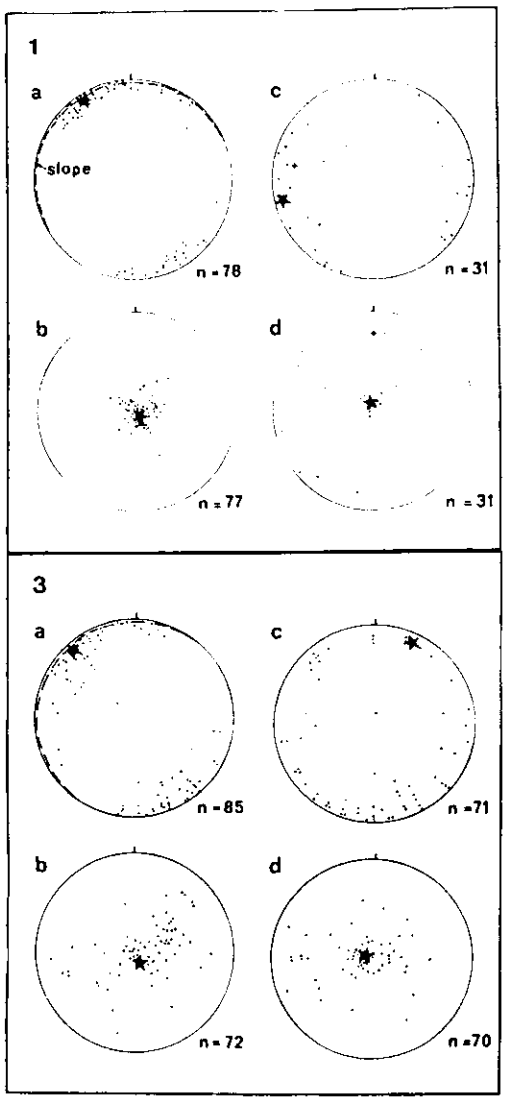

Fig. 6. Location of three areas where detailed structural analysis of the Green tuff has been made, together with generalized lineation trends in the northeast of Pantelleria (from Fig. 3); stipple: Green tuff; diamond rule: younger basalt lava and scoria; squared rule: younger rhyolite lava. Stereograms are lower hemisphere equal area plots of orientation data from the three areas: (a) lineations, (b) poles to foliation, (c) fold hinge lines, (d) poles to axial surfaces. Crosses are for refolds; stars indicate the means. Dashed lines on plots of lineations are maximum slope directions.

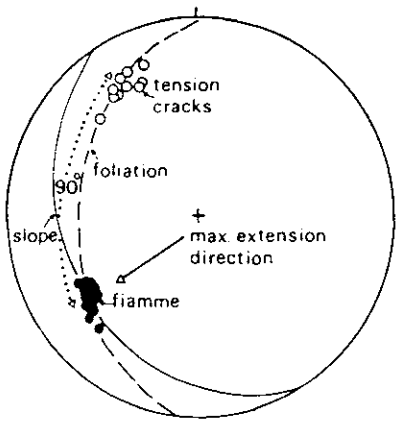

Fig. 7. Lower hemisphere equal area plot of orientation data in Fig. 5B.

approximate estimate of the movement axis. The dispersal is due to fold initiation at any angle to flow direction within the plane of the sheet; with continuing movement, the hinges will gradually rotate until they are perpendicular to the flow direction (Borradaile, 1972; Sanderson, 1973). The dip of fold axial surfaces varies from upright to recumbent (Fleuty, 1964) (Fig. 6). There is some correlation between interlimb angle and fold attitude (Fig. 9), tighter folds having more gently inclined axial surfaces than open folds. This

Fig. 8. Flow folds in rheomorphic welded tuffs. A. Folded fiamme in a welded ignimbrite from Gran Canaria. Diameter of film cap is 3.5 cm. B. Folded foliation in a tight overturned fold nearing recumbency (Fleuty, 1964) in the Green tuff, Pantelleria. Extended length of compass is 15 cm. C. Refolded fold in the Green tuff showing a type 2 interference pattern (Ramsay, 1967).

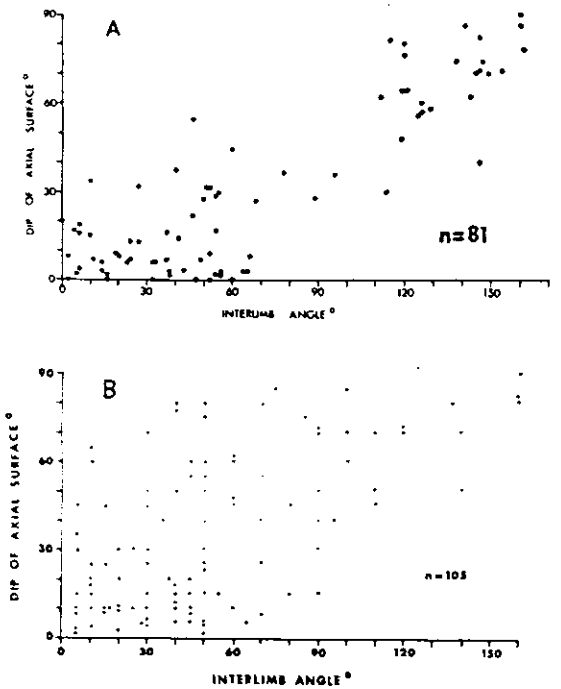

Fig. 9. Relation between the dip of the axial surface and the interlimb angle of folds in welded ignimbrites of southwest Gran Canaria (A), and the Green tuff, Pantelleria (B).

indicates that folds were initiated as gentle upright structures in the plane of the welded tuff sheet; with progressive deformation, tightening and overturning of the folds towards recumbency occurred. Slump folds show an analogous deformation history (Woodcock, 1976).

Fold surface shapes have been classified according to the harmonic analysis method of Huddleston (1973a). "Quarter wavelength units" of folds have been fitted to a function of the form:

$$f(x) = b_1 \sin x + b_3 \sin 3x + \ldots$$

where b_1 and b_3 are constants for a given unit. Results are shown on a plot of b_1 vs. b_3 calibrated by the "shape" and "amplitude" factors of Huddleston (Fig. 10). The range of shapes, from variable at low amplitude towards semi-elliptical at high amplitude, is similar to that found from small-scale tectonic folds (Huddleston, 1973b) and sedimentary slump folds (Woodcock, 1976).

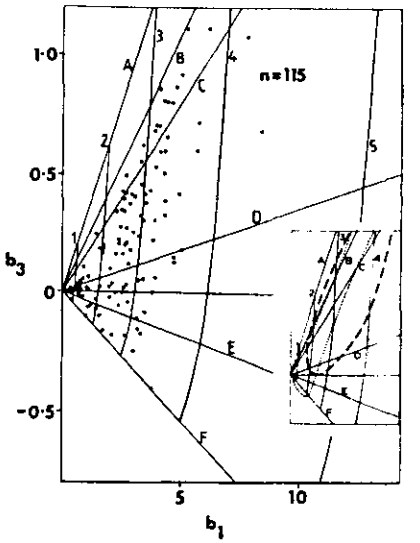

Fig. 10. Plot of harmonic coefficients b_1 vs. b_3 for rheomorphic folds in the welded tuffs of Gran Canaria and Pantelleria. The folds shapes represented by the shape factors A—F of Huddleston (1973a) are: A = box folds; C = semi-ellipses; D = parabolas; b_3 = 0: sine waves; F = chevron folds. *Inset*: dashed line: field of small scale tectonic folds (Huddleston, 1973b); dotted line: field of sedimentary slump folds (Woodcock, 1976).

However, rheomorphic folds show a larger amplitude variation for any one shape.

Fold layer shapes occupy the whole range of Ramsay's classification (1967, pp. 365—372), class 1c being the most common (Fig. 11). In the ignimbrites class 1b (parallel) folds, in association with class 3 layers, are generally restricted to individual fiamme folded on the centimeter scale (Fig. 11e). This reflects a competence contrast between fiamme and matrix; fiamme may be either more or less competent than the matrix. Such folds are rare in the Pantelleria rocks. Class 2 (similar folds are found in both areas, particularly where the texture is folded on the scale of tens of centimeters to a few meters. Where recumbent, such folds may propagate along the axial plane for several tens of meters.

Development of both similar and parallel styles indicates the operation of both heterogeneous simple shear and flexural slip mechanisms respectively during folding. The importance of heterogeneous simple shear is seen in the folded-lineation patterns of large folds (Fig. 12), deformed lineation loci showing no marked discontinuity across the axial surface; the small discontinuity in Fig. 12b suggests a minor buckling component in fold development

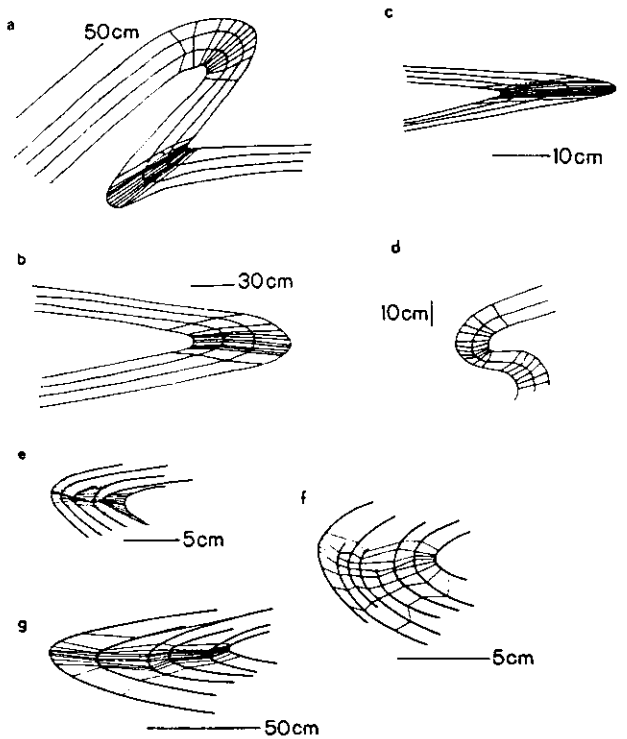

Fig. 11. Examples of rheomorphic folds with dip isogons constructed at 15° intervals. (a) Class 1c folds, with divergent dip isogons, and class 2 (similar) fold, with nearly parallel dip isogons, Green tuff, Pantelleria. (b) Class 1c fold, Green tuff, Pantelleria. (c) Class 2 fold, Green tuff, Pantelleria. (d) Class 1 folds, Green tuff, Pantelleria. (e) Alternating class 3 layers, with convergent dip isogons, and class 1 layers, Gran Canaria ignimbrite. (f) Class 1 fold, Gran Canaria ignimbrite. (g) Approximately similar fold, Gran Canaria ignimbrite.

(Ramsey, 1967, p. 463). Heterogeneous simple shear is, however, the dominant folding mechanism in the welded sheets.

Some of the larger folds have associated minor folds; the fold axes and axial planes of these are parallel to the major structure. An axial planar cleavage is also sometimes found.

Interference patterns, due to superimposition of folds, are found and may be locally abundant (Fig. 8C). Types 2 and 3 (Ramsay, 1967, pp. 520—534) are the most common. Both types are formed when recumbent folds are

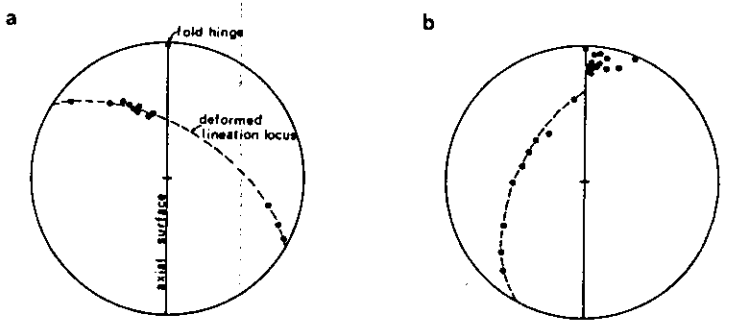

Fig. 12. Lower hemisphere equal area plots of two examples of deformed lineation loci from the Green tuff, Pantelleria.

refolded by new structures with steeply inclined axial surfaces, and their presence is thus consistent with continuous fold initiation and development over a period of time. Occasional patterns of great complexity are also seen, suggesting several folding deformations.

The analogy between deformational processes operating in rheomorphic tuffs and sedimentary slump sheets is considered to be good; both are gravity-induced sheet deformations of materials with high bulk ductilities (compared with those normally encountered in structural geology). Fold styles have been examined in some detail, to see whether they exhibit any characteristics diagnostic of their origin. However, as with slump folds (Woodcock, 1976), there is no criterion of style by which folds in rheomorphic tuffs may be distinguished from tectonic structures in ancient deformed volcanic terrains; large (10—50 m wavelength) rheomorphic folds which deform welding-zone boundaries could easily be misinterpreted as having a tectonic origin in such cases.

Imbricate structure

This is characterized by eutaxitic texture having a consistent upslope dip of about 30°; it is commonly found in the basal 1 m of the densely welded zone and persists to the very base of this zone (Fig. 13). It is restricted to the ignimbrites, and its occurrence appears to preclude the presence of any other rheomorphic feature. It may persist throughout the densely welded zone where this is unusually thin (< 5 m). Generally, however, it passes upwards into densely foliated rock with decreasing dip and increasing flattening of fiamme. Rarely, where individual flow units can be distinguished, the structure is seen in the basal part of several flows in the same cooling unit. These features indicate that the structure forms rapidly and during the initial stages of welding.

Fig. 13. Imbricated fiamme in basal part of a welded ignimbrite, Gran Canaria. *1* = underlying ignimbrite, *2* = basal non-welded zone, *3* = imbricate structure, *4* = foliated densely welded tuff. Diameter of film cap is 3.5 cm. The primary pyroclastic flow moved from left to right in the photograph.

The mechanism suggested here is shearing of individual clasts as the primary flow collapses and starts to weld (see "Discussion"). Hence the structure is not, strictly speaking, a rheomorphic one; however it is only likely to form in those ignimbrites which are composed of material sufficiently plastic to flow after deposition and welding.

DISCUSSION

Compaction during welding of tuff can be modelled by the expression (Riehle, 1973):

$$\beta = \frac{\sigma_z(\Delta t)}{\ln(P_f - 1)/(P_i - 1)} \qquad (1)$$

where β is the compaction coefficient, σ_z is the vertical uniaxial stress, and P_i, P_f are the tuff porosities before and after the time increment Δt respectively. Riehle gives values for β of 10^{10}–10^{12} P for rhyolites over a range of temperatures and clast porosities at p_{H_2O} = 10 bars. The compaction coefficient is related to clast viscosity. Peralkaline melts have lower viscosities than calc-alkaline rhyolites (Fig. 14) and a value of 10^{10} P is here adopted as the maximum compaction coefficient of peralkaline pyroclasts at near-liquidus temperatures. From equation (1), complete compaction occurs in less than 20 hours for an uniaxial stress of 1 bar (the load pressure produced by 4 m

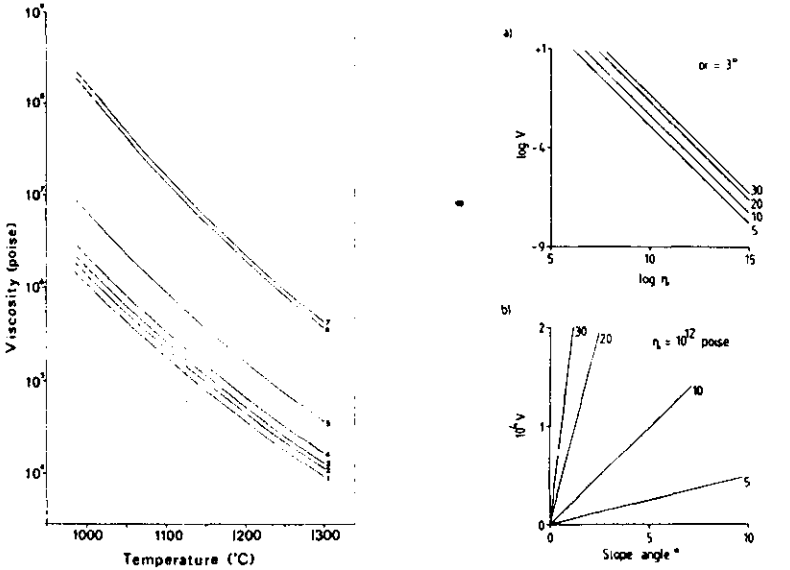

Fig. 14. Viscosity/temperature curves calculated by the method of Shaw (1972) for the following analyses recalculated volatile-free: *1*; *3* = the Green tuff, Pantelleria (Villari, 1974); *2* = the Fantale tuff, Ethiopia (Gibson, 1970); *4*, *5* = Gran Canaria ignimbrites (Schmincke and Swanson, 1967); *6* = average rhyolite (from Carmichael et al., 1974, p. 9); *7* = average New Zealand ignimbrite (from Carmichael et al., 1974; p. 554). Analyses *1*—*5* are peralkaline in composition; *6* and *7* are calc-alkaline. Dotted extrapolation of curves is for subliquidus temperatures. The model assumes Newtonian rheology which is not valid for real silicate liquids. However, rheological contrasts between different compositions are considered to be represented in a qualitative manner.

Fig. 15. Flow velocities computed from equation (2) for Newtonian liquids, for flows of 5, 10, 15, 20, and 30 m depth. (a) Flow velocity as a function of viscosity for a slope of 3°. (b) Flow velocity as a function of slope for a liquid of viscosity 10^{12} P.

dense rock equivalent of overlying tuff). Riehle's temperature profiles demonstrate that the greater part of a welded tuff sheet initially 10 m thick remains at the emplacement temperature for several days after formation. Hence for most of this time the bulk of the sheet will have zero porosity and its physical properties will be those of an equivalent lava.

The flow velocity of a Newtonian fluid is given by:

$$V = \frac{\rho g \sin \alpha d^2}{n\eta} \qquad (2)$$

where ρ is the density, α is the slope, d is the flow depth, η is the viscosity and n is a factor dependent on channel morphology. For a wide channel, $n = 2$. The dependence of flow velocity on (a) slope, and (b) viscosity, computed from equation (2), is shown in Fig. 15. For viscosities $> 10^6$ P, these velocities are attained from rest in a few seconds or less. Use of liquidus viscosities (Fig. 14) calculated by the method of Shaw (1972) gives velocities which suggest that several kilometers of lateral movement can occur in the time available during cooling of the welded sheets. However, the maximum flow distance compatible with field evidence is a few hundred meters in the case of the Green tuff of Pantelleria; in other cases a figure of tens of meters is more realistic. Hence apparent viscosities of 10^{11}–10^{12} P *at the prevailing strain rates* are considered to be more appropriate; composition-based calculations of high viscosities at near-liquidus temperatures are subject to large errors (Shaw, 1972).

In general, magmas at the earth's surface have a non-Newtonian rheology (Hulme, 1974). Hulme (1974) has shown that lavas approximate to Bingham materials with a finite yield stress. The yield stress shows a direct relation to SiO_2 content of the lava (Hulme and Fielder, 1977). The required yield stresses of the magmas considered here (approximately 5×10^3 N m^{-2}) are anomalously low compared with high-SiO_2 lavas. However, calculated Newtonian viscosities of peralkaline melts are much lower than for other silicic types (Fig. 14). The melt structure factors affecting yield stress, in the Bingham model, will be broadly the same as those affecting viscosity, in the Newtonian model. Also, peralkaline magmas have appreciable fluorine contents (Carmichael et al., 1974, p. 318). Fluorine in silicate melts is an extremely effective network modifier and is likely to have a drastic effect on rheology (R. Lowry, personal communication). In the absence of more quantitative data, it is sufficient to note that low yield stresses for peralkaline liquids are not inconsistent with their compositions. The situation is complicated by the assumption of perfect Bingham behavior; strongly pseudo-plastic behavior (Fig. 16) is more probable. Apparent viscosities of Bingham and pseudo-plastic materials are strain-rate dependent (Fig. 16) and are high in low strain-rate situations, such as compaction and rheomorphism.

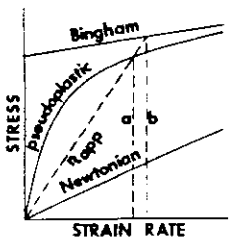

Fig. 16. Flow curves for a Bingham, a pseudo-plastic, and a Newtonian material (Skelland, 1967); η_{app} is the apparent viscosity of the pseudoplastic material at strain rate a, and of the Bingham material at strain rate b.

At higher strain rates, for example in a volcanic conduit, apparent viscosities will be much lower.

It is now possible to explain the generation of the imbricate structure found in the ignimbrites. Sparks (1976), Wright (1979), Wright and Walker (1981), and Wilson (1980) emphasize that pyroclastic flows are emplaced as high concentration debris flows in many ways analogous to mud flows. Such flows halt rapidly rather than gradually, resulting in a high shear stress being momentarily imposed on the constituent clasts. Transient clast strain rates will be high and shearing of clasts results, giving a uniformly oriented fabric. The fabric is preserved at the base of the welded sheet, where cooling is sufficiently rapid to preclude the onset of rheomorphism. Self (1973) invoked shearing of clasts during primary flowage to account for the presence of a planar fabric in the basal part of the peralkaline Lajes ignimbrite, Terceira, not compactional flattening.

CONCLUSIONS

Schmincke and Swanson (1967) invoked late-stage primary viscous flowage to account for the features of the Gran Canaria welded ignimbrites. We have shown however, that in these specific examples, and in general, such structures can be generated by rheomorphic (secondary) flowage over a wide area in welded tuffs emplaced on gentle slopes, provided that the initial temperature is sufficiently high. Flowage structures in welded air-fall tuffs can only be interpreted as a secondary phenomenon, after deposition and initial compactional deformation. The correspondence between flowage structures in welded ignimbrites and welded air-fall tuffs indicates that a common origin is probable. There is a close similarity in structural style between rheomorphic welded tuffs and other analogous gravity-induced sheet deformations (see Woodcock, 1976).

We regard the distinction between primary and secondary flow to be important. Only one of the structures (imbrication of fiamme) we describe is a primary flowage feature. When one considers the emplacement and depositional mechanisms of pyroclastic flows it is unlikely that primary laminar flowage structures could form. Both field studies (Sparks, 1976; Wright, 1979; Wright and Walker, 1981) and laboratory fluidization experiments (Wilson, 1980) indicate that pyroclastic flows do not gradually slow down, but halt suddenly by "freezing" of the flow; the imbricate structures described form as a consequence of this sudden freezing. Directional fabrics in welded tuffs are controlled by palaeoslope. Although, because ignimbrites generally slope away from their source volcano, these are likely to reflect movement direction as suggested by other workers (Elston and Smith, 1970; Rhodes and Smith, 1972).

Our studies and others (Schmincke and Swanson, 1967; Walker and Swanson, 1968; Parker, 1972) have indicated a correlation between the occurrence of rheomorphism in welded tuffs and peralkaline magmas. This, apparently, is not

always the case. The welded tuff showing rheomorphic structures described by Chapin and Lowell (1979) is a calc-alkaline rhyolite. Several Icelandic tuffs show rheomorphic structures yet are not peralkaline (H. Sigurdsson, personal communication). These include the rhyolitic Askja welded air-fall tuff (Sparks and Wright, 1979) in which case superheating brought about by mixing with hotter basic magma may have promoted lower glass viscosities; although, rheomorphic structures in the Askja welded tuff cannot be compared to the scale of structures described herein. We can conclude, however, that compositional factors favour the development of rheomorphism in densely welded tuffs of peralkaline type.

The answer to the question of why many welded tuffs in other areas, such as the thick cooling units seen in the western United States, do not exhibit the rheomorphic structures we have described is considered to lie in the non-Newtonian rheology of their magmas; at stresses generated by gravity in welded tuffs, apparent viscosities are extremely high for the majority of magmas. Also, heat is efficiently retained by pyroclasts during the emplacement of gas-poor peralkaline ignimbrites (Sparks et al., 1978). Calc-alkaline rhyolites generally contain more water than their peralkaline equivalents and cool considerably during emplacement (Sparks et al., 1978) to a temperature several hundred degrees below the rhyolite liquidus. Thus even in thick calc-alkaline sheets the process of welding and rheomorphism may be halted at an early stage by devitrification and crystallization of the groundmass.

ACKNOWLEDGEMENTS

This work was funded by the Natural Environmental Research Council of Great Britain. We would like to thank Prof. G.P.L. Walker, Dr. S. Self, C.J.N. Wilson, and Dr. R. Lowry for useful discussions. Both S. Self and C.J.N. Wilson gave invaluable reviews of an earlier version of the manuscript which we appreciate.

REFERENCES

Borradaile, G.J., 1972. Variably orientated co-planar folds. Geol. Mag., 109: 89—98.
Borsi, S., Marinelli, G., Mazzoncini, F., Mittempergher, M. and Tedesco, C., 1963. Reconnaissance of some ignimbrites of Pantelleria and Eolian Islands. Bull. Volcanol., 25: 359—367.
Carmichael, I.S.E., Turner, F.J. and Verhoogen, J., 1974. Igneous Petrology. McGraw-Hill, New York, N.Y., 739 pp.
Chapin, C.E. and Lowell, G.R., 1979. Primary and secondary flow structures in ash-flow tuffs of the Gribbles Run paleovalley, central Colorado. In: C.E. Chapin and W.E. Elston (Editors), Ash-Flow Tuffs. Geol. Soc. Am., Spec. Paper, 180: 137—154.
Christiansen, R.L. and Lipman, P.W., 1966. Emplacement and thermal history of a rhyolite lava flow near Fortymile Canyon, Southern Nevada. Geol. Soc. Am. Bull., 77: 671—684.
Cobbold, P.R., Cosgrove, J.W. and Summers, J.M., 1971. Development of internal structures in deformed anisotropic rocks. Tectonophysics, 12: 23—53.

Deal, E.G., 1973. Primary laminar flow structures in the rhyolite ash-flow tuff of A.L. Peak, San Mateo Mountains, New Mexico. Geol. Soc. Am., Abstr. Progr., 5: 475.
Elston, W.E. and Smith, E.I., 1970. Determination of flow direction of rhyolitic ash-flow tuffs from fluidal textures. Geol. Soc. Am. Bull., 81: 3393—3406.
Fleuty, M.J., 1964. The description of folds. Proc. Geol. Assoc., 75: 461—492.
Flinn, D., 1962. On folding during three-dimensional progressive deformation. Q.J. Geol. Soc. London, 118: 385—433.
Gibson, I.L., 1970. A pantelleritic welded ash-flow from the Ethiopian Rift Valley. Contrib. Mineral. Petrol., 23: 89—111.
Huddleston, P.J., 1973a. Fold morphology and some geometrical implications of theories of fold development. Tectonophysics, 16: 1—46.
Huddleston, P.J., 1973b. An analysis of single layer folds developed experimentally in viscous media. Tectonophysics, 16: 189—214.
Huddleston, P.J., 1973c. An analysis and interpretation of minor folds in the Moine rocks of Monar, Scotland. Tectonophysics, 17: 89—132.
Hulme, G., 1974. The interpretation of lava flow morphology. Geophys. J. R. Astron. Soc., 39: 361—383.
Hulme, G. and Fielder, G., 1977. Effusion rates and rheology of lunar lavas. Philos. Trans. R. Soc. London, Ser. A, 285: 227—234.
Lock, B.E., 1972. A Lower Palaeozoic rheo-ignimbrite from White Bay, Newfoundland. Can. J. Earth Sci., 9: 1495—1503.
McCall, G.J.H., 1964. Froth flows in Kenya. Geol. Rundsch., 54: 1148—1195.
Noble, D.C., 1968. Laminar viscous flowage structures in ash-flow tuffs from Gran Canaria, Canary Islands: a discussion. J. Geol., 76: 721—723.
Parker, D.F., 1972. Laminar flow in a peralkaline ash-flow sheet, Davis Mountains, Texas. Geol. Soc. Am., Abstr. Progr., 4: 288.
Ragan, D.M. and Sheridan, M.F., 1972. Compaction of the Bishop Tuff, California. Geol. Soc. Am. Bull., 83: 95—106.
Ramsay, J.G., 1967. Folding and Fracturing of Rocks. McGraw-Hill, New York, N.Y., 568 pp.
Rhodes, R.C. and Smith, E.I., 1972. Distribution and directional fabric of ash-flow sheets in the north-western Mogollon Plateau, New Mexico. Geol. Soc. Am. Bull., 83: 1863—1868.
Riehle, J.R., 1973. Calculated compaction profiles of rhyolitic ash-flow tuffs. Geol. Soc. Am. Bull., 84: 2193—2216.
Rittman, A., 1958. Cenni sulle colate di ignimbriti. Catania Acad. Gioenia di Sci., Nat. Boll., Ser. 4, 4: 524—533.
Rittman, A., 1962. Volcanoes and Their Activity. Interscience, New York, N.Y., 305 pp.
Rutten, M.G. and Van Everdingen, R.O., 1961. Rheo-ignimbrites of the Ramnes volcano, Permian, Oslo Graben. Geol. Mijnbouw, 40: 49—57.
Sanderson, D.J., 1973. The development of fold axes oblique to the regional trend. Tectonophysics, 16: 55—70.
Schmincke, H.U., 1969. Ignimbrite sequence on Gran Canaria. Bull. Volcanol., 33: 1199—1219.
Schmincke, H.U. and Swanson, D.A., 1967. Laminar viscous flowage structures in ash-flow tuffs from Gran Canaria, Canary Islands. J. Geol., 75: 641—664.
Self, S., 1973. Recent volcanism on Terceira, Azores. Ph.D. Thesis, Imperial College, London.
Shaw, H.R., 1972. Viscosities of magmatic silicate liquids: an empirical method of prediction. Am. J. Sci., 272: 870—893.
Skelland, A.H.P., 1967. Non-Newtonian flow and heat transfer. Wiley-Interscience, New York, N.Y., 432 pp.
Smith, R.L., 1960. Zones and zonal variations in welded ash-flows. U.S. Geol. Surv., Prof. Paper, 354-F: 149—159.

Sparks, R.S.J., 1976. Grain size variations in ignimbrites and implications for the transport of pyroclastic flows. Sedimentology, 23: 147—188.
Sparks, R.S.J. and Wright, J.V., 1979. Welded air-fall tuffs, In: C.E. Chapin and W.E. Elston (Editors), Ash-Flow Tuffs. Geol. Soc. Am., Spec. Paper, 180: 155—166.
Sparks, R.S.J., Self, S. and Walker, G.P.L., 1973. Products of ignimbrite eruptions. Geology, 1: 115—118.
Sparks, R.S.J., Wilson, L. and Hulme, G., 1978. Theoretical modelling of the generation, movement and emplacement of pyroclastic flows by column collapse.J. Geophys. Res., 83 (B4): 1727—1739.
Villari, L., 1969. On particular ignimbrites of the Island of Pantelleria (Channel of Silicy). Bull. Volcanol., 33: 828—839.
Villari, L., 1974. The Island of Pantelleria. Bull. Volcanol., 33: 680—724.
Walker, G.W. and Swanson, D.A., 1968. Laminar flowage in a Pleistocene soda rhyolite ash-flow tuff, Lake and Harney Countries, Oregon. U.S. Geol. Surv., Prof. Paper, 600-B: 37—47.
Wilson, C.J.N., 1980. The role of fluidization in the emplacement of pyroclastic flows. J. Volcanol. Geotherm. Res., 8: 231—249.
Woodcock, N.H., 1976. Structural style in slump sheets: Ludlow Series, Powys, Wales. J. Geol. Soc. London, 132: 399—415.
Wright, J.V., 1979. Formation, transport and deposition of ignimbrites and welded tuffs. Ph.D. Thesis, Imperial College, London, 451 pp.
Wright, J.V., 1980. Stratigraphy and geology of the welded air-fall tuffs of Pantelleria, Italy. Geol. Rundsch., 69: 263—291.
Wright, J.V. and Walker, G.P.L., 1981. Eruption, transport and deposition of ignimbrite: a case study from Mexico. J. Volcanol. Geotherm. Res. 9: 111—131.
Wright, J.V., Smith, A.L. and Self, S., 1980. A working terminology of pyroclastic deposits. J. Volcanol. Geotherm. Res., 8: 315—336.

Formation of the Green Tuff, Pantelleria

J. A. WOLFF — *Department of Geology, Imperial College, London SW7 2BP, U.K.*

J. V. WRIGHT — *Department of Earth Sciences, Monash University, Clayton, Victoria 3168, Australia*

ABSTRACT

The strongly peralkaline Green Tuff, Pantelleria, is an example of a thin, densely welded air-fall tuff which mantles an area of at least 85 km². Offshore the tuff is correlated with the Y-6 ash layer in the central Mediterranean Sea, and the total volume of the eruption is estimated at 7 km³ D.R.E. New petrological data suggests that the tuff was erupted from a zoned magma chamber containing a cooler, more fractionated upper zone relative to be bulk of the magma. Analysis of the distribution of accessory lithic fragments in terms of existing models of eruption dynamics indicates emplacement by a plinian-type eruption. It is shown that, due to the low viscosity of pantelleritic ejecta, dense welding can occur at moderate tephra accumulation rates and a rate of the order of 1 cm/minute is suggested for the Green Tuff; this yields an estimate for the eruption duration of rather less than one day. It is predicted that welded tuff should be formed during large plinian eruptions of pantelleritic magma, and therefore that welded air-fall tuffs should be common in areas of peralkaline volcanism.

INTRODUCTION

Extensive, thin densely welded tuff sheets are not an uncommon volcanic rock and they are most frequently encountered in areas of peralkaline volcanism. SCHMINCKE (1974) lists several occurrences described as ignimbrites and WALLACE *et al.* (1980) quote examples from Nevada. The island of Pantelleria, Italy, contains many welded tuffs originally described as ignimbrites (VILLARI, 1974), since re-interpreted as welded air-fall tuffs (WRIGHT, 1980). The most spectacular of these is the Green Tuff, which in its original distribution mantled the entire island (85 km²) with over 5 m of densely welded tuff (Fig. 1). Rheomorphism of the hot welded viscous sheet resulted in redistribution and the internal development of various secondary flowage structures (WOLFF and WRIGHT, 1981). The present work interprets new petrological data and considers the volcanological formation of the tuff.

FIELD CHARACTERISTICS

The Green Tuff has been previously described by VILLARI (1974), WRIGHT (1980) and WOLFF and WRIGHT (1981). We shall here summarize those aspects pertinent to the present analysis.

The Green Tuff is found throughout Pantelleria except where covered by younger rocks, and is usually welded throughout its thickness. At most locations a basal vitrophyre passes upward into revesiculated rheomorphic tuff which constitutes the bulk of the sheet. An incipiently welded top and non-welded basal pumice have also been found. The tuff drapes the former topography and is ponded in depressions. The overall geometry thus resembles that of pyroclastic surges (WRIGHT *et al.*, 1980) and low aspect ratio ignimbrites (WALKER *et al.*, 1980). We conclude that the tuff was formed by an air-fall mechanism for the following reasons:

1. The grain-size distribution, particularly that of non-welded pumice, is characteristic of pyroclastic fall deposits;
2. At favourable exposures, stratification and individual fall-units can be distinguished;
3. There is no correlation between degree of welding and thickness, as would be expected were the thickness variation a

primary feature, and the evidence presented by WRIGHT (1980) suggests that the observed variation is the result of downslope movement during rheomorphism, and is thus of secondary origin.

The 20 cm lithic isopleth encloses ca. 100 km^2, and the tuff is therefore of plinian type according to the criteria of WALKER (1980).

ESTIMATE OF TOTAL ERUPTED VOLUME

Because of rheomorphic ponding in depressions an isopach map of the tuff cannot be constructed. The volume on Pantelleria can however be estimated by comparing average topography with the welded tuff's dependence of thickness on ground slope (WRIGHT, 1980). This gives a value of 0.6 km^3 of revesiculated welded tuff or approximately 1.2 km^3 of primary uncompacted tephra (of density 0.85×10^3 kgm^{-3}).

An estimate can also be made of the volume of material that fell in the sea, if it is assumed that the primary distribution of tephra was similar to that of other widely-dispersed air-fall deposits. On an «area» diagram (Fig. 2) we have plotted a straight line to satisfy the volume of proximal Green Tuff on the island parallel with the slope of other plinian deposits near source (WALKER, 1980; WALKER *et al.*, 1981), and, for the distal part, this has been extrapolated parallel to the slope of the Taupo pumice fall deposit (WALKER, 1980) to a limiting thickness of 1 µm. This gives a volume estimate for the Green Tuff of 20 km^3 of primary vesicular tephra or 7 km^3 D.R.E. (dense rock equivalent).

KELLER *et al.* (1978) have detailed the deep-sea ash layer stratigraphy of the Mediterranean for the past 200,000 years. Among the layers they describe is Y-6, a widespread strongly peralkaline horizon with an interpolated age of 45,000 years B. P., correlated with Pantelleria. Both Y-6 and the Green Tuff are chemically characterised by high ratios of total iron and alkalies to alumina, and compositions have therefore been compared by plotting in K_2O-FeO-Al_2O_3 (Fig. 3). Na_2O was omitted since it is readily affected by post-eruptive processes. Y-6 compositions are closely

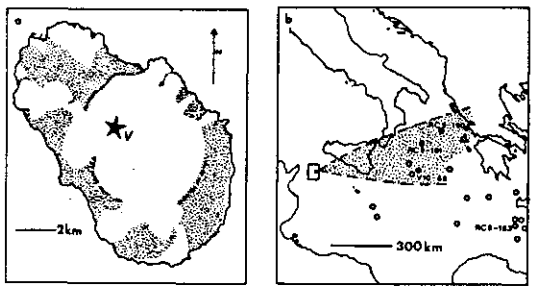

FIG. 1 — Location and distribution maps of the Green Tuff. *a*) Present outcrop of densely welded rheomorphic tuff on Pantelleria (stipple), from VILLARI (1974) and WRIGHT (1980). Star with V is the assumed vent position we have used in our analysis based on the distribution of large lithic fragments (WRIGHT, 1980), and this agrees closely with the observations of MAHOOD and HILDRETH (1980) that Cuddia di Mida is the vent of the Green Tuff. Dashed line is the exposed caldera rim which is mantled by the Green Tuff. *b*) The 45,000 B.P. Y-6 ash layer in the Mediterranean Sea (stipple), correlated with the Green Tuff (see text). Labelled solid circles are deep sea cores in which Y-6 is reported, and open circles, those where it is not (data from KELLER *et al.*, 1978, and W. Cornell, unpublished). There is some confusion in KELLER *et al.* (1978) as to whether Y-6 occurs in core RC9-183. This has been checked with the authors who report (J. KELLER, pers. comm.) that Y-6 was not confirmed by petrographic examination.

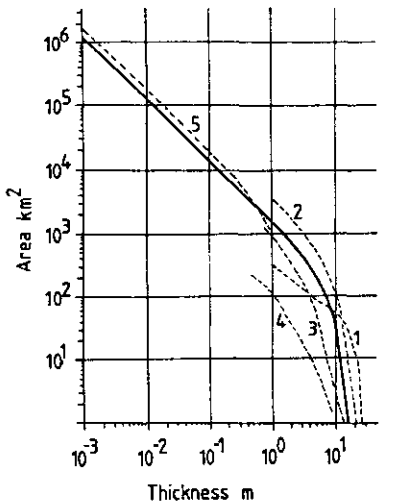

FIG. 2 — «Area» plot of the Green tuff (solid curve). Dashed lines are the plinian fall deposits which form the basis of our volume estimation of the Green Tuff as explained in the text; near-vent 1 — Fogo A, 2 — La Prrimavera B, 3 — La Primavera J, 4 — Fogo 1563, and distally 5 — Taupo. The data comes from WALKER (1980), and WALKER *et al.* (1981).

bracketed by those of the Green Tuff (Fig. 3) and are distinct both from other deep-sea ash layers and other tuff units on Pantelleria. Furthermore, Y-6 is dispersed to the east of Pantelleria (Fig. 1b), which approximately corresponds to the south-easterly dispersal direction of the Green Tuff on the island (WRIGHT, 1980). Other Pantelleria air-fall deposits of comparable size show different dispersal axes (WRIGHT, 1980). We therefore conclude that Y-6 represents distal ash fallout from the Green Tuff eruption. The implied dispersal area is 10^5 km^2 from Pantelleria to the central Mediterranean (Fig. 1b), where cored Y-6 thicknesses are 1-2 cm (J. KELLER, pers. comm.). This is fully consistent with the estimated total volume; from Fig. 2 the 1 cm Green Tuff isopach covers 1.2×10^5 km^2.

PETROLOGY

The petrology of the tuff has previously been described by KORRINGA and NOBLE (1972) and VILLARI (1974).

Petrographically the tuff consists of phenocrysts set in a finely crystallized matrix, although original glass is preserved in the basal vitrophyre. Both glassy and crystalline groundmasses have been intensely revesiculated. As original clast outlines have been obscured by welding, the total magmatic abundance of phenocrysts cannot be estimated; an upper limit of 19% is imposed by the observed modal abundance. Two distinct phenocryst assemblages are present: the bulk of the rock has anorthoclase + clinopyroxene + aenigmatite + magnetite + + ilmenite + fayalite + apatite ± quartz, while the basal vitrophyre contains anorthoclase + aenigmatite + clinopyroxene + + quartz + apatite. Representative microprobe analyses of phenocrysts and glass are given in Table 1.

Phenocrysts

Quartz is abundant in the vitrophyre but rare in the crystallized tuff.

Large tabular crystals of anorthoclase up to 1.3 cm in length are ubiquitous. Occasionally, rounded and embayed examples are seen, suggesting a degree of post-eruptive resorption. Crystals are essentially unzoned. Compositions vary between $Ab_{67}Or_{33}$ and $Ab_{65}Or_{35}$ in the crystalline tuff, and $Ab_{64}Or_{36}$ and $Ab_{62}Or_{38}$ in the vitrophyre.

The pale to deep green pyroxenes are hedenbergitic with a minor acmite component ($Na_2O \leq 2.2$ wt. %). Those in the basal vitrophyre have a slightly higher Fe^{2+}/Mg ratio than those in the bulk of the tuff, although zoned examples are found which span the two compositions (Fig. 4).

Occasionally strongly resorbed crystals of olivine are found in the crystalline tuff.

No compositional variation is found within the precision limits of the microprobe. The composition is $Fa_{85}Fo_9Tp_5La_1$.

Aenigmatite is found throughout the tuff but is especially abundant in the vitrophyre. Compositions are constant, and closely similar to those described from other peralkaline rhyolites (NICHOLLS and CARMICHAEL, 1969).

Iron-titanium oxides are absent from the basal vitrophyre but are found as microphenocrysts and as inclusions in silicate phases throughout the rest of the tuff. Two ilmenites are found; one has a mean hematite content of 4%, the other 2%. Only the former is found in equilibrium with magnetite, which has a mean ulvospinel content of 71%.

Apatite and rare pyrrhotite occur as accessory phases.

Pre-eruptive Conditions in the Magma Chamber

The processes of extraction of magma from the chamber, explosive eruption,

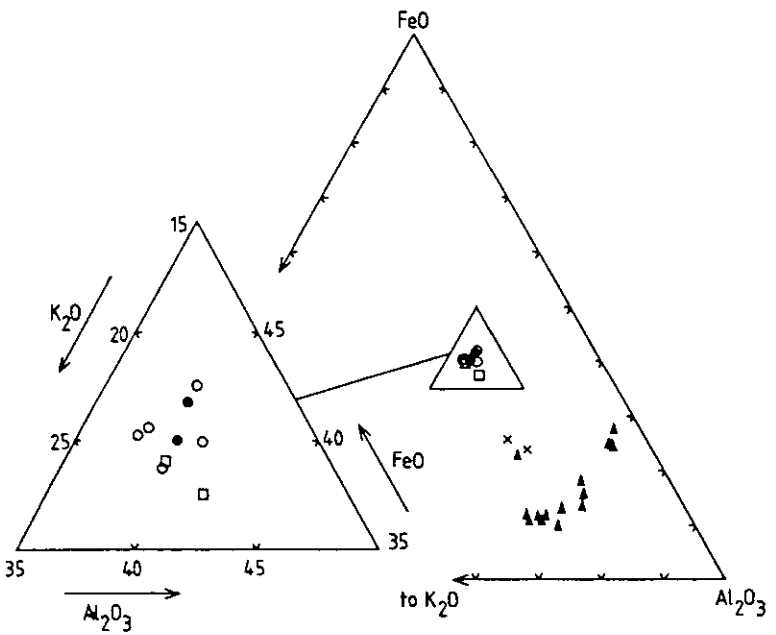

FIG. 3 — Geochemical correlation of deep-sea ash layer Y-6 with the Green Tuff. Analyses plotted in wt% K_2O-FeO-Al_2O_3, where FeO represents total iron. Open circles are Green Tuff glasses (KORRINGA and NOBLE, 1972; additional analyses by the authors and W. Cornell); closed circles are Y-6 glasses (KELLER *et al.*, 1978; W. CORNELL, pers. comm.); filled triangles are other ash layers in the central Mediterranean (KELLER *et al.*, 1978; W. CORNELL, pers. comm.); open squares are whole-rock analyses of Green Tuff (VILLARI, 1974); crosses are whole-rock analyses of other welded tuffs on Pantelleria (VILLARI, 1974).

TABLE 1 — Representative microprobe analyses for phenocrysts and unhydrated glass from the Green tuff.

	1	2	3	4	5	6	7	8	9	10	11
SiO_2	67.4	67.3	49.3	49.2	40.9	41.0	0.4	0.2	0.3	30.5	70.0
TiO_2	-	-	0.4	0.5	9.2	9.0	24.4	50.5	51.5	-	0.5
Al_2O_3	18.1	18.0	0.2	-	0.5	0.7	0.2	-	-	-	7.4
FeO*	1.0	1.0	26.4	23.4	39.7	39.9	70.8	46.4	46.3	61.5	8.1
MnO	-	-	1.5	1.4	1.0	1.1	1.7	2.2	2.2	3.9	-
MgO	-	-	2.5	4.6	0.9	1.1	-	0.3	-	3.4	-
CaO	-	-	17.3	19.2	0.7	0.6	-	-	-	0.5	0.3
Na_2O	7.3	7.4	2.2	1.1	7.2	7.2	-	-	-	-	6.5
K_2O	6.2	5.9	-	-	-	-	-	-	-	-	3.6
P_2O_5	-	-	-	-	-	-	-	-	-	-	-
Total	100.0	99.6	99.6	99.4	100.1	100.6	97.5	99.6	100.3	99.7	96.2†
Fe_2O_3	-	-	5.3	2.8	-	-	20.3	3.8	2.2	-	
FeO	-	-	21.6	20.9	-	-	52.5	43.0	44.4	-	
Total	100.0	99.6	100.1	99.7	100.1	100.6	99.5	100.0	100.6	99.8	98.2

* Total iron as FeO
† Includes 0.9% Cl, 0.3% S, 0.6% ZrO_2

1 and 2, feldspar; 3 and 4, clinopyroxene; 5 and 6, aenigmatites; 7, titanomagnetite; 8 and 9, ilmenite; 10, olivine; 11, glass. Analyses 1, 3, 5 and 11 from basal vitrophyre while remainder from crystalline tuff. All phases analysed on the Microscan V E.D.S. at Imperial College. Totals are recalculated for those phases whose Fe_2O_3 content can be estimated.

atmospheric flight, and rheomorphism are conducive to the mixing of portions of magma from originally widely separated locations in the magma chamber. Thus only phenocrysts from a single aggregate grain can be reasonably assumed to have been in chemical equilibrium. Using this criterion, temperature estimates for the Green Tuff magma have been obtained from the Fe-Ti oxides geothermometer (BUDDINGTON and LINDSLEY, 1964; CARMICHAEL, 1967; POWELL and POWELL, 1977) and the olivine-clinopyroxene geothermometer (POWELL and POWELL, 1974). The validity of the latter geothermometer has been severely criticised by

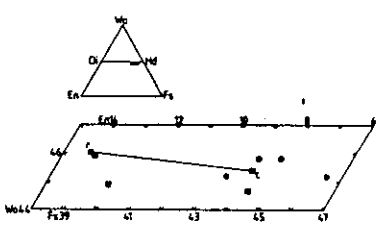

FIG. 4 — Pyroxene compositions in the Green Tuff. Squares are phenocrysts from crystalline tuff, circles are phenocrysts from basal vitrophyre.

TABLE 2 — Geothermometry and oxygen barometry for phenocrysts from the crystalline part of the Green Tuff.

Geothermometer	T(°C)	fO_2 ($\log_{10}$ bars)
Fe-Ti oxides (i) (Carmichael, 1967; Buddington and Lindsley, 1964)	960 ± 30	-12.1 ± 0.7
Fe-Ti oxides (ii) (Powell and Powell, 1977)	935 ± 55	-12.8 ± 1.2
Olivine-clinopyroxene (Powell and Powell, 1974)	960	-

WOOD (1976), but POWELL (1978) reasserts its usefulness for mineral compositions similar to those considered here. A temperature of 950 °C is indicated for the bulk of the Green Tuff magma (Table 2).

NICHOLLS and CARMICHAEL (1969) have demonstrated the existence of a «no-oxide» field in T-f_{O_2} space for peralkaline rhyolites within which Fe-Ti oxides are unstable and replaced by aenigmatite. This field (Fig. 5) is bounded by the reactions:

$$\underset{\text{magnet-ite}}{4\,Fe_3O_4} + 6\,Na_2Si_2O_5 + 12\,SiO_2 + O_2 = 12\,NaFeSi_2O_6 \qquad (1)$$
$$\text{liquid} \qquad \text{quartz} \qquad \text{pyroxene}$$

$$Na_2Fe_5TiSi_6O_{20} + Na_2Si_2O_5 + O_2 = 4\,NaFeSi_2O_6 + FeTiO_3 \qquad (2)$$
$$\text{aenigmatite} \qquad \text{liquid} \qquad \text{pyroxene} \qquad \text{ilmenite}$$

$$6\,Fe_2SiO_4 + 6\,Na_2Si_2O_5 + 6\,SiO_2 + 3\,O_2 = 12\,NaFeSi_2O_6 \qquad (3)$$
$$\text{olivine} \qquad \text{liquid} \qquad \text{quartz} \qquad \text{pyroxene}$$

The position of the «no-oxide» field varies with varying activities of $Na_2Si_2O_5$ in the silicate liquid and $NaFeSi_2O_6$ in pyroxene and cannot be precisely delineated for the Green Tuff. However the relative abundance of aenigmatite and absence of Fe-Ti oxides in the basal vitrophyre suggests that the portion of the magma represented by this horizon equilibrated internally at a lower temperature than the 950 °C found for the bulk of the magma (Fig. 5). This observation is supported by the presence of abundant quartz and relatively less-magnesian pyroxene in the vitrophyre.

During eruption, the first magma to be tapped from the chamber will be that nearest the point of entry of the volcanic conduit. The slightly more evolved nature of the vitrophyre layer therefore suggests that the Green Tuff was erupted from a vertically zoned magma chamber with a relatively fractionated roof zone; similar zonation has been recognized in many other volcanic areas (SMITH, 1979; HILDRETH, 1979; WOLFF *et al.*, in press).

ESTIMATION OF PHYSICAL PARAMETERS FOR THE ERUPTION

For any plinian eruption, it is theoretically possible to deduce such physical parameters as muzzle velocity, vent radius and eruption column height from measurements of eruption duration, grain-size

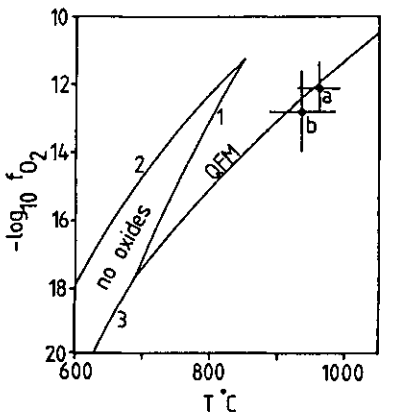

FIG. 5 — Fugacity of oxygen vs. temperature showing the position of the «no-oxide» field for unit activities of acmite and sodium disilicate, after NICHOLLS and CARMICHAEL (1969). Points *a* and *b* are the equilibration conditions of Fe-Ti oxides deduced from the methods of BUDDINGTON and LINDSLEY (1974) and POWELL and POWELL (1977) respectively. Numbers 1-3 refer to the reactions given in the text. The presence of olivine and titanomagnetite in the phenocryst assemblage is reflected in the proximity of points *a* and *b* to the QFM (quartz-fayalite-magnetite) buffer curve.

distribution and total volume of the resultant pyroclastic fall deposit (WILSON, 1976; WILSON *et al.*, 1978). In the case of the Green Tuff much information has been destroyed by the processes of welding and rheomorphism. However, since rheomorphism is very unlikely to have involved bulk movements of welded tuff over distances greater than a few hundred meters (WOLFF and WRIGHT, 1981) the primary lithic size distribution may be considered to have survived largely unchanged, and is thus used as the basis of the following analysis.

Average maximum lithic size data are plotted against distance from vent (Fig. 1); a line drawn along the top of the resulting scatter of points gives the maximum range of fragments of a given size (Fig. 6). The line shows an inflexion at about 5 km from source, indicating the maximum range of ballistic clasts (those largely unaffected by aerodynamic factors). Such particle size distributions are common among plinian deposits (WALKER and CROASDALE, 1971; BOOTH *et al.*, 1978). Extrapolation of this graph to zero range yields a value of 4.3 m for the maximum diameter of lithics at the vent. This value receives some corroboration from the existence of 5 m blocks in the tuff in the deduced vent area; although moved by rheomorphism (WRIGHT, 1980), we now consider that they may be ballistic ejecta. Applying equation (6) of WILSON (1976) gives 500 ms^{-1} as the maximum muzzle velocity during the eruption; the average velocity may conveniently be taken as half this value (WILSON, 1976).

The instantaneous mass rate of eruption of material from a vent of radius b_o is $\dot{m}$ where

$$\dot{m} = \frac{100}{n}\,\rho_o\,u_o\,\pi\,b_o^2,$$

where ρ_o is the gas density at the vent, n is the percentage of magmatic volatiles, and u_o is the muzzle velocity (WILSON,

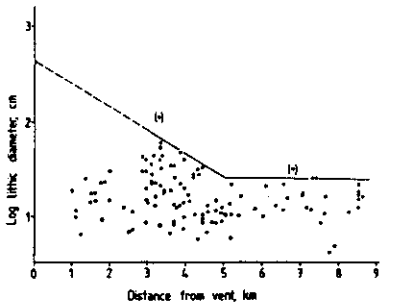

FIG. 6 — Average maximum diameter vs. distance from vent for the Green tuff. Each data point is the average of the five largest lithic clasts found at any one locality. The solid and dashed lines are explained in the text.

1976). Assuming the magmatic gas to be H_2O, Fig. 7 shows the relation between volumetric eruption discarge rate, magma gas content, and vent radius for the Green Tuff eruption. For certain combinations of these variables, column collapse to form pyroclastic flows occurs (SPARKS and WILSON, 1976). Since we have concluded that the tuff is of air-fall origin, the «collapse boundary» limits the conditions of formation as show.

The degree of welding of an air-fall deposit is principally dependent on tephra accumulation rate (SPARKS and WRIGHT, 1979), but few data are available on the critical rate required for welding to occur. SPARKS and WRIGHT (1979) estimate rates of 2-4 and 20 cm/minutes respectively for the production of incipiently welded and densely welded rhyolitic air-fal tuff

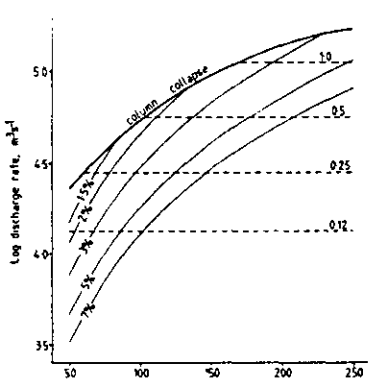

FIG. 7 — Variation of volumetric discharge rate of tephra as dense rock (density 2.5×10^3 kgm^{-3}) in a plinian eruption column with vent radius for five values of magmatic volatile content (assumed to be entirely water) in weight % and a muzzle velocity of 250 ms^{-1}, from the model of WILSON (1976). Dashed lines indicate the discharge rates required to accumulate 10 m uncompacted tephra (maximum thickness of the Green Tuff at maximum range on Pantelleria) at four values of tephra accumulation rate (in cm/minute) for a total erupted volume of 20 km^3 of vesicular tephra.

during the eruption of Askja, 1875. The Green Tuff magma was unusually fluid, both by reason of chemical composition (WOLFF and WRIGHT, 1981), and the high magmatic temperature. Assuming that high initial magmatic temperature will result in high residual temperature of deposited tephra, pyroclasts from the eruption may have had a viscosity as low as 10^{-3} times that of «normal» rhyolitic pumice. Compaction of the deposit must therefore have occurred very rapidly (WOLFF and WRIGHT, 1981); field evidence for rapid compaction is seen in the revesiculation, which accounts for 20% by volume of the Green Tuff. Calculations of SPARKS (1978) suggest that the excess residual volatile content of pumice is lost in the first few hours after eruption. Compaction must therefore have reached the point where vesicle interconnections were destroyed (perhaps 10% porosity) before this time period elapsed. The prolate shape of some vesicles shows that the welded sheet was still internally exsolving gas after the initiation of rheomorphic flow (WOLFF and WRIGHT, 1981). Compaction of tuff during welding is dependent on the compaction coefficient, β, as follows:

$$\beta \propto 1/ln\left(\frac{P_f - 1}{P_i - 1}\right)$$

where P_i and P_f are the initial and final tuff porosities for the time increment under consideration (RIEHLE, 1973). β has only been characterised for rhyolitic ash, but is primarily related to pumice glass viscosity. It can be seen that conditions required to produce incipiently welded rhyolitic tuff (taken as 1% porosity decrease) will cause complete compaction of pantelleritic tuff.

Comparison of pumice glass viscosities with the data of SPARKS and WRIGHT (1979) suggests that an accumulation rate of 1 cm/minute is sufficiently to produce a densely welded air-fall tuff of similar composition to the Green Tuff. Figure 7 indicates that the mean accumulation rate at maximum range on Pantelleria is unlikely to have been much greater, and gives a corresponding eruption discarge rate of 1.1×10^5 m^3 s^{-1} D.R.E., which yields a value of 18 hours for the eruption duration. Using the method of WILSON *et al.* (1978), the eruption column height was approximately 30 km, and the total energy released is estimated at 10^{18}-10^{19} J. These values indicate a moderately powerful plinian eruption comparable in intensity to that of Bezymianny, 1956 (GORSHKOV, 1959). More importantly, our analysis predicts that widespread pantelleritic welded air-fall tuffs can form at typical plinian discharge rates.

DISCUSSION

The foregoing analysis is necessarily approximate and based on several assumptions; perhaps the least valid of these is that the magmatic volatile component consisted entirely of water, in view of the dryness of peralkaline magmas (NICHOLLS and CARMICHAEL, 1969). Fluorine, however, is an abundant constituent of such magmas (NICHOLLS and CARMICHAEL, 1969) and HF may have accounted for part of the phase; its gas density is similar to that of steam. Furthermore, dissolved fluorine lowers the viscosity of silicate liquids, and thus will promote rapid welding (WOLFF and WRIGHT, 1981).

To a first approximation, we have shown that the formation of the Green Tuff can be understood in terms of plinian eruption column dynamics; the widespread dense welding and rheomorphism are solely a consequence of the unusual fluidity of the magma, as has been intuitively suggested by other workers (*e.g.* SCHMINCKE, 1974). A corollary of this study is that any powerful plinian eruption of pantelleritic magma will result in the formation of a widespread welded air-fall tuff. We suggest, therefore, that many extensive thin welded tuffs in other areas of peralkaline volcanism may have an air-fall origin.

An extreme example may be noted. HAY *et al.* (1979) describe a very thin (maximum thickness 2.5 m) welded tuff sheet covering 300 km^2 around Mt. Suswa, Kenya. The sheet mantles topography, passes upwards into air-fall pumice, and exhibits stratification and an irregular compaction profile; these features are diagnostic of an air-fall origin (SPARKS and WRIGHT, 1979). The magmatic composition, Fe-rich peralkaline phonolite, has a calculated viscosity (HAY *et al.*, 1979) lower than that of the Green Tuff, and the welding could therefore have occurred at accumulation rates much less than 1 cm/minute.

ACKNOWLEDGEMENTS

We thank the Natural Environment Research Council of Great Britain for postgraduate research studentships at Imperial College, and for funding fieldwork by J. V. W. on Pantelleria. Paul Suddaby and Neil Wilkinson are thanked for their assisstance with microprobe facilities at Imperial College. Additional microprobe work, kindly carried out by Winton Cornell, was facilitated by National Science Foundation Grants EAR-76-22083 and OCE-7513296 to Drs. H. Sigurdsson and J-G. Schilling for use of the electron probe at the University of Rhode Island. We also thank Dr. Floyd McCoy for supplying us with a sample of Y-6 ash from the Lamont-Doherty G. O. repository, funded by National Science Foundation Grant OCE-78-25448 and the Office of Naval Research Contract N00014-80-C-0098. Dr. J. Keller, F. McCoy and W. Cornell all kindly gave us information about the Mediterranean deep-sea cores.

REFERENCES

BOOTH, B., CROASDALE, R., and WALKER, G. P. L., 1978, *A Quantitative Study of Five Thousand Years of Volcanism on Sao Miguel, Azores*. Philos. Trans. R. Soc. Lond., *A 288*, p. 271-319.

BUDDINGTON, A. F., and LINDSLEY, D. M., 1964, *Iron-Titanium Oxide Minerals and Synthetic Equivalents*. J. Petrol., *5*, p. 310-357.

CARMICHAEL, I. S. E., 1967, *The Iron-Titanium Oxide Minerals of Salic Volcanic Rocks and Their Associated Ferromagnesian Silicates*. Contrib. Mineral. Petrol., *14*, p. 36-64.

GORSHKOV, G. S., 1959, *Gigantic Eruption of the Volcano Bezymianny.* Bull. Volcanol., *20*, p. 77-109.

HAY, R. L., HILDRETH, W., and LAMBE, R. N., 1979, *Globule Ignimbrite of Mount Suswa, Kenya.* Geol. Soc. America Spec. Paper 180, p. 167-175.

HILDRETH, W., 1979, *The Bishop Tuff: Evidence for the Origin of Compositional Zonation in Silicic Magma Chambers.* Geol. Soc. America Spec. Paper 180, p. 43-75.

KELLER, J., RYAN, W. B. F., NINKOVICH, D., and ALTHERR, R., 1978, *Explosive Volcanic Activity in the Mediterranean Over the Past 200,000 Years as Recorded in Deep Sea Sediments.* Geol. Soc. America Bull., *89*, p. 591-604.

KORRINGA, M. K., and NOBLE, C. D., 1972, *Genetic Significance of Chemical, Isotopic, and Petrographic Features of Some Peralkaline Salic Rocks from the Island of Pantelleria.* Earth Planet. Sci. Lett., *17*, p. 258-262.

MAHOOD, G., and HILDRETH, W., 1980, *Pantelleria, A New Interpretation* (abs). Eos., *61*, p. 1141.

NICHOLLS, J., and CARMICHAEL, I. S. E., 1969, *Peralkaline Acid Liquids: A Petrological Study.* Contrib. Mineral. Petrol., *20*, p. 265-294.

POWELL, M., 1978, *The Crystallization of the Igdlerfigssalik Nepheline Syenite Intrusion, Greenland.* Lithos, *11*, p. 99-120.

———, and POWELL, R., 1974, *An Olivine-Clinopyroxene Geothermeter.* Contrib. Mineral. Petrol., *48*, p. 249-263.

POWELL, R., and POWELL, M., 1977, *Geothermometry and Oxygen Barometry Using Co-Existing Iron-Titanium Oxides: A Reappraisal.* Min. Mag., *41*, p. 257-263.

RIEHLE, J. R., 1973, *Calculated Compaction Profiles of Rhyolitic Ash-Flow Tuffs.* Geo. Soc. America Bull., *84*, p. 2193-2216.

SCHMINCKE, H. U., 1974, *Volcanological Aspects of Peralkaline Silicic Welded Ash-Flow Tuffs.* Bull. Volcanol., *38*, p. 594-636.

SMITH, R. L., 1979, *Ash-Flow Magmatism.* Geol. Soc. America Spec. Paper 180, p. 5-27.

SPARKS, R. S. J., 1978, *Gas Release Rates from Pyroclastic Flows: As Assessment of the Role of Fluidisation in Their Emplacement.* Bull. Volcanol., *41*, p. 1-9.

———, and WILSON, L., 1976, *Model for Ignimbrite Formation by Gravitational Column Collapse.* J. Geol. Soc. Lond., *132*, p. 441-451.

SPARKS, R. S. J., and WRIGHT, J. V., 1979, *Welded Air-Fall Tuffs.* Geol. Soc. America Spec. Paper 180, p. 155-166.

VILLARI, L., 1974, *The Island of Pantelleria.* Bull. Volcanol., *38*, p. 680-724.

WALKER, G. P. L., 1980, *The Taupo Pumice: Product of the Most Powerful Known (Ultraplinian) Eruption?* J. Volcanol. Geother. Res., *8*, p. 69-94.

———, and CROASDALE, R., 1971, *Two Plinian-Type Eruptions in the Azores.* J. Geol. Soc. Lond., *127*, p. 17-55.

———, HEMING, R. F., and WILSON, C. J. N., 1980, *Low Aspect Ratio Ignimbrites.* Nature, *283*, p. 286-287.

———, WRIGHT, J. V., CLOUGH, B. J., and BOOTH, B., 1981, *Pyroclastic Geology of the Rhyolitic Volcano of La Primavera, Mexico.* Geol. Rundsch., *70*, p. 1100-1118.

WALLACE, A. B., DREXLER, J. W., GRANT, N. K., and NOBLE, D. C., 1980, *Icelandite and Aenigmatite-Bearing Pantellerite from the McDermitt Caldera Complex, Nevada-Oregon.* Geology, *8*, p. 380-384.

WILSON, L., 1976, *Explosive Volcanic Eruptions, III. Plinian Eruption Columns.* Geophys. J. R. Astron. Soc., *45*, p. 543-556.

———, SPARKS, R. S. J., HUANG, T. C., and WATKINS, N. D., 1978, *The Control of Volcanic Column Heights by Eruption Column Energetics and Dynamics.* J. Geophys. Res., *83*, p. 1829-1836.

WOLFF, J. A., and WRIGHT, J. V., 1981, *Rheomorphism of Welded Tuffs.* J. Volcanol. Geotherm. Res., *10*, p. 13-34.

———, ———, SMITH, A. L., CLOUGH, B. J., ROOBOL, M. J., and SELF, S., in press, *Mixed Pumice Eruptions: Field Characteristics.* Proc. IX Carib. Conf., Santo Domingo, 1980.

WOOD, B. G., 1976, *An Olivine-Clinopyroxene Geothermometer - A Discussion.* Contrib. Mineral. Petrol., *56*, p. 297-303.

WRIGHT, J. V., 1980, *Stratigraphy and Geology of the Welded Air-Fall Tuffs of Pantelleria, Italy.* Geol. Rundsch., *69*, p. 263-291.

———, SMITH, A. L., and SELF, S., 1980, *A Working Terminology of Pyroclastic Deposits. J. Volcanol. Geotherm. Res., 8*, p. 315-336.

Ms. received May 1981; sent to review June 1981. Revised ms. received and accepted March 1982.

From Transactions of the 9th Caribbean Conference, Vol.1, 1980

Mixed pumice eruptions: field characteristics

J.A. WOLFF*
J.V. WRIGHT**
A.L. SMITH**
B.J. CLOUGH*
M.J. ROOBOL**
S.SELF***

ABSTRACT

Pumice deposits, of both ignimbrite and airfall type, which contain two juvenile components of contrasting composition (one salic, the other more mafic) are extremely common. This paper concentrates on descriptions of field characteristics of such deposits. Their frequency of occurrence in pyroclastic successions described from a number of Quaternary volcanic areas, including the Lesser Antilles, shows they form in widely differing volcanotectonic settings.

In many examples the salic and mafic pumices are respectively acidic and intermediate in composition; close chemical similarity between the two members can also be found and an example of two mixed rhyolites is described. Colour banding in the mixed pumices is explained by the relative iron contents and Fe^{III}/Fe^{II} ratios of the two components. Detailed geochemical examination of any one deposit may provide an insight into conditions in magma chambers before eruption and examples are given. It is suggested that the "lithic" fraction in many deposits is partly derived from juvenile mafic material. Magma mixing may affect ignimbrite formation and also welding of both ignimbrite and airfall deposits.

RESUMEN

Son extremadamente comunes los depósitos de pomez, tanto de tipo ignimbrita como de toba de caída aérea, los cuales contienen dos componentes juveniles de composición contrastante (uno sialico y el otro más máfico). Este trabajo se concentra en la descripción de características de campo de tales depósitos. La frecuencia de ocurrencia en secuencias piroclásticas, descritas de un número de áreas volcánicas del Cuaternario, incluyendo Las Antillas Menores, muestran que ellos se forman en ambientes volcano-tectónicos extremadamente diferentes.

En muchos ejemplos las pomez siálicas y máficas son de composición ácida e intermedia, respectivamente; cercanas similitudes químicas entre los dos miembros pueden también ser encontradas y se ha descrito un ejemplo de dos riolitas mezcladas. El bandeamiento de color en las pomez mezcladas se explica por los contenidos relativos de hierro y las relaciones Fe^{III}/Fe^{II} de los dos componentes. El examen geoquímico detallado de cualquier depósito puede proporcionar un análisis interno de las condiciones de las cámaras magmáticas antes de la erupción y se dan algunos ejemplos. Se sugiere que la fracción "lítica" en muchos depósitos sea parcialmente derivada de material máfico juvenil. La mezcla de los magmas puede haber afectado la formación de la ignimbrita y también el soldamiento de ambos: ignimbritas y depósitos de caída libre aérea.

INTRODUCTION

A mixed pumice deposit is one which contains two juvenile components: one salic, the other more mafic. The salic component is normally the more abundant. Occurrences are known from several different volcano-tectonic settings (Table 1). In this paper we will concentrate on descriptions of field characteristics of such deposits. Examples of pyroclastic flow and fall deposits displaying co-existing, contrasting magma types are described from Tenerife, Mexico, the Western United States, the Lesser Antilles, and Santorini. It is proposed that the incidence of mixed tephra is sufficiently high to postulate the co-existence of two or more different liquids as a general feature of many types of explosive volcanic activity.

DESCRIPTION

The most conspicuous mode of occurrence of mafic material in mixed pumice deposits is as glassy, vesiculated blebs and streaks enclosed within salic pumice, occasionally the reciprocal relationship is observed. Extremely intimate

*) Department of Geology, Imperial College, London, England.
**) Department of Geology, University of Puerto Rico, Mayaguez, Puerto Rico, 00708
***) Department of Geology, Arizona State University, Tempe, Arizona, 85281.

associations may be found in mixed clasts, with delicate interfingering of the two components being observed on all scales. This banding and interfingering is usually truncated by the clast outlines. Partial homogenisation is sometimes apparent in such samples. The mafic fraction may also occur as small, rounded, poorly—or non—vesiculated glassy or finely crystalline clots intermixed with salic and banded pumice.

Mixed pumice clasts are distinctive in thin sections. Colourless salic glass contrasts strongly with medium to dark brown mafic glass. Phenocrysts in the two components may differ in both type and composition. In favourable cases detailed petrographic and electron microprobe examination reveals two or more phenocryst populations defined on the basis of the compositions of phases found associated in aggregate grains. However, relations are frequently complex, particularly where several original phenocryst assemblages appear to be present. For example, phenocrysts representative of the entire magmatic range of the parent volcano have been found within a single pumice clast from a non-welded ignimbrite from Tenerife.

The following examples are, however, largely restricted to cases where only two components appear to be present. In all cases the available evidence points to two contrasting magmas having come together when both were in a largely fluid state.

FIELD OCCURRENCES

As can be seen from Table 1, mixed pumice deposits have been described from several geographical and volcanotectonic settings, while Table 2 indicates that there is also a wide range of magma types which can give rise to such deposits. In this section, deposits from five areas, of oceanic island, island arc, continental interior and continental margin settings, are described.

1) Tenerife

Tenerife, the largest island in the Canary archipelago, has a complex sequence of phonolitic pyroclastics which are particularly well exposed in the south-east of the island (Booth and Walker, in prep.). The deposits include plinian pumice falls, welded and non-welded ignimbrites and pyroclastic surges, intercalated with mudflows and lavas ranging in composition from ankaramite to phonolite. Nearly every major tephra deposit on Tenerife is composed of mixed pumice. Two of these deposits are described below.

Fall deposit A (maximum thickness 70 cm) is perhaps the best example of a compositionally zoned pumice in the area (Figs. 1 and 2). The bulk consists of creamy-white angular pumice. At 60 cm above the base this passes abruptly, but with no sign of an eruption break, into material containing a predominance of dense, porphyritic more mafic pumice of intermediate composition (Table 2), with minor mixed pumice clasts.

One of the larger airfall deposits on Tenerife, E (total volume 8 km^3, Booth and Walker, in prep.) is a widespread plinian pumice deposit. Minor quantities of millimetre-sized, finely crystalline basaltic inclusions in pumice occur throughout the fall. Basalt is also present in the lithic fraction. Occasional banded pumice clasts are found in the topmost few centimetres of the fall deposit. Locally the fall is capped by an ignimbrite, the product of a later phase of the same eruption. Mixed and dark clasts are plentiful in this ignimbrite, together with hybrid pumice intermediate in shade between light and dark types. When analysed, the two glasses are found to be chemically similar (Table 2). The more mafic material accounts for 10%—15% of the ignimbrite but for less than 1% of the pumice fall; the significance of this is discussed later.

2) Mexico

Several examples of mixed pyroclastics have been discovered near Guadalajara, Mexico. Three occurrences are described here.

The Acatlan ignimbrite outcrops in an area 40 km SW of Guadalajara (Wright and Walker, 1977; 1980). It has several flow units and displays vertical compositional zoning. In the lower flow units the juvenile component is exclusively an aphyric white or pink rhyolitic pumice with associated shards. In the uppermost main flow unit (Figs. 3 and 4), the lower part is composed of white or pink rhyolitic pumice and the upper part of black andesitic pumice, clasts of which may contain silky white rhyolitic streaks. Chemical analyses are given in Wright and Walker (1980) and see Wright *et al.* (these Transactions). A passage zone about 3 m thick between the lower and upper parts contains pumice of both types (Fig. 4), the mafic component gradually increasing upwards in amount. No sign of a flow unit boundary is visible within this passage zone.

The superposition of two pumice types within a single flow unit implies that transport was by laminar flow, as turbulent flow would not be expected to preserve the compositional zonation (Wright and Walker, 1980). Over part of the outcrop, the mafic portion is densely welded (Fig. 3); welding continues to the very top of the deposit despite lack of evidence for the significant erosion of material from the ignimbrite.

Associated with the ignimbrite is a co-ignimbrite lag fall deposit (Wright and Walker, 1977); it displays the same compositional zonation. In both deposits the mafic pumices are on average larger than the salic clasts (Table 3).

The Rio Caliente ignimbrite is a large, complex intraplinian deposit erupted from La Primavera volcano, a Quaternary rhyolite centre near Guadalajara. The stratigraphy of the eruption is presented elsewhere (Walker *et al.*, 1980 and see Wright *et al.*, these Transactions). Throughout most of the deposit the only juvenile component is a white, aphyric tubular pumice. However, mixed pumice flow units containing a dark, almost aphyric and banded pumice locally occur near the top of the ignimbrite near the source area, where thickest (Figs. 5 and 6). These units constitute less than 5% of the total volume of the ignimbrite. They can contain over 75% of dark and banded pumice (Fig. 5). The uppermost flow units of the ignimbrite and the overlying co-eruptive plinian fall deposit however lack this dark pumice. When analysed the two glasses are found to be almost identical chemically and are both rhyolites (Table 2). The darker glass even has a very slightly higher silica content. However, possibly more important is the iron content (see section Origin of banding). The mixed pumice flow units frequently display well-developed pumice concentration horizons (Fig. 6a). Such horizons form in the mixed pumice flow units as a consequence of a greater

average size of the darker as compared to salic pumice. As only clasts above a certain cut-off diameter are subject to grading processes in ignimbrites (Sparks, 1976), such horizons are therefore much more fully developed in the mixed than in the purely salic flow units. The variations in pumice-type content are mirrored in a co-ignimbrite lag fall deposit found close to the believed source.

Las Planillas, a polygenetic satellite centre of La Primavera, has erupted a total of 4 km^3 (dense rock equivalent) of comenditic lavas and airfall pumice. The largest plinian fall is capped by a single deposit of porphyritic mafic spatter found over a restricted area close to the vent.

Microscopically, the spatter shows small wisps of salic glass, indicating contamination of the mafic by the salic liquid. The composition of the erupted spatter (Table 2) may therefore be appreciably more acidic than the initial composition of the mafic magma.

3) Western United States

In this section we just want to note that two of the best known large rhyolitic pyroclastic deposits in Western United States were mixed pumice eruptions. Both the Bandelier tuff and Bishop tuff contain minor amounts of mafic and streaky pumice. In the Bishop tuff streaky pumice is found in a pumice concentration zone at the base of the ignimbrite produced in the eruption. The Bandelier tuff is in fact the product of two large ignimbrite-forming eruptions (Smith and Bailey, 1966; Wright *et al.*, 1980). Mixed pumice has been found in both plinian and ignimbrite phases of these eruptions. Preliminary chemical data from a mixed pumice clast from the Lower Bandelier plinian layer shows mixing between andesite (SiO_2=61%) and rhyolite (SiO_2=72%).

4) The Lesser Antilles

Mixed tephra deposits have been described from at least six of the potentially active volcanoes of the Lesser Antilles island arc (Table 1). The commonest modes of occurrence are as plinian airfall deposits and ignimbrites although they are also found as pyroclastic flow and surge deposits produced by nuée ardente eruptions of St. Vincent and Peléan type. In most instances the deposits appear to show no vertical variation in the relative amounts of the two components.

Unlike most of the other examples described, in the Lesser Antilles the end- members of the mixed deposits are invariably basic (basalt, basaltic andesite) and intermediate (andesite), rather than basic–acid or intermediate–acid (Table 2). In addition to clasts of end-member composition, most deposits contain clasts showing intermixing of the two components as well as apparently homogeneous clasts of intermediate composition.

5) Santorini

Several mixed pumice deposits are exposed in the caldera walls of Santorini volcano, Greece. Three are discussed here: the Middle Pumice and the stratigraphically younger Thera and Therasia welded tuffs, all are of airfall type.

The Middle Pumice is exposed in the south of the island as a distinctive layer up to 24.5 m thick (Fig. 7). The deposit has two main fall units. The lower (maximum thickness 3.5 m) consists entirely of salic pumice. The upper unit (maximum thickness 21 m) contains in addition mafic pumice, the ratio mafic/salic showing a steady upward increase (Fig. 7); chemical analyses are given in Table 2. Near the base of the unit, large ballistic clasts up to 1 m in diameter of mixed and mafic pumice are common. Incipient welding of fine material is found around some of these clasts; the deposit is otherwise completely non-welded. The mafic fraction forms between 20% and 25% of the whole deposit.

The Thera and Therasia welded tuffs have been described in detail by Sparks and Wright (1979). Features of these tuffs such as variation in grain size in the vertical profile, good sorting ($6\phi<2$), and mantle bedding indicate that they are of airfall origin. Both deposits contain two pumice types and abundant streaky mixed pumice. Mafic pumice constitutes 25% and 40% of the Thera and Therasia tuffs respectively; it is present throughout the Thera tuff but is absent from the base of the Therasia layer. Chemical analyses of glasses from each are given in Sparks and Wright (1979). The salic component of both tuffs is dacitic while the mafic shows considerable heterogeneity, ranging from andesitic to dacitic in composition. The heterogeneity is characterised by increasing FeO, CaO, MgO and TiO_2 with decreasing SiO_2, indicating progressive contamination of the mafic liquid by the salic liquid.

DISCUSSION

1) Origin of banding

The principal physical characteristic common to all mixed pumice deposits we have studied is the presence of banded pumice. Invariably a clear glass and a dark-brown to black glass are present. In all other respects the two glasses may be closely similar physically, and can even be almost identical chemically, such as in the Rio Caliente ignimbrite.

An explanation of this colour difference is found by considering the relative iron contents of the two different components (Table 2). The Fe^{III} cation is the principal colouring agent present in natural glasses. The ratio Fe^{III}/Fe^{II} increases in magmas with decreasing temperature and increasing alkali concentration (Carmichael and Nicholls, 1967). Thus evolved liquids (rhyolite, phonolite, etc.) commonly have higher Fe^{III}/Fe^{II} ratios than more primitive types, although their low total iron contents result in a low *absolute* concentration of Fe^{III} and hence pale colouration. If a more basic liquid, with higher total iron content but lower Fe^{III}/Fe^{II} ratio, is now mixed with the salic magma, the value of the ratio will adjust towards that of the salic magma. This will cause an abnormally high absolute concentration of Fe^{III} in the more basic component, thus intensifying its colouration. If the mixed magma is now quenched before chemical homogenisation occurs, the distinct colour contrast is preserved in the glass and streaky or banded pumice is produced.

Following the above argument, in the case of the Rio Caliente ignimbrite the dark pumice could have been produced from a rhyolitic magma with lower f_{O_2}. However, more chemical data is needed to clarify the story of the origin of the Rio Caliente mixed pumice. Preliminary data

indicates that the darker pumice has less evolved trace element abundances.

2) Origin of mixed volcanic rocks

We are here more concerned with the processes immediately pertaining to the eruption of mixed material than with the ultimate origin of two liquids found in close association, a question which has been discussed by Yoder (1973). It may be noted here that liquid immiscibility, which has recently received some attention in the literature, is not a viable mechanism for the production of the relationships we have observed. In particular, co-existing immiscible liquids cannot generate two phenocryst populations in gross disequilibrium with each other.

Blake *et al.* (1965) and more recently Sparks *et al.* (1977) have suggested that acid-basic mixed magma eruptions are triggered by the injection of basic liquid, derived at depth, into a body of acid magma already present in the upper crust. It is worth commenting that heat supplied by repeated basic injections into a salic magma chamber, without any eruption, will tend to retard the cooling of the acid body such that it may remain in a largely liquid condition for a very long time. The apparent availability of basic magma in many salic volcanic areas may signify that this process of "stoking" is fairly common. Stoking may result in the slow build-up of unstable conditions over a long period of time, culminating in a major explosive eruption involving a significant proportion of the entire contents of the chamber. Some of the resulting ejecta would then be intermediate in composition; Bowman *et al.* (1973) and Eichelberger (1974) have presented evidence that the mixing process, when carried to completion, may result in intermediate magma types.

The chemical data presented in Table 2 would seem to suggest that a true acid-basic association may be rare among erupted material, and that acid-intermediate or basic-intermediate occurrences are more common. In some instances two glasses found among the products of a mixed-magma eruption are chemically quite similar (Table 2, e.g. analyses 2a and 2b), although still retaining their identities. Such eruptions may result from the disruption of a stably-zoned magma chamber by such a scheme as shown in Fig. 8, where magma from different parts of the chamber is simultaneously drawn into the vent. Such type of mixing is a consequence rather than a triggering mechanism or cause of an explosive eruption.

For the basic-intermediate type mixed magma eruptions of the Lesser Antilles, Smith *et al.* (1980) have proposed a mechanism schematically described in Fig. 9. Here andesitic magma, produced by fractional crystallisation, is brought to reside in a relatively high level magma chamber. Mixed eruptions are triggered when realtively undifferentiated basic magma encounters such chambers. However the presence of mixed deposits in which both components are andesitic suggests the possibility of the existence of more than one magma chamber, their products being mixed within the volcanic edifice itself.

It should also be pointed out that the triggering mechanism of Sparks *et al.* (1977), if it operates on an unhomogeneous magma chamber, will produce tephra in which several end-member magmatic compositions may be present in close association. Such relations are seen in two cases from Tenerife (J.A. W. unpub. data).

3) Eruption of mixed magma

Magma mixing may influence both the course of an explosive eruption and the detailed nature of the resulting deposit.

The change in eruptive style of the Tenerife E deposit, from plinian fall to ignimbrite, coincides with a sudden increase in the amount of mafic material in the deposit, and, in general, ignimbrites on Tenerife are richer in mafic pumice than are fall deposits. Sparks and Wilson (1976) and Sparks *et al.* (1978) have proposed a model for the formation of ignimbrite by gravitational collapse of a plinian eruption column, the transition from plinian to ignimbrite-forming activity occurring at some critical value of magma water content (for a fixed vent radius). Salic liquids generally have higher water contents than associated more basic magma; in mixed deposits this is reflected in the vesicularity contrast between salic and mafic pumices. Thus a cause of column collapse may be the tapping of liquid in the magma chamber which contains an increased proportion of the mafic component.

The chilling of basic magma against acid has been described before (Wager and Bailey, 1953). During magma mixing, a proportion of the invading basic liquid will be chilled to small, glassy or microcrystalline clots (e.g. see chemical analyses of the Middle Pumice, Table 2). Pumice clasts form during an explosive eruption by the fragmentation of rising vesiculating magma in the volcanic conduit. This fragmentation will be partly controlled by the distribution of points of weakness in the magma. Such points of weakness are provided by solid bodies such as phenocrysts, xenoliths, and crystallised fragments of juvenile material. Hence some of this material is released as free particles in the eruption column and enters the dense fraction (lithics + crystals) of the resulting deposit. Therefore the mafic component of a mixed pumice deposit may contribute to the lithic fraction, and the presence of a high proportion of basic lithics in an otherwise unmixed salic pumice horizon will suggest the existence of a mixed deposit. Basaltic lithics are ubiquitous in the pumice deposits of Tenerife.

The occurrence of aureoles of incipient welding around large mafic clasts in the otherwise non-welded Santorini Middle Pumice suggests that the presence of a more basic ejecta in an acidic pumice deposit may promote welding. More importantly, pre-eruptive superheating of salic magma during the mixing process will result in a substantial viscosity reduction and ejecta formed from superheated material will therefore be more liable to plastic deformation. The Santorini and Askja welded airfall deposits described by Sparks and Wright (1979) are mixed; whether substantial mixing is more common among welded falls than non-welded falls is uncertain. Likewise, mixing is a common feature of non-welded ignimbrites; how frequently it occurs among welded ignimbrites may be difficult to establish as the presence of two pumice types in a densely welded, oxidised and devitrified cooling unit will be far from obvious in the field. In the case of the Acatlan ignimbrite, the occurrence of a zone of dense welding is governed by the compositional change in that only the mafic component is welded (Fig. 3). There is apparently no correlation between

mixing and welding zone development in the Rio Caliente ignimbrite (Fig. 5). Whether or not magma mixing is generally a major factor affecting the welding of tuff deposits remains uncertain.

ACKNOWLEDGEMENTS

The authors are grateful to Prof. G.P.L. Walker for invaluable discussions and for reading an early version of the manuscript, J.A.W., J.V.W. and B.J.C. thank the Natural Environment Research Council of Great Britain for studentships at Imperial College. A.L.S. and M.J.R. acknowledges the support of National Science Foundation grant EAR 73–00194. S.S. acknowledges the support of NASA grant NSG 5145. Fieldwork in Mexico (J.V.W. and B.J.C.) was funded by NERC and the Instituto de Geologia, University of Mexico (UNAM). J.V.W. thanks the Lindermann Trust Fellowship for funding fieldwork in the U.S.A.

REFERENCES

Anderson, A.T., 1976. Magma mixing: Petrological process and volcanological tool. J. Volcanol. Geotherm. Res., v. 1, 3–33.

Blake, D.H., Elwell, R.W.D., Gibson, I.L., Shelhorn, R.R. and Walker, G.P.L., 1965. Some relationships from the intimate association of acid and basic magmas. Q.J. Geol. Soc. Lond., v. 122, 31–49.

Bond, A. and Sparks, R.S.J., 1976. The Minoan eruption of Santorini, Greece. J. Geol. Soc. Lond., v. 132, 1–16.

Booth, B. and Walker, G.P.L., in prep. The Quaternary pumice deposits of Tenerife, Canary Islands.

Booth, B., Croasdale, R. and Walker, G.P.L., 1978. A quantitative study of five thousand years of volcanism on Sao Miguel, Azores. Phil. Trans. R. Soc. Lond., Ser. A, v. 288, 271–319.

Bowman, H.R., Asaro, F. and Perlman, I., 1973. On the uniformity of composition of obsidian and evidence for magmatic mixing. J. Geol., v. 81, 312–326.

Carey, S.N. and Sigurdsson, H., 1978. Deep-sea evidence for distribution of tephra from the mixed magma eruption of the Soufriere on St. Vincent, 1902. Ash turbidites and air fall. Geology, v. 6, 271–274.

Carmichael, I.S.E. and Nicholls, J., 1967. Iron-Titanium oxides and oxygen fugacities in volcanic rocks. J. Geophys. Res., v. 72, 4665–4687.

Curtis, G.H., 1968. The stratigraphy of the ejecta from the 1912 eruption of Mount Katmai and Novarupta, Alaska, *in* Coats, R.R., Hay, R.L. and Anderson, C.A., *eds.*, Studies in Volcanology (Howell Williams volume). Geol. Soc. America Mem. 116, 153–210.

Eichelberger, J.C., 1974. Magma contamination within the volcanic pile: Origin of andesite and dacite. Geology, v. 2, 29–34.

Ewart, A., 1963. Petrology and petrogenesis of the Quaternary pumice ash in the Taupo area, New Zealand. J. Petrol., v. 4, 392–431.

Guest, J.E., 1968. Banded pumice in a Chilean ignimbrite. Geol. Mag., v. 105, 177–184.

Gunn, B.M., Roobol, M.J. and Smith, A.L., 1976. Petrogenetic implications of a basaltic andesite-andesite-rhyolite suite on St. Eustatius, Lesser Antilles [abs.]. Geol. Soc. America Abstr. with Prog., v. 8, 896–897.

Johnson, D.A., 1966. Evidence for a zoned magma chamber 6 to 10 km beneath Augustine volcano, Alaska [abs.]. Geol. Soc. America Abstr. with Prog., v. 8, 942–943.

MacDonald, G.A. and Katsura, T., 1965. Eruption of Lassen Peak, Cascade Range, California in 1915: An example of mixed magmas. Geol. Soc. America Bull., v. 76, 475–482.

McBirney, A.R., 1968. Compositional variations of the climatic eruption of Mount Mazama. *in* Dole, H.M., *ed.*, Andesite Conference Guidebook, State of Oregon Department of Geology and Mineral Industries Bull. G2, 53–56.

Miller, T.P. and Smith, R.L., 1977. Spectacular mobility of ash flows around Aniakchak and Fisher Calderas, Alaska. Geology, v. 5, 173–176.

Peterson, P.S., 1980. Tephra of the Laguna de Ayarza calderas of southeastern Guatemala and its correlation to units of the Guatemalan Highlands. M.S. Thesis, Michigan Tech. Univ., 108p.

Rea, W.J., 1974. The volcanic geology and petrology of Montserrat, West Indes. J. Geol. Soc. Lond., v. 130, 341–366.

Roobol, M.J. and Smith, A.L., 1976. Mount Pelée, Martinique: A pattern of alternating eruptive styles. Geology, v. 4, 521–524.

Roobol, M.J., Smith, A.L., and Wright, J.V., in prep. Late Pleistocene to Recent eruptions of Mt. Misery, St. Kitts, Lesser Antilles: A reappraisal of the volcanic hazard.

Rose, W.I., Jr., Hahn, G.A., Drexler, J.W., Love, M.A., Peterson, P.S. and Wunderman, R.L., 1980. Quaternary tephra of northern Central America: Tephrachronology of a complex calc-alkalic, silicic sequence [abs.]. Nato ASI, Tephra studies as a tool in Quaternary Research, Abstracts.

Schmincke, H.–U., 1969. Ignimbrite sequence on Gran Canaria. Bull. Volcanol., v. 33, 1199–1219.

Self, S. and Williams, S.N., 1980. Triggering of the October 1902 eruption of Santa Maria volcano, Guatemala by a magma mixing event. Eos, v. 61, 68.

Shepherd, J.B., Aspinall, W.P., Rowley, K.C., Pereira, J.A., Sigurdsson, H., Fiske, R.S. and Tomblin, J.F., 1979. The eruption of Soufriere volcano, St. Vincent, April–June 1979. Nature, v. 282, 24–28.

Smith, A.L., Gunn, B.M. and Roobol, M.J., 1975. Guadaloupe and island arc andesites [abs.]. Eos., v. 56, 474.

Smith, A.L., Roobol, M.J. and Gunn, B.M., 1980. The Lesser Antilles: An example of island arc volcanism. Bull. Volcanol., v. 43, in press.

Smith, R.L., 1979. Ash-flow magmatism. *in* Chapman, C.E. and Elston, W.E., *eds.*, Ash-flow tuffs. Geol. Soc. America Spec. Pap., 180, 5–27.

Smith, R.L. and Bailey, R.A., 1966. The Bandelier Tuff, a study of ashflow eruption cycles from zoned magma chambers. Bull. Volcanol., v. 29, 83–104.

Sparks, R.S.J., 1975. Stratigraphy and geology of the ignimbrites of Vulsini volcano, Central Italy. Geol. Rundsch., v. 64, 497–523.

Sparks, R.S.J., 1976. Grain size variations in ignimbrites and implications for the transport of pyroclastic flows. Sedimentology, v. 23, 147–188.

Sparks, R.S.J. and Wilson, L., 1976. A model for the formation of ignimbrite by gravitational column collapse. J. Geol. Soc. Lond., v. 132, 441–452.

Sparks, R.S.J. and Wright, J.V., 1979. Welded air-fall tuffs. *in* Chapin, C.E. and Elston, W.E., *eds.*, Ash-flow tuffs. Geol. Soc. America Spec. Pap., 180, 155–166.

Sparks, R.S.J., Sigurdsson, H. and Wilson, L., 1977. Magma mixing: A mechanism for triggering acid explosive eruptions. Nature, v. 267, 315–318.

Sparks, R.S.J., Wilson, L. and Hulme, G., 1978. Theoretical modelling of the generation, movement and emplacement of pyroclastic flows by column collapse. J. Geophys. Res., v. 83, B4, 1727–1739.

Wager, L.R. and Bailey, E.B., 1953. Basic magma chilled against acid magma. Nature, v. 172, 68–70.

Walker, G.P.L., 1962. Tertiary welded tuffs in Eastern Iceland. Q.J. Geol. Soc. Lond., v. 118, 275–293.

Walker, G.P.L., Wright, J.V., Clough, B.J. and Booth, B., 1980. Pyroclastic geology of the rhyolitic volcano of La Primavera, Mexico. Geol. Rundsch., in press.

Wright, J.V., 1980. Stratigraphy and geology of the welded air-fall tuffs of Pantelleria, Italy. Geol. Rundsch., v. 69, 263–291.

Wright, J.V. and Walker, G.P.L., 1977. The ignimbrite source problem: Significance of a co-ignimbrite lag-fall deposit. Geology, v. 5, 729–732.

Wright, J.V. and Walker, G.P.L., 1980. Eruption, transport and deposition of ignimbrite: A case study from Mexico. J. Volcanol. Geotherm. Res., in press.

Wright, J.V., Self, S. and Fisher, R.V., 1980. Towards a facies model for ignimbrite-forming eruptions: Bandelier tuffs, Jemez volcano, New Mexico. Nato ASI, Tephra studies as a tool in Quaternary Research, in press.

Wright, J.V., Smith, A.L. and Roobol, M.J., these Transactions. Ignimbrites from island arcs and continents: A comparison of examples from the Lesser Antilles and Mexico.

Yoder, H.S., 1973. Contemporaneous basaltic and rhyolitic magmas Am. Mineral., v. 58, 153–171.

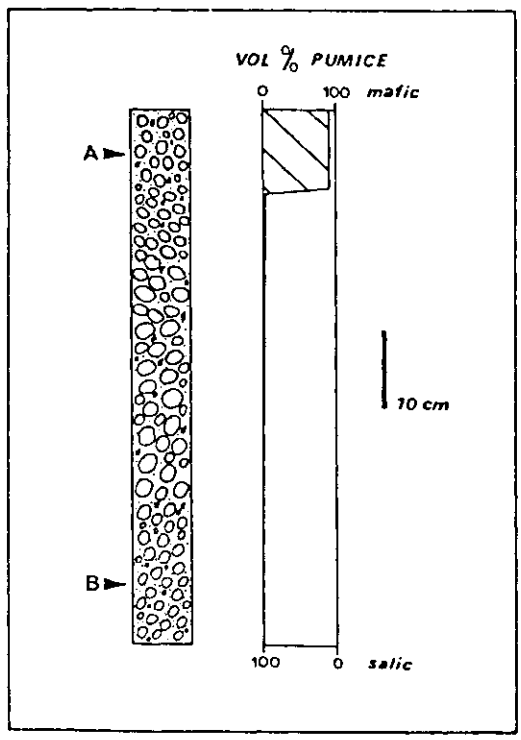

Fig. 1. Pumice Fall deposit A, Tenerife, showing variation in salic pumice (blank) and mafic pumice (diagonal rule). A and B refer to the stratigraphic position of pumice samples shown in Fig. 2.

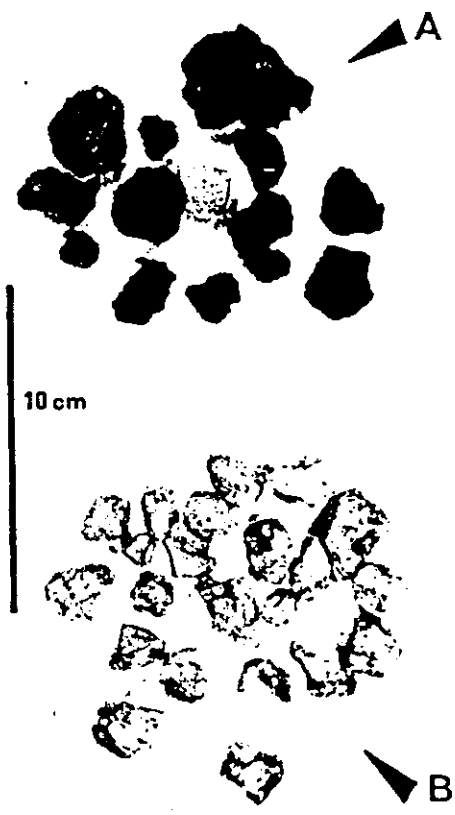

Fig. 2. Pumice samples from the respective mafic (A) and salic (B) parts of pumice fall A, Tenerife.

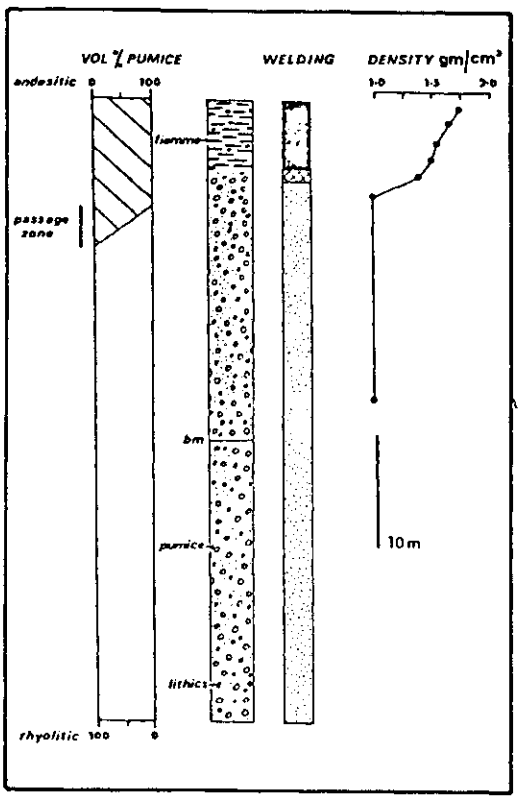

Fig. 3. Generalised section through the Acatlan ignimbrite near Ahuisculco, Mexico. Compositional variation is shown as in Fig. 1; bm marks the base of the main compositionally zoned flow unit; welding zones are represented by, stipple: non-welded, cross-hatch: incipiently welded, black: densely welded with fiamme.

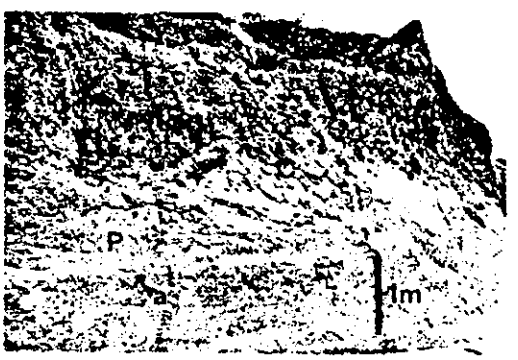

Fig. 4. Unwelded top of the Acatlan ignimbrite near Acatlan; M: mafic top, P: passage zone; a: points to a large mafic pumice in the passage zone; C: marks colour change from pink to dark grey at base of mafic part.

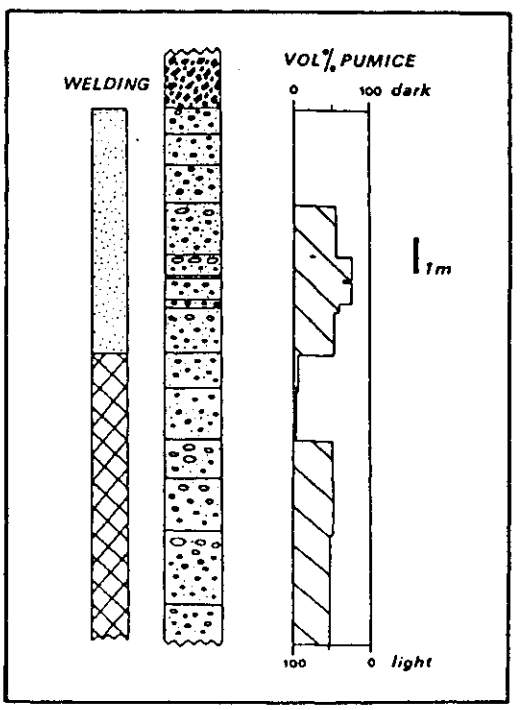

Fig. 5. Generalised section through the Rio Caliente ignimbrite, at Rio Caliente, Mexico. The ignimbrite is shown overlain by a redeposited rhyolite breccia; at other exposures a co-eruptive plinian fall deposit only containing white pumice is found. Ornament is as in Fig. 3.

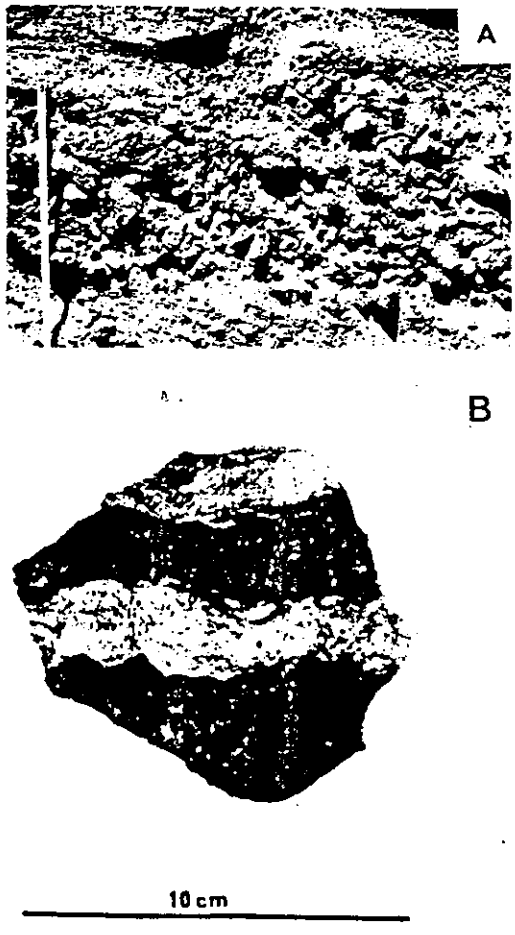

Fig. 6. a) Mixed pumice flow unit of the Rio Caliente ignimbrite with an extreme concentration zone of large pumice which shows reverse grading. Ruler is extended to 45 cm. b) Banded mixed pumice clast from the Rio Caliente ignimbrite.

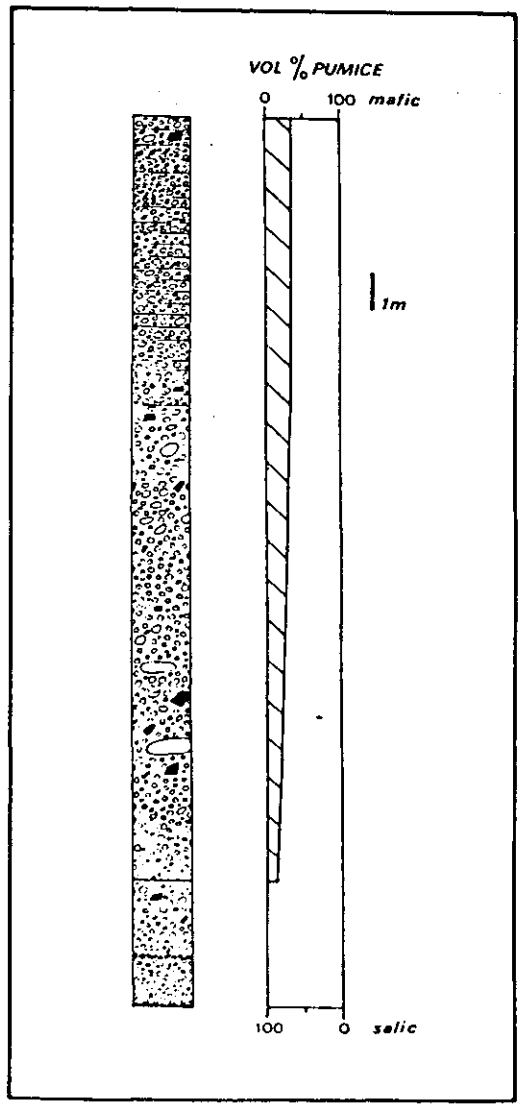

Fig. 7. Generalised section through the Middle Pumice, exposed in the caldera wall south of Thira, Santorini. Ornament is as in Fig. 1.

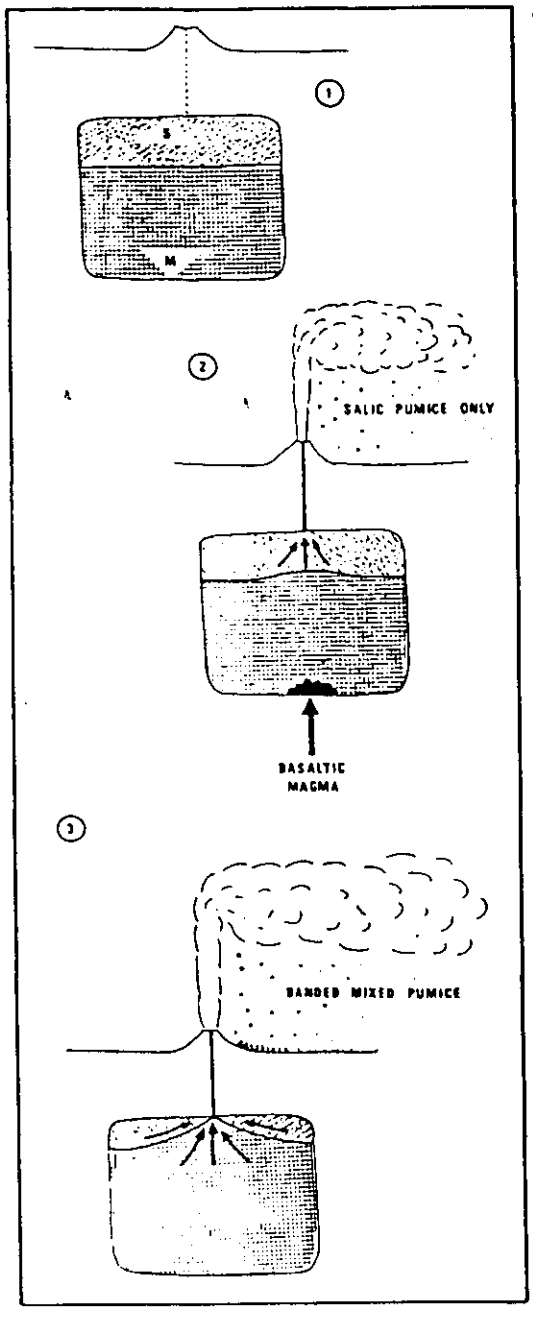

Fig. 8. Model to explain close chemical similarity of some mixed pumice types. 1) Stably zoned magma chamber with S: salic magma, and M: more mafic magma. 2) Eruption commences (may still be triggered by injection of basaltic magma at base of chamber); magma drawn into conduit while compositional boundary migrates upwards more rapidly in centre towards conduit. At this stage only salic pumice is erupted. 3) Both salic and mafic magma types are drawn into conduit giving streaky banded pumice. A mixed pumice is erupted and proportion of M should increase with time. Mixed pumice will be erupted until all of S is used up and if the eruption continues then only the more mafic magma will be erupted. It should be noted that in the case of the Rio Caliente ignimbrite this model cannot explain the observed geological relationships (Fig. 5).

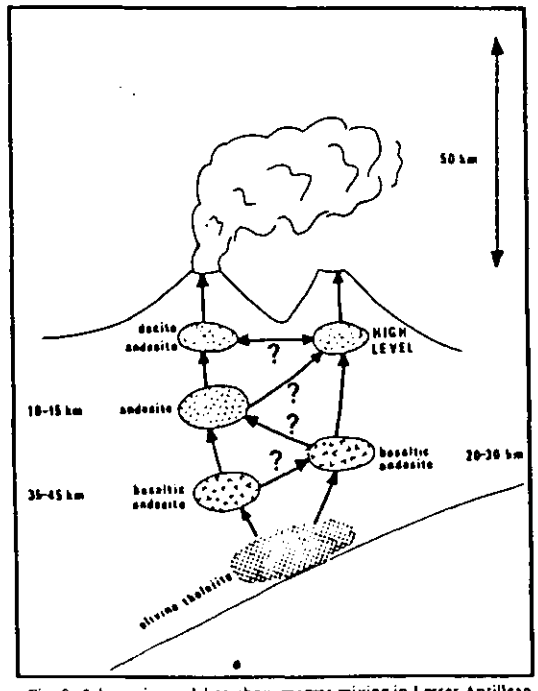

Fig. 9. Schematic model to show magma mixing in Lesser Antillean volcanoes (after Smith *et al.*, 1980). Primary basalts are generated by partial melting of mantle wedge above subduction zone at about 50–80 km depth

TABLE 1
KNOWN OCCURRENCES OF MIXED PUMICE

Locality	Type of Deposit	Source
LESSER ANTILLES:		
1) Statia	Scoria flows, block and ash-flow ignimbrites, and falls.	Gunn *et al.* (1976) This paper
2) Montserrat	Ignimbrite	Rea (1974)
3) Guadaloupe	Ignimbrite	Smith *et al.* (1975) This paper
4) Martinique	Ignimbrites and pumice falls	Roobol and Smith (1976) This paper
5) St. Vincent	Scoria flows and falls	Carey and Sigurdsson (1978) Shepherd et al. (1979)
6) St. Kitts	Scoria flows	Roobol *et al.* (in prep.)
CENTRAL AND SOUTH AMERICA		
1) Guadalajara, Mexico	Ignimbrite and airfall	This paper
2) Guatemala	Ignimbrites and Pumice falls	Peterson (1980) Rose *et al.* (1980) Self and Williams (1980)
3) Chile	Ignimbrite	Guest (1968)
UNITED STATES		
1) Bandelier, New Mexico	Ignimbrites and plinian falls	This paper
2) Bishop, California	Ignimbrite	This paper
3) Crater Lake, Oregon	Ignimbrite	McBirney (1968)
4) Lassen Peak, California	Block and ash flow	MacDonald and Katsura (1965)
5) East San Butte, California	Scoria fall	Anderson (1976)
6) Katmai, Alaska	Ignimbrite and pumice fall	Curtis (1968)
7) Aniakchak, Alaska	Ignimbrite	Miller and Smith (1977)
8) Augustine Island, Alaska	Ignimbrite	Johnson (1976) Smith (1979)
MEDITERRANEAN		
1) Vesuvius, Italy	Plinian falls	Lirer *et al.* (1973)
2) Vulsini, Italy	Ignimbrite E	Sparks (1975)
3) Pantelleria, Italy	Welded air-fall C	Wright (1980)
4) Santorini, Greeece	Ignimbrites and pumice falls	Bond and Sparks (1976) Sparks *et al.* 1977) Sparks and Wright (1979) This paper
MID—ATLANTIC OCEAN		
1) Tenerife, Canary Islands	Ignimbrites and pumice falls	This paper
2) Gran Canaria, Canary Islands	Ignimbrite	Schmincke (1969)
3) Azores	Pumice falls	Booth *et al* (1978)
4) Skessa, Iceland	Ignimbrite	Walker (1962)
5) Askja, Iceland	Plinian airfall	Sparks *et al.* (1977)
NEW ZEALAND	Pumice falls	Ewart (1963)

TABLE 2
CHEMICAL ANALYSIS OF MIXED PUMICE

	1a	1b	2a	2b	3a	3b	4a	4b	5a	5b	6a	6b	7a	7b	8a	8b	9a	9b	10a	10b
SiO_2	63.3	56.9	63.5	61.2	61.4	58.2	63.5	56.7	77.34	77.64	77.4	61.9	64.1	56.4	59.4	54.0	60.0	57.9	61.0	57.9
TiO_2	0.4	1.8	0.9	1.6	0.5	1.6	0.9	2.2	0.07	0.13	0.1	1.0	1.4	1.4	0.6	0.7	0.8	0.7	0.6	0.7
Al_2O_3	19.9	19.1	19.4	19.1	20 8	19.3	20.1	18.7	11.73	11.67	11.8	17.2	19.3	16.6	17.5	18.5	17.6	17.9	17.5	17.9
FeO	2.6	5.9	3.4	4.8	2.7	4.6	3.4	6.1	1.45	1.69	1.5	5.6	4.0	9.4	7.1	8.3	7.1	7.8	5.9	6.4
MnO	0.2	0.2				0.3						0.1		0.2	0.2	0.2	0.2	0.2	0.3	0.2
MgO	0.3	1.8	0.6	1.0		1.2		1.1	0.01	0.00	0.1	2.3	0.7	3.5	2.4	4.4	2.8	3.7	2.6	3.7
CaO	0.8	4.9	1.8	3.2	1.0	3.5	1.1	4.9	0.05	0.03	0.2	5.2	2.1	7.6	6.6	8.9	7.4	8.1	6.4	7.9
Na_2O	5.1	5.3	5.1	5.0	7.4	6.1	5.5	5.6	4.97	4.09	4.6	3.9	3.5	3.9	3.4	3.1	3.1	2.8	4.9	4.4
K_2O	7.3	3.6	4.9	3.7	6.1	4.6	5.5	3.6	4.37	4.72	4.4	2.6	4.4	1.2	1.1	0.8	1.0	0.8	0.6	0.6
P_2O_5	0.1	0.5	0.5	0.5		0.6		1.2				0.3	0.5	0.3	0.1	0.1	0.1	0.1	0.2	0.2

1a. Salic pumice, fall deposit A, Tenerife.
1b. Mafic pumice, fall deposit A, Tenerife.
2a. Salic glass, ignimbrite E, Tenerife.
2b. Mafic glass, ignimbrite E, Tenerife.
3a. Salic glass, undesignated ignimbrite, La Caleta, Tenerife.
3b. Mafic glass, undesignated ignimbrite, La Caleta, Tenerife.
4a. Salic glass ignimbrite 0, Tenerife.
4b. Mafic glass, ignimbrite 0, Tenerife.
5a. Light coloured glass (from mixed clast in Fig. 6b), Rio Caliente ignimbrite Mexico.
5b. Dark glass (from mixed clast in Fig. 6b) Rio Caliente ignimbrite, Mexico.
6a. Pumice, Las Planillas, Mexico.
6b. Mafic spatter, Las Planillas, Mexico.
7a. Salic glass, Middle Pumice, Santorini.
7b. Mafic clot in pumice, Middle Pumice, Santorini.
8a. Salic pumice, ignimbrite, Mt. Pelée.
8b. Mafic pumice, ignimbrite, Mt. Pelée.
9a. Salic pumice, ignimbrite, Soufriere, Guadeloupe.
9b. Mafic pumice, ignimbrite, Soufriere, Guadeloupe.
10a. Salic block, block and ash flow deposit (nuée ardente), Quill, Statia.
10b. Mafic block, block and ash flow deposit (nuée ardente), Quill, Statia

Analyses 2a, 2b, 3a, 3b, 4a, 4b, 5a, 5b, 6a, 6b by electron microprobe; remainder by X.R.F.
Post-eruptive hydration of glasses has resulted in greatly differing measured water contents in salic and mafic pumice; to facilitate comparison, all analyses are therefore presented normalised to 100% on a volatile-free basis.
Total iron is expressed as FeO.

TABLE 3
RELATIVE SIZES OF SALIC AND MAFIC PUMICE CLASTS*

	Salic pumices (cm)	Mafic pumices (cm)
Thera welded tuff	15	44
Therasia welded tuff	6	23
Middle Pumice	16	56
Acatlan ignimbrite	17	47
Acatlan co-ignimbrite lag fall	12	79

*) Average maximum diameters[1] of mafic and salic pumice clasts from the Santorini tuffs and the Acatlan ignimbrite.

1) Average of the five largest clasts measured